Tracing the diversity of hot subdwarf evolution

Surface composition, magnetic fields, and populations

Der Naturwissenschaftlichen Fakultät
der Friedrich-Alexander-Universität
Erlangen-Nürnberg

zur

Erlangung des Doktorgrades Dr. rer. nat.

vorgelegt von

Matti Dorsch
aus Bamberg

Als Dissertation genehmigt
von der Naturwissenschaftlichen Fakultät
der Friedrich-Alexander-Universität Erlangen-Nürnberg
Tag der mündlichen Prüfung: 21. Dezember 2023

Gutachter: Prof. Dr. Ulrich Heber
Prof. Dr. Artemio Herrero Davo
Prof. Dr. Philipp Podsiadlowski

Abstract

Hot subdwarf stars of spectral types O and B (sdO/B) represent late stages of stellar evolution. They are located close to the hot end of the horizontal branch, and most of them are core helium burning stars. At radii of roughly $0.2\,R_{\odot}$, they lack the extensive hydrogen envelopes of cooler horizontal branch stars. The formation of these objects and their evolutionary links to other classes of stars are still not fully understood, but their majority seems to result from binary evolution: Roche lobe overflow, common envelope episodes, and several types of stellar mergers. It was the aim of this thesis to provide an observational overview of the properties of hot subdwarfs as an important step towards understanding their complex formation and evolution. Therefore, both the overall hot subdwarf population and several peculiar stars were studied in detail.

In the first part, individual hot subdwarfs were studied in great detail to establish them as testbeds for stellar evolution, in particular by determining their chemical signatures from high-quality ultraviolet and optical spectra. This includes two typical He-poor sdOB stars as reference objects: as determined from archival far-ultraviolet spectra, CPD −56° 464 and the Schweizer-Middleditch Star exhibit similar surface compositions, including a distinct CNO-cycle pattern. Several heavy elements were identified for the first time in He-poor sdOB stars. The resulting heavy metal abundances are high compared to the Sun but lower compared to peculiar stars like LS IV−14°116. The absence of silicon in the Schweizer-Middleditch star likely results from the combination of diffusion and weak stellar winds. In contrast, CPD −56° 464 has a silicon abundance about a third of solar, among the highest observed in helium-poor sdOB stars.

Three of the most chemically peculiar stars, the so-called heavy-metal helium-rich sdOBs, were analysed with unprecedented detail and precision. High-quality UVES spectra of the Zr-rich LS IV−14°116 and Feige 46 revealed many strong lines corresponding to transitions of various heavy metals, some of which have not previously been observed in any star. The surface abundance of 19 metals is nearly identical in both stars. These abundance patterns differ significantly from those of typical He-poor hot subdwarfs with similar temperatures. The observed extreme overabundance of heavy metals suggests the presence of strong atmospheric diffusion processes that affect both stars similarly, although a contribution by s-process fusion is not excluded. The comparable abundances of C, N, O, and Ne in both stars provide evidence of a shared evolutionary origin. Recently proposed evolutionary models involving the merging of a hybrid He/C/O white dwarf with a more massive helium-core white dwarf offer a promising formation scenario for stars similar to LS IV−14°116. This scenario explains the atmospheric parameters, single-star nature, and unique pulsations observed in LS IV−14°116.

The next analysis showed the lead-rich He-sdOB EC 22536−5304 to be in a binary system with an extremely metal-poor subdwarf F-type companion. As a result, the derived lead abundance in the hot subdwarf is even larger than originally thought: about a million times solar, making it the most lead-rich star known to date. Based on the metallicity and atmospheric parameters of the F-type companion, the EC 22536−5304 system seems to be older than about 10 Gyr. The system has an orbital period of about 457 days and was therefore formed through stable Roche lobe overflow. The experience gained with EC 22536−5304 was then applied to another peculiar binary system: the sdOB + K-type subgiant BD −7° 5977. The system was extensively observed with high-resolution far-UV, optical, and infra-red spectrographs. This allowed us to test the Roche lobe overflow scenario by determining the companion's ^{12}C/^{13}C isotopic ratio, which may have been decreased by accreted material. The resulting ratio (28 ± 5) is clearly lower than the solar value (89), likely due to a combination of both mass transfer and mixing caused by convective dredge-up in the K-type companion.

Magnetic fields are considered a smoking gun for the formation of single hot subdwarfs in the merger scenario, but despite several dedicated searches they have long eluded detection. Here we report the discovery of four magnetic He-sdOs and carry out spectral analyses based on high-quality optical spectra by modelling their Zeeman-split hydrogen, helium, and metal lines. The first magnetic hot subdwarf to be analysed, J0809-2627, was discovered by a low-resolution spectrum and later confirmed by X-shooter and UVES spectra. This intermediately helium-rich sdO star exhibits strongly Zeeman-split lines, indicating an average field strength of about 350 kG.

Although the star has a low projected rotation velocity, its overall properties are best explained as the product of a double helium white dwarf merger. In the next step, three additional magnetic He-sdOs that were discovered in the SDSS survey were analysed. These stars are almost identical to J0809-2627 in terms of atmospheric parameters, rotation, and field strengths. The occurrence of these magnetic stars suggests a lower limit of about 2 % for the magnetic fraction in the He-sdO population. It remains unclear why the majority of He-sdO stars do not exhibit detectable magnetic fields, even though they are also thought to be formed by mergers.

The *Gaia* space mission has provided photometric and astrometric measurements for more than one billion stars, which have transformed Galactic astrophysics in general and research into hot subdwarf stars in particular. Combined with large ground-based spectroscopic surveys and other photometric surveys, this huge dataset finally allows the study of statistically significant samples of the comparatively rare hot subdwarf stars. In the second part of this thesis, two analyses based on these datasets were performed. The analysis of spectral energy distributions (SEDs), from the UV to the infra-red, combined with *Gaia* parallaxes provided fundamental stellar parameters and characterised the population F/G/K-type companions to hot subdwarfs. In addition, the computation of Galactic orbits based on radial velocities and *Gaia* astrometry provided age estimates for various sub-populations of hot subdwarfs.

The SED fits performed here are the most extensive so far: they include all ~6600 spectroscopically identified hot subdwarfs listed in the latest version of the hot subdwarf catalogue. In this study, 27% of these known hot subdwarfs turned out to belong to composite-SED systems, meaning that an F/G/K-type companion star was detected. An interesting result is that F- and K-type companions seem to be more common than G-types, which is currently not explained by theory. Further investigations based on *Gaia* parallax measurements, angular diameters from the SED, and spectroscopic surface gravities allowed the determination of radii, luminosities, and masses. As expected, the He-poor sdB stars on the extreme horizontal branch can be divided into two groups: a cooler one and a hotter one. These groups evolve into two groups of He-poor sdO stars once helium fusion moves from the core to a shell around it. The extremely He-rich sdO stars, which lack F/G/K-type companions, exhibit higher masses compared to other hot subdwarf classes, indicating that they were formed by merger channels. The intermediately He-rich sdOB stars are divided into two subgroups: the more luminous stars show a similar lack of companions, which suggests that low-mass white dwarf mergers contribute to their formation. In contrast, more compact He-sdOB stars have a companion fraction that is more comparable to the He-poor sdOB stars. Both the newly observed binary fractions for each spectral type and the lack of G-type companions should be compared to updated binary population synthesis models. From the observational side, future spectral analyses should be performed in a homogeneous fashion, which would improve the precision in particular in the important mass determination.

Gaia parallaxes, proper motions, and literature radial velocities were then used to study the current Galactic velocities and orbital properties of the known hot subdwarfs. This kinematic analysis showed that most of these stars are associated with the Galactic thin and thick disk, each contributing about 44 %, while the metal weak-thick disk and halo population contribute about 3 % and 10 %, respectively. In particular the helium-poor and helium-rich populations of hot subdwarfs show different kinematic properties. Helium-rich stars at effective temperatures of more than 32 000 K have a larger contribution by the thick disk and halo populations – these stars must therefore be predominantly formed in old stellar populations. The opposite is true for cooler helium-rich sdB stars, which seem to be dominated by the thin disk. In addition, the difference in age between the helium-rich sdOB stars and their more common helium-poor sdB counterparts seems to exclude the proposition that He-sdOB stars may evolve to become sdB stars.

In conclusion, this thesis provides several detailed analyses of hot subdwarf stars, encompassing their abundance patterns, magnetic properties, binary nature, fundamental stellar parameters, and kinematic age. These results form an observational basis that can be combined with binary evolution models to shed light on the diverse formation mechanisms of hot subdwarfs and their evolution. In that sense, the observations performed here also contribute to the broader context of binary evolution, in particular in old stellar populations – in our Galaxy and beyond.

Contents

Chapter 1

Introduction and background

1.1 Introduction

The structure and evolution of low-mass single stars has been studied for many decades and many facets are well-understood. Numerical models are able to predict their evolution from the start of hydrogen fusion to their end as inert white dwarf remnants, even if some details still require further clarification. However, the same level of understanding does not exist for close binary stars because their evolution is changed by phases of interaction and mass transfer. This is particularly true for stars in the later stages of their evolution, where these processes may occur after one of the components has expanded to giant dimensions. There is growing evidence that some classes of stars can only be understood by invoking close binary evolution. A prominent example of such a class are the hot subdwarf stars.

Although most hot subdwarf stars are less massive and smaller than the Sun, they have surface temperatures of more than 20000 K – a combination of properties that never occurs in standard stellar evolution models. Hot subdwarf stars of various types have been proposed to form via several distinct evolutionary paths, usually involving binary star interactions. From observations of hot subdwarfs in the Galactic field population, Pelisoli et al. (2020) argued that binary interaction is in fact always required to form hot subdwarf stars. The goal of this work is to provide observational constraints on the formation of hot subdwarf stars, by studying both their overall population and individual stars. The population of hot subdwarf stars is relevant to many astrophysical fields, for example:

- *Elliptical galaxies.* Main sequence stars in old stellar populations do not produce significant amounts of ultraviolet (UV) light because the lifetimes of hot and massive stars are short. Consequently, it was surprising when strong UV fluxes were observed in elliptical galaxies and the bulges of spiral galaxies (O'Connell 1999; Yi 2008). This excess UV flux is thought to be generated by helium-burning hot subdwarf stars (Catelan 2009; Podsiadlowski et al. 2008), which have to be considered when modelling the stellar population of these galaxies (Conroy et al. 2009).

- *Globular clusters.* Hot subdwarf stars are also observed in many (but not all) globular clusters, which represent old and metal-poor stellar populations. The formation of hot subdwarfs in globular clusters may be related to poorly understood processes in red giant stars or the formation of the globular clusters themselves (Moehler 2010; Catelan et al. 2010).

- *Thermonuclear supernovae.* Type Ia supernovae (SNe) are the results of a thermonuclear explosion of a white dwarf (WD) in a close binary system (Iben & Tutukov 1984a; Webbink 1984). Many binaries between a hot subdwarf and a massive WD have been observed, some of which will start to transfer mass to the WD while the hot subdwarf is still fusing helium (Geier et al. 2013b; Pelisoli et al. 2021; Kupfer et al. 2021, 2022). Once a sufficient amount of helium has accumulated on the surface of the WD, there are three possible outcomes. If the combined mass of the system exceeds about 1.4 $M_{\odot}$ (the Chandrasekhar limit), the

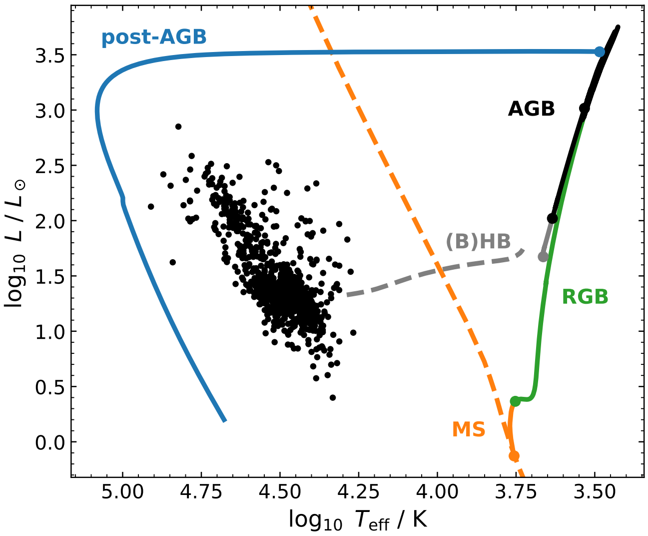

Figure 1.1.1. Evolution of a Sun-like star in the Hertzsprung-Russell diagram (HRD), as predicted by a MIST model (Choi et al. 2016). Evolutionary stages are labelled. Dashed lines represent the solar-metallicity zero-age main sequence (orange) and the horizontal branch (grey) for low metallicity. Hot subdwarf stars are shown in black (see Sect. 4.1.2).

WD is no longer able to stabilise after the mass transfer. Upon contracting, this massive WD heats up and ignites carbon and subsequent fusion and explodes in a SN Ia. Below the Chandrasekhar limit, a subluminous supernova may occur if accretion ignites helium fusion in the envelope, which then triggers carbon fusion in the core: the so-called double-detonation scenario (Livne 1990; Shen et al. 2018). Supernovae that are consistent with this scenario have already been observed: SN2018byg (De et al. 2019) and SN2016hnk (Jacobson-Galán et al. 2020). For even lower masses, the detonation of the transferred helium fails to ignite carbon fusion (Kato et al. 1989). A possible example of this is the bright helium nova V445 Puppis (Kato et al. 2008). In the supernova scenario, the hot subdwarf donor star may survive and is ejected at extreme velocities (Neunteufel 2020; Liu et al. 2021). In fact, one such donor is known to escape the Galaxy as a hyper-velocity star: the subdwarf O-type (sdO) US 708 (Hirsch et al. 2005; Geier et al. 2015b).

The following sections provide a brief introduction to hot subdwarf stars, which is based on the detailed reviews of Heber (2009, 2016). As discussed in Sect. 1.2, the canonical single-star evolution can not account for the formation of hot subdwarf stars. The observed properties of the hot subdwarf population are described in Sect. 1.3. Formation scenarios are discussed in the context of non-canonical single-star evolution in Sect. 1.4 and via binary evolution in Sect. 1.5. The two most significant physical processes that impact the observed surface composition of hot subdwarfs, nuclear fusion and atomic diffusion, are described in Sect. 1.6 and Sect. 1.7, respectively. Section 1.8 outlines the analyses carried out as part of this thesis.

1.2 Canonical evolution of single low-mass stars

To understand the uniqueness of hot subdwarf stars, one should first consider the standard evolution of single low-mass stars. In simple terms, this evolution follows five stages, starting on the main sequence and ending in the white dwarf stage:

- *Main sequence.* All stars spend most of their life fusing hydrogen to helium in their cores. Stellar masses in the Galactic disk range from 0.07 $M_\odot$ (Saumon & Marley 2008) to about 150 $M_\odot$ (Figer 2005). These stars form the main sequence (MS) in the Hertzsprung-Russell diagram (HRD, see Fig. 1.1.1), which plots the stellar effective temperature T_eff against the luminosity L. The lifetimes on the main sequence vary strongly with mass; the Sun is predicted to spend about 8 Gyr on the MS while a star with a mass of 0.8 $M_\odot$ would spend about 13 Gyr, close to the age of the Milky Way galaxy. In contrast, a B-type star with a mass of 10 $M_\odot$ has a total lifetime of only about 30 Myr.

- *First giant branch.* Once hydrogen is exhausted in the core, fusion continues in a shell closely surrounding the core, and the star leaves the main sequence. As the helium core contracts, the envelope expands at a nearly constant luminosity. This subgiant evolution ends when the star begins to ascend the red giant branch (RGB) by drastically expanding. Why does this happen? For low-mass stars, the answer lies in the electron-degenerate nature of the helium core. Such degenerate cores *contract* as their mass is steadily increasing as a result of hydrogen-fusion in the shell. Therefore, the pressure, density, and temperature in the shell increase, which leads to higher nuclear luminosity. This increased luminosity can only be radiated away by an expanding envelope. Why intermediate-mass stars also become red giants is an avid topic of discussion, one that has not yet found a universally accepted answer (Miller Bertolami 2022; Renzini 2023). The helium cores of stars with less than 2 $M_{\odot}$ are unable to ignite helium fusion before contracting to electron-degenerate densities. Such stars continue to ascend the RGB until their cores have reached a mass of about 0.5 $M_{\odot}$. At this point, their central temperatures reach about 10^8 K, which violently ignites helium fusion (Härm & Schwarzschild 1961). Because the pressure in electron-degenerate cores is independent of temperature, such cores cannot immediately expand, which leads to run-away fusion that heats up the core dramatically: the so-called helium-flash. This vicious cycle is terminated once the thermal energy reaches the Fermi level and the degeneracy of the electron gas is lifted.
- *Horizontal branch.* After the helium-flash, a new equilibrium is reached where helium is burned in the core and hydrogen in a shell surrounding it. This causes the star to contract towards the horizontal branch (HB) in the HRD. The morphology of the HB is determined by properties of the hydrogen envelope, specifically its mass and radius. The Sun is predicted to reach the HB at about ten solar radii, and a surface temperature of about 4800 K (Hidalgo et al. 2018), placing it in the so-called red clump. Some HB stars have much thinner hydrogen envelopes and can reach T_{eff} of up to 20 000 K. These blue horizontal branch (BHB) stars are often observed in globular clusters and are thought to form in old stellar populations. This is because their thin envelopes require low-mass progenitors, roughly between 0.8 and 0.9 $M_{\odot}$. These stars exhaust most of their hydrogen envelope on the RGB before their core reaches the mass required for the He-flash about 12 to 13 Gyr after their formation (Tailo et al. 2021). The low metal abundances common for old stellar populations lead to less opaque and therefore more compact envelopes, which further contributes to higher T_{eff} on the HB. However, neither the exact conditions at the time of the He-flash, nor the flash itself are well understood, and several theories have been proposed to explain the formation of BHB stars (Moehler 2001).
- *Second giant branch.* After about 100 Myr, even helium is exhausted in the core. Most post-HB stars then proceed to fuse helium and hydrogen in two shells above the core, and thus ascend the asymptotic giant branch (AGB). Low-mass AGB stars never reach temperatures high enough for carbon fusion. They continue to expand until the weakly bound envelope is finally ejected by a combination of radial pulsations and strong stellar winds. This leaves a very hot core that is no longer performing nuclear fusion: a young white dwarf, briefly surrounded by a planetary nebula that forms from the ionised ejected envelope. This stellar remnant then contracts and finally cools down in the white dwarf sequence.

This standard picture of single stellar evolution struggles to explain BHB stars. It fails completely for hot subdwarf stars with their even thinner hydrogen envelopes. These stars populate the extreme blue end of the horizontal branch (EHB). Such stars can reach temperatures of up to about 35 000 K, at which point they purely consist of the helium core. The hottest EHB stars in globular clusters are referred to as “blue hook” stars. The majority of hot subdwarf stars have core masses that are close to the mass required for the He-flash: about 0.5 $M_{\odot}$ (Iben 1968), which is consistent with the observations of Fontaine et al. (2012). Even hotter temperatures are possible with higher core masses, which form the helium main sequence (e. g. Paczyński 1971). Many subdwarf O stars (sdO) are located close to this sequence, and are termed He-sdO given their helium-rich surfaces.

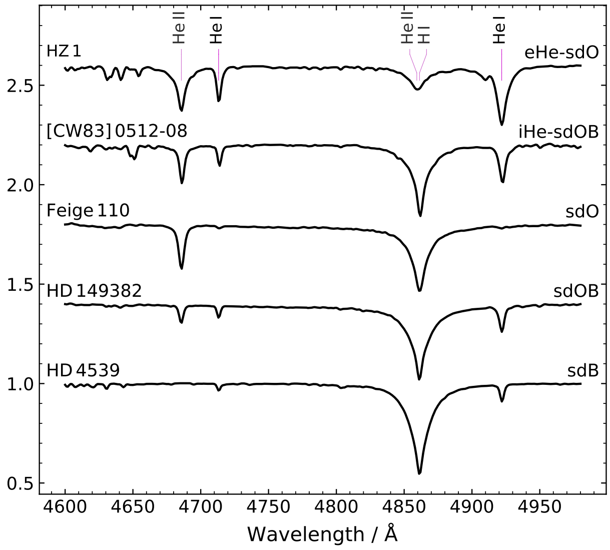

Figure 1.3.1. Example rough classification of hot subdwarf stars using the He II 4686 Å, He I 4713, 4922 Å, and H I 4861 Å lines. All spectra were taken with the X-shooter spectrograph and are shown for a reduced resolution of $\Delta\lambda = 2.5$ Å. Each star is labelled with its name (left) and classification (right).

1.3 The population of hot subdwarf stars

Some of the brightest hot subdwarf stars were originally classified in the spectroscopic Henry Draper catalogue (HD; Cannon & Pickering 1918), although they were not recognised as distinct from other hot (O/B/A-type) stars then. Hot subdwarf stars were first identified as subluminous compared to hot main sequence stars by Humason & Zwicky (1947, HZ) in a photometric survey that targeted blue stars at high Galactic latitudes. Since then, the search for hot subdwarf stars picked up speed, through projects like the Palomar-Green (PG; Green 1976), the Hamburg-ESO (HE; Wisotzki et al. 1991), and the Edinburgh-Cape surveys (EC; Kilkenny et al. 1991). The most recent catalogue of candidate hot subdwarf stars was constructed using photometry and astrometric measurements from the *Gaia* space observatory, and includes about 60 000 field stars (Culpan et al. 2022).

1.3.1 Spectral classification.

The population of hot subdwarfs is not homogeneous, but comprised of subclasses that may differ in their origin. Figure 1.3.1 shows examples of five basic spectroscopic classes: sdB, sdOB, sdO, intermediate helium-sdOB (iHe-sdOB), and extreme helium-sdO (eHe-sdO). Exemplary spectra for each of these classes are shown in Fig. 1.3.1. Due to their low helium abundances, sdB, sdOB, and sdO stars have weak helium lines. Ionised helium lines are absent in the spectra of helium-poor sdB stars while neutral helium is absent in sdO stars. Both iHe-sdOB and eHe-sdO stars show strong neutral and ionised helium lines. Hydrogen lines are weak or even absent in eHe-sdO stars. A much more detailed classification scheme was introduced by Drilling et al. (2013).

1.3.2 Atmospheric parameters

Surface properties such as the effective temperature T_{eff}, the surface gravity g, and the helium-to-hydrogen ratio by number[1] $n(\mathrm{He})/n(\mathrm{H})$ can be determined from spectroscopic observations by constructing models of the stellar atmosphere – see Sect. 2.1 for a detailed discussion. Large spectroscopic surveys such as SDSS (Kepler et al. 2019) and LAMOST (Luo et al. 2021) have increased the number of spectroscopically identified hot subdwarf stars to more than 6500 (Geier 2020; Culpan et al. 2022) in the Galactic field population.

---

[1] The surface gravity is often expressed in the logarithm $\log g$, where g has the unit $\mathrm{g\,cm^{-2}}$. Similarly, the helium abundance is often expressed as $\log n(\mathrm{He})/n(\mathrm{H})$.

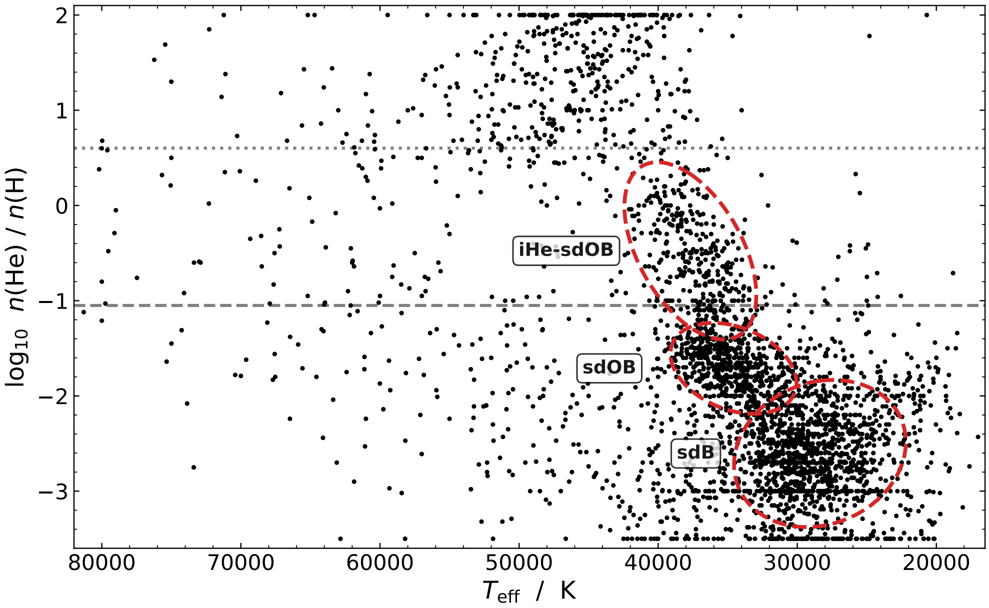

Figure 1.3.2. Distribution of helium abundances in the sample of known hot subdwarfs in the Galactic field, as collected by Culpan et al. (2022). The dashed line indicates the solar helium abundance while the dotted line distinguishes intermediate helium-enrichment from extreme enrichment. Abundances outside the plotted range are shown at the plot limits.

Helium abundance. An intriguing spectral property of hot subdwarfs are their typically non-solar helium abundances. Figure 1.3.2 shows the distribution of helium abundances with effective temperature for this large sample. Most sdBs have low helium abundances between $\log n(\mathrm{He})/n(\mathrm{H}) = -4$ and -2. This depletion is a result of atmospheric diffusion processes, as first proposed by (Greenstein 1967): the balance between gravitational settling of heavier ions and the radiative levitation that results from their absorption of photons[2]. The surface composition of a diffusive atmosphere therefore depends on both $\log g$ and T_eff. Several helium-poor sdBs at T_eff close to 29 000 K show a relative enhancement in ^{3}He (Geier et al. 2013c; Schneider et al. 2018), a result of gravitational settling of the heavier ^{4}He isotope (Michaud et al. 2011). The abundance of helium increases with T_eff and reaches an average value of $\log n(\mathrm{He})/n(\mathrm{H}) = -1.7$ for sdOB stars, still sub-solar. Intermediate-helium sdOB-stars follow a similar sequence between about solar helium abundances and atmospheres dominated by helium. The distinction between intermediately and extremely helium-rich hot subdwarfs is usually made at $\log n(\mathrm{He})/n(\mathrm{H}) = +0.6$. The hot sdO stars are the most diverse in helium abundance. Most are extremely depleted in hydrogen (eHe-sdO), often to the point where hydrogen becomes undetectable. The complete absence of hydrogen can be explained by formation scenarios that involve mixing any remaining hydrogen envelope into deeper layers, where it is burned. A minority of sdO stars are helium-poor; they are thought to be the progeny of sdB and sdOB stars that have exhausted the helium supply in their cores. Due to the lack of a hydrogen burning shell, these post-EHB stars do not ascend the AGB but evolve to higher T_eff during their helium-shell burning phase.

Surface gravity. An important characteristic of hot subdwarf stars is the high gravitational acceleration at their surface

$$g = GM/R^2, \tag{1.3.1}$$

where G is the gravitational constant, M is the stellar mass, and R is the stellar radius. Typical values for hot subdwarf stars are $4.5 < \log g < 6.5$, which places them in between main-sequence O/B stars ($3 < \log g < 4$) and the WD sequence ($7 < \log g < 9$). The surface gravities for the

---

[2] Refer to Sect. 1.7 for a short introduction to atmospheric diffusion.

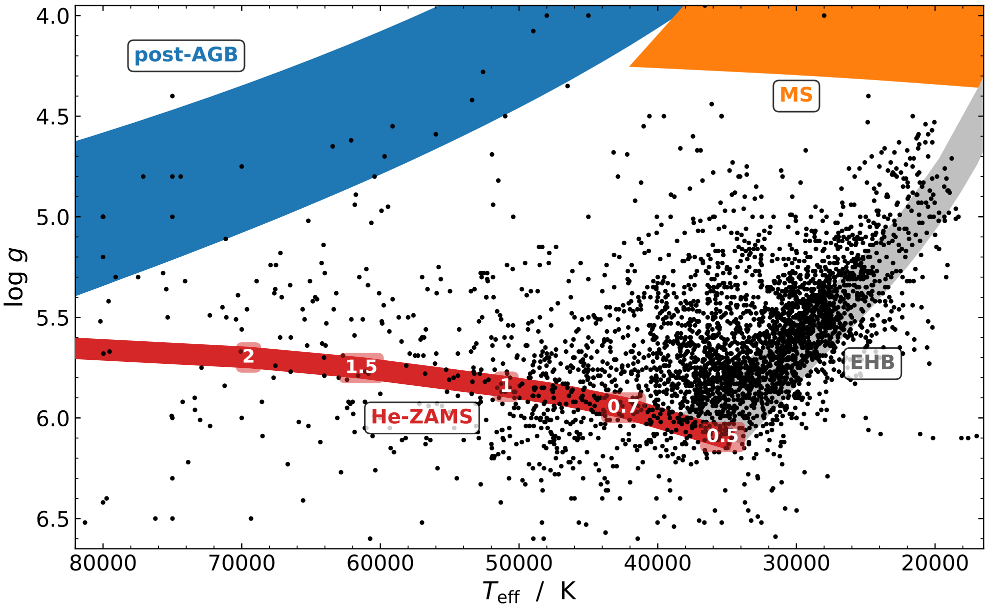

Figure 1.3.3. Kiel diagram showing the population of spectroscopically classified hot subdwarf stars collected by Culpan et al. (2022). The blue shaded region corresponds to post-AGB tracks from Miller Bertolami (2016), for final masses between 0.53 and 0.83 $M_\odot$. The solar-metallicity main sequence of Choi et al. (2016) is marked in orange. The broad red line marks the He-ZAMS of Paczyński (1971); its masses are labelled in $M_\odot$. The grey shaded region shows the HB from Dorman et al. (1993) for a core mass of 0.49 $M_\odot$ and 1/30th of the solar metallicity, partly extrapolated to extend to the He-ZAMS.

spectroscopic hot subdwarf sample are shown in Fig. 1.3.3. The vast majority of hot subdwarfs cluster close to the EHB, or are already evolving towards hotter temperatures and lower surface gravities. Also the helium main sequence is well populated. The number of stars decreases at $T_{\mathrm{eff}} > 50\,000$ K, which would correspond to helium cores more massive than about one solar mass. The hottest stars spectroscopically classified as hot subdwarfs are post-AGB stars, which are formed independent of the remaining hot subdwarf population.

Metal abundances. The surface abundance of metals[3] is known for much fewer stars because they require detailed analyses based on high-quality spectra. The metal abundances of hot subdwarfs vary strongly from star to star and are often far from solar values. Optical spectra allow access to spectral lines of light metals such as carbon, nitrogen, oxygen, and silicon in ionisation stages ii (singly ionised) to iv (triply ionised), which are often less abundant than in the Sun (e. g. Geier 2013). Metal lines of the iron group are weak in optical spectra of sdOB and especially sdO stars. When determined from strong lines in far-UV spectra, the abundance of iron is often close to solar while other iron-group elements are often enhanced by factors of 10 to 100 relative to the Sun (Chayer et al. 2006; O'Toole & Heber 2006; Blanchette et al. 2008). In addition, Geier (2013) and Möller (2021) found a trend of increasing abundances with higher T_{eff} for metals such as argon, titanium, and chromium.

Extreme enrichment in even heavier metals is observed in a group of intermediate He-sdOB stars. Relative to the solar abundance, zirconium was discovered to be enhanced by factors of about 10 000 in LS IV−14°116 (Naslim et al. 2011), Feige 46 (Latour et al. 2019b; Dorsch et al. 2020), and PHL 417 (Østensen et al. 2020). All three stars in this class also show peculiar pulsations that are not observed in other hot subdwarfs. Several other iHe-sdOB stars were observed to be extremely enhanced in lead (Naslim et al. 2013; Jeffery et al. 2017; Dorsch et al. 2021). Next to zirconium and lead, these "heavy metal" stars also show extreme enrichments in other

---

[3] As usual in astrophysics, all elements heavier than helium are considered to be "metals" in this thesis.

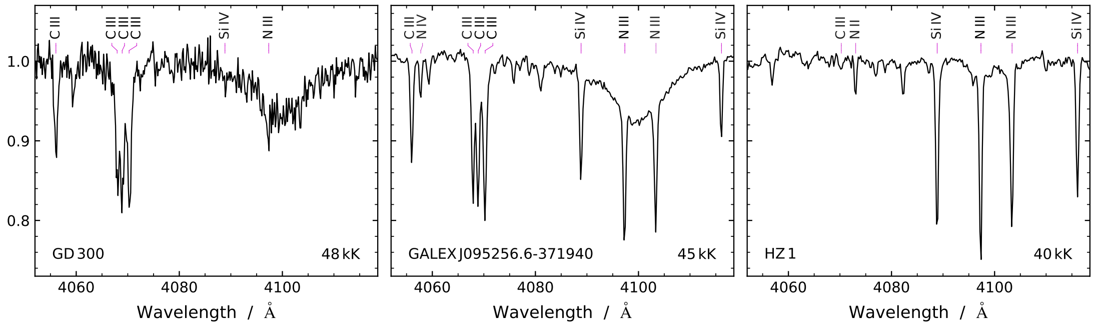

Figure 1.3.4. Characteristic metal lines for three types of extreme He-sdO: C-type (left), CN-type (centre), N-type (right). The effective temperature decreases from left to right.

observable elements with atomic number $Z > 30$.

Like the helium abundance, the metal abundance trends in hot subdwarfs have long been suspected to be the result of strong atmospheric diffusion (Baschek et al. 1982a). As discussed in more detail in Sect. 1.7, the diffusion models of Michaud et al. (2011) are able to qualitatively reproduce the surface abundances of sdB and sdOB stars. Although diffusion models are not currently available for iHe-sdOB stars, their extreme surface chemistry is thought to be supported by diffusion processes as well, possibly alongside nuclear fusion during their formation. The strong diffusion in the atmospheres of hot subdwarf stars also means that their observed metal abundances do not necessarily contain information about their initial metallicity, which complicates the determination of their ages.

Diffusion seems to be less effective for eHe-sdO stars, possibly due to atmospheric convection caused by the ionisation of He II (Groth et al. 1985)[4]. According to the studies of Stroeer et al. (2007) and Hirsch (2009), eHe-sdOs can be classified into three types based on their carbon and nitrogen abundances (see Fig. 1.3.4). The majority of eHe-sdOs in the temperature range between 40 kK and 43 kK exhibit enrichment in nitrogen, but depletion in carbon and oxygen, referred to as "N-type". Another group of eHe-sdOs is characterised by enrichment in both carbon and nitrogen ("CN-type") and is found close to $T_{\mathrm{eff}} = 44$ kK. The smallest and hottest group of eHe-sdOs is enriched in carbon but less so in nitrogen ("C-type"), typically found at T_{eff} up to 50 kK. Very recently, Werner et al. (2022a) discovered two hot (55 kK) eHe-sdOs that are enriched in both carbon and oxygen, representing a fourth class of eHe-sdOs. Intermediate He-sdOB stars are observed to show enhanced nitrogen while carbon is often close to solar (Naslim et al. 2010).

1.4 Formation of hot subdwarf stars: single evolution

Despite extensive searches for companions, most helium-rich sdO stars appear to be single (Napiwotzki 2008), as does a significant fraction of helium-poor sdO/B stars (Napiwotzki et al. 2004). Similarly, almost no binaries are found among EHB stars in globular clusters (Moni Bidin et al. 2009, 2011). The hot flasher scenario was proposed to explain such stars without a strict need for binary interaction.

1.4.1 Hot flashers

As discussed in Sect. 1.2, low-mass giant stars leave the RGB once their degenerate cores ignite helium fusion. However, if the hydrogen shell is exhausted before the core ignites helium fusion, a star may leave the RGB early. If at this point the temperature of the helium core is nearly high enough to ignite fusion, a delayed He-flash may occur while the star is contracting. This "late hot flash" has been proposed as the explanation of EHB stars in globular clusters (D'Cruz et al. 1996). Evolutionary models of this kind require unusually thin hydrogen envelopes at the tip

---

[4] This analysis is confirmed in Appendix A.1 based on modern atmospheric models.

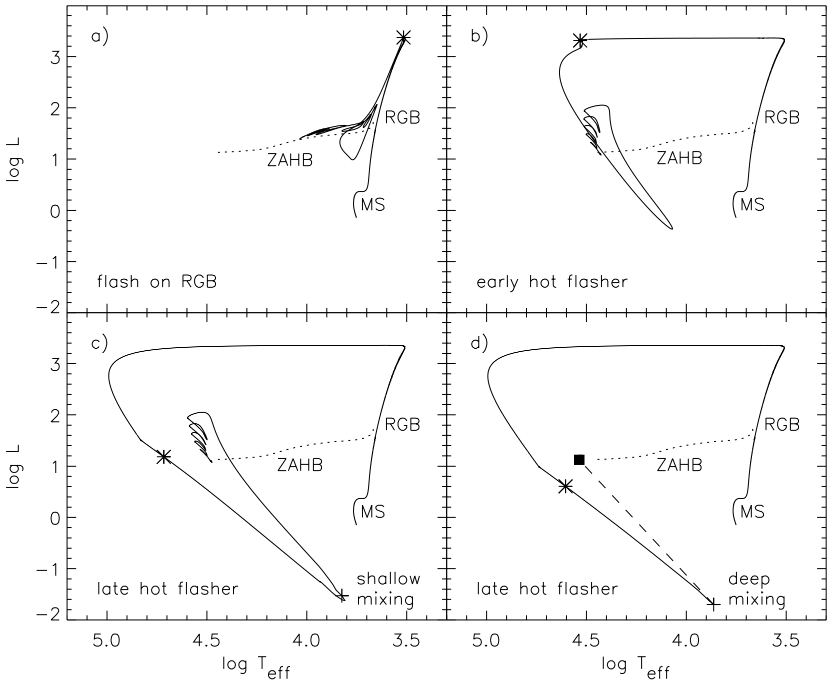

Figure 1.4.1. Evolutionary tracks from the MS to stable helium fusion from Lanz et al. (2004). The mass loss at the tip of the RGB is artificially increased from panels b) to d). The asterisks mark the initial helium flash. In the case of a hot flasher in panels c) and d), hydrogen is mixed into the core and causes a hydrogen flash, which is marked by the plus sign. The evolution from deep mixing to the zero-age horizontal branch was not computed and is shown by a dashed line.

of the RGB. This may be achieved through strong stellar winds (Castellani & Castellani 1993), increased mixing of helium into the envelope (Sweigart 1997), rapid core rotation (Tailo et al. 2015), or initially high helium abundances (Gratton et al. 2010), which would allow low-mass stars to reach the tip of RGB within the age of the Galaxy. An established scenario that can produce a late hot flash is envelope stripping through stable Roche lobe overflow (Han et al. 2002), which of course would require a binary system.

The usual approach to model “hot flashers” is to artificially increase the mass-loss at the tip of RGB. Recent calculations of this kind were performed by Lanz et al. (2004), Miller Bertolami et al. (2008), and Battich et al. (2018). Four evolutionary tracks from Lanz et al. (2004) are shown in Fig. 1.4.1. Increasing the mass-loss at the tip of the RGB leads to increasingly hot and helium-rich HB stars:

a) Without increased mass-loss, the He-flash occurs on the RGB. In this canonical case, the result is a HB star that retains a relatively thick hydrogen envelope without changes to its surface composition.

b) In the *early hot flasher* case, the helium flash occurs when the post-RGB star is already contracting and the remaining hydrogen-burning shell is still able to sustain a high luminosity. Due to neutrino-cooling in the core, the first helium flash occurs slightly off-centre. The helium burning region then propagates inward through a series of helium shell flashes, which cause loops during the evolution towards the quiescent core-burning HB. The convection region caused by an early helium flash never reaches the stellar surface, which therefore remains unaffected. The resulting star then appears as a sdB-type hot subdwarf. Its surface composition is later altered by atmospheric diffusion processes, as discussed in Sect. 1.7.

c) In a *late hot helium flash*, the hydrogen-burning shell is very thin, and no longer serves as a strong barrier against the convection zone caused by the helium flash. In this *shallow-mixing* case, the hydrogen envelope is mixed with the outer layers of the core, but not lost completely. This results in helium-enrichment of the surface, similar to that observed for iHe-sdOB stars.

d) In the *deep mixing* case, the residual hydrogen shell is fully mixed into the core, where it is burned in the CNO-cycle. The result is an extremely hydrogen-poor surface that is further enriched in material processed by helium fusion, in particular carbon (Cassisi et al. 2003). Such compositions are observed in many eHe-sdO stars (Hirsch & Heber 2009).

It is difficult to predict the exact chemical abundances on the surface because mixing effects in the interior of the star as well as in the atmosphere have to be considered. Miller Bertolami et al. (2008) and Battich et al. (2018) have created models for both late-flasher cases, including predictions for the final surface composition. They find that all considered hot flasher scenarios lead to a subdwarf with a carbon- and nitrogen-enriched surface. In a detailed spectroscopic study, Schindewolf et al. (2018) found good agreement between predicted surface abundances from the deep-mixing hot flasher scenario and their measurements of "C"- and "CN"-type eHe-sdOs.

The hot flasher channel is not only relevant for He-sdO stars. For example, a post-RGB origin of single He-poor sdB stars through the early hot flasher scenario is supported by their slow core rotation rates, as determined from their pulsations (Charpinet et al. 2018).

1.5 Formation of hot subdwarf stars: binary evolution

About 30 to 50 % of sdB stars are found in binaries with M-dwarf (dM), brown-dwarf, or white dwarf companions (Maxted et al. 2001; Copperwheat et al. 2011; Schaffenroth et al. 2022). Such systems have short orbital periods, ranging from about one hour up to one day (+dM) or several days (+WD; Kupfer et al. 2015; Schaffenroth et al. 2022). Due to their strong radial velocity variations, which can reach amplitudes of several hundred km s^{-1}, such systems can be identified using time-series spectroscopy. In addition, many binaries are close enough to show light variations due to eclipses, ellipsoidal deformation of the sdB, Doppler boosting, gravitational self-lensing, or a partially irradiated M-dwarf or brown-dwarf companion ("reflection effect").

Given the large number of sdB and sdOB stars in close binary systems known today, it is clear that binary interaction must contribute significantly to their formation. This was proposed early on by Baschek & Norris (1975) and Mengel et al. (1976), who found that sdB stars in the Galactic field are likely to be younger than their GC counterparts and would therefore be expected to have much more extended hydrogen envelopes. Although no binary sdBs had been clearly identified at that time, they realised that binary interaction is an efficient means of stripping the envelopes of RGB-type stars, thus forming a hot subdwarf.

1.5.1 Common envelope evolution

The closest binary systems are thought to result from common envelope evolution (Paczynski 1976), as sketched in Fig. 1.5.1b. Consider an initial binary of two main sequence stars with different masses. The more massive star will evolve first and will, if the system is close enough, fill its Roche lobe when it expands to giant dimensions. If one star is much less massive than the other (mass ratio $q := M_{\mathrm{donor}}/M_{\mathrm{accretor}} \gtrsim 1.2$ to 1.5; Podsiadlowski et al. 2008), the mass transfer is dynamically unstable. This leads to the formation of a common envelope, which engulfs the companion and the stripped star's remaining helium core. The orbital motion within this envelope creates drag forces which transfer orbital momentum and energy to the envelope, thus decreasing the distance between both stars and shortening the orbital period. Eventually, the envelope becomes unbound to the system and is ejected. If this process happens at the very tip of the RGB, the stripped star may still ignite helium fusion and thus becomes a hot subdwarf star. If the envelope is ejected during an earlier stage, the result is instead a helium-core white dwarf (He-WD[5]; Iben & Tutukov 1986a), which consists of a degenerate and inert helium core, surrounded by a thin hydrogen envelope (Driebe et al. 1998). In both cases, the companion star remains on the main

---

[5] If the mass is $< 0.3\,M_\odot$, they are also called extremely low-mass (ELM) white dwarfs.

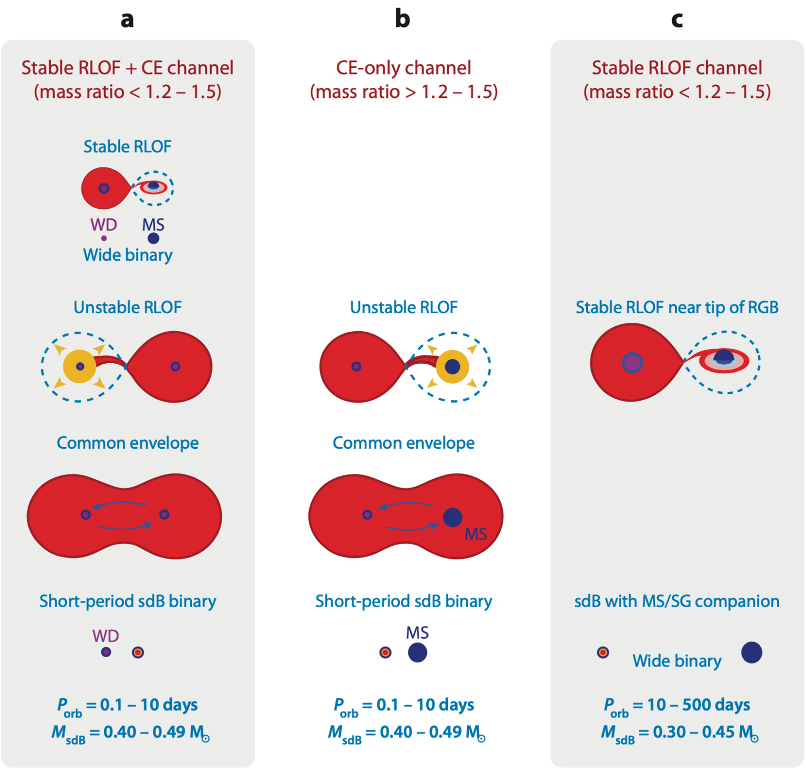

Figure 1.5.1. Binary evolution channels that lead to the formation of hot subdwarf stars. The observed orbital periods P_{orb} for post-RLOF models are actually longer than 500 days (Vos et al. 2018). Adopted from Heber (2016), originally by Podsiadlowski et al. (2008).

sequence. The resulting system therefore consists of a hot subdwarf (or He-WD) and a main-sequence star on a short-period orbit. In the case of systems containing a hot subdwarf, the mass of the main sequence companion must be low; the observed systems contain late K- and M-type stars down to brown dwarfs. The further evolution of the close binary is driven by gravitational wave radiation and magnetic breaking. Iben & Tutukov (1984b) already predicted orbital periods for such systems in the range from 2 h to 15 h, roughly consistent with the observed period distribution (Kupfer et al. 2015; Kawka et al. 2015; Schaffenroth et al. 2022).

1.5.2 Stable Roche lobe overflow

A second large group of hot subdwarfs, about 20 % to 30 % of the field population, can be identified by their unusually red colours (Thejll et al. 1995; Ulla & Thejll 1998; Stark & Wade 2003; Girven et al. 2012; Schaffenroth 2016; Solano et al. 2022). They are characterised by a double-humped flux distribution in which the sdB dominates the blue part and the F/G/K-type companion dominates the red part. The orbital periods of such systems are of the order of 500 to 1500 days (Barlow et al. 2012; Vos et al. 2019; Molina et al. 2022). Despite their larger separation, many long-period systems have experienced mass transfer through stable Roche lobe overflow (RLOF, Fig. 1.5.1c), which can happen if the binary consists of two stars of similar initial mass ($q \lesssim 1.2$). The initially more massive (primary) star is stripped, forming either a hot subdwarf or He-WD, while the companion remains on the main sequence.

Such systems may evolve further once the secondary star ascends the RGB. At this point, the hot subdwarf star has already exhausted its helium core and evolved to become a low-mass carbon-oxygen (CO) WD. This leads to a large mass ratio and unstable mass transfer through a second common envelope episode (Fig. 1.5.1a). This process is analogous to the first CE, and can therefore form either an He-WD or hot subdwarf in a close binary with a WD.

1.5.3 White dwarf mergers

The hot flasher scenario is widely accepted as the explanation for hot subdwarf stars in globular clusters, even though the cause of the mass loss at the tip of RGB is unknown. Another way to produce single hot subdwarf stars is a stellar merger involving at least one helium-core white dwarf (Webbink 1984). Jeffery & Zhang (2020) provide a recent and brief overview of double white dwarf mergers, which can produce a wide variety of remnants, including the low-mass and helium-rich supergiant R Coronae Borealis (RCB) stars (Webbink 1984; Saio & Jeffery 2002), the extreme helium (EHe) giants, and He-sdOs.

Double-degenerate binary systems are formed through various channels, including the second CE scenario discussed above. Yu & Jeffery (2010) predict about 300 million such systems to exist in the Galactic disk. More than 100 ELM WDs in close binaries were already discovered as part of the SPY (Napiwotzki et al. 2020), SDSS (Breedt et al. 2017), and ELM surveys (Brown et al. 2022), including several double He-WD systems (Brown et al. 2020; Burdge et al. 2020a,b). Many of these close binary He-WD systems will start to transfer mass once the emission of gravitational waves has sufficiently shortened their orbital period. Due to its electron-degenerate nature, the lower-mass WD is the larger component and becomes the donor ($q := M_{\text{donor}}/M_{\text{accretor}} < 1$). This donor further expands upon losing mass. If a critical mass ratio is reached, the increase in donor radius is faster than the widening of the orbit due to angular momentum transfer, which means that the mass transfer is self-reinforcing. At this point, the donor is tidally disrupted on a dynamical time-scale, so within seconds. Several types of mergers are able to produce hot subdwarf stars:

- *He-WD+He-WD:* Detailed double He-WD merger sequences have been computed by several authors (Iben 1990; Saio & Jeffery 2000; Zhang & Jeffery 2012; Hall & Jeffery 2016; Schwab et al. 2012; Schwab 2018; Yu et al. 2021). The merged star is always predicted to have a helium-rich surface, while the abundance of metals depends on the details of the simulation, in particular on how the mass of the disrupted donor is transferred to the more massive star. According to Zhang & Jeffery (2012), there are three main scenarios:
    - *Slow.* The disrupted donor may form a cold disk that is accreted on time-scales of millions of years. In this case, the surface abundances of the He-sdO remnant are expected to resemble the bulk composition of a He-WD: nitrogen is enhanced and carbon depleted, both as a result of hydrogen fusion in the CNO cycle before the merger[6]. This matches the observation of N-type He-sdO stars around $T_{\text{eff}} = 40\,\text{kK}$ (Hirsch 2009; Dorsch et al. 2019; Jeffery et al. 2021).
    - *Fast.* Alternatively, the donor may form a corona around the primary, which is accreted in a few minutes. As a result, helium fusion ignites in a shell around the core that reaches peak temperatures of 400 million Kelvin. Helium fusion at such high temperatures produces carbon, oxygen (destroying nitrogen), and to a lesser degree neon. Because the envelope is convective immediately following the merger, these newly generated metals are brought to the surface. Once the merger has settled on the helium main sequence, the result is a eHe-sdO star rich in carbon, oxygen, and neon, but depleted in nitrogen. Hirsch (2009) observed three eHe-sdOs that match the expected carbon and nitrogen abundances: HE 1142-2311, HE 1251+0159, and HE 1203-1048.
    - *Composite.* Finally, both the fast and slow accretion may take place. Some fraction of the disrupted mass forms a corona and is quickly accreted while the rest forms a cold disk. Zhang & Jeffery (2012) predict that carbon produced by helium fusion during the merger is mixed to the surface for final masses $\gtrsim 0.65\,M_{\odot}$. Due to accretion of nitrogen-rich material from the disk, the resulting surface is not depleted in nitrogen like it would be in a fast merger. The resulting carbon-enhanced surface abundances are consistent with those observed for CN-type eHe-sdOs (Hirsch 2009).

---

[6] See the next Section for more details on nucleosynthesis.

C-rich He-sdOs may also be formed by the hot flasher scenario, which however is unable to produce He-sdOs with masses $\gtrsim 0.5\,M_\odot$. The maximum He-sdO mass formed via the double He-WD merger scenario is close to $0.8\,M_\odot$.

- *He-WD+CO-WD:* A double He-WD merger is not the only type of merger that can produce hot subdwarf stars. For example, the CO-type He-sdOs of Werner et al. (2022a) seem to be the result of a merger between a He-WD and a less massive CO-WD (Miller Bertolami et al. 2022). For a total mass of less than $0.55\,M_\odot$, this type of merger may also be able to explain the formation of CN-rich intermediate He-sdOB stars. In this case, the predicted sub-surface enhancement in carbon and oxygen is predicted to drive the unusual pulsations observed for several iHe-sdOB stars (Saio & Jeffery 2019; Miller Bertolami et al. 2022): LS IV−14°116 (Ahmad & Jeffery 2005), Feige 46 (Latour et al. 2019a), and PHL 417 (Østensen et al. 2020). Also the hybrid HeCO-WD + He-WD channel of Justham et al. (2011) is be able to create He-sdO stars. Mergers between a more massive CO-WD and a He-WD would rather produce EHe and RCB stars that are much more luminous and cooler than He-sdO stars (e. g. Saio & Jeffery 2002; Schwab 2019).
- *He-WD+MS:* Single helium-poor subdwarf stars may also be formed by mergers between a He-WD and a low-mass MS star (Clausen et al. 2012; Zhang et al. 2017, 2018). The surface of such merger products is predicted to be helium-normal once stable helium fusion is established, and then becomes helium-poor as a result of diffusion. They may therefore account for a fraction of the observed single sdB population.

Given the high angular momentum of a merging binary, one may expect high rotation rates for hot subdwarfs formed by such channels. Double He-WD merger remnants would in fact be super-critically rotating if no angular momentum were lost (Gourgouliatos & Jeffery 2006). However, most He-sdO stars are known to be slow rotators at $\upsilon_\mathrm{rot}\sin i < 30\,\mathrm{km\,s^{-1}}$ (Hirsch 2009) and helium-poor sdB stars typically rotate even less (Geier & Heber 2012). In the double He-WD merger models of Schwab (2018), angular momentum loss by mass loss during the merging is able to produce hot subdwarfs with rotational velocities between 30 and $100\,\mathrm{km\,s^{-1}}$– still too high. Additional angular momentum could be lost through magnetodipole radiation (García-Berro et al. 2012) and magnetized stellar winds (Iben & Tutukov 1986b). Although strong magnetic fields are predicted to be generated by dynamo action in white dwarf mergers (e. g. Zhu et al. 2015), large spectropolarimetric surveys have failed to detect any such fields in hot subwarfs (Landstreet et al. 2012; Mathys et al. 2012). The first analysis of the first magnetic hot subdwarfs is presented as a part of this thesis.

1.6 Nucleosynthesis

Nuclear synthesis during the formation of a hot subdwarf star can directly impact its observable composition. Mixing processes can bring processed material from the core or shell to the surface. In addition, accreted material may be heated to sufficiently high temperature for fusion to take place, for example during mergers. The most important fusion processes are summarised in the following.

- Hydrogen fusion in the proton-proton (p-p) chain is the dominant source of energy for low-mass main sequence stars such as the Sun. The most important variant is the pp-I branch

$$\begin{aligned} \mathrm{p} + \mathrm{p} &\rightarrow {}^{2}\mathrm{H} + \mathrm{e}^{+} + \nu_\mathrm{e} \\ {}^{2}\mathrm{H} + \mathrm{p} &\rightarrow {}^{3}\mathrm{He} + \gamma \\ {}^{3}\mathrm{He} + {}^{3}\mathrm{He} &\rightarrow {}^{4}\mathrm{He} + 2\mathrm{p}. \end{aligned}$$

  Because the first two steps have to occur twice before the last step, the total reaction is $4\mathrm{p} + 2\mathrm{e}^{-} \rightarrow {}^{4}\mathrm{He} + 2\nu_\mathrm{e}$, releasing a total energy of 26.7 MeV. This process therefore leads to enrichment of helium, but does not modify the abundance of heavier elements.

- At higher temperatures, hydrogen fusion in the carbon-nitrogen-oxygen (CNO) cycle becomes more important. This process has the same net result as the pp-cycle, but achieves it with C, N, O as catalysts, which was already proposed by von Weizsäcker (1937, 1938) and Bethe (1939). The temperature required for the CNO process, about 1.7×10^7 K, is reached in the cores of stars more massive than about $1.3\,M_\odot$ (Schuler et al. 2009), as well as in the shells of RGB stars. Because the CNO cycle is strongly temperature-dependent ($\propto T^{17}$), stellar cores with dominant CNO-cycle fusion are convective. The most important variant of the CNO-process is the CNO-I branch:

$$\begin{aligned} {}^{12}\mathrm{C} + \mathrm{p} &\rightarrow {}^{13}\mathrm{N} + \gamma, & {}^{14}\mathrm{N} + \mathrm{p} &\rightarrow {}^{15}\mathrm{O} + \gamma \\ {}^{13}\mathrm{N} &\rightarrow {}^{13}\mathrm{C} + \mathrm{e}^+ + \nu_\mathrm{e}, & {}^{15}\mathrm{O} &\rightarrow {}^{15}\mathrm{N} + \mathrm{e}^+ + \nu_\mathrm{e} \\ {}^{13}\mathrm{C} + \mathrm{p} &\rightarrow {}^{14}\mathrm{N} + \gamma, & {}^{15}\mathrm{N} + \mathrm{p} &\rightarrow {}^{12}\mathrm{C} + {}^{4}\mathrm{He}. \end{aligned}$$

  This branch is also called the “CN”-cycle due to the very quick β^+ decays of ^{13}N and ^{15}O. Despite its cyclical nature, the abundances of C, N, and O are strongly modified by the CNO cycle. This is because all reaction time scales are short compared to $^{14}\mathrm{N} + \mathrm{p} \rightarrow {}^{15}\mathrm{O}$, resulting in a high equilibrium abundance of nitrogen. This nitrogen-enrichment, accompanied by depletion of carbon and oxygen relative to their initial abundances, is therefore called the CNO-cycle pattern. Similarly, fusion in the CN cycle decreases the isotopic $^{12}\mathrm{C}/^{13}\mathrm{C}$ ratio from the solar value of about 89 (IAEA 1995) to about 4 (Wollman 1973). The observation of a low $^{12}\mathrm{C}/^{13}\mathrm{C}$ ratio is therefore a clear sign of CNO-processed material.

- Stable hydrogen fusion does not take place in hot subdwarf stars. Their energy is instead generated by helium to carbon fusion in the triple alpha process

$$\begin{aligned} &{}^{4}\mathrm{He} + {}^{4}\mathrm{He} \rightarrow {}^{8}\mathrm{Be} \\ &{}^{4}\mathrm{He} + {}^{8}\mathrm{Be} \rightarrow {}^{12}\mathrm{C} + \gamma. \end{aligned}$$

  As first realised by Hoyle (1954), this process is the main source of carbon in the universe. It requires a core temperature of roughly 10^8 K; otherwise ^{8}Be decays before it can fuse with ^{4}He. These temperatures are reached in the degenerate cores of low-mass RGB stars once they reach a mass of about $0.5\,M_\odot$, which causes the helium-flash as discussed above. Due to the extreme temperature-dependence ($\propto T^{40}$), stellar cores powered by helium fusion are convective. The treatment of their convective boundary is a topic of current research and has a strong impact on the evolution hot subdwarf stars and their observed pulsation modes (Ostrowski et al. 2021; Li & Li 2021).

- Helium fusion can continue with successively heavier metals through the so-called alpha ladder

$$\begin{aligned} &{}^{12}\mathrm{C} + {}^{4}\mathrm{He} \rightarrow {}^{16}\mathrm{O} + \gamma \\ &{}^{16}\mathrm{O} + {}^{4}\mathrm{He} \rightarrow {}^{20}\mathrm{Ne} + \gamma \\ &\qquad\qquad \vdots \\ &{}^{52}\mathrm{Fe} + {}^{4}\mathrm{He} \rightarrow {}^{56}\mathrm{Ni} + \gamma \rightarrow {}^{56}\mathrm{Fe} + \mathrm{e}^+ + \nu_\mathrm{e} \end{aligned}$$

  Each of these reactions requires higher temperatures than the previous. These temperatures are not sustained during the formation or evolution of hot subdwarf stars, given their typical masses of only $0.5\,M_\odot$. However, the initial helium flashes in the hot flasher scenario, as well as fast mergers may produce metals up to neon, in particular through the $^{14}\mathrm{N}(\alpha,\gamma)^{18}\mathrm{O}$ and $^{18}\mathrm{O}(\alpha,\gamma)^{22}\mathrm{Ne}$ reactions (Zhang & Jeffery 2012; Battich et al. 2018). Even in massive stars, the alpha ladder ends at ^{56}Ni, which β^--decays to form ^{56}Fe. This is because photodisintegration becomes increasingly important in the last fusion stages (Burbidge et al. 1957).

The atmospheres of most hot subdwarf stars are enriched in elements heavier than iron to some degree. Such heavy metals are mostly formed by neutron capture reactions (Arcones & Thielemann 2023). Seed nuclei that have captured one or more neutrons are often unstable and will eventually undergo radioactive decay. In the case of rapid neutron capture (r-process), neutrons captures occur faster than the nuclei can decay. This is only possible in extremely high neutron densities, such as neutron star merger events. In the case lower but still high neutron densities, slow neutron capture can occur: the s-process. Here, unstable products of neutron capture have enough time to typically β^--decay, thus converting a neutron into a proton. In the course of stellar nucleosynthesis there are very few processes that release neutrons. Actually, the only relevant chains are $^{13}\mathrm{C}(\alpha, n)^{16}\mathrm{O}$ and $^{22}\mathrm{Ne}(\alpha, n)^{25}\mathrm{Mg}$, which occur in AGB stars (Busso et al. 1999). Starting from a seed nucleus, most importantly iron, the s-process produces among other elements Sr, Y, Zr, Sn, Ba, and Pb. Since most hot subdwarf stars have not evolved through the AGB phase, they are thought to be unable to produce substantial amounts of heavy elements. However, the conditions during the initial helium-flashes may be able to form small amounts of heavy metals (Battich et al. 2023). Cristallo et al. (2009) showed that the s-process in low-metallicity AGB stars favours the production of heavy elements, in particular lead, which may also apply to neutron capture during helium-flashes in hot subdwarf stars.

1.7 Atomic diffusion

The surface composition of helium-rich hot subdwarfs would be determined by their initial metallicity and past nuclear fusion if there were no additional physical processes. Today it is evident that the observed abundances of helium-poor sdB stars are dominated by atomic diffusion processes and their interaction with accretion, convection and mass loss, as was first proposed by Greenstein (1967). The following short introduction to diffusion in hot subdwarf stars is based the detailed review of Michaud et al. (2015).

Definition. Radiative forces in the atmospheres of sdB stars were first explored by Michaud et al. (1985) and Bergeron et al. (1988). The term diffusion refers to the interplay of gravitational settling and radiative levitation, alongside statistical diffusion. This radiative acceleration g_{rad} is caused by the absorption of outward-travelling photons, the strength of which depends on the depth in the atmosphere and is different for each element. Its calculation requires detailed knowledge of the involved atomic data[7]. Elements that are not sufficiently supported by radiative acceleration will eventually sink in the stellar atmosphere while others may become enriched at a specific depth. Various types of stars exhibit peculiar surface compositions due to diffusion, including many main-sequence A/F-type stars, BHB stars, hot subdwarfs, and white dwarfs.

In HB stars. Both gravitational settling and radiative levitation are suppressed by surface mixing processes. It is the absence of convection and the slow rotation rates of B-type BHB stars (Behr 2003) that allow diffusion to operate in the first place (Quievy et al. 2009). The cooler A-type BHB stars show higher rotation rates and are separated from B-BHB stars by a gap at about 11500 K, the so-called Grundahl et al. (1999) jump. LeBlanc et al. (2009) were able to show that diffusion leads to atmospheric stratification of the iron abundance in B-BHB stars, while A-BHB stars retain their homogeneously low initial iron abundances. The resulting differences in the atmospheric structure of A/B-BHB stars cause the observed Grundahl gap (LeBlanc et al. 2010). Much like B-BHB stars, most sdB stars are slow rotators (Geier & Heber 2012), which leads to the same type of diffusion effects.

Time-dependent diffusion. The simplest approach to diffusion models is to assume an equilibrium between gravitational settling and radiative acceleration, i. e. setting $g_{\mathrm{grav}} = -g_{\mathrm{rad}}$. However, this equilibrium is not necessarily reached within the helium-burning lifetime of a HB star. This means that diffusion calculations have to be performed while following the evolution to the zero-age HB and beyond, as done by Michaud et al. (2011) and Hu et al. (2011). As shown in Fig.

---

[7] These data are discussed in the context of stellar photospheres in Sect. 2.1.4.

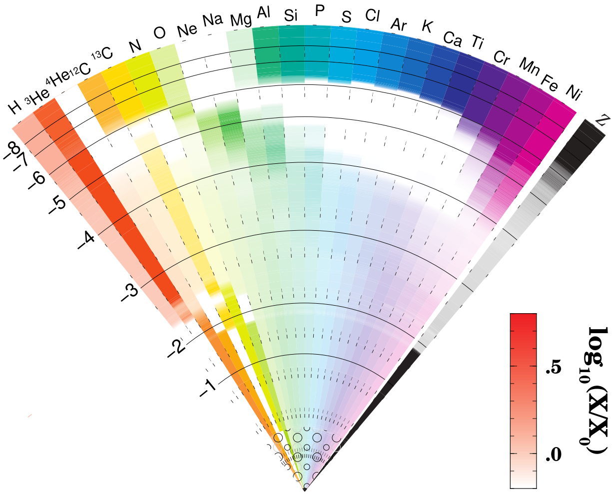

Figure 1.7.1. Concentration of elements relative to the initial abundances in a diffusion model, adopted from Michaud et al. (2011). The model is for a sdB at $T_{\text{eff}} = 30\,\text{kK}$ and 25 Myr after the start of stable core helium fusion. The inset shows the concentration scale. The radius scale is linear and the mass coordinate is indicated by solid lines, labelled logarithmically in units of the contained fractional stellar mass $\Delta M / M_\star$.

1.7.1, these non-equilibrium models predict strong abundance variations due to diffusion in the envelope, whereas deeper layers are affected by helium fusion. The observed abundances correspond to those at the very surface of the star, the photosphere, which roughly covers the outer 10^{-17} to 10^{-11} $M_\star$ in hot subdwarf stars.

Damped diffusion. Atomic diffusion alone can not reproduce the surface composition of hot subdwarf stars. Several sdOB stars are characterized by extremely low silicon abundances[8], which can only explained by diffusion if the uppermost layers of the atmosphere are removed by a weak stellar wind (Michaud et al. 1985). An the same time, diffusion calculations underestimate the surface abundances of several elements, including helium (Byrne et al. 2018) and light metals. Better agreement with the observation can be achieved by assuming damped diffusion in the presence of a weak stellar wind, amounting to a mass loss of about 10^{-14} to 10^{-13} $M_\odot\,\text{yr}^{-1}$ (Fontaine & Chayer 1997; Unglaub & Bues 2001). Such radiation driven winds were predicted to exist in sdB stars by Unglaub (2008). The diffusion models of Michaud et al. (2011) are able to reproduce the surface composition of sdB stars by assuming a generic mixing in the outermost $10^{-7.5}$ $M_\odot$ of the envelope.

Pulsation driving. As significant fraction of hot subdwarf stars show multiperiodic light variations at low amplitudes. A minority of sdOBs are pressure-mode pulsators with periods of the order of minutes (Kilkenny et al. 1997; Østensen et al. 2011). In addition, almost all sdBs close to $T_{\text{eff}} = 28\,\text{kK}$ show gravity-mode pulsations with periods of up to two hours (Green et al. 2003). Both types of pulsations are driven by the ionisation of iron-peak elements below the photosphere, which are enriched at this depth due to radiative levitation (Charpinet et al. 1997; Jeffery & Saio 2006; Bloemen et al. 2014). Hu et al. (2011) argue that stellar winds can not account for sufficient damping of diffusion as they would at the same time suppress the observed pulsations.

Helium-rich atmospheres. Unfortunately, no metal diffusion calculations are available for the most chemically peculiar hot subdwarfs: the “heavy metal” iHe-sdOBs. The only available predictions are concerned with the helium to hydrogen ratio and CNO abundances. In the models of Unglaub (2005), diffusion turns He-sdOBs into helium-poor sdOBs after about 10 Myr if the initial hydrogen abundance exceeds 1% by number (left panel of Fig. 1.7.2). However, these models did not assume any additional mixing which would suppress this transformation. Unglaub (2010) demonstrated that a CN-type He-sdO formed via the deep-mixing hot flasher channel of Miller Bertolami et al. (2008) would quickly transform into an N-type He-sdO if less than the outer 10^{-8} $M_\odot$ are affected to mixing processes (right panel of Fig. 1.7.2). Based on such calculations it has been proposed that iHe-sdOB stars may be remnants of recent mergers that are currently evolving towards the EHB and will eventually turn into helium-poor sdOBs (Naslim et al. 2013), a hypothesis that has not been confirmed to date.

---

[8] See Sect. 3.2 for an extreme example.

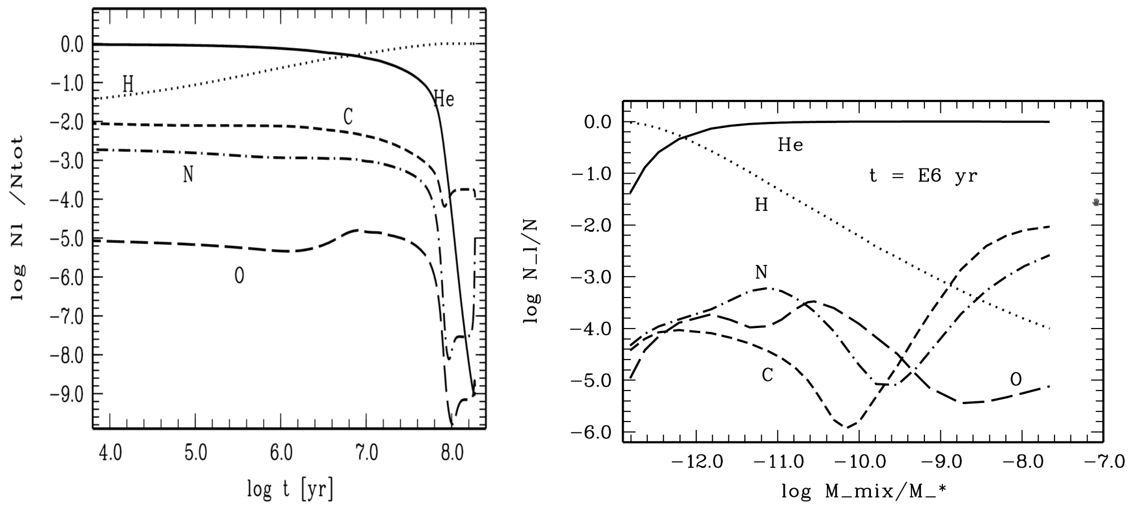

Figure 1.7.2. *Left*: Predicted gravitational settling of helium in a He-sdO by Unglaub (2005) for a mass loss rate of $10^{-13.6}\,M_\odot\,\mathrm{yr}^{-1}$ and without surface layer mixing. *Right*: Surface abundances in a He-sdO model by Unglaub (2010) after one million years, depending on the amount of artificial surface layer mixing.

1.8 Outline of the thesis

Both nuclear fusion and diffusion can alter the surface composition of hot subdwarf stars. Detailed studies of individual stars are required to measure this composition accurately. The necessary methods, in particular model atmospheres are discussed in Chapter 2. Such studies have the potential to distinguish between the hot flasher and merger scenarios for helium-rich hot subdwarfs, as well as identify new formation channels. The detailed studies presented in Chapter 3 serve as benchmarks for evolutionary models, since all observed features should be replicated by a successful theory. Several detailed studies are performed in the first part of this thesis:

- **Heavy-metal sdOBs.** The group of “heavy-metal” He-sdOBs is distinct from most sdOB stars not only by their extreme enhancement in zirconium or lead, but also their pulsations and extreme Galactic orbits. The connection between helium-rich and helium-poor sdOB stars is explored in the first analyses in Chapter 3 by performing detailed spectral, photometric, and kinematic analyses for both He-poor and He-rich sdOB stars.

- **Long-period binaries.** The formation of hot subdwarfs through Roche lobe overflow is tested by studying the first heavy-metal He-sdOB in a binary system, which turns out to have a very low initial metallicity. In addition, the molecular lines in the infra-red spectra of another long-period companion to a sdOB star are used to test whether or not mass transfer has occurred in this system.

- **Magnetic hot subdwarfs.** Magnetic hot subdwarf stars have long eluded detection, despite extensive searches. The analysis of the first magnetic hot subdwarf stars is finally presented here, including a basic spectral analysis of their magnetic fields. This new class of strongly magnetic He-sdO stars seems to be formed via the merging of binary helium white dwarfs, but poses several challenges to these models.

It is likely that all formation scenarios mentioned here contribute to the hot subdwarf population, along with other and possibly unknown scenarios. A good understanding of the population as a whole can only be achieved by comparing its statistical properties with theoretical predictions, as reviewed by Han et al. (2020). A large set of binary population synthesis (BPS) models for hot subdwarfs was calculated by Han et al. (2002) and Han et al. (2003). These models predict a wide range of properties, including the distribution in T_{eff} and $\log g$, in radius, luminosity, and mass, as well as the properties of binary systems.

Recently, large surveys have provided photometric, spectroscopic, and astrometric data for millions of stars. Parallax measurements by DR2 and DR3 of the *Gaia* space observatory not only finally provided distance measurements for thousands of hot subdwarf stars, but also very accurate photometry and proper motions. The second part of this work sets out to use these data in statistically significant studies of the hot subdwarf population in terms of stellar parameters, composite binary nature, and Galactic kinematics:

- **Stellar parameters and composite binaries.** The fundamental stellar parameters radius, luminosity, and mass are currently only known for few hot subdwarf stars. Section 4.1 presents the first large-scale study of stellar parameters, based on a combination of spectroscopic T_{eff} and $\log g$ from the literature, distance measurements from *Gaia*, and the analysis of photometric measurements. This study also provides the largest sample of hot subdwarfs in composite-color binary systems, likely formed by the stable Roche lobe overflow channel. Both types of results are discussed for each spectroscopic sub-class of hot subdwarf stars to asses differences in the formation of these classes. The overall observed distributions are compared to evolutionary tracks and the BPS models. In particular the radii and temperatures of the observed cool companion population present a challenge to the BPS models of Han et al. (2003), which suggests that these models need significant updates.

- **Galactic kinematics.** As discussed in Sect. 1.7, the surface metallicity of hot subdwarf stars is affected by strong diffusion effects and thus cannot be used to estimate their ages. An alternative method for estimating their ages is to analyse their Galactic orbits. In a simple picture, such orbits can be classified to belong to the Galactic thin disk, thick disk, or halo population, in order of increasing age. Section 4.2 presents the Galactic kinematics of the spectroscopically identified hot subdwarf sample. This sample can be compared to the results of Luo et al. (2021) for the LAMOST sample of hot subdwarf stars. Again, significant differences between the spectroscopic classes are identified.

The conclusions derived from the various analyses presented in this thesis are summarised in Chapter 5. Lastly, the potential for further studies on hot subdwarf populations is highlighted.

Chapter 2

Methods

2.1 Model atmospheres and synthetic spectra

Stellar spectra contain a wealth of information that sets the observational foundation of our theory of stars and their evolution. Examples range from the stellar effective temperature $T_{\rm eff}$, surface gravity g, the atmospheric chemical composition and magnetic field strength to the radial velocity $\upsilon_{\rm rad}$ and projected rotational velocity $\upsilon_{\rm rot}\sin i$. This information can be extracted by constructing models of the stellar photosphere[1], the deepest region from which photons can escape. Detailed explanations of the physics involved, in particular for hot and compact stars, are provided by Gray (2005), Irrgang (2014), Hubeny & Mihalas (2014), and Hubeny & Lanz (2017b), on which the following brief overview is based.

2.1.1 Radiative transfer equation

The specific photon intensity at the bottom of the photosphere is simply given by the Planck function

$$B_\nu(T) = \frac{2h\nu^3}{c^3}\frac{1}{e^{h\nu/k_{\rm B}T} - 1}, \tag{2.1.1}$$

where ν is the photon frequency, T is the local temperature, c is the speed of light, h is the Planck constant, and $k_{\rm B}$ is the Boltzmann constant.

The radiative transfer equation describes the transfer of a photon beam towards the surface. For z increasing towards the stellar surface, the specific intensity $I_{\mu\nu}$ of a beam of photons changes as

$$\mu\frac{\partial I_{\mu\nu}}{\partial z} = \eta_\nu^{\rm tot} - \chi_\nu I_{\mu\nu}, \tag{2.1.2}$$

where χ_ν is the total absorption coefficient, also called opacity, $\eta_\nu^{\rm tot}$ is the total emission coefficient, and μ is the cosine of the polar angle Θ, which spans between the direction of propagation and the normal to the stellar surface. The specific intensity emergent from the stellar surface is then

$$I_{\mu\nu}(\tau_\nu = 0) = \int_{\tau_1=0}^{\tau_2=\infty} S_\nu(t_\nu)\, e^{-t_\nu/\mu}\, \mathrm{d}t_\nu/\mu, \tag{2.1.3}$$

where $S_\nu(\tau_\nu) = \chi_\nu/\eta_\nu^{\rm tot}$ is the source function and $\tau_\nu(z) = \int_z^{z_{\rm max}} \chi_\nu(z')\mathrm{d}z'$ is the optical depth, which decreases towards the surface. The factor $e^{-\tau_\nu/\mu}$ is called the extinction. In practice, model emergent spectra specify the first angular moment of the specific intensity

$$F_\nu(\tau = 0) = 2\pi\int_{-1}^{1} I_{\mu\nu}(\tau_\nu = 0)\,\mu\,\mathrm{d}\mu, \tag{2.1.4}$$

---

[1] Because stellar chromospheres, coronae, and winds are not important in the context of this work, the terms "photosphere" and "atmosphere" may be used interchangeably here.

often as the Eddington flux $H_\nu = F_\nu/4\pi$ and in units of erg cm^2 s^{-1} Å^{-1}. This flux can only be determined if the source function is known, which requires knowledge of the atmospheric structure, in particular the stratifications of temperature and (electron) density, as well as the atomic energy level occupation numbers down to a depth where the atmosphere becomes opaque.

2.1.2 Standard assumptions

The classical stellar atmosphere code used in this work, Tlusty 205 (Hubeny 1988; Hubeny & Lanz 2017a), makes several approximations. The atmosphere is considered to be one-dimensional and *plane-parallel* with the coordinate z increasing towards the surface. There are three main additional assumptions that determine the atmospheric structure:

- *Hydrostatic equilibrium* – radiative and gas pressure are balanced against the gravitational pressure:

  $$-\frac{\mathrm{d}P_{\mathrm{total}}}{\mathrm{d}z} + \rho g = 0, \tag{2.1.5}$$

  where P_{total} is the sum of radiation and gas pressure and ρ is the mass density. The surface gravity $g = GM_*/R_*^2$ is one of the fundamental parameters of stellar atmospheres. Here, M_* and R_* are the stellar mass and radius while G is the gravitational constant. The atmospheric structure is therefore considered to be static, which introduces the restriction that stellar winds can not be modelled.

- *Radiative equilibrium* – the absorption and the emission of photons is balanced in each volume element when integrated over all frequencies

  $$\int_0^\infty (\kappa_\nu J_\nu - \eta_\nu)\,\mathrm{d}\nu = 0, \tag{2.1.6}$$

  where κ_ν and η_ν are the thermal absorption and emission coefficients and $J_\nu = \int_{-1}^{1} I_{\mu\nu}\,\mathrm{d}\mu$ is the mean intensity of radiation. Here, the energy transport is assumed to be entirely due to photons. Convective energy transport is negligible for the hot stars discussed here. An equivalent formulation is possible using the flux conservation

  $$\int_0^\infty F_\nu\,\mathrm{d}\nu = \sigma_{\mathrm{SB}} T_{\mathrm{eff}}^4. \tag{2.1.7}$$

  Here, the effective temperature T_{eff} is one of the basic atmospheric parameters and σ_{SB} is the Stefan–Boltzmann constant.

- *Kinetic (statistical) equilibrium* – the population density n_i for any atomic energy level i is time-independent, including levels in higher ionisation stages. This means that the total population and the de-population rates are balanced

  $$n_i \sum_{i \neq j} P_{ij} - \sum_{j \neq i} (n_j P_{ji}) = 0 \quad \forall\ i \tag{2.1.8}$$

  where P_{ij} is the depopulation rate from level i to level j and P_{ji} is the reverse rate. These rates consist of the radiative rate R_{ij} and the collisional rate C_{ij}

  $$P_{ij} = R_{ij} + C_{ij}. \tag{2.1.9}$$

  For known radiative and collisional rates, these equations can be combined with the abundance definition of a particular element to derive its level populations in all ionisation stages.

The rate equations (2.1.8) not only depend on radiative and collisional transition cross sections, but also on the mean intensity of radiation. The radiation field itself depends on the source function, which in turn depends on the level populations. Therefore the kinetic (2.1.8) and radiative transfer (2.1.2) equations are highly coupled. In model atmosphere codes, these equations are solved in an iterative way, the details of which are described by Hubeny & Mihalas (2014).

2.1.3 The LTE approximation

Whenever collisional rates dominate over radiative rates, the population of energy levels is coupled only to the density and temperature of the local plasma. Because the mean free path of photons $1/\chi_\nu$ is then very small compared to the distance over which the temperature changes, one can assume local thermal equilibrium (LTE). The LTE assumption simplifies the model atmosphere problem significantly. In particular,

- the particle velocity distribution is a Maxwell-Boltzmann distribution

  $$f(v)\,\mathrm{d}v = 4\pi \left(\frac{m}{2\pi k_\mathrm{B} T}\right)^{3/2} v^2 e^{-mv^2/2k_\mathrm{B}T}\,\mathrm{d}v, \tag{2.1.10}$$

  where T is the local temperature, v is the particle velocity, and m is its mass. This approximation is always valid for electrons in the stellar photosphere due to their short free paths. The most probable velocity is $\bar{v} = \sqrt{2k_\mathrm{B}T/m}$.

- The ratio of the populations of any two energy levels i and j in the same ion is given by the Boltzmann equation

  $$\frac{n_i^*}{n_j^*} = \frac{g_i}{g_j} e^{-(E_i-E_k)/k_\mathrm{B}T}, \tag{2.1.11}$$

  where n_i^* is the LTE population of level i, E_i is its energy with respect to the ground state. The statistical weights g_i are defined by

  $$g_i = 2J_i + 1, \tag{2.1.12}$$

  where J_i is the total angular momentum quantum number. The LTE population of a level i relative to the total number density N_I^* of its ionisation stage I is then given by

  $$\frac{N_i^*}{N_I^*} = \frac{g_i e^{-E_i/k_\mathrm{B}T}}{\sum_k g_k e^{-E_k/k_\mathrm{B}T}} = \frac{g_i e^{-E_i/k_\mathrm{B}T}}{U_I}, \tag{2.1.13}$$

  where U_I is called the partition function.

- The LTE number ratio of atoms in two subsequent ionisation stages is given by the Saha equation

  $$\frac{N_{I+1}^*}{N_I^*} = \frac{2U_{I+1}}{U_I} \frac{\lambda_\mathrm{th}^3}{n_\mathrm{e}} e^{-\chi_I/k_\mathrm{B}T}, \tag{2.1.14}$$

  where n_e is the local electron density and $\lambda_\mathrm{th} = \sqrt{\frac{2\pi m_\mathrm{e} k_\mathrm{B} T}{h^2}}$ is the thermal de Broglie wavelength with the electron mass m_e. The Saha equation can be combined with the condition of charge conservation to obtain the ionisation fractions for all atoms. Therefore, once the partition functions for all levels are known, the only additional atomic data needed are the ionisation energies χ_I.

2.1.4 Atomic data

The LTE approximation breaks down in the hot atmospheres discussed here. There, radiative rates often dominate over collisional rates and the occupation numbers of atomic levels depend on the non-local radiation field. In this non-LTE case, the Saha and Boltzmann equations have to be replaced by the kinetic equilibrium equations (2.1.8).

Atomic data are required to compute the transition rates and the opacity and emissivity as the combination of several processes. In particular, the total transition rate P_{ij} is the sum of the radiative bound-bound (bb) and bound-free (bf) transition rate and the collisional rate

$$P_{ij} = R_{ij}^\mathrm{bb} + R_{ij}^\mathrm{bf} + C_{ij}, \tag{2.1.15}$$

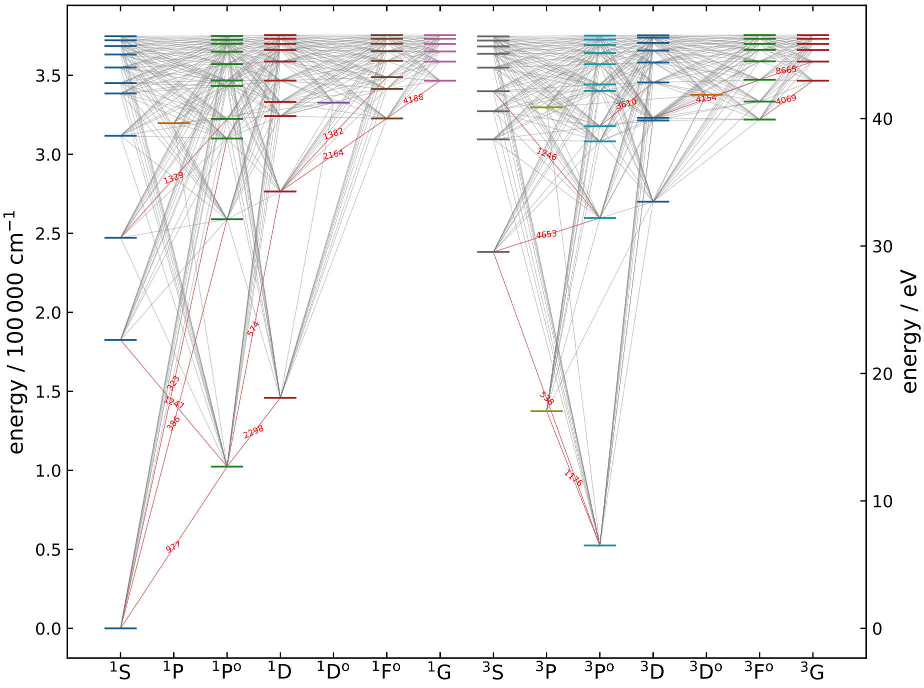

Figure 2.1.1. Grotrian diagram for a new C III model ion. The 94 considered energy levels are ordered by their *LS*-coupling terms, separated by the singlet and triplet systems. The most important transitions are marked in red and labelled with their wavelength in Å.

where the latter is dominated by collisions with free electrons in hot atmospheres. Both the opacity and emissivity are the sum of a scattering and a thermal term, here for the opacity

$$\chi_\nu = \kappa_\nu^{\text{scatter}} + \underbrace{\sum_i \sum_{j>i} \kappa_{ij}^{\text{bb}} + \sum_i \kappa_{ij}^{\text{bf}} + \sum_k \kappa_k^{\text{ff}}}_{\equiv \kappa_\nu^{\text{thermal}}}, \tag{2.1.16}$$

where free-free (ff) transitions involve collisions between atoms and electrons that are unbound before and after the interaction. The scattering term accounts for electron (Thomson) and Rayleigh scattering. The former is an important source of opacity for O- and B-type stars.

The atomic data required to compute the radiative and collisional rates as well as the source function are often combined in so-called model atoms. A TLUSTY model atom consists of three blocks: level energies, bound-bound transition data, and photoionisation cross sections. For many ions, these data were provided by the Opacity Project (OP, Seaton et al. 1992), focussing on radiative data, and the Iron Project (IP, Hummer et al. 1993), which focussed on collisional data. The following paragraphs describe the necessary atomic data only to the degree that they are used in the subsequent analyses.

Energy levels. Due to computational limitations, only a subset of all energy levels in each ion can be considered in model atmospheres – typically no more than 2000 levels in total. For most atoms up to the iron group, the angular momenta of individual electrons can be considered to couple in the Russel-Saunders (or *LS*) coupling scheme. In the *LS* coupling scheme, the (absolute) total spin angular momentum S and the total orbital angular momentum L are considered as conserved quantum numbers. They can be summarised as a term symbol

$$^{2S+1}L_J,$$

where $2S+1$ is the spin multiplicity. Terms with $S = 0, \frac{1}{2}, 1$ belong to the so-called singlet, doublet, and triplet systems. For historic reasons, L is labelled by letters (S, P, D, F, G, ...)

instead of numbers. The total angular momentum quantum number J splits each term into fine structure energy levels, which is often ignored in atmospheric structure calculations. Electron configurations and their LS terms have either an even or an odd parity. The latter is indicated by a superscript ° to the term symbol. An example level structure is shown in Fig. 2.1.1 for a C III model ion constructed from OP data.

Ab-initio calculations of level energies usually lack the accuracy required to match observed transition wavelengths. Theoretical energies should therefore be replaced with the more accurate experimental values whenever possible.

Bound-bound transitions. Spectral lines result from transitions between a lower (i) and upper (j) energy level. These electronic dipole transitions obey the following so-called selection rules:

- The parity of the initial and final level must differ.
- $\Delta J = 0$ or ± 1, but not $J = 0 \leftrightarrow 0$.
- No intersystem lines, so $\Delta S = 0$.
- $\Delta L = 0$ or ± 1.

Photon transitions between two bound levels are possible in three processes:

- The lower level absorbs a photon, thus exciting an electron to the upper level. This is described by *Einstein's absorption probability* B_{ij}.
- An excited electron spontaneously drops to the lower level, emitting a photon. The corresponding probability is *Einstein's spontaneous emission probability* A_{ji}.
- An excited electron may be induced to jump to the lower level by other photons that have the same energy as the thus emitted photon. This process can be considered negative absorption, described by *Einstein's induced emission probability* B_{ji}.

These Einstein coefficients are determined by the intrinsic quantum mechanical properties of an atom and are related as

$$A_{ji} = \frac{2h\nu}{c^2} B_{ji} = \frac{2h\nu}{c^2} B_{ij} \frac{g_i}{g_j}. \tag{2.1.17}$$

Model atmosphere calculations can therefore make use of a single cross section

$$\sigma_{ij}(\nu) = \frac{\pi e^2}{m_e c} f_{ij} \, \phi_{ij}(\nu), \tag{2.1.18}$$

where ϕ_{ij} is the normalised absorption profile coefficient that results from line broadening processes. The oscillator strength used in (2.1.18) is simply given by

$$f_{ij} = \frac{\varepsilon_0 m_e c^3}{2\pi e^2 \nu^2} \frac{g_j}{g_i} A_{ji}, \tag{2.1.19}$$

where ε_0 is the electric constant. Defining $G_{ij} = g_i/g_j$ for bound-bound transitions, the radiative rates are then given by

$$R^{\mathrm{bb}}_{ij} = \frac{4\pi}{h} \int_0^\infty \frac{\sigma_{ij}(\nu)}{\nu} J_\nu \, \mathrm{d}\nu, \qquad R^{\mathrm{bb}}_{ji} = \frac{4\pi}{h} \int_0^\infty \frac{\sigma_{ij}(\nu)}{\nu} G_{ij} \left(\frac{2h\nu^3}{c^2} + J_\nu \right) \mathrm{d}\nu, \tag{2.1.20}$$

where the first and second terms in R^{bb}_{ji} correspond to spontaneous and induced emission, respectively. The line cross section similarly enters the opacity and emissivity

$$\kappa^{\mathrm{bb}}_{ij}(\nu) = (n_i - n_j G_{ij}) \, \sigma_{ij}(\nu), \qquad \eta^{\mathrm{bb}}_{ij}(\nu) = \frac{2h\nu^3}{c^2} n_j G_{ij} \, \sigma_{ij}(\nu). \tag{2.1.21}$$

Bound-bound transitions from many elements contribute significantly to the total opacity in (hot) stellar atmospheres. In particular the many transitions in ions of the iron group are an important

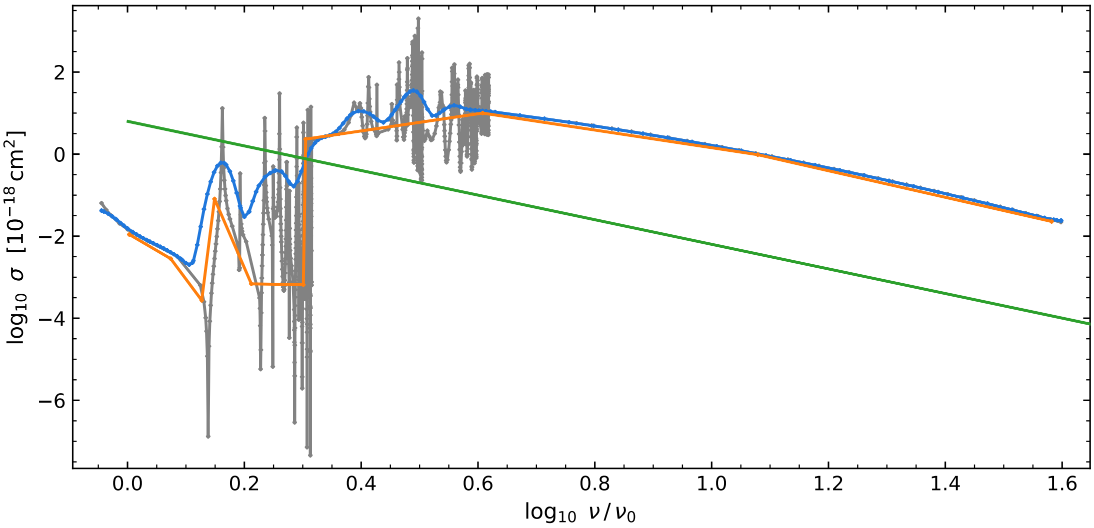

Figure 2.1.2. Detailed (grey), resonance-averaged (blue), and standard Tlusty (orange) OP cross sections compared to the hydrogenic approximation (green) for the lowest C ii ^{2}D° level.

source of opacity that directly influences the temperature stratification. Despite their importance, oscillator strengths are often poorly known because they require complex computations or laboratory measurements.

Spectral line strengths are often expressed using the equivalent width. Given a flux that considers a single bound-bound transition F_ν^{ji}, the equivalent width is defined as

$$W_{ji} := \int_0^\infty A_\nu^{ji}\,\mathrm{d}\nu. \tag{2.1.22}$$

Here $A_\nu^{ji} := \frac{F_\nu^{\mathrm{c}} - F_\nu^{ji}}{F_\nu^{\mathrm{c}}}$ is the line depth with respect to the continuum flux F_ν^{c}, which is simply the flux without the contribution of bound-bound transitions. The emergent continuum flux is useful to define a normalised flux

$$F_\lambda^{\mathrm{norm}} = F_\nu^{\mathrm{norm}} := F_\nu / F_\nu^c, \tag{2.1.23}$$

which will be used to show the strength of spectral lines throughout this work.

Bound-free transitions. If the energy of an incident photon exceeds the binding energy of an electron, it may remove the electron through photoionisation. As shown by Milne (1924), the photoionisation rate and its inverse, the recombination rate, are analogous to bound-bound transitions (Eq. 2.1.20). For bound-free transitions, G_{ij} is given by the Saha-Boltzman factor

$$n_e \Phi_i(T) = \frac{g_i}{2 g_1^+} \frac{n_e}{\lambda_{\mathrm{th}}^3} e^{(\chi_I - E_i)/k_{\mathrm{B}} T}, \tag{2.1.24}$$

where g_1^+ is the statistical weight of the ground state of the next ion. In hot atmospheres, hydrogen and helium photoionisation contributes significantly to the opacity and emissivity, analogous to Eq. (2.1.21). In F-type or cooler stars, the strongest continuous absorption in the optical range is due the ionisation of the H$^-$ ion (Gray 2005).

Theoretical photoionisation cross sections for many ions were computed as part of the Opacity Project (OP; Seaton et al. 1992). Figure 2.1.2 shows an example OP cross section for the lowest ^{2}D° level of C ii. The sharp peaks in the original OP cross sections (grey) result from resonances that are associated with excited levels of C iii. The exact position of the resonances is subject to uncertainties in the level energy calculation. It is therefore beneficial to smooth the ionisation cross sections, creating so-called resonance-averaged photoionisation (RAP) cross sections (Bautista et al. 1998; Allende Prieto et al. 2003). The blue line in Fig. 2.1.2 shows a RAP cross section using a Gaussian kernel with a standard deviation of $\delta\nu = 0.03\nu$. The cross sections originally implemented in Tlusty model atoms (orange) sometimes disregard the resonances entirely, in which case they should be replaced by RAP cross sections.

If no data are available, photoionisation cross sections can be approximated using a scaled formula based on the hydrogen atom (green in Fig. 2.1.2). Photoionisation from an energy level with an effective principal quantum number n can be approximated as

$$\sigma_{\text{hyd}}(\nu) = 2.815 \times 10^{-29}\, Z^4\, \nu^{-3}\, n^{-5} g^{\text{bf}}(n, \nu),$$

where Z is the nuclear charge and g^{bf} is the Gaunt factor, a quantum mechanical correction factor close to unity. While this hydrogenic approximation is roughly correct for the ground state of hydrogenic atoms such as He II and C VI, it is not accurate for excited states, even in hydrogenic ions.

Collisional transitions. Collisional transitions are important because they couple the energy level populations to the local electron temperature, thus bringing them closer to LTE. The collisional transition rate, both bound-bound and bound-free, is

$$C_{ij} = n_e \int_{v_0}^{\infty} \sigma_{ij}\, f(v)\, \mathrm{d}v, \qquad\qquad C_{ji} = \frac{n_i^*}{n_j^*}\, C_{ij}, \tag{2.1.25}$$

where is $f(v)$ is given by Eq. (2.1.10) and $v_0 = \sqrt{2E_{ij}/m}$ is the minimum velocity to match the threshold energy E_{ij}. Here, the ratio of LTE populations n_i^*/n_j^* is a correction for induced emission. Like radiative cross sections, accurate collisional cross sections can only be derived from complex quantum mechanical models or experimental measurements. In cases where these are not available, bound-bound rates are usually approximated using the formula of van Regemorter (1962) while collisional ionisation is approximated by the Seaton (1962) formula.

2.1.5 Atmospheric structure and spectral features

Model atmospheres are computed for a set of discrete depth points, usually between 50 and 100. The depth of these points can be described by the optical depth $\tau_\nu(z)$, which strongly depends on the frequency. To avoid this dependency, one may instead use the column mass

$$m(z) = \int_z^{\infty} \rho(z')\, \mathrm{d}z', \tag{2.1.26}$$

which strongly depends on the surface gravity, or the Rosseland mean optical depth

$$\tau_{\text{Ross}} \equiv 1/\chi_{\text{Ross}} \equiv \int_0^{\infty} \frac{1}{\chi_\nu} \frac{\partial B_\nu}{\partial T}\, \mathrm{d}\nu \bigg/ \int_0^{\infty} \frac{\partial B_\nu}{\partial T}\, \mathrm{d}\nu\,, \tag{2.1.27}$$

which increases with increasing depth in the atmosphere and reaches a value close to unity in the line forming region. While the atmospheric structure has to be computed down to deep layers, only the photons that escape the atmosphere are actually observable.

It is instructive to consider how the atmospheric structures and their emergent flux, described by Eq. (2.1.4), depend on the basic atmospheric parameters T_{eff} and $\log g$. This is shown in Fig. 2.1.3 for helium-dominated atmospheres. As shown in panel (a), higher values of T_{eff} lead to higher local temperatures at all depths. This increases the degree of ionisation (c) – an atmosphere at $T_{\text{eff}} = 25$ kK is still dominated by He II while most helium atoms are fully ionised at $T_{\text{eff}} \gtrsim 45$ kK. The electron density is barely affected by the value of T_{eff}: higher degrees of ionisation are counteracted by the simultaneous increase in radiative pressure which leads to lower (electron) densities. Conversely, increasing the surface gravity (b) barely affects the temperature structure, but leads to much higher (electron) densities. As can be understood from the Saha equation (2.1.14), lower values of $\log g$ therefore lead to higher degrees of ionisation (d). Although He II is the dominant ionisation stage even at $T_{\text{eff}} = 25$ kK, He II lines are weak at that temperature (e). This is because the specific levels involved in optical He II transitions are populated only at higher temperatures. Similarly, He I lines are still strong in the emergent spectra at $T_{\text{eff}} = 40$ kK even though less than 0.1 % of all helium atoms are neutral at that T_{eff} (f).

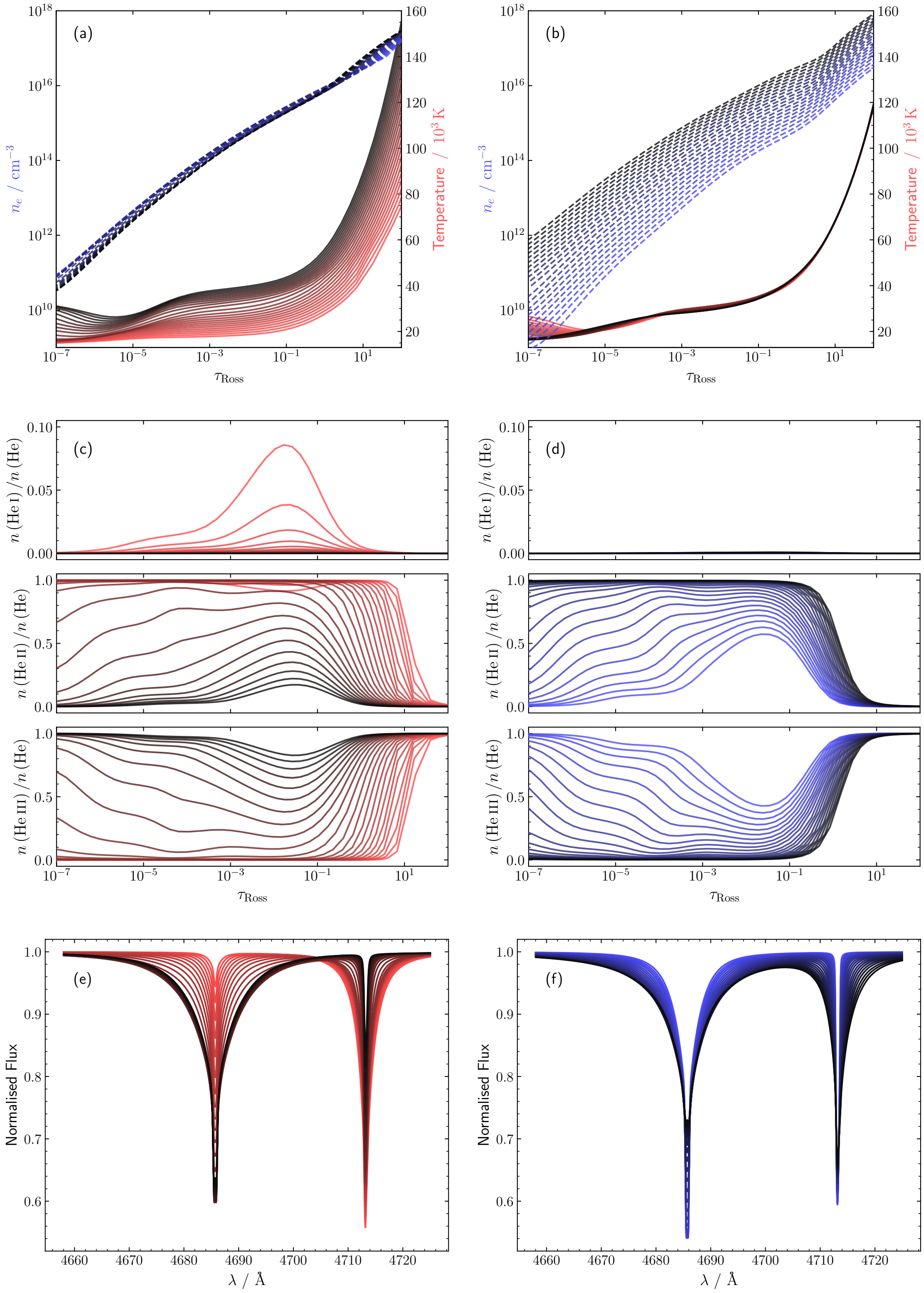

Figure 2.1.3. *Top:* Atmospheric temperature (solid red) and electron density (dashed blue) structures: left from $T_{\rm eff}$ = 25 000 K (light) to 52500 K (dark) in steps of 1250 K and at $\log g = 5.5$; right from $\log g = 4.0$ (light) to 6.5 (dark) in steps of 0.125 and at $T_{\rm eff}$ = 40 000 K. All models are for $\log n(\mathrm{He})/n(\mathrm{H}) = +1$. *Middle:* The helium ionisation fractions for the same model atmospheres. *Bottom:* The emergent He II 4686 Å and He I 4713 Å lines based on these models. Only the contribution of bound-bound transitions is shown in these normalised spectra.

2.1.6 Line broadening

Apart from the absolute strength of spectral lines, both the temperature and (electron) density stratification also affect spectral line shapes through the absorption profile $\phi_{ij}(\nu)$. The absorption profile $\phi_{ij}(\nu)$ is equal to the emission profile $\phi_{ji}(\nu)$ if all transitions are assumed to be balanced by their inverse (so-called detailed balance). Various effects contribute to the spectral line shapes:

- *Natural (radiative) broadening:* all energy levels except for the ground state have a finite characteristic lifetime Δt_j. Their energy is therefore broadened according to Heisenberg's uncertainty principle

  $$\Delta E_j \gtrsim \hbar/\Delta t_j. \tag{2.1.28}$$

  Similar to a damped classical oscillator, the resulting line profile follows a Lorentz function

  $$\phi_{ji}^{\mathrm{Natural}}(\nu) = \frac{\Gamma_{ji}/4\pi^2}{(\nu-\nu_0)^2 + (\Gamma_{ji}/4\pi)^2}, \tag{2.1.29}$$

  where $\Gamma_{ji} = (\Gamma_j + \Gamma_i)/2$ is the damping constant and $\Gamma_k = \sum_{l<k} A_{kl}$ for $k \in \{i, j\}$. This natural broadening is only important in low-density environments such as the interstellar medium. The following effects are much stronger in stellar atmospheres.

- *Collisional (pressure) broadening:* radiating atoms in stellar atmospheres are affected by Coulomb interactions during collisions with neutral and charged particles. The large number of charged particles in hot atmospheres leads to statistical broadening of energy levels through the Stark effect. Linear Stark broadening is important for atoms with an intrinsic dipole moment, in particular (nearly) hydrogenic levels, that is levels with a single bound electron. The quadratic Stark effect is important for all non-hydrogenic atoms in hot atmospheres. In cooler stars, collisions with neutral hydrogen through van der Waals (vdW) interactions become more important.

  All pressure broadening effects lead to an approximately Lorentzian line shape (Eq. 2.1.29), so a common damping constant $\Gamma = \Gamma^{\mathrm{Stark}} + \Gamma^{\mathrm{vdW}}$ can be used. In reality, detailed Stark broadening calculations for hydrogen and in particular neutral helium (He I) are often non-Lorentzian. Such Stark broadening tables are vital for the determination of the surface gravity from the spectra of hot stars. They are typically computed in two different approximations. The *impact approximation*, used for fast moving electron perturbers, considers an interruption to the emitted electromagnetic wave that creates a phase shift; it is valid for non-overlapping collisions. The heavier and thus slowly moving ions are usually approximated as *quasi-static* particles that statistically perturb the level energies around some average value.

- *Thermal broadening:* particles in stellar atmospheres are constantly moving in the line of sight, which means that the rest frequency of emitted photons ν_0 is shifted by the Doppler effect

  $$(\nu_0 - \nu)/\nu = \upsilon/c. \tag{2.1.30}$$

  Because the line of sight velocity dispersion is given by

  $$p(\upsilon) = \frac{1}{\sqrt{\pi}\bar{\upsilon}}\, e^{-\upsilon^2/\bar{\upsilon}^2}, \tag{2.1.31}$$

  the resulting profile is Gaussian

  $$\phi^{\mathrm{Doppler}}(\nu) = p(\upsilon)\left|\frac{\mathrm{d}\upsilon}{\mathrm{d}\nu}\right| \overset{\upsilon \ll c}{\approx} e^{-x^2}/(\Delta\nu_{\mathrm{th}}\sqrt{\pi}), \tag{2.1.32}$$

  where $x = (\nu - \nu_0)/\Delta\nu_{\mathrm{th}}$ and $\Delta\nu_{\mathrm{th}} = \bar{\upsilon}\nu_0/c$ is the thermal Doppler width.

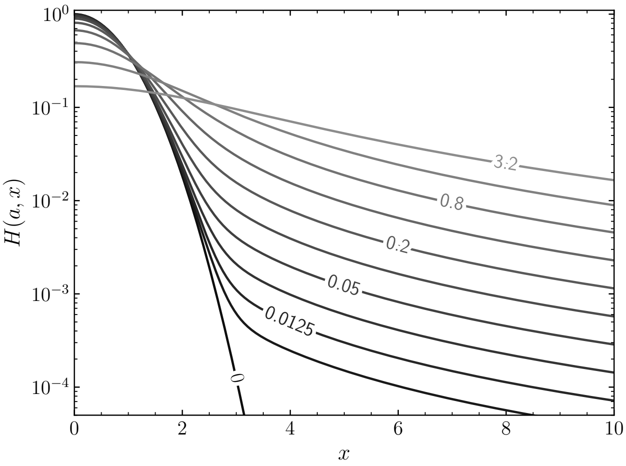

Figure 2.1.4. Hjerting function for various values of a. For high a (grey), it is close to a Lorentz function with pronounced line wings. A Gauss function is approached for $a \to 0$ (black).

- *Microturbulance:* Small-scale motions below the photon mean free path $1/\tau_{\text{Ross}}$ are neglected by hydrostatic models. These motions introduce Dopper broadening additional to the thermal component. This micro-turbulent velocity ξ is therefore treated as an increased Doppler width $\Delta\nu_{\text{D}} = \sqrt{\bar{v}^2 + \xi^2}\nu_0/c$ in Eq. (2.1.32). For most hot subdwarf stars there is no evidence for significant microturbulance.

All of these effects contribute to the broadening of spectral lines, the shapes of which therefore result from the convolution of Lorentzian and Gaussian profiles as

$$\phi_{ji} = \phi_{ji}^{\text{Natural}} * \phi_{ji}^{\text{Pressure}} * \phi^{\text{Thermal}} * \phi^{\text{Micro}} \approx \phi^{\text{Lorentz}} * \phi^{\text{Gauss}}. \tag{2.1.33}$$

The convolution of a Lorentzian and Gaussian profile is called a Voigt profile

$$\begin{aligned}\phi^{\text{Voigt}}(x) \equiv \phi^{\text{Lorentz}} * \phi^{\text{Gauss}} &:= \int_{-\infty}^{+\infty} \phi^{\text{Lorentz}}(x)\, \phi^{\text{Gauss}}(x-y)\,\mathrm{d}y \\ &= \frac{1}{\sqrt{\pi}}\frac{a}{\pi}\int_{-\infty}^{+\infty} \frac{e^{-y^2}}{(x-y)^2 + a^2}\mathrm{d}y = \frac{1}{\sqrt{\pi}}H(a,x).\end{aligned} \tag{2.1.34}$$

Here, both the frequency difference $x = (\nu - \nu_0)/\Delta\nu_{\text{D}}$ and the damping parameter $a = \frac{\Gamma}{4\pi\,\Delta\nu_{\text{D}}}$ are expressed in units of the Doppler width. The physical damping parameter is given by $\Gamma = \Gamma^{\text{Natural}} + \Gamma^{\text{Stark}} + \Gamma^{\text{vdW}}$. The Hjerting function $H(a,x)$ is shown in Fig. 2.1.4. It can be seen as having two components: a Doppler-broadened core and pressure-broadened wings to each side.

There are two additional broadening mechanisms that broaden spectral lines after their formation in the stellar photosphere, namely

- *Rotation and limb darkening:* most stars rotate with some equatorial velocity v_{rot}, ranging from a few to several hundreds of $\text{km}\,\text{s}^{-1}$. Given an inclination i of the rotation axis with respect to the line of sight, the projected rotational velocity $v_{\text{rot}}\sin i$ leads to changing Doppler shifts across the stellar disk. Because stellar surfaces can usually not be resolved by the observation, this introduces broadening of spectral lines. Following Gray (2005), the corresponding broadening profile can be approximated as

$$\phi^{\text{Rot}}(x) = \begin{cases} \dfrac{2(1-\epsilon)\sqrt{1-x^2} + \pi\epsilon(1-x^2)/2}{\pi\Delta\lambda_L(1-\epsilon/3)} & \text{if } |x| \leq \Delta\lambda_L, \\ 0 & \text{otherwise.} \end{cases} \tag{2.1.35}$$

Here, λ_0 is the rest wavelength, $x = (\lambda - \lambda_0)/\lambda_L$, and $\Delta\lambda_L = v_{\text{rot}}\sin(i)\,\lambda_0/c$ is the Doppler shift at the stellar equator. As described by Eq. (2.1.3), the extinction increases towards the edges of the stellar disk ($|\mu| \to 1$), an effect called limb darkening. One can approximate this effect by assuming $I_{\mu\nu} = I_{1\nu}(1 - \epsilon + \epsilon\mu)$, where ϵ is the linear limb darkening coefficient

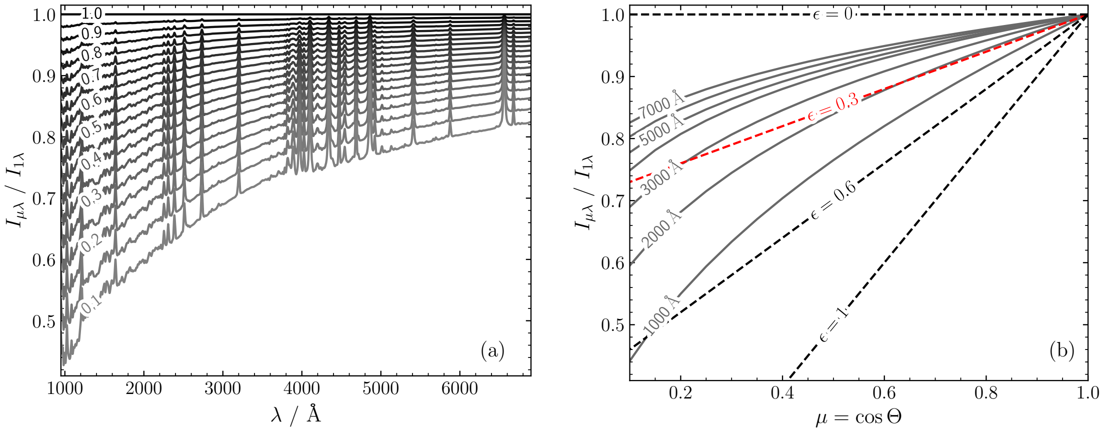

Figure 2.1.5. *Top left:* Specific intensity relative to the disk centre for a TLUSTY/SYNSPEC sdO model at $T_{\text{eff}} = 38\,000$ K, $\log g = 5.9$, and $\log n(\text{He})/n(\text{H}) = -0.75$ for various μ. Several helium lines show a weak limb darkening effect compared to the continuum. *Top right:* Predicted limb darkening from the same models for various wavelengths (solid grey), compared to linear approximations (dashed black) for $\epsilon = 0$ to 1. *Bottom:* Rotational broadening profiles for ϵ in steps of 0.1, where the adopted profile is marked red.

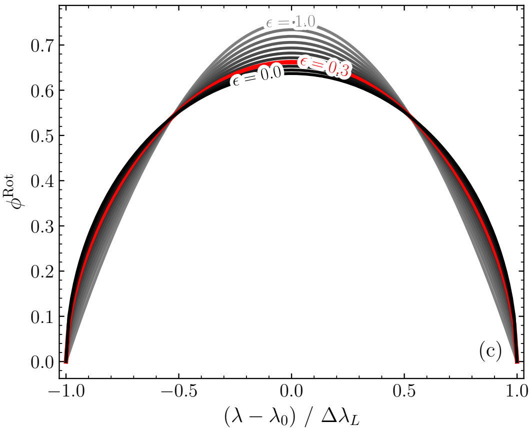

(Milne 1921). This coefficient is a function of T_{eff}, $\log g$, and wavelength – the latter is shown in Fig. 2.1.5a. It is reasonable to use a constant value of $\epsilon = 0.3$ (Fig. 2.1.5b), given that ϵ has a relatively minor effect on ϕ^{Rot} (Fig. 2.1.5c). Most hot subdwarfs are very slow rotators (Geier & Heber 2012) with projected rotational velocities below the detection limit of typically 5 km s^{-1}. In close binary systems the subdwarf may be spun up by tidal interaction, which leads to $v_{\text{rot}} \sin i$ exceeding 100 km s^{-1} in the most extreme cases (e. g. Kupfer et al. 2022).

- *Instrumental broadening:* observed spectra are obtained with spectrographs that have a limited wavelength resolution. Although the corresponding instrumental broadening profile can be complex, it is usually assumed to have a Gaussian shape

$$\phi^{\text{Instr}}(x) \approx \frac{2\sqrt{\ln 2}}{\Delta\lambda\sqrt{\pi}}\, e^{-4x^2 \ln 2}, \tag{2.1.36}$$

  where $x = (\lambda - \lambda_0)/\Delta\lambda$ and $\Delta\lambda$ is the full width at half maximum. For spectrographs with a single dispersion element $\Delta\lambda$ is approximately constant. High-resolution spectrographs usually use two dispersion elements (gratings or prisms) to split the incoming light, in which case they are called Échelle spectrographs. As discussed by Irrgang (2014), Échelle spectrographs feature a roughly constant spectral resolving power $R := \lambda/\Delta\lambda$, which means that $\Delta\lambda$ is a function of wavelength.

Both of these broadening effects can be applied after the computation of synthetic spectra and conserve the equivalent width of spectral lines.

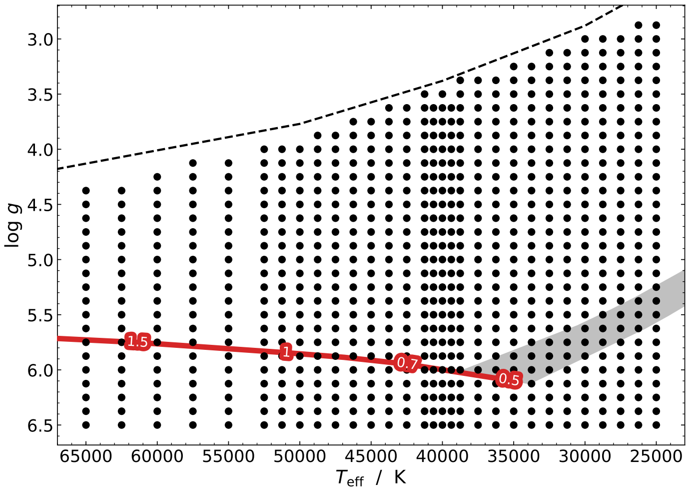

Figure 2.2.1. Models in the "sdOstar" grid for $\log n(\mathrm{He})/n(\mathrm{H}) = +1$. The location of the helium main sequence of Paczyński (1971) is shown in red, where masses are labelled in $M_{\odot}$. The grey band shows the solar-metallicity EHB of Dorman et al. (1993). The dashed line shows an approximate Eddington limit, which constrains the lowest possible hydrostatic surface gravities (Langer & Kudritzki 2014).

2.2 Hot subdwarf model grids

The first step in the spectral analysis of hot subdwarf stars is to obtain their basic atmospheric parameters: T_{eff}, $\log g$, and helium abundance $\log n(\mathrm{He})/n(\mathrm{H})$. These parameters are typically derived from the strengths and shapes of optical hydrogen and helium lines, which depend on the details of the model atmospheres (see Sect. 2.1.5). This therefore requires a grid of accurate model atmospheres that varies in all three dimensions and covers a large parameter space.

2.2.1 Previous model grids

Model grids for hot subdwarf stars are often subject to one of three limitations: small size, the assumption of LTE, or a lack of metal line opacity. Even if metal lines are not used for the spectral analysis, the opacity provided by metal lines has a strong impact on the atmospheric structure. Their effect is often described as "line-blanketing" – the additional opacity of a "blanket" of lines in the UV region leads to heating in continuum-forming layers ("backwarming") and cooling close to the surface (for a detailed discussion, see Hubeny & Mihalas 2014, p. 587). These effects appear in all model atmospheres; examples using TLUSTY are given by Lanz & Hubeny (2003).

Metal line blanketing can easily be treated under the assumption of LTE because level populations can then be computed using the Boltzmann equation (2.1.13). This approach has been used extensively for sdB stars, e. g. in the LINFOR (Heber et al. 2000) and STERNE codes (Behara & Jeffery 2006). Because the assumption of LTE breaks down for the hotter sdO stars, non-LTE models need to be applied. Early non-LTE models only considered hydrogen and helium (e. g. Husfeld et al. 1989; Stroeer et al. 2007) and were therefore lacking metal line blanketing. Non-LTE models with several hundred metal energy levels have been successfully applied to sdO stars since the 1990s, in particular using the Tübingen Model Atmosphere Package (TMAP, Dreizler 1993; Dreizler & Werner 1993) and similarly TLUSTY (Lanz et al. 1997). These analyses were limited to few stars and a relatively small parameter range. Non-LTE models that include hydrogen, helium, and few light elements were later used to fit large samples of hot subdwarf stars by Hirsch (2009, C or N) and Németh et al. (2012, C, N, O), but were still affected by a lack of metal opacity. In parallel, Przybilla et al. (2006) successfully tested a hybrid LTE/non-LTE approach to model sdB stars, which combined the advantages of LTE (fast computation, treatment of many metals) with approximate departures from LTE: the combination of the ATLAS/DETAIL/SURFACE (ADS) codes. This ADS method was later applied to more sdB stars by Latour et al. (2016) and Schneider et al. (2018) and is well-suited for sdO/B-type stars up to at least $T_{\mathrm{eff}} = 40\,000$ K (Schneider 2022). However, no extensive[2] grid of rigorous non-LTE model atmospheres is available that also considers the opacity of even the most important metals (i. e. up to iron and nickel).

---

[2] The non-LTE grid of Pacheco et al. (2021) is not suitable for spectral analysis due to its very sparse T_{eff} and $\log g$ sampling and lack of helium abundances.

Table 2.2.1. Model atoms used for the “sdOstar2020” grid with their number of explicit levels (L) and “super-levels” (SL). The latter consolidate several levels with similar energies and the same principal quantum number n. All model ions are based on those distributed with Tlusty 205 (Hubeny & Lanz 2017a).

Ion	L	SL	Ion	L	SL	Ion	L	SL
H I	17	–	O IV	31	8	S V	12	–
He I	19	5	O V	34	6	S VI	13	3
He II	20	–	O VI	15	5	Fe III	–	50
C II	17	5	Ne II	11	4	Fe IV	–	43
C III	16	7	Ne III	12	2	Fe V	–	42
C IV	21	4	Ne IV	10	2	Fe VI	–	42
N II	18	8	Si III	24	6	Ni III	–	36
N III	25	7	Si IV	19	4	Ni IV	–	38
N IV	15	8	P IV	14	–	Ni V	–	48
N V	10	6	P V	13	4	Ni VI	–	42
O II	21	6	S III	16	4			
O III	20	9	S IV	15	–	Total	463	440

2.2.2 The “sdOstar” model grid

Motived by the lack of a line-blanketed non-LTE model grid, we have computed a new and extensive grid based on non-LTE Tlusty 205 model atmospheres and Synspec 51 model spectra. The specific versions of both codes used here are described in the three-part manual of Hubeny & Lanz (2017a,b,c). A similar grid was already computed for O-type stars on the main sequence: the non-LTE “Ostar” grid of Lanz & Hubeny (2003), which includes metal opacity up to nickel. While this grid does not vary in helium abundance and does not extend to high surface gravities, it could serve as the basis of our new grid, which is therefore referred to as the “sdOstar” grid. Lanz & Hubeny (2003) provide a detailed description of the included physics – the following description of the “sdOstar” grid is limited to deviations from the “Ostar” grid.

Although the “sdOstar” grid was originally intended for the study of He-sdO stars, it also covers much of the sdB parameter space: from $T_{\rm eff} = 25\,000$ to $65\,000$ K, $\log g = 3.0$ to 6.5 in steps of 0.125, and $\log n({\rm He})/n({\rm H}) = -1.75$ to $+4.00$ (in steps of 0.25 up to +2.5, then steps of 0.5). The grids also extends to low surface gravities suitable for hot EHe and luminous post-AGB stars. Much of the O-Type and early B-Type MS parameter space is covered, including stars with non-solar helium abundances. The coverage in the $T_{\rm eff}$ - $\log g$ plane for one helium abundance is shown in Fig. 2.2.1. The model grid is not rectangular because stars beyond the Eddington limit (dashed lines in Fig. 2.2.1) are unstable. While the “Ostar” grid is comprised of 680 models, the “sdOstar” grid includes nearly 17 000 models. Each of these models took at least 12 hours to compute on a single CPU core. The computation of such are large model grid was possible by using the Remeis computer cluster, which allows up to 155 computations in parallel.

2.2.2.1 Metals and model atoms

The “Ostar” grid was computed for several scaled-solar metal abundances, ranging from metal-free to twice solar. Hot subdwarf stars show large variations in the abundance of metals (Geier 2013), but their iron abundances are often close to solar (e. g. O’Toole & Heber 2006). Here, the metal abundances were set to the solar values of Asplund et al. (2009), except for C (2× solar), O (1/10th solar), Ne (2× solar), Fe (1.5× solar), and Ni (10× solar). The latter enhancements compensate the lack of opacity from other iron-group elements, which is also why a relatively high microturbulent velocity of $\xi = 5\,{\rm km\,s^{-1}}$ was adopted. Such approaches have successfully been applied to individual hot subdwarfs, e. g. to the sdO BD +28° 4211 (Latour et al. 2015).

Table 2.2.2. Multiplets involved in the formation of important He i lines and their wavelengths in Å. Terms are prefaced with their principal quantum number *n*. Levels included as part of "super-levels" in the 24-level atom are marked in italics while missing terms are marked in boldface.

	Final state								
Initial state	2 P$^\circ$	3 P$^\circ$	4 P$^\circ$	*5 P$^\circ$*	*6 P$^\circ$*	*7 P$^\circ$*	*8 P$^\circ$*	***9 P$^\circ$***	***10 P$^\circ$***
1 ^{1}S	584.3	537.0	522.2	515.6	512.1	510.0	508.6	507.7	507.1
		3 P$^\circ$	4 P$^\circ$	*5 P$^\circ$*	*6 P$^\circ$*	*7 P$^\circ$*	*8 P$^\circ$*	***9 P$^\circ$***	***10 P$^\circ$***
2 ^{3}S		10830	3889	3188					
2 ^{1}S		5016	3965	3614	3448	3355			
		3 S	4 S	*5 S*	*6 S*	*7 S*	*8 S*	***9 S***	***10 S***
2 ^{3}P$^\circ$		7065	4713	4121	3868	3733	3652		
2 ^{1}P$^\circ$		7281	5048	4438	4169	4024	3936		
		3 P$^\circ$	4 P$^\circ$	*5 P$^\circ$*	*6 P$^\circ$*	*7 P$^\circ$*	*8 P$^\circ$*	***9 P$^\circ$***	***10 P$^\circ$***
2 ^{3}P$^\circ$			4517†	4045†	3829†				
2 ^{1}P$^\circ$			4911†	4383†	4141†				
		3 D	4 D	*5 D*	*6 D*	*7 D*	*8 D*	***9 D***	***10 D***
2 ^{3}P$^\circ$		5876	4472	4026	3820	3705	3634	3587	3554
2 ^{1}P$^\circ$		6678	4922	4388	4144	4009	3927	3872	
		3 F$^\circ$	4 F$^\circ$	*5 F$^\circ$*	*6 F$^\circ$*	*7 F$^\circ$*	*8 F$^\circ$*	***9 F$^\circ$***	***10 F$^\circ$***
2 ^{3}P$^\circ$			4470†	4025†					
2 ^{1}P$^\circ$			4921†						

Notes. $^{(\dagger)}$ Dipole forbidden transition.

The included model ions are listed in Table 2.2.1. An additional ionisation stage for each element was included by its ground state only. Because our intention was not to model the metal lines in the emergent spectrum but only their effect on the atmospheric structure, these model atoms are small and mostly include low-lying lines that contribute to the UV opacity. The model atoms are almost identical to those used for the "Ostar" grid; the most notable difference is the use of a larger 17-level H i atom here.

Tlusty treats most lines as depth-independent Doppler profiles, which systematically underestimates the strength of strong pressure broadened lines. Because this broadening becomes important at the high surface gravities of hot subdwarf stars, we treated more He i, C iii-iv and O iii-v lines as depth-dependent Voigt profiles and allowed existing profiles to be broader. Other metal lines were sampled at a frequency spacing of 0.75 Doppler widths, including about five million iron and nickel lines. The resulting number of considered frequencies is about 300 000.

2.2.2.2 Treatment of neutral helium

The optical spectra of helium-enriched hot subdwarf stars show strong He i lines, listed in Table 2.2.2. These lines have to be well reproduced to obtain reliable atmospheric parameters. The two main improvements to the treatment of He i in the "sdOstar" grid are described in the following.

Level dissolution. Energy levels close to the ionisation threshold have a probability to be *dissolved*, which means that electron is in fact not bound but free (Däppen et al. 1987; Hubeny et al. 1994). This effectively reduces the occupation numbers of these high-lying levels, an effect that was considered for H i and He ii in the "Ostar" grid. Level dissolution is more important at the

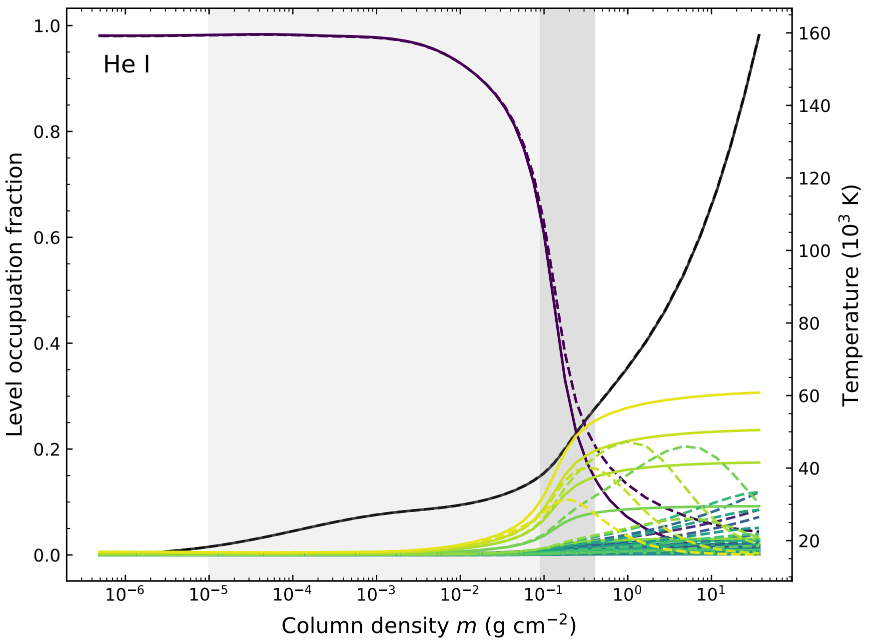

Figure 2.2.2. He I level occupation fraction without (solid) and with (dashed) level dissolution. The latter model is from the "sdOstar" grid and both were computed for $T_{\rm eff}$ = 40 000 K, $\log g$ = 6, and $\log n({\rm He})/n({\rm H})$ = +1. Yellow colors indicate high-lying levels. The continuum-forming region is marked in dark grey, while the light grey shade marks the origin of the strongest metal lines.

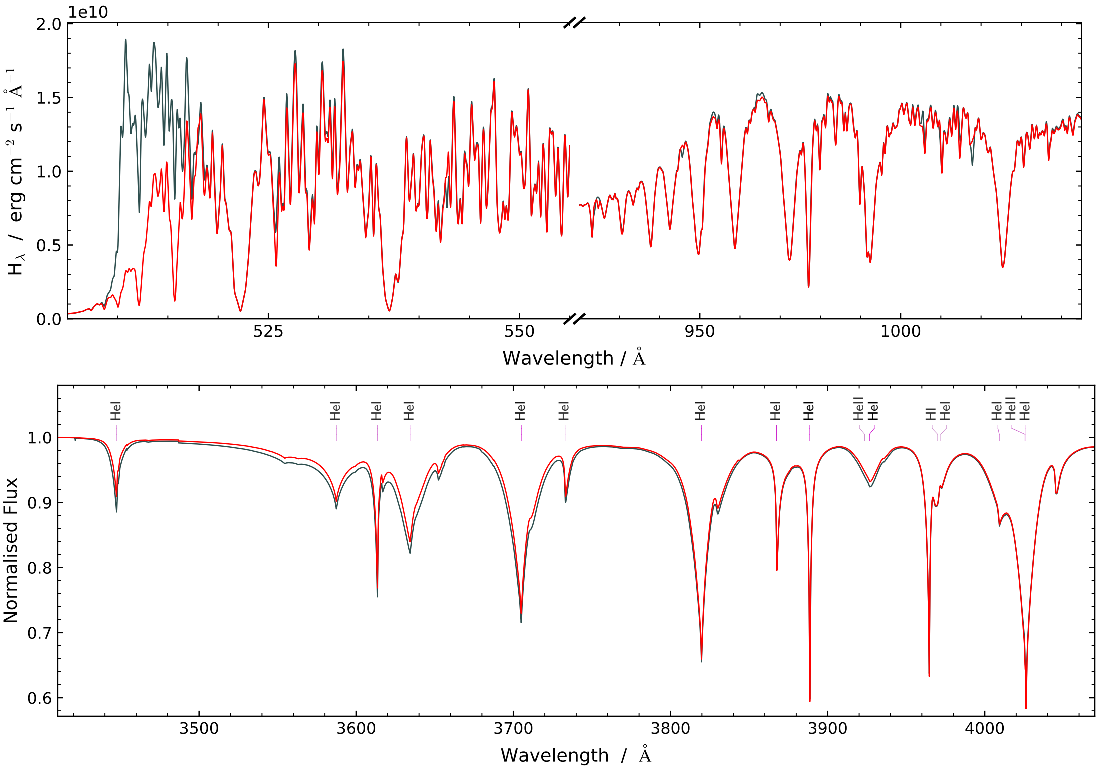

Figure 2.2.3. *Top*: TLUSTY emergent flux around the He I and H I ground state continua in the same models as Fig. 2.2.2: with (red) and without (grey) the updates to Voigt profiles, He I level dissolution, and pseudo-continua. For clarity, both spectra were convolved with Gaussian profiles at R = 2000. *Bottom*: SYNSPEC spectra from these models in the near-UV/blue range.

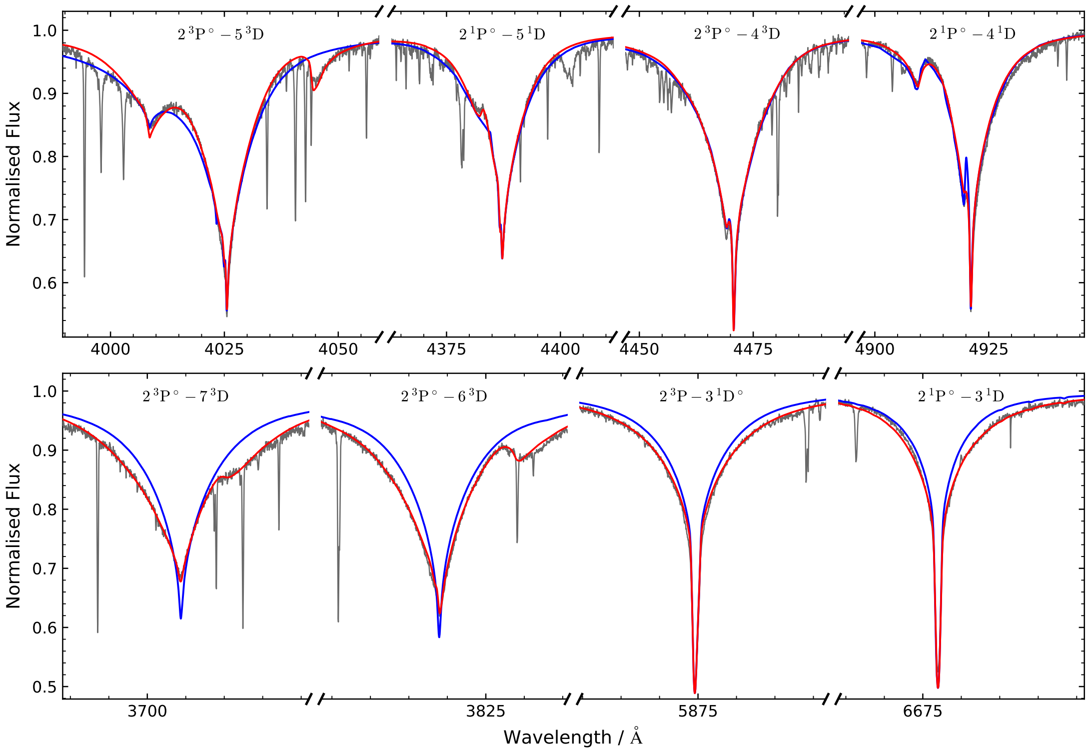

Figure 2.2.4. Models using the standard Synspec treatment of He I lines (blue) and the updated tables (red), both for fixed $T_{\rm eff}$ = 38 500 K, $\log g$ = 5.7, and $\log n({\rm He})/n({\rm H}) = +1.6$. The UVES observation of BD+25° 4655 (grey) is shown for comparison. *Top:* the four lines covered by the Shamey (1969) and Barnard et al. (1974) tables. *Bottom:* the strongest He I lines that previously had no broadening tables. The central He I lines are labelled with their lower and upper terms.

higher surface gravities of hot subdwarf stars. The “sdOstar” grid therefore also considers level dissolution for He I, the effect of which is shown Fig. 2.2.2. The highest included He I level is a so-called “super-level” that consolidates all $n = 8$ levels. It is strongly dissolved in the deepest line-forming region of hot subdwarf stars.

Transitions from these dissolved levels form a quasi-continuous source of opacity, the so-called *pseudo-continuum*, which adds to the photoionisation continuum. The “Ostar” grid considers pseudo-continua for the first three levels of H I, the first two levels of He II, and the ground state of He I. The “sdOstar” grid further includes pseudo-continua for the first five levels of He I and the first four levels of He II, and allows all pseudo-continua to extend to longer wavelengths. The updated He I and H I ground state continua are compared with the standard Tlusty treatment in the top panel of Fig. 2.2.3. Despite the increased opacity close to the He I ground state ionisation edge, the effect on the overall flux distribution is small. However, some optical He I lines are noticeably affected, as shown in the bottom panel of Fig. 2.2.3. These differences are mostly due to the He I 2p ^{3}P° (3423 Å) and 2p ^{1}P° (3681 Å) pseudo-continua. The He I 3636 Å (2p ^{3}P° ↔ 8d ^{3}D°) and 3927 Å (2p ^{1}P° ↔ 8s ^{1}D°) lines are affected by the dissolution of their upper level, which also applies to several lines with high-lying upper levels that are not included in the model atom. This pressure-dependence of He I line strengths is very useful for the determination of the surface gravity, which makes these improvements important.

Stark broadening tables. As discussed in Sect. 2.1.6, the shape of hydrogen and helium lines in hot subdwarf spectra is dominated by the Stark effect. The “sdOstar” grid makes use of detailed Stark broadening tables for hydrogen (Tremblay & Bergeron 2009), ionised helium (Schöning & Butler 1989), and neutral helium. The standard version of Synspec uses the broadening tables of Shamey (1969) for He I 4026, 4388, and 4922 Å and results from Barnard et al. (1974) for He I 4472 Å. These tables are well-tested but only cover four lines. Beauchamp et al. (1997) have calculated new profiles for 37 He I lines, tabulated for temperatures of 10 000, 20 000, and 40 000

K and electron densities of 10^{14} to $6{\times}10^{17}$ cm^{-3}. These tables were implemented in Synspec by Bédard et al. (2020), who kindly made the tables and his implementation available to us.

While testing, it became obvious that not all tabulated profiles are normalised to one; some have much smaller wavelength integrals. This is the case at low densities, where line profiles become narrow to the point that thermal Doppler broadening becomes more important than Stark broadening. In these cases, the line cores were not sampled in the calculation of Beauchamp et al. (1997). Because Doppler broadening was still applied, the predicted tables appear reasonable at first glance but have significantly too small integrals. Using these profiles in the spectrum synthesis would lead to incorrectly weak lines, so the affected profiles were not considered here. Because of this sampling issue, we instead used the tables of Gigosos & González (2009) for He I 4472 Å and the tables of Lara et al. (2012) for He I 4922 Å, both of which were implemented by Andreas Irrgang.

Figure 2.2.4 compares the standard Synspec treatment of He I and the updated Beauchamp et al. (1997) tables with the observed UVES spectrum of the He-sdO BD+25° 4655. Especially lines that previously lacked broadening tables, as well as their forbidden components are much improved and can now be used for the determination of surface gravities with the “sdOstar” grid. Even more detailed Stark broadening calculations for He I were performed by Tremblay et al. (2020), but could not be used for the present work because they are not yet publicly available. Future improvements should also include updates to the He II broadening tables of Schöning & Butler (1989), which do not cover all strong He II lines in the optical range, specifically the $n = 5$ series and lines blueward of 4101 Å.

2.2.3 Non-linear least squares fitting

The best model f_{mod} for an observation f_{obs} can be found by optimising some measure of fit quality. The standard method in spectroscopy is least squares fitting: one first computes for each data point i the weighted deviation

$$\chi_i = \frac{f_{\text{obs},i} - f_{\text{mod},i}}{\sigma_i}, \tag{2.2.1}$$

given uncorrelated Gaussian uncertainties σ_i. The goodness of fit is then the sum of squared χ_i,

$$\chi^2 = \sum_i^n \chi_i^2, \tag{2.2.2}$$

where n is the number of data points. The model at the global minimum of χ^2 is considered to be the best-fit. The reduced chi-square is defined as $\chi_r^2 := \chi^2/k$, where $k \approx n - m$ is the degree of freedom for m model parameters. For a perfect model and realistic uncertainties, χ_r^2 has an expected value of unity[3]. Large $\chi_r^2 > 1$ indicate a poor model or underestimated uncertainties while $\chi_r^2 < 1$ may result from overestimated uncertainties or too many free parameters (“overfitting”).

The evaluation of the model in Eq. (2.2.1) for a requested set of parameters requires interpolation in the model grid. Because the model grids used in this work are finely sampled in all dimensions, this is done using linear interpolation. This interpolated model must be re-sampled to the wavelength grid of the observation, preserving the total flux as described by Carnall (2017).

Most model fits in this work were performed using the Interactive Spectral Interpretation System (ISIS, Houck & Denicola 2000). The implementation of spectral fits in ISIS is described in detail by Irrgang (2014). These spectral fits are usually performed for the full spectrum, removing only regions that can not be reproduced by the model. The resulting χ^2 landscape is typically smooth enough that the minimum χ^2 can be found using the Levenberg–Marquardt algorithm (Levenberg 1944; Marquardt 1963), sometimes combined with the method of Powell (1964). Some analyses were also performed by using the Python libraries Scipy (Virtanen et al. 2020) for interpolation and LMFIT (Newville et al. 2014) for fitting. Least-squares fitting is extensively used in astrophysics; another application in this work are spectral energy distribution fits, as described in the next section.

---

[3] This is an approximation because the degree of freedom k is not known for non-linear models (Andrae et al. 2010).

2.3 Spectral energy distributions

A spectral energy distribution (SED) is usually defined as the energy emitted by an object as a function of wavelength or frequency. Instead of energy, the following will use the term SED to refer to the observed spectral flux density F_λ, as usual in stellar astrophysics.

Modern CCD technology has enabled several large and deep photometric surveys to image the sky using various filters that cover spectral regions from the ultra-violet (UV) to the infrared (IR). Combining apparent magnitudes from these and older surveys allows us to construct the SED for all except the very faintest or blended stars, many more than can be observed spectroscopically. Some of the most important modern photometric surveys in the optical range are SDSS (Alam et al. 2015a), APASS (Henden et al. 2015), Pan-STARRS (Magnier et al. 2020), SkyMapper (Onken et al. 2019), DES (Abbott et al. 2021), and *Gaia* (Riello et al. 2021). The *Gaia* mission also provided photometric low-resolution spectra that were considered as a sequence of 14 box filters here. The near-infrared range is covered by the ground-based 2MASS survey (Cutri et al. 2003), the UKIDSS survey (Lawrence et al. 2007), and several surveys carried out at the VISTA telescope, such as VHS (McMahon et al. 2013) and VIKING (Edge et al. 2013). Further data in the near- to mid-infrared are provided by the WISE satellite (Schlafly et al. 2019). The coverage is usually worst in the UV, where the only comprehensive modern survey was performed by the small GALEX satellite (Bianchi et al. 2017). Additional UV coverage for several bright hot subdwarfs was provided by low-resolution IUE spectra (González-Riestra et al. 2001).

2.3.1 SED fits as a powerful tool

Performing model fits to SEDs constructed from several observed magnitudes allows a determination of the effective temperature of a star, as well as its angular diameter on the sky Θ. The latter simply scales the model flux independent of wavelength. The details of our SED fitting method are described in Sect. 2.3.2, while its precision is tested in Appendix A.3.

F/G/K-type stars emit most of their flux between the near-UV and mid-IR spectral ranges. Because observed SEDs often cover these wavelength ranges well, it is possible to derive precise temperatures for such stars. Hotter stars emit most of their flux in the far- or even extreme-UV bands, which are more difficult to observe because of telluric[4] and interstellar absorption. Therefore, only the low-energy tail of their SED is observable. This means that the determination of effective temperatures from the SED is less accurate than for cool stars, especially if no far-UV photometry is available. On the other hand, the results for cool companions are less accurate if IR measurements are not available.

The SED fitting method is a powerful tool – especially if both UV and IR measurements are available. For example, samples of hot subdwarf and BHB candidates can be cross-checked for cool contaminants using photometric effective temperatures. For large samples, the number of main sequence F/G/K-type companions can be estimated for both the hot subdwarf and BHB catalogues. The SED of a binary system that consists of a fairly hot and a notably cooler star is double-peaked – such SEDs are usually termed composite. In the case of binary systems that contain a hot subdwarf and a main-sequence F/G/K-type star, both components can clearly be distinguished. Fainter companions to hot subdwarfs, such as M-type dwarfs or white dwarfs are usually not detectable because they are far less luminous than the hot component, even at IR wavelengths. Vice versa, sdO companions to main-sequence B or A-type stars are hard to detect with photometric measurements because the larger MS star outshines the hot subdwarf at all observable wavelengths.

2.3.2 The SED fitting method

Our SED fitting method is based on and a direct update to that of Heber et al. (2018). It was initially implemented and maintained by Andreas Irrgang. As the first step, photometric mea-

---

[4] Absorption by the Earth's atmosphere, see Moehler et al. (2014).

[5] the CALSPEC Vega spectrum of Bohlin et al. (2014), `alpha_lyr_stis_008.fits`.

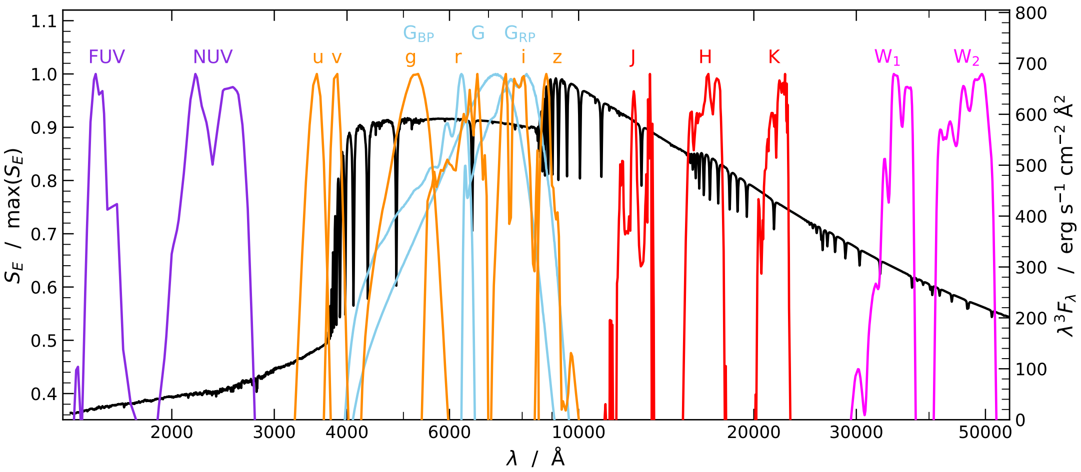

Figure 2.3.1. Energy response curves S_E for GALEX (violet), SkyMapper (orange), *Gaia* (light blue), 2MASS (red), and the first two WISE filters (fuchsia). The black curve shows the reference flux-calibrated Vega spectrum[5], multiplied with λ^3 for better visualisation.

surements are collected automatically by querying from more than 70 individual catalogues. This functionality was developed mainly by Kreuzer (2021). Many surveys can be queried via the Table Access Protocol (TAP) using the Astronomical Data Query Language (ADQL), a variant of the Structured Query Language (SQL). This makes it possible to automatically filter and retrieve photometric measurements, usually around the coordinates of an individual star. Many surveys can be queried through the VizieR[6] database (Ochsenbein et al. 2000). Recent additions to the SED query tool include the deep DES survey (Abbott et al. 2021), the 12-filter J-PLUS (López-Sanjuan et al. 2023) and S-PLUS surveys (Almeida-Fernandes et al. 2022), data from the Spitzer IR satellite (Spitzer Science 2009), and box filters constructed from the low-resolution BP/RP spectra provided by *Gaia* DR3 (De Angeli et al. 2023).

During the computation of synthetic magnitudes that can be compared to the observed magnitudes, one has to account for the complex optical systems that are used for photometric measurements. Before their detection on a CCD chip, photons travel through the Earth's atmosphere, are reflected through sets of telescope mirrors, and pass through a photometric filter that is transparent in a specific wavelength range. Near-UV and near-IR filters of ground-based surveys are especially affected by the weather-dependent telluric absorption, which, although corrected during the data reduction, still represents an important source of uncertainty. To compare synthetic spectra with such photometric measurements, the full optical response functions need to be known. These functions are either specified as the photon response function $S_P(\lambda)$, which is appropriate for photon-counting detectors such as a CCD, or the energy response function $S_E(\lambda) = \lambda S_P(\lambda)$, which is more appropriate for photocathodes. Some of the most important energy response functions are shown in Fig. 2.3.1, along with the observed SED of Vega. An excellent summary of photometric definitions is given in appendix A of Bessell & Murphy (2012).

Synthetic magnitudes are then for each filter constructed from a model spectrum. In general, a photometric system is defined by a reference flux density distribution F_ref in the form

$$\begin{aligned}\text{magnitude} &= -2.5\log\frac{\int F_\lambda \cdot S_E(\lambda)\,\mathrm{d}\lambda}{\int F_{\lambda,\mathrm{ref}} \cdot S_E(\lambda)\,\mathrm{d}\lambda}\\ &= -2.5\log\frac{\int F_\nu \cdot S_E(\nu)\,\mathrm{d}\nu}{\int F_{\nu,\mathrm{ref}} \cdot S_E(\nu)\,\mathrm{d}\nu}\end{aligned} \tag{2.3.1}$$

where F_λ is the model flux density. Here, we use the AB_ν absolute magnitude scale of Oke & Gunn (1983). In the AB_ν system, an object with zero magnitude has the same filter-averaged

---

[6] http://vizier.u-strasbg.fr/

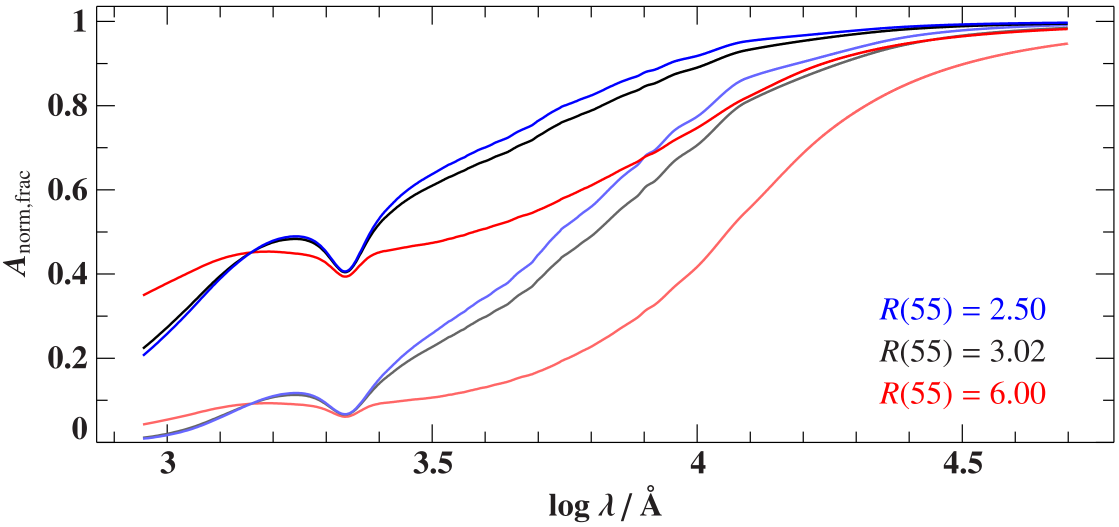

Figure 2.3.2. Empirical fractional normalised extinction curves for the Milky Way from Fitzpatrick et al. (2019) for different values of $R(55)$. The darker curves are for a colour excess $E(44-55) = 0.1$ mag while the lighter curves are for 0.3 mag. Note the logarithmic wavelength scale. The exact origin of the UV extinction bump at 2175 Å is still under debate; it is likely caused by a mixture of molecules (Ma et al. 2020).

flux as a source with constant flux per frequency interval $F_{\nu,\mathrm{ref}} = 10^{-48.6/2.5}\,\mathrm{erg\,s^{-1}\,cm^{-2}\,Hz^{-1}}$. A synthetic AB$_\nu$ magnitude for a model SED F_λ in a specific filter with an energy response S_E is therefore computed as

$$\begin{aligned}\mathrm{AB}_\nu &= -2.5\log\frac{\int F_\nu \cdot S_E(\nu)\,\mathrm{d}\nu}{\int S_E(\nu)\,\mathrm{d}\nu} - 48.6\\ &= -2.5\log\frac{\int F_\lambda \cdot S_E(\lambda)\,\mathrm{d}\lambda}{\int S_E(\nu)\,\mathrm{d}\nu} - 48.6\\ &= -2.5\log\frac{\int F_\lambda \cdot S_E(\lambda)\,\mathrm{d}\lambda}{\int -S_E(\lambda)\,\mathrm{d}\lambda^{-1}} + 2.5\log(c10^{-48.6/2.5})\end{aligned} \tag{2.3.2}$$

where c is the speed of light, and given that $F_\nu = F_\lambda\lambda^2/c$ and $\mathrm{d}\nu/\mathrm{d}\lambda = -c/\lambda^2$.

These synthetic AB magnitudes are then converted to the system used for each observed magnitude by adding a zero point. For a conversion from the AB system to the VEGAMAG system, this zero point is equivalent to the negative AB magnitude of Vega, which can be calculated by replacing F_λ with the observed SED of Vega $f_{\lambda,\mathrm{Vega}}$ in Eq. 2.3.2. Even surveys that were calibrated to the AB system often state a so-called zero-point correction that has to be removed from the provided observed magnitudes to bring them to the AB system. These zero point corrections are often larger than the statistical uncertainty associated with observed magnitudes and therefore represent an important source of uncertainty.

The flux distribution is altered by interaction with the interstellar medium (ISM) and depends on the column density of intervening ISM material along the line of sight. The ISM, here in the sense of dust grains between the Solar system and the observed star, scatters and absorbs light. This extinction is wavelength dependent such that blue light is more affected than red light, which is sometimes referred to as the "reddening" effect. Interstellar extinction is considered here using the empirical extinction curves of Fitzpatrick et al. (2019). The total extinction in monochromatic magnitudes is defined as

$$A(\lambda) := -2.5\log\frac{f_\lambda}{F_\lambda} + 5\log\frac{\Theta}{2} =: A_{\mathrm{norm}}(\lambda) + A_\Theta(\lambda). \tag{2.3.3}$$

Here, f_λ is the observed and F_λ the intrinsic SED. Because the angular diameter Θ is not known ab initio, the total extinction is usually normalised. Following Fitzpatrick et al. (2019), this normalisation is given as

$$k(\lambda - 55) = \frac{A(\lambda) - A(55)}{A(44) - A(55)} \tag{2.3.4}$$

where $k(\lambda - 55)$ is the average Milky Way extinction curve given by Table 3 of Fitzpatrick et al. (2019) and 44 and 55 are short for 4400 Å and 5500 Å. The extinction model of Fitzpatrick et al. (2019) is parametrised with the monochromatic colour excess $E(44 - 55)$ and the extinction parameter

$$R(55) \coloneqq \frac{A(55)}{E(44 - 55)}. \tag{2.3.5}$$

For a fixed value of $R(55)$, the colour excess governs the overall strength of the extinction, as visualised in Fig. 2.3.2. One can combine

$$A_{\mathrm{norm}}(\lambda) = E(44 - 55) \cdot (k(\lambda - 55) + R(55))\,. \tag{2.3.6}$$

The fractional extinction curve can be computed from the extinction in magnitudes $A(\lambda)$ as

$$A_{\mathrm{norm,frac}} = 10^{-A(\lambda)/2.5} \tag{2.3.7}$$

and is applied to the model fluxes before synthetic magnitudes are computed. The second part of the extinction is applied to the synthetic AB magnitudes as

$$\mathrm{AB}_{\mathrm{corrected}} = \mathrm{AB} - 5\log\frac{\Theta}{2}. \tag{2.3.8}$$

Similar to spectroscopic fits, a least squares method is used to minimise the differences between the synthetic and the observed magnitudes. The colour excess is usually a free parameter in our SED fits while the extinction parameter $R(55)$ is usually fixed to 3.02, an average value for the Milky Way's diffuse ISM.

2.3.3 From atmospheric to stellar parameters: the role of the parallax

Photometric angular diameters are especially powerful when combined with parallax measurements ϖ, because they allow the determination of stellar radii R and luminosities L. The stellar radius is simply given by the geometric relation

$$R = \frac{\Theta}{2\varpi} \tag{2.3.9}$$

while the stellar luminosity can be derived from the radius and effective temperature

$$L = 4\pi R^2 \sigma_{\mathrm{SB}} T_{\mathrm{eff}}^4, \tag{2.3.10}$$

where σ_{SB} is the Stefan-Boltzmann constant. Here, T_{eff} can be determined from the SED itself but can also be fixed to the spectroscopic value, if available. If also the surface gravity g is known, the stellar mass M can be derived as

$$M = g\frac{R^2}{G}, \tag{2.3.11}$$

where G is the gravitational constant. The surface gravity can either be measured by independent spectroscopy, or, for A- and B-type stars with very good photometry, from the strength of the hydrogen Balmer jump.

Because of the lack of parallax measurements, stellar radii and luminosities have never been determined for large samples of hot subdwarf and blue horizontal branch stars. This has changed with the advent of precise parallax data from the *Gaia* mission (Gaia Collaboration et al. 2016), especially *Gaia* EDR3 (Gaia Collaboration et al. 2021), which is used throughout this work. Zero-point corrections are performed following Lindegren et al. (2021), and the parallax uncertainty is inflated according to equation 16 of El-Badry et al. (2021). In particular radii can be determined very accurately and with small systematic uncertainties.

Chapter 3

A close up on individual hot subdwarfs

This chapter presents six detailed analyses of particularly interesting hot subdwarf stars that can serve as benchmarks for evolutionary models. Section 3.1 provides a detailed analysis of the prototypical "heavy-metal" iHe-sdOB LS IV−14°116 and its twin Feige 46. Newly identified lines in their optical spectra are used to derive the abundance of 19 metals, which are found to differ strongly from those of He-poor hot subdwarfs of similar temperature. The heavy metal abundances of two such helium-poor sdOB stars are obtained from an analysis of far-UV spectra in Sect. 3.2. Section 3.3 presents a detailed spectroscopic study of the lead-rich iHe-sdOB EC 22536−5304, which is not only found to be the most lead-rich star known, but is also identified to be in a binary system with a very metal-poor F-type subdwarf. Another unique long-period binary is studied in Sect. 3.4: BD −7° 5977, which consists of a sdOB and a subgiant K-type star. High-resolution infra-red spectra of the K-type allow a measurement of its $^{12}C/^{13}C$ ratio, which can be used to test whether or not mass transfer has occurred. The analysis of the first magnetic hot subdwarf stars is performed in Sections 3.5 and 3.6. These helium-rich sdO stars are found to have strong and time-variable magnetic fields of the order of 300 kG and will eventually evolve to become strongly magnetic white dwarfs.

3.1 Heavy-metal subdwarfs: the UVES spectra of LS IV−14°116 and Feige 46

The analysis presented in this section was published as a part of the Dorsch et al. (2020) paper. Large parts of the content of this chapter are taken verbatim from this paper. Because new parallax measurements became available for both stars after the publication of this paper, the stellar parameters for both LS IV−14° 116 and Feige 46 as presented in Sect. 3.1.2 were updated for this thesis. Other results are unaffected by this update.

3.1.1 Introduction

As discussed in Sect. 1.3, the atmospheres of most sdBs are dominated by hydrogen as a result of atomic diffusion, damped by turbulence and mass loss (Michaud et al. 2011; Hu et al. 2011). In contrast, many sdO stars are extremely helium-enhanced and show almost no hydrogen in their atmospheres (Stroeer et al. 2007; Németh et al. 2012; Fontaine et al. 2014). Helium-rich sdO stars are thought to be the result of either a delayed He-flash at the top of the red giant branch (Miller Bertolami et al. 2008) or the merging of two low-mass stars, for example two He-WDs (Zhang & Jeffery 2012). Unlike the He-poor sdB stars, these He-sdOs do not seem to be influenced by diffusion processes (due to convection caused by the ionisation of He II; Groth et al. 1985). Two questions arise: will most He-sdOs evolve to become He-poor sdBs or do they represent a distinct population? And at which point in the stellar evolution does atmospheric diffusion become important? Both Feige 46 and LS IV−14°116 are part of the small population of intermediately He-rich sdOB (iHe-sdOB) stars that is of special interest when trying to address these questions (Jeffery et al. 2012). They share many physical properties, which make them a unique pair not only among the iHe-sdOBs.

Kinematic analyses of LS IV−14°116 (Randall et al. 2015) and Feige 46 (Latour et al. 2019a) have shown that both stars are likely to be members of the galactic halo, unlike most helium-rich hot subdwarfs (Martin et al. 2017). Both stars show light variations due to pulsations. Since its light variations were discovered by Ahmad & Jeffery (2005) LS IV−14°116 remained the sole member of its class of pulsating stars, now termed V366 Aqr variables, until Latour et al. (2019a) identified similar pulsations in Feige 46. Ahmad & Jeffery (2005) found two periods of 1950 s and 2900 s in the light variations of LS IV−14°116. These pulsations have been confirmed in follow-up observations by Jeffery (2011) and Green et al. (2011) who identified four additional periods up to 5084 s. Pulsational light variations in sdB stars are well established. Both pressure (p-mode) and gravity (g-mode) oscillations have been observed in hot subdwarf stars – the former have periods of a few minutes (short periods), whereas the periods of the latter range from 30 minutes to a few hours (long periods; for recent compilations see Holdsworth et al. 2017; Reed et al. 2018).

The pulsations observed in He-poor sdB stars are thought to be driven by an opacity (κ-) mechanism which is related to an iron/nickel opacity bump in their thin stellar envelope. This mechanism can produce both short period oscillations (Charpinet et al. 1996, 1997) at the temperature of LS IV−14°116 and Feige 46 (~35 000 K) and long periods (Green et al. 2003; Jeffery & Saio 2006) at lower temperatures. The detection of long periods in LS IV−14°116 is remarkable because the κ-mechanism predicts that short-period pulsations should be excited at the high effective temperature and surface gravity of LS IV−14°116, which, however, are not observed. How the observed long-period pulsations are excited in LS IV−14°116 remains an open question. Battich et al. (2018) and Miller Bertolami et al. (2011, 2020) show that gravity modes stochastically excited by He-flash driven convection are able to produce long-period pulsation similar to that observed in LS IV−14°116. This would place LS IV−14°116 in an evolutionary state immediately following one of the first He-core flashes, subsequent to either a late hot He-flash or the merging of two He-WDs. Alternatively, Saio & Jeffery (2019) show that the pulsation of LS IV−14°116 could also be explained by carbon and oxygen opacity bumps, but would require very substantial C/O enrichment at temperatures around 10^6 K.

Another striking peculiarity of LS IV−14°116 and Feige 46 is their chemical composition characterised by extreme overabundances of heavy metals. Naslim et al. (2011) found LS IV−14° 116 to be enriched in strontium, yttrium, and zirconium to the order of 10 000 times solar values. A very similar abundance pattern was found in Feige 46 by Latour et al. (2019b). Other recently discovered "heavy metal" subdwarfs include the lead-rich iHe-sdOBs [CW83] 0825+15 (Jeffery et al. 2017), EC 22536-4304 (Jeffery & Miszalski 2019), PG 1559+048, and FBS 1749+373 (Naslim et al. 2020). This extreme enrichment compared to solar values is thought to be the result of strong atmospheric diffusion processes. While the population of known "heavy metal" subdwarfs continues to grow, it remains too small to relate the observed differences in enrichment to specific ranges in their atmospheric parameters. In addition, theoretical diffusion calculations for iHe-sdOB stars are still lacking.

In this investigation we focus on the determination and comparison of the detailed abundance patterns of LS IV−14°116 and Feige 46. We have recently obtained high-resolution spectra for Feige 46 at the ESO VLT, while archival spectra were retrieved for LS IV−14°116. Already a coarse inspection of the spectra showed them to be strikingly similar. The same metal lines are detected in both stars at very similar strength, indicating that the abundances are similar as well. It is therefore tempting to study both stars jointly.

Before addressing the main aim of the study we derive the mass, radius, and luminosity of both stars in Sect. 3.1.2, based on photometric measurements, *Gaia* astrometry, and the spectroscopic surface gravity and effective temperature. In Sect. 3.1.3, we give an overview of the available spectra. The atmospheric parameters used for our abundance analysis are described in Sect. 3.1.4 while the abundance analysis itself is described in Sect. 3.1.5. We summarise our results in Sect. 3.1.6.

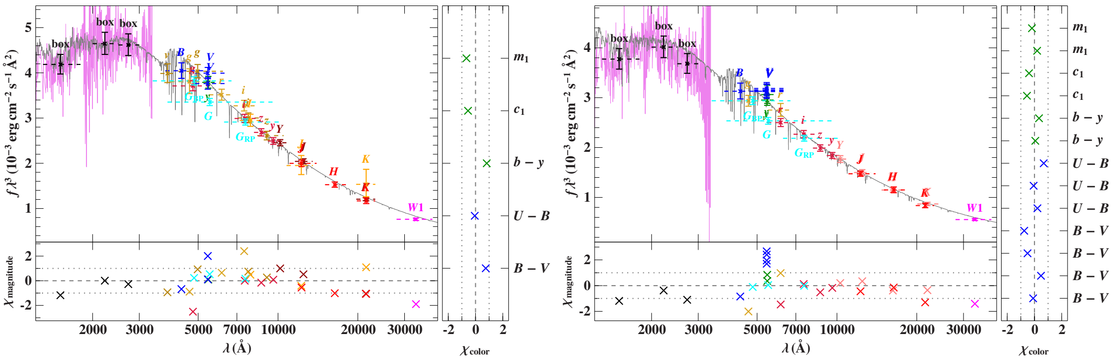

Figure 3.1.1. Comparison of the smoothed final synthetic spectrum (grey line) of LS IV−14°116 (left) and Feige 46 (right) with photometric data. For LS IV−14°116, the two black data points labelled "box" are binned fluxes from an IUE spectrum (LWP10814LL, magenta line, Wamsteker et al. 2000). Three IUE spectra were used to construct the box filters for Feige 46 (SWP17466RL, SWP20342L, LWR16264LL). Filter-averaged fluxes are shown as coloured data points that were converted from observed magnitudes. The dashed horizontal lines indicate filter widths. The residual panels at the bottom and right side respectively show the differences between synthetic and observed magnitudes/colours. The following colour codes are used to identify the photometric systems: SDSS (yellow, Henden et al. 2015; Alam et al. 2015a), SkyMapper (dark yellow, Wolf et al. 2018), Pan-STARRS1 (red, Chambers et al. 2016), Johnson-Cousins (blue, Mermilliod 1994; Henden et al. 2015; O'Donoghue et al. 2013), Strömgren (green, Kilkenny et al. 1988; Hauck & Mermilliod 1998), *Gaia* (cyan, Gaia Collaboration 2018), UKIDSS (rose, Lawrence et al. 2013), VISTA (dark red, McMahon et al. 2013), DENIS (orange, DENIS Consortium 2005), 2MASS (bright red, Cutri et al. 2003), and WISE (magenta, Schlafly et al. 2019).

3.1.2 Parallax, spectral energy distribution and stellar parameters

Combining the geometric parallax with photometry allows us to convert atmospheric parameters to the fundamental stellar parameters mass, radius, and luminosity without relying on predictions from evolutionary models. Here, photometry is required to derive the angular diameters of the stars. We have combined apparent magnitudes from the ultraviolet to the infrared to construct new observed spectral energy distributions of LS IV−14°116 and Feige 46 (see Fig. 3.1.1). For each star, our final synthetic spectrum was then scaled to fit this SED using χ^2 minimisation using the method described in Sect. 2.3. Interstellar reddening is considered after Fitzpatrick et al. (2019), assuming an extinction parameter $R(55) = 3.02$. Fit parameters are the angular diameter Θ and $E(44-55)$, which is the monochromatic analogon of the colour excess $E(B–V)$.

To derive the stellar radius R, the *Gaia* parallax ϖ is combined with the best-fit angular diameter $\Theta = 2R\varpi$. Since the publication of Dorsch et al. (2020), the data release EDR3 of the *Gaia* mission provided updated parallaxes for LS IV−14°116 and Feige 46, the latter of which changed considerably (1.86 ± 0.07 mas to 2.03 ± 0.06 mas). This allowed us to redetermine the stellar parameters of Feige 46, while the parameters of LS IV−14°116 remained essentially unchanged. The stellar mass M is then derived using the spectroscopic surface gravity $g = GM/R^2$, where G is the gravitational constant ($\log g = 5.85$ for LS IV−14°116). The stellar luminosity L is based on the spectroscopic effective temperature ($T_{\rm eff} = 35500$ K). The atmospheric parameters used for the SED are the same as those for the spectroscopic analysis and are described in Sect. 3.1.4. For both stars, we assumed systematic errors of 0.1 dex in $\log g$ and 1000 K in $T_{\rm eff}$. The results of this analysis are listed in Table 3.1.1. In contrast to the results of Dorsch et al. (2020), the derived stellar mass for Feige 46 ($0.44 \pm 0.12\,M_\odot$) is identical within our uncertainties to the value obtained for LS IV−14°116 ($0.38 \pm 0.10\,M_\odot$). As before, both masses are consistent with the canonical mass suggested by extreme horizontal branch models, about $\sim 0.47\,M_\odot$ depending on metallicity (Dorman et al. 1993; Han et al. 2003).

Table 3.1.1. Parallax and parameters derived from the SED fitting. The atmospheric parameters $T_{\rm eff}$ and $\log g$ are derived from spectroscopy and discussed in Sect. 3.1.4. To be consistent with Dorsch et al. (2020), stellar parameters are stated as mean values, rather than the mode.

	LS IV−14°116	Feige 46
ϖ (mas)	2.38 ± 0.07	2.03 ± 0.06
d (pc)	420 ± 12	493 ± 15
$\log \Theta$ (rad)	−10.882 ± 0.009	−10.959 ± 0.009
$E(44-55)$ (mag)	0.034 ± 0.005	0.012 ± 0.005
$T_{\rm eff}$ (K)	35500 ± 1000	36100 ± 1000
$\log g$	5.85 ± 0.10	5.93 ± 0.10
$R/R_\odot$	0.122 ± 0.005	0.119 ± 0.005
$M/M_\odot$	0.38 ± 0.10	0.44 ± 0.12
$L/L_\odot$	21 ± 3	22 ± 3

Table 3.1.2. UVES spectra used in the present analysis. For LS IV−14°116, only spectra with a sufficient signal-to-noise ratio for cross-correlation were used. Total exposure times are given per wavelength range and resolution.

Star	Range / Å	R	$n_{\rm exp}$	$\sum t_{\rm exp}$ / s	Run ID
Feige 46	3305 – 4525	40970	4	5920	0104.D-0206(A)
	4620 – 6645	42310	4	5920	
LS IV−14°116	3290 – 4525	40970	12	3600	087.D-0950(A)
	4788 – 6835	42310	15	4500	
	3290 – 4525	49620	18	3600	095.D-0733(A)
	4788 – 6835	51690	18	3600	
	3290 – 4525	58640	64	12800	
	4788 – 6835	66320	71	14200	

3.1.3 Spectroscopic observations

We have obtained four VLT/UVES spectra of Feige 46 in February 2020 with a total exposure time of 5920 s (ID 0104.D-0206(A)). These spectra have a resolving power of $R \approx 41000$ and cover the spectral range from 3305 Å to 6645 Å with gaps at 4525 – 4620 Å and 5599 – 5678 Å. The individual spectra were stacked after cross-correlation to obtain a single spectrum with an increased signal-to-noise ratio (S/N) of about 80. The radial velocity obtained, $\upsilon_{\rm rad} = 89$ km s^{-1}, is fully consistent with the value found by Drilling & Heber (1987), 90 ± 4 km s^{-1}. For the spectral analysis the observed spectrum was shifted to the stellar rest frame. We refer to Latour et al. (2019b) for the description and analysis of older spectra of Feige 46, including ultraviolet observations.

LS IV−14°116 has been observed extensively with the UVES spectrograph. A total of 788 spectra are available in the ESO archive (corresponding to 394 exposures). Spectra were taken as part of two programmes: on 7 September 2011 (ID 087.D-0950(A)) and between 23 and 27 August 2015 (ID 095.D-0733(A)). These programs have used time-resolved spectroscopy in order to relate the observed photometric variability to radial velocity variations (Jeffery et al. 2015; Martin et al. 2017). We have combined spectra from both runs to create a high-S/N spectrum that is suitable for a detailed abundance analysis. For each resolution, spectra with the highest S/N, typically S/N = 16 to 25, were cross-correlated and stacked. These stacked spectra were convolved with a Gaussian function to match the lowest common resolutions, $R = 40970$ for the blue and $R = 42310$ for the red range, and were then co-added. We then shifted the spectrum to

Table 3.1.3. Sources of oscillator strengths for detected lines of heavy metals in Feige 46 and LS IV−14°116.

Ion	N_{ident}	Reference
Ga III	9	O'Reilly & Dunne (1998)
Ge III	3	Naslim et al. (2011)
Ge IV	6	O'Reilly & Dunne (1998)
Kr III	17	Raineri et al. (1998)
Sr II	2	Fernández-Menchero et al. (2020)
	3	Kurucz/Linelists
Sr III	35	Kurucz/Atoms
Y III	2	Naslim et al. (2011)
	3	Fernández-Menchero et al. (2020)
Zr III	2	Kurucz/Linelists
Zr IV	16	Rauch et al. (2017)
Sn IV	2	Kaur et al. (2020)
Pb IV	1	Safronova & Johnson (2004)

the stellar rest frame, correcting for the high radial velocity of about $v_{\text{rad}} = -154\ \text{km s}^{-1}$. The final spectrum has a mean effective S/N of about 200, limited by small-scale artefacts. Details of the UVES spectra used in the present analysis are given in Table 3.1.2.

Randall et al. (2015) have carried out spectropolarimetry of LS IV−14°116 with VLT/FORS2 to search for a magnetic field. While no polarisation could be detected, their observations produced a flux spectrum of excellent quality (spectral resolution $\Delta\lambda \approx 1.8$ Å, S/N ≈ 700). In contrast to the UVES spectra, this long-slit spectrum does not have the normalisation issues that frequently occur in the reduction procedure of Échelle spectra. The FORS2 spectrum is therefore useful for determining atmospheric parameters based on broad hydrogen and helium lines.

3.1.4 Methods

The excellent UVES spectra enable a detailed abundance analysis, as well as a consistent comparison of abundances between LS IV−14°116 and Feige 46, which is described in the following section. To minimise systematic errors, we have analysed the spectra of both Feige 46 and LS IV−14° 116 using the same fitting method and the same type of model atmospheres, following the procedure described by Latour et al. (2019b) and Dorsch et al. (2019). This analysis is based on model atmospheres and synthetic spectra computed using the hydrostatic, homogeneous, plane-parallel, non local thermodynamic equilibrium (non-LTE) codes TLUSTY and SYNSPEC (Hubeny 1988; Hubeny & Lanz 2017a).

Our line list is based on atomic data provided by R. Kurucz[1]. We have extended this line list to include lines from additional heavy ions. The atomic data previously collected are described in Dorsch et al. (2019) and Latour et al. (2019b). This list was further extended to model the rich spectrum of Feige 46. The main sources for detected lines of heavy ions are listed in Table 3.1.3. Heavy elements (here $Z > 30$) in ionisation stages I-III are included in LTE using the treatment of Proffitt et al. (2001) who added ionisation energies and partition functions from R. Kurucz's ATLAS9 code (Kurucz 1993) to SYNSPEC. Partition functions for higher ionisation stages are calculated as described by Latour et al. (2019b).

As in our previous analysis of Feige 46 (Latour et al. 2019b), all model atmospheres were calculated using the atmospheric parameters derived by Latour et al. (2019a), namely $T_{\text{eff}} = 36\,100$ K, $\log g = 5.93$, and a helium abundance of $\log n(\text{He})/n(\text{H}) = -0.32$. Atmospheric parameters for LS IV−14°116 were derived by Randall et al. (2015) based on a high S/N FORS2 spectrum

---

[1] `http://kurucz.harvard.edu/linelists/gfnew/gfall08oct17.dat`; see also Kurucz (2018).

(T_{eff} = 35 150 K, $\log g$ = 5.88, $\log n(\text{He})/n(\text{H})$ = −0.62). We used a grid of line-blanketed non-LTE models to re-fit the same FORS2 spectrum and we obtained T_{eff} = 35 500 K, $\log g$ = 5.85, $\log n(\text{He})/n(\text{H})$ = −0.60, which is fully compatible with the results of Randall et al. (2015). The model grid used for this fit includes H, He, C, N, O, Ne, Mg, Al, Si, and Fe in non-LTE with abundances appropriate for LS IV−14°116.

Using the atmospheric parameters reported above for each star, we then constructed series of models by varying the abundance of one element at a time. These models also include nickel in non-LTE. Based on these grids, we have determined metal abundances using the χ^2-fitting program SPAS developed by Hirsch (2009).

Both Feige 46 and LS IV−14°116 show slightly broadened lines that are best reproduced at a projected rotational velocity of $\upsilon_{\text{rot}} \sin i = 9\,\text{km}\,\text{s}^{-1}$. This broadening is not solely caused by rotation but instead results from unresolved high-order pulsations. Indeed, Jeffery et al. (2015) found that the principal pulsation mode in LS IV−14°116 (1950 s) leads to radial velocity variations with a semi-amplitude of about $5.5\,\text{km}\,\text{s}^{-1}$. They also came to the conclusion that other pulsation periods lead to additional unresolved motion. Similar variability could be present in Feige 46, which would explain the observed broadening, given that the UVES exposure times (1480 s) cover a significant fraction of the shortest period observed in Feige 46 (2295 s). However, the exposure times of the UVES spectra of LS IV−14°116 were much shorter (200 s or 300 s). The remaining broadening, despite cross-correlating individual exposures before co-adding, may be explained by a combination of uncertainties in the cross-correlation, high-order pulsations, unresolved motion due to multiple periods, and actual rotation. Jeffery et al. (2015) also found evidence for differential pulsation: line strength and pulsation amplitude might be correlated. Therefore, correlating single spectra using specific strong lines would not perfectly mitigate the broadening in the stacked spectrum for weak lines. However, differential pulsation was not confirmed in the radial velocity study of Martin et al. (2017). Additional broadening may be caused by microturbulence (υ_{tb}). However, as shown by Latour et al. (2019b), a microturbulence of $5\,\text{km}^{-1}$ is too high to simultaneously reproduce UV and optical lines in Feige 46. We have therefore adopted $\upsilon_{\text{tb}} = 2\,\text{km}\,\text{s}^{-1}$ for both stars which leads to negligible broadening.

3.1.5 Individual abundances

In the following section, we present the result of our abundance analysis for each element in detail. A summary of the abundances derived for Feige 46 and LS IV−14°116 is given in Table 3.1.4. Abundances stated in the text are always relative to solar values. Examples of the strongest lines from light elements for both stars along with the final models are shown in the top panels of Fig. 3.1.2. The full spectra are presented in Sect. B.1. The following paragraphs summarise the derivation of abundances for light metals and the iron group.

Carbon, nitrogen, and oxygen: Plenty of carbon, nitrogen, and oxygen lines are available to determine abundances, including the lines shown in Fig. 3.1.2. Both stars have a carbon abundance close to the solar number fraction; slightly enhanced for Feige 46 (+0.25 dex) and somewhat depleted for LS IV−14°116 (−0.19 dex). Nitrogen is overabundant in both stars by 0.46 dex and 0.28 dex, respectively, while oxygen is significantly underabundant by −1.03 dex and −1.23 dex. On average, the CNO content of LS IV−14°116 is lower than that of Feige 46 by about 0.2 dex. Although the general fit for carbon lines is good, there is some discrepancy between the strongest C II and C III lines. We attribute this mostly to non-LTE effects that are not perfectly modelled. For instance, the C II 4267.3 Å doublet is too strong in our synthetic spectra, while the C III triplet 4152.5, 4156.5, 4162.9 Å is slightly too weak. C II 5661.9 Å is predicted to be in emission although no line is observed at this position in the UVES spectrum of LS IV−14°116. Some nitrogen lines display similar behaviour: N II 4630.5, 4643.1, 4803.3, 5005.2, 5179.5, and 5710.8 Å are too weak in our models and were not considered for determining the nitrogen abundance. These lines also appeared in emission in the synthetic spectra of the iHe-sdO HD 127493 by Dorsch et al. (2019), who used the same model atoms. Resolving these issues is a complex task because almost all optical lines of C II-III and N II originate from high-lying levels. The population

Table 3.1.4. Abundance results for Feige 46 and LS IV−14°116 by number fraction ($\log \epsilon$) and number fraction relative to solar ($\log \epsilon/\epsilon_\odot$). The number of resolved lines used per ionisation stage is given in the last column.

	Feige 46			LS IV−14°116		
	$\log \epsilon$	$\log \epsilon/\epsilon_\odot$	$N_{\rm lines}$	$\log \epsilon$	$\log \epsilon/\epsilon_\odot$	$N_{\rm lines}$
H	-0.17 ± 0.02	-0.13 ± 0.02		-0.10 ± 0.02	-0.06 ± 0.02	
He	-0.49 ± 0.03	0.62 ± 0.04		-0.70 ± 0.08	0.41 ± 0.08	
C II-IV	-3.36 ± 0.13	0.25 ± 0.14	6/16/1	-3.80 ± 0.12	-0.19 ± 0.13	6/9
N II-III	-3.74 ± 0.08	0.46 ± 0.10	23/14	-3.92 ± 0.06	0.28 ± 0.08	20/3
O II-III	-4.38 ± 0.10	-1.03 ± 0.11	12/1	-4.57 ± 0.10	-1.23 ± 0.11	11/1
F	$<-5.79^{+0.50}$	$<1.69^{+0.53}$		$<-5.99^{+0.50}$	$<1.49^{+0.53}$	
Ne II	-4.48 ± 0.07	-0.38 ± 0.12	18	-4.60 ± 0.06	-0.49 ± 0.12	13
Na				$<-5.65^{+0.50}$	$<0.15^{+0.50}$	
Mg II	-5.22 ± 0.02	-0.79 ± 0.04	1	-5.50 ± 0.02	-1.07 ± 0.05	1
Al III	$<-6.33^{+0.40}$	$<-0.74^{+0.40}$		$<-6.52^{+0.30}$	$<-0.93^{+0.30}$	
Si III-IV	-5.68 ± 0.03	-1.15 ± 0.04	1/3	-6.13 ± 0.07	-1.60 ± 0.07	1/2
P III	-6.61 ± 0.05	0.02 ± 0.06	1	-6.85 ± 0.05	-0.23 ± 0.06	1
S	$<-5.77^{+0.30}$	$<-0.85^{+0.30}$		$<-6.10^{+0.30}$	$<-1.18^{+0.30}$	
Cl	$<-6.22^{+0.40}$	$<0.32^{+0.45}$		$<-6.41^{+0.40}$	$<0.13^{+0.45}$	
Ar III	-5.92 ± 0.14	-0.28 ± 0.20	3	-5.64 ± 0.04	-0.01 ± 0.14	2
Ca	$<-6.32^{+0.40}$	$<-0.62^{+0.40}$		$<-6.46^{+0.30}$	$<-0.76^{+0.30}$	
Ti III-IV	-5.68 ± 0.12	1.41 ± 0.13	3/2	-5.79 ± 0.12	1.30 ± 0.13	3/2
*Cr	-5.85 ± 0.17	0.55 ± 0.18				
*Mn	$<-5.86^{+0.40}$	$<0.75^{+0.40}$				
*Fe	-4.81 ± 0.14	-0.27 ± 0.15		$<-5.00^{+0.30}$	$<-0.46^{+0.30}$	
*Co	-6.02 ± 0.21	1.03 ± 0.23				
Ni III	-4.70 ± 0.19	1.12 ± 0.19	8	-4.72 ± 0.13	1.10 ± 0.14	14
Zn III	-4.96 ± 0.12	2.51 ± 0.13	13	-5.02 ± 0.08	2.46 ± 0.09	15
Ga III	-5.66 ± 0.12	3.34 ± 0.15	10	-5.72 ± 0.06	3.28 ± 0.11	7
Ge III-IV	-5.06 ± 0.15	3.33 ± 0.19	3/3	-5.14 ± 0.10	3.24 ± 0.14	3/5
Kr III	-5.07 ± 0.07	3.72 ± 0.10	11	-5.01 ± 0.11	3.77 ± 0.12	10
Sr II-III	-4.68 ± 0.09	4.49 ± 0.12	3/19	-4.54 ± 0.09	4.63 ± 0.11	4/21
Y III	-5.40 ± 0.02	4.43 ± 0.05	2	-5.23 ± 0.01	4.60 ± 0.05	2
Zr III-IV	-5.17 ± 0.08	4.29 ± 0.09	1/12	-4.85 ± 0.09	4.60 ± 0.10	1/13
Sn IV	-6.43 ± 0.06	3.57 ± 0.12	2	-5.65 ± 0.04	4.34 ± 0.11	2
*Pb IV	$<-7.46^{+0.60}$	$<2.83^{+0.60}$		-6.84 ± 0.40	3.44 ± 0.42	1

of these levels is very sensitive to the photo-ionisation (radiative bound-free) cross-sections used. The development of new TLUSTY model atoms would be required for at least C II-III and N II, which is an elaborate process and beyond of the scope of the present investigation. For the time being, the best fit to lines of C, N, and O can be considered satisfactory. The derived abundances of C, N, and O for Feige 46 do not differ significantly from the values given by Latour et al. (2019b).

Neon: The slightly sub-solar neon abundance for both stars is based on several Ne II lines in the blue range, for example Ne II 3334.8, 3664.1, and 3694.2 Å.

Magnesium: The Mg II 4481 Å doublet is observed in both stars and best reproduced at abundances of −0.79 dex for Feige 46 and −1.07 dex for LS IV−14°116.

Aluminium: The strongest predicted aluminium lines, Al III 4479.9, 4512.6, and 5696.6 Å, are not detected in Feige 46 or LS IV−14°116. The upper limit derived from these lines is slightly sub-solar.

Silicon: Sub-solar silicon abundances are based mainly on the Si IV 4088.9, 4116.1 Å doublet.

Table 3.1.5. Updated line positions. Observed positions are accurate to about 0.02 Å depending on the specific line strengths.

Ion	$\lambda_{\rm lit}$ / Å	$\lambda_{\rm obs}$ / Å	$\Delta\lambda$ / Å	Ion	$\lambda_{\rm lit}$ / Å	$\lambda_{\rm obs}$ / Å	$\Delta\lambda$ / Å
Zn III	5075.243	5075.330	+0.087	Kr III	3311.540	3311.490	−0.050
Zn III	5157.431	5157.580	+0.149	Kr III	3474.750	3474.650	−0.100
Ge III	4178.960	4179.078	+0.118	Sr III	3976.706	3976.033	−0.673
Ge IV	3320.410	3320.530	+0.120	Sr III	3991.587	3992.272	+0.685
Ge IV	3333.640	3333.785	+0.145	Y III	4039.602	4039.576	−0.026
Ge IV	3554.190	3554.257	+0.067	Zr IV	5462.333	5462.380	+0.047
Ge IV	3676.650	3676.735	+0.085	Zr IV	5779.843	5779.880	+0.037
Ge IV	4979.190	4979.987	+0.797	Sn IV	3862.051	3861.207	−0.844
Ge IV	5072.900	5073.330	+0.430	Sn IV	4217.184	4216.192	−0.992

Phosphorus: The only phosphorus line observed in Feige 46, P III 4222.2 Å, is very weak but present in LS IV−14°116 as well. The derived abundance based on this line is solar for Feige 46 and slightly sub-solar for LS IV−14°116.

Sulphur: No sulphur lines are detected in either star. The upper limit derived for Feige 46 is consistent with the value found by Latour et al. (2019b) from the UV spectrum.

Argon: The argon abundance for Feige 46 is based on the weak Ar III 3311.6 and 3503.6 Å lines. The same lines could not be used for LS IV−14°116, where the Ar abundance (about solar) is instead based on Ar III 3336.1 and 3511.2 Å. Significant uncertainty (~0.2 dex) is introduced by the continuum placement since all argon lines are very weak.

Calcium: The upper limits derived for calcium are based on the non-detection of the Ca II 3933.7 Å resonance line, which is well separated from interstellar lines in both stars. These upper limits indicate severe underabundances (by about 0.7 dex) for both stars, which is consistent with the non-detection of the Ca III 4233.7 and 4240.7 Å lines that are usually observed in He-poor sdOB stars.

Titanium: Weak titanium lines are observed in both stars. We used Ti III 3354.7, 4215.5, 4285.6 Å and Ti IV 3541.4, 3576.5, 4971.2, and 5398.9 Å to derive super-solar abundances.

Chromium, manganese, iron, and cobalt: No lines from the iron-peak elements chromium, manganese, iron, and cobalt are observed in UVES spectra of either star. For completeness, we list the abundances derived from UV lines for Feige 46 by Latour et al. (2019b) in Table 3.1.4. The absence of high-resolution UV spectra of LS IV−14°116 means that no information on the abundance of these elements can be obtained for that star, except for iron. The iron upper limit for LS IV−14°116 (0.35 times solar) is based on the non-detection of Fe III 5243.3 and 5891.9 Å, which are too strong in the final model. Fe III 4137.8 and 4164.7 Å are well reproduced at this abundance.

Nickel: Several weak nickel lines could be used to derive abundances for both stars, for example Ni III 5332.2, 5436.9, 5481.3 and 5482.3 Å. The Ni abundance derived from the optical lines for Feige 46 is the same as that obtained from the UV lines: overabundant by about 1 dex with respect to solar.

Zinc: The zinc abundances for Feige 46 and LS IV−14°116 (about 300 times solar) are based on 13 and 16 strong lines, respectively (e. g. Zn III 3683.4, 4818.9, 4970.8, 5075.2, 5249.7, and 5563.7 Å; see Fig. 3.1.2).

From a spectroscopic perspective, the prevalence of strong lines of heavy elements (here $Z > 30$) is the most striking feature of LS IV−14°116 and Feige 46. Nevertheless, many lines of heavy metals remained either undetected in the previous analyses (Naslim et al. 2011; Latour et al. 2019b), owing to the limited S/N and wavelength coverage of the spectra available, or unidentified

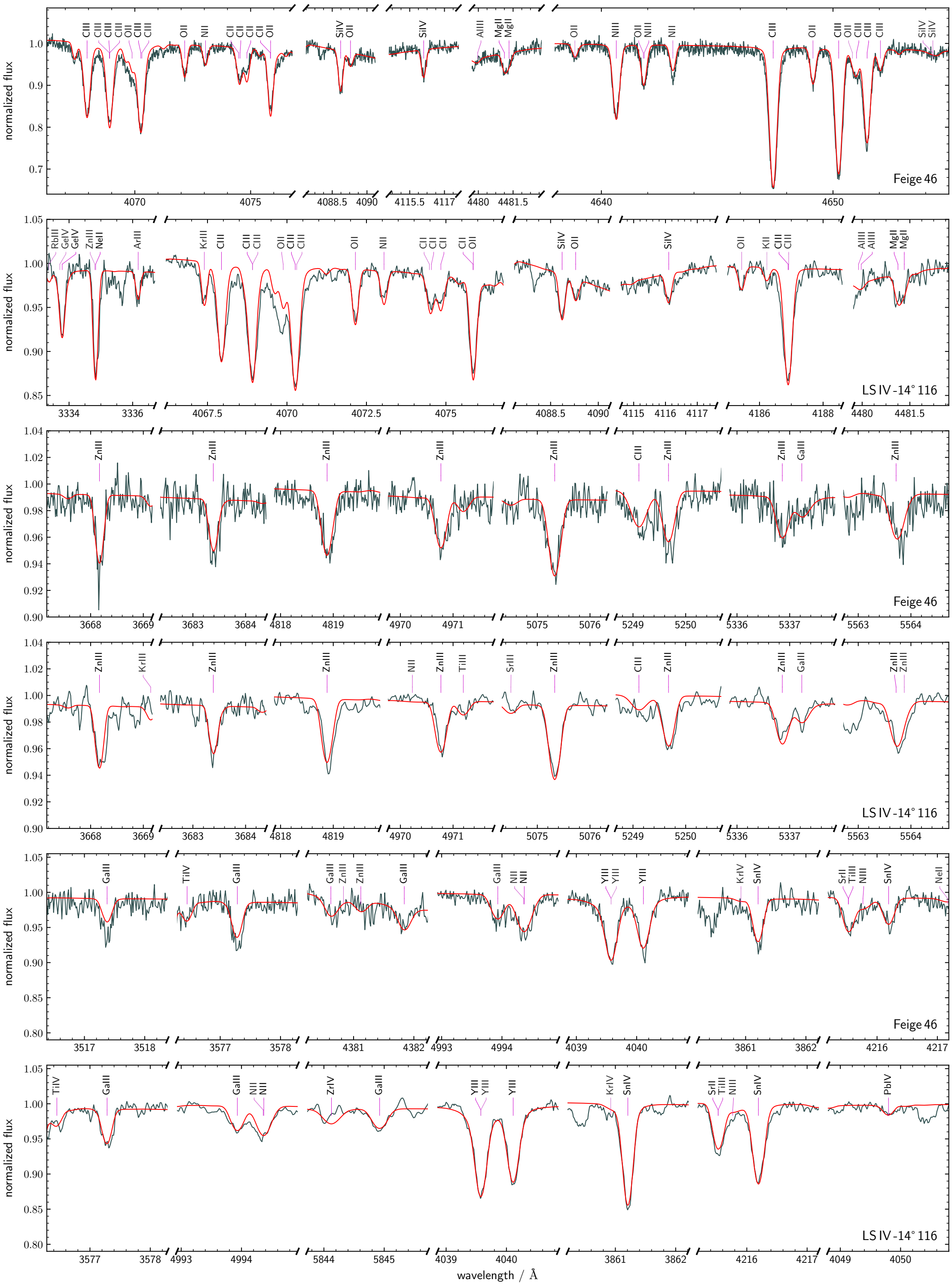

Figure 3.1.2. Representative regions in the UVES spectra of Feige 46 and LS IV−14°116. The best fit models are shown in red. Adopted from Dorsch et al. (2020).

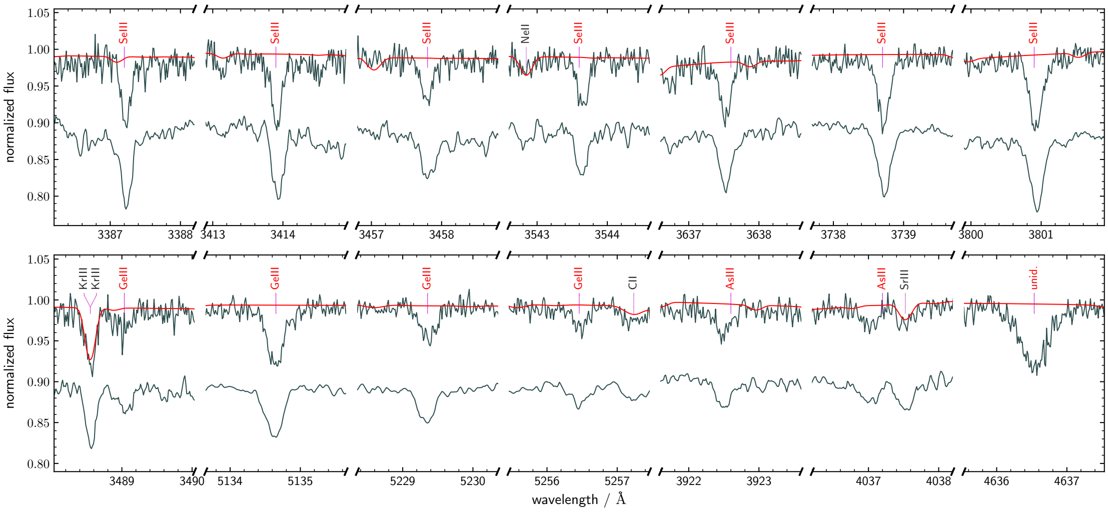

Figure 3.1.3. Additional regions in the UVES spectrum of Feige 46 showing newly identified lines that are lacking oscillator strengths and the strongest unidentified line observed. The UVES spectrum of LS IV−14°116 is shown for comparison, offset by −0.1. Adopted from Dorsch et al. (2020).

due to the scarcity of atomic data. Therefore, we set out to identify all heavy-metal lines that are present both in LS IV−14°116 and Feige 46.

Oscillator strengths are available for many ions that are expected to show spectral lines in the programme stars. However, several of these lines have remained unidentified so far because their rest wavelengths are not known with sufficient precision. The large wavelength coverage and good S/N of our spectra allowed us to identify lines of such ions from predicted relative intensities by adjusting the theoretical wavelengths to match the position of observed lines. These empirical wavelengths may also be useful in future atomic structure calculations.

Lines that required significant shifts to match observed lines are listed in Table 3.1.5. All 102 detected heavy-metal lines with available oscillator strengths are listed in Table 3.1.6. This includes strong previously unidentified lines noted by Naslim et al. (2011) at 4007 Å and 4216 Å that we now associate with Sr III and Sn IV, respectively. An additional 21 newly identified lines that lack oscillator strengths are listed in Table 3.1.7; some of these are shown in Fig. 3.1.3. The 51 remaining unidentified lines are listed in Table B.1.1. In the following paragraphs, we briefly describe the analysis for each heavy element detected. The strongest modelled lines for each heavy element are shown in Fig. 3.1.2 (Ga, Y, Sn, Pb), Fig. 3.1.4 (Ge, Kr, Sr), and Fig. 3.1.5 (Zr) for both stars.

Gallium: We identified several Ga III lines in the spectra of Feige 46 and LS IV−14°116. Oscillator strengths for optical Ga III lines were provided by O'Reilly & Dunne (1998). In particular, Ga III 3517.4, 3577.3, 3806.7, 4380.6, 4381.8, 4993.9, 5337.2, 5358.2, 5844.9, and 5993.9 Å could be used to derive an abundance of about 2000 times solar for both stars. To our knowledge, they have never been observed in any star.

Germanium: Naslim et al. (2011) identified and provide oscillator strengths for three Ge III lines in the optical spectrum of LS IV−14°116. Oscillator strengths for optical lines of Ge IV were provided by O'Reilly & Dunne (1998). However, these Ge IV lines have never been used to derive abundances, and their wavelengths had to be shifted to match the observed ones as listed in Table 3.1.5. We used three Ge III lines as well as four Ge IV lines to derive a germanium abundance of 2000 times solar for both stars. There is a mismatch between Ge III and Ge IV lines, which systematically appear too weak in our synthetic spectra. This may be due to non-LTE effects or systematic differences between the atomic data used for Ge III and Ge IV.

An effective temperature of 35920 K would be required for LS IV−14°116 to simultaneously reproduce both ionisation stages. However, this temperature is too high by about 400 K to be able to reproduce the ionisation balance of most other elements.

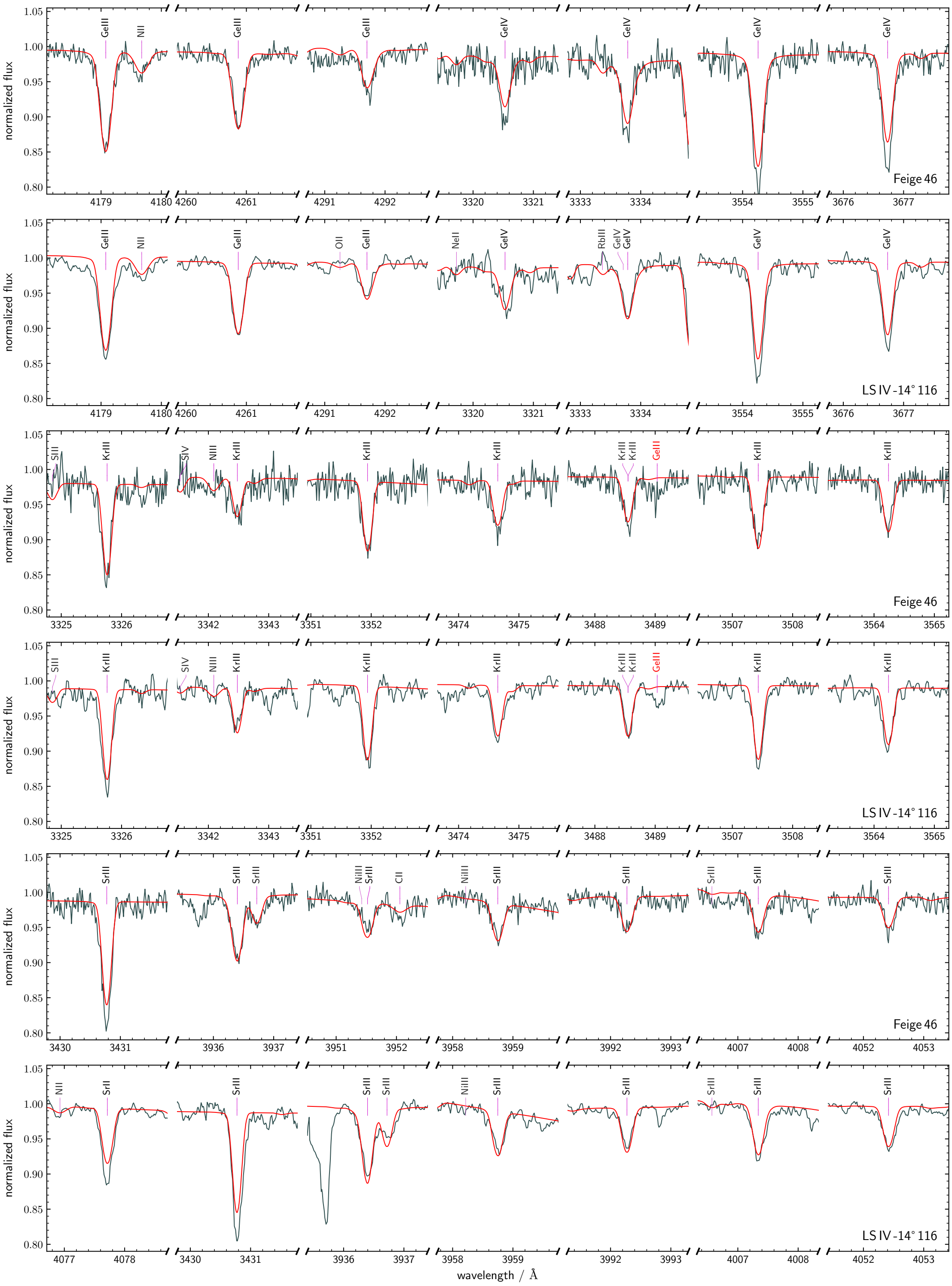

Figure 3.1.4. Strongest lines identified in the UVES spectra of Feige 46 and LS IV−14°116 for elements Ge, Kr, and Sr. Adopted from Dorsch et al. (2020).

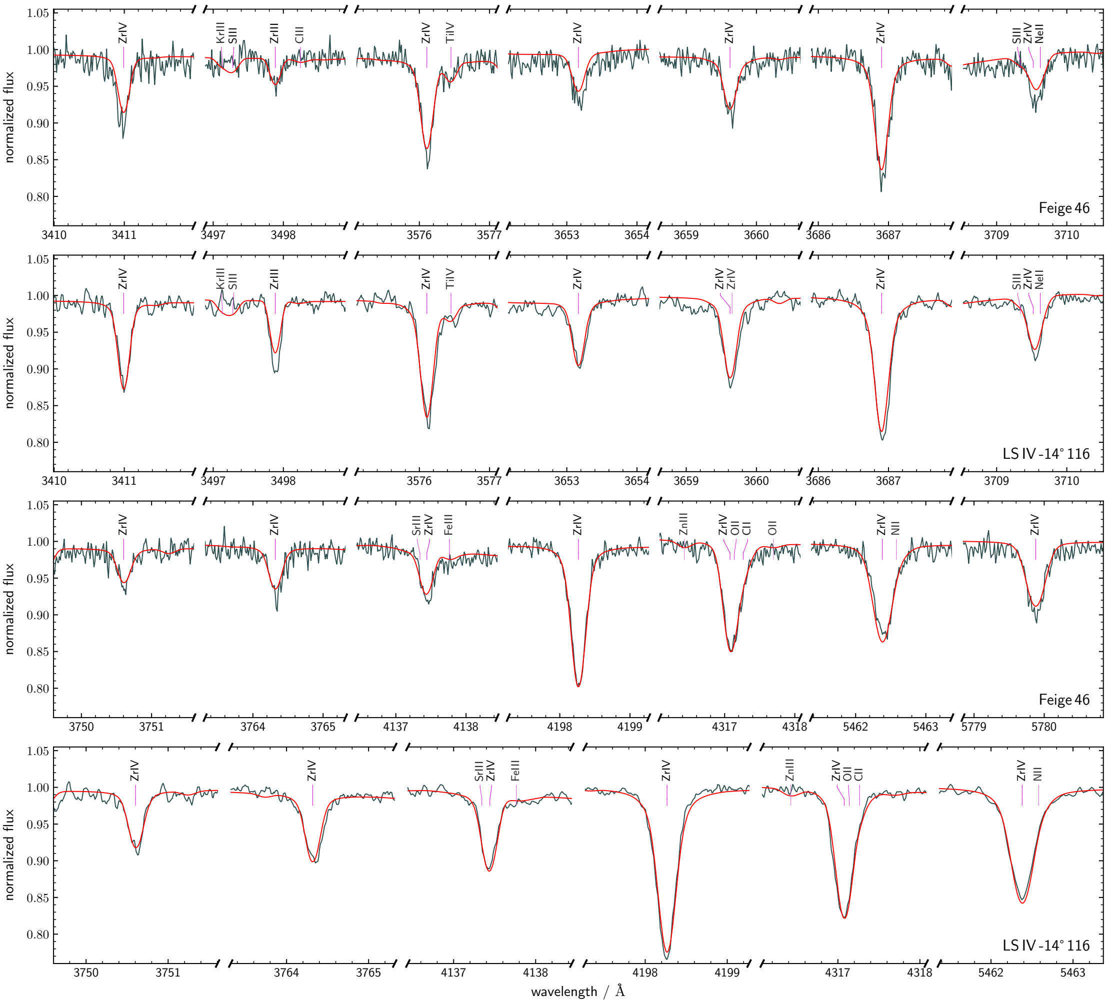

Figure 3.1.5. Zr IV lines and one Zr III line identified in UVES spectra of Feige 46 and LS IV−14°116 at the best fit abundances. Adopted from Dorsch et al. (2020).

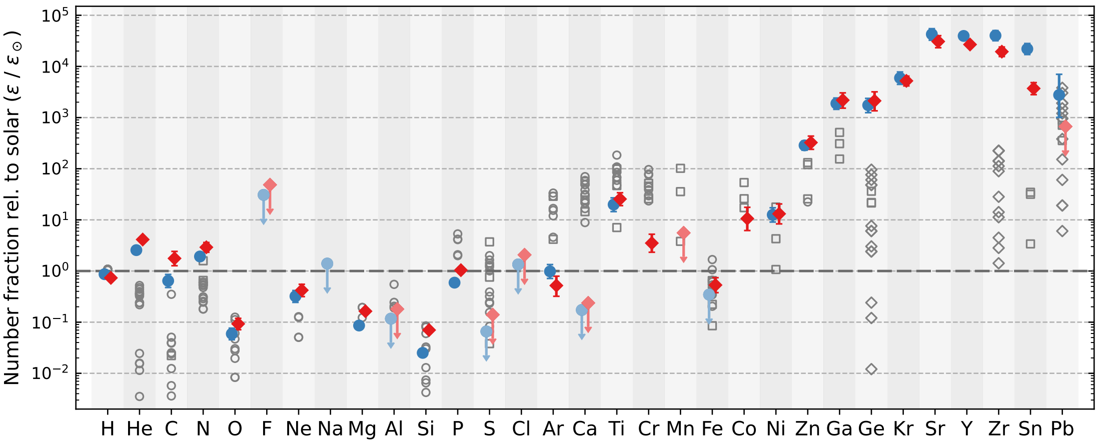

Figure 3.1.6. Abundance patterns of LS IV−14°116 and Feige 46 relative to that of the Sun (by number fraction). Only elements with an abundance measurement are shown. Upper limits are marked with an arrow and less saturated colours. For comparison, abundance measurements for He-poor sdOB stars (33000 K < T_{eff} < 36500 K) are shown as grey open circles (Geier 2013, based on optical data), diamonds (Chayer et al. 2006, based on far-UV data), and squares (O'Toole & Heber 2006, based on UV data).

Arsenic: Two weak and unidentified lines at 3922.5 Å and 4037 Å are observed close to experimental As III wavelengths provided by Lang (1928), as listed in NIST.[2] We are not aware of oscillator strengths for optical As III lines, and, therefore, cannot derive the abundance.

Selenium: Fifteen previously unidentified lines were identified with Se III using the experimental wavelengths of Badami & Rao (1933), as shown in Fig. 3.1.3. This is the first time that these lines have been observed in any star. They are visible in both Feige 46 and LS IV−14°116; a list of identifications is given in Table 3.1.7. Unfortunately, no oscillator strengths are available for optical Se III lines.

Krypton: Many Kr III lines that are observed in the UVES spectra of Feige 46 and LS IV−14°116 have never been identified in any star as far as we know.[3] Fortunately, oscillator strengths were provided by Raineri et al. (1998). Some lines were shifted to match their observed position; they are listed in Table 3.1.5. We have used Kr III 3325.76, 3342.48, 3351.94, 3474.65, 3488.55, 3564.24, 3641.35, 3690.66, and 4067.40 Å to derive an abundance of about 5500 times solar for both stars. The predicted Kr III 3308.22, 3396.72 Å lines do not match observed lines. Alternative oscillator strengths by Eser & Özdemir (2018) are even larger for these two transitions. These lines might therefore have inaccurate oscillator strength or require large shifts.

Strontium: A total of 35 previously unidentified lines can clearly be attributed to Sr III, for example the strong 3430.8, 3936.4 Å lines. To our knowledge, these lines have never before been reported in stellar spectra. Wavelengths and oscillator strengths for Sr II-III were provided by R. Kurucz, allowing us to determine the strontium abundance. The resonance lines Sr II 4077.7, 4215.5 Å used by Naslim et al. (2011) to derive the strontium abundance in LS IV−14°116 are also observed in Feige 46. To model these lines, we used oscillator strengths from Fernández-Menchero et al. (2020), who recently investigated Sr II in detail (along with Y III and Zr IV). Both stars also show Sr II lines at 3380.7, 3464.5, and 4305.4 Å. Fitting four Sr II lines (three for Feige 46) as well as 21 Sr III lines (19 for Feige 46) results in an abundance of 43 000 times solar for LS IV−14°116 and 31 000 times solar for Feige 46.

Yttrium: Naslim et al. (2011) identified two strong yttrium lines in the spectrum of LS IV−14° 116: Y III 4039.602 and 4040.112 Å. Fitting these lines (Y III 4039.6 Å at a slightly revised position) results in abundances of 27 000 times solar for Feige 46 and 40 000 times solar for LS IV−14° 116. Oscillator strengths for additional Y III lines observed at 5102.9, 5238.1, and 5602.2 Å were provided by Fernández-Menchero et al. (2020). However, these lines are not consistent with Y III 4039.6, 4040.1 Å and were therefore not considered for the abundance determination.

Zirconium: By far the strongest lines from heavy metals in the optical spectrum of both stars originate from zirconium IV transitions (see Fig. 3.1.5). Oscillator strengths for four Zr IV lines were provided by Naslim et al. (2011) and for two additional lines by Naslim et al. (2013). Rauch et al. (2017) also provide oscillator strengths for a large number of UV and optical Zr IV lines, while Fernández-Menchero et al. (2020) have recently computed oscillator strengths for eight Zr IV lines that are observed in the UVES spectra of both stars. We exclusively rely on data from Rauch et al. (2017), as they provide the most extensive list. A single strong Zr III line is observed at 3497.9 Å and is somewhat too weak in our models. We used this line as well as several Zr IV lines to determine the abundance in both stars, including the four Zr IV lines used by Naslim et al. (2011). The best-fit Zr abundance for LS IV−14°116, 40 000 times solar, is significantly higher than that for Feige 46 (20 000 times solar). As shown in Fig. 3.1.5, Zr IV lines are very well reproduced in both stars with the exception of Zr IV 3919.3 and 5462.3 Å, which are somewhat too strong in our models. In addition, we slightly revised the position of two Zr IV lines: Zr IV 5462.38 and 5779.88 Å.

---

[2] National Institute of Standards and Technology, `https://physics.nist.gov/PhysRefData/ASD/lines_form.html`; see also Kramida et al. (2019).

[3] Around 2012, N. Naslim reported the possible presence of krypton lines to Simon Jeffery; this could not be confirmed at the time.

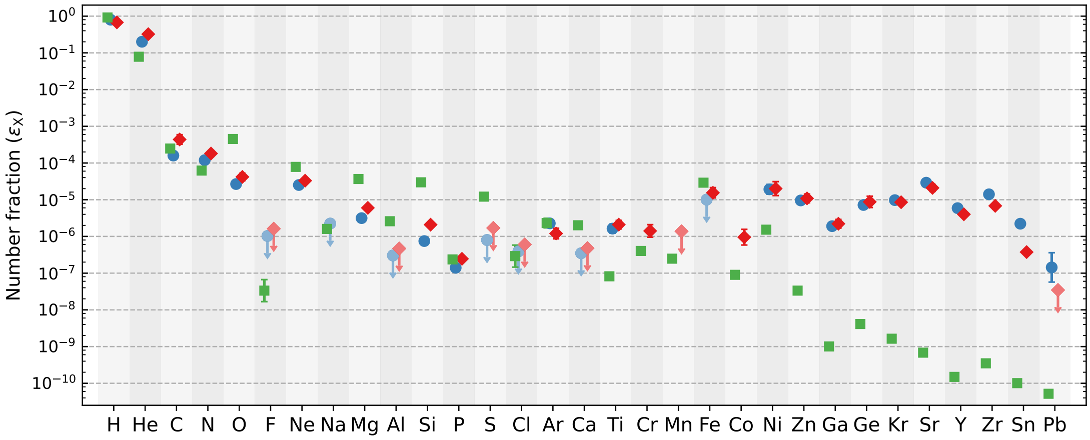

Figure 3.1.7. Atmospheric abundances for LS IV−14°116 (blue) and Feige 46 (red) by number fraction, compared with solar values (green) from Asplund et al. (2009).

Tin: Strong spectral lines of Sn iv at 3862.1 and 4217.2 Å are visible in the UVES spectra of Feige 46 and LS IV−14°116. These lines have not been previously identified in any star. To model these lines, we used oscillator strengths provided by Kaur et al. (2020) after adjusting their rest wavelengths (see Table 3.1.5). The abundance of tin derived from the two newly identified lines turns out to be 22 000 times solar for LS IV−14°116 and 3700 times solar for Feige 46, which is consistent with the value derived from UV lines by Latour et al. (2019b).

Lead: The lead abundance of LS IV−14°116, 2800 times solar, is based on a very weak Pb iv 4049.8 Å line. No other lead lines are detected and thus the abundance has a large uncertainty. Based on the Pb iv 1313 Å resonance line, Latour et al. (2019b) determined an upper limit of 680 times solar for Feige 46, which is likely close to the actual abundance. Although this upper limit is consistent with the non-detection of lead lines in the optical spectrum of Feige 46, it would have to be confirmed by UV observations of higher quality than the low S/N IUE spectrum that is currently available.

Undetected elements: We searched unsuccessfully for lines of fluorine, sodium, chlorine, potassium, scandium, vanadium, rubidium, and xenon. F ii 3505.6, 3847.1, 3850.0, and 4246.2 Å exclude abundances higher than about 100 times solar in LS IV−14°116. The very weak photospheric resonance lines Na i 5889.94 and 5889.96 Å are well separated from the interstellar lines, but unfortunately blended with the stronger C ii 5889.78 Å. These lines as well as Na ii 3533.1 Å seem to exclude abundances higher than about five times solar in LS IV−14°116, whereas no sensible upper limit could be derived for Feige 46. Chlorine abundances higher than six times solar for Feige 46 and about four times solar for LS IV−14°116 are excluded based on the non-detection of Cl iii 3530.0 and 3601.9 Å. The upper limits derived for other elements are either too high to be of use or too uncertain because of poorly known line positions. We therefore refrain from stating even an upper limit for the following elements. K ii 4186.2 Å seems to fit a weak line in LS IV−14°116 at an abundance of about 30 times solar. However, this abundance seems to be excluded by K iii 3322.4, 3358.4, and 3364.3 Å, which suggest an upper limit of about ten times solar. The upper limit derived from the non-detection of very weak predicted Sc iii and V iii lines are next to meaningless for both stars. Zhang et al. (2014) provide atomic data for Rb iii. However, because these lines have never been observed, their positions are likely not accurate. They do not match observed lines in Feige 46 or LS IV−14°116. The same is true for optical Xe iv lines as predicted by Rauch et al. (2017).

Both stars show almost the same abundance pattern, as illustrated in Fig. 3.1.6. When compared to solar values, nitrogen is enhanced and oxygen is depleted. Carbon is slightly super-solar in Feige 46 and slightly sub-solar in LS IV−14°116. The light metals C, N, O, Ne, Mg, Si, and P are all slightly more abundant in Feige 46 but otherwise follow the same pattern as in LS IV−14°116. The abundances of elements from argon to krypton, when known, are almost

Table 3.1.6. Identified lines of heavy metals ($Z > 30$) in the UVES spectra of LS IV−14°116 and Feige 46 for which oscillator strengths are available. Equivalent widths are given for LS IV−14°116.

Ion	$\lambda_{\rm obs}$ / Å	EW / mÅ	Ion	$\lambda_{\rm obs}$ / Å	EW / mÅ	Ion	$\lambda_{\rm obs}$ / Å	EW / mÅ
Zr IV	3297.858	20.0	Zr IV	3709.552	18.0	Ge III	4291.700	11.9
Sr III	3302.730	5.2	Zr IV	3750.608	15.9	Sr II	4305.406	5.7
Kr III	3311.490	13.0	Zr IV	3764.335	25.6	Zr IV	4317.073	49.8
Ge IV	3320.530	20.6	Kr III	3792.666	4.1	Ga III	4380.662	9.9
Kr III	3325.752	29.9	Sr III	3821.965	7.3	Ga III	4381.793	11.9
Ge IV	3333.785	15.4	Zr III	3829.240	1.9	Ge IV	4979.987	7.9
Kr III	3342.461	10.2	Sr III	3855.913	5.6	Ga III	4993.940	11.7
Kr III	3351.938	22.4	Sn IV	3861.207	30.0	Sr III	5022.702	7.7
Kr III	3374.961	5.7	Kr III	3868.793	3.8	Sr III	5071.126	4.3
Sr II	3380.702	7.4	Sr III	3874.278	11.6	Ge IV	5073.330	13.2
Zr IV	3410.999	23.3	Sr III	3874.755	2.8	Sr III	5074.551	1.4
Sr III	3430.775	36.5	Zr IV	3919.332	11.9	Y III	5102.901	8.4
Sr III	3444.874	8.4	Sr III	3936.403	25.9	Sr III	5158.291	3.5
Sr II	3464.480	12.6	Sr III	3936.740	14.8	Y III	5238.110	22.4
Kr III	3474.650	16.3	Sr III	3951.546	12.9	Sr III	5257.763	13.0
Kr III	3488.558	12.6	Sr III	3958.762	12.8	Sr III	5262.211	8.2
Zr III	3497.889	17.4	Sr III	3976.033	8.2	Y III	5263.580	2.5
Kr III	3507.435	22.8	Sr III	3992.272	11.7	Sr III	5288.360	7.5
Ga III	3517.392	9.9	Sr III	4007.348	16.8	Ga III	5337.238	2.9
Kr III	3549.408	3.9	Sr III	4037.534	8.3	Ga III	5358.205	5.5
Ge IV	3554.257	35.0	Y III	4039.576	32.8	Sr III	5391.037	11.8
Sr III	3559.674	8.0	Y III	4040.115	26.0	Sr III	5405.448	5.1
Kr III	3564.223	17.8	Sr III	4052.432	13.8	Sr III	5417.570	3.9
Kr IV	3567.647	3.7	Kr III	4067.382	10.5	Sr III	5421.061	7.3
Zr IV	3576.123	39.0	Sr II	4077.711	23.4	Sr III	5443.479	16.9
Ga III	3577.291	12.0	Sr III	4094.047	7.1	Zr IV	5462.380	52.8
Kr III	3641.332	6.5	Zr IV	4137.430	23.4	Sr III	5463.942	9.0
Sr III	3650.734	9.6	Kr III	4154.452	4.2	Y III	5602.151	5.8
Zr IV	3653.182	19.8	Ge III	4179.078	30.3	Sr III	5664.628	4.5
Zr IV	3659.634	30.1	Zr IV	4198.255	65.2	Sr III	5689.761	5.4
Ge IV	3676.735	26.4	Sr II	4215.531	19.6	Zr IV	5779.880	26.4
Zr IV	3686.914	49.6	Sn IV	4216.192	27.1	Ga III	5844.912	9.3
Sr III	3688.299	6.1	Kr III	4226.580	6.4	Ga III	5993.887	6.1
Kr III	3690.652	5.0	Ge III	4260.865	24.2	Zr IV	6443.235	13.5

identical and calcium is depleted in both stars. Heavy elements are enriched to very high values, from zinc at about 300 times solar to zirconium well above 20 000 times solar. While being highly enriched when compared to solar values, the concentration of Sr, Y, Zr, Sn, and Pb in the line-forming region of Feige 46 is progressively less extreme when compared to that of LS IV−14°116. This enrichment is nevertheless notable when compared to He-poor sdOB stars, which have been observed to be enhanced in Zn, Ga, Ge, Zr, and Sn to about 10 to 200 times the solar value (O'Toole & Heber 2006; Chayer et al. 2006; Blanchette et al. 2008). Not only the extreme enrichment in heavy metals but also the abundances of lighter metals are different to those observed in He-poor sdOB stars. In particular, the argon and calcium abundances in LS IV−14°116 and Feige 46 are significantly lower than the super-solar values Geier (2013) obtained for He-poor sdOBs of similar temperatures.

Table 3.1.7. Observed wavelengths for newly identified lines that lack oscillator strengths in the spectra of LS IV−14°116 and Feige 46. Equivalent widths are given for LS IV−14°116.

Ion	$\lambda_{\rm lit}$ / Å	$\lambda_{\rm obs}$ / Å	$\Delta\lambda$ / Å	EW / mÅ
Ge III	3489.034	3489.055	+0.021	6.3
Ge III	5134.652	5134.626	−0.026	18.2
Ge III	5229.354	5229.336	−0.018	12.3
Ge III	5256.459	5256.466	+0.007	8.8
As III	3922.6	3922.499	−0.101	8.2
As III	4037.2	4037.015	−0.185	9.3
Se III	3387.2	3387.232	+0.032	16.4
Se III	3413.9	3413.931	+0.031	17.2
Se III	3428.4	3428.398	−0.002	9.4
Se III	3457.8	3457.817	+0.017	17.4
Se III	3543.6	3543.638	+0.038	12.6
Se III	3570.2	3570.191	−0.009	10.0
Se III	3637.6	3637.526	−0.074	15.9
Se III	3711.7	3711.683	−0.017	12.7
Se III	3738.7	3738.727	+0.027	20.6
Se III	3743.0	3742.921	−0.079	6.7
Se III	3800.9	3800.938	+0.038	21.8
Se III	4046.7	4046.733	+0.033	6.5
Se III	4083.2	4083.164	−0.036	8.4
Se III	4169.1	4169.070	−0.030	15.8
Se III	4637.9	4637.896	−0.004	5.7

Such strong deficiency when compared to He-poor sdOB stars (2 dex for calcuium) can not be explained by a lower initial metallicity that might be expected for LS IV−14°116 and Feige 46 due to their halo kinematics. It is worth mentioning that this calcium deficiency is not observed in lead-rich iHe-sdOB stars such as [CW83] 0825+15 (Jeffery et al. 2017), FBS 1749+373, and PG 1559+048 (Naslim et al. 2020). These stars show calcium abundances in line with those observed in He-poor sdOB stars. In contrast to this, the carbon and nitrogen abundances in LS IV−14°116 and Feige 46 are higher than in the average He-poor sdOB star.

Enrichment helium and nitrogen is likely caused by material processed by hydrogen fusion in the CNO-cycle. In addition, helium fusion in the 3α process may explain the increased carbon abundance in the atmospheres of LS IV−14°116 and Feige 46 when compared to He-poor sdOB stars. Such patterns were predicted for both the hot flasher (Miller Bertolami et al. 2008) and helium white dwarf merger scenarios (Zhang & Jeffery 2012). This is also consistent with the positive correlation between the helium and carbon abundances of sdOB stars in the globular cluster ω Cen as found by Latour et al. (2014). In addition, the abundances of C, N, and O might still be affected by diffusion processes to some degree – both in He-poor and iHe-sdOB stars.

3.1.6 Discussion and conclusions

We have performed a detailed spectral analysis of Feige 46 and LS IV−14°116. This consistent analysis of both stars enables an accurate and direct comparison of their abundance patterns, which would be hampered by the use of different analysis methods.

The abundance patterns of both stars, as well as their differences, can likely be explained with atmospheric diffusion processes that may affect heavy metals more than the CNO abundances. In this context it is convenient to consider the abundance pattern as number fraction without the comparison to solar values (Fig. 3.1.7). It is easy to recognise that the overall abundance of light metals from carbon to phosphor drops off by three orders of magnitude from $\log \epsilon \approx$

−3.5 to about −6.5 dex. Unlike in the Sun, the abundances of heavier elements (except calcium) do not continue to drop further, but follow a more constant pattern. A comparison of detailed diffusion calculations with these observed abundance patterns is required to resolve the question whether diffusion alone is enough to produce such high enrichment of heavy metals. In addition, atmospheric models that consider atmospheric stratification are required to determine whether the observed enrichment in heavy metals can be explained by thin layers of enriched material in the line-forming region.

Thanks to the excellent quality and wavelength coverage of the available UVES spectra we have been able to identify many previously unidentified lines in Feige 46 and LS IV−14°116 with transitions of heavy ions. Strong lines with available oscillator strengths originate from ions such as Ge IV, Kr III, Sr III, Zr III, and Sn IV. Their identification will enable the determination of abundances in future analyses of other "heavy metal" stars, even with spectra of lower quality. Atomic data are still lacking for some heavy elements and ionisation stages III-IV, including several newly identified lines of Ge III, Se III, and Y III. We also provide observed wavelengths for lines that may be useful in future atomic structure calculations. About 50 mostly weak lines detected in the spectra of LS IV−14°116 and Feige 46 remain unidentified and could belong to elements not yet identified in either star.

Stellar parameters (mass, radius, and luminosity) were derived from the high-quality *Gaia* parallax by combining it with spectroscopic atmospheric parameters and the spectral energy distribution. The mass determination for both stars is limited by the uncertainty on the surface gravity, but is consistent with both the canonical subdwarf mass predicted by hot flasher models ($0.47 M_\odot$, Dorman et al. 1993; Han et al. 2003) and the lowest-mass He-WD mergers (Zhang & Jeffery 2012).

The similarity of LS IV−14°116 and Feige 46 in terms of atmospheric parameters, abundances, pulsation, and galactic kinematics remains puzzling. A larger sample of intermediately He-rich sdOB stars with detailed observed abundance patterns is required to draw conclusions on the causal relation between these features. Such a sample would also be required to answer the questions:

- What makes the heavy-metal stars different from the normal sdOB stars? Because other chemically peculiar stars such as helium-rich main-sequence B stars and Ap stars have strong magnetic fields, it has been suggested that the heavy-metal stars are magnetic too, but no magnetic field has been detected in LS IV−14°116 (down to 300 G, Randall et al. 2015).
- Do most iHe-sdOB stars represent an intermediate stage in the evolution of He-sdOs towards the He-poor sdBs?
- At which point in their evolution will atmospheric diffusion become important?

Fortunately, recent surveys such as the LAMOST survey (e. g. Lei et al. 2020) and the SALT survey (e. g. Jeffery et al. 2021) are discovering many new helium-rich subdwarf stars. Future analyses of a larger sample of stars that share the atmospheric parameters of LS IV−14°116 and Feige 46 (intermediate He-enrichment and T_{eff} around 35 000 K), but also of their potential progenitors, the extreme He-sdOs, might give important clues on the evolution of He-rich subdwarf stars. In particular the determination of masses using *Gaia* parallaxes will be useful to test formation models; an analysis in this direction is performed later in this thesis in Sect. 4.1.

3.2 He-poor sdOBs: CPD −56°464 and the Schweizer-Middleditch Star

By now, more than 12 intermediate He-sdOBs such as LS IV−14°116 and Feige 46 have been discovered to be extremely enriched in heavy metals (here $Z > 30$), including zirconium or lead. The observed abundances of heavy metals can reach up to 10^6 times their Solar value. In contrast, helium-poor sdOB stars are typically observed with much weaker enrichment of heavy metals, at most of the order of 10^2 – 10^3 times solar (O'Toole & Heber 2006; Chayer et al. 2006; Blanchette et al. 2008). There is one exception to this rule: the recent discovery of Németh et al. (2021) who found lead in the He-poor and rather hot ($T_{\text{eff}} = 37$ kK) sdOB component of SB 744, a sdOB+G1V type spectroscopic binary.

Because iHe-sdOBs have temperatures and gravities similar to those of He-poor sdOBs, one might expect that similar radiative levitation in their atmospheres would lead to similar enrichment of heavy metals. Diffusion clearly operates in the photospheres of He-poor sdOBs, whose helium-deficient atmospheres result from gravitational settling of helium below a thin layer of hydrogen. The diffusion calculations of Michaud et al. (2011) have shown that an equilibrium is not reached for He-poor sdOBs during their first 30 Myr on the extreme horizontal branch. The lack of extreme enrichment and the lower helium abundance compared to the "heavy metal" iHe-sdOBs may partly be caused by differences in age – the metal-rich layers may have had more time to sink in He-poor sdOBs while hydrogen had more time to float to the surface. Whether or not there is a direct evolutionary connection between He-rich and He-poor sdOBs is still unclear. The differences in the abundance patterns of He-rich and -poor sdOB stars therefore represent an important test of the evolution of hot subdwarf stars.

Heavy metal lines in the FUV spectra of 24 sdOB and sdB stars were discovered by O'Toole (2004). Fontaine et al. (2004) later determined abundances up to nickel for four He-poor sdBs based on FUSE spectra. Three mayor papers have since determined trans-iron element abundances of He-poor sdBs. O'Toole & Heber (2006) derived detailed metal abundance patterns up to lead for five He-poor sdOBs with temperatures between 27.5 kK and 35.4 kK from high-resolution STIS spectra, using metal line-blanketed LTE model atmospheres computed with Atlas6. Chayer et al. (2006) used Synspec synthetic spectra based on metal-free LTE atmospheres computed with Tlusty to derive Ge, Zr, and Pb abundances from FUSE spectra of 18 He-poor sdBs, with effective temperatures ranging from 23.9 to 33.9 kK. Blanchette et al. (2008) used the same type of models to derive extensive metal abundance patterns up to lead for five long-period sdB pulsators with temperatures from 24 kK to 29 kK based on FUSE spectra. Geier (2013) combined high-resolution optical spectra with metal line-blanketed LTE model spectra to derive abundances up to cobalt for 106 He-poor sdB stars, an effort that was continued by Möller (2021).

In the following section, we present an explorative analysis of two helium-poor sdOBs: CPD −56° 464 and the SM Star. We selected these two stars for three reasons:

- Both stars are relatively hot He-poor sdOBs at temperatures around 31 kK.
- Both CPD −56° 464 and the SM Star have been observed extensively in the UV region and the photospheric lines in these spectra have not been analysed yet. This allowed us to measure the abundances of heavy metals even at relatively low enrichments.
- CPD −56° 464 has an excellent FUSE spectrum while the SM Star has a broad coverage of UV data, including FUSE and STIS/E140M, although the S/N of its individual spectra is lower. The lack of coverage for CPD −56° 464 is partly compensated by the STIS spectrum of the SM Star. For many metals, the analysis of the FUSE spectrum of CPD −56° 464 can be performed using lines that were shown to be consistent between lines in the STIS and FUSE ranges in the spectrum of the SM Star. Vice versa, the high quality of the FUSE spectrum of the CPD −56° 464 can be used to identify trustworthy lines in the FUSE spectrum of the SM Star. The parallel analysis of both stars has the further advantage that blends with interstellar lines appear at different wavelengths, which also helps to asses the reliability of photospheric lines for the determination of metal abundances.

3.2.1 CPD –56°464

CPD –56° 464 is a relatively bright ($V = 12$ mag) and He-poor field sdOB. A first spectroscopic analysis based on low-resolution IUE and optical spectra taken with the Boller & Chivens spectrograph was performed by Viton et al. (1991). However, no further analyses are available.

The star was used extensively as a calibration source for the FUSE satellite. A total of 17 spectra from three observing programmes (P205, I819, U106) result in a mean S/N of about 70 for the coadded spectrum, which is very high for FUSE spectra of hot subdwarfs. These spectra have not been analysed before and enabled us to derive a complete abundance pattern for CPD –56° 464, including heavy metals that are only observable in the far-UV.

Its atmospheric parameters place CPD –56° 464 right in between the two main sdB instability strips: the short-period *p*-mode V361 Hya pulsators (Kilkenny et al. 1997) and the hotter long-period *g*-mode V1093 Her pulsators (Green et al. 2003). CPD –56° 464 was observed in sector 2 of TESS, but no pulsations were detected.

3.2.2 Schweizer-Middleditch Star

In a search for a blue star that might be associated with the supernova remnant (SNR) SN 1006, Schweizer & Middleditch (1980) found a relatively faint sdOB star which is now known as the Schweizer-Middleditch Star (or short: SM Star). Despite being relatively faint ($V = 16.6$ mag), the SM Star has been observed extensively in the far-UV with FUSE, COS, STIS, and FOS. These spectra were used to study to the expanding SN ejecta in the line of sight.

There are two strong features of SN ejecta in the UV spectrum of the SM Star. Strong and broad Fe II absorption features at about 2400 Å and 2600 Å in the FOS spectrum were used by Wu et al. (1993) to analyse the SNR velocity profile and estimate the amount of Fe II contained in the remnant. In addition, a broad and strong red-shifted absorption feature due to Si II 1260 Å is observed between about 1270 and 1290 Å. Hamilton et al. (2007) have used this feature in the STIS spectrum to determine the velocities of the SN ejecta at the reverse shock (where the ejecta are shocked by the ISM). The same feature was later used by Winkler et al. (2011) to measure how this speed changed between 1999 (using STIS spectra) and 2010 (using COS). A weaker redshifted Si III 1206.5 Å feature is present between about 1225 and 1235 Å (Hamilton et al. 1997). However, most spectral regions are not affected by the SNR and can therefore be used to study the photospheric abundances of the SM Star itself.

Due its faintness the FUSE spectrum of the SM Star shows strong telluric N I and O I emission lines. The spectrum is also affected by strong interstellar absorption lines due to H I, H_2, and both neutral and ionised metals. For the present analysis, all FUSE exposures were corrected for radial velocity trends and then co-added. Telluric lines were removed where possible. The resulting spectrum has a low S/N, but its resolving power is high enough that the spectrum is still useful when smoothed with a 4-pixel “box” filter.

As mentioned above, the SM Star was also observed with COS. However, this spectrum is inferior to the STIS spectrum and was therefore not used in the present analysis. Additional FOS spectra cover a broad spectral range from the FUV to the NUV and are well reproduced by our models, but they did not contribute to our abundance determinations because of their low resolution.

3.2.3 Atmospheric parameters

While this analysis is focussed on metal abundances from far-UV spectra, the basic atmospheric parameters are usually determined from optical spectra. The atmospheric parameters of the SM Star were first determined by Burleigh et al. (2000), using a low-resolution optical spectrum obtained at the SAAO Ratcliffe Telescope using the Unit spectrograph. We used the same spectrum for our determination of atmospheric parameters. A new optical spectrum of CPD –56° 464 was obtained with EFOSC2, a low-resolution spectrograph mounted at the ESO 3.6m telescope at La Silla Observatory. A summary of all spectra used for our analysis is given in Table 3.2.1.

Table 3.2.1. Spectra available for CPD −56° 464 and the SM Star.

Star	Instrument	Range (Å)	R	S/N^a
CPD −56° 464	FUSE/LWRS	905 – 1188	~17000	73
	EFOSC2	3720 – 5100	6.2 Å^b	320
SM Star	FUSE/LWRS	905 – 1188	~17000	5
	STIS/E140M	1170 – 1708	~45800	5
	SAAO/US	3720 – 5100	4.0 Å^b	17

Notes. $^{(a)}$ The signal-to-noise ratio is the average over the spectrum. $^{(b)}$ The resolution for long-slit spectrographs is given instead as $\Delta\lambda$.

Table 3.2.2. Atmospheric parameters derived from optical spectroscopy. Uncertainties are stated as the quadratic sum of (small) statistical uncertainties and estimated systematic uncertainties.

Name	$T_{\rm eff}$ / K	$\log g$	$\log y$	Grid	Spectrum	Ref
CPD −56° 464	29240 ± 900	5.49 ± 0.10	−1.98 ± 0.10	ADS/sdB	EFOSC2	1
	30670 ± 900	5.50 ± 0.10	−1.96 ± 0.10	TLUSTY	EFOSC2	1
	30000 ± 500	5.50 ± 0.20	−1.80 ± 0.20	LTE	IUE/B&C	2
SM Star	31200 ± 1400	6.03 ± 0.14	−1.77 ± 0.14	ADS/sdB	SAAO/US	1
	32900 ± 1500	6.18 ± 0.30	−1.70 ± 0.30	NLTE/HHe	SAAO/US	3

Notes. References: (1) this work. (2) Viton et al. (1991). (3) Burleigh et al. (2000).

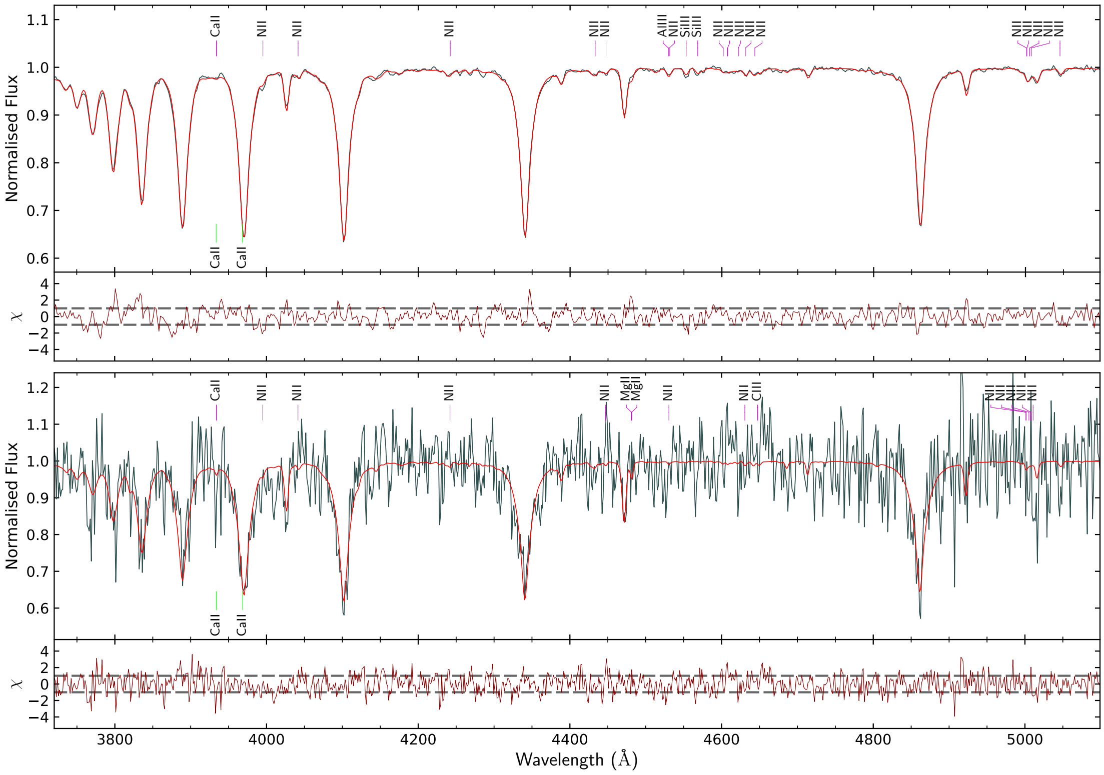

Figure 3.2.1. *Top*: NTT/EFOSC2 spectrum of CPD −56° 464 (grey) and the final synthetic spectrum (red). The residuals for each spectrum are shown in the lower panels. *Bottom*: Best fit to the SAAO/US spectrum of the SM Star.

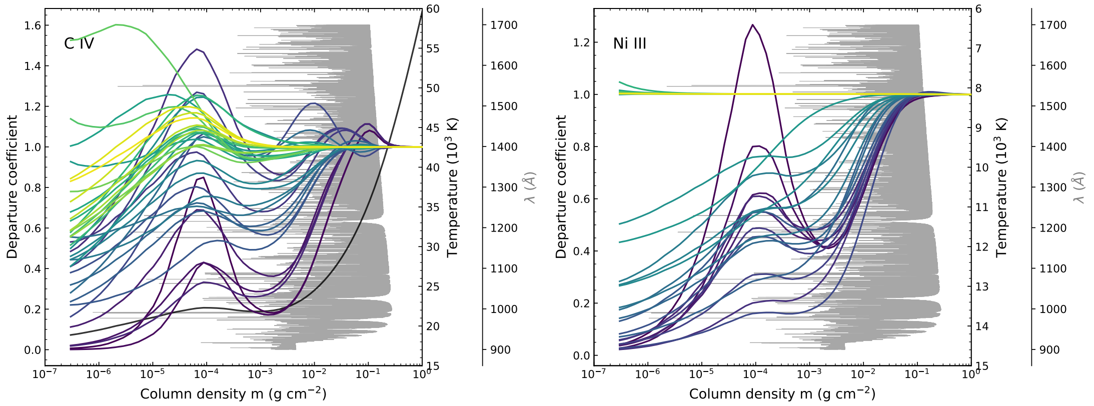

Figure 3.2.2. Examples for departure coefficients for ions in the final model of the SM Star. Dark lines correspond to low-lying levels. The black line (left) shows the temperature profile, whereas the grey background spectrum shows the formation depths for lines in the FUV spectrum.

We derived atmospheric parameters from χ^2 fits to these low-resolution optical spectra using our standard large grid of line-blanketed hybrid LTE/non-LTE ADS models, computed using mean sdB abundances from Pereira (2011). Because our metal abundance analysis for the SM Star and CPD −56° 464 is not based on ADS models, but line-blanketed Tlusty/Synspec models, we repeated the fit for CPD −56° 464 using the "sdOstar2020" model grid[4]. As stated in Table 3.2.2, the results using both grids are consistent with each other, as well as literature values. We assume systematic uncertainties of 3 % for $T_{\rm eff}$ and 0.1 dex for $\log g$ and $\log n(\mathrm{He})/n(\mathrm{H})$. Our final best-fit models are compared with the optical spectra in Fig. 3.2.1. In order to reproduce the Lyman series in the FUSE spectra, these models use slightly different parameters than the best fits derived from optical spectra. For CPD −56° 464, we used $T_{\rm eff} = 30250\,\mathrm{K}$, $\log g = 5.45$, and $\log n(\mathrm{He})/n(\mathrm{H}) = -1.9$, while $T_{\rm eff} = 32000\,\mathrm{K}$, $\log g = 5.90$, and $\log n(\mathrm{He})/n(\mathrm{H}) = -1.7$ was used for the SM Star. These parameters are within the uncertainties stated in Table 3.2.2. Because the far-UV spectra of both stars are affected by interstellar lines, a simple model of interstellar absorption was developed. It is described in Appendix A.2.

3.2.4 Weak non-LTE effects

Previous studies of He-poor sdOBs were often based on LTE atmospheres or non-LTE models with limited line blanketing. Like Dorsch et al. (2019), Latour et al. (2019b), and Dorsch et al. (2020), we use Tlusty model atmospheres that include metal ions up to iron and nickel in non-LTE – Tlusty non-LTE model ions are not yet available for heavier atoms. Our model for CPD −56° 464 includes in non-LTE H, He, C, N, O, Mg, Si, S, Fe, and Ni, while the model for the SM Star also includes Al in non-LTE. All metals were included at approximately the correct abundance for each star, based an a previous coarse analysis.

At effective temperatures of about 30 000 K and surface gravities of 5.9 and 5.5, the SM Star and CPD −56° 464 occupy a parameter space in which non-LTE effects start to become important. Departure coefficients for almost all levels of all elements significantly deviate from unity at column densities of less than $10^{-2}\,\mathrm{g\,cm^{-2}}$; they typically range between 2 and 0.1 (see Fig. 3.2.2). However, almost all FUV lines are formed at larger column densities – only the very cores of strong resonance lines are formed in the outer photosphere. Non-LTE effects on predicted metal lines in the UV region therefore generally remain small. Figure 3.2.3 shows those lines that are most affected by non-LTE departures in the STIS spectrum of the SM Star. This means that our approach to use the LTE assumption to model heavy metal ions, which lack the necessary atomic data to be modelled in non-LTE, is likely still acceptable.

---

[4] For a detailed description of the "sdOstar2020" grid, see Sect. 2.2.2.

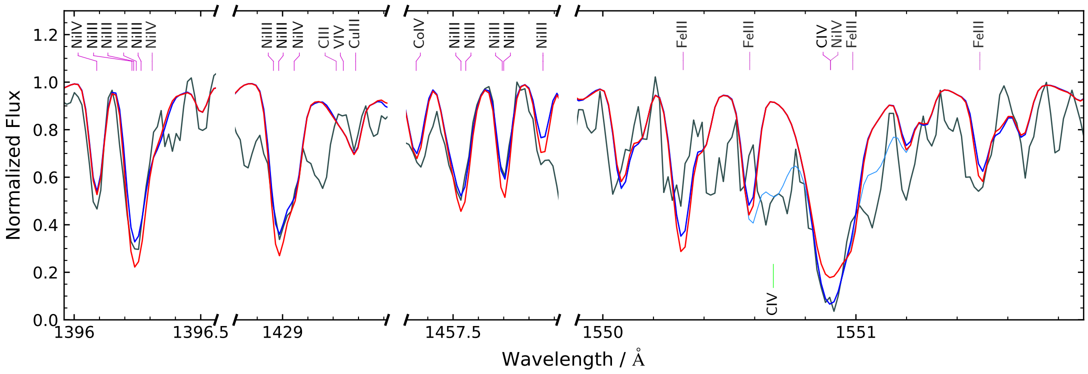

Figure 3.2.3. Effects of non-LTE level populations in the STIS spectrum of the SM Star. The red model was computed with LTE populations while the blue model includes non-LTE populations. Both are based on the same final non-LTE atmospheric structure.

3.2.5 Metal abundances

In the following, the determination of metal abundances for CPD −56° 464 and the SM Star is summarised by element. A total of 27 and 28 metals were detected for CPD −56° 464 and the SM Star, respectively. We use atomic data for heavy elements as collected by Dorsch et al. (2019) and Dorsch et al. (2020) with some minor updates, mostly to the position of individual lines. Abundances in the text are always stated as number fractions relative to the solar value of Asplund et al. (2009). A summary of abundances is given in Table 3.2.3 and the full best fits to the UV spectra are shown in Appendix B.2. Upper limits in this table are stated as the abundance at which the observation is best reproduced, with an “uncertainty” that indicates the abundance at which predicted features become clearly too strong. The upper limits stated in the text refer to this more conservative value.

Carbon. The C III 977 Å resonance line is very strong in both stars, but partially blended with a telluric O I emission line for the SM Star. The C IV 1548.2, 1550.8 Å resonance lines in the STIS spectrum of the SM Star seem to be blended with interstellar C IV lines. The carbon abundance can be determined from several other C II-III lines, such as the strong C III 1176 Å sextuplet, and is close to 1/10 solar for both stars.

Nitrogen. The N III 989.8, 991.6 Å resonance lines in the FUSE spectrum of the SM Star are blended with strong telluric O I emission lines. The strong N II 1085 Å ground-state triplet lines are blended with unidentified emission lines. The nitrogen abundance in the SM Star, about two times solar, is therefore based on the isolated N II 1006 Å line, as well as several weaker lines (the strongest being N III 1324, 1387 Å, N IV 955.3 Å, and N V 1242.8 Å). The strong nitrogen lines observed in the FUSE spectrum of CPD −56° 464 are not blended with emission lines and are best reproduced an abundance of about three times solar.

Oxygen. The oxygen abundance of CPD −56° 464, −1.7 dex relative to solar, is based on the isolated O III 1153.8 Å line. Other O III lines at 1138.5, 1149.6, and 1150.9 Å, are consistent with this abundance, but are blended with either identified or unidentified lines. Due to the lower quality of the FUSE spectrum of the SM Star, no isolated oxygen lines are detected. Also O IV 1343.5 Å in the STIS spectrum is not detected, which excludes oxygen abundances of more than about 1/20 solar.

Neon. No neon lines are detected for either star. Because Ne II-III lines are also not observed in the FUV spectra of other sdB stars, their central wavelengths can not be confirmed. We therefore prefer not to state upper limits, although abundances higher than 1.3 dex relative to solar seem unlikely.

Magnesium. No magnesium lines are clearly detected for the SM Star and non-detection of Mg II 1369, 1478 Å excludes abundances of more than 10 times solar. While the EFOSC2 spectrum of CPD −56° 464 covers the Mg II 4481 Å doublet at high S/N, its low resolution means

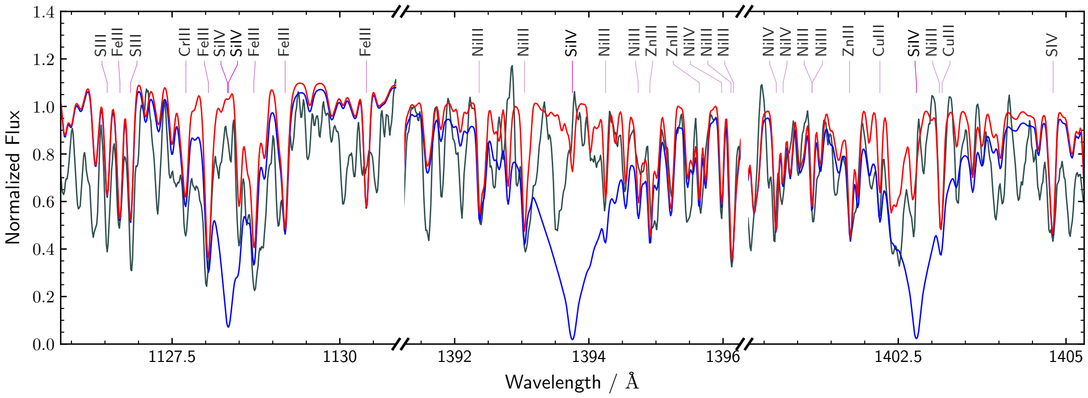

Figure 3.2.4. FUSE and STIS spectral ranges showing the lack of silicon lines in the SM Star. The blue model is identical to the final model for the SM Star (red), except that the silicon abundance is set to the (still sub-solar) value of CPD −56° 464.

that these lines are blended with the Al III 4479 Å doublet, making them useless for abundance determination.

Aluminium. Aluminium III lines at 1605.77 Å and 1611.87 Å in the STIS spectrum of the SM Star are best reproduced at an abundance of about −2.3 dex solar. The only detected aluminium line in the FUSE spectrum of CPD −56° 464, Al III 1162.6 Å, would be well reproduced at an abundance of 1.5 times solar, which would be much larger than the abundance of the SM Star. Because the line is blended with two unidentified lines and its theoretical wavelength may be slightly off, we only state an upper limit of 6 times solar.

Silicon. No silicon lines are observed in the spectrum of the SM Star. Even the Si IV 1393.76, 1402.77 Å resonance doublet is too weak to be detected, as shown in Fig. 3.2.4. These lines are very strong in CPD −56° 464 despite its low silicon abundance of about 1/3 solar. Although several Si III lines are detected in CPD −56° 464, none are detected in the SM Star. This lack of Si III-IV lines allows us to set a very low upper limit on the silicon abundance of the SM Star, about 1 / 300 000 solar (−5.5 dex). Such low silicon abundances have been observed before in hot subdwarfs at $T_{\mathrm{eff}} \gtrsim 32000$ K, such as the He-poor sdOB Feige 66 (Baschek et al. 1982b; O'Toole & Heber 2006).

Phosphorus. The phosphorus abundance of CPD −56° 464, −1.5 dex relative to solar, is based on P III 998 Å, as well as P IV 1030.5, 1033.1, 1035.5 Å in its FUSE spectrum. These P IV lines are clearly detected for the SM Star as well and are well reproduced at the same abundance. There are no detectable phosphorus lines in the STIS spectrum of the SM Star.

Sulphur. Several strong S II-V lines are observed FUV spectrum of the SM Star, the strongest being the S IV resonance triplet at 1062.7, 1073.0, and 1073.5 Å, S IV 1098.9 Å, S III 1015.5 Å, as well as the resonance S III sextuplet around 1198 Å. S V 1501.8 Å is too weak in the best-fit model, but might be blended with an unidentified line. S III-IV lines are best reproduced at an abundance of about 1.3 times solar. The sulphur abundance of CPD −56° 464 is close to solar.

Chlorine. A sub-solar abundance, −2.5 dex relative to solar, was derived for the SM Star from strong Cl IV resonance lines at 977.6 Å and 986 Å. The latter is blended with an equally strong Mn III line and several weaker lines. The chlorine abundance of CPD −56° 464, −1.5 dex, is also strongly sub-solar.

Argon. The strongest isolated argon lines in the FUV spectra of the SM Star, Ar III 1295.6, 1669.3, 1669.7 Å, are best reproduced at an abundance of about 20 times solar. Several other argon lines would be consistent with higher abundances, but might be blended with unidentified lines. The strongest usable argon lines in the FUSE spectrum of CPD −56° 464, Ar III 983.04, 986.07, 1042.7 Å, as well as Ar IV 1002.1 Å are all weaker than 20 mÅ and blended with lines of similar strength. The best-fit abundance, about 3.4 times solar, is therefore rather uncertain.

Table 3.2.3. Abundance results for CPD −56° 464 and the SM Star by number fraction ($\log \epsilon$) and number fraction relative to the photospheric solar values of Asplund et al. (2009, $\log \epsilon/\epsilon_\odot$).

	$\log \epsilon$		$\log \epsilon/\epsilon_\odot$	
Element	CPD −56° 464	SM Star	CPD −56° 464	SM Star
H	−0.01 ± 0.00	−0.01 ± 0.00	0.03 ± 0.00	0.03 ± 0.00
He	−1.91 ± 0.20	−1.71 ± 0.20	−0.80 ± 0.20	−0.60 ± 0.20
C	−4.71 ± 0.20	−4.71 ± 0.30	−1.10 ± 0.21	−1.10 ± 0.31
N	−3.71 ± 0.20	−3.89 ± 0.40	0.50 ± 0.21	0.31 ± 0.41
O	−5.01 ± 0.50	−5.01 ± 0.30	−1.66 ± 0.51	−1.66 ± 0.31
Mg		−3.83 ± 0.40		0.60 ± 0.40
Al	$<-5.41^{+0.60}$	−7.89 ± 0.30	$<0.18^{+0.60}$	−2.31 ± 0.30
Si	−5.01 ± 0.30	$<-10.01^{+1.00}$	−0.48 ± 0.30	$<-5.48^{+1.00}$
P	−8.16 ± 0.30	−8.11 ± 0.40	−1.53 ± 0.30	−1.48 ± 0.40
S	−4.91 ± 0.40	−4.81 ± 0.30	0.01 ± 0.40	0.11 ± 0.30
Cl	−8.01 ± 0.40	−9.01 ± 0.60	−1.47 ± 0.55	−2.47 ± 0.81
Ar	−5.11 ± 0.40	−4.31 ± 0.40	0.53 ± 0.43	1.33 ± 0.43
Ca	−4.71 ± 0.50	−4.01 ± 0.30	0.99 ± 0.50	1.69 ± 0.30
Ti	−6.01 ± 0.40	−5.78 ± 0.20	1.08 ± 0.41	1.31 ± 0.21
Sc		−7.01 ± 0.40		1.88 ± 0.40
V	−7.06 ± 0.25	−6.53 ± 0.20	1.05 ± 0.27	1.57 ± 0.22
Cr	−5.61 ± 0.30	−5.31 ± 0.30	0.79 ± 0.30	1.09 ± 0.30
Mn	−5.93 ± 0.30	−6.01 ± 0.40	0.68 ± 0.30	0.60 ± 0.40
Fe	−4.59 ± 0.30	−5.16 ± 0.25	−0.05 ± 0.30	−0.62 ± 0.25
Co	−6.81 ± 0.35	−6.16 ± 0.40	0.24 ± 0.36	0.89 ± 0.41
Ni	−4.91 ± 0.25	−5.23 ± 0.15	0.91 ± 0.25	0.59 ± 0.16
Cu	−6.01 ± 0.50	−6.13 ± 0.20	1.84 ± 0.50	1.71 ± 0.20
Zn	−6.11 ± 0.40	−5.46 ± 0.20	1.37 ± 0.41	2.02 ± 0.21
Ga	−7.16 ± 0.60	−6.49 ± 0.25	1.84 ± 0.62	2.51 ± 0.27
Ge		−6.23 ± 0.30		2.16 ± 0.32
As	−8.61 ± 0.40	−7.11 ± 0.30	1.13 ± 0.40	2.63 ± 0.30
Se	−8.21 ± 0.60		0.49 ± 0.60	
Kr	−6.41 ± 0.50	−5.71 ± 0.50	2.38 ± 0.51	3.08 ± 0.51
Y	−7.11 ± 0.40		2.72 ± 0.41	
Zr	−6.76 ± 0.40	−7.41 ± 0.60	2.70 ± 0.40	2.05 ± 0.60
Nb		$<-7.21^{+0.60}$		$<3.37^{+0.60}$
Mo	$<-8.01^{+0.60}$	−6.61 ± 0.80	$<2.15^{+0.60}$	3.55 ± 0.82
Sn	−8.31 ± 0.40	−8.41 ± 0.30	1.69 ± 0.42	1.59 ± 0.32
Sb	−10.31 ± 0.50	−9.41 ± 0.50	0.72 ± 0.51	1.62 ± 0.51
Te	$<-7.51^{+0.60}$	$<-7.71^{+0.60}$	$<2.35^{+0.60}$	$<2.15^{+0.60}$
Pb	−8.36 ± 0.35	−7.41 ± 0.30	1.93 ± 0.37	2.88 ± 0.32
Bi	$<-9.91^{+0.60}$	$<-8.71^{+1.00}$	$<1.48^{+0.60}$	$<2.68^{+1.00}$

Calcium. Several strong and isolated Ca II-III lines are present in the STIS spectrum of the SM Star (e. g. Ca II 1553.2, 1554.6 Å and Ca III 1298.0, 1317.7, 1385.4, 1397.7 Å). Most lines are best reproduced at an abundance about 50 times solar, although there is some scatter between individual lines. The calcium abundance of CPD −56° 464 is identical to that of the SM Star and was determined based on the weak but isolated Ca III 955.9, 960.2 Å lines, as well as Ca III 1001.3 Å, which is blended with a Cr III line.

Scandium. Two strong scandium lines, Sc III 1603.1, 1610.2 Å, are observed in the STIS spectrum of the SM Star. They are best reproduced at an abundance of about 80 times solar. It is not possible to determine an abundance for CPD −56° 464 because the rest wavelengths of the weak predicted Sc III lines in the FUSE rage, e. g. at about 1168.6 Å, seem to be poorly known.

Titanium. Several strong and isolated titanium lines are observed in the STIS spectrum of the SM Star, for example Ti III 1293.2, 1422.4, 1455.2 Å and Ti IV 1451.7, 1467.3 Å. These lines are best reproduced at an abundance of about 20 times solar. The Ti IV 1183.6 Å line in the FUSE spectrum of CPD −56° 464 is well reproduced at an abundance of 12 times solar, although the Ti III 1005 Å sextuplet is slightly too strong at this abundance. Because Ti IV 1183.6 Å is well reproduced in the FUSE spectrum of the iHe-sdOB HZ 44 at an abundance derived from optical lines (Dorsch et al. 2019), we choose to trust this line rather than the weaker and blended Ti III lines.

Vanadium. Strong isolated V III lines at 1254.0 Å and 1335.1 Å, as well as several V III lines between 1150 Å and 1165 Å in the FUV spectra of the SM Star are best reproduced at an abundance of about 40 times solar. This abundance is consistent with several V IV lines. e. g. at 1317.6, 1355.1, and 1403.6 Å. The clearly detected V III lines in FUSE spectrum of CPD −56° 464 can be used to estimate its vanadium abundance to about 10 times solar.

Chromium. Many strong and isolated chromium lines are detected in the STIS and FUSE spectra of the SM Star. Several Cr III lines in the 1245 – 1265 Å range are best matched at an abundance of about twelve times solar. This is consistent with strong Cr III lines in the 1030 – 1165 Å range, and Cr IV lines, for example at 1319.7 Å and 1380.5 Å. Since there is some scatter between individual lines, we adopt a relatively large uncertainty of 0.3 dex. Chromium III lines are also strong in the spectrum of CPD −56° 464 and show the same scatter. They are best reproduced at an abundance of about six times solar. In the future, the atomic data used for chromium lines should be re-evaluated using a non-LTE model atom. This would require accurate photoionisation cross-sections, which are currently not available.

Manganese. Many manganese lines are predicted in the FUV spectrum of the SM Star, although most lie between 940 and 960 Å, where the S/N of the FUSE spectrum is very low. The strongest Mn IV lines are observed between 1650 and 1670 Å, where the S/N of the STIS spectrum is low, while Mn III 1283.6, 1287.6 Å are blended with a Si II feature. However, several other lines, such as Mn III 1111.1, 1114.5, 1239.2 Å and Mn IV 1252.0, 1257.3, 1667.0 Å, are well reproduced at an abundance of about four times solar. We adopt this abundance with a high uncertainty of 0.4 dex. Due to the higher S/N of its FUSE spectrum, the manganese abundance of CPD −56° 464, about 5 times solar, can be determined more precisely.

Iron. Many strong Fe III-IV lines in the STIS spectrum of the SM Star, in particular in the 1500 – 1670 Å range, are best matched at an abundance of about 1/4 solar. Also the FUSE spectrum of the SM Star shows many strong Fe III lines. The same lines are stronger in the FUSE spectrum of CPD −56° 464, where they are best reproduced at an abundance close to solar.

Cobalt. Both the FUSE and STIS spectra of the SM Star show many strong cobalt lines, such as Co III 1043.2, 1044.3, 1095.5 Å and Co IV 1502.2, 1521.6 Å. They are best reproduced on average at an abundance of about 8 times solar. The cobalt abundance for CPD −56° 464, about twice solar, is mostly based on the aforementioned Co III lines, as well as Co III 944.8 Å.

Nickel. Many strong Ni III-IV lines are observed in the 1300 – 1670 Å range of the SM Star, including isolated lines. They are best reproduced at an abundance of about four times solar. This abundance is consistent with the isolated Ni III 1070.5 Å line and the blended but strong

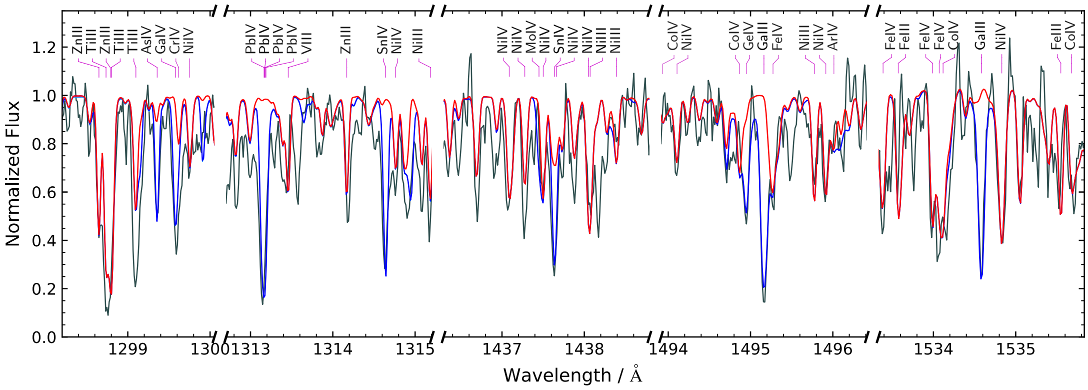

Figure 3.2.5. Strong Ga III-IV, Ge IV, As IV, Sn IV, and Pb IV lines in the STIS spectrum of the SM Star. Modelled heavy metal lines are shown in blue, other lines in red.

Ni III 979.6 Å line. Due to the higher S/N and smaller interstellar column densities, more nickel lines are visible in the FUSE spectrum of CPD −56° 464. Strong and fairly isolated nickel lines, most notably Ni III 955.0, 965.5, 994.1, and 1070.5 Å are on average best reproduced at an abundance of 8 times solar.

Copper. Several strong and isolated Cu III lines are detected in the 1330 – 1680 Å range in the STIS spectrum of the SM Star, for example Cu III 1376.8, 1593.8, 1628.3, 1639.0 Å. These lines are best matched at abundance of about 50 times solar. There are no observable Cu III lines in the FUSE range. The Cu IV lines predicted in this range are weak at the temperature of the SM Star and CPD −56° 464, making it more difficult to determine the copper abundance for CPD −56° 464. The Cu IV 1058.0, 1064.0 Å lines are consistent with Cu III lines observed in the STIS range in the SM Star. These lines are also present in the FUSE spectrum of CPD −56° 464, which, due to its higher S/N, also shows many other Cu IV lines. Although the scatter is large between individual lines, it is possible to estimate an abundance of about 70 times solar.

Zinc. Many strong and well isolated Zn III and Zn IV lines in the STIS spectrum of the SM Star are best reproduced at an abundance of about 200 times solar, e. g. Zn III 1473.4, 1491.0, 1499.4 Å and Zn IV 1320.7, 1349.9 Å. Zinc lines in the FUSE spectrum are weaker and show some scatter – the atomic data for Zn IV lines in the FUSE range seem to be subject to large uncertainties. Because TOSS data for Zn IV (Rauch et al. 2014) do not include lines from high-lying levels, Kurucz data are used. It is still possible to roughly estimate the zinc abundance of CPD −56° 464 using lines that were consistent between the STIS and FUSE spectra of the SM Star, such as Zn IV 979.3, 998.5, 1001.9, 1177.5 Å. These lines are best reproduced at an abundance of about 20 times solar. Despite its large uncertainty, this abundance is significantly lower than that of the SM Star.

Gallium. The STIS spectrum of the SM Star shows strong gallium lines. The particularly strong resonance Ga III lines at 1495.045, 1534.462 Å are well reproduced at an abundance of about 320 times solar (see Fig. 3.2.5). Many weaker but still isolated Ga IV lines are consistent with this value, including Ga IV 1195.0, 1245.5, 1258.8, 1264.6 Å in the STIS spectrum and Ga IV 1170.6 Å in the FUSE spectrum. This latter line was used to determine the gallium abundance in CPD −56° 464 to about 70 times solar (see Fig. 3.2.7), consistent with the blended Ga IV 965.2, 986.8 Å.

Germanium. The strongest germanium lines in the spectra of the SM Star are by far the Ge IV 1189.0, 1229.8 Å resonance lines, the latter being blended with a SN 1006 Si II feature. Both lines have been used extensively in previous studies of sdB stars, and their oscillator strengths are relatively well known. Ge IV 1189 Å is best reproduced at an abundance of about 300 times solar, but at this abundance, the strong Ge III 1088.5 Å resonance line in the FUSE spectrum

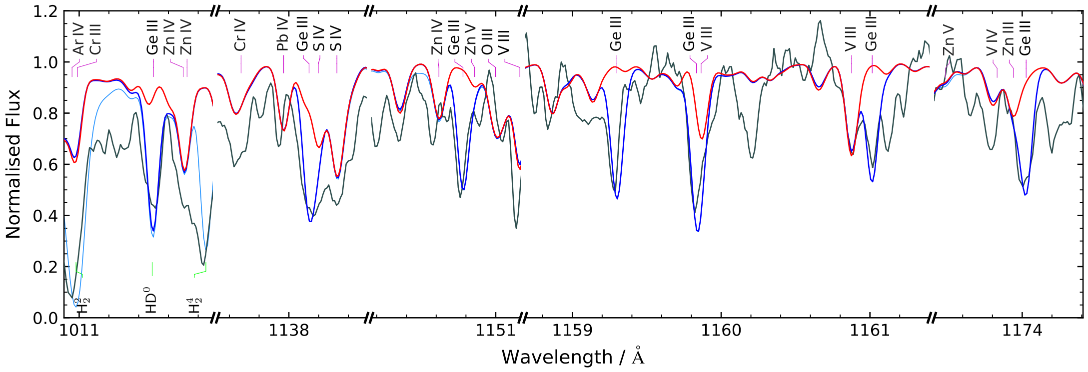

Figure 3.2.6. Newly identified Ge III lines (blue) in the FUSE spectrum of the SM Star at an abundance of 150 times solar. In addition, interstellar lines are shown in light blue.

is too strong. Based on atomic data by Claudio Mendoza (priv. comm.)[5], the newly identified Ge III 1011.4, 1138.0, 1150.7, 1159.2, 1159.7, 1160.9, 1173.9 Å prefer about 150 times solar, which is the adopted value (see Fig. 3.2.6). The Ge III 1088.5 Å line in the FUSE spectrum of CPD −56° 464 appears to be broadened by the Stark effect and would require experimental Stark broadening parameters to be well reproduced, which are not available. Because most germanium lines are not covered for CPD −56° 464 we do not state an abundance for this star.

Arsenic. The strong As IV 1299.3 Å line in the STIS spectrum of the SM Star is best reproduced at an abundance of about 430 times solar, as shown in Fig. 3.2.5. The weaker As V 987.7, 1029.5 Å lines are consistent with this value, but blended with interstellar lines. The former line is strong and fairly isolated in the FUSE spectrum of CPD −56° 464 and well reproduced at an abundance of 13 times solar (see Fig. 3.2.7). This is considerably less than the abundance derived for the SM Star.

Selenium. The strongest selenium line observed in the FUSE spectrum of CPD −56° 464 is Se IV 996.71 Å, which is best reproduced at an abundance of three times solar. This is consistent with several weak and blended Se III-IV lines. Here, we used data from Morton (2000) for three Se IV lines and data from Tauheed & Hala (2012) for 38 Se III lines. Due to the lack of more comprehensive and reliable data for Se III-IV, we assume a large uncertainty of 0.6 dex. No selenium lines are clearly detectable in the STIS and FUSE spectra of the SM Star, although Se IV 996.71 Å would be consistent with an abundance of three times solar, if its position is assumed to be correct. The enrichment of selenium observed for both stars therefore seems to be lower than that of other heavy metals.

Krypton. Like Dorsch et al. (2019), we used atomic data from Rauch et al. (2016) for Kr IV, but we have added data for Kr III from Raineri et al. (1998), which were also used for the analysis of the optical spectrum of Feige 46 and LS IV−14° 116 by Dorsch et al. (2020). The strongest krypton lines in the STIS spectrum of the SM Star, Kr IV 1525.17, 1538.21, 1558.51, and 1569.82 Å, have equivalent widths between 20 and 25 mÅ. They are best reproduced at an abundance of about 1200 times solar. Most other predicted krypton lines are consistent with this abundance, including the equally strong Kr III 987.23 Å. This line is also present in the FUSE spectrum of CPD −56° 464, but had to be shifted to 987.527 Å in order to be consistent with Kr IV 983.053 Å (see Fig. 3.2.7). These lines are then well reproduced at an abundance of 240 times solar.

Strontium. Strontium lines were observed in the FUV spectrum of Feige 46 by Latour et al. (2019b), the strongest being Sr IV 1331.13 Å. The same line can not be detected clearly in the STIS spectrum of the SM Star. Several Sr III lines in the FUSE spectrum of CPD −56° 464 almost match to the position of otherwise unidentified lines, for example Sr III 1044.92, 1098.77, 1125.50 Å, but are too weak to be clearly identified. We therefore prefer not to state a strontium abundance for the SM Star and CPD −56° 464.

---

[5] These data were computed using Cowan's codes, as described by Cowan (1981), briefly summarised by e. g. Kramida (2019).

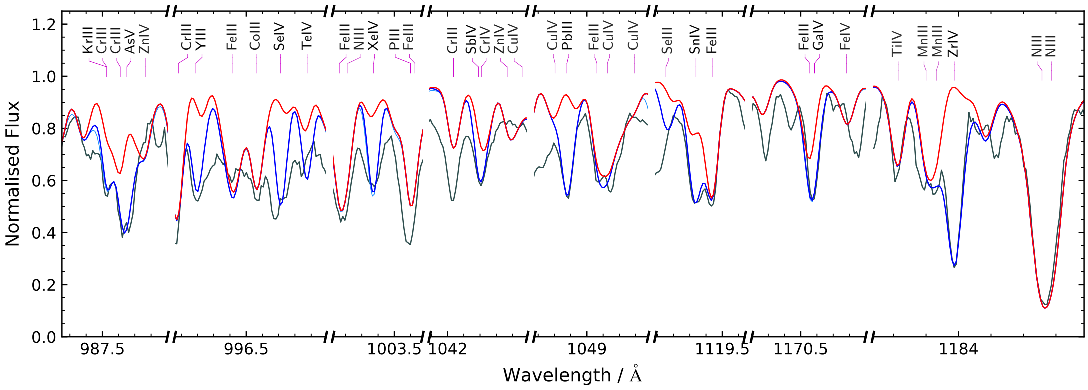

Figure 3.2.7. Strong Kr III, As V, Y III, Se IV, Te IV, Xe IV, Sb IV, Pb III, Sn IV, Ga IV, and Zr IV lines in the FUSE spectrum of CPD −56° 464. The model is red (blue with heavy metal lines).

Yttrium. We used atomic data from Fernández-Menchero et al. (2020) for Y III lines in the UV. Two fairly isolated yttrium lines, Y III 989.079 and 996.190 Å, are present in the FUSE spectrum of CPD −56° 464. They are best reproduced at an abundance of 500 times solar. Unfortunately, the FUSE spectrum of the SM Star is severely affected by interstellar and telluric lines around 990 Å, so it was not possible to determine the yttrium abundance for this star. The dominant ionisation stage in the photosphere of CPD −56° 464 and the SM Star is Y IV. Loginov & Tuchkin (2001) provided radiative lifetimes for Y IV that can be converted into oscillator strengths. Because no corresponding experimental wavelengths are available, they had to be calculated from level energies provided by NIST. Unfortunately, all Y IV resonance lines lie in the extreme UV, which means that they are not observable. Since most Y IV ions are in the ground state, the remaining predicted lines for CPD −56° 464 and the SM Star are very weak and therefore not useful for the abundance determination. These lines, for example Y IV 1034.5 and 1275.2 Å, become strong in somewhat hotter stars, such as the iHe-sdOB HZ 44 (39 kK; Dorsch et al. 2019).

Zirconium. As shown in Fig. 3.2.7, the strongest zirconium line in the UV spectra of CPD −56 464 and the SM Star is Zr IV 1184 Å, for which we used the oscillator strength of Chayer et al. (2006), $\log gf = 0$. This oscillator strength was also used by Blanchette et al. (2008). In the FUSE spectrum of CPD −56° 464, this line is best reproduced at an abundance of 500 times solar. The SM Star requires a lower abundance of 200 times solar. The blended Zr IV 1201.8 and 1469.5 Å lines are well reproduced at this abundance, whereas Zr IV 1546.2 and 1599.0 Å would be consistent with much a higher zirconium abundance. It is notable that Zr IV 4200 Å would be observable in a high-resolution and high S/N (≈150) spectrum of CPD −56° 464, given its predicted equivalent width of 20 mÅ. While such spectra do not exist for CPD −56° 464, they are available for similar He-poor sdOBs. High-resolution spectra that cover the near-UV might further be able to detect Kr III 3245.69 and 3325.76 Å at predicted equivalent widths of 20 mÅ and 13 mÅ, respectively. These lines were detected in UVES spectra of Feige 46 and LS IV−14°116 by Dorsch et al. (2020, see Sect. 3.1).

Niobium. Several strong and otherwise unidentified lines in the FUSE and STIS spectra of the SM Star can be matched with predicted niobium lines at an abundance of about 2300 times solar, e. g. Nb IV 1005.7, 1049.6, 1107.8, 1447.5, 1510.8 Å, and Nb V 1267.5 Å. However, several other Nb IV lines are too strong to match the FUSE spectrum of the SM Star when included at this abundance, e. g. Nb IV 1020.4, 1030.3, and 1044.9 Å. This may be due to inaccurate wavelengths, wrong oscillator strengths, or the low quality of the FUSE spectrum of the SM Star. Unfortunately, none of the predicted niobium lines can clearly identified in the much better FUSE spectrum of CPD −56° 464. Because no spectrum covering the range between 1200 and 1700 Å is available for CPD −56° 464, its niobium abundance can not be determined independent of the FUSE spectrum, so it is not possible to draw conclusions on the quality of atomic data for niobium lines in the FUSE range. We therefore only state an upper limit of 10 000 times solar for the SM Star and no upper limit for CPD −56° 464.

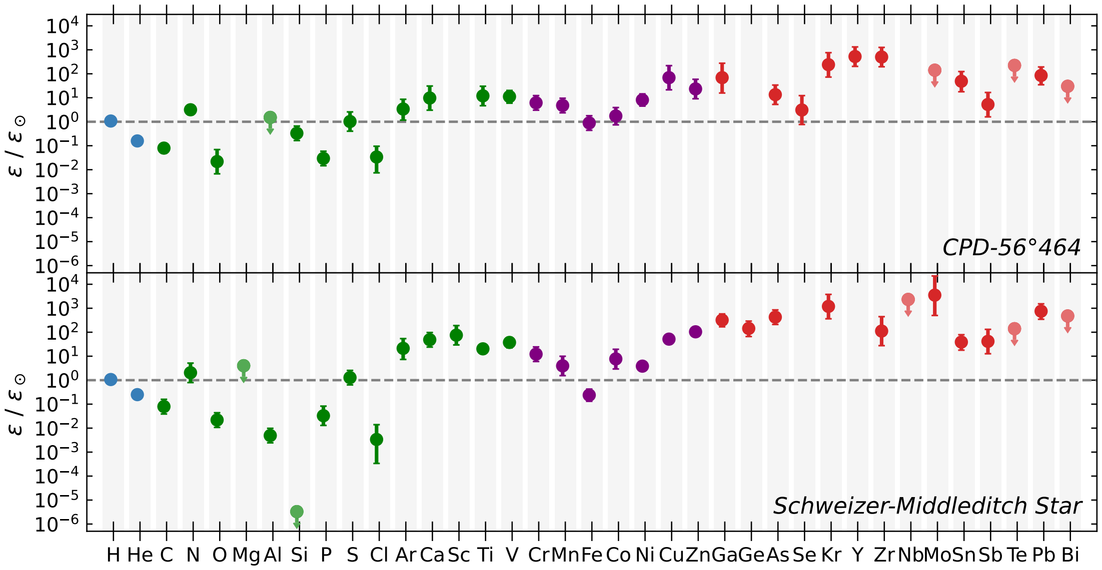

Figure 3.2.8. Abundance pattern relative to solar values for CPD −56° 464 and the SM Star.

Molybdenum. Many Mo III-V lines with estimated equivalent widths around 20 mÅ are predicted in the FUSE and STIS spectral ranges of the SM Star if molybdenum is included at an abundance of 3500 times solar. Many of these lines match the position of otherwise unidentified lines such that the overall fit is improved, for example Mo III 1295.4 Å and Mo IV 941.1, 1099.2, 1344.9, 1399.1, and 1431.2 Å. However, not all lines are well reproduced, possibly due to inaccurate atomic data or non-LTE effects. We therefore assume a high uncertainty of 0.8 dex for the molybdenum abundance of the SM Star. The molybdenum abundance of CPD −56° 464 is much lower – we derive an upper limit of 600 times solar from Mo IV 941.1, 958.9, and 966.6 Å.

Tin. The tin abundance of the SM Star, about 40 times solar, is based on the strong Sn IV 1314.54 Å and 1437.53 Å lines (see Fig. 3.2.5). Sn III 1251.39 Å is also present, but blended with the slightly weaker Cr III 1251.41 Å line. In the FUSE spectrum, Sn IV 1119.34 Å is detected, but may be blended with an unidentified IS or photospheric line while Sn IV 1044.49 Å is blended with the strong Co III 1044.29 Å line. The Sn IV 1119.34 Å line is clearly detected in CPD −56° 464 and very well reproduced at an abundance of about 50 times solar (see Fig. 3.2.7). The second tin line, Sn IV 1044.49 Å, is blended with Co III 1044.29 Å, which is too strong and inconsistent with other cobalt lines. Because interstellar lines are weaker in CPD −56° 464, Sn IV 1119.34 Å is likely not blended. We therefore adopt 50 times solar as the tin abundance for CPD −56° 464.

Antimony. Two of the three predicted antimony lines are fairly isolated and match the position of otherwise unidentified lines in the spectrum of the SM Star. The strong Sb IV 1042.19 Å line (see Fig. 3.2.7) is best reproduced at an abundance of about 40 times solar, consistent with Sb V 1226.00 Å (although blended with the blue-shifted Si II feature). Only Sb V 1104.23 Å seems to be slightly too strong at this abundance – this might be due to an inaccurate predicted central wavelength. We therefore adopt 50 times solar as the abundance, but state a large uncertainty of 0.5 dex. Sb IV 1042.19 Å is clearly detected in the FUSE spectrum of CPD −56° 464, while Sb V 1104.23 Å seems to be blended with an unidentified line. We determine an abundance of about five times solar for CPD −56° 464.

Tellurium. The dominant tellurium ions in the photospheres of CPD −56° 464 and the SM Star are Te IV-V. Unfortunately, no line positions and oscillator strengths are available for Te IV lines beyond the EUV. Line positions can be estimated from level energies and configurations as stated on NIST. Three Te IV lines at about 996.9, 1077.9, and 1168.4 Å seem to match the position of previously unidentified lines in the FUSE spectrum of CPD −56° 464 if weighted oscillator strengths of $\log gf = -1$ are assumed. Two predicted tellurium lines in the spectrum of the SM Star are strong enough to be detected. Te VI 1071.41 Å would be best reproduced at an abundance

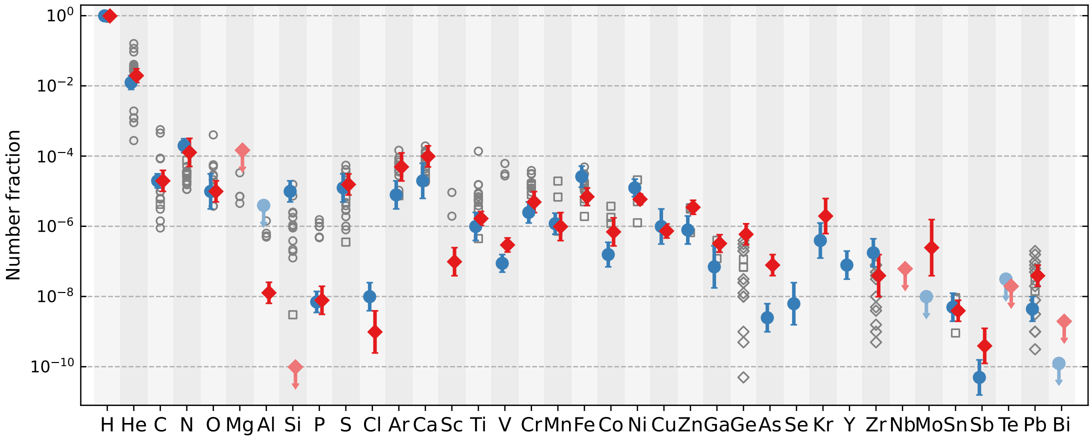

Figure 3.2.9. Abundance patterns of CPD −56° 464 (blue) and the SM Star (red) by number fraction. Upper limits are marked with an arrow and less saturated colors. For comparison, abundances for He-poor sdOB stars (27000 K $< T_{\mathrm{eff}} <$ 36000 K) are shown as grey open circles (Geier 2013), diamonds (Chayer et al. 2006), and squares (O'Toole & Heber 2006).

of about 60 times solar. The second tellurium line, Te v 1281.67 Å, is blended with the red-shifted Si ii feature. We therefore only state an upper limit of 560 times solar, based on Te vi 1071.41 Å.

Xenon. The dominant ionisation stages for xenon in the photospheres of CPD −56° 464 and the SM Star range from Xe iii to Xe v. We use atomic data for low-lying Xe iii lines from Eser & Özdemir (2017), all of which are very weak due to low weighted oscillator strengths. Like Dorsch et al. (2019), we use data from Rauch et al. (2017) for Xe iv-v. The strongest xenon line in the FUSE spectrum of CPD −56° 464 is Xe iv 1003.373 Å, which is fairly isolated and clearly detected (see Fig. 3.2.7) – the same line is blended with interstellar H_2 in the spectrum of the SM Star. Unfortunately, this line appears to be significantly affected by the Stark effect, which not only broadens but also increases the strength of the line. Because no Stark broadening parameters are available, we can therefore not use this line for abundance measurements. No other xenon lines could be identified with certainty, so no abundance or upper limit is stated for either star.

Lead. The lead abundance for the SM Star, about 760 times solar, is based on the strong the resonance lines Pb iv 1028.6 Å, Pb iv 1313.1 Å, and Pb iii 1048.9 Å. We assume a solar isotopic ratio for Pb iv 1313.1 Å. Pb iv 1028.6 Å and Pb iii 1048.9 Å (see Fig. 3.2.7) are also clearly detected in the FUSE spectrum of CPD −56° 464, where they are best reproduced at an abundance of 85 times solar. This is significantly less than derived for the SM Star.

Bismuth. Both Bi v 1139.55 Å and Bi iv 1317.07 Å match the position of observed lines in the spectrum of the SM Star. The Bi v 1139.55 Å line would best reproduced at an abundance of about 1400 times solar and it becomes clearly too strong at an abundance of 4600 solar. The stronger Bi iv 1317.07 Å line requires an abundance of only about 480 times solar. We therefore adopt an upper limit of 4600 times solar for the SM Star. A weak Bi v 1139.55 Å line is marginally detected in the FUSE spectrum of CPD −56° 464 and sets an upper limit of about 120 times solar.

The abundance patterns of CPD −56° 464 and the SM Star are compared to solar values in Fig. 3.2.8. As could be expected from their similar atmospheric parameters, these patterns are generally quite similar. Both stars show a distinctive CNO cyle-like pattern; carbon and oxygen are depleted while nitrogen is enriched. The first major difference is the abundance of silicon, which is extremely depleted in the photosphere of the SM Star but only slightly subsolar in CPD −56° 464. Iron and nickel are less abundant in the SM Star compared to CPD −56° 464, whereas most heavy metals are more abundant in the SM Star. All detected heavy metals are enriched in both stars, with the possible exception of selenium in CPD −56° 464. While these enrichments are not as extreme as observed for the "heavy metal" iHe-sdOBs, they still reach values as high as about 1000 times solar.

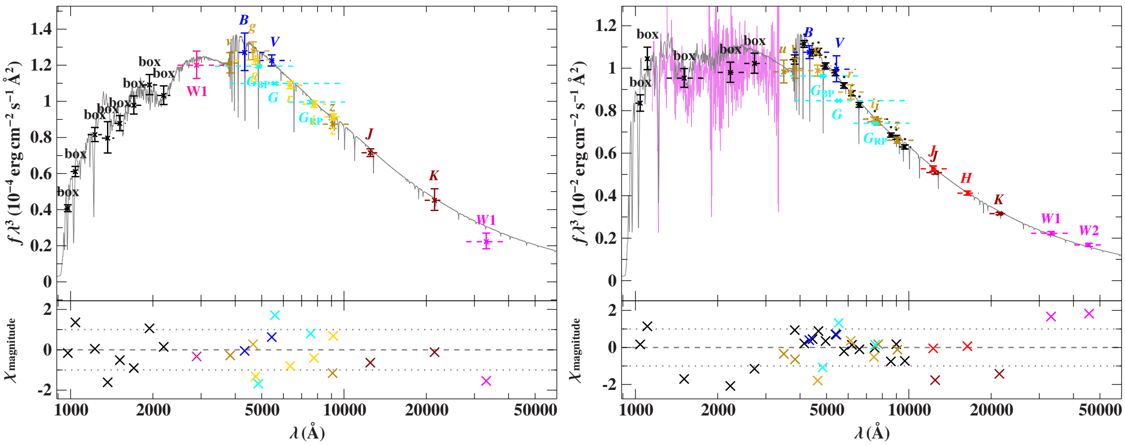

Figure 3.2.10. SED fit for the SM Star (left) and CPD −56° 464 (right). The grey line shows the best-fit model while filter-averaged flux measurements are indicated by dashed horizontal lines. Box filters constructed from HST/FOS and FUSE spectra are labelled "box" while box filters constructed from *Gaia* low-resolution spectra (De Angeli et al. 2023) are marked with a dot. Photometric surveys are identified by colour codes: XMM (hot pink, Page et al. 2012), Johnson (blue, Kilkenny et al. 1988; Girard et al. 2011), APASS (yellow, Henden et al. 2015), SkyMapper (dark yellow, Onken et al. 2019), *Gaia* (cyan, Riello et al. 2021), DECam (bright yellow, Schlafly et al. 2018; Drlica-Wagner et al. 2021), VISTA (dark red, McMahon et al. 2013), 2MASS (red, Skrutskie et al. 2006), and WISE (magenta, Schlafly et al. 2019).

A comparison with the abundances of He-poor sdOBs from literature studies is shown in Fig. 3.2.9. The abundances of light metals in CPD −56° 464 are mostly similar to the results of Geier (2013), except for low abundances of phosphorus and vanadium. These abundances are likely below the detection threshold of the optical spectra of Geier (2013), who could only determine upper limits for many stars (not shown in Fig. 3.2.9). The same is true for aluminium, silicon, and scandium in the case of the SM Star. While the gallium, tin, and lead abundances of both stars are not unusual given the large scatter observed in the studied sample of He-poor sdOBs, they seem to be more zirconium-rich than most He-poor sdOBs. Also the germanium abundance of the SM Star is slightly higher than that observed for other He-poor sdOBs.

3.2.6 Photometry and stellar parameters

The spectral energy distributions of both stars were constructed by combining magnitudes from various photometric surveys with box filters constructed from the far-UV spectra. These SEDs were modelled using the ADS/sdB model grid with $\log n(\mathrm{He})/n(\mathrm{H})$ and $\log g$ fixed to the spectroscopic values. The metallicity was a free parameter and is constrained by the far-UV magnitudes. Additional free parameters were $T_{\rm eff}$, the angular diameter, and the colour excess. The best-fit SEDs are shown in Fig. 3.2.10 and the resulting stellar parameters are listed in Table 3.2.4.

Although CPD −56° 464 and the SM Star are very similar in terms of $T_{\rm eff}$ and $\log n(\mathrm{He})/n(\mathrm{H})$, CPD −56° 464 is the much larger star. At a radius of only 0.1 $R_\odot$ the SM Star is located somewhat below the zero-age EHB, which would be expected from a core mass of less than the canonical 0.47 $M_\odot$. This is in line with the best-fit mass of 0.4 $M_\odot$, although both stars are also consistent with a mass of 0.47 $M_\odot$. Given its large radius of 0.2 $R_\odot$, CPD −56° 464 might already perform helium shell burning. This would mean that CPD −56° 464 is in the final stages of its EHB lifetime, whereas the SM Star is likely to be closer to the start of core helium fusion.

3.2.7 Conclusions

A detailed analysis of the FUV spectra of two He-poor sdOBs can only make a small contribution to the collective knowledge about the evolution of the metal abundances in He-poor sdB stars.

Table 3.2.4. Parameters derived from the SED fitting, stated as median values and using 68 % confidence. Also listed are the *Gaia* parallax and spectroscopic $T_{\rm eff}$ and $\log g$, discussed in Sect. 3.2.3.

	SM Star	CPD −56° 464
ϖ (mas)	0.60 ± 0.09	2.50 ± 0.05
d (pc)	1600^{+270}_{-210}	399^{+8}_{-7}
$\log \Theta$ (rad)	$-11.564^{+0.012}_{-0.011}$	$-10.616^{+0.012}_{-0.011}$
$E(44-55)$ (mag)	0.0805 ± 0.0029	0.0126 ± 0.0018
$z^{\dagger}$ (dex)	0.38 ± 0.11	-0.30 ± 0.17
$T_{\rm eff}^{\ddagger}$ (K)	31200 ± 1000 K	29200 ± 1000
$\log g^{\ddagger}$	6.03 ± 0.15	5.49 ± 0.10
$R(R_{\odot})$	$0.101^{+0.018}_{-0.013}$	0.215 ± 0.007
$L(L_{\odot})$	$8.7^{+3.5}_{-2.3}$	30 ± 5
$M(M_{\odot})$	$0.40^{+0.24}_{-0.15}$	$0.52^{+0.14}_{-0.11}$

Notes. $^{(\dagger)}$ The metallicity is relative to the average sdB values of Pereira (2011). $^{(\ddagger)}$ Prescribed from the spectroscopic best-fit.

However, we have shown that Tlusty/Synspec models are suitable for the analysis of such stars, and that a large number of metal abundances can be assessed without relying on optical spectra. Some of the observed ions were identified for the first time in any helium poor sdOB, including As, Se, Kr, Y, Mo, and Sb. Possibly except for selenium in CPD −56° 464, all trans-iron elements are enriched in both stars. The enrichments are systematically stronger in the SM Star. Therefore, atmospheric diffusion seems to operate more strongly in the SM Star.

The SM Star is extremely depleted in silicon, by a factor more than 300 000 compared to the Sun, while CPD −56° 464 is only moderately depleted. Michaud et al. (1985) suggested that the depletion of silicon and the observed carbon and nitrogen abundances of sdOB stars could result from a weak *homogeneous* stellar wind that strips off the very top layers of a diffusive atmosphere, in their example at a mass-loss rate of $2.5 \times 10^{-15}\,M_{\odot}\,{\rm yr}^{-1}$. Similar calculations were performed by Unglaub & Bues (2001), also assuming homogeneous winds. Due to its radius of only $0.1\,R_{\odot}$, the SM Star is indeed expected to have a weak stellar wind, even with its super-solar heavy metal abundances. Unglaub (2008) predicted a likely over-estimated mass-loss rate of about $10^{-13}\,M_{\odot}\,{\rm yr}^{-1}$ at $T_{\rm eff} \approx 30\,{\rm kK}$ and $\log g = 6$. According to his models, this mass loss is weak enough to be chemically *non-homogeneous* in the sense that the metals that drive the wind decouple from hydrogen and helium, as well as each other. O'Toole (2004) proposed such a fractionated wind as the explanation for both the depletion of silicon and the enrichment of heavy metals, when combined with diffusion. He assumed that silicon is radiatively accelerated to a velocity of about $2000\,{\rm km\,s^{-1}}$, which would be beyond the escape velocity of the SM Star, $\upsilon_{\rm esc} = \sqrt{2gR} = 1190^{+250}_{-210}\,{\rm km\,s^{-1}}$. At the same acceleration, heavier elements would be expected to be slower than $\upsilon_{\rm esc}$ and therefore fall back on the surface.

Higher mass loss rates are expected for CPD −56° 464 due to its larger radius of $0.2\,R_{\odot}$. According to Unglaub (2008), such winds might be chemically homogeneous, thereby damping diffusion processes without selective mass loss. This would explain both the moderate silicon depletion in CPD −56° 464 and its weaker heavy-metal enrichment compared to the SM Star.

More detailed diffusion calculations are required to differentiate between the hypotheses of Michaud et al. (1985) and O'Toole (2004), as well as the turbulence-damped diffusion approach of Michaud et al. (2011). As noted by Michaud et al. (2011), these models should include mass loss instead of turbulence as the mixing process competing with diffusion. Metals beyond the iron group should be considered as well. Future theoretical and observational abundance studies should further treat a larger sample with broader $T_{\rm eff}$, radius, and helium abundance ranges.

3.3 EC 22536−5304: a lead-rich and metal-poor long-period binary

The analysis presented in this chapter was published as a part of the Dorsch et al. (2021) paper. Large parts of the content of this chapter are taken verbatim from this paper.

3.3.1 Introduction

The hot component of EC 22536−5304 was identified as an extremely lead-rich iHe-sdOB by Jeffery & Miszalski (2019) – in fact the most lead-rich star known to date. Like the depletion of helium observed in the photospheres of most sdB stars, the strong enrichment in heavy metals is usually attributed to diffusion and selective radiative acceleration. However, quantitative predictions are still lacking for atomic diffusion in the atmospheres of iHe-sdOB stars.

A close inspection of new high-resolution spectra taken with SALT/HRS reveals a second component in the spectrum of EC 22536−5304: a metal-poor subdwarf F-type (sdF) main sequence (MS) star, which was not considered in the previous analysis. Many helium-poor sdB stars are found in binary systems with low-mass MS stars or white dwarfs at short orbital periods of the order of ten days or less (Kupfer et al. 2015). They are thought to be formed following a common envelope phase, in which the red giant progenitor to the sdB has lost most of its hydrogen-rich envelope, just before it ignites helium fusion in the core (Han et al. 2002).

The orbital properties of all 23 solved helium-poor sdB stars in long-period binaries have recently been published by Vos et al. (2019). They find that the orbital periods of these sdB + F/G/K-type systems range from about 500 to 1400 days. The hot subdwarf stars in such systems are the result of stable Roche overflow that occurred when the progenitor star to the sdB reached the tip of the red giant branch (RGB, Han et al. 2003; Chen et al. 2013). Only two helium-rich subdwarf stars in long-period binary systems are known: the post-asymptotic giant branch He-sdOs HD 128220 (Rauch 1993) and HD 113001 (Tomley 1970). The latter is a visually resolved binary with a very long orbital period that has likely not undergone mass transfer (Goy 1980; Orlov et al. 2010).

EC 22536−5304 is the first heavy-metal subdwarf found to be in a binary system (long- or short-period), together with the lead-rich helium-poor sdOB SB 744 (Németh et al. 2021). As we will show in the following, EC 22536−5304 is part of a long-period binary system, the first such system found at a metallicity below [Fe/H] = −1. It therefore presents a unique opportunity to study the RLOF evolutionary scenario, especially once additional spectra become available that will further constrain the orbital parameters of the system.

3.3.2 Spectral energy distribution

Due to the large difference in their effective temperatures, both components of EC 22536−5304 are easily distinguished in the SED of the system. To get an initial estimate for the atmospheric parameters of both components, a first photometric fit was performed before the spectral analysis. Free fit parameters were the effective temperature of both components, the angular diameter of the sdOB Θ_A, and the surface ratio $A_\mathrm{sdF}/A_\mathrm{sdOB}$. Here we used the same large model grids as for the spectroscopic analysis, which are described in Sect. 3.3.4. Interstellar reddening was considered after Fitzpatrick et al. (2019), assuming an extinction parameter $R(55) = 3.02$. Since no reliable UV magnitudes are available, we have constrained the colour excess not to exceed the line-of-sight value given by Schlegel et al. (1998), $E(B-V) = 0.0126\,\mathrm{mag}$[6].

The first fit was later refined by fixing the helium abundance of the hot component, the metallicity and alpha-element enhancement of the cool component, and both surface gravities to values derived from the spectral analysis. The final SED fit is shown in Fig. 3.3.1, and Table 3.3.1 compares results of the SED fit with parameters derived from the spectral fit, which is described in detail in Sect. 3.3.4.

---

[6] Dorsch et al. (2021) stated $E(B-V) = 0.126\,\mathrm{mag}$, which includes a typing error.

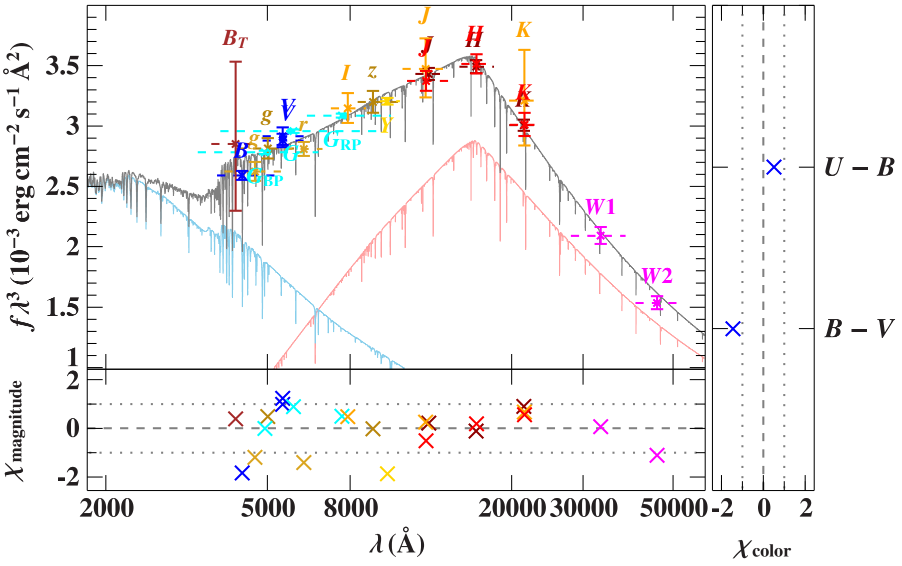

Figure 3.3.1. Photometric fit for EC 22536−5304. Filter-averaged fluxes are shown as coloured data points that were converted from observed magnitudes. Filter widths are indicated by dashed horizontal lines. The grey line visualises the combined model spectrum while individual contributions are shown in blue (A) and red (B). The residual panels at the bottom and right side respectively show the differences between synthetic and observed magnitudes and colours. The following colour codes are used to identify the photometric systems: Tycho (brown, Høg et al. 2000), Johnson-Cousins (blue, Henden et al. 2015; Kilkenny et al. 2016), SDSS (yellow, Henden et al. 2015), SkyMapper (dark yellow, Wolf et al. 2018), *Gaia* (cyan, Riello et al. 2021), DENIS (orange, DENIS Consortium 2005), DES (bright yellow, Abbott et al. 2018), VISTA (dark red, McMahon et al. 2013), 2MASS (bright red, Cutri et al. 2003), and WISE (magenta, Cutri et al. 2021). Adopted from Dorsch et al. (2021).

Table 3.3.1. SED fit and spectroscopic fit results for the hot (A) and cool component (B) of EC 22536−5304.

	SED fit	Spectral fit
$\log \Theta_{\rm A}$ (rad)	$-11.09^{+0.09}_{-0.05}$	–
$T_{\rm eff,A}$ (K)	38000^{+5000}_{-7000}	38000 ± 400
$\log g_{\rm A}$		5.81 ± 0.04
$\log n({\rm He})/n({\rm H})$		-0.15 ± 0.04
$v_{\rm tb,A}$ (km s^{-1})		2.1 ± 0.2
$v_{\rm rot} \sin i_{\rm A}$ (km s^{-1})	–	$0.0^{+1.0}_{-0.0}$
$T_{\rm eff,B}$ (K)	6460^{+90}_{-190}	6210 ± 70
$\log g_{\rm B}$		4.64 ± 0.10
$[{\rm Fe/H}]_{\rm B}$		-1.95 ± 0.04
$[\alpha/{\rm Fe}]_{\rm B}$		$+0.40 \pm 0.04$
$v_{\rm tb,B}$ (km s^{-1})		1.83 ± 0.05
$v_{\rm rot} \sin i_{\rm B}$ (km s^{-1})	–	15.3 ± 0.2
Surface ratio	34 ± 9	34 ± 5

Table 3.3.2. Spectroscopic data available for EC 22536−5304[a] .

Spectrograph	Range / Å	R	$n_{\rm exp}$	S/N
HRS/blue	3895 – 5520	43000	25	200
HRS/red	5500 – 8870	41000	9	120
RSS	3850 – 5100	1.6 Å[b]	2	100
UVES/blue	3740 – 4525	41000	3	50
UVES/red	5655 – 9463	42000	2	25

Notes. (a) The signal-to-noise ratio is the maximum reached in a combined spectrum. (b) The resolution for RSS is given as $\Delta\lambda$.

3.3.3 Spectroscopic observations

The spectroscopic data available for EC 22536−5304 are summarised in Table 3.3.2. EC 22536−5304 has been observed extensively with the Southern African Large telescope (SALT) using both the Robert Stobie Spectrograph (RSS) and the High Resolution Spectrograph (HRS). The setups used for both spectrographs are described in detail in Jeffery & Miszalski (2019). They used two long-slit RSS spectra taken in June 2018, as well as HRS spectra taken on 2017 May 18 and 2018 November 15, with exposure times of 2 × 2000 s on both occasions. These individual HRS spectra have mean signal-to-noise ratios (S/N) of about 30. Twenty-one additional blue HRS spectra were taken between 2019 May 9 and 23, increasing the combined S/N to about 200. The HRS spectra consist of short échelle orders which make order merging difficult. We use a technique which normalises all orders simultaneously, ensuring continuity across the order overlaps, before stitching the individual orders together. Some residual anomalies persist, so we have re-normalised the order-merged spectra before performing the spectral analysis. As a result, broad hydrogen and helium lines in these spectra could not be used to estimate atmospheric parameters. The HRS spectra remained essential for the detection of weak metal lines of both components, as well as the Mg I triplet. Coverage of the Mg I triplet is especially important because it is sensitive to the metallicity, alpha-enhancement, and surface gravity of the F-type companion.

In addition to the blue HRS spectra, nine red HRS spectra of sufficient quality are available. These spectra were taken on the same dates as the blue HRS spectra. Their near infrared coverage is especially useful since it includes the Ca II triplet of the F-type star, as well as He I 6678, 7065, and 7281 Å for the sdOB, all of which help to constrain the surface ratio.

We also make use of archival UVES spectra, which were obtained in October and December 2011 by M. R. Schreiber under Programme ID 088.D-0364(A). Because normalisation issues are less pronounced in the blue UVES spectra than in the HRS spectra, UVES spectra proved to be valuable for the determination of atmospheric parameters from broad hydrogen and helium lines, despite their lower S/N.

3.3.4 Spectral analysis and atmospheric parameters

As before, we used non-LTE and line-blanketed Tlusty/Synspec spectra to model the contribution of the sdOB component. Heavy metals were included in LTE in the spectrum synthesis as described by Latour et al. (2019b). The first estimate of the atmospheric parameters was obtained using the "sdOstar2020" model grid[7]. A smaller grid was then constructed around the best-fit parameters for the sdOB obtained with the first grid. To be consistent with the models used for the metal abundance analysis performed in Sect. 3.3.6, this second grid uses the largest model atoms distributed with Tlusty 205. Because these model atoms include more energy levels, optical transitions that involve high-lying levels were treated in non-LTE. The grid considers H, He, C, N, O, Ne, Mg, Al, Si, P, S, Ar, Ca, Fe, and Ni in non-LTE at abundances close to those derived

---

[7] For a detailed description of the "sdOstar2020" grid, see Sect. 2.2.2.

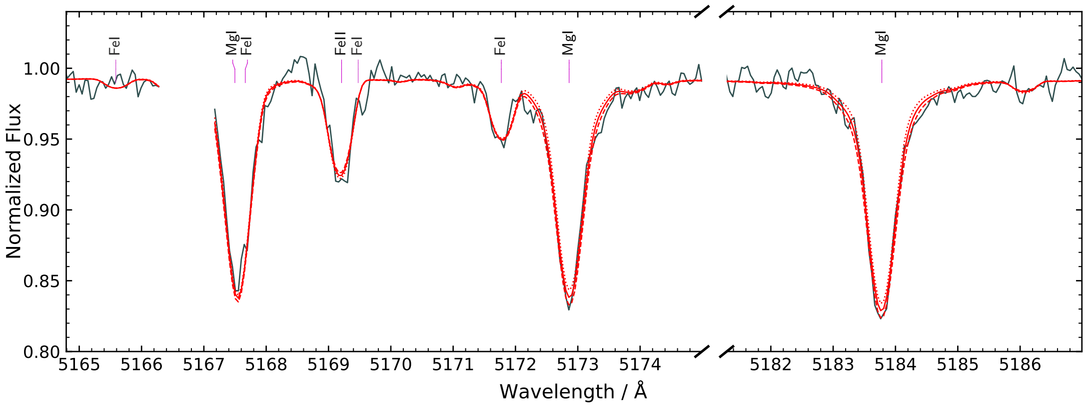

Figure 3.3.2. The Mg I triplet in the HRS spectrum of EC 22536−5304 (grey). The model spectrum (red) is the sum of the contributions of the sdOB and F-type star at the best fit. The dashed spectrum was computed at $\log g_{\mathrm{B}} = 4.9$ while the dotted spectrum uses $\log g_{\mathrm{B}} = 4.55$. Adopted from Dorsch et al. (2021).

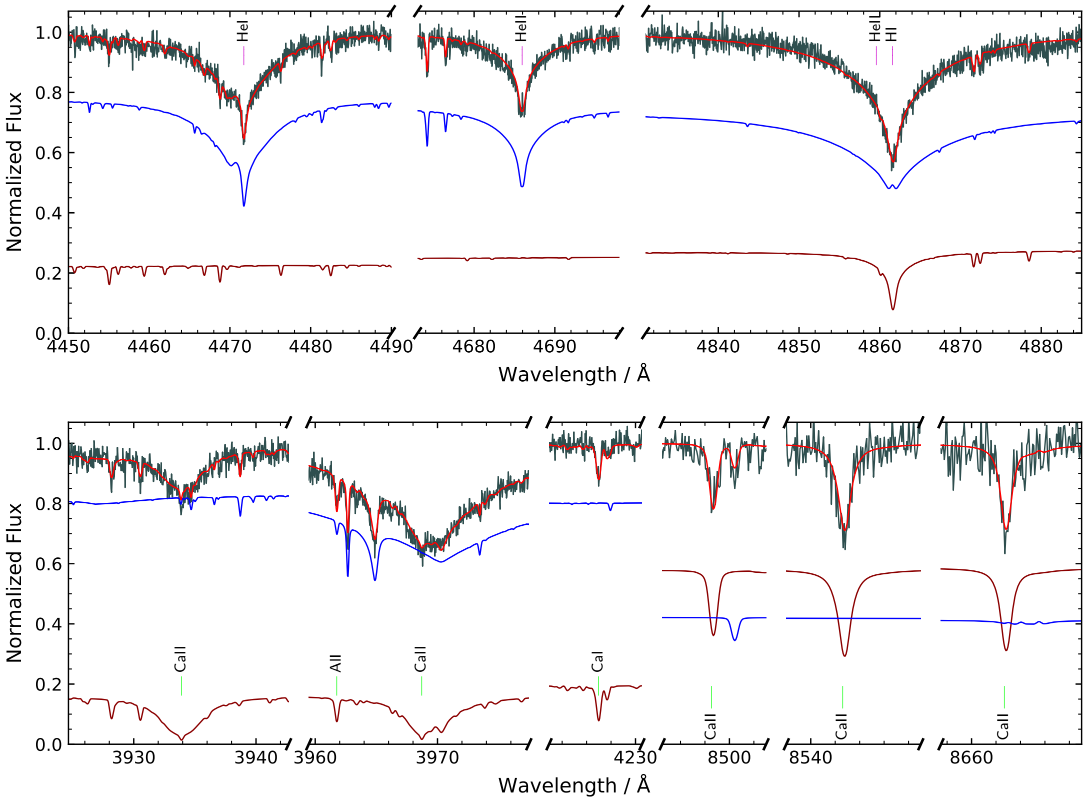

Figure 3.3.3. *Top*: Examples of prominent helium and hydrogen lines in an individual UVES spectrum of EC 22536−5304 (grey). The combined model spectrum (red) is the sum of the contributions of the sdOB (blue) and F-type star (dark red). *Bottom*: Similarly, the strongest calcium lines in blue and red UVES spectra. The lines of the sdF are labelled at the bottom. Adopted from Dorsch et al. (2021).

for the sdOB. The abundances of metals that could not be determined from the available spectra (most importantly Fe and Ni) were set to the values derived for the iHe-sdOB HZ 44 (Dorsch et al. 2019).

Similarly, the cool companion was initially modelled using a large grid of model spectra. Here, we used LTE model atmospheres and synthetic spectra computed with Atlas12 (Kurucz 1996) and Synthe (Kurucz 1993). The initial grid extends from $T_{\mathrm{eff}} = 4000$ to 8000 K, $\log g = 2.0$ to 5.2, [Fe/H] = −2.0 to +0.5 dex, and covers microturbulent velocities of $\upsilon_{\mathrm{tb}} = 0$, 1, and 2 km s^{-1}. A solar helium abundance was assumed. The F-type companion is metal poor ([Fe/H] = −1.9) and strongly alpha enhanced, which is typical for halo stars (e. g. Fuhrmann 1998). The initial grid was therefore computed using a fixed alpha enhancement of $[\alpha/\mathrm{Fe}] = 0.4$ dex relative to the photospheric solar values of Asplund et al. (2009). Like for the sdOB component, a second, smaller grid was constructed around the best-fit parameters. This grid also uses Atlas12/Synthe model spectra, but was additionally allowed to vary in alpha enhancement. The dimensions of all four grids of synthetic spectra used in this analysis are summarised in Table B.3.1.

It is challenging to determine the surface gravity of the F-type companion accurately. The wings of hydrogen lines, which are typically used to determine the surface gravity of sdB stars, are less useful for F-type stars because they are less sensitive to the density and correlate strongly with temperature. In EC 22536−5304, this is further complicated by the contribution of the sdOB, which has very broad hydrogen lines. The strength of the bluest Balmer and Paschen lines is sensitive to the surface gravity due to level dissolution. Unfortunately, our spectra lack coverage of these high Balmer lines while the high Paschen lines are below the detection limit. The observed Balmer series, from H_{α} up to H_{11}, excludes surface gravities $\log g_{\mathrm{B}} < 4.0$. Instead, the surface gravity of cool (F/G-type) stars is often derived from the Fe I-II ionisation equilibrium, which also depends on the effective temperature. The strengths of the Mg I triplet and the Ca II 3934, 3968 Å resonance lines are sensitive to the surface gravity and the respective abundances. As shown in Fig. 3.3.2, the Mg I triplet in EC 22536−5304 is well reproduced at $\log g_{\mathrm{B}} = 4.7$, assuming an alpha enhancement of 0.4 dex.

We have performed global spectral fits in order to consider all sensitive absorption lines in the observed spectra. Examples for strong hydrogen, helium, and calcium lines are shown in Fig. 3.3.3. The atmospheric parameters of both components and the surface ratio were varied simultaneously. The individual UVES and HRS exposures were not stacked but evaluated at the same time. This is necessary because the radial velocity difference between both components is not constant over more than a few days. Spectral regions that were not well reproduced were removed before performing the final fit. This includes metal lines with uncertain atomic data, as well as the cores of Ca II resonance and hydrogen Balmer lines, which are poorly modelled in our LTE models for the cool component. After a first fit using large model grids, a second global fit was performed that used tailored grids for both components, as described above.

The atmospheric parameters derived from the final spectral fit are listed in Table 3.3.1 and the full spectra are shown in Appendix B.3. They are consistent with the results obtained from the SED fit in Sect. 3.3.2, but more precise. We use 1-σ intervals for the statistical uncertainties. Due to the high resolution and high total S/N of our spectra, purely statistical uncertainties are small. The total uncertainties are dominated by systematic effects, such as deficiencies in the synthetic spectra or limited accuracy in the normalisation of our spectra. We estimate systematic uncertainties of 1% in T_{eff}, as well as 0.04 in $\log g_{\mathrm{A}}$, $\log n(\mathrm{He})/n(\mathrm{H})$, $[\mathrm{Fe/H}]_{\mathrm{B}}$, and $[\alpha/\mathrm{Fe}]_{\mathrm{B}}$. These systematic uncertainties were added in quadrature to the smaller statistical errors. We use a higher uncertainty of 0.10 dex for the surface gravity of the cool component, $\log g_{\mathrm{B}}$, for two reasons. First, there is no spectral feature that is strongly dependent on $\log g_{\mathrm{B}}$. Second, $\log g_{\mathrm{B}}$ is strongly correlated with the other free parameters $T_{\mathrm{eff,B}}$, the surface ratio, and the alpha enhancement.

We obtained a projected rotational velocity of 15.3 ± 0.2 km s^{-1} for the sdF-type companion. This rotation is relatively slow compared to the values Vos et al. (2018) found for the cool companions in their sample of nine long-period sdB + F/G/K-type systems. The sdOB is well reproduced without rotation, which is not unusual given that most hot subdwarfs are slow rotators, including those in wide binaries (Geier & Heber 2012).

Table 3.3.3. Stellar parameters for EC 22536−5304 as derived by combining the SED with atmospheric parameters from spectroscopy and the parallax distance. The mode and the highest density interval of each quantity are given for 1-σ probability (see Bailer-Jones et al. 2018).

	A	B
$R/R_\odot$	0.132 ± 0.007	0.75 ± 0.07
$M/M_\odot$	0.40 ± 0.06	$0.84^{+0.29}_{-0.23}$
$L/L_\odot$	32 ± 4	$0.74^{+0.15}_{-0.14}$

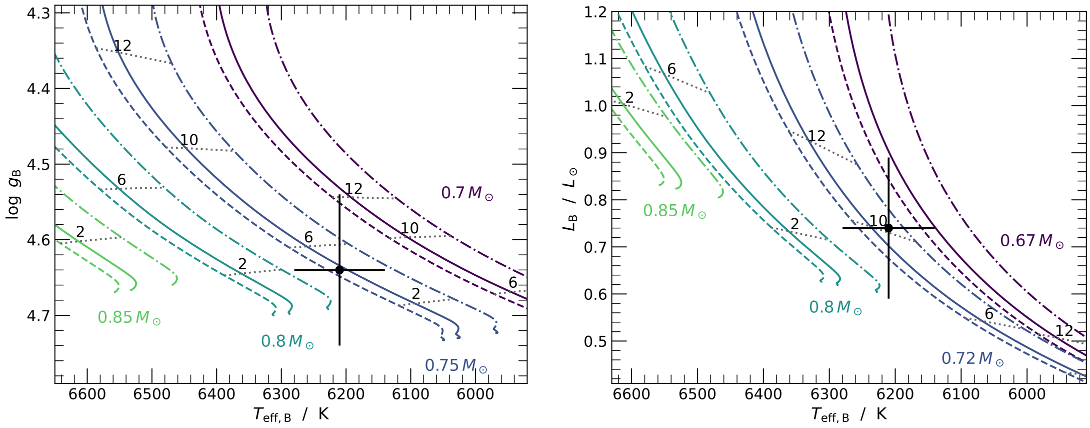

Figure 3.3.4. Main-sequence evolutionary tracks from MIST (Choi et al. 2016) for [Fe/H] = −2.1 (dashed), −1.9 (solid), and −1.6 (dash-dotted), as well as for four initial masses. The left panel shows the Kiel diagram while the Hertzsprung-Russell diagram is shown in the right panel. The dotted grey lines indicate equal age and are labelled in Gyr. The parameters of EC 22536−5304 B and their uncertainties are marked by the cross. Adopted from Dorsch et al. (2021).

3.3.5 Mass, radius, and luminosity

Stellar parameters can be derived using the precise parallax measurement provided by *Gaia* EDR3 (Gaia Collaboration et al. 2021), $\varpi = 1.40 \pm 0.04$ mas, corrected for its zero point offset (Lindegren et al. 2021) and uncertainty (El-Badry et al. 2021). Stellar radii are then given as $R = \Theta/(2\varpi)$. Here, Θ refers to the individual angular diameters determined from the SED. In contrast to the SED fit performed in Sect. 3.3.2, the angular diameter used here, $\log \Theta_{\rm A}/{\rm rad} = -11.078^{+0.018}_{-0.022}$, was obtained while keeping all atmospheric parameters fixed to the more precise spectroscopic values as listed in Table 3.3.1. The stellar parameters for both components are listed in Table 3.3.3, where uncertainties were propagated using the Monte Carlo method.

Due to the high uncertainty in surface gravity and surface ratio, the mass for the sdF component is poorly constrained. As discussed in Sect. 3.3.7, it is likely that the EC 22536−5304 system has formed through Roche lobe overflow. However, (Vos et al. 2018) predicted that a mass of less than about than 0.03 $M_\odot$ is accreted onto the cool companion in this process. Given the relatively slow projected rotation of EC 22536−5304 B, one could even argue that the transferred mass might be below this value here. We can therefore estimate a mass for the sdF component based on its spectroscopic effective temperature and surface gravity by using single-star evolutionary tracks. Figure 3.3.4 shows such evolutionary tracks from the MIST project (Choi et al. 2016) for metallicities of [Fe/H] = -1.9 ± 0.3. In the Kiel diagram (Fig. 3.3.4; left panel), our atmospheric parameters of EC 22536−5304 B are consistent with masses between about 0.8 and 0.7 $M_\odot$. We can not estimate an evolutionary age directly from the atmospheric parameters since our surface gravity puts EC 22536−5304 B close to the predicted zero-age MS. Given the low metallicity of EC 22536−5304 B, one would expect an age of the order of about 10 Gyr or more. The spectroscopic surface gravity for the sdF may therefore be slightly overestimated.

Table 3.3.4. Metal abundance results for EC 22536−5304 A by number fraction ($\log \epsilon = \log n_X / \sum_i n_i$) and number fraction relative to solar ($\log \epsilon/\epsilon_\odot$, Asplund et al. 2009). The number of resolved lines used per ionisation stage is given in the last column (with equivalent widths > 10 mÅ).

Element	$\log \epsilon$	$\log \epsilon/\epsilon_\odot$	N_{lines}
C II-IV	-2.88 ± 0.20	0.73 ± 0.21	19/45/2
N II-III	-3.73 ± 0.20	0.48 ± 0.21	22/9
O II-III	-3.46 ± 0.20	-0.11 ± 0.21	46/4
Mg II	-5.07 ± 0.30	-0.64 ± 0.30	1
Si III-IV	-5.52 ± 0.25	-0.99 ± 0.25	1/2
P III-IV	-5.92 ± 0.30	0.70 ± 0.30	1/1
S III-IV	-5.76 ± 0.30	-0.84 ± 0.30	1/1
Ar	$<-5.80^{+0.40}$	$<-0.17^{+0.41}$	
Ca	$<-5.42^{+0.40}$	$<0.27^{+0.40}$	
Ti	$<-5.84^{+0.50}$	$<1.24^{+0.50}$	
Fe	$<-4.30^{+0.30}$	$<0.23^{+0.30}$	
Zn	$<-5.36^{+0.40}$	$<2.11^{+0.40}$	
Ga	$<-5.82^{+0.40}$	$<3.18^{+0.40}$	
Ge	$<-5.89^{+0.40}$	$<2.50^{+0.40}$	
Kr	$<-4.89^{+0.40}$	$<3.90^{+0.40}$	
Sr	$<-5.27^{+0.40}$	$<3.90^{+0.40}$	
Y	$<-5.76^{+0.40}$	$<4.07^{+0.40}$	
Zr	$<-6.71^{+0.40}$	$<2.75^{+0.40}$	
Sn	$<-6.44^{+0.40}$	$<3.56^{+0.40}$	
Pb III-IV	-4.01 ± 0.30	6.27 ± 0.32	5/7

It is useful to consider the position of EC 22536−5304 B in the Hertzsprung-Russell diagram, given that the luminosity is (almost) independent of the spectroscopic surface gravity. As shown in the right panel of Fig. 3.3.4, our estimates for the luminosity and effective temperature of the sdF are consistent with a lower evolutionary mass, about 0.7 $M_\odot$. While this mass would be consistent with the expected age, the uncertainties are large.

It is not possible to directly derive an evolutionary mass for the sdOB because too many evolutionary tracks cross its position in the T_{eff} - $\log g$ plane. However, the mass expected for a sdOB that was formed through RLOF is close to the core mass that is required for the helium-flash at the top of the RGB, or about 0.49 $M_\odot$ at [Fe/H] ≈ -2 (Dorman et al. 1993). Although higher than the $0.40 \pm 0.06\, M_\odot$ found for EC 22536−5304 A, the lower value observed here is still consistent with it being a core helium burning star.

3.3.6 Metal abundance analysis

The atmospheric parameters of both components were kept fixed for the metal abundance analysis. The spectrum of the cool companion was modelled using Atlas12/Synthe using the final best-fit atmospheric parameters. We used the global χ^2 fitting procedure developed by Irrgang et al. (2014) to simultaneously determine the abundances for all metals that show sufficiently strong lines in the hot component (C, N, O, Mg, Si, P, Pb). A grid of synthetic spectra that includes lines of one metal only was computed for each metal using Synspec, always based on the same Tlusty atmosphere. This model atmosphere was calculated for the best-fit atmospheric parameters derived in Sect. 3.3.4. To allow an estimation of the microturbulent velocity, each grid was calculated for microturbulent velocities of 0 and 3 km s^{-1}. The full synthetic spectrum was then constructed by multiplication of all individual (normalised) metal spectra, which were

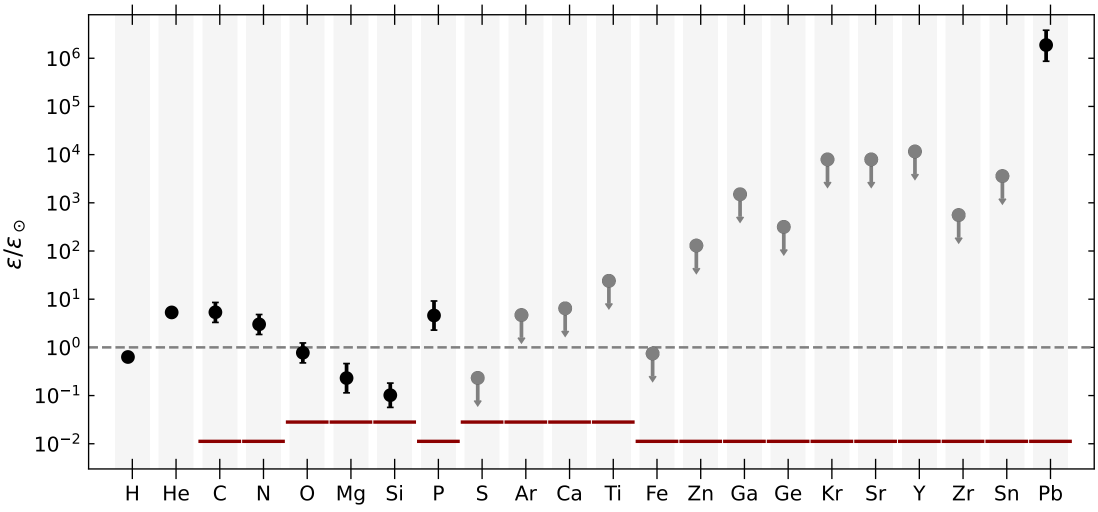

Figure 3.3.5. Photospheric abundances for EC 22536−5304 A relative to solar number fractions from Asplund et al. (2009). Abundance measurements are shown as black dots while upper limits are marked with grey arrows. Solid red lines show the corresponding metal abundances adopted in our model for EC 22536−5304 B, as given by the best-fit [Fe/H] and [α/Fe]. The solar reference is indicated by the dashed grey line.

interpolated to the desired abundances. This method is well tested for sdB and other B-type stars (e. g. Schaffenroth et al. 2021; Irrgang et al. 2020). It assumes that small changes in the metal abundances do not influence the atmospheric structure and that there are few intrinsic blends between lines of different metals. The abundance fitting procedure was repeated using a Tlusty atmosphere that consistently includes the abundances from a first fit. As before, spectral regions that were not well reproduced were removed from the fit.

Because the observed lines that originate from the sdOB component show no strong signs of a microturbulent velocity, the best-fit $v_{\mathrm{tb,A}} = 2.1 \pm 0.2\,\mathrm{km\,s^{-1}}$ can be considered as an upper limit. The final abundance pattern for EC 22536−5304 A is listed in Table 3.3.4 and shown in Fig. 3.3.5. Upper limits were derived by eye. They are stated as best-fit values, with an uncertainty that indicates at which abundance the predicted lines become clearly too strong. The analysis of individual metal abundances is described in the following.

Plenty of strong C ii-iv, N ii-iii, and O ii-iii lines are present in the spectrum of EC 22536−5304A. The C ii atom was updated to use resonance-averaged photo-ionisation cross-sections using data from TOPbase (Cunto et al. 1993). This slightly changes the strengths of C ii lines, but has little effect on the general atmospheric structure because C ii represents a small fraction of all carbon ions throughout the atmosphere (< 2 %). The sdOB star is enriched in carbon and nitrogen and has an approximately solar oxygen abundance. The carbon, nitrogen, and oxygen lines in the spectrum of the F-type companion are too weak to be detected. The Mg ii 4481 Å doublet is present in both components, but the contribution of the sdOB is larger, despite its subsolar magnesium abundance. This is because the flux contribution of the sdOB star is more than twice that of the F-type companion in this specific range. The derived silicon abundance for the sdOB, about 1/10th solar, is mostly based on the strong Si iv 4088.9, 4116.1 Å lines and the weaker Si iii 4552.6 Å line. The only detected silicon line that originates from the cool companion, Si i 3905.52 Å, is consistent with an alpha-enhancement of 0.4 dex. Two weak phosphorus lines in the spectrum of the sdOB, P iii 4222.2 Å and P iv 4249.7 Å, are clearly identified. They are best reproduced at an abundance of about five times solar. All detected calcium lines originate from the cool component. Most notably the Ca i 4226.7 Å resonance line and the Ca ii 8498, 8542, 8662 Å triplet are well reproduced at an alpha-enhancement of 0.4 dex.

As shown in Fig. 3.3.6, strong Pb iv lines are present at rest wavelengths of 3962.5, 4049.8, 4174.5, 4496.2, 4534.4, 4534.9, and 4605.4 Å. Although weaker, Pb iii lines at 3854.1, 4272.7, 4571.2, 4761.1, and 4798.6 Å are clearly detected. All identified lead lines are listed in Table

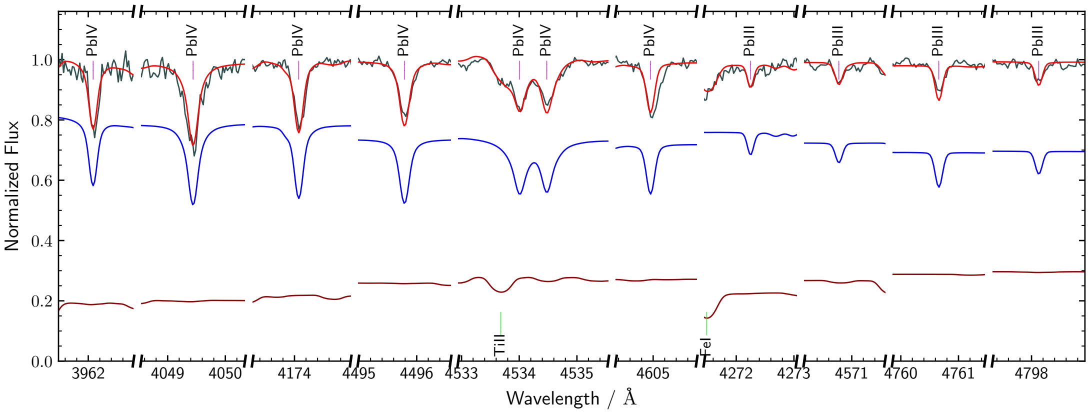

Figure 3.3.6. Very strong lead lines in the HRS spectrum of EC 22536−5304 (grey). The combined model spectrum (red) is the sum of the contributions of the sdOB (blue) and the F-type star (dark red). Adopted from Dorsch et al. (2021).

Table 3.3.5. Lead lines detected in the spectrum of EC 22536−5304. References for the oscillator strengths are stated in the last column.

Ion	λ / Å	$\log gf$	Ref.
Pb III	3854.080	+0.302	1
Pb III	4272.660	−0.462	1
Pb III	4571.219	+0.029	1
Pb III	4761.120	+0.012	1
Pb III	4798.590	−0.356	1
Pb IV	3962.467	−0.047	2
Pb IV	4049.832	−0.065	2
Pb IV	4174.478	−0.444	3
Pb IV	4496.223	−0.437	3
Pb IV	4534.447	+1.190	3
Pb IV	4534.917	+1.102	3
Pb IV	4605.400	−0.991	3

Notes. (1) Alonso-Medina et al. (2009), (2) Safronova & Johnson (2004), (3) Alonso-Medina et al. (2011).

3.3.5. The 2019 HRS spectra were shifted to the rest frame of the sdOB and co-added to update the wavelengths of newly observed lead lines. This co-added spectrum was not used for the abundance fit, which, as before, was performed using all individual spectra. All modelled lead lines are reasonably well reproduced at an abundance between one and two million times solar, or 100 million times larger compared to the scaled solar abundance at the metallicity of the cool companion. This is significantly more than the 4.8 dex enrichment derived by Jeffery & Miszalski (2019), who were unaware of any flux contribution from a companion.

Table 3.3.4 also lists upper limits for several elements that have been detected in other iHe-sdOBs, in particular Feige 46 and LS IV−14°116 (Dorsch et al. 2020). Since no lines from these elements are detected, any “best-fit” abundance obtained from a χ^2 fit would strongly depend on the location of the continuum. We therefore prefer to obtain upper limits by eye. All lines used to derive upper limits for EC 22536−5304 A up to iron are known to be well-reproduced in our models of other He-sdOB stars. For sulphur, we use the weak S IV 4485.7, 4504.2 Å lines, which seem to be just below the detection limit of the HRS and UVES spectra of EC 22536−5304. The only usable predicted argon line is Ar III 4183.0 Å. The upper limits for calcium and titanium are based on Ca III 4233.7, 4240.7 Å and Ti IV 4618.2, 5398.9, 5492.5 Å, respectively. The upper limit for iron is based on the non-detection of Fe III 4164.7, 4304.8, 4310.4 Å. In addition to lead, we have also searched for heavy metals that have been detected in optical spectra of the intermediate He-sdOBs Feige 46 and LS IV−14°116: Zn, Ga, Ge, Kr, Sr, Y, Zr, and Sn. Upper limits for these elements are based on the non-detection of Zn III 4818.9, 5075.2 Å, Ga III 4380.6, 4381.8, 4993.9 Å, Ge III 4179.1, 4260.9 Å, Kr III 4067.4, 4226.6 Å, Sr III 3936.4 Å, Y III 4039.6, 4040.1 Å, Zr IV 4198.3, 5462.4 Å, and Sn IV 4216.2 Å. We used the same atomic data as Dorsch et al. (2020) for these ions. The resulting upper limits rule out extreme enrichments as observed for lead, but would still be consistent with strong enrichment compared to solar or even mean sdB values. Ultraviolet spectra would enable us to determine abundances for most of these heavy metals, but are not presently available. A small number of lines in the UVES and HRS spectra remain unidentified. The identification of these lines is complicated by the composite nature of EC 22536−5304, since the lines of the F-type companion are only slightly more broadened by rotation than those of the sdOB. Table B.3.2 lists the rest wavelengths of all detected unidentified lines, assuming that they originate from the sdOB component. We only list lines that are present in both coadded HRS and coadded UVES spectra, or are strong enough to be detected in single exposures.

The overall abundance pattern for EC 22536−5304 A is similar to that derived by Jeffery & Miszalski (2019), but shifted to higher abundances due to the contribution of the sdF star (unaccounted for previously). Carbon, nitrogen and phosphorus are enhanced relative to solar values, while the oxygen abundance is about solar. Magnesium, silicon, and sulphur are sub-solar. With respect to the system's primordial abundances as approximated by the observed abundances of the sdF, all detected elements would be enhanced in the sdOB. The observed sdOB abundances for the light metals are similar to other heavy-metal iHe-sdOBs: the zirconium-rich Feige 46 and LS IV−14°116 (Naslim et al. 2011; Dorsch et al. 2020), the zirconium- and lead-rich HE 2359-2844 and HE 1256-2738 (Naslim et al. 2013), the lead-rich PG 1559+048 and FBS 1749+373 (Naslim et al. 2020), as well as PG 0909+276 and UVO 0512-08 (Edelmann 2003; Wild & Jeffery 2018), which are extremely enriched in iron-group elements. Unlike the somewhat lead-rich iHe-sdOBs UVO 0825+15 (Jeffery et al. 2017), HZ 44, and HD 127493 (Dorsch et al. 2019), EC 22536−5304 A does not show a distinct CNO-cycle pattern (strong N, weak C and O). Interestingly, the metal abundance pattern is not shifted to lower values when compared to other heavy-metal iHe-sdOBs. This indicates that the metal abundance patterns observed for iHe-sdOB stars are not strongly dependent on their initial metallicity. The abundances derived for C, N, O, and Si are almost identical to those of HE 1256-2738, an apparently single lead-rich iHe-sdOB found to be a Galactic halo member by Martin et al. (2017).

EC 22536−5304 A does not seem to share the extreme zirconium abundance observed in some iHe-sdOBs or the extreme enrichment in iron-group elements found in others, although our upper limits are high. The latter may be due to the very low primordial metallicity of the system. The lead enhancement of EC 22536−5304 A is the most extreme found in any hot subdwarf, or, to our knowledge, in any star. The strong enrichment of heavy metals in the photospheres of heavy-metal sdOBs is usually discussed in terms of selective radiative levitation. In this picture, the strong heavy metal lines observed in the emergent spectrum are the result of a chemically stratified envelope, in which a thin metal-rich layer overlaps with the line-forming region. As mentioned by Jeffery & Miszalski (2019), atmospheric models that include a physical treatment of stratification by diffusion are required to estimate the total amount of lead in the enriched layers. These models would then have to be compared with lines that form at various optical depths, ideally using both far-UV and optical spectra.

The flux contribution of the sdF overtakes that of the sdOB only at about 7200 Å in our best-fit model. Therefore, and due to its low metallicity, relatively few metal lines that originate from the sdF component are detectable in our spectra. Most of them are well reproduced at the best-fit metallicity and alpha-enhancement. The strongest metal lines detected include transitions in the Na I, Mg I, Al I, Si I, Ca I-II, Ti II, Cr I, Mn I, Fe I-II, and Ni I atoms. The strontium lines Sr II 4077.7, 4215.5 Å seem to be well reproduced at the scaled solar abundance. We also detect Ba II 4554.0, 4934.1 Å, which are somewhat too weak in our models at the scaled solar abundance. This discrepancy may be due to a weak enrichment in barium, but may also be caused by deficiencies

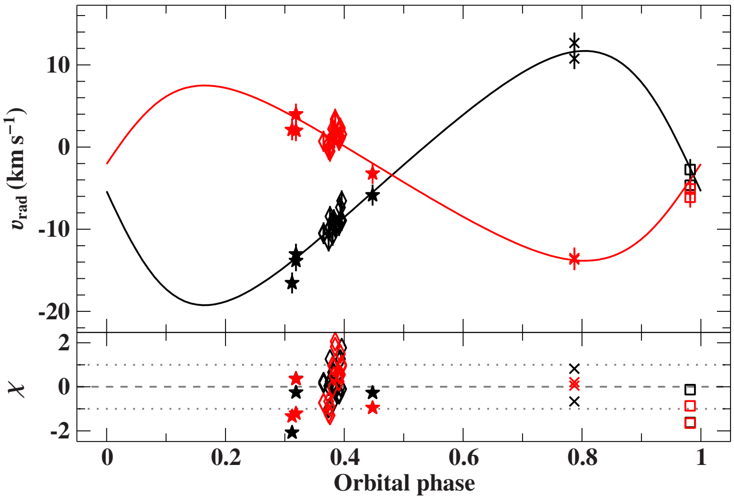

Figure 3.3.7. Elliptic orbits fit to the radial velocities of both EC 22536−5304 A (black) and B (red). Asterisks indicate UVES measurements, while HRS data from 2017, 2018, and 2019 are marked by crosses, squares, and diamonds, respectively. Adopted from Dorsch et al. (2021).

in our synthetic spectra, such as inaccurate atomic data or non-NLTE effects. The existence of dwarf barium stars is usually explained with pollution through wind accretion or RLOF from an AGB star (Jorissen & Boffin 1992; Gray et al. 2011). Given that EC 22536−5304 A is likely still on the horizontal branch, it seems unlikely that the sdF component is a barium star.

It is likely that the present EC 22536−5304 system has formed through mass transfer from an RGB star to the sdF companion. One can therefore expect at least some pollution of the sdF companion by material processed in the CNO-cycle, although diluted by convection. Unfortunately, no carbon, nitrogen, or oxygen lines that originate from the sdF are detectable in our spectra.

3.3.7 Analysis of the radial velocity curve

A total of 27 HRS and UVES spectra have sufficient quality to measure the radial velocities of both components, which are listed in Table B.3.3. These spectra cover a time span of Δt = 2880 days, but were taken in only five observing runs, the longest of which was just two weeks. This coverage is too irregular to determine the orbital parameters of the EC 22536−5304 system precisely. We initially searched for orbital periods by fitting circular orbits to all available radial velocities, corrected for the gravitational redshifts. A unique best orbital period, $P \approx 457$ days, was obtained by finely sampling orbital frequencies between 1/330 and 1/550 d^{-1} with steps of $0.01/\Delta t = 3.6 \times 10^{-6}$ d^{-1}. Fitting eccentric orbits resulted in a somewhat eccentric orbit with the same 457 day period and velocity semiamplitudes of $K_A = 15.5 \pm 1.7$ km s^{-1} and $K_B = 10.7 \pm 1.4$ km s^{-1} (see Table 3.3.6). The phased radial velocity curves are shown in Fig. 3.3.7. More observations are required to improve the orbital solution, in particular for the eccentricity.

Since the orbital period of EC 22536−5304 is certainly larger than 50 days, it is likely that the system was formed through stable Roche lobe overflow. Vos et al. (2017) have discovered a positive correlation between the eccentricity and orbital period for post-RLOF systems. Given the orbital period of about 457 days, one would expect a low eccentricity for the orbit of EC 22536−5304. We find an eccentricity of $e = 0.22^{+0.13}_{-0.08}$, which however strongly depends on the radial velocities derived from the HRS spectra taken in 2017.

A correlation between the orbital period and mass ratio of post-RLOF sdB+MS binaries has been found by Vos et al. (2019). Subsequently, Vos et al. (2020) showed that the observed relation can be explained in terms of the system's metallicity. In order to produce a sdB, the mass transfer must happen close to the top of the RGB, so that the RGB star can ignite helium burning in its core. Orbital periods of sdB+MS systems decrease with metallicity because low-metallicity donor stars have smaller radii at the top of the RGB. Low-metallicity systems therefore have shorter initial periods, which leads to shorter final periods once the mass transfer has stopped. For halo systems at [Fe/H] = −1.8 ± 0.5, Vos et al. (2020) predict orbital periods of 300 to 500 days and mass ratios $q = M_{\rm sdB}/M_{\rm MS}$ of 0.6 to 0.8, which is consistent with our (preliminary) result for EC 22536−5304, $q = K_B/K_A = M_A/M_B = 0.69 \pm 0.06$. Assuming a canonical mass of $M_{\rm sdB} = 0.49\,M_\odot$ for the sdOB, the mass ratio would put the mass of the sdF to $0.71 \pm 0.06\,M_\odot$.

Table 3.3.6. Orbital parameters for EC 22536−5304. The gravitational redshift v_{grav} is calculated from the stellar parameters listed in Table 3.3.3.

Parameter	Value
Period P	$457.0^{+1.2}_{-1.5}$ d
Epoch of periastron $T_{\mathrm{periastron}}$	56160^{+21}_{-17} MJD
Eccentricity e	$0.22^{+0.13}_{-0.08}$
Longitude of periastron ω	276^{+21}_{-18} deg
Velocity semiamplitude K_A	$15.5^{+1.7}_{-1.6}$ km s^{-1}
Velocity semiamplitude K_B	10.7 ± 1.4 km s^{-1}
Gravitational redshift $v_{\mathrm{grav}_\mathrm{A}}$	$1.95^{+0.22}_{-0.20}$ km s^{-1}
Gravitational redshift $v_{\mathrm{grav}_\mathrm{B}}$	$0.72^{+0.21}_{-0.17}$ km s^{-1}
Systemic velocity γ	-3.3 ± 0.4 km s^{-1}
Derived parameter	**Value**
Mass ratio $q = K_B/K_A = M_A/M_B$	$0.69^{+0.06}_{-0.05}$
Projected semimajor axis $a_A \sin(i)$	0.63 ± 0.05 au
Projected semimajor axis $a_B \sin(i)$	0.44 ± 0.04 au

3.3.8 Kinematics

Proper motions and the parallax from *Gaia* EDR3 combined with the system's radial velocity can be used to derive the present 3D space velocity of EC 22536−5304. The Galactic orbit of EC 22536−5304 can then be traced back in time using a model for the Galactic potential; here for 10 Gyr. We used Model I of Irrgang et al. (2013) for the Galactic potential, which is a revision of the Allen & Santillan (1991) potential. Given the sparse coverage of our radial velocities, we adopted an uncertainty of 5 km s^{-1} on the system's radial velocity. The resulting orbit for EC 22536−5304 has a low angular momentum perpendicular to the Galactic disc $L_Z = 930 \pm 40$ kpc km s^{-1}, but a relatively high eccentricity of $e = 0.53 \pm 0.02$.

The current velocity towards the Galactic centre U, perpendicular to the disc W, and in direction of Galactic rotation V can be used to place EC 22536−5304 in the Toomre diagram. When compared to the Toomre parameters predicted from Besançon Galactic models (Robin et al. 2003) the location of EC 22536−5304 in this diagram is consistent with either a thick disc or halo origin (see Fig. 3.3.8). Although most hot subdwarf stars seem to be part of the thin disc, several intermediate He-sdO/Bs in the sample of Martin et al. (2017) have been classified as thick disc or halo. To facilitate the comparison with EC 22536−5304, we have repeated the orbit calculation for iHe-sdOBs from this sample using reliable *Gaia* EDR3 proper motions and parallaxes ($\sigma_{\varpi}/\varpi < 10\,\%$). The heavy-metal iHe-sdOBs Feige 46 and HZ 44 (Dorsch et al. 2019, 2020) were considered in addition. We corrected the proper motions provided by *Gaia* EDR3 for bright stars ($G < 13$ mag) following Cantat-Gaudin & Brandt (2021). As before, we applied corrections to the parallax measurements (Lindegren et al. 2021) and their uncertainty (El-Badry et al. 2021). The resulting orbital parameters are summarised in Table B.3.4.

Given the low metallicity of EC 22536−5304, the system may be part of the low-metallicity tail of the thick disc, also termed metal-weak thick disc (MWTD). According to Chiba & Beers (2000), the low-metallicity cut-off of the MWTD is close to [Fe/H] = −2, comparable to the metallicity of EC 22536−5304 B. At this low metallicity, the halo population in their sample dominates even at small distances from the Galactic disc, such as the $Z = -593^{+13}_{-16}$ pc observed for EC 22536−5304. However, is not possible to discern between a MWTD or halo origin for any particular system that shows disc-like kinematics (see, e. g. Reddy & Lambert 2008).

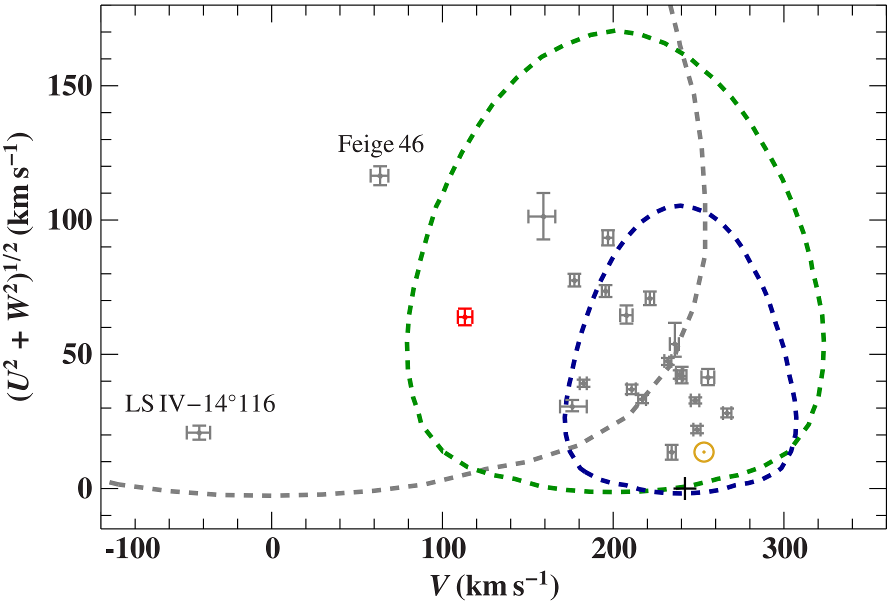

Figure 3.3.8. Toomre diagram showing space velocities with respect to the Galactic centre. The velocity component V is measured in the direction of the rotation of the Galaxy, U towards the Galactic centre, and W perpendicular to the plane. The position of EC 22536−5304, the Sun, and the local standard of rest (LSR) are marked by the red cross, yellow circled dot, and black plus, respectively. The grey, green, and blue dashed lines indicate 2-σ velocity dispersions from Robin et al. (2003) for the halo, thick disc, and old thin disc, respectively. Stars from the sample of intermediate He-sdO/Bs studied by Martin et al. (2017), updated using *Gaia* EDR3 parallaxes and proper motions are shown in grey. Probable halo stars are labelled. Adopted from Dorsch et al. (2021).

3.3.9 Conclusions

We have performed a detailed analysis of high-resolution spectra of EC 22536−5304, and can confirm that the system contains an extremely lead-rich intermediate He-sdOB as found by Jeffery & Miszalski (2019). However, we find a second component in its spectrum: a strongly alpha-enhanced and metal-poor F-type subdwarf. EC 22536−5304 A is the first heavy-metal sdOB found in a binary system. Our updated metal abundances for the sdOB component are similar to those derived in the previous analysis, but shifted to higher abundances. EC 22536−5304 A therefore remains the most lead-rich hot subdwarf known. Although the initial metallicity of the system is low, the abundances for the hot component are quite similar to those of other iHe-sdOB stars, some of which probably have significantly higher initial metallicities, given that they belong to the younger thin disc population (such as PG 1559+048, see Sect. 3.3.8). The observed abundance pattern of EC 22536−5304 A is likely the result of strong diffusion processes. Ultraviolet spectroscopy would enable us to derive a more complete abundance pattern for the sdOB component. These spectra would also provide access to lead lines at various formation depths that could then be used to probe the stratification of a proposed layer of lead in the atmosphere of EC 22536−5304 A. In fact, such spectra are currently being taken by the STIS spectrograph mounted on the Hubble space telescope.

EC 22536−5304 A is the first hot subdwarf found to be in a long-period binary with a known metallicity $[\mathrm{Fe/H}] < -1$. The low metallicity ($[\mathrm{Fe/H}]_\mathrm{B} = -1.95$) and strong alpha enhancement ($[\alpha/\mathrm{Fe}]_\mathrm{B} = 0.4$) derived for the sdF component indicate that the system is part of the Galactic halo or metal-weak thick disc. The system is therefore likely old ($\gtrsim$10 Gyr, e. g. Helmi 2020). Other hot subdwarfs with a low known metallicity are part of globular clusters, but are typically not found in binary systems (Latour et al. 2018b). Still, the stellar evolution models of Han (2008) predict a significant fraction of old sdO/Bs to be formed through stable RLOF, which seems to be the case for EC 22536−5304.

To determine the stellar parameters mass, radius, and luminosity for both components, we have combined the parallax provided by *Gaia* EDR3 with the angular diameter derived from a SED fit and our spectroscopic atmospheric parameters. The resulting mass for EC 22536−5304 A, $0.40 \pm 0.06\,M_\odot$, is consistent with the range of masses expected for hot subdwarf stars on the extreme horizontal branch. The spectroscopic mass for EC 22536−5304 B, $0.84^{+0.29}_{-0.23}\,M_\odot$, is associated with a high uncertainty because its surface gravity is not easily determined. In fact, the comparison of MIST evolutionary tracks with our effective temperature and luminosity points to a lower mass for the sdF, about $0.7\,M_\odot$. This mass would be consistent with an evolutionary age of about 10 Gyr.

Radial velocity variations suggest that the system is a wide binary with an orbital period of about 457 days. An eccentric fit to the radial velocities results in a mass ratio $q = M_A/M_B = 0.69 \pm 0.06$. Vos et al. (2019) have recently found a strong relation between the orbital period and mass ratio for long-period hot subdwarf binaries. This relation could be explained by a correlation between the final orbital period and the metallicity of such systems found by Vos et al. (2020), which results from different radii of the progenitors at the tip of the RGB, which is the point at which mass transfer started. Given the low metallicity of EC 22536−5304, the system will help to constrain these relations at much lower metallicity than before. The current results for the orbital period, mass ratio, and metallicity are consistent with the predictions of Vos et al. (2020) for post-RLOF systems. Additional spectra that sample the full orbital period are required to obtain reliable orbital parameters.

We have also performed a kinematic analysis, based on the system's radial velocity determined from the current radial velocity curve. EC 22536−5304 is on an eccentric orbit around the Galactic centre, which is consistent with a halo or thick disc membership. Several heavy-metal iHe-sdOB stars have been found in the Galactic halo. From the *Gaia* EDR3 data we can confirm that the zirconium-rich Feige 46 and LS IV−14°116 (Latour et al. 2019a; Dorsch et al. 2020) are halo members.

3.4 BD−07° 5977: a post Roche-lobe overflow system

BD −7° 5977 is the brightest known hot subdwarf star with a K-type companion. Its binary nature was first identified by Viton et al. (1991) using low-resolution IUE spectra, who classified it as sdOB+K0III-IV. Vos et al. (2017) studied the system in detail and found an orbital period of 1262 days. They also derived atmospheric parameters for both components by combining the mass ratio from the orbital solution with an SED fit and spectral analysis of the cool component. Their results show that the cool component is indeed a K-type subgiant, which distinguishes it from the more common main-sequence companions to other hot subdwarfs, as discussed in Sect. 4.1.2.3. Although long, this orbital period is short enough that stable Roche lobe overflow from the sdOB's progenitor may have occurred. If this was the case, the transferred CNO-processed material would have altered the surface composition of the (now) K-type subgiant. This can be tested by determining the ^{12}C/^{13}C ratio which is lowered to about 4 in the equilibrium CN cycle (Wollman 1973), much lower than the terrestrial value of about 89 (Coplen et al. 2002).

Stars polluted by mass transfer are commonly observed. Prominent examples are dwarf carbon (Dearborn et al. 1986; Heber et al. 1993) and dwarf barium (Gray et al. 2011) stars, as well as extrinsic giant barium and CH stars (McClure et al. 1980; Jorissen & Boffin 1992). These dwarf and RGB stars have not yet experienced *s*-process fusion in their envelopes that could produce barium and neither have they ignited helium fusion that would produce carbon. Therefore, all of these stars are thought to be enriched in metals by mass transfer from AGB-type companions that have since evolved to become white dwarfs. This proposition is supported by long-term radial velocity monitoring, which showed that the binary fraction of these stars approaches 100 % (Jorissen et al. 2019; Escorza et al. 2019).

The ^{12}C/^{13}C ratio is best measured from molecular CO transitions in the infrared spectra of K-type stars, which was first proposed as a test of common-envelope evolution by Sarna et al. (1995). Such studies have previously been performed for the secondary stars of cataclysmic variables, for example SS Cyg (Dhillon et al. 2002; Harrison & Marra 2017). In this section, this method is applied to BD −7° 5977.

3.4.1 The K-giant Arcturus as a benchmark

To test our analysis method, we selected Arcturus, a K-type giant and the brightest star in the northern hemisphere, as a reference point. This choice was made due to its extensive analyses in existing literature. Excellent spectra including the Hinkle et al. (1995) infrared spectral atlas are readily available and allow us to derive its ^{12}C/^{13}C ratio and compare to literature values. A high photospheric ^{12}C/^{13}C ratio is expected for Arcturus because the star has evolved through the first dredge-up (FDU). As stars begin to ascend the RGB, their convective envelopes extend down to deep regions that contain material processed by hydrogen fusion in the CNO cycle. This material is dredged up by convection, which leads to enrichment in nitrogen and a lowered ^{12}C/^{13}C ratio, typically to down to values between 15 and 30 (Weiss et al. 2000).

The ^{12}C/^{13}C ratio observed for Arcturus is in fact even lower than expected from the canonical FDU scenario: Hinkle et al. (1976) measured it as 7 ± 1.5 by using the curve of growth method and the 2.3μm CO lines, while Day et al. (1973) measured a value of 7.2 ± 1.5 using the 0.8μm CN bands. A more recent study by Abia et al. (2012) based on 1D LTE atmospheres similar to those used here found $^{12}\mathrm{C}/^{13}\mathrm{C} = 9 \pm 2$ using CO lines. The exceptionally low ^{12}C/^{13}C ratio of Arcturus and other evolved RGB stars seems to be related to additional mixing that takes place when the outward-moving H-burning shell reaches the chemical discontinuity left behind by the first dredge-up (Abia et al. 2012), a process that causes a bump of the luminosity function on the RGB. Although Arcturus is an ideal benchmark for our spectroscopic fit method, the star is therefore not suitable as a direct comparison to BD −7° 5977, which, as a subgiant, is less evolved and did not yet pass the RGB luminosity bump.

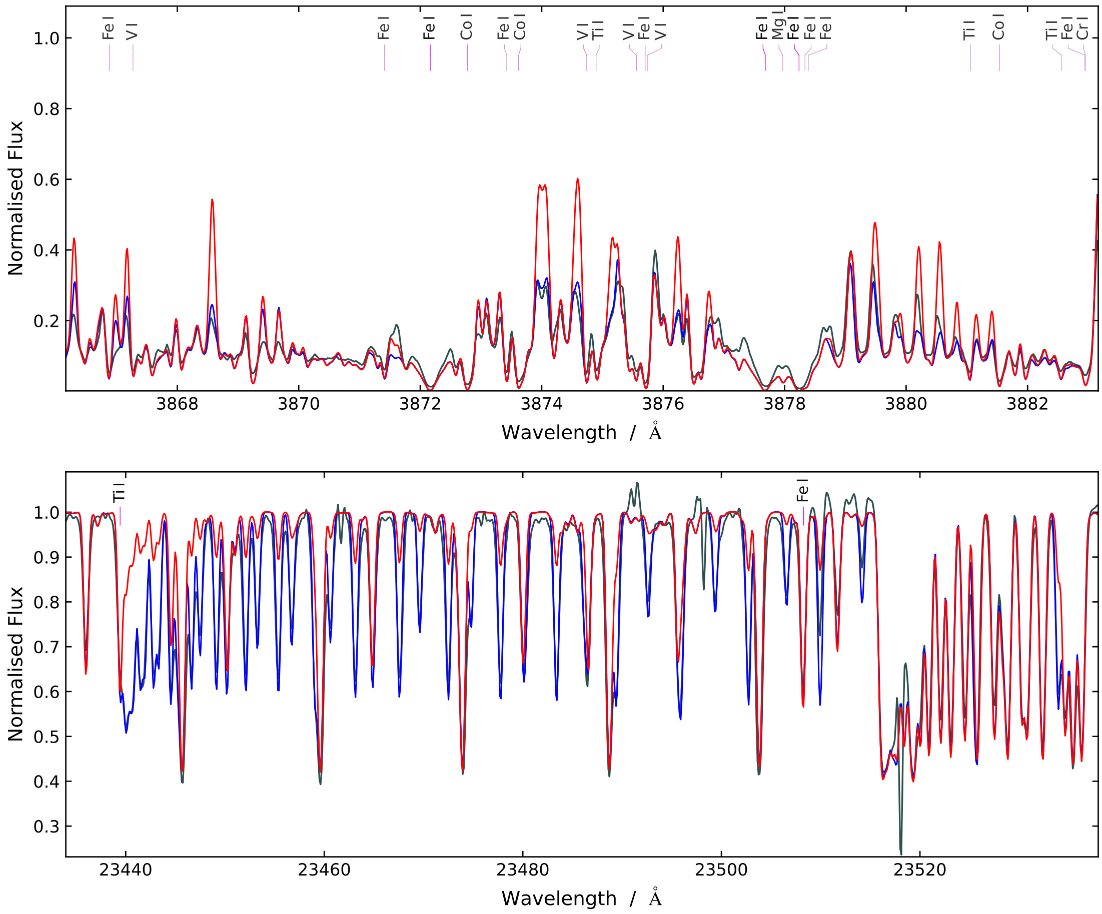

Figure 3.4.1. *Top*: Part of the near-UV CH band in the UVES spectrum of Arcturus. *Bottom*: the Arcturus spectral atlas of Hinkle et al. (1995), showing ^{13}CO and ^{12}CO band heads at 23441 and 23518 Å, respectively. The red spectrum was computed with ^{12}C/^{13}C = 89 while the ratio is seven for the blue spectrum. The strongest metal lines are labelled.

Models. We have computed Synthe spectra for different values of ^{12}C/^{13}C based on R. Kurucz's Atlas12 structure for Arcturus[8], which assumes $T_{\rm eff}$ = 4300 K, $\log g$ = 1.5, [Fe/H] = −0.5, and slight α-enhancement. This structure notably considers the decrease in mircoturblent velocity from the bottom of the atmosphere ($\upsilon_{\rm tb}$ = 3.58 km s^{-1}), where is corresponds to the maximum convective velocity, up to the surface ($\upsilon_{\rm tb}$ = 0.98 km s^{-1}, Kurucz 2002). Since the convective velocity increases with decreasing surface gravity, a good treatment of microturbulence is more important for the giant Arcturus ($\log g \approx 1.5$) than for the subgiant BD −7° 5977 B ($\log g \approx 2.8$).

Spectral fit. The Arcturus infrared spectral atlas of Hinkle et al. (1995) covers the CO lines at a resolution of R = 100 000 and high S/N. The very strong telluric lines in this spectral region were removed by building the ratio to a spectrum of the Earth's atmosphere. In addition, the 3040 – 10400 Å range is covered by archival UVES spectra at a high resolution and signal-to-noise ratio.

As shown in Fig. 3.4.1, ^{12}CO and ^{13}CO bands are clearly visible in the IR spectrum of Arcturus and are well reproduced at ^{12}C/^{13}C = 7 using our Atlas12/Synthe models. Even the heavily blended NUV CH bands are reasonably well reproduced. Fitting the 23430 Å – 23870 Å range in the spectrum of Arcturus using a grid that varies in the carbon isotopic ratio results in ^{12}C/^{13}C = 6.74 ± 0.2 and $\upsilon_{\rm rot} \sin i$ = 4.0 ± 0.1 km s^{-1} (1σ statistical errors only). This is perfectly consistent with the results of Hinkle et al. (1976) and Abia et al. (2012). We are therefore confident that this method can be applied to BD −7° 5977 A as well and will yield results that are comparable to 1D-LTE analyses of other stars.

---

[8] http://kurucz.harvard.edu/stars/arcturus/modat4300g15kvd.dat

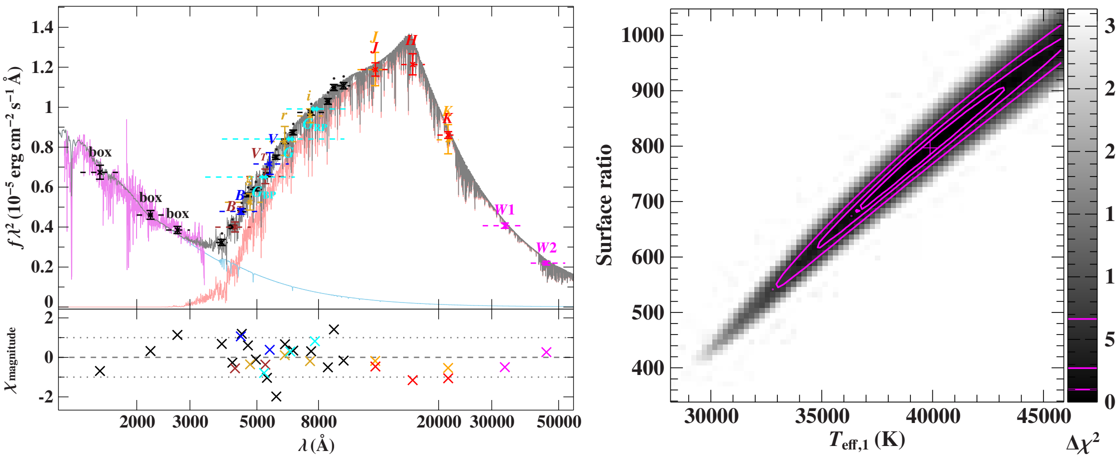

Figure 3.4.2. *Left*: Best-fit SED of BD −7° 5977 for a fixed colour excess $E(44-55) = 0.035$ mag, the line-of-sight value provided by the Schlegel et al. (1998) reddening map. *Right*: Confidence map showing the correlation between the hot subdwarf's $T_{\rm eff}$ and the surface ratio. Note that other parameters beyond those shown are fixed in such confidence maps, here including $E(44-55)$.

3.4.2 Application to BD−7° 5977

Observations. Following the initial discovery of the UV excess in BD −7° 5977 by Spacelab-1 on the Space Shuttle (Viton et al. 1991), the system was also observed using the IUE satellite, providing both low- and high-resolution far-UV spectra. Vos et al. (2017) later observed BD −7° 5977 extensively using the optical HERMES spectrograph at a resolving power of $R \approx 85000$ to determine the system's orbital properties. In addition, a single FEROS spectrum is available in the ESO archive under programme ID 098.A-9019(A). Infra-red spectra taken from the ground are constrained by transmission windows in Earth's atmosphere, the so-called J-, H-, and K-bands. Molecular CO bands of utmost importance to determine the ^{12}C/^{13}C ratio are located in the K-band and have been recorded at the ESO/VLT with CRIRES[9], covering the range range from 22.77 to 23.81 μm at a resolving power of $R \approx 100\,000$. These spectra were taken before the CRIRES upgrade and are therefore made up of eight segments with small gaps in between. They are complemented by J- and H-band spectra taken with CARMENES[10] at the Calar Alto 3.6m telescope, which range from 9.6 to 17.1 μm at a resolving power of $R \approx 80400$ and thus cover the CN molecular bands.

Basic parameters. Before performing a detailed study for the K-type companion, the basic parameters of both components had to be estimated: $T_{\rm eff}$, $\log g$, and $\log n(\mathrm{He})/n(\mathrm{H})$ for the hot subdwarf, $T_{\rm eff}$, $\log g$, and [Fe/H] for the companion, as well as the surface ratio. In the following, the K-type was modelled using Atlas12/Synthe as described above, while the sdOB was modelled using Tlusty/Synspec models, similar to the analysis of EC 22536−5304 (see Sect. 3.3).

Because the optical spectrum is almost completely dominated by the K-type, it is impossible to rely on optical and IR spectroscopy alone. An alternative approach is to use the system's SED to estimate the effective temperature of both components and their surface ratio. As shown in Fig. 3.4.2 (left), this SED is well covered, ranging from the far-UV up to the mid-infrared. Nevertheless, there are strong correlations between the $T_{\rm eff}$ of the hot subdwarf, the surface ratio (right), and the interstellar extinction. This prevents a reliable estimate of the system's parameters.

There is, however, an additional piece of information: the high-resolution UV spectrum taken with the IUE[11] satellite that covers the 1150 to 1970 Å range. Because of the low $T_{\rm eff}$ of the subgiant companion, the UV spectral range is fully dominated by the hot subdwarf component. Through the relative strengths of metal lines in various ionisation stages – the so-called ionisation

---

[9] The CRIRES spectra were taken under IDs 088.C-0707(B) and 089.D-0875(A).

[10] The CARMENES spectra were obtained by Ulrich Heber in 2016 and were reduced by Evangelos Nagel.

[11] The high-resolution IUE spectrum has the ID SWP34463HL and was obtained from the INES archive.

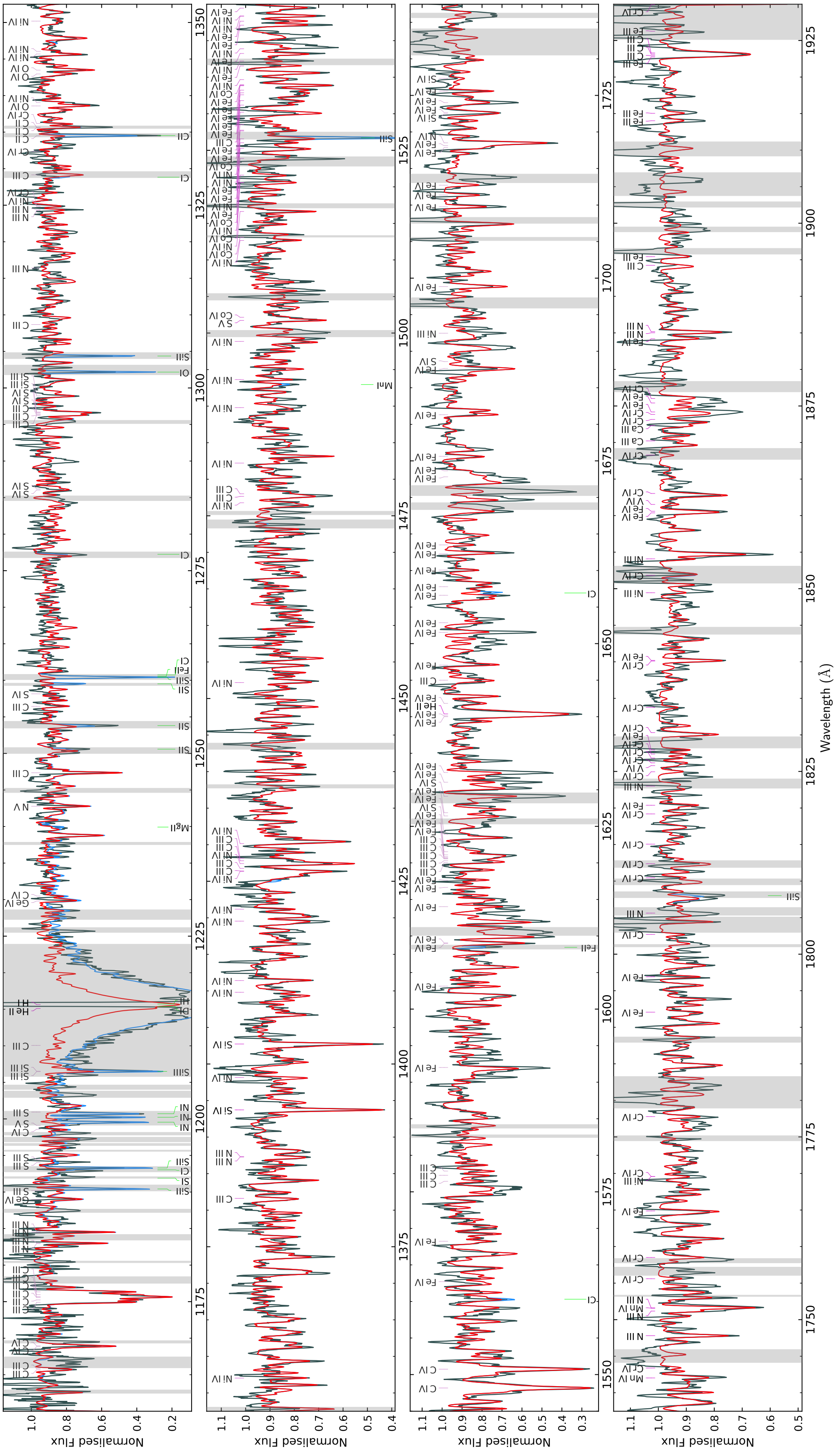

Figure 3.4.3. The high-resolution IUE spectrum of BD −7° 5977 (grey, with 5× binning) compared to the best-fit model (red). Free parameters were $T_{\rm eff}$ and the abundances of C, N, O, Al, Si, Cr, Fe, Ni, and Zn. Spectral regions excluded from the χ^2 fit are shaded grey, including several interstellar lines that are shown in blue and labelled at the bottom (see also Appendix A.2).

Table 3.4.1. Parameters for BD −7° 5977 as obtained by combining the analyses of its SED and its IUE, optical, and infrared spectra. Estimated systematic uncertainties are stated here since the statistical uncertainties are much smaller. Arcturus is listed for comparison, the parameters of which are from the analysis of Ramírez & Allende Prieto (2011), besides N (from Kurucz's model) and $v_{\rm rot} \sin i$ and ^{12}C/^{13}C (this analysis).

	BD −7° 5977 A	BD −7° 5977 B	Arcturus
$T_{\rm eff}$ (K)	38400 ± 2500	4850 ± 100	4300
$\log g$	5.2 ± 0.3	2.8 ± 0.3	1.7
$\log n(\rm He)/n(\rm H)$	−2.0 ± 0.4	−1.0 (fix)	–
$v_{\rm rot} \sin i$ (km s^{-1})	–	4.2 ± 1	4
ξ (km s^{-1})	–	1.5 (fix)	variable
[Fe/H]	–	−0.20 ± 0.05	−0.5
[α/Fe]	–	+0.07 ± 0.05	–
[C/Fe]	–	+0.04 ± 0.15	+0.4
[N/Fe]	–	+0.88 ± 0.20	+0.6
[O/Fe]	–	+0.40 ± 0.20	+0.5
^{12}C/^{13}C	–	28 ± 5	7
Surface ratio = $R_{\rm B}^2$ / $R_{\rm A}^2$	–	715 ± 100	–
R / $R_\odot$	0.30 ± 0.02	8.0 ± 0.6	25

balance – it allows an independent determination of the subdwarf's $T_{\rm eff}$, in particular through the C III/IV and N III/IV/V balances. This temperature information was extracted by fitting the spectrum with a grid of TLUSTY/SYNSPEC model spectra for the hot subdwarf that was allowed to simultaneously vary in $T_{\rm eff}$ and the abundances of C, N, O, Al, Si, Cr, Fe, Ni, and Zn. Such a high-dimensional grid is necessary due to the frequently overlapping spectral lines and the correlation between metal abundances and $T_{\rm eff}$. The computation of this grid was made feasible by varying the metal abundances in SYNSPEC only, thus ignoring the small effect that changing the metal abundances has on the atmospheric structure. This approach remains viable because the metal abundances of the underlying TLUSTY models, which treated C, N, O, Si, S, Fe, and Ni in non-LTE, were close to the best-fit values. The best fit as shown in Fig. 3.4.3 was achieved at $T_{\rm eff}$ = 38400 ± 2500 K, stated here with an estimated systematic uncertainty. Vos et al. (2017) could not determine $T_{\rm eff}$ from their optical and infra-red SED fit of BD −7° 5977 to sufficient accuracy, but their $T_{\rm eff}$ = 30000 ± 7000 K is still consistent with our value.

The improved $T_{\rm eff}$ = 38400 K from the IUE spectrum could now be fixed to redo the SED analysis, thus breaking the aforementioned degeneracies. This fit resulted in a more reliable surface ratio and $T_{\rm eff}$ for the K-type companion, which were then fixed for the spectral analysis. Note that the masses as derived from SED and parallax are not stated here, while the radii are listed. This is because the large uncertainties on the surface gravities preclude meaningful results for the masses. In addition, the currently available *Gaia* parallax may be affected by the system's binary motion and may thus be inaccurate, which would also affect the radius estimate.

Spectral fit. In the next step, a simultaneous χ^2 fit to the optical and infrared spectra was performed to determine the remaining parameters of the system. The global spectral fit approach used here for the abundance analysis is analogous to the spectral analysis of the sdOB+sdF binary EC 22536−5304 presented in Sect. 3.3. The interactive python code used to perform χ^2 fits was extended to deal with more free parameters of the K-type star: next to $T_{\rm eff}$, $\log g$, $v_{\rm rot} \sin i$, surface ratio, and the overall metallicity [Fe/H], also the alpha enhancement [α/Fe], the individual abundances of carbon, nitrogen, and oxygen, and the ^{12}C/^{13}C ratio were allowed to vary. The microturbulent velocity for the K-type was set to ξ = 1.5 km s^{-1}. In particular the variable C, N, O abundances are important since they are correlated with the ^{12}C/^{13}C value, given that this

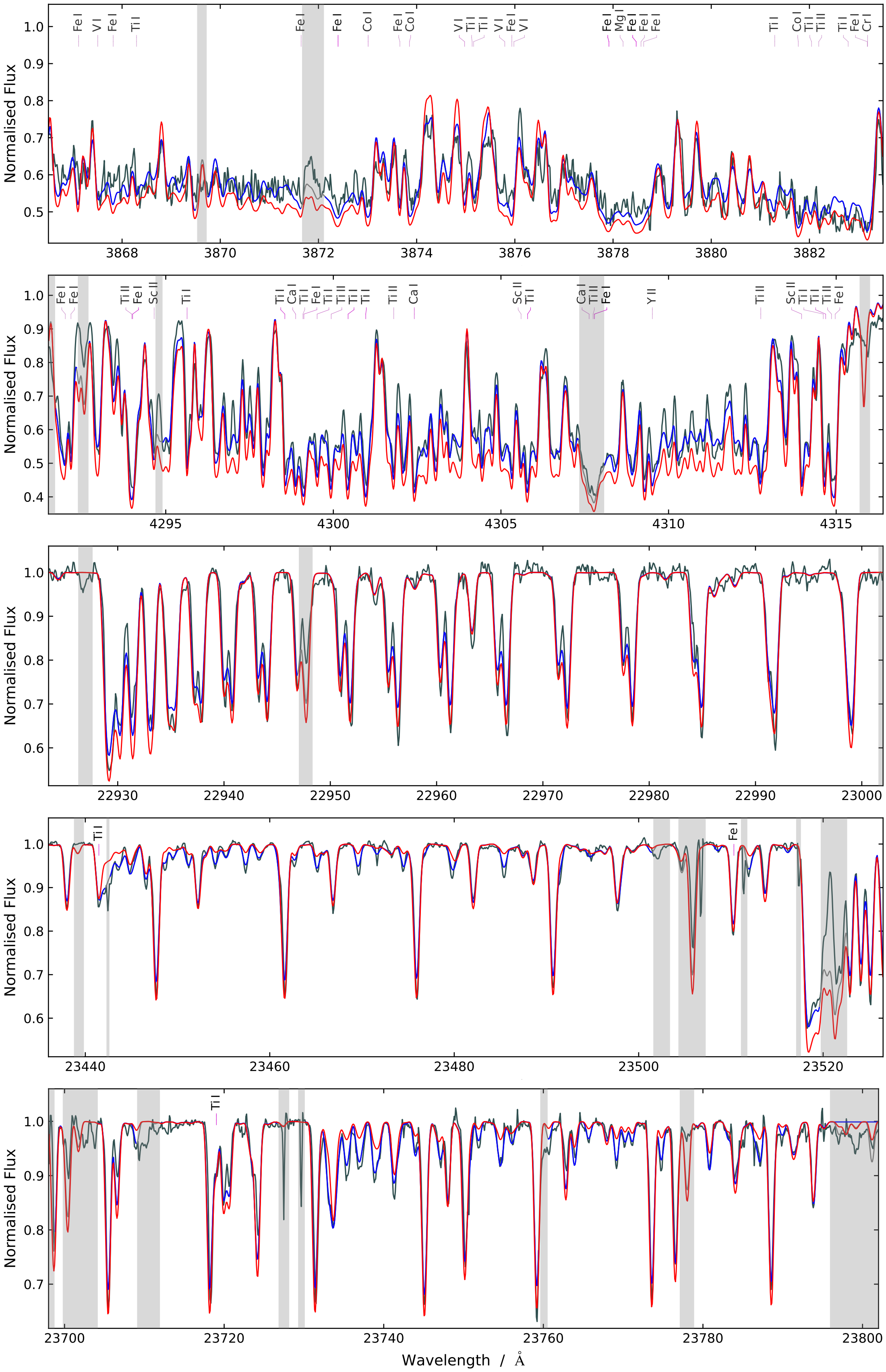

Figure 3.4.4. Spectral fit of BD −7° 5977: sections of the near-UV and optical CH bands in the HERMES spectrum are shown in the upper two panels, while sections of the CRIRES spectra covering the ^{13}CO and ^{12}CO bands are shown in the lower panels. The blue line is the best-fit model at ^{12}C/^{13}C = 28, while the red model is for ^{12}C/^{13}C = 89, the terrestrial value. Regions that were excluded during the χ^2 fit are shaded grey. The strongest atomic transitions are labelled.

is determined mostly from CO molecular bands. Because O is more abundant than C and N, its abundance has a strong effect on the formation of the CN molecule; lowered oxygen abundances drastically increase the strength of CN bands. Such correlations result in the large uncertainties on the abundances of C, N, and O as stated in Table 3.4.1, which lists the best fit parameters. The FEROS and CRIRES spectra are compared to the best fit in Appendix B.4.

The most important diagnostic regions for the value of $^{12}C/^{13}C$ are shown in Fig. 3.4.4, namely the CH-bands covered by HERMES and the CO-bands covered by CRIRES. The combinations of these bands and the CN bands are also what determines the carbon, nitrogen and oxygen abundances. Despite the remaining correlations, the fit clearly prefers a lowered $^{12}C/^{13}C$ ratio. There are two main results:

- The K-type is strongly enriched in nitrogen ([N/Fe] = +0.88) compared to the metallicity-scaled solar abundance ([Fe/H] = −0.2), while the carbon is close to scaled solar. Such abundance patterns are produced by hydrogen fusion in the CNO-cycle at low temperature (Caughlan & Fowler 1962). The enhanced oxygen abundance ([O/Fe] = +0.40) may in part result from an initial enrichment in α-process elements, but is larger than expected given the relatively high metallicity.
- The $^{12}C/^{13}C$ isotopic ratio of BD −7° 5977 B of 28 ± 5 is intermediate between the terrestrial value of 89 and the CNO-process equilibrium value of 4.

3.4.3 Conclusions

The main goal of the analysis of BD −7° 5977 was to determine the K-type's $^{12}C/^{13}C$ ratio of 28 ± 5 as a tracer of pollution of its atmosphere by RLOF from the hot subdwarf's progenitor. Because the accretor is a subgiant, it is in an evolutionary phase of hydrogen shell burning. It can therefore not be excluded that atmospheric $^{12}C/^{13}C$ ratio has been altered by internal mixing processes as opposed to external pollution. $^{12}C/^{13}C$ ratios as low as 20 are commonly observed at the base of the RGB (Dearborn et al. 1976; Afşar et al. 2012), close to the parameters of BD −7° 5977 B. In addition, is it unclear if enough mass is transferred during the RLOF episode to significantly affect the composition of a cool companion star. Vos et al. (2020) predict that less than about 0.05 $M_\odot$ is accreted during RLOF – the rest is lost from the system. It seems likely that it is a combination of convective dredge-up and pollution through RLOF that led to the current surface composition of BD −7° 5977 B, which complicates conclusions on either process.

Future high-resolution infrared studies aimed at finding evidence of mass-transfer to long-period K-type companions of hot subdwarf stars should therefore focus on companions on the main sequence. However, the infared spectra of BD −7° 5977 are still useful to characterise the K-type companion, and further analysis beyond the present work is possible. For example, the $^{16}O/^{17}O$ and $^{16}O/^{18}O$ isotopic ratios could be used to estimate the companion mass from FDU models, as performed for Arcturus by Abia et al. (2012). This mass could be compared to the mass derived from combining the SED fit with the *Gaia* parallax, as well as to the mass obtained from the solved orbit of BD −7° 5977. Such an analysis would require a *Gaia* parallax measurement that accounts for the orbital motion. Due to the long orbital period of the system (42 months), such measurements will only become available in a future data release. The analysis performed here, for the first time, provided reliable measurements of the atmospheric parameters of the hot subdwarf component. Based on its rather high T_{eff}, the hot subdwarf should be classified as sdOB rather than sdB, as already done by Viton et al. (1991). It is important to note that while the sdOB's mass is presently not very well determined, its large radius of 0.3 $R_\odot$ indicates that the star has evolved off the EHB and is currently performing helium shell fusion.

3.5 J0809-2627: discovery and spectroscopic analysis of a magnetic He-sdO

The analysis presented in this section was published as a part of Dorsch et al. (2022). Large parts of the content of this section are taken verbatim from this paper.

3.5.1 Introduction

About 20 % of all white dwarf (WD) stars within 20 pc are known to host surface magnetic fields, with strengths ranging from a few kG to several hundred MG (Hollands et al. 2018; Landstreet & Bagnulo 2019; Bagnulo & Landstreet 2020, 2021). In contrast, magnetic fields have not yet been directly observed for any hot subdwarf star. A study by Landstreet et al. (2012) based on spectropolarimetry for 40 sdB and sdO stars found no evidence for magnetic fields, with upper limits of about 1 to 2 kG. Mathys et al. (2012) found no significant magnetic fields in ten He-poor sdB stars using FORS2 spectropolarimetric observations at similar upper limits. Similar FORS2 observations of the metal-rich intermediate He-sdOB LS IV$-14°116$ excluded magnetic field strengths above 300 G (Randall et al. 2015).

Recently, Momany et al. (2020) studied the light curves of EHB stars in globular clusters and found a significant fraction to be variable at periods between 2 and 50 days. They argue that this variability can only be explained with the presence of stellar spots that result from weak magnetic fields of the order of hundreds of Gauss. Jeffery et al. (2013) discovered small-amplitude photometric variability with a period of about four days in the helium-rich sdO KIC 10449976, and suggested stellar spots as a possible explanation. Using TESS photometry, Balona et al. (2019) detected rotational modulation and a flare event in SB 290, a quickly rotating helium-poor sdB star (Geier et al. 2013a). However, a magnetic field could not be detected for this star using FORS1 spectropolarimetry (Bagnulo et al. 2015). Vos et al. (2021) reported complex line profiles and light curve variability for the He-poor sdB J22564-5910, which they argued to be consistent with a magnetic field; however, they noted that a disc could also explain the observed properties without a magnetic field being required. Strong and irregular radial velocity (RV) variations were found for several helium-rich sdO stars by Geier et al. (2015b). These authors also found irregular photometric variability for one of their RV-variable He-sdOs. Similar photometric variability was observed for several other sdO stars (Green et al. 2014; Østensen et al. 2010). Whether or not these irregular variations are related to magnetic fields is still an open question.

A first He-sdO star with a significant magnetic field (300 – 700 kG) was identified spectroscopically by Heber et al. (2013), although this star has not been analysed to date. The following sections present the first spectroscopic analysis of a hot subdwarf star with a strong magnetic field, specifically the He-sdO Gaia DR2 5694207034772278400, or short J0809-2627.

3.5.2 Observations

J0809-2627 was identified as a candidate hot subdwarf by Geier et al. (2019). We obtained follow-up spectroscopy with the IDS spectrograph at the Isaac Newton Telescope (INT) to confirm this classification and identified the star as a helium-rich sdO star. Two spectra were taken in direct succession with exposure times of 750 s, which resulted in a mean signal to noise ratio of 50 for the coadded spectrum. There is no significant radial velocity shift between the two exposures. At a resolution of $\Delta\lambda \approx 4$ Å the coadded IDS spectrum shows strongly broadened hydrogen and helium lines (see Fig. 3.5.1, left), which we tentatively interpreted as rapid rotation.

Because hot subdwarf stars are known to be slow rotators (Geier & Heber 2012), the strongly broadened lines of J0809-2627 are unusual. Therefore, the star was observed again in April 2021 with the medium-resolution spectrograph X-shooter at the ESO-VLT. This observation was part of the HOTFUSS programme (ID: 105.206H.001). We used the 3070 – 7400 Å range of the UVB and VIS channels, which covers all relevant spectral lines at a mean S/N of about 80 and a resolving power of $R = \lambda/\Delta\lambda \approx 10\,000$. At this resolution, eight times better than IDS, strong

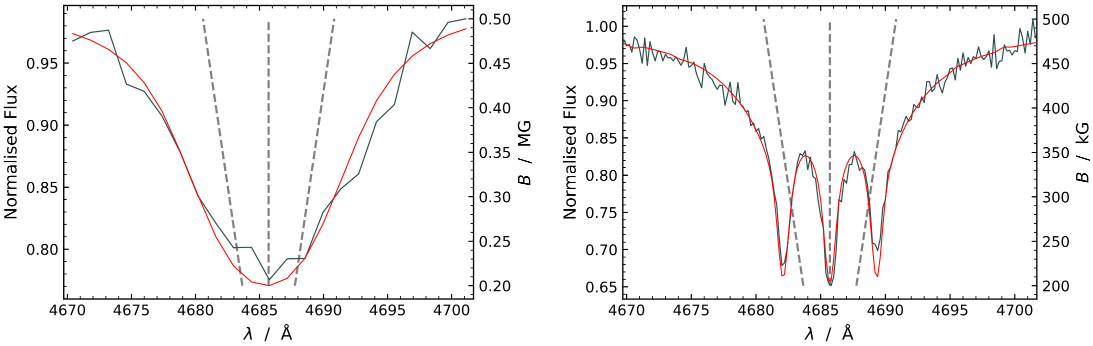

Figure 3.5.1. *Left*: The strongly broadened He II 4686 Å in the radial velocity corrected IDS spectrum of J0809-2627 (grey). *Right*: Resolved Zeeman-splits for the same line in the X-shooter spectrum of J0809-2627 (grey). The dashed lines visualise the positions of the three components that depend on the magnetic field strength due to the linear Zeeman effect. The best-fit model to the X-shooter spectrum is shown in red. Adopted from Dorsch et al. (2022).

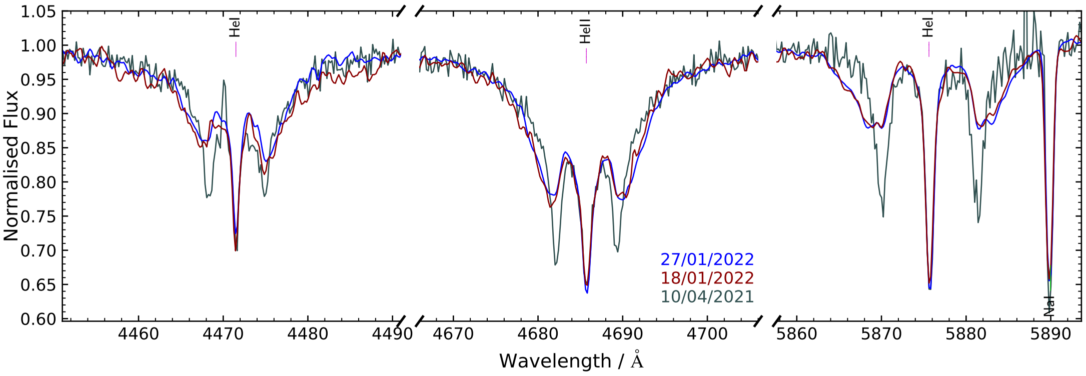

Figure 3.5.2. Zeeman-split He I 4471 Å, He II 4686 Å, and He I 5878 Å lines in the radial velocity-corrected X-shooter (grey) and UVES (blue, red) spectra of J0809-2627. Here, the UVES spectra were convolved to match the $R = 10\,000$ of X-shooter.

Zeeman-split multiplets are clearly visible, demonstrating that the line broadening is not due to rapid rotation but is caused by the presence of a magnetic field (Fig. 3.5.1, right).

J0809-2627 was also observed by the high-resolution spectrograph UVES at the ESO-VLT (ID: 108.225R.001), on January 18th and 27nd 2022. These spectra cover the 3070 – 6630 Å range at $R \approx 40\,000$. The radial velocity determined from the UVES spectra is consistent with that determined from the X-shooter spectrum ($v_{\rm rad} = 33\,{\rm km\,s^{-1}}$). J0809-2627 is therefore likely not radial velocity variable, although further observations are required to support this conclusion. As shown in Fig. 3.5.2, the displaced Zeeman components in the UVES spectra are significantly broader and on average more strongly shifted than those in the X-shooter spectrum. This means that the strength and geometry of the magnetic field on the visible hemisphere of J0809-2627 are time-dependent, possibly due to rotation on a time scale of months. The UVES spectra require a strongly non-homogenous magnetic field, with strengths ranging from about 300 kG to 600 kG. The following analysis focuses on the X-shooter spectrum, which is easier to model and has higher S/N than the UVES spectra.

3.5.3 Models

We used a grid of atmospheric structures computed with the Tlusty code as the basis of our spectroscopic analysis. For a description of the code, see Hubeny & Lanz (2017a,b,c). These models are plane-parallel, homogeneous, hydrostatic, and include H, He, C, N, O, Si, P, S, Fe, and Ni in non-local thermodynamic equilibrium.

Table 3.5.1. Relative intensities for the π and σ Zeeman components following Hönl (1925). The quantum numbers J and m refer to the initial level and $\Delta J = J_{\text{final}} - J_{\text{initial}}$.

ΔJ	π	$\pm\sigma$
0	m^2	$\frac{1}{4}(J \mp m)(J \pm m + 1)$
+1	$(J+1)^2 - m^2$	$\frac{1}{4}(J \pm m + 1)(J \pm m + 2)$
−1	$J^2 - m^2$	$\frac{1}{4}(J \mp m)(J \mp m - 1)$

The observed line splittings can be explained by the linear Zeeman effect caused by the presence of a strong surface magnetic field. Here we used a simplified model for the magnetic field. The magnetic field is assumed to be uniform in both direction and strength B across the visible surface. Its axis is allowed to be inclined at an angle ψ with respect to the line of sight. The magnetic field in J0809-2627 is not strong enough to have a large effect on the atmospheric structure beyond the additional metal line opacity in the UV region (Wickramasinghe & Martin 1986; Tremblay et al. 2015)[12]. In addition, the linear Zeeman effect dominates over the quadratic Zeeman effect at strengths below about 1 MG (Garstang & Kemic 1974). Therefore, our approach was to consider only the linear Zeeman effect as expected from a homogeneous magnetic field. Line splittings due to the linear Zeeman effect were considered in the spectrum synthesis only. We therefore modified the spectrum synthesis code Synspec (Hubeny & Lanz 2017a) to include linear Zeeman multiplets for hydrogen, helium, and detectable metal lines. Kawka & Vennes (2011) used a similar method to model the spectrum of the cool magnetic white dwarf NLTT 10480 which has a magnetic field strength similar to J0809-2627 (about 500 kG).

We assume LS coupling for all metal line transitions, given that the heaviest observed element is sulphur. A LS-coupling state is described by its orbital angular momentum L, its spin angular momentum S, and its total angular momentum J. For each included line, the upper and lower LS states are split into to $2J + 1$ components with magnetic quantum numbers from $m = -J$ to $m = +J$. Only transitions with $\Delta m = 0$ or ± 1 were considered.

For a transition between lower and upper states with magnetic quantum numbers m_l and m_u, the wavelength shift with respect to the rest wavelength at zero magnetic field λ_0 is given as

$$\Delta\lambda = \frac{eB\lambda_0^2}{4\pi m_e c^2} \cdot (m_\text{l} g_\text{l} - m_\text{u} g_\text{u}) \tag{3.5.1}$$

where e is the elementary charge in cgs units, B is the magnetic field strength, m_e is the electron mass, c is the speed of light, and g_l and g_u are the Landé g-factors for the lower and upper level.

In the case of LS-coupling the Landé g-factor is given as

$$g = 1 + \frac{J(J+1) + S(S+1) - L(L+1)}{2J(J+1)}. \tag{3.5.2}$$

Transitions between levels of hydrogen and singly ionised helium represent special cases in this simple model for the magnetic field because these levels are sufficiently described by a main quantum number n. The Landé g-factors were set to unity for these levels and neutral helium.

Analytic expressions for the relative intensities of the components of any linear Zeeman multiplet were first presented by Hönl (1925). They are summarised in Table 3.5.1. Unlike the Landé g-factors, these relative intensities depend only on J and m, and are therefore valid in any coupling scheme. The relative intensity I of the central (π) and displaced (σ) components depends on the angle ψ between the magnetic field axis and the line of sight. The angular dependence given by Condon & Shortley (1935) is for the π (central) component

$$\frac{I(\psi)}{I(90°)} = \sin^2\psi \tag{3.5.3}$$

---

[12] Although iron and nickel lines are not observed in the optical spectrum of J0809-2627, they were still included in our models at abundances of three times their solar value. This is necessary because the opacity of Zeeman-spilt iron group lines in the UV region likely has a significant effect on the atmospheric structure. For the same reason, we used a microturbulent velocity of 6 km s^{-1} for the atmospheric structure calculations only.

Table 3.5.2. Atmospheric parameters derived from spectroscopy. Elemental abundances are stated by number fraction and relative to solar ($\log \epsilon/\epsilon_{\odot}$, Asplund et al. 2009). Upper limits are given as best fit values, while their uncertainties represent values that can clearly be excluded.

	Spectral fit	Element	$\log n_X / \sum_i n_i$	$\log \epsilon/\epsilon_{\odot}$
$T_{\rm eff}$ (K)	44900 ± 1000	H	-0.46 ± 0.07	-0.43 ± 0.07
$\log g$	5.93 ± 0.15	He	-0.18 ± 0.04	0.92 ± 0.04
$\log n({\rm He})/n({\rm H})$	$+0.28 \pm 0.10$	C	$<-3.74^{+0.40}$	$<-0.14^{+0.40}$
B (kG)	353 ± 10	N	-2.98 ± 0.20	1.22 ± 0.20
ψ (°)	64 ± 25	O	$<-3.92^{+0.30}$	$<-0.57^{+0.30}$
$v_{\rm rad}$ (km s^{-1})	33 ± 2	Si	-4.26 ± 0.30	0.27 ± 0.30
$v_{\rm rot} \sin i$ (km s^{-1})	< 25	S	-4.16 ± 0.30	0.75 ± 0.30

and for the σ components

$$\frac{I(\psi)}{I(90^\circ)} = 1 + \cos^2 \psi. \tag{3.5.4}$$

3.5.4 Spectral fits

We performed a global χ^2 fit to the X-shooter spectrum of J0809-2627 to determine its atmospheric parameters, including ψ and B. Spectral regions that are not well reproduced by our models were excluded from the fit. This includes several metal lines, as well as some neutral helium lines. Especially narrow He I lines from the triplet ($S = 1$) system, such as He I 5876 Å, and lines with strong forbidden components, such as He I 4472, 4922 Å, are not well modelled. This is to be expected given the simple nature of our model for the magnetic field, as well as the lack of helium broadening tables in the presence of a magnetic field. The strongest hydrogen and helium lines that could be used for the fit are shown in Fig. 3.5.3. The χ^2 fit prefers a projected rotational velocity of $v_{\rm rot} \sin i = 34\,{\rm km\,s^{-1}}$. However, $v_{\rm rot} \sin i$ is not well constrained because broadening of the displaced Zeeman components may also be caused by a more complex magnetic field geometry. Possibly for the same reason, the central components of several helium lines are sharper in the observation than predicted by our model. These central components in the UVES spectra seem to exclude $v_{\rm rot} \sin i > 25\,{\rm km\,s^{-1}}$. The strength of the central components of Zeeman triplets may also be somewhat increased by magneto-optical effects (Martin & Wickramasinghe 1981), which are not included in our models. Most observed metal lines appear sharp given the limited resolution of the X-shooter spectra. The final atmospheric parameters as derived from the X-shooter spectra are listed in the left part of Table 3.5.2 while the full spectra are shown in Fig. B.5.2. All uncertainties are estimated because they are dominated by systematic effects rather than noise.

As presented in Fig. 3.5.4, the X-shooter spectrum of J0809-2627 shows strong N III-IV, Si IV, and S IV lines. The determination of abundances was complicated not only by the magnetic field but also because most transitions originate from high-lying energy levels that are hard to model even in non-magnetic sdO stars. This meant that some predicted lines could not be used for the abundance determination, for example the C III triplet at 4070 Å and N III 4379 Å. Metal abundances were therefore estimated by eye, that is by comparing the observed spectra with models with different abundances, and keeping the atmospheric parameters fixed to the best-fit values. The derived abundances are listed in the right part of Table 3.5.2. J0809-2627 is enriched in nitrogen at close to 20 times the solar abundance (by number). Carbon and oxygen seem to be at least somewhat subsolar because no lines from these elements are clearly detected – in particular the C III 4159 Å, C IV 5805 Å, and O III 3760 Å multiplets. The photosphere therefore likely consists of material processed by hydrogen fusion in the CNO-cycle. Silicon and sulphur are enriched at about two and six times their solar value, respectively.

The X-shooter and UVES spectra allowed a good determination of the radial velocity of

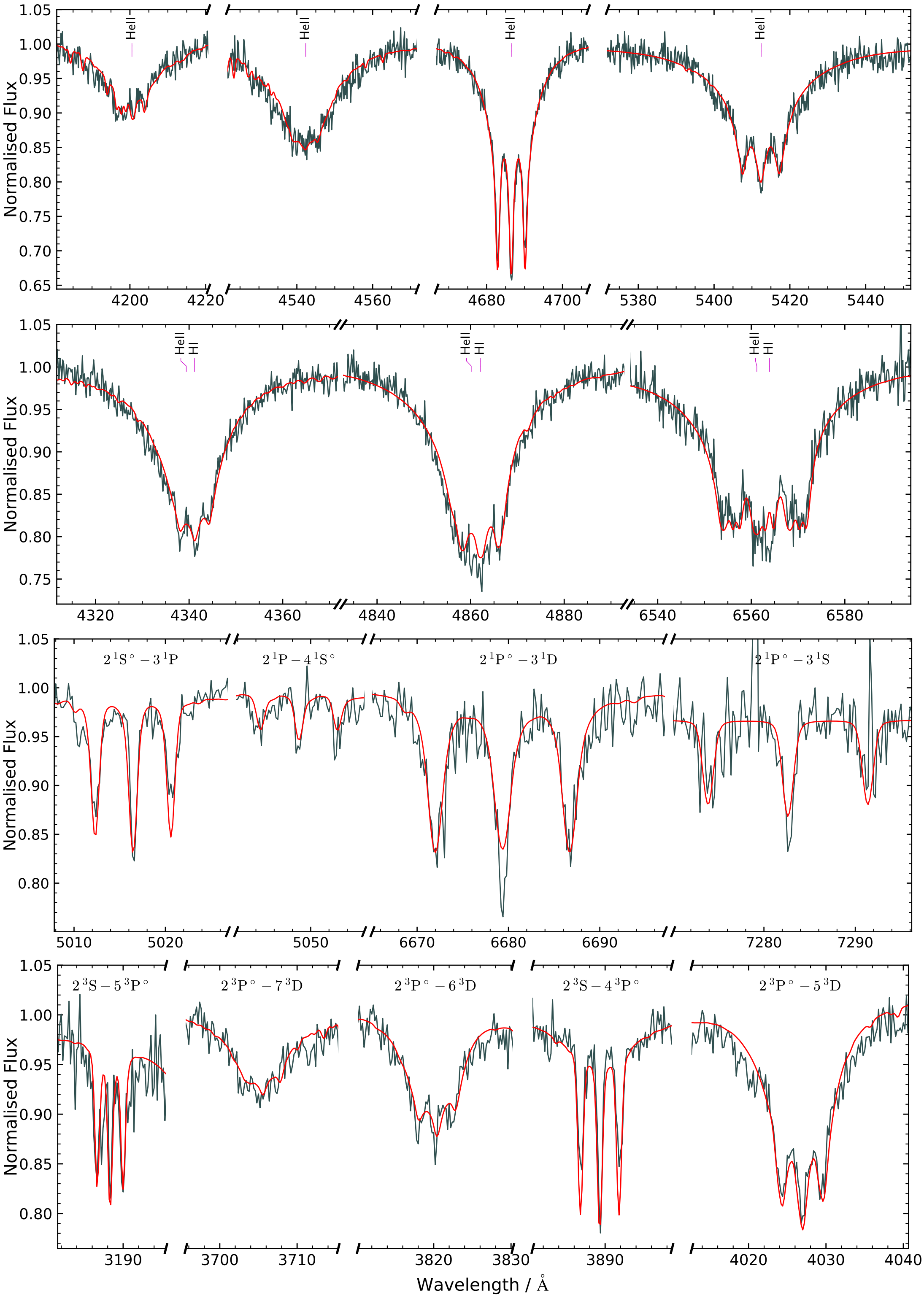

Figure 3.5.3. The strongest He II and H I lines, as well as the best-fitting He I lines in the X-shooter spectrum of J0809-2627. The observed spectrum is shown in grey while the best model is shown in red. Labels indicate He II and H I line positions for zero magnetic field, as well as the lower and upper *LS* terms for He I lines. Adopted from Dorsch et al. (2022).

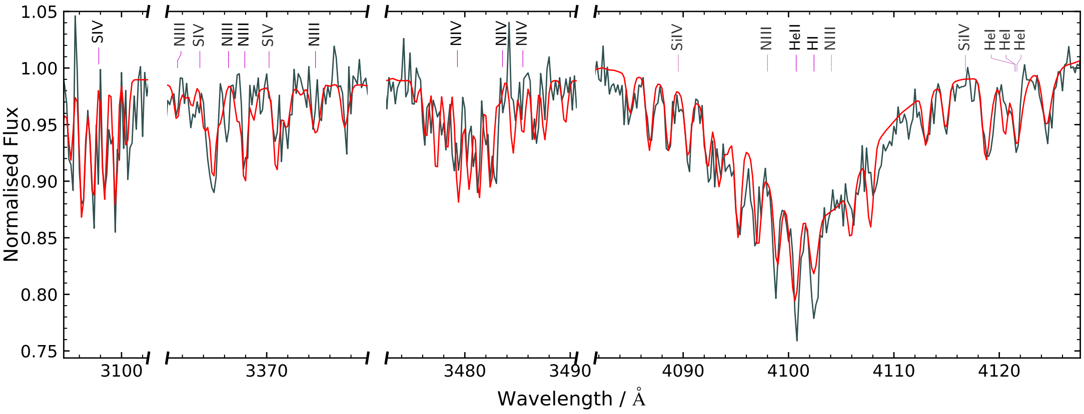

Figure 3.5.4. Zeeman-split N III-IV, Si IV, and S IV lines in the X-shooter spectrum (grey) and the best model (red) of J0809-2627. The projected rotational velocity is set to $v_{\mathrm{rot}} \sin i = 20\ \mathrm{km\,s^{-1}}$. Line positions at zero magnetic field are labelled. Adopted from Dorsch et al. (2022).

J0809-2627, which seems to be constant. If the radial velocity is taken as constant and combined with the parallax and proper motions provided by EDR3 of the *Gaia* satellite (Gaia Collaboration et al. 2021), one can compute the current Galactic space velocity vector of J0809-2627, that is the current velocity towards the Galactic centre U, perpendicular to the disc W, and in direction of Galactic rotation V. The resulting space velocities $(U, V, W) = (-17.3 \pm 2.0, 230.1 \pm 2.7, 7.1 \pm 0.8)\ \mathrm{km\,s^{-1}}$ are consistent with a membership to the thin disk population.

3.5.5 Mass, radius, and luminosity

As described in Sect. 2.3, mass, radius, and luminosity can be derived by combining the spectroscopic surface gravity, the parallax, and the spectral energy distribution. Two SED fits were performed for J0809-2627, with T_{eff} either as a free parameter or fixed to the value derived by the spectroscopic fit. The latter is useful because $T_{\mathrm{eff}} \gtrsim 35\,000$ K are not well constrained from optical and infrared magnitudes alone. The surface gravity and helium abundance were always fixed to spectroscopic values, while the angular diameter Θ was a free parameter. Interstellar extinction was accounted for using the reddening law of Fitzpatrick et al. (2019), where the colour excess $E(44-55)$ was a free parameter. An extinction parameter $R(55) = 3.02$ was assumed.

The angular diameter derived from the SED with fixed T_{eff} was combined with the parallax measurement provided by *Gaia* EDR3 and the spectroscopic surface gravity to estimate the stellar parameters mass, radius, and luminosity for J0809-2627. Here, the parallax measurement of $\varpi = 0.68 \pm 0.04$ mas was corrected for its zero point offset following Lindegren et al. (2021) while the corresponding uncertainty was inflated using the function of El-Badry et al. (2021). The SED fit and stellar parameters are summarised in Table 3.5.3. The top left panel of Fig. B.5.1 shows the SED fit with T_{eff} fixed to the spectroscopic value.

While the stellar radius of J0809-2627, $0.184 \pm 0.011\,R_{\odot}$, and its luminosity, $123^{+19}_{-16}\,L_{\odot}$, are typical for He-sdO stars, the derived mass of $0.93^{+0.44}_{-0.30}\,M_{\odot}$ is rather high. The uncertainty on the mass is considerable due the uncertain spectroscopic surface gravity. These parameters place J0809-2627 close to the zero-age helium main sequence at about $0.8\,M_{\odot}$ (Paczyński 1971), which means that it likely consists of a helium core with next to no hydrogen envelope left.

3.5.6 Evolutionary status

In the following, we discuss the evolution of J0809-2627 in the Hertzsprung-Russell diagram (Fig. 3.5.5). Any possible scenario must be able to explain the location of J0809-2627 on the helium main sequence for a mass of $0.8\,M_{\odot}$. Three scenarios are discussed:

i) Canonical post-EHB evolution. Most hydrogen-rich sdO stars can be explained by post-EHB evolution. When core helium burning ceases, the EHB (sdB) star will evolve to higher

Table 3.5.3. SED fit and stellar parameters. The stellar parameters result from the SED fit with a prescribed $T_{\text{eff}} = 44900 \pm 1000\,\text{K}$. The mode and the highest density interval of each quantity are given for 1-σ probability (see Bailer-Jones et al. 2018).

	SED fit
T_{eff} (K)	47000^{+11000}_{-3000}
$\log\Theta$ (rad)	$-11.246^{+0.005}_{-0.004}$
$E(44-55)$ (mag)	$0.073^{+0.004}_{-0.004}$
Radius $R = \Theta/(2\varpi)$	$0.184^{+0.011}_{-0.010}\,R_\odot$
Mass $M = gR^2/G$	$0.93^{+0.44}_{-0.30}\,M_\odot$
Luminosity $L/L_\odot = (R/R_\odot)^2(T_{\text{eff}}/T_{\text{eff},\odot})^4$	123^{+19}_{-16}

temperatures and towards the white dwarf cooling sequence. However, this scenario is unlikely for J0809-2627. Although the position of J0809-2627 in the HRD (Fig. 3.5.5) is crossed by a post-EHB track of Dorman et al. (1993), this track would require a mass of $0.47\,M_\odot$ – inconsistent with the adopted mass of $0.93^{+0.44}_{-0.30}\,M_\odot$. Moreover, J0809-2627 is a helium-rich sdO, while most sdB stars are helium-poor due to atomic diffusion processes (Michaud et al. 2011). It is unlikely that the helium-poor composition of the sdB progenitor could transform into a helium-rich one (Groth et al. 1985). Furthermore, there would be no explanation for the strong magnetic field.

ii) Intermediate mass progenitor. Richer et al. (2019) and Caiazzo et al. (2020) recently discovered three massive magnetic DA white dwarf stars in young open clusters, and propose that these are the progeny of intermediate-mass stars. They suggested that the strong surface magnetic fields observed for these WDs are fossil fields that were first generated by dynamo effects in the progenitors' convective core. Fuller et al. (2015) and Stello et al. (2016) used asteroseismic observations to show that most massive ($\gtrsim 1.5\,M_\odot$) red giant branch stars have strongly magnetic cores, with strengths exceeding 100 kG. Similar fields may exist in red clump stars (Cantiello et al. 2016; Sandquist et al. 2020). Given its relatively high mass ($\approx 0.9\,M_\odot$), one might consider J0809-2627 as an intermediate mass star that was stripped of its envelope by a compact unseen companion, thus revealing the magnetic field in its core. Models for stripped intermediate mass stars were provided by Götberg et al. (2018). These models can produce a He-sdO with the surface composition and effective temperature observed for J0809-2627 by stripping a $\approx 4.9\,M_\odot$ star of solar metallicity. The resulting He-sdO has a mass of $0.98\,M_\odot$ but is larger, more luminous, and has a lower surface gravity when compared to J0809-2627 (see also Fig. 3.5.5). The stripping would require an unseen companion that would likely be detectable through radial velocity variations. Based on the three spectra shown in Fig. 3.5.2, J0809-2627 seems to have a constant radial velocity, which is a strong argument against this "stripped star" scenario.

iii) Merging of two white dwarfs. Given that there is presently no evidence for binarity, the merging of two helium-core WD stars is the preferred scenario for the formation of J0809-2627. This scenario would have difficulty in making an object with a mass as high as $0.93\,M_\odot$, but is predicted to produce significant numbers of He-sdOs with masses up to about $0.8\,M_\odot$ (Han et al. 2003), which would be well within the uncertainty of our mass for J0809-2627. Indeed, the $0.8\,M_\odot$ slow merger model of Zhang & Jeffery (2012) matches the effective temperature and luminosity of J0809-2627 well at the onset of core helium burning, as shown in Fig. 3.5.5.

The presence of a strong magnetic field as been proposed as a smoking gun for stellar mergers (Schneider et al. 2019). Based on three dimensional simulations of CO white dwarf mergers (Yoon et al. 2007; Lorén-Aguilar et al. 2009), García-Berro et al. (2012) showed that strong magnetic fields can be generated in a the hot, convective, and differentially rotating corona surrounding the primary during the mass transfer. These magnetic fields are predicted to be frozen to the outer layers of the final merger product. Magnetodipole radiation rapidly spins down the newly formed magnetic white dwarf if magnetic and rotation axes are not aligned. These predictions

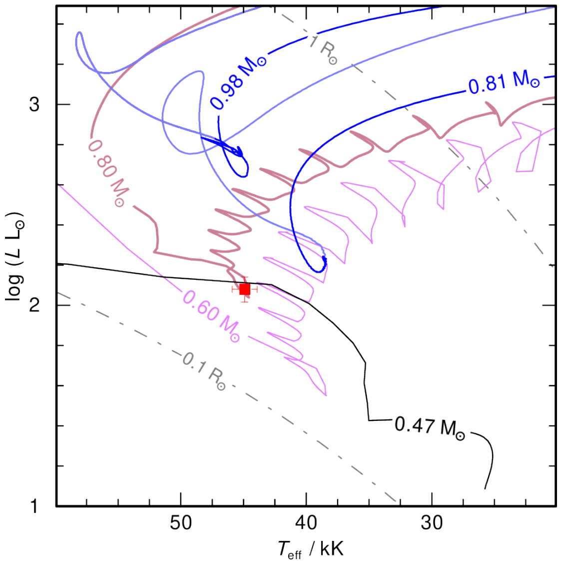

Figure 3.5.5. Position of J0809-2627 (red) compared to several evolutionary tracks. Blue: two stripped massive star tracks from Götberg et al. (2018), where dark and light blue colours indicate the pre- and post-He core burning phases. The 0.98 $M_\odot$ track is for solar metallicity ($Z = 0.014$) while the 0.81 $M_\odot$ track is for $Z = 0.006$. Pink: two double He-WD slow-merger tracks from Zhang & Jeffery (2012). Black: solar metallicity post-EHB track from Dorman et al. (1993). The grey dashed-dotted lines indicate radii of 0.1 and 1 $R_\odot$. The final masses for all tracks are labelled. Adopted from Dorsch et al. (2022).

appear to be consistent with recent results of Bagnulo & Landstreet (2021), who found that young WDs with fields exceeding 1 MG are more massive than canonical WDs. Similarly, J0809-2627 will evolve through a helium shell burning phase and eventually become a white dwarf. If the magnetic flux would be conserved until J0809-2627 reaches the WD stage ($B \sim R^{-2}$), its surface field strength would reach about 100 MG at a radius of 0.01 $R_\odot$.

The unusual surface chemical composition, slow rotation, and strong magnetic field of J0809-2627 provide important constraints on merger models. As discussed in Sect. 1.5.3, evolutionary calculations for He-WD+He-WD mergers were performed by Zhang & Jeffery (2012), Hall & Jeffery (2016), and Schwab (2018). Zhang & Jeffery (2012) predict nitrogen-rich surfaces for slow double He-WD mergers, similar to what we find for J0809-2627. Such systems retain the initial composition of the secondary He-WD, which includes a nitrogen-rich signature as observed for J0809-2627. Fast hot mergers would produce C-rich, N-poor surfaces and composite models lead to C&N-rich surfaces. Expanding on the work of Zhang & Jeffery (2012), Yu et al. (2021) found that the masses of the merging white dwarfs are important, with lower masses forming N-rich systems and larger masses leading to C-enrichment. Given the large estimated mass of J0809-2627, carbon-enrichment would be expected. Such enrichment is not excluded by the presently available optical data. Coverage of the far-UV C IV 1548, 1551 Å resonance doublet would be required to derive an accurate carbon abundance that could be compared to these models.

A related formation channel for He-sdOs is the merger of a He-WD with a post-sdB WD, i. e. a hybrid HeCO-WD (Justham et al. 2011, following the pioneering models of Iben 1990). This channel is a natural consequence of one of the common-envelope formation channels for sdB stars described by Han et al. (2002), and seems likely to contribute substantially to the population of single He-sdO stars. Moreover, the inferred effective temperature and surface gravity of J0809-2627 are close to the densest region of the population predictions of Justham et al. (2011) in which a hybrid WD of only 0.35 $M_\odot$ accretes 0.15–0.3 $M_\odot$ from a He-WD. However, only the more massive of those merger models are within the mass range we infer for J0809-2627. It seems plausible that the resulting surface abundances resemble J0809-2627 as long as the He-WD is disrupted rather than the hybrid HeCO-WD, i. e., that the He-WD is the less massive component of the merging binary. This differentiates this scenario from the merger models of Miller Bertolami et al. (2022), in which a HeCO-WD is accreted by a more massive He-WD.

The best-fit surface hydrogen abundance for J0809-2627 is higher than that observed for most (extreme) He-sdO stars (see e. g. Stroeer et al. 2007; Schindewolf et al. 2018). Model predictions are difficult to make for merger models because the atmosphere corresponds to a very small fraction of the stellar envelope. For double He-WD mergers, attempts have been made by Hall & Jeffery (2016), and Schwab (2018). In these models, the surface hydrogen abundance depends on the rotational velocities after the merging – models that include rotation result in very hydrogen-poor surfaces. In fact, Schwab (2018) predict rotational velocities of about 30 km s^{-1} once a

$0.5\,M_\odot$ merger remnant reaches the core helium burning phase, which would be consistent with the elemental abundance pattern of J0809-2627. However, the more relevant $0.7\,M_\odot$ merger remnant is predicted to be a fast rotator at $\upsilon_{\mathrm{rot}} \approx 100\,\mathrm{km\,s^{-1}}$, which would require a low inclination for J0809-2627. Such a fast rotation is also in contradiction with the non-variability between the two UVES spectra of J0809-2627, which were separated by nine days. In this $0.7\,M_\odot$ merger model, the surface becomes enriched in carbon and extremely hydrogen-poor, which is not observed for J0809-2627.

3.5.7 Summary and conclusions

We performed a detailed spectral analysis of the magnetic He-sdO J0809-2627 and used a simple uniform model to derive a mean magnetic field strength of $353 \pm 10\,\mathrm{kG}$ at an inclination of $\psi = 64 \pm 25\,^\circ$. While our uniform model for the magnetic field generally results in good fits for most lines in the X-shooter spectrum of J0809-2627, the magnetic field geometry is certainly more complicated in reality. In fact, the comparison between UVES and X-shooter exposures showed that the magnetic field is variable on time-scales of weeks to months, and clearly non-uniform. The magnetic field variability may be caused by magnetic spots combined with slow stellar rotation. However, the TESS light curve of J0809-2627 does not show significant variations, as discussed by Dorsch et al. (2022)[13]. Constant radial velocity measurements between the three high-resolution spectra, separated by nine days and nine months, respectively, indicate that J0809-2627 is a single star.

Apart from its strong magnetic field, J0809-2627 has a relatively low helium abundance at $\log n(\mathrm{He})/n(\mathrm{H}) = +0.28 \pm 0.10$ compared to typical non-magnetic He-sdOs, while its effective temperature, $T_{\mathrm{eff}} = 44900 \pm 1000\,\mathrm{K}$, and surface gravity, $\log g = 5.93 \pm 0.15$, are not unusual. The He-sdO is nitrogen-rich and seems to be carbon- and oxygen-poor, although only upper limits could be derived for C and O. This is consistent with the metal abundances expected for a slow double He-WD merger (Zhang & Jeffery 2012) or a stripped intermediate-mass star (Götberg et al. 2018). We combined astrometry, photometry and spectroscopy to derive stellar parameters of $R = 0.184 \pm 0.011\,R_\odot$, $L = 123^{+19}_{-16}\,L_\odot$, and $M = 0.93^{+0.44}_{-0.30}\,M_\odot$. Placing it in the HRD, J0809-2627 is located on the helium main sequence, which implies that it lost any hydrogen envelope completely. J0809-2627 is therefore more compact than the stripped star models of Götberg et al. (2018) at similar temperature and mass.

In summary, the combination of its position on the helium zero-age main sequence, its high mass estimate, CNO-processed chemical composition, and the absence of a close stellar companion presents compelling evidence in support of the double-degenerate merger scenario for J0809-2627. The UVES spectra exclude projected rotation velocities of more than about $25\,\mathrm{km\,s^{-1}}$, which is inconsistent with the $\upsilon_{\mathrm{rot}} \approx 100\,\mathrm{km\,s^{-1}}$ Schwab (2018) predicted for a $0.7\,M_\odot$ double He-WD merger remnant – these merger models likely overestimate rotation rates. As noted by Schwab (2018), magneto-hydrodynamic simulations would be required for double He-WD mergers, similar to those performed for CO-WD mergers by Ji et al. (2013) and Zhu et al. (2015).

A double He-WD merger is also the favoured scenario for the formation of the more common non-magnetic He-sdO stars. Therefore, the question remains why the vast majority of He-sdO stars are apparently non-magnetic, whereas J0809-2627 has a strong magnetic field. One possibility would be that the surface magnetic field observed for J0809-2627 is not stable and weakens quickly after a merging event. Spectropolarimetric or high-resolution monitoring observations would provide more information about the global magnetic field geometry and its stability.

In addition, ultraviolet observations would allow us to improve on the determination of the abundances of carbon and oxygen, for which only upper limits are available at present, and would provide abundance measurements for many more metals, including neon and the iron group. A complete abundance pattern is crucial to establish the composition of any accreted and fusion-processed material. This would provide the basis of a better understanding of the relevant merger channels and the fusion reactions that take place during the merging.

---

[13] This analysis was performed by Ingrid Pelisoli and is therefore not discussed here.

Table 3.6.1. List of archival WHT/ISIS spectra of J0415+2538, J1303+2646, and J1603+3412.

Star	Date	Grating	Central wavelength (Å) Blue	Central wavelength (Å) Red	Number of spectra
J0415+2538	20140203	R600	4300	6403	2
J0415+2538	20140204	R600	4300	6403	2
J0415+2538	20150822	R600	4298	6201	4
J0415+2538	20150823	R600	4298	6201	4
J0415+2538	20150824	R600	4298	6201	4
J0415+2538	20150825	R600	4298	6201	4
J0415+2538	20151215	R600	4498	6900	3
J1303+2646	20050225	R1200	4501	6199	1
J1303+2646	20120531	R600	4351	6558	4
J1303+2646	20150615	R1200	4750	6799	4
J1303+2646	20150616	R1200	4750	6799	6
J1603+3412	20150615	R1200	4750	6799	4
J1603+3412	20150616	R1200	4750	6799	5

3.6 J0415+2538, J1303+2646, and J1603+3412: a triplet of magnetic He-sdOs

The analysis presented in this chapter was published as a part of Pelisoli et al. (2022). Large parts of the content of this chapter are taken verbatim from this paper.

3.6.1 Introduction and observations

The first magnetic He-sdO star analysed, J0809-2627 (Sect. 3.5), is not the first one to be discovered. Already in the since 2010, Boris Gänsicke discovered three additional magnetic He-sdOs in the SDSS spectroscopic survey: SDSS J041536.05+253857.1, SDSS J130346.61+264630.6[14], and SDSS J160325.52+341237.4 (henceforth J0415+2538, J1303+2646, J1603+3412, respectively). These stars were analysed for the first time as part of this thesis, also published as part of the Pelisoli et al. (2022) paper. Since their discovery in SDSS, additional spectra were taken using the ISIS spectrograph mounted at the William Herschel Telescope (WHT) on La Palma, which are summarised in Table 3.6.1. These spectra were retrieved from the database of the Isaac Newton Group of telescopes[15] and reduced by Ingrid Pelisoli. Both the R600 and the R1200 gratings were used, which have spectral resolutions of about 1.9 Å and 0.8 Å, respectively.

3.6.2 Spectral and SED analysis

The spectral analysis for the three targets discussed in this section was based on the method used by Dorsch et al. (2022) to model the prototype magnetic He-sdO J0809-2627, as described in Sect. 3.5.3. We performed global χ^2 fits to the WHT/ISIS spectra of each star. Initially we fitted the Doppler-corrected co-added spectra to evaluate the performance of our simple treatment of the magnetic field. The free parameters were the effective temperature T_{eff}, the surface gravity $\log g$, the helium abundance $\log n(\text{He})/n(\text{H})$, and the mean magnetic field strength B. This initial fit showed that the spectra of J1303+2646 clearly display broadened displaced Zeeman components (see Fig. 3.6.1), which indicates that the magnetic field across the surface of this star is non-homogeneous. To account for this, we constructed toy models consisting of more than one homogeneous component, which allowed us to roughly emulate a non-homogeneous

---

[14] This is the then undisclosed star mentioned by Heber et al. (2013).

[15] http://casu.ast.cam.ac.uk/casuadc/ingarch/query

Table 3.6.2. Atmospheric parameters from fits with one, two, or three field components to the co-added WHT/ISIS spectra of the three targets. The components' area is denoted A_i.

Star	$T_{\rm eff}$/K	$\log g$	$\log n(\mathrm{He})/n(\mathrm{H})$	B_1/kG	B_2/kG	B_3/kG	A_2/A_1	A_3/A_1	χ^2_r
J0415+2538	46730	6.02	−0.15	280	–	–	–	–	2.56
J0415+2538	46460	5.95	−0.12	266	420	–	0.24	–	2.31
J0415+2538	46430	5.96	−0.13	262	377	469	0.21	0.10	2.45
J1303+2646	48880	6.07	+0.22	415	–	–	–	–	2.66
J1303+2646	47920	5.87	+0.32	384	571	–	0.56	–	1.99
J1303+2646	47790	5.84	+0.33	364	584	442	0.67	0.61	1.89
J1603+3412	46620	6.08	+0.06	340	–	–	–	–	2.33
J1603+3412	45980	6.03	+0.05	291	395	–	0.82	–	2.10
J1603+3412	45700	5.95	+0.06	284	377	523	0.90	0.27	2.07

magnetic field geometry that causes significant variation of the magnetic field strength across the stellar surface. For each star, we re-fitted the co-added spectra with one and two additional homogeneous magnetic field components that were allowed to vary in the field strength and surface contribution. This exercise is visualised in Fig. 3.6.1 and its results are summarised in Table 3.6.2.

Importantly, our toy model also allowed us to investigate the systematic uncertainties on the derived atmospheric parameters that result from our approximation of a uniform magnetic field. The resulting $T_{\rm eff}$ values change insignificantly because they are dominantly constrained by the helium ionisation equilibrium rather than by the detailed spectral line shapes. The surface gravities as well as the hydrogen to helium ratios, however, are derived mainly from the shapes of the hydrogen and helium lines. Therefore, changes of 0.1–0.2 dex are observed when introducing a second component. Adding a third component leads to considerably smaller changes of the atmospheric parameters, which we judge to be insignificant for J0415+2538 and J1603+3412. We therefore adopted the two-component models for these two stars. The field structure of J1303+2646 is more complex, which led us to adopt three components.

Once the number of components was fixed, all available spectra were fitted simultaneously with the selected number of components to determine $T_{\rm eff}$, $\log g$, $\log n(\mathrm{He})/n(\mathrm{H})$, the mean magnetic field strength B, and the surface contribution of each component, as well as the radial velocities $\upsilon_{\rm rad}$. We only allowed $\upsilon_{\rm rad}$ to be different for the individual spectra, forcing a global best-fit for the atmospheric parameters. The magnetic field axis was forced to be inclined at an angle $\psi = 90°$ with respect to the line of sight because our simplified model for the magnetic field geometry does not allow for a physical interpretation of this angle. The projected rotational velocity was fixed to $\upsilon_{\rm rot} \sin i = 0\,\mathrm{km\,s^{-1}}$ for all stars because it is not well constrained by the low-resolution WHT/ISIS spectra. We only derived upper limits based on the value preferred by a free $\upsilon_{\rm rot} \sin i$ fit. Spectral regions that were poorly reproduced by our models were excluded from the fit. This includes He I 4471 Å, as well as regions that are affected by metal lines. Important metal line blends are due to strong N III lines, partly blended with H I/He II 4101, 4862 Å and He II 4201, 4543 Å.

Our best-fit models are compared with the merged and radial velocity-corrected WHT/ISIS spectra in Fig. 3.6.1. The best-fit parameters are listed in Table 3.6.3, including the average magnetic field for each star. The strengths and relative surface ratios of the components are given in Table B.5.1. The uncertainties of the atmospheric parameters stated in Table 3.6.3 are estimated systematical uncertainties because the statistical uncertainties are negligible in comparison. For the radial velocities, we state the average values and their standard deviations. For J0415+2538, we exclude the radial velocity measurements taken on 2015 December 15, given that no arc lamp was taken with the same pointing as the target, making the radial velocities unreliable due to instrumental shifts. In all three cases, there is no evidence of significant radial velocity variability on time scales of thousands of days. This is comparable to the longest orbital periods observed

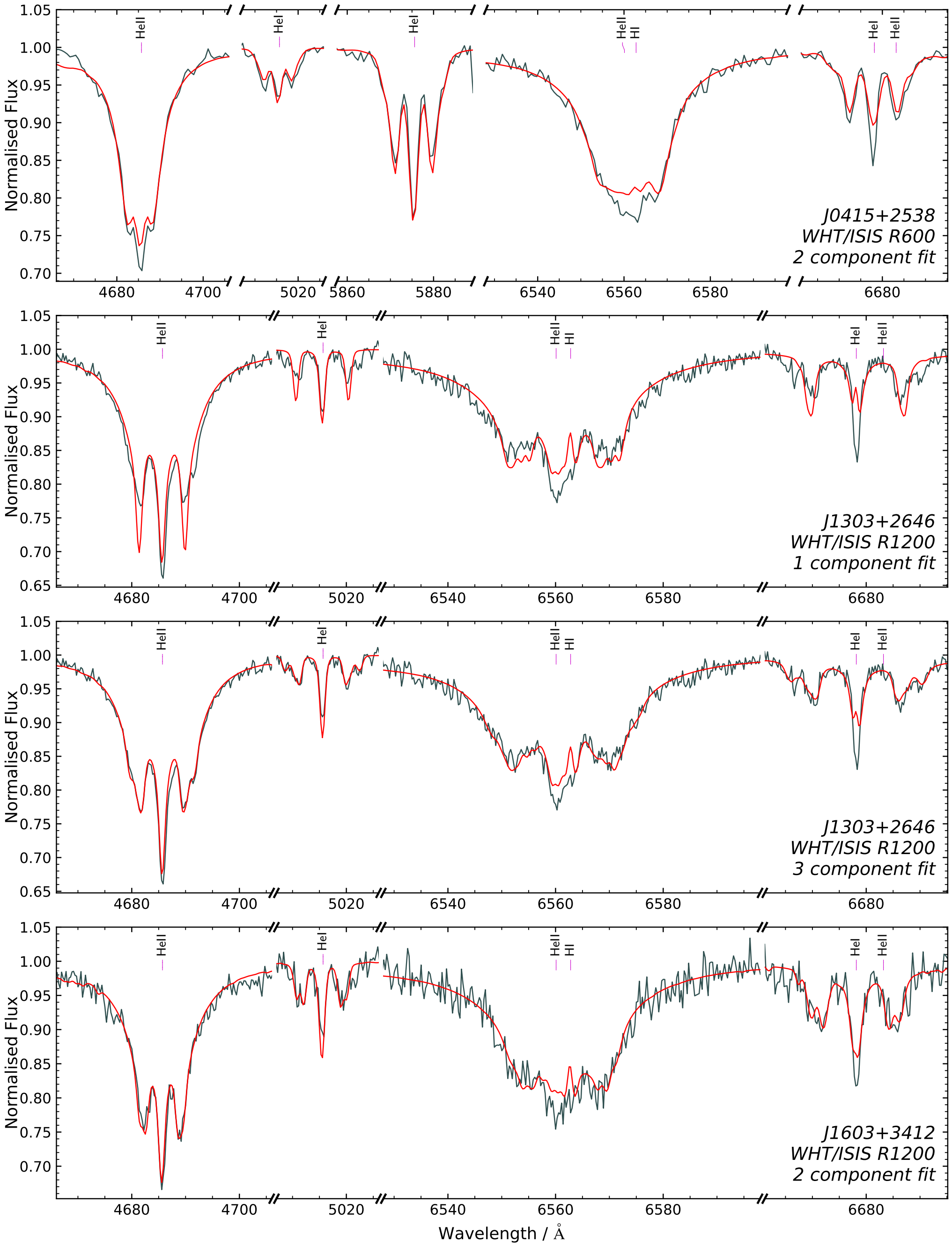

Figure 3.6.1. H I, He I, and He II lines in the merged and radial velocity-corrected WHT/ISIS spectra for each target. The best model is shown in red, not including metal lines. Labels indicate H I and He I-II line positions at $B = 0$. The top panel shows our best fit for J0415+2538. The two middle panels show fits for J1303+2646: initially using only one magnetic field component, which leads to a poor fit to the Zeeman components, and using three components, which can much better approximate the complex magnetic field geometry. The bottom panel shows the final fit for the merged spectrum of J1603+3412. Adopted from Pelisoli et al. (2022).

Figure 3.6.2. Co-added and radial velocity corrected WHT/ISIS spectra from top to bottom for J1603+3412, J1303+2646, and J0415+2538. The spectra are offset in steps of 0.1 for better visibility. The origin of the broad and smooth feature centred at about 4631 Å is unknown. Adopted from Pelisoli et al. (2022).

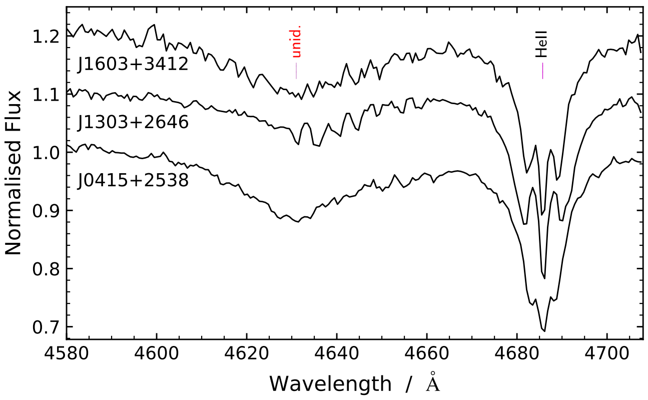

for hot subdwarfs (Vos et al. 2019) and indicates that the three stars are single, like J0809-2627.

The similarities between the atmospheric parameters of all four known magnetic He-sdOs are remarkable. All stars share an intermediate helium abundance, with almost the same number of hydrogen and helium atoms in their photospheres. This is highly unusual for He-sdO stars at $T_{\rm eff}$ > 43 000 K, which are almost always either extremely hydrogen-poor or helium-poor (Stroeer et al. 2007). Due to the low resolution of the available spectra, we could not determine detailed abundance patterns. All stars seem to lack strong carbon lines, similar to J0809-2627. Hints of the C IV lines at 5805 Å and the C III 4070 Å triplet are observed in the co-added ISIS spectrum of J0415+2538 and to a lesser degree in the SDSS spectrum of J1603+3412, but are absent in the ISIS spectrum of J1303+2646. This suggests that carbon is not strongly enriched, although solar carbon abundances cannot be excluded. The N III 4517, 4639 Å multiplets in the ISIS spectra of J1303+2646 are best reproduced at a nitrogen abundance of about ten times solar. The same lines are weaker in the spectra of J0415+2538 and J1603+3412, suggesting nitrogen abundances between two and six times solar. In short, there is evidence that the magnetic objects are nitrogen-rich, but better spectra are needed to probe the carbon content and all other metal abundances.

In addition, all stars show a strong and broad feature in the 4629 – 4660 Å range, centred at about 4631 Å (see Fig. 3.6.2). The origin of this feature remains unclear. A photospheric origin seems to be excluded by the lack of similar features at other wavelengths. The same argument can be used to exclude both ultra-high excitation lines, which are observed for some DO-type white dwarfs (Werner et al. 1995; Reindl et al. 2019), and diffuse interstellar bands. An instrumental effect is excluded because the feature is also observed in the SDSS spectra. The feature is present in the X-shooter spectrum of J0809-2627 as well, but weaker than in the three new stars.

The individual spectra of J0415+2538 and J1303+2646 were taken over a timespan of years; one might therefore expect a variable field strength and geometry as observed for J0809-2627 (see Fig. 3.5.2). We see no significant variation in the ISIS spectra of these two stars, although these spectra are of lesser quality than the spectra of J0809-2627. Any variation in the fields at the times of observation must have been less drastic than for J0809-2627.

We also fitted the SED of the three stars, as done for J0809-2627[16]. The effective temperature, $\log g$, and $\log n(\mathrm{He})/n(\mathrm{H})$ were fixed to the values determined from spectroscopy, while the angular diameter Θ and the colour excess $E(44-55)$ were left as free parameters. We find a significant reddening of $E(44-55) = 0.298 \pm 0.005$ mag for J0415+2538, in agreement with reddening maps (e. g. Lallement et al. 2018), whereas J1303+2646 and J1603+3412 are not strongly reddened at $E(44-55) = 0.005 \pm 0.003$ mag and $E(44-55) = 0.025 \pm 0.006$ mag, respectively. The best-fit SEDs are plotted in Fig. B.5.1, while their parameters and the resulting radii and luminosities are listed in Table 3.6.3. In principle, stellar masses could be determined from the radius and $\log g$ measurements, but the large $\log g$ and parallax uncertainties preclude any meaningful results. The luminosities of all magnetic He-sdOs are close to $100\,L_\odot$ and therefore comparable with what has been previously derived for He-sdOs (e. g. Stroeer et al. 2007) – see also Sect. 4.1 for accurate luminosities for a large sample of He-sdOs and other hot subdwarf stars.

---

[16] For more details on the SED fitting method, refer to Sect. 2.3.

Table 3.6.3. Stellar parameters derived from spectroscopic and SED fits. We include the values for the prototype J0809-2627 from Dorsch et al. (2022, Sect. 3.5) for comparison. For $T_{\rm eff}$, $\log g$, and $\log n({\rm He})/n({\rm H})$, we quote estimated systematic uncertainties, which are dominant over the statistical ones. For $\upsilon_{\rm rad}$, we quote the average and standard deviation over the multiple measurements. For R and L, the quoted values are the mode and the 68 % confidence interval.

	J0809-2627	J0415+2538	J1303+2646	J1603+3412
$T_{\rm eff}$ (K)	44900 ± 1000	46580 ± 1500	47950 ± 1500	46450 ± 1500
$\log g$	5.93 ± 0.15	5.98 ± 0.25	5.97 ± 0.30	6.06 ± 0.20
$\log n({\rm He})/n({\rm H})$	+0.28 ± 0.10	−0.10 ± 0.15	+0.25 ± 0.15	+0.07 ± 0.15
$B_{\rm avg}$ (kG)	353 ± 10	305 ± 20	450 ± 20	335 ± 15
$\upsilon_{\rm rad}$ (km s^{-1})	33 ± 2	−17 ± 10	−37 ± 8	6 ± 5
$\upsilon_{\rm rot} \sin i$ (km s^{-1})	< 25	< 45	< 60	< 65
R ($R_\odot$)	$0.184^{+0.011}_{-0.010}$	$0.148^{+0.020}_{-0.015}$	$0.19^{+0.05}_{-0.04}$	$0.14^{+0.06}_{-0.04}$
L ($L_\odot$)	123^{+19}_{-16}	91^{+29}_{-21}	160^{+100}_{-60}	70^{+80}_{-40}

3.6.3 Magnetic fields in the hot subdwarf population

Our three new detections increase the number of hot subdwarfs with confirmed magnetic fields from one to four[17]. Considering the sample size of 2036 hot subdwarfs identified from SDSS spectra (Geier 2020), and assuming that there is no bias in selecting magnetic systems (which is reasonable since their colours do not seem to be strongly affected), the three detections from SDSS spectra imply a lower limit to the fraction of strongly magnetic hot subdwarfs of 0.15 ± 0.10 %[18]. At 1.8 ± 1.2 %, the lower limit is higher amongst the He-sdOs, which represent about 8 % of the overall SDSS sample. Given the low resolution of SDSS ($\Delta\lambda \approx 2.9$ Å), only field strengths larger than ≈200 kG can be identified from visual inspection, implying that lower fields would remain undetected. This detection limit is significantly improved for high resolution ($R \approx 20000$), which would reveal fields down to ≈50 kG. However, high resolution spectra are available for a smaller number of stars (≈200) that furthermore are not homogeneously selected.

Previous searches for magnetic fields in hot subdwarfs mainly used low-resolution spectropolarimetry (Landstreet et al. 2012; Mathys et al. 2012), which has the advantage of lower detection limits of the order of a few hundred gauss to kilogauss, but the disadvantage of requiring the targets to be fairly bright. These searches targeted forty stars of quite different spectral types in various stages of stellar evolution, including sdB stars in close binary systems with white dwarfs or low-mass main sequence companions – see Appendix B.5 and Table B.5.2 for a summary. Most observations were carried out with the FORS spectropolarimeter at the ESO VLT. Landstreet et al. (2012) and Bagnulo et al. (2012) reanalysed most FORS observations of hot subdwarfs and found no detections even at 2σ level, concluding that there is “no evidence for the presence of magnetic fields at the level of 1 kG”.

There are five He-sdOs that have been probed by spectropolarimetry: two eHe-sdO stars and three iHe-sdO stars. Landstreet et al. (2012) derived a mean longitudinal field strength B_z = 90 ± 140 G for the eHe-sdO CD−31 4800 and B_z = 232 ± 178 G for the iHe-sdO HD 127493. Randall et al. (2015) reported an upper 3σ limit of 300 G for a magnetic field of the iHe-sdOB LS IV−14°116. Hence, no magnetic fields at a level of a few hundred gauss are present in these three He-sdOs. Earlier work by Elkin (1996) targeted the eHe-sdO star BD+25 4655 and the iHe-sdO BD+75 325. They measured circularly polarised spectra using the 6-metre telescope at the Russian Academy of Sciences Special Astronomical Observatory and determined a magnetic

---

[17] The object mentioned by Heber et al. (2013) is in fact part of our sample.

[18] This value corresponds to the median and 68 % quantiles obtained by drawing samples from the corresponding binomial distribution.

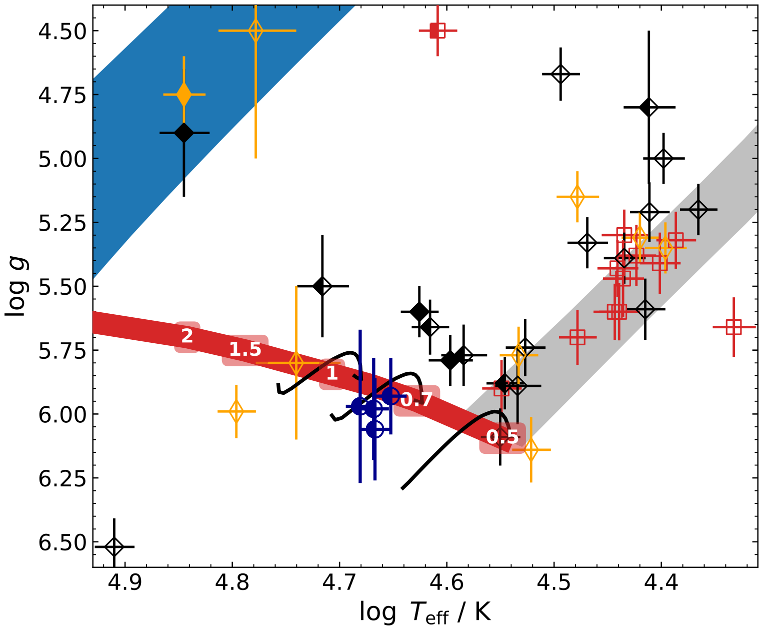

Figure 3.6.3. Kiel diagram showing sdO/B stars that have been probed for magnetic fields using spectropolarimetry. The four known magnetic He-sdOs are shown as blue circles. Black diamonds mark apparently single (non-$v_{\rm rad}$ variable) stars, red squares show known close binaries with white dwarf or low-mass main sequence/brown dwarf companions, and orange thin diamonds indicate unknown $v_{\rm rad}$ variability. Helium-poor stars are marked by open symbols, extremely He-rich stars by filled symbols, and intermediately He-rich stars by half filled symbols. The solid black lines indicate the core helium burning phase in the merger tracks of Yu et al. (2021) for a metallicity of $Z = 0.01$ and remnant masses of 0.45, 0.65, 0.85 $M_{\odot}$. The grey shaded region marks the location of the EHB by Dorman et al. (1993) for solar metallicity, the blue shaded region marks the range of post-AGB tracks of Miller Bertolami (2016), and thick red line indicates the zero-age helium MS from Paczyński (1971). Adopted from Pelisoli et al. (2022).

field strength of $B_z = 1680 \pm 60$ G in BD+75 325. Three additional measurements of BD+75 325 pointed at a variable field strength (Elkin 1998). In addition, Elkin (1998) failed to detect a magnetic field at the 400 G level from three observations of BD+25 4655. Hence, BD+75 325 would be the only hot subdwarf with a detected magnetic field of a few kG. However, Landstreet et al. (2012) argue that the real uncertainties in these measurements are likely of the order of 1 kG, so of the same order as the reported fields. Confirmation with more sensitive methods would therefore be required. In summary, the fields of the four confirmed magnetic He-sdOs are larger by a factor of at least a thousand than those of the few probed He-sdOs.

A Kiel diagram of all hot subdwarfs probed for magnetic fields using spectropolarimetriy, as well as the four magnetic He-sdOs is shown in Fig. 3.6.3; see Table B.5.2 for more details on the objects. The binary status of the stars, inferred from $v_{\rm rad}$ variability, is also indicated, as is the helium abundance. About 60 % of the previously studied stars with sufficient $v_{\rm rad}$ measurements show no evidence of a binary companion, like the known magnetic systems. Strikingly, the four magnetic He-sdO stars cluster very closely together in the Kiel diagram, and none of the previously probed stars are found in this region. This suggests that a very specific formation scenario is required to generate a magnetic field. Spectropolarimetric studies of a larger number of stars would be necessary to confirm that magnetism does not occur for hot subdwarfs in other regions of the Kiel diagram.

Other He-rich hot subdwarfs likely formed by mergers were observed by the SPY survey (Napiwotzki et al. 2003; Lisker et al. 2005; Stroeer et al. 2007; Hirsch 2009), which obtained high resolution spectra ($R \approx 20\,000$) of tens of hot subwarfs. More recent spectral analyses of He-rich sdO stars from high resolution spectroscopy have been reported by Schindewolf et al.

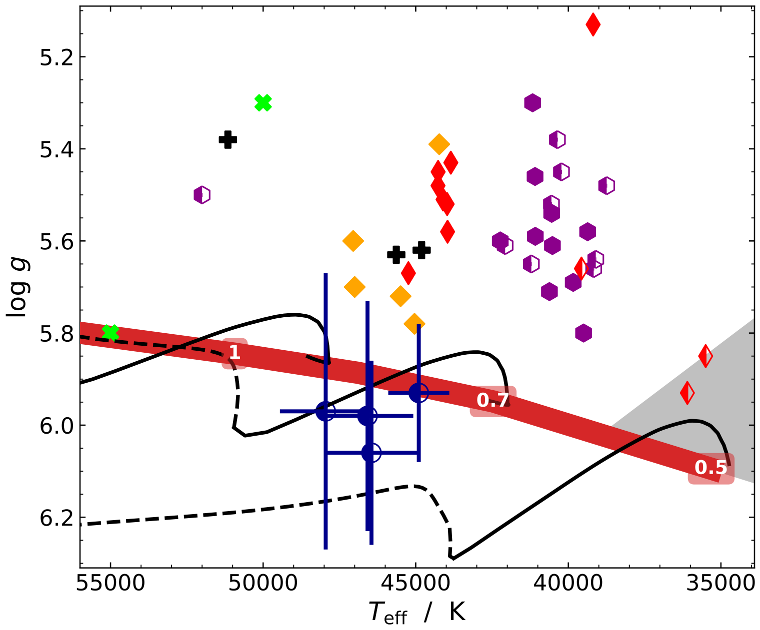

Figure 3.6.4. Similar to Fig. 3.6.3, but for the distribution of He-rich hot subdwarf stars by metal composition, indicated as purple hexagons (N-rich), red thin diamonds (C&N-rich), orange diamonds (C-rich), or black pluses (C-rich, N-poor). The CO-rich He-sdOs from Werner et al. (2022a) are green cross-marks. Here, solid lines correspond to the core helium burning phase and dashed lines indicate helium shell burning for the Yu et al. (2021) tracks. Adopted from Pelisoli et al. (2022).

(2018), Naslim et al. (2013, 2020), Dorsch et al. (2019), Jeffery et al. (2021), and Werner et al. (2022b), while Latour et al. (2018b) analysed four He-poor sdOs. Spectroscopic analyses based on even higher resolution spectroscopy are available for well over a hundred sdB stars (e. g. Edelmann et al. 2005; Geier 2013; Schneider et al. 2018). No hint of Zeeman splitting or broadening has been found in any of them. The surface magnetic fields of these stars observed with high-resolution spectroscopy must be much weaker than observed for the four magnetic He-sdOs; less than about 20 to 50 kG. Finally, Werner et al. (2022a) recently found two CO-rich subtype of He-sdOs whose origin has been attributed to mergers (Miller Bertolami et al. 2022). Their low-resolution spectra show no Zeeman splitting, excluding magnetic fields of the order of 100 kG.

3.6.4 Formation scenarios for magnetic hot subdwarfs

The formation of the prototypical magnetic He-sdO J0809-2627 was already discussed in Sect. 3.5.6. Considering stellar and atmospheric parameters, it was likely formed by either a double He-WD merger or a He-WD + hybrid He/CO-WD merger. The similarity between the known magnetic hot subdwarfs suggests that all four stars were formed by the same evolutionary channel. Further evidence for a merger origin for magnetic He-sdOs is provided by the lack of radial velocity variability for the three stars presented here. Indeed, there is growing evidence that the majority of He-rich sdO stars result from mergers. While the fraction of hydrogen-rich subdwarfs in close binaries is high (about 50 %, Maxted et al. 2001; Napiwotzki et al. 2004), Geier et al. (2022) showed that radial velocity variables are very rare amongst He-sdOs, concluding that their majority is likely formed by mergers.

The Kiel diagram in Fig. 3.6.4 compares the four magnetic subdwarfs to the He-rich subdwarfs from the SPY project and other detailed high-resolution studies (Lanz et al. 1997; Schindewolf et al. 2018; Dorsch et al. 2019, 2020, 2022), as well as the CO He-sdOs of Werner et al. (2022a). The four magnetic He-sdOs form an isolated group at fairly high log g. The three main He-sdO subtypes (N-rich, C-rich, C&N-rich) cluster in two ranges; the N-rich stars are cooler

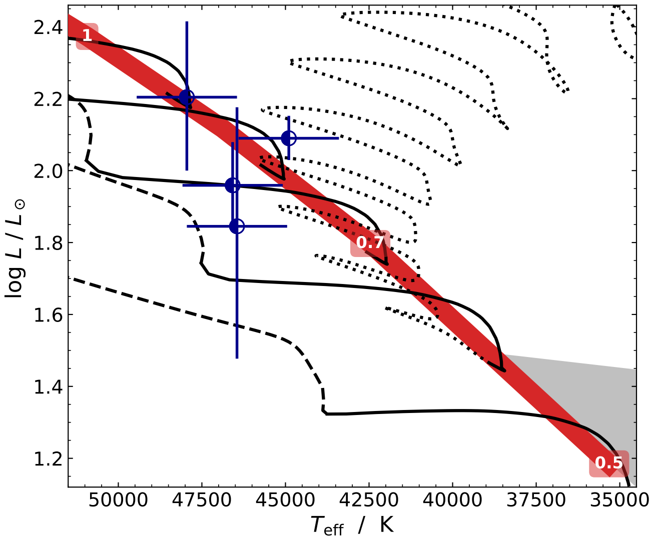

Figure 3.6.5. The four magnetic He-sdOs (blue) in the HRD. The black merger tracks are the same as in Fig. 3.6.4, as are the He-ZAMS (red) and EHB band (grey). For the 0.55 $M_\odot$ track, the pre-helium main sequence phase is shown as a dotted line. Adopted from Pelisoli et al. (2022).

than the C and C&N-rich types. The two known CO-He-sdOs and the three N-poor eHe-sdOs are amongst the hottest He-sdOs. The four magnetic iHe-sdOs are also hot, but all of them seem to be rich in nitrogen. Because we have no good constraints on their surface carbon abundances, these stars may be similar to the C&N- or N-type He-sdOs, or even each show different abundances.

All four magnetic He-sdOs are located very close to the He-ZAMS of Paczyński (1971), not only in terms of surface gravity but also luminosity. As shown in Fig. 3.6.5, the models of Yu et al. (2021), which are similar to those of Zhang & Jeffery (2012), are able to explain the observed $T_{\rm eff}$ and luminosity of all magnetic iHe-sdOs. It is puzzling that no He-sdO stars other than the four discussed here have been found to be magnetic, if mergers were to always lead to magnetic fields. This suggests that some fine-tuning is required for the formation of magnetic He-sdOs.

Another puzzle is the division of He-sdOs according to hydrogen content into iHe- and eHe-sdOs, as discussed extensively by Luo et al. (2021). The double He-WD merger models of Hall & Jeffery (2016) and Schwab (2018), the only to consider hydrogen, predict surfaces poor in hydrogen. While this is at odds with the intermediate helium abundances of all four magnetic He-sdOs, we do find these stars to lie close to the helium main sequence. This means that their hydrogen envelopes must be small. The discrepancy between observed and predicted abundances is likely due to limitations on the modelling of the merger, rather than an issue with the idea of a merger itself. For instance, the hydrogen abundance is strongly dependent on rotation, which in turn depends on the angle between the rotation and magnetic axes (García-Berro et al. 2012). This effect is not included in the available merger models. Our fits to the available observations of the magnetic He-sdOs do not constrain the magnetic field geometry well, as that would require higher-resolution spectra that better resolve the shape of the Zeeman components. The observed fields are clearly non-homogeneous, given that multiple homogeneous components were required by our models. This non-homogeneity was also observed in J0809-2627 (see Fig. 3.5.2).

The observed projected rotation velocities are typically low in hot subdwarfs, irrespective of their chemical composition (see e. g. Geier & Heber 2012). The magnetic systems seem to be no exception, as suggested by our upper limits on $v_{\rm rot} \sin i$. Dorsch et al. (2022) found no signs of a rotation period in the TESS light curve of J0809-2627. Indeed, similar light curve analyses by Pelisoli et al. (2022) led to the same conclusion for the three other magnetic He-sdOs[19]. Although magnetism is certainly able to induce stellar spots, it seems that detectable spots are uncommon in the case of strongly magnetic He-sdOs.

Apart from mergers, another scenario that could cause magnetism during the hot subdwarf phase is a dynamo acting in the convective core during the main sequence, which has been invoked to explain a fraction of magnetic white dwarfs (Bagnulo & Landstreet 2021). In this scenario, the

---

[19] All light curve analyses were performed by Ingrid Pelisoli and are therefore not part of this thesis. Please refer to Dorsch et al. (2022) and Pelisoli et al. (2022) for more details.

field would be exposed when the progenitor star loses its outer layers due to binary interaction. As discussed in Sect. 3.5.6, the stripped star models of Götberg et al. (2018) are not able to match the luminosity and surface gravity of J0809-2627, which applies to all four magnetic He-sdOs. An additional argument against this scenario is given by the fact that no binary hot subdwarfs have been found to be magnetic. Finally, the fossil field scenario would also apply to helium-poor sdB stars, none of which were found to be magnetic to date. To explain the lack of detection, the fraction of systems with detectable magnetic fields must be a few percent at most, which was also the conclusion of Landstreet et al. (2012).

3.6.5 Summary and conclusions

We identified three new magnetic hot subdwarfs from their SDSS spectra, bringing the total to four. Using archival WHT/ISIS spectra and SED fits, we estimated their temperatures, surface gravities, and helium abundances, as well as radii and luminosities, all of which turned out to be similar between the stars. The observed magnetic fields range between 300and 500 kG. Assuming conservation of magnetic flux, this implies fields of the order of $50 - 150$ MG at the white dwarf stage, consistent with typically observed values (Kepler et al. 2013; Bagnulo & Landstreet 2021). The similarity between the stellar parameters of all four known magnetic hot subdwarfs points at a common origin for all of them. Their lack of radial velocity variability and surface composition is consistent with a merger origin, although better data, as well as more complete merger models including hydrogen and magnetic fields, are required to constrain the exact channel. In addition, it seems that a merger alone is not sufficient to trigger a magnetic field, given the lack of detection in high-resolution spectra of likely merger remnants, for example by Napiwotzki et al. (2004) and Werner et al. (2022a). Still, our findings provide evidence that mergers are indeed responsible for a fraction of magnetic white dwarfs, in particular those with strong ($\gtrsim$50 MG) fields.

The stripped star scenario seems to be excluded for the magnetic He-sdOs, based on their lack of radial velocity variably and comparatively low luminosities. However, the stripping of intermediate-mass red giants with magnetic cores ($M \gtrsim 1.1\,M_\odot$, Stello et al. 2016) may still be a relevant formation scenario for other hot subdwarfs. Götberg et al. (2018) predict helium-poor sdBs with normal luminosities as the result of stripping stars with masses in the 2 to 4 $M_\odot$ range. Such stripped stars have non-canonical masses, i. e. different from the 0.47 $M_\odot$ that is required for the He-flash at solar metallicity. Therefore, it may be profitable to focus future spectropolarimetric searches on low- or high-mass hot subdwarfs.

It may seem surprising that all known magnetic He-sdOs have field strengths in excess of 300 kG – the upper limits for non-magnetic hot subdwarfs are much lower (1 to 50 kG), leaving a gap in the intermediate field strength range. In order to search for the missing weaker-field magnetic hot subdwarfs, magnetic model fits to all hot subdwarfs in the SDSS and LAMOST archives should be performed; such efforts are underway. Future and current large spectroscopic surveys such as WEAVE, SDSS-V, and 4MOST are likely to discover many more magnetic subdwarfs, which will hopefully shed light on the mergers channels form them.

Finally, we propose that, in analogy to white dwarf classes, an ‘H’ should be added to the spectral class of magnetic hot subdwarfs that show Zeeman splitting, which would make J0415+2538, J1303+2646, J1603+3412, and the prototype J0809-2627 He-sd**OH**s.

Chapter 4

Large samples of hot subdwarfs

Detailed analyses of single stars are important to constrain the physical processes of their formation and evolution. However, such analyses can not constrain important quantities such as the relative frequency of their specific formation channels or the parameter ranges that these channels can produce. This information can only be obtained from statistically significant samples of stars, such as those discussed in this chapter.

4.1 Stellar parameters and binary fraction from SED and parallax

Because radii and luminosities are a natural output of theoretical stellar population synthesis models, they represent a valuable constraint on these models and therefore also on the formation of hot subdwarf stars. The luminosities of horizontal branch stars have the interesting property that they are approximately independent of mass or effective temperature. In principle, stellar masses would provide the best constraint on the evolution of horizontal branch stars because they do not change significantly during the helium burning lifetime. However, the necessary surface gravity measurement usually requires high-quality spectroscopic observations and is often too uncertain to constrain the stellar mass. The following analyses will therefore focus on stellar radii and luminosities.

The large samples discussed in the following require an automated fitting procedure that can deal with thousands of stars. This method is described in Sect. 4.1.1. Subsequently, stellar parameters and the fraction of binary (composite SED) systems are derived for the sample of known hot subdwarfs in Sect. 4.1.2. Such studies provide an important counterpart to theoretical population synthesis studies and allow direct comparisons between observed and the predicted distribution of luminosities and radii for large samples of hot subdwarf and BHB stars.

Table 4.1.1. Model grids used in the automatic SED fitting procedure.

Name	Code	T_{eff} / K	$\log g$	$\log n(\mathrm{He})/n(\mathrm{H})$
sdB[a]	ADS	15000 to 55000	4.6 to 6.6	−5.0 to +1.0
ELM[a]	ADS	9000 to 20000	3.8 to 7.0	−5.0 to −0.3
sdOstar2020[b]	Tlusty/Synspec	26250 to 57500	4.250 to 6.375	−1.75 to +4.0
DA[c]	TMAP	40000 to 180000	6.0 to 9.5	pure H
DO[c]	TMAP	40000 to 180000	6.0 to 9.5	pure He
PHOENIX[d,e]	PHOENIX	2300 to 15000	2.0 to 5.5	−2.0 to +0.0

Notes. (a) Provided by Ulrich Heber and Andreas Irrgang. (b) See Sect. 2.2.2. (c) Provided by Nicole Reindl. (d) From Husser et al. (2013). (e) The helium abundance is solar and [Fe/H] is stated instead.

4.1.1 Automated SED fitting procedure

The automated fitting procedure used here is analogous to the SED fit of a single star, but can be performed in parallel for many stars. The Remeis cluster of computers used for this work allows up to 155 simultaneous SED fits, which means that composite SED fits for samples of the order of 50 000 stars can be performed in one or two days. Photometric data are collected using variable search radii depending on the astrometric accuracy achieved by each queried survey. Observations with various bad quality flags are excluded before starting the SED fit. The key point is that the thus constructed SEDs are automatically fitted using several model grids that cover a large parameter range: from cool M-type stars to hot DO white dwarfs. Each SED fit is repeated until the best grid was found; a summary of the grids used in this automatic SED fitting procedure is given in Table 4.1.1. During the fitting procedure, outlier magnitudes are automatically removed using multiple consecutive 6-σ cuts. This value is a reasonable compromise between an efficient removal of erroneous data and the risk of removing accurate data if the currently selected model grid is not appropriate.

For systems with a reliable *Gaia* DR3 parallax measurement, the radius, luminosity, and mass can be calculated as described in Sect. 2.3.1. Here, the uncertainties in parallax, angular diameter, $T_{\rm eff}$, and $\log g$ are propagated using the Monte Carlo method. This results in histograms for each parameter, corresponding to estimated probability densities. The following section will use the corresponding mode and highest density interval (68 % confidence) for radius and luminosity measurements, for which the difference between mode and median is small. The assumed uncertainty on $\log g$ has a strong impact on the asymmetric shape of the mass probability density, which shifts the corresponding mode value. This $\log g$ uncertainty is often not well known and not necessarily Gaussian. Therefore, the more robust median and quantiles are stated for SED-based mass measurements, unless otherwise mentioned.

In this method, SED fits are possible using both single star and binary models. Here, the binary fits were set up to deal with hot subdwarf stars with F/G/K-type companions on the main sequence. The metallicity and surface gravity of cool companions can usually not be determined from the SED alone and must therefore be fixed, here to $[\mathrm{Fe/H}] = -0.3$ and $\log g = 4.4$ as average values for F/G/K-type MS stars. The surface ratio $A_{\rm cool}/A_{\rm hot}$ was constrained to not exceed a value of 2000 because an sdB or WD component would not be detectable at higher surface ratios. In addition, the companion temperature was constrained to not exceed 10 000 K, beyond which the companion and hot subdwarf SED would become very similar. In case the best-fit uncertainty was consistent with a single hot subdwarf or hot white dwarf model, the secondary component was removed from the fit. The colour excess $E(44-55)$ was forced to not exceed the value reported by the 3D reddening map of Capitanio et al. (2017) by more than 0.15 mag. If no distance measurement was available, the limit was imposed using the line-of-sight values of Schlegel et al. (1998) or Schlafly & Finkbeiner (2011). This is especially important for composite-SED systems that have no UV measurements. In such cases, there is a strong negative correlation between the colour excess and the surface ratio: an overestimated colour excess leads to an underestimated surface ratio. Limiting the colour excess to the literature value would lead to spurious detections of composite SEDs. This is likely due to underestimated colour excess in the reddening maps for some directions, caused by their limited angular resolution.

An important task is the automatic identification of physical composite binary systems based on the χ^2 fit results. Here, several filters were used to determine whether or not a cool companion was detected in each SED. The most important filter was based on the flux ratios between the hot component and the cool component at 1600 Å and 28000 Å, estimated using black body models at the best-fit effective temperatures and surface ratio $A_{\rm cool}/A_{\rm hot}$. An example of the two-dimensional flux ratio diagram used for classification is shown in Fig. 4.1.1, here for the sample of spectroscopically identified hot subdwarfs of Culpan et al. (2022), which is discussed in Sect. 4.1.2. This diagram only includes SEDs to which the best-fit companion model contributes significantly – simple single-component SEDs are outside the plot limits. In addition, the surface ratio of composite SEDs was required to exceed a value of one and the best-fit companion $T_{\rm eff}$ was required to be consistent with at least 2400 K (2900 K if $A_{\rm cool}/A_{\rm hot} < 100$).

Figure 4.1.1. Composite SED identification for the sample discussed in Sect. 4.1.2 using black body flux ratios at 1600 Å and 28000 Å. Most systems are identified as either binary (red) or single (blue). The majority of single hot subdwarfs are located outside the plot limits. Binary systems must be within the manually defined polygon shown as a dashed black line. Black points correspond to SEDs in which no hot component could be detected or fits that require two similar components. The grey tracks are described in the text.

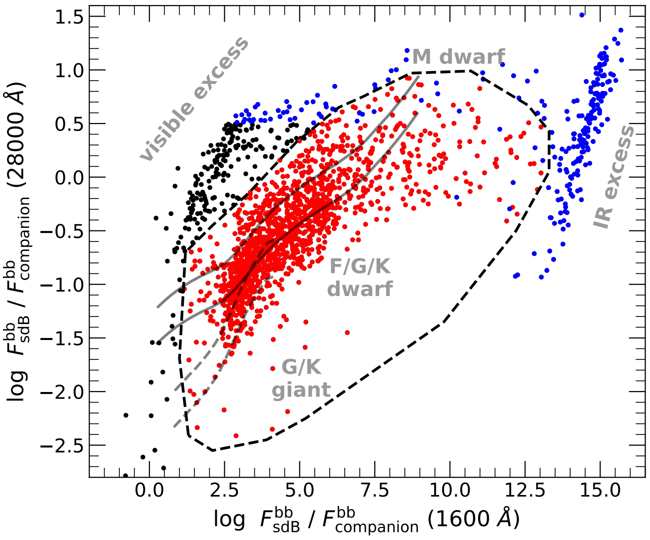

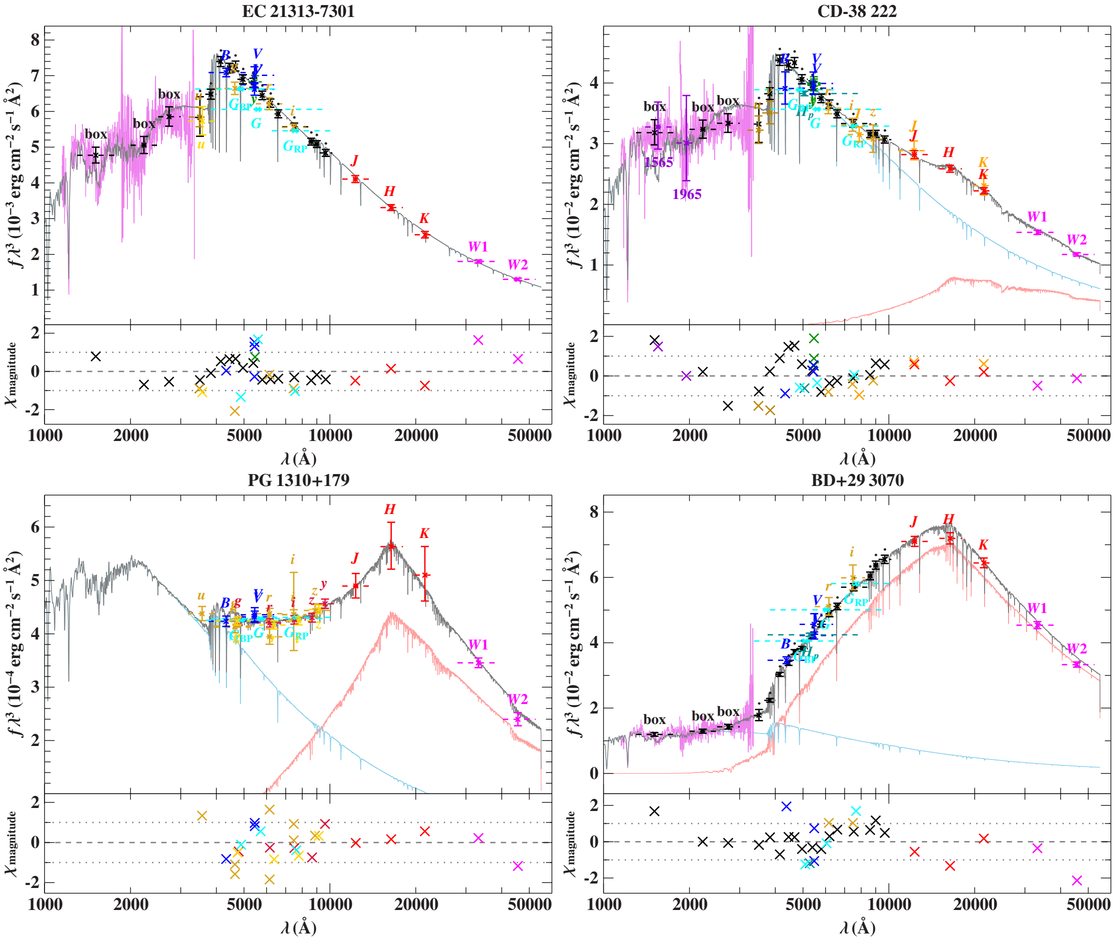

Figure 4.1.2. Examples for good SED fits: the single sdB EC 21313-7301 and three composite-SED binaries, increasing by secondary contribution: CD-38 222 (sdB+M0V), PG1310+179 (sdB+K2V), BD+29 3070 (sdB+F5V). The combined model fit is shown in grey; for composite SEDs, the contribution of the hotter component (the sdB) is shown in blue while the MS companion is shown in red. The black data points labelled “box” are binned fluxes constructed from IUE spectra. Black points marked by small dots are fluxes constructed from *Gaia* DR3 XP spectra. The remaining data points are provided by various photometric surveys.

The main cluster of systems in this diagram (red) corresponds to hot subdwarfs with main sequence F/G/K-type companions, which is confirmed by two sets of binary star sequences. Two solid grey lines show the expected location of binary systems that contain a $T_{\text{eff}} = 35\,000\,\text{K}$ (lower) or $T_{\text{eff}} = 25\,000\,\text{K}$ (upper) hot subdwarf on the EHB and a companion star on the zero-age main sequence, with masses ranging from $0.3\,M_\odot$ to $2.0\,M_\odot$. The dashed grey lines are similar, but for terminal-age main sequence (TAMS) companions, with masses ranging from $0.75\,M_\odot$ to $2.0\,M_\odot$. All tracks are based on the BaSTI models of Hidalgo et al. (2018) for [Fe/H] = −0.3. The few G/K-type giants in the sample are located at the bottom of Fig. 4.1.1, below the TAMS companions, because they outshine their hot subdwarf companions by factors of up to several hundred in the near-IR. These systems are only identifiable with excellent UV data, such as IUE or HST spectra.

A smaller and well-separated group of SEDs, located above the main group, is best reproduced by hot subdwarfs with putative A-type companions and is labelled “visible excess” in Fig. 4.1.1. These fits are affected by two issues. First, the SED fitting method can not reliably identify binary systems that consist of similar components, especially if the colour excess is poorly constrained. Second, there seems to be a group of hot subdwarfs in the sample of Culpan et al. (2022) for which the published T_{eff} are overestimated. A fraction of these stars appear to have real F/G/K-type companions; the inaccurate spectroscopic T_{eff} measurements may then be the result of single-component fits to composite spectra in the literature. Because these overestimated T_{eff} values were kept fixed during the SED fits, this resulted in spurious A- or B-type companions. These objects were therefore not considered for further analysis.

A distinct group of SEDs at the top right of Fig. 4.1.1 shows an infrared excess that can not be explained by a companion star. In case their IR fluxes are not overestimated (for example due to blends with close M-type stars or quasars), the IR excess might be caused by a cool disk or shell. These systems are considered as “single” in the following because the infrared excess is effectively removed by the (unphysical) best-fit M-type companion. Hot subdwarf components are not detectable in some SEDs; these are located at the very bottom or left of Fig. 4.1.1. They can be matched with a synthetic spectrum of a single late type star and were excluded from further analysis. Vice versa, some SEDs at the very top are almost completely dominated by the hot subdwarf component; they are considered as non-composite hot subdwarfs in the following (coloured blue).

4.1.2 Spectroscopically identified hot subdwarfs

Spectral energy distribution fits for a sample of 4500 spectroscopically identified hot subdwarf stars were performed in the Master’s thesis of Schaffenroth (2016). The following analysis is an extension and update of that work, making use of many more photometric surveys and in particular the *Gaia* parallaxes. A list of spectroscopically identified hot subdwarf stars was compiled by Geier (2020), which was recently updated to include 6616 stars by Culpan et al. (2022). The analysis performed in this section provides SED fits for the latter catalogue, including the following information:

- Photometric effective temperatures in case they were not yet known from spectroscopy.
- Identification of minor contamination in the catalogue of Culpan et al. (2022) by stars other than hot subdwarfs, such as main sequence or BHB stars.
- Stellar radii and luminosities for apparently single hot subdwarf stars using precise *Gaia* EDR3 parallaxes.
- Identification of composite spectrum binaries, including previously unknown binaries.
- Stellar effective temperatures and surface ratios for the companions stars, as well as companion radii and luminosities when parallaxes are available.

The sample of Culpan et al. (2022) has the advantage that atmospheric parameters for many stars are already well determined from spectroscopic observations. For the purpose of this analysis,

T_{eff}, $\log g$, and the helium abundance were fixed to spectroscopic values from the literature, if available. This is especially important for the hot sdO stars, for which the determination of effective temperatures from photometry alone becomes highly uncertain (see Fig. A.3.1). Fixing T_{eff} allows the determination of reasonably accurate luminosities and radii even for the hottest sdO or post-AGB stars, if an accurate parallax is available.

Automated SED fits were performed using the method described in Sect. 4.1.1 for all 6616 stars in the spectroscopic catalogue of Culpan et al. (2022). Examples for good fits to the SEDs of an apparently single and three composite-spectrum hot subdwarfs are shown in Fig. 4.1.2. These fits were manually checked, fixing issues such as outlier magnitudes or, in rare cases, blends with close stars or background galaxies. Blends with close stars are especially problematic for 2MASS and WISE infrared magnitudes because of the low spatial resolution of these surveys. A total of 6265 SEDs considered were based on at least 5 photometric filters in the final fit and had a reduced χ^2 close to unity. The rest were excluded from further analysis. Some objects in the input catalogue are not well reproduced by our models. Examples are systems with strong non-stellar contribution such as nebula emission lines in the SEDs of central stars of planetary nebulae (CSPNe) or the accretion disk in cataclysmic variables, which can dominate the overall flux. Such systems were removed if known from the literature using Simbad database[1] classifications and the HASH[2] database of CSPNe. Also hot subdwarfs in globular clusters were removed, e. g. from the new General Catalogue of non-stellar objects (NGC; Dreyer 1888). In addition, stars from the OGLE survey (Pietrukowicz et al. 2013) that targeted the Galactic Bulge were excluded because of the extreme blending and extinction in this region, which makes automatic SED fits impractical.

Several quality cuts on the *Gaia* EDR3 parallax were applied for the analysis of radii and luminosities. Only stars with parallax $\varpi \geq 0.10$ mas and parallax uncertainties of less than 25 % were considered. Because composite SED binaries are known to often exceed the generic recommended RUWE value of 1.4, a cut was applied at RUWE < 10 instead (c.f. fig. 11 in Culpan et al. 2022). This cut ensures that most hot subdwarfs from the sample of solved long-period sdB binaries of Vos et al. (2018) remain part of the good-parallax SED sample, but still provides some filter for possibly erroneous parallax measurements.

Before discussing the stellar parameters derived through SED fitting, it should be noted that not all stars in the catalogue of known hot subdwarf stars seem to be bona-fide hot subdwarf stars. About 450 stars, or 7 % of the sample, have best-fit temperatures that are below 20 000 K at the 68 % confidence level, which is too cool for sdB (EHB) stars. These stars might rather be BHB stars or other B-type stars. Because most of them have poor parallax measurements, they were already removed by the previously mentioned quality cuts.

4.1.2.1 The HR and temperature-radius diagrams

Figure 4.1.3 shows overviews of the HRD and radius - T_{eff} diagrams for non-composite sdO/Bs in this cleaned sample. The sample includes stars in a variety of evolutionary stages. Several hot and luminous stars lie on post-AGB tracks (Miller Bertolami 2016), which are shown as a blue shaded band. A more detailed view of the EHB and its transition to the pure helium main sequence (He-MS) is given in Fig. 4.1.5, where stars are coloured according to their spectral class. These spectral classes are defined using the helium abundance - effective temperature space, as shown in Fig. 4.1.4. The following paragraphs will discuss the distribution of stars in Fig. 4.1.5 by spectral class and point out examples of interesting objects.

The EHB. The majority of stars at $T_{\mathrm{eff}} < 40000$ K are located on the EHB band of Dorman et al. (1993), which is marked by the grey shaded region. Except for some iHe-sdOB stars at the very hot end of the EHB, all of these stars are classified as He-poor sdB stars. In the HRD, most of these stars seem to lie within one of two ellipses, both of which are marked dashed red in Fig.

---

[1] Wenger et al. (2000); `https://simbad.cds.unistra.fr/simbad/`

[2] Parker et al. (2022); `http://hashpn.space`

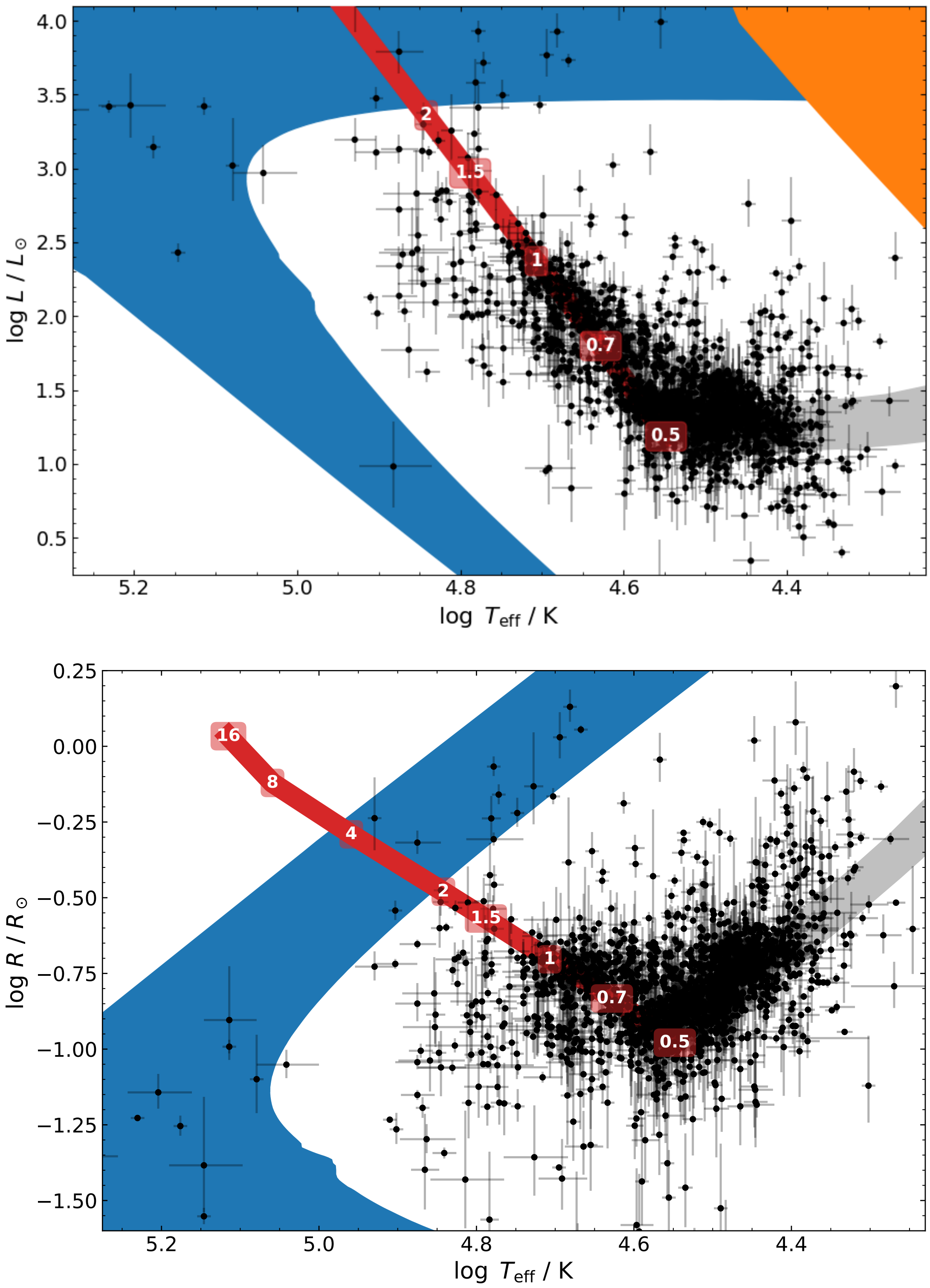

Figure 4.1.3. *Top:* HRD for non-composite stars in the cleaned known hot subdwarf sample of Culpan et al. (2022) (black dots) compared with evolutionary tracks. For clarity, only stars with uncertainties of less than 0.3 dex in log L, 0.2 dex log R, and 10 % in $T_{\rm eff}$ are shown. The blue shaded region corresponds to post-AGB tracks from Miller Bertolami (2016), for final (initial) masses between 0.53 (1) $M_\odot$ and 0.83 (4) $M_\odot$. The [Fe/H] = −1 hydrogen-burning main sequence of Hidalgo et al. (2018) is marked in orange. The broad red line marks the He-ZAMS of Paczyński (1971); its masses are labelled in $M_\odot$. The grey shaded region shows the HB from Dorman et al. (1993) for a core mass of 0.47 $M_\odot$ and solar metallicity, partly extrapolated to extend to the He-ZAMS. *Bottom:* similar, but for radii instead of luminosities.

Figure 4.1.4. Definition of spectral classes for the sample of known hot subdwarfs. Stars are classified as eHe-sdO (red), iHe-sdOB (orange), He-poor sdO (blue), He-poor sdB (grey), or iHe-sdB (green), depending on their helium abundance and effective temperature (separated by solid lines). The the colors of the lettering used in the figure are used for these classes throughout this work. Stars that show composite SEDs are marked in red while apparently single hot subdwarfs are coloured blue. Composite-SED systems are discussed in Sect. 4.1.2.3.

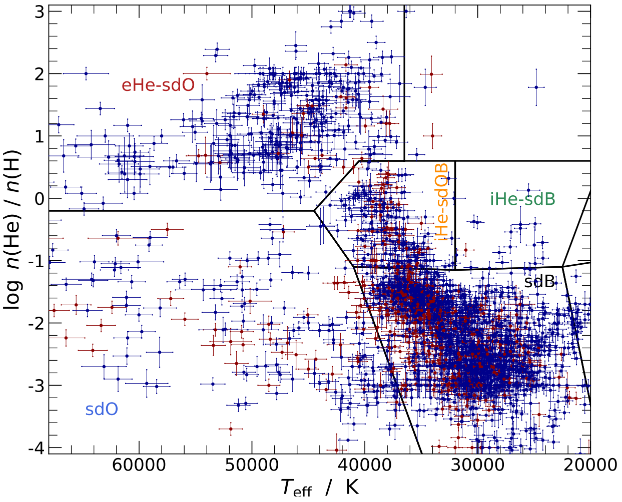

4.1.5: one centred at about 28 000 K ("EHB1"), the other at about 33 000 K ("EHB2"). While the physical nature of these overlapping ellipses is not confirmed, they match the two groups of He-poor sdB stars identified by Németh et al. (2012, their fig. 4), Luo et al. (2021, their figs. 4 and 17), and Geier et al. (2022, their fig. 3). The ellipsoidal shape of both populations can be understood in terms of evolution during the core helium-burning EHB lifetime, during which sdBs increase in luminosity and $T_{\rm eff}$ (Dorman et al. 1993; Han et al. 2003).

Above and beyond the EHB. The region above the EHB in terms of radius and luminosity is also well populated, as would be expected from the fact that it is crossed by both stars that are evolving towards and away from the EHB (Dorman et al. 1993). The latter have exhausted the helium in their cores, after which helium shell burning lasts for about 20 Myr (Dorman et al. 1993). During this phase, they are observable as He-poor sdB and sdO stars above the EHB band in terms of luminosity. Notably, there are two groups of He-poor sdO stars: one above the HeMS and one below it. There is a remarkable lack of He-poor sdO stars next to the HeMS. This can be understood in the sense that most He-poor sdO stars, both above and below the HeMS, are currently in the stable helium shell burning phase. The higher-luminosity He-poor sdOs might then be considered post-EHB1 stars, while the lower-luminosity group below the HeMS would be post-EHB2 stars. A qualitative agreement between the two observed He-poor sdO populations and such post-EHB tracks (in cyan) is shown in Fig. 4.1.5.

Below the EHB. Several other stars have luminosities and radii that place them below the EHB – these typically helium-poor stars are good candidates for hot subdwarfs with masses between the canonical mass of about 0.47 $M_\odot$ and the helium burning limit of about 0.3 $M_\odot$ (Han et al. 2003). The same region is thought to be crossed by pre-extremely low-mass white dwarfs (pre-ELMs) that are not massive enough to ignite helium in their cores (Driebe et al. 1998; Althaus et al. 2013; Istrate et al. 2016). A prominent example is the known pre-ELM HD 188112 (Heber et al. 2003; Latour et al. 2016). Several other stars in the sample are good candidates for bright pre-ELM or very low-mass EHB stars, given that they lie close to or below the 0.35 $M_\odot$ zero-age EHB of Han et al. (2003). This includes the previously unclassified and fairly bright PG 2208+014, GALEX J080510.9-105834, Ton 263, HS 2033+0507, RL 105, and KUV 07528+4113.

Intermediate He-sdBs. All iHe-sdB stars with good SED fits are located above the EHB, which is in line with their low spectroscopic surface gravities. Prominent examples of this group are JL 87 (Ahmad et al. 2007) and KIC 1718290, a known gravity-mode pulsator (Østensen et al. 2012). Also the well-known sdB + WD binary HZ 22 (Young et al. 1972; Greenstein 1973) is classified as He-sdB here, given that its solar helium abundance is much higher than the typically sub-solar helium abundances observed for normal sdB stars. Although this system is spectroscopically similar to a main-sequence B-type star (Saffer et al. 1997), the primary is predicted to have

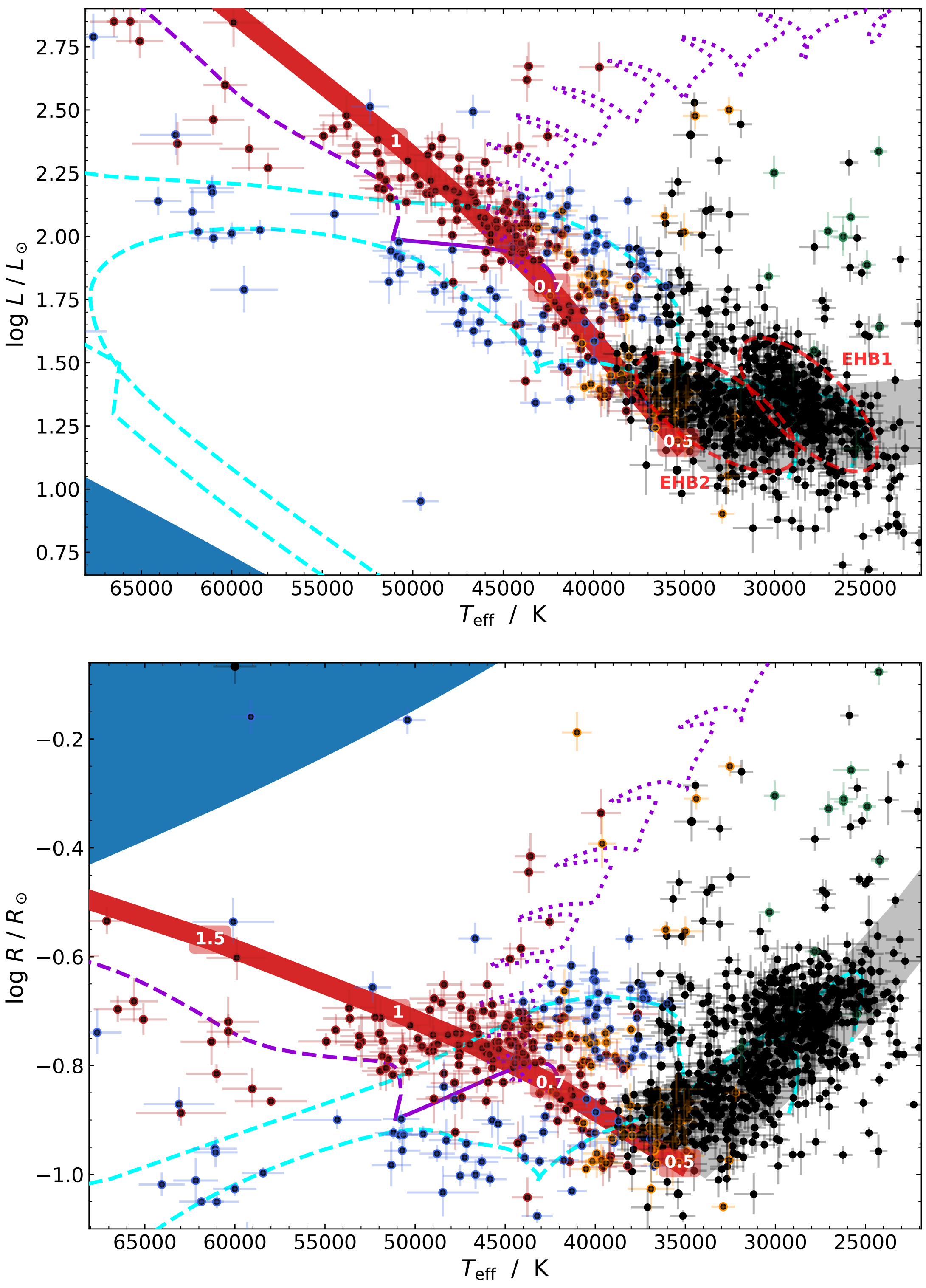

Figure 4.1.5. Like Fig. 4.1.3, but a more detailed view. For clarity, only stars with uncertainties of less than 0.1 dex in $\log L$, 0.05 dex $\log R$, and 5 % in T_{eff} are shown. Known CSPNe are not shown. Stars are coloured according to their spectral classification, as visualised in Fig. 4.1.4: He-poor sdB (black), He-poor sdO (blue), iHe-sdOB (orange), eHe-sdOB (red), and iHe-sdB (green). In the upper panel, the "EHB1" and "EHB2" groups of He-poor sdBs are marked by dotted red ellipses. Two (post-)EHB tracks are shown in cyan, both for solar metallicity: the 0.45 $M_\odot$ track of Han et al. (2003) with an envelope mass of 0.001 $M_\odot$ and the 0.47 $M_\odot$ track of Dorman et al. (1993) with an envelope mass of 0.002 $M_\odot$. Their post core-burning evolution is indicated by dashed lines.

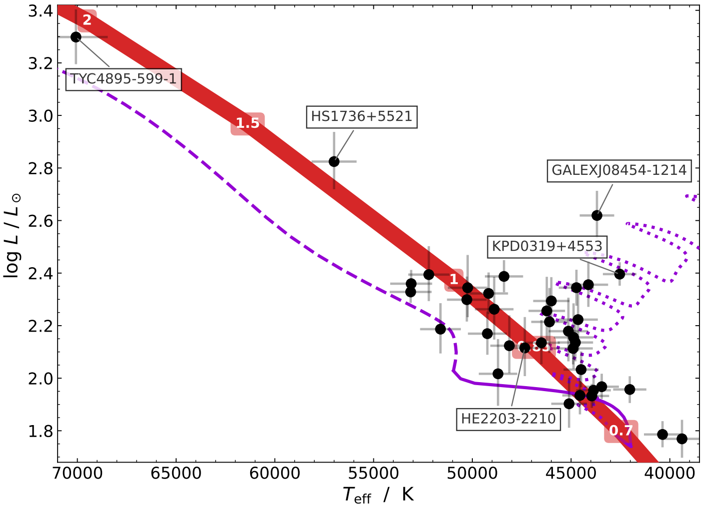

Figure 4.1.6. Candidates for single He-sdOs with masses larger than 0.8 $M_\odot$ and uncertainties of less than 40 %. Most of the 37 candidates lie close to the He-ZAMS of Paczyński (1971), marked in red. The masses of several candidates that exceed 1 $M_\odot$ might be overestimated; their surface gravities should be re-examined.

a low mass of 0.39 ± 0.05 $M_\odot$ (Schönberner 1978) and can therefore be considered a hot subdwarf star. Similar iHe-sdB + WD binaries are CPD −20°1123 (Naslim et al. 2012; Löbling 2020) and KPD 0422+5421 (Koen et al. 1998). Several other He-sdBs are less well known; their spectral parameters were obtained as part of the LAMOST (Luo et al. 2021) and SALT surveys (Jeffery et al. 2021).

Intermediate He-sdOBs. It is interesting to note that there seem to be two main groups of iHe-sdOB stars in terms of radius and luminosity, both coloured orange in Fig. 4.1.5: a compact group at the intersection of He-ZAMS and EHB and a more luminous group somewhat above the He-ZAMS. Almost all members of the spectroscopic class of extremely heavy metal enriched iHe-sdOBs are part of the more compact group (Jeffery et al. 2017; Naslim et al. 2020; Dorsch et al. 2020, see also Sect. 3.1). This includes the heavy metal iHe-sdOB + sdF binary EC 22536-5304 discussed in Sect. 3.3 (Dorsch et al. 2021); the only exceptions are HZ 44 and HD 127493 (Dorsch et al. 2019). Extreme enrichment in heavy metals is usually attributed to atmospheric diffusion effects, which can be suppressed by atmospheric convection (Unglaub 2010). As discussed in Sect. A.1 and shown in Fig. A.1.5, atmospheric convection resulting from the ionization of He II turns off only for the more compact iHe-sdOB stars (at $\log g \approx 6.0$), which could explain the observed lack of luminous heavy-metal iHe-sdOB stars. Increased stellar winds for luminous iHe-sdOB stars would have a similar effect (Unglaub 2008). A major difference between the compact and the luminous group of iHe-sdOBs seems to be their composite-SED fraction; as discussed in Sect. 4.1.2.3, the overall iHe-sdOB population has a high composite fraction (about 29 %). However, the composite fraction of the more luminous group seems to be similar to that of the eHe-sdOs ($\lesssim 10$ %), which would support the idea that this group is formed by evolutionary channels similar to the eHe-sdO population. The most luminous iHe-sdOBs, far above the He-ZAMS, include peculiar stars, such as the known inflated sdO+WD binary EVR-CB-004 (Ratzloff et al. 2020) and the similarly variable (Heinze et al. 2018) but unstudied ATO J089.4285+27.7808. These luminous stars are also expected to show strong wind lines in the far-UV, as observed in low-resolution IUE spectra of Ton 927.

Extreme He-sdOs. Most eHe-sdO stars, marked red in Fig. 4.1.5, lie close to the zero-age HeMS, both in terms of radius and luminosity. This suggests that they are either currently fusing helium in their cores or have evolved off the He-MS and are now going through the helium shell burning phase. If most eHe-sdOs that lie close to the He-ZAMS are indeed core helium burning stars, they would be expected to have masses of 0.6 $M_\odot$ (at 40 000 K) to about 1.2 $M_\odot$ (at 55 000 K), based on the models of Paczyński (1971). Many eHe-sdOs seem to cluster at $T_{\rm eff} \approx$ 44 000 K, on or slightly above the He-ZAMS – they would be expected to have masses of about 0.75 $M_\odot$. This clustering is predicted by evolutionary models: the evolution of a 0.75 $M_\odot$ double

He-WD merger remnant towards the HeMS is predicted to be much faster (≈1 Myr) than its core (≈30 Myr) and shell (≈10 Myr) helium-burning lifetimes (Yu et al. 2021). Late hot flasher tracks, such as those of Miller Bertolami et al. (2008) and Battich et al. (2018) would also be able to produce eHe-sdO stars that follow a very similar evolution close to the He-ZAMS. He-sdO stars at $T_{\mathrm{eff}} > 55\,000\,\mathrm{K}$ are predominantly found below the He-ZAMS, which indicates a post-HeMS helium shell burning nature and masses of less than about $1.2\,M_{\odot}$. Previous studies based on high-resolution spectra by Hirsch (2009) and Schindewolf et al. (2018) have derived rather low surface gravities for their samples of He-sdO stars, which would be more consistent with stars that are currently evolving towards the zero-age HeMS. This is not observed here.

Masses were derived from the parallax, angular diameter, and spectroscopic surface gravity measurements, as described in Sect. 2.3.1. Figure 4.1.6 shows the HRD for single eHe-sdO stars with observational masses of more than $0.8\,M_{\odot}$ and uncertainties of less than 40 %. Most of them lie close to the He-ZAMS at predicted masses of more than $0.7\,M_{\odot}$, which seems to confirm their high masses. However, the derived masses for some of these candidates are larger than those that would be expected from their position on the He-ZAMS. The most massive candidates are KPD 0319+4553 ($1.83^{+0.50}_{-0.39}\,M_{\odot}$), HE 2203-2210 ($1.82^{+0.74}_{-0.51}\,M_{\odot}$), and TYC 4895-599-1 ($1.67^{+0.64}_{-0.45}\,M_{\odot}$). KPD 0319+4553 lies significantly above the He-ZAMS while HE 2203-2210 is located on the He-ZAMS at a theoretical mass of about $0.85\,M_{\odot}$, which is not consistent with its high observational mass. As the hottest candidate, the high observational mass of TYC 4895-599-1 is matched by the high mass expected from its position on the He-ZAMS ($\lesssim 2\,M_{\odot}$), which makes this star a strong high-mass candidate. The same is true of the second hot candidate, HS 1736+5521 ($1.11^{+0.44}_{-0.31}\,M_{\odot}$), for which the theoretical mass would be about $1.3\,M_{\odot}$. Because they were derived using inhomogeneous methods, the literature surface gravity measurements of all massive He-sdO candidates should be verified using state-of-the-art model spectra. At a radius of $0.36^{+0.04}_{-0.03}\,R_{\odot}$, GALEXJ08454-1214 is the largest massive He-sdO candidate. It has a mass of $0.85^{+0.30}_{-0.22}\,M_{\odot}$ based on the atmospheric parameters obtained by Jeffery et al. (2021). Interestingly, the fairly massive eHe-sdO PG 1444+076 ($0.68^{+0.24}_{-0.18}\,M_{\odot}$) is a retrograde halo star, as will be discussed in Sect. 4.2.6.

4.1.2.2 Radius, luminosity, and mass distributions

The overall distributions of radii, luminosities, and masses for non-composite stars in the known hot subdwarf sample are shown in Fig. 4.1.7, where the contribution of H-sdB, H-sdO stars, iHe-sdOBs, and eHe-sdOs is marked in grey, blue, orange, and red, respectively. These distributions can be used to confirm and quantify the substructures in the HRD (Fig. 4.1.5). Uncertainties in the angular diameter and parallax measurements, as well as the spectroscopic uncertainties in T_{eff} and $\log g$ are explicitly considered. If no uncertainties were stated in the table of Culpan et al. (2022), 2 % in T_{eff} and 0.1 in $\log g$ were assumed. The distribution of the radii of non-composite helium-poor sdBs is not well reproduced by a single-peaked function. This is not necessarily unexpected, given that they form the EHB band, rather than scatter around one specific radius. However, the radius distribution could also be reproduced by two distinct, but overlapping distributions, such as the “EHB1” and “EHB2” populations discussed above. The radius distribution of He-poor sdO stars is clearly double peaked – some are observed at radii that place them above the EHB and HeMS bands, while their majority are below both bands. These two groups are likely explained as post-“EHB1” and post-“EHB2” stars. Also the radius distribution of iHe-sdOBs seems to be double-peaked – most of them are located at the intersection of HeMS and EHB, at $\log R/R_{\odot} \approx -0.95$, while a second group lies closer to the population of eHe-sdO stars, at radii around $\log R/R_{\odot} \approx -0.75$. The latter group would be expected to be more massive than the first, if one would assume that both were formed by merger events. The bimodal nature of the iHe-sdOB population is also observed in their luminosity distribution, which again is split into a group at the hot end of the EHB and one that more closely resembles the eHe-sdO population at larger radii. Due to the steeper slope of post-EHB tracks in the HRD, the bimodal nature of the population of He-poor sdO stars is not visible in their luminosity distribution. The luminosity distributions of sdB, sdO, and eHe-sdO stars peak at roughly 20, 50, and $100\,L_{\odot}$, respectively.

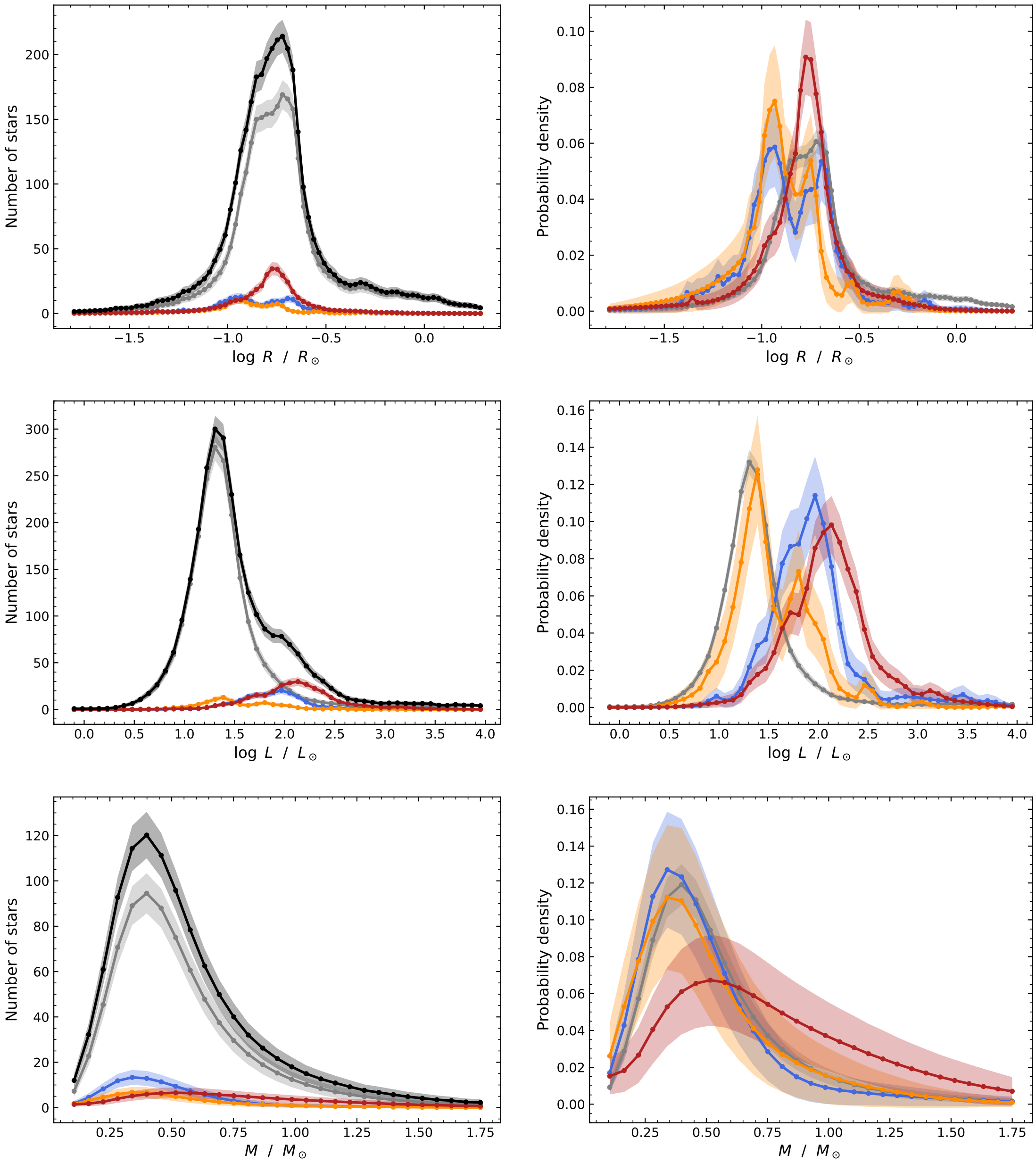

Figure 4.1.7. Histograms of radii, luminosities, and masses for non-composite hot subdwarfs from the sample of Culpan et al. (2022). The left column shows absolute histograms, while the right column shows normalised histograms for four spectral populations: H-sdBs (grey), H-sdOs (blue), iHe-sdOBs (orange), and eHe-sdOs (red). The black lines in the left panels correspond to the combined sample. Interpolated lines are shown for clarity. The following quality cuts were applied: uncertainties were better than 0.3 dex in $\log R$ (3551 stars) and $\log L$ (2713 stars), while the uncertainty on the mass was less than 40 % (1070 stars). For each histogram, the uncertainties in the variable and spectral classification were considered using the MC method. The resulting uncertainties in each bin are shown as lightly shaded regions.

Figure 4.1.7 also shows the mass distribution of 1070 stars that satisfy two quality criteria: (1) they were classified as single by the SED fitting procedure and (2) they have uncertainties of less than 40 % on their masses. Because the spectroscopic surface gravities in the catalogue of Culpan et al. (2022) were derived using different models, methods, and data qualities, these mass distributions should be treated with caution. Keeping this in mind, the mass distributions of hydrogen-rich sdB, sdO, and intermediate He-sdOB stars seem to be almost identical. They feature a tail towards high masses and peak below the "canonical" mass of $0.47\,M_\odot$, at about $0.4\,M_\odot$. This can partly be explained by the assumption of Gaussian uncertainties on the parallax and $\log g$ measurements. Because the non-logarithmic surface gravity enters in the mass calculation (Eq. 2.3.11), the mass probability distribution for each individual star has a tail towards high masses but is peaked at a lower mass than would be obtained from the best-fit $\log g$. Consequently, the median value of each mass distribution is larger than the corresponding mode (cf. Sect. 4.1.1). Specifically, the median mass is $0.45^{+0.25}_{-0.13}\,M_\odot$ for the He-poor sdBs, $0.43^{+0.15}_{-0.14}\,M_\odot$ for the He-poor sdOs, $0.43^{+0.20}_{-0.15}\,M_\odot$ for the iHe-sdOBs, and $0.68^{+0.44}_{-0.27}\,M_\odot$ for the eHe-sdOs. Again, note that these values are based on inhomogeneously derived surface gravities that may be affected by systematic uncertainties. Despite the large uncertainty, the median mass derived for He-poor sdB stars is very close to the more precise $0.47 \pm 0.03\,M_\odot$ found by Fontaine et al. (2012) for their sample of 22 sdB pulsators and eclipsing binaries. In particular for helium-rich stars, the masses derived here differ from the masses of Lei et al. (2023), who performed a similar analysis for hot subdwarfs based on LAMOST spectra and SED fits using VOSA[3]. A comparison to the theoretical mass distribution of Han et al. (2003, their fig. 22) will only be possible once a more homogeneous spectral analysis of the known hot subdwarf sample becomes available, providing reliable surface gravity estimates.

Despite the large uncertainties, the population of extreme He-sdOs is clearly more massive than the other spectral classes. In addition, it shows a pronounced tail that extends to about $1.5\,M_\odot$. These masses are often but not always in line with the masses expected of He-sdO stars from their position on the zero-age HeMS, as is shown in Fig. 4.1.6. It may seem peculiar that the mass distributions of extreme He-sdOs and intermediate He-sdOBs do not match, given that both classes of stars have been suggested to be formed by the merging of two low-mass white dwarfs. However, most intermediate He-sdOBs are located close to the low-temperature end of the HeMS and would therefore be expected to have lower masses than the mostly hotter extreme He-sdOs. In addition, the bimodal distribution of iHe-sdOBs in radius and luminosity suggest that this spectral class might comprise stars from several evolutionary channels that differ in their intrinsic mass distribution.

4.1.2.3 Composite-SED hot subdwarf binaries

The automated fits also provided stellar parameters for the companion stars, if present. An automated classification based on the filters described in Sect. 4.1.1 led to the identification of 1518 composite-SED candidates, which corresponds to 27 % of the clean sample. This value depends on the exact flux ratio cuts used, as well as the upper limit set for the colour excess; a systematic uncertainty of at least 5 % should be assumed. However, the composite-SED fraction found here is consistent with previous studies. The first study to systematically identify composite-colour hot subdwarfs was performed by Ferguson et al. (1984) based on the Palomar-Green survey (PG; Green et al. 1986). Dedicated infrared searches for cool companions to known hot subdwarfs were performed by Thejll et al. (1995) and Ulla & Thejll (1998), who found significant infrared excess for more than 20 % of hot subdwarfs in their samples. Later, Stark & Wade (2003) used 2MASS infrared magnitudes to find a composite fraction of about 30 % for an approximately volume-limited sample of hot subdwarfs.

Binary fraction by spectral class. As shown in Fig. 4.1.8, the observed fraction of composite SED hot subdwarfs depends on the spectral class of the hot subdwarf primary. The total com-

---

[3] VO Sed Analyzer (VOSA) of the Spanish Virtual Observatory (Bayo et al. 2008).

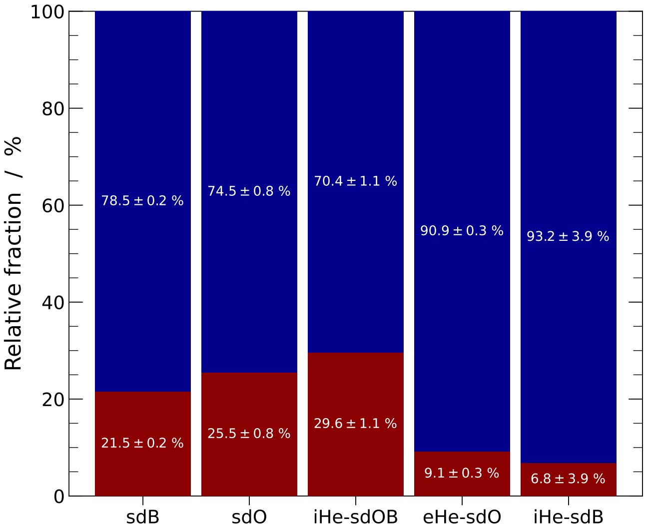

Figure 4.1.8. Fraction of detected composite (red) and non-composite SEDs (blue) for the He-poor sdB and sdO, iHe-sdOB, eHe-sdO, and iHe-sdB populations in the known hot subdwarf sample. The uncertainties stated here are purely statistical and do not account for systematic uncertainties in the detection of composite SEDs. The location of spectral classes in the helium abundance - T_{eff} diagram is shown in Fig. 4.1.4.

posite fraction in the sample is somewhat higher than the composite fraction of hot subdwarfs with measured parameters, likely because composite spectra are often discarded from spectral analyses. The helium-poor sdB and sdO populations have similar fractions of composites: 21 % and 26 %, respectively. This suggests that they represent connected evolutionary stages of the same underlying population, as expected from the canonical theory that identifies most He-poor sdO stars as helium shell burning post-EHB stars. The composite fraction found here for He-poor sdOs is consistent with the 31 % Allard et al. (1994) obtained from their sample of 100 sdOs, if an uncertainty of 5 % is assumed. The fraction of composite SEDs in the eHe-sdO population is only about 9 %. Perhaps most surprisingly, the iHe-sdOB population contains the largest fraction of composite SEDs at about 30 %. The large difference in the binary fractions of iHe-sdOB and eHe-sdO stars can not be explained by selection effects alone. Therefore, stable Roche lobe overflow seems to contribute significantly more to the formation of iHe-sdOBs than to the formation of eHe-sdO stars. The bi-modal radius distribution of iHe-sdOBs may indicate that this spectroscopic class itself is formed by at least two different evolutionary channels. Binaries seem to be more abundant in the compact subgroup of iHe-sdOBs while the composite-SED fraction of the luminous subgroup is close to the fraction observed for eHe-sdO stars ($\lesssim$10 %). Finally, only a single cool iHe-sdB is marginally identified as a composite system with an M-type companion, which corresponds to a fraction of less than 7 ± 4 %. This low fraction suggests these stars are either formed by mergers or common envelope evolution with white dwarf or M-type companions. As discussed above, several iHe-sdBs have already been confirmed to be in such short-period binaries. In addition, most iHe-sdB in the known sample are kinematically young (see Sect. 4.2), which also favours the common envelope scenario.

Comparisons to binary stellar population (BPS) models are difficult, not only because of selection effects that affect the observation, but also because the BPS models depend on several parameters, some of which are poorly known. For example, the BPS models of Yu & Li (2009) do predict the formation of sdB, sdOB, and sdO stars through stable RLOF, but always predict relatively thick hydrogen envelopes – inconsistent with the helium-enriched sdOBs.

The HRD of companions. Most cool companions identified in the current sample are F-, G-, and K-type stars. This is consistent with previous studies, both based on spectral analyses (Lisker et al. 2005) and SED fits (Aznar Cuadrado & Jeffery 2001; Girven et al. 2012). A cleaned HRD for the companions is shown in Fig. 4.1.9. Almost all F/G/K-type companions lie close to the main sequence, except for a small number of known systems that contain G- or K-type giants. HD 185510 (Fekel & Simon 1985; Jeffery et al. 1992) and BD −7° 5977 (Viton et al. 1991, see also Sect. 3.4) are located close to the RGB. The G-type giant HD 128220 A (Wallerstein et al. 1963) is more luminous than expected for an RGB star with initial mass of 2 $M_{\odot}$, as already observed by Howarth & Heber (1990). The eclipsing system BD −3° 5357 (FF Aqr; Dworetsky

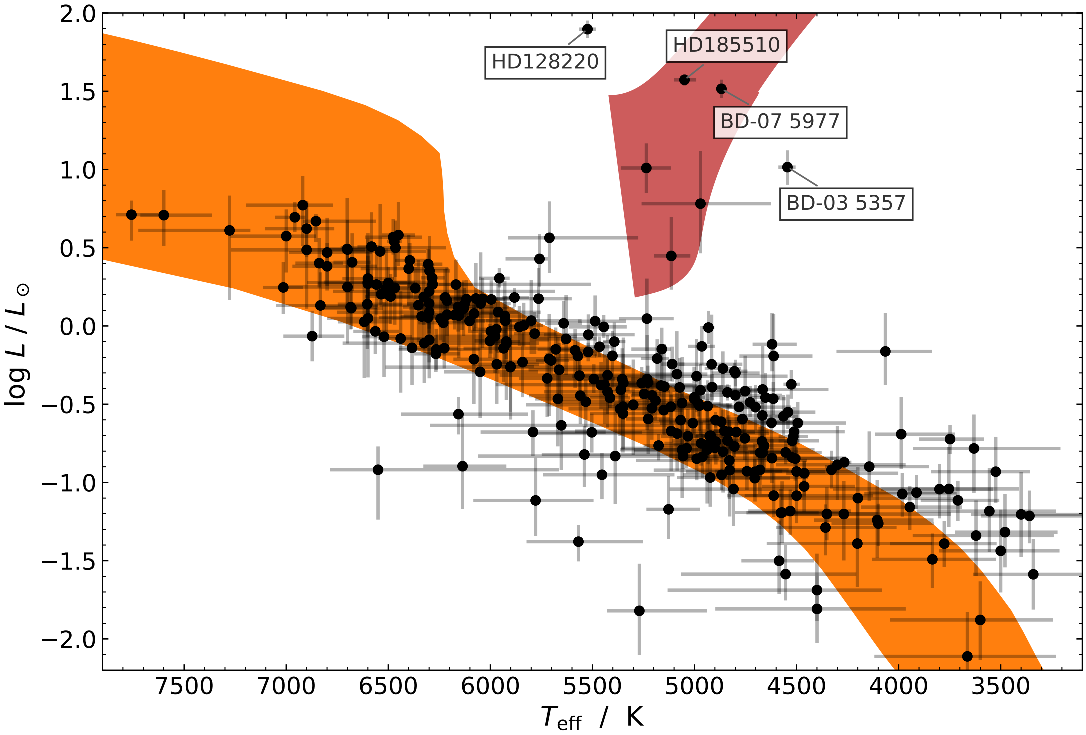

Figure 4.1.9. Cool companions to known hot subdwarfs in the HRD. Only systems with an uncertainty of less than 0.3 dex in the luminosity of the cool component are shown. The filled orange region spans between the MS at [Fe/H] = −3.2 and an age of 100 Myr and the [Fe/H] = +0.06 MS at the time when the core hydrogen mass fraction drops to 30 %. The position of expected RGB companions with masses of 0.75 $M_\odot$ to 2 $M_\odot$ is marked red, using [Fe/H] = −0.4. All evolutionary regions were constructed from BaSTI tracks (Hidalgo et al. 2018).

et al. 1977) is dominated by a companion on the RGB; its unusually low SED temperature might be affected by its variable nature (Vaccaro & Wilson 2003). Other companions appear to lie below the [Fe/H] = −3.2 ZAMS. These systems seem to be affected by overestimated *Gaia* parallaxes because the best-fit radii of both components are unphysically small.

The observed abundance of K-type companions on the main sequence is remarkable, because the BPS calculations of Han et al. (2003) do not predict such stars to be formed by the Roche lobe overflow channel, as shown in their fig. 15. For systems formed through stable Roche lobe overflow, these authors instead predict K-type companions that on the RGB. Hot subwdarfs with main-sequence K-type companions are only predicted as a result of the first common envelope channel. If these models were correct, one would expect systems with K-type companions on the main sequence to have short periods, which is not observed (Vos et al. 2018, 2020). Independent BPS calculations focusing on hot subdwarfs were performed by Clausen et al. (2012), who found their results to be highly sensitive to the uncertain parameters used to simulate binary evolution, including the critical mass ratio for stable mass transfer q_crit and the common-envelope efficiency α_CE. The existence of the large population of observed main sequence K-type + hot subdwarf systems may help constrain these parameters, especially once their orbital periods are measured. A significant fraction of K-type main sequence companions to hot subdwarfs were also found by Girven et al. (2012), who already stated that “the predictions of neither Han et al. (2003) nor Clausen et al. (2012) match the observed distribution completely”. The most recent BPS calculations for hot subwdarfs from the RLOF channel were performed by Vos et al. (2020), based on MESA models. The HRD of predicted companions in their models is very similar to the HRD shown in Fig. 4.1.9, including the MS K-type companions (Joris Vos, priv. comm.). A systematic study using such BPS models would be an important step towards a better understanding of both the RLOF and CE evolutionary channels.

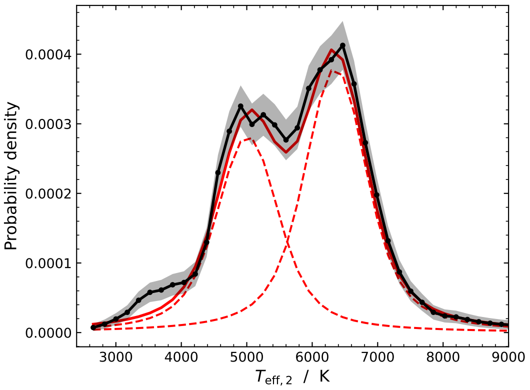

Figure 4.1.10. Distribution of companion T_{eff}, constructed from 1364 binary candidates with uncertainties of less than 15 % in T_{eff}. Two Voigt functions (dashed red) were fitted to the observed distribution (black, uncertainties are shown in grey). The curves are centred at 5010 ± 30 K and 6360 ± 20 K, and contribute 42 ± 3 % and 58 ± 3 %, respectively. The combined model (solid red) reproduces the observation fairly well, which is clearly bi-modal.

The significant contribution of K-type companions becomes even clearer in the distribution of companion T_{eff}, shown in Fig. 4.1.10. The distribution is clearly bi-modal, with peaks in the early K- and late F-type ranges. The observed lack of G-type companions is unlikely to be caused by selection effects and can not be explained by any currently available BPS models.

Figures 4.1.9 and 4.1.10 show a small excess of early to mid M-type candidate companions close to the MS. Such companions are only detectable using the SED method when excellent infrared photometry is available or for the most compact hot subdwarf primaries, such as the hot sdO Feige 34 (Latour et al. 2018a). An early M-type companion was also detected for the quickly rotating sdB CD −38 222 (Geier et al. 2013a), the SED of which is shown in Fig. 4.1.2. This star was previously not known to show a composite SED and was classified as single by Stark & Wade (2003). Several other M-type companions observed here are located slightly above the main sequence in the HRD (Fig. 4.1.9). Because M-type dwarfs did not yet have the time to evolve off the main sequence, this position can not easily be explained. This issue is likely caused by the fixed parameters of the hot subdwarf star: if the T_{eff} of the hot subdwarf is overestimated from spectroscopy, the companion T_{eff} will be underestimated. Most of the overluminous “M-type” dwarfs that result from such χ^2 fits are therefore more likely to be K-type dwarfs on the main sequence. An example of this is LB 1695, for which an SED fit with fixed primary T_{eff} leads to a large M-type companion, but a fit with free primary T_{eff} leads to a companion in the mid-K type range on the main sequence.

Observational biases. The BPS models of Han et al. (2003) predict large numbers of hot subdwarfs with A-type companions on the main sequence, formed through the stable RLOF channel. Such systems are not observed here, which might be the result of selection effects to some degree. Many hot subdwarfs were originally identified by their blue colours, which introduces a bias against binaries with significant optical contribution of a cooler companion. This means that the input catalogue is biased against systems with early F-type and A-type companions, that often lie close to the main sequence in optical and infrared colours. The same applies to F/G/K-type (sub-)giant companions. Post-EHB1 and eHe-sdO hot subdwarfs are intrinsically brighter in the optical range than sdB stars (see Fig. 4.1.5). As a result, eHe-sdOs and post-EHB1 sdOs are more likely to be identified as hot subdwarfs despite the contribution of a relatively bright F-type companion. Figure 4.1.11 clearly shows that K-type companions contribute more to the observed population of composite-SED He-poor sdBs than F-type companions, whereas the opposite applies to the composite He-poor sdO population. This is likely an observational bias, assuming that most He-poor sdO stars are the progeny of He-poor sdBs.

4.1.2.4 Summary and outlook

The SED analyses performed in this chapter, combined with the spectroscopic parameters from the literature, provide a rich data set that can be used to study many aspects of the hot subdwarf population. The most important conclusions discussed here are summarised as follows:

- The EHB band shows structure. There seem to be two groups of He-poor sdB stars on the

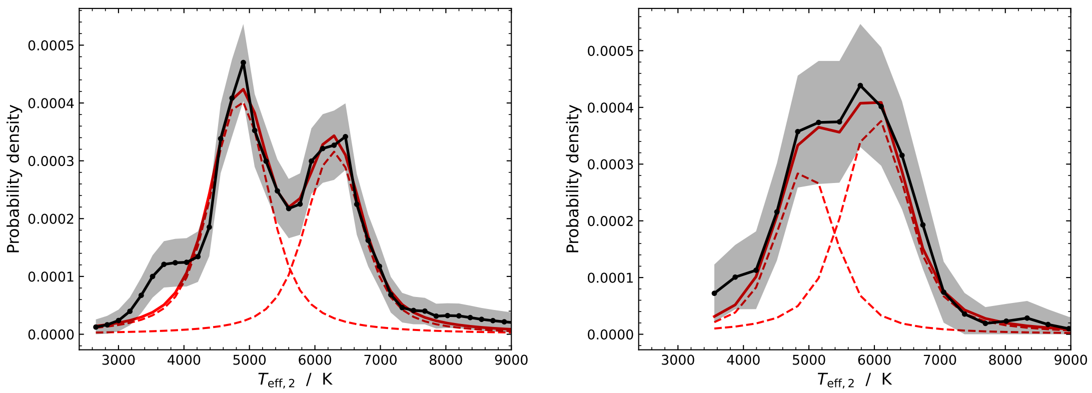

Figure 4.1.11. Like Fig. 4.1.10, but separated by spectral class: He-poor sdBs (left) and He-poor sdOs (right). The absolute number of binary candidates among the other spectral classes is too low to construct well-resolved histograms.

EHB, as already suggested by Németh et al. (2012).

- The progeny of these two groups are He-poor sdOs, which also appear in two groups.
- The population of iHe-sdOBs, as defined in the helium abundance - T_{eff} diagram is split into two subgroups: a luminous one with a low fraction of composite binaries and a more compact one with a high fraction of composite binaries.
- Most eHe-sdO stars are non-composite and seem to have masses of more than $0.5\,M_{\odot}$, but less than about $1\,M_{\odot}$. As expected from merger models, they have a distinct mass distribution compared to the other spectral classes of hot subdwarf stars, skewed to higher masses.
- The observed population of cool companions to hot subdwarfs is dominated by F-type and K-type stars on the main sequence. There seems to be a dearth of G-type companions that can not be explained by selection effects.
- The stellar parameters and binary candidates presented here allow the identification of many interesting systems that should be studied in more detail.

These conclusions are mostly not consistent with available binary population synthesis models. In particular the distribution of companion types would profit from updated BPS calculations. In addition, follow-up spectroscopy should be performed for the newly identified composite systems, which would not only provide measurements of their metallicity, but also allow their orbits to be solved. Also many of the non-composite hot subdwarf are interesting targets for follow-up, including candidate massive He-sdO stars. As a next step, the available spectra for the full sample discussed here should be re-analysed with consistent methods. Spectra from the SDSS and LAMOST surveys, which are available for many hot subdwarfs, are particularity well suited for this task. A consistent spectroscopic analysis would not only provide more reliable surface gravity measurements and thus improved mass distributions, but also improve the identification of structure in the distribution of hot subdwarfs in the HRD, such as the “EHB1” and “EHB2” groups. Spectroscopic fits to composite-SED systems that consider both components would provide more reliable parameters and help with the characterisation of many binary systems.

The SED fitting method is quick, can be applied to many types of stars, and photometric observations are readily available. Future applications will include updated versions of the parallax- and proper motion selected samples of candidate hot subdwarfs of Culpan et al. (2022), the candidate BHB sample of Culpan et al. (2021), and the extremely low-mass white dwarf candidates of Pelisoli & Vos (2019). In addition, SED analyses for a well-known sample of hot subdwarf stars can be used to refine the calibration of large photometric surveys. This is possible by deriving systematic differences between the predicted and observed magnitudes, under the assumptions that the SED model is accurate and that there exists a mean calibration derived from the collection of all available photometric data.

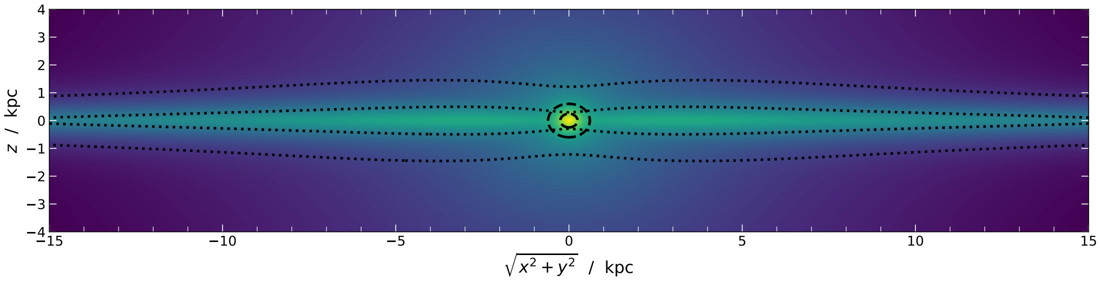

Figure 4.2.1. Mass density map of the axisymmetric Milky Way model I of Irrgang et al. (2013) on an arbitrary logarithmic scale. The dotted and dashed lines indicate the 1- and 2-σ contours of the disk and bulge components, respectively. Even the 1-σ contour for the halo exceeds the plot limits, at $r \approx 28$ kpc.

4.2 Galactic kinematics

Stars are characterised not only by their radius, luminosity, mass, and atmospheric parameters, but also by their motion within the Galactic potential. The kinematic properties of stellar populations are closely linked to their age, a direct result of the formation and evolution of the Milky Way. Therefore, stellar kinematics are a central tool for the study of the structure and evolution of our Galaxy (for reviews, see Bland-Hawthorn & Gerhard 2016; Helmi 2020). Conversely, the orbital properties of individual stars in the Galaxy can be used to constrain their age, which is especially important for hot subdwarf stars. This is because the metallicity of hot subdwarf stars is not a reliable indicator of age. The chemical composition of their surface is modified by strong diffusion effects (Michaud et al. 2011), as was discussed in Sect. 1.7. The interplay between radiative levitation and gravitational settling in the atmosphere of helium-poor hot subdwarf stars affects all ions in different ways, which can completely alter the chemical composition of their surface. In the following, the methods necessary to study the kinematic properties for a large sample of stars are introduced, which are then applied to the sample of known hot subdwarfs.

4.2.1 Galactocentric coordinate systems

The following section uses both the Cartesian and cylindric Galactic coordinate frames, centred on the Galactic Centre (GC). Here, the x-axis is pointed from the GC in the direction opposite to the Sun, the y-axis points in the direction of the Sun's orbit, and the z-axis points towards the north Galactic pole. The cylindrical radial distance from the GC is defined as $r = \sqrt{x^2 + y^2}$ and the angular coordinate is denoted φ. The same left-handed system is used for the velocity components, defining the Galactic radial velocity $U \equiv v_r$ as negative towards the GC, the Galactic tangential velocity $V \equiv v_\varphi$ as positive in the direction of Galactic rotation, and the vertical velocity $W \equiv v_z$ as positive towards the north Galactic pole. These velocities can be derived without the assumption of a specific Galactic potential or the calculation of orbits. They can be calculated from the radial velocity, the position and proper motion on the sky, and the distance to a star (for details, see Johnson & Soderblom 1987). For the transformation from Heliocentric to Galactocentric coordinates, the solar position and velocity relative to the GC have to be known. Because the following analyses are based on the methods developed by Irrgang (2014), the values of Irrgang et al. (2013) were used. The solar distance from the GC was assumed to be

$$r_\odot = 8.4\ \mathrm{kpc},$$

while the circular velocity of the local standard of rest (LSR) was taken as

$$V_\mathrm{LSR} = 242\ \mathrm{km\,s^{-1}}.$$

In addition, the solar velocities with respect to the LSR were assumed to be

$$(U_\odot, V_\odot, W_\odot) = (11.1, 12.2, 7.3)\ \mathrm{km\,s^{-1}},$$

based on the results of Schönrich et al. (2010). If the current Galactocentric position and velocities of a star are well-constrained, its orbit can be traced back in time by assuming a model for the Galactic gravitational potential. These orbits can then be studied in terms of their eccentricity e and (specific) total energy E_{tot}, which is the conserved sum of their (specific) potential and kinetic energy. In the following analysis, model I of Irrgang et al. (2013) was used. This model is an updated version of the Allen & Santillan (1991) model and is comprised of three components: the halo, the central bulge, and the Galactic disk. The combined mass density for this model is shown in Fig. 4.2.1. Irrgang et al. (2018) used the model to study the kinematics and origin of hypervelocity stars, that is stars that are likely to be unbound to the Milky Way, and Irrgang et al. (2021) used it to study a sample of somewhat slower extreme disk-runaway stars.

4.2.2 Metallicity and α-enhancement

The chemical composition of stars in the Universe has changed considerably since its first stars, the virtually metal-free population III stars, were formed. Over time, stellar nucleosynthesis followed by supernova explosions progressively enriched the star-forming gas in metals, forming a constant cycle of matter (for a review, see Nomoto et al. 2013). The age of stellar populations is therefore correlated with their photospheric chemical composition, at least for stars that do not exhibit strong atmospheric diffusion. This means that Galactic stellar populations defined based on their spectroscopically measurable chemical compositions differ in their kinematic properties (see e. g., Sharma et al. 2022).

At an age of about 4.6 Gyr (Bonanno et al. 2002), the Sun is a relatively young star. Old stellar populations consequently have a low metallicity relative to the Sun. Because the iron abundance is easy to determine for most stars, it is used as a proxy for the overall metallicity of a star. The metallicity relative to the Sun is therefore usually defined as

$$[\mathrm{Fe/H}] = \log_{10}(n_{\mathrm{Fe}}/n_{\mathrm{H}}) - \log_{10}(n_{\mathrm{Fe}}/n_{\mathrm{H}})_{\odot},$$

where n_{H} and n_{Fe} are the number densities of hydrogen and iron, respectively. In addition, old stellar populations feature an enhancement of the so-called α-process elements (O, Ne, Mg, Si, S, Ar, and Ca) relative to the abundance of iron when compared to the solar ratio. This quantity is usually referred to as the α-enhancement

$$[\alpha/\mathrm{Fe}] = \log_{10}(n_{\alpha}/n_{\mathrm{Fe}}) - \log_{10}(n_{\alpha}/n_{\mathrm{Fe}})_{\odot}$$

and was first used by Aller & Greenstein (1960) and Wallerstein (1962). The enhancement of magnesium [Mg/Fe] is often used as a proxy for the α-enhancement.

Supernovae caused by massive and therefore short-lived stars are able to enrich the interstellar medium in α-elements that were produced e. g. through thermonuclear fusion of helium. However, they contribute less to the enrichment of heavier elements such as iron, because these metals partly become trapped in the neutron star or black hole remnant (Nomoto et al. 2013). A large portion of the iron in star-forming material is instead produced by Type Ia supernovae (Tinsley 1979), explosions of accreting (single-degenerate; Whelan & Iben 1973) or merging (double-degenerate; Webbink 1984) white dwarfs that typically leave no remnant. Because of their less massive progenitor stars, white dwarfs can require billions of years before producing a thermonuclear supernova through binary interaction (Maoz & Mannucci 2012). Compared to the Sun, old stellar populations have had less time to be affected by iron enrichment through exploding white dwarfs. These old populations are therefore α-enhanced. In addition, stars formed in dwarf galaxies or globular clusters are intrinsically less metal-rich than the Milky Way (Kirby et al. 2013) and are less enriched in α-elements due to their longer star formation timescales (Conroy et al. 2014). Therefore, the metallicity [Fe/H] and enrichment in α-processed metals [α/Fe] are essential tools to define various stellar populations in the Milky Way that differ in their age and origin.

Chemically-defined kinematic studies using thousands of stars in the Solar neighbourhood were performed by Chiba & Beers (2000), Soubiran et al. (2003), and Fuhrmann (2011), among others. Several spectroscopic surveys have since observed much larger samples, often exceeding

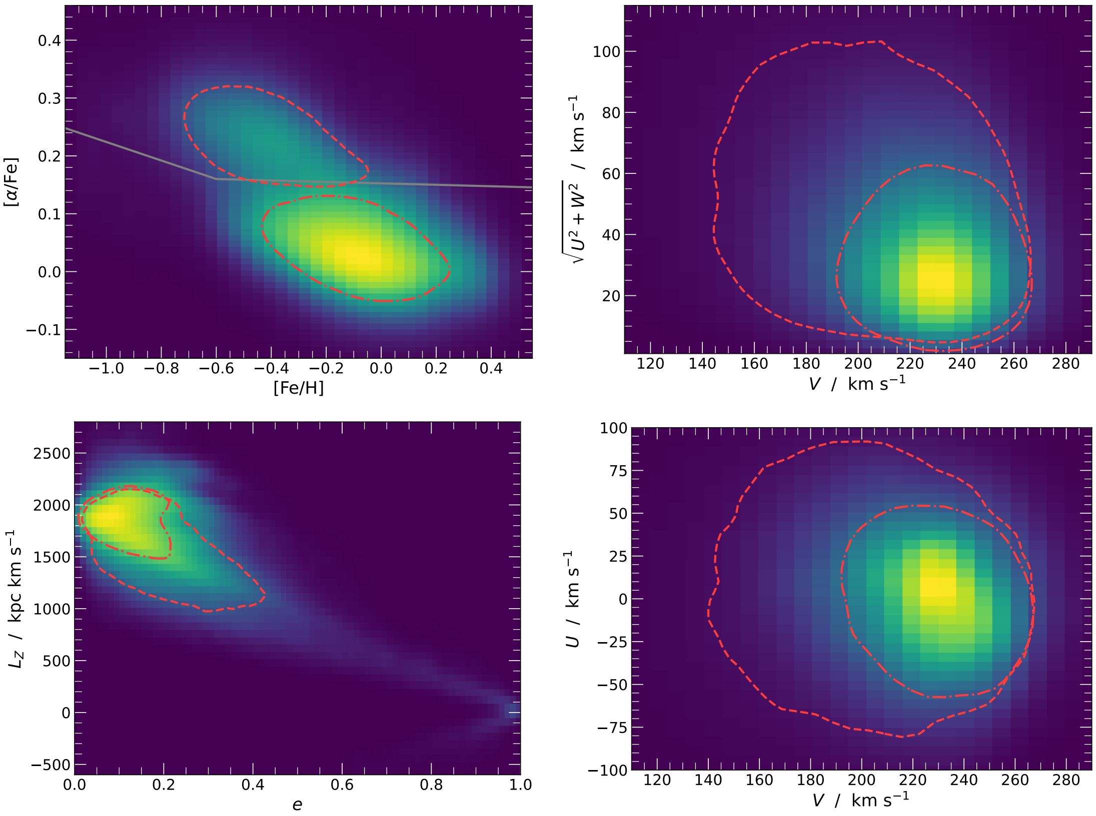

Figure 4.2.2. Top left: the [α/Fe] - [Fe/H] space based on data of the GALAH+ DR3 sample of Buder et al. (2021). The brightness is proportional to the density of the sample. The approximate separation between the low- and high-[α/Fe] populations is shown as a grey line. The 1-σ contours for the densities of the two populations separated by this line are shown as dash-dotted and dashed lines. The other panels show the density of the same sample in the Toomre, U-V, and L_z-e diagrams, as well as the corresponding 1-σ contours.

500 000 stars. This includes samples based on low resolution spectroscopy, most notably SEGUE (Bond et al. 2010) and LAMOST (Wu et al. 2021; Xiang & Rix 2022), but also high resolution surveys such as Gaia-ESO (Hayden et al. 2018), APOGEE (Anguiano et al. 2020; Lagarde et al. 2021), and GALAH+ (Buder et al. 2021). The kinematic properties of the Galactic stellar populations can also be derived from population synthesis calculations, such as the Besançon model (Robin et al. 2003, 2017). In a simplified picture, stars are often classified as members of either the Galactic bulge, thin disk, thick disk, or the halo population. The following discussion will omit the Galactic bulge population because hot subdwarf stars in the bulge are distant and faint (Busso et al. 2005).

4.2.3 Galactic populations: Overview

Like the Sun, the majority of stars in the Milky Way are **thin disk** stars that orbit the Galactic centre on near-circular and almost co-planar orbits. Because it is the youngest of the three populations, the thin disk population consists mostly of fairly metal-rich stars that are not significantly enriched in α-processed metals. A typical definition for the thin disk in terms of metallicity and α-enrichment is that of Anguiano et al. (2020): $-0.7 < \mathrm{[Fe/H]} < +0.5$ and $-0.1 < \mathrm{[Mg/Fe]} < +0.17$. The top left panel of Fig. 4.2.2 shows the clear distinction between the chemically defined thin and thick disk in the GALAH+ sample of Buder et al. (2021) as a grey line. The thus defined thin disk shows little scatter in the distribution of circular velocities, which is centred at about $V = 230\ \mathrm{km\,s^{-1}}$, close to the solar value (Eilers et al. 2019; Lagarde et al. 2021). At a vertical scale height of about 300 pc (Gilmore & Reid 1983), the orbits of thin disk stars do not extend far above or below the Galactic plane – hence the name. Due to their low scale height and low

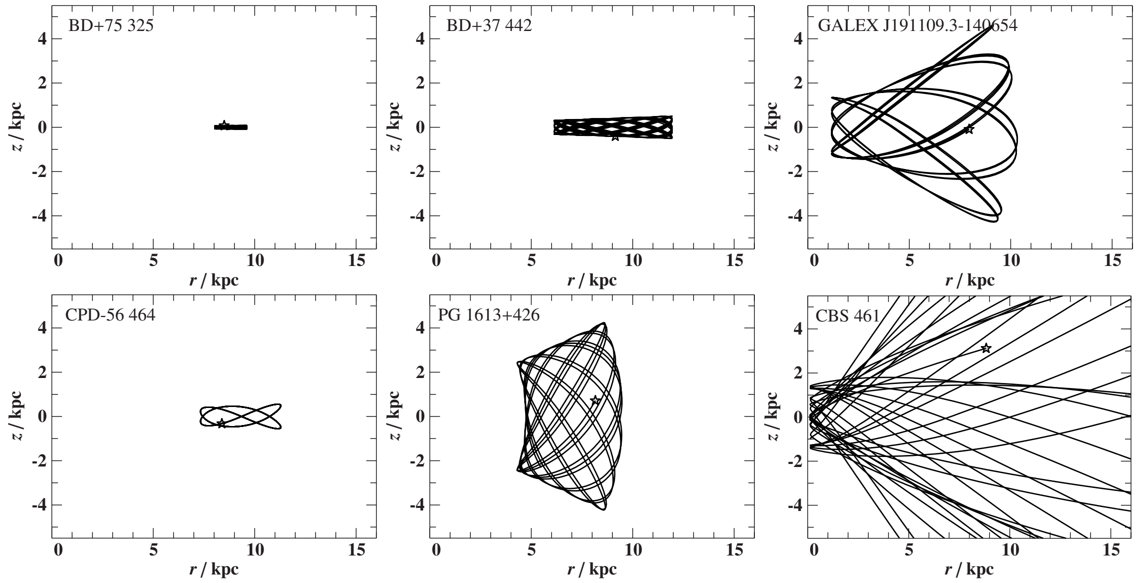

Figure 4.2.3. Example orbits of stars from the sample of known hot subdwarfs discussed in Sect. 4.2.6, projected to the z - r plane. The three columns show orbits for thin disk, thick disk, and halo stars, respectively. The orbits become more extreme from top to bottom and from left to right. The current positions are marked by star symbols and the trajectories are computed into the past.

eccentricities, the orbits of thin disk stars are confined to a small box when projected to the z - r plane, as shown in Fig. 4.2.3. The velocity distribution of stars in the solar neighbourhood is highly structured, as revealed by the *Gaia* satellite (Kushniruk et al. 2017; Gaia Collaboration et al. 2018; Ramos et al. 2018).

Compared to the thin disk, **thick disk** stars form an older population (Kilic et al. 2017). Chemically, they are separated from the thin disk by their roughly 0.15 dex higher α-enhancement and overall lower metallicity, roughly in the range $-1 <$ [Fe/H] < 0. Although this chemical classification can be used to discern the kinematic distributions of the thin and thick disk populations, there is a considerable overlap in the kinematic properties. Differences are especially obvious in the distribution of circular velocities V – compared to the thin disk, the thick disk population has a lower average Galactic rotation velocity of about 190 km s^{-1} (Anguiano et al. 2020), a property often described as the “asymmetric drift”. Its larger contours in Fig. 4.2.2 further show that the thick disk velocity and eccentricity distributions have higher standard deviations than the thin disk. Thick disk orbits are on average less circular than those of thin disk stars and tend to extend further above and below the Galactic plane, as exemplified in Fig. 4.2.3. A standard value for the vertical scale height of the thick disk is about 900 pc (Bland-Hawthorn & Gerhard 2016). The actual definition of the thick disk, as intermediate between the thin disk and the halo, is not straight-forward. Bovy et al. (2012) found that there is no thin-thick disk bi-modality in the scale height distribution, which they interpreted as indication that the thin and thick disk are a continuous population of stars. Sharma et al. (2021) were able to explain the two sequences in the α-enhancement - metallicity space by an increase in the α-enhancement for stars older than about 10 Gyr, which is in line with the observations of Sharma et al. (2022). In their model, effects of radial migration and kinematic heating over time lead to the larger scale height of the α-enhanced thick disk, compared to the younger, low-α thin disk. Based on the ages of main-sequence turn-off stars, Bonaca et al. (2020) argued that the α-enhanced disk was formed gradually up to about 8.3 Gyr ago, when star formation in this population was abruptly truncated. Competing models attribute the two α-sequences to two major episodes of gas infall during the formation of the Milky Way, where the first episode formed the thick disk and the second episode formed the thin disk (Chiappini et al. 1997; Spitoni et al. 2020; Hu & Shao 2022).

Furthermore, a low-metallicity tail of the thick disk, the so-called metal-weak thick disk (MWTD), seems to extend to even lower metallicities (see e.g. Chiba & Beers 2000; Beers et al. 2014; Yan et al. 2022). In a chemodynamical study of stars in the solar neighbourhood, Carollo et al. (2019) found that the MWTD population is a distinct population from the canonical thick disk, showing distinct but overlapping distributions in both [α/Fe] and its kinematic properties. In particular, they found the circular rotation of the MWTD to lag about 30 km s^{-1} behind the thick disk. The origin of this MWTD population is not currently known although several theories exist, ranging from kinetic heating of old disk stars induced by a merger event to radial migration of bulge stars (Carollo et al. 2019).

The Galactic **halo** as a whole can be very roughly approximated as spherical in space, and as lacking a preferred direction of rotation V. Halo stars can follow highly eccentric trajectories, examples of which are shown in Fig. 4.2.3. The accepted picture of the stellar halo has evolved considerably in recent years. It is the oldest population of stars in the Galaxy and was often simply defined as the population of stars that have [Fe/H] < -1. Nissen & Schuster (2010) identified two sequences of kinematically extreme low-metallicity stars at [Fe/H] < -0.8: a low-α and a high-α population. They suggested that the high-α population is comprised of old (thick) disk or bulge stars that were kinematically heated to halo orbits, which is why this population is also referred to as the "in-situ" halo. Recent studies suggest that this high-α population has the same origin as the MWTD (Di Matteo et al. 2019; Buder et al. 2022). Similarly, some halo stars on highly eccentric orbits were observed to have higher metallicities than most other halo stars and are therefore thought to have been formed in the Galactic disk at a later time, before experiencing substantial changes to their orbits (Bonaca et al. 2017). For the low-α population, Nissen & Schuster (2010) proposed that it has been accreted from dwarf galaxies. This theory recently received overwhelming support and data from the *Gaia* satellite even allowed the detection of several distinct substructures in the low-α Galactic halo that differ in their origin. For example, a stream of stars is associated with the Sagittarius dwarf spheroidal galaxy, which is currently in the process of merging with the Milky Way (Ibata et al. 1994). Many other stars in the halo appear to have been accreted from a single dwarf galaxy, now termed the Gaia-Enceladus (Helmi et al. 2018). Comparing stellar ages obtained from colour-magnitude fitting and spectroscopic α-enhancements with cosmological simulations led Gallart et al. (2019) to conclude that the thick disk and high-α halo populations correspond to old Milky Way stars that were kinematically heated by the Gaia-Enceladus merger event about 10 Gyr ago, while the low-α population corresponds to stars accreted from the Gaia-Enceladus galaxy. Similar conclusions were reached by Xiang & Rix (2022) based on the ages of subgiant stars. The presence of smaller subgroups of halo stars that share kinematic properties and chemistries indicates that a number of smaller merger events also contributed to the halo population (Naidu et al. 2020; Bonaca et al. 2021).

4.2.4 Previous kinematic analyses of hot subdwarfs

Because the abundances of metals in the photospheres of hot subdwarf stars are affected by strong diffusion effects, it is not generally possible to measure their initial metallicity or α-enhancement. This means that a classification in thin disk, thick disk, and halo stars has to rely on the kinematic analysis alone. This is also the case for white dwarf stars such as those in the samples of Pauli et al. (2006) and Raddi et al. (2022). The age of white dwarf stars can be estimated from cooling tracks, which, combined with a kinematic analysis even allows age estimates for the Galactic halo (Oppenheimer et al. 2001). This is not possible for the helium-burning hot subdwarf stars. A kinematic analysis is therefore the most important tool to roughly estimate the age of the Galactic hot subdwarf population.

Because hot subdwarf stars were first identified at high Galactic latitudes (Humason & Zwicky 1947), it has long been suspected that many are members of the old disk or even halo. Indeed, early kinematic analysis, such as those of Colin et al. (1994) and de Boer et al. (1997) found the hot subdwarf population to show orbits that match the thick disk population, although their samples were small. These authors found the vertical scale height z_0 of the known subdwarf population to be close to 1 kpc, similar to the thick disk. This value was supported by Altmann et al. (2004) using a sample of 114 sdBs, who further found halo stars to contribute with a scale height of about 7 kpc, identifying about 15 % of their sample of as halo stars. The Galactic orbits

Table 4.2.1. The central positions μ and standard deviations σ for the distributions of the chemically defined thin disk, thick disk, and halo populations of Anguiano et al. (2020). All values are stated as $\mu \pm \sigma$ in km s^{-1}.

	U	V	W
Thin disk	-0.52 ± 37.61	229.43 ± 25.01	0.02 ± 18.63
Thick disk	-3.04 ± 64.68	191.40 ± 40.10	0.02 ± 43.60
Halo	-2.90 ± 165.50	-2.30 ± 95.10	-5.00 ± 94.10

of 179 sdB binaries were studied by Kawka et al. (2015), who concluded that the populations of binary and single sdB stars share the same Galactic kinematics. Using a sample of 88 hot subdwarfs, Martin et al. (2017) found that helium-rich hot subdwarfs show on average more extreme kinematic properties than the helium-poor sdBs. In fact, one of the few stars that are known to currently escape from the Milky Way is the helium-rich sdO US 708 (HVS 2, Hirsch et al. 2005; Geier et al. 2015a).

Before the second data release of the *Gaia* space mission, kinematic analyses of hot subdwarf stars had to rely on ground-based proper motions and spectroscopic distances for most stars, such as the searches for high-velocity hot subdwarf stars by Tillich et al. (2011) and Ziegerer et al. (2017). In addition, they were limited by the small size of their samples. Early astrometric satellites such as Tycho (Høg et al. 2000) and Hipparcos (van Leeuwen 2007) provided parallaxes and proper motions for only a few of the brightest hot subdwarf stars. The first study to resolve these issues was performed by Luo et al. (2021), who used *Gaia* EDR3 astrometry and LAMOST DR7 spectroscopy to study the orbits of 1587 hot subdwarfs. They defined several groups of hot subdwarfs based on their helium content and effective temperatures and found that some of these populations seem to differ in their kinematic properties. In particular, they found more hydrogen-deficient stars in the halo and thick disk compared to the thin disk. Overall, Luo et al. (2021) classified 49 % of their sample as thin disk, 36 % as thick disk, and 15 % as halo stars.

4.2.5 Classification methods and systematics

Most studies of hot subdwarfs have classified stars as part of either the thin disk, thick disk, or halo populations. These classifications were based on the current Galactic motions (U, V, W), in particular in the Toomre- and U-V diagrams, as well as the L_z-eccentricity diagram, as shown in Fig. 4.2.2. Here, the z-component of the (specific) angular momentum L_z is given as

$$L_z = y \cdot v_x - x \cdot v_y = V \cdot r,$$

which is a conserved quantity in an axisymmetric Galactic model. The eccentricity is defined as

$$e = \frac{R_{\max} - R_{\min}}{R_{\max} + R_{\min}}$$

where $R = \sqrt{x^2 + y^2 + z^2}$ and $R_{\min}$ and $R_{\max}$ are the minimum and maximum distances from the Galactic centre. Some studies have additionally based their classifications on visual inspection of stellar trajectories in the vertical height - galactrocentric radius diagrams as shown in Fig. 4.2.3 or on the histogram of mean vertical heights. Similar approaches have been used by Pauli et al. (2003) and Pauli et al. (2006) to classify their sample of white dwarfs from the SPY survey. As the most recent and largest example, Luo et al. (2021) classified hot subdwarf stars as thin/thick disk if they were within the respective 3-σ contours of Pauli et al. (2006) in the U-V diagram and in specific boxes in the L_z-e diagram. In the overlapping regions of thin and thick disk, stars were classified as thin disk. The contours in U, V, and W and the boxes in L_z-e were defined by Pauli et al. (2003) by comparison with a sample of 137 F-/G-type stars for which metallicities were known. This method is straight-forward to understand and implement, and is well suited

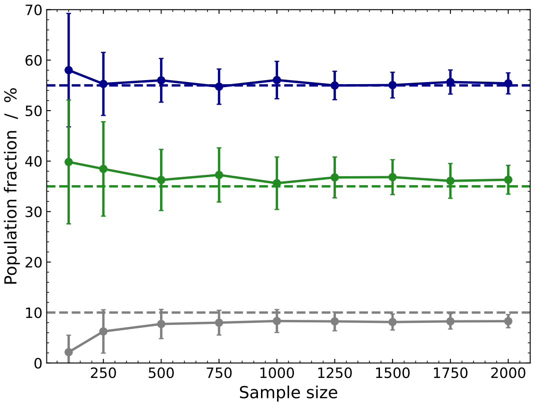

Figure 4.2.4. Performance of the histogram fitting method as a function of the sample size. In this example, the simulated thin disk (blue), thick disk (green), and halo populations (grey) made up 55%, 35%, and 10%, respectively. These fractions are indicated by the dashed lines.

for the identification of outliers, such as halo or hyper-velocity stars. However, it may lead to a biased classification, both for individual stars and the overall relative population fractions. The choice of the exact classification regions in the L_z-e diagram and the choice of the significance level used in the U-V diagram are somewhat subjective and should be adjusted for each sample. For example, the use of the 3-σ thin disk contour may be appropriate for a sample that contains mainly thin disk stars, such as that of Pauli et al. (2006), but would lead to misclassifications in a sample that is dominated by halo or thick disk stars. In the latter example, many stars would be falsely classified as thin disk stars because of overlapping contours.

Instead of using only their contours, it is possible to directly use the Gaussian probability density functions (PDFs) of each population in the one-dimensional U-, V-, W-histograms, as defined by reference studies such as those of Robin et al. (2003) and Anguiano et al. (2020). This method requires knowledge about the relative contribution of each population to the underlying sample – the normalisation of each Gaussian component. These can be estimated directly from the observed sample of stars by simultaneously fitting the histograms in U, V, and W with multiple PDFs, one for each population. It is necessary to limit the number of free parameters during the fit, because the number of bins is limited and, more importantly, because the parameters of the Gaussian models tend to be strongly correlated. These correlations result from the overlap between the Gaussian components. The histogram fits have a minimum of two free parameters if three populations are assumed: the normalisation of the thick disk A_{thick} and halo A_{halo}. The third normalisation A_{thin} results from the condition that $1 = A_{\text{thin}} + A_{\text{thin}} + A_{\text{halo}}$. In the present analysis, the central positions and standard deviations of the Gaussian models were fixed to the values of Anguiano et al. (2020), as derived from the APOGEE DR16 sample of main sequence and giant stars. These values are stated in Table 4.2.1.

A crucial aspect of histogram fitting is the treatment of the uncertainties of the bin heights. Here, a Monte Carlo (MC) approach was used to estimate the distributions of each bin height based on the uncertainties of the observed variables, using 10^5 samples for each bin – this is equivalent to 10^5 realisations of each histogram. Estimated probability densities for individual $U/V/W$ measurements were constructed from asymmetrical uncertainties using the two-piece normal function, which is also called the Fechner function (Wallis 2014). The final height of each bin then corresponds to the corresponding mean of bin heights in the MC calculation and the corresponding uncertainty is given by the standard deviation.

Once the total population fractions were estimated, membership probabilities of individual stars were assigned by evaluating the best-fit one-dimensional Gaussian PDFs in $U/V/W$ at the observed values. This results in different population membership probabilities for each of the $U/V/W$-histograms. The combined population membership probability from all histograms was then estimated by constructing the 3-dimensional normal distributions for all populations, which can easily be evaluated for each star. This means that the weak correlations between $U/V/W$ are disregarded. While this method works well and is easy to implement, it introduces a slight bias that favours a thin disk classification and that suppresses halo classifications relative to the best-fit

Table 4.2.2. Population fractions in percent. Uncertainties for the histogram fitting method used here refer to 1-σ statistical uncertainties only. Uncertainties for the literature samples are usually not stated and were estimated from the number of stars N_k in each population k as $\sigma_k \approx \sqrt{N_k}$.

Sample	Thin disk	Thick disk	Halo	"fourth"	Reference
Known subdwarfs	43.0 ± 0.8	44.3 ± 1.3	9.9 ± 2.2	2.8 ± 2.1	this work
LAMOST DR7	34.6 ± 0.4	47.7 ± 0.7	13.4 ± 1.1	4.3 ± 1.1	this work
LAMOST DR7	49.1 ± 2.1	35.8 ± 1.7	15.1 ± 1.0	–	Luo et al. (2021)
Martin et al. (2017)	51.1 ± 9.4	40.8 ± 8.1	8.0 ± 3.1	–	Martin et al. (2017)

normalisations. Specifically,

$$A_i \neq \frac{\sum_k^n p_{k,i}}{\sum_k^n \sum_i^m p_{k,i}} =: A_i^*$$

where i is any population, m is the number of considered populations, k is an individual star, n is the number of stars in the sample, $p_{k,i}$ is the combined membership probability, A_i is the best-fit normalisation, and A_i^* is the biased normalisation. The difference $|A_i^* - A_i|$ is always smaller than about 3 % for the known hot subdwarf sample studied in Sect. 4.2.6 and smaller than 5 % for the sample of Luo et al. (2021). The bias is caused by the mutual (redundant) information contained in the U-, V-, and W-histograms – information that is used multiple times in the current method, which should be remedied in the future.

It is useful to test the histogram fitting method using simulated samples before applying it to samples of hot subdwarf stars. Simulated samples can be constructed by modelling the distribution of thin disk, thick disk, and halo stars in U, V, W as Gaussian PDFs, using the mean values and standard deviations of Anguiano et al. (2020). In this case, the relative population fractions are known, allowing the performance of the histogram fitting method to be tested depending on the sample size by drawing a limited number of stars from the model. The results of this exercise are visualised in Fig. 4.2.4 for a simulated sample that contains 55% thin disk, 35% thick disk, and 10% halo stars. The mean best-fit population fractions and their uncertainties for each sample size were estimated by drawing the sample 100 times, each time performing the histogram fit. The fitting method performs well for simulated sample sizes larger than about 500 stars, although the fraction of halo stars was systematically underestimated by 1.7% in this specific example.

4.2.6 The known hot subdwarf sample

The catalogue of hot subdwarfs of Geier (2020), updated by Culpan et al. (2022), is the largest collection of spectroscopically identified hot subdwarf stars. It contains the brightest hot subdwarfs, but also fainter stars from surveys such as LAMOST (Luo et al. 2021). Because the catalogue includes radial velocity measurements for most stars, it can be used as the basis of a large kinematic study. Here, orbit calculations were performed for stars in the catalogue of Culpan et al. (2022) that satisfied reasonable quality criteria. Stars with radial velocity uncertainties larger than 100 km s^{-1} were excluded. The sample was further limited to stars with *Gaia* EDR3 parallaxes larger than 0.25 mas, with parallax uncertainties of less than 30 %, and with RUWE values of less than 2.0. At 1824 stars, the resulting sample is slightly larger than that of Luo et al. (2021). Hot subdwarf stars often reside in binary systems and are therefore radial velocity variable. Because the orbits of these systems are often not solved, their systemic radial velocities are unknown. Known radial velocity variable stars were therefore removed using the lists of Culpan et al. (2022) and Geier et al. (2022). In addition, hot subdwarfs that were found to show composite SEDs in Section 4.1.2 were removed. This left 999 hot subdwarf stars in the cleaned sample, which will be referred to as the "known hot subdwarf sample" in the following. About 59 % of these stars are also part of the sample of Luo et al. (2021).

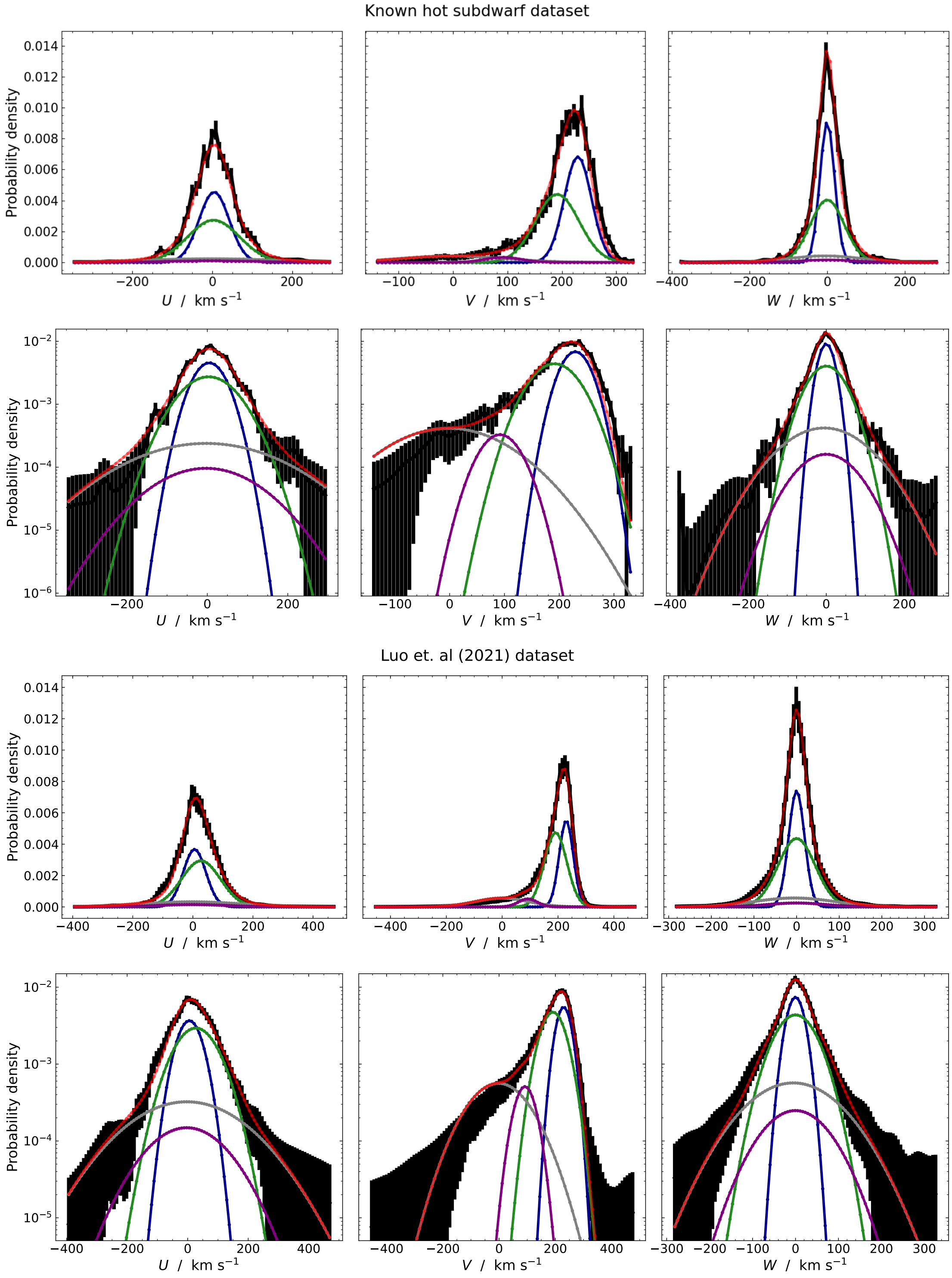

Figure 4.2.5. Simultaneous fit to the empirical probability density in the U, V, and W histograms of the known hot subdwarf sample and that of Luo et al. (2021). Four populations were modelled by simple Gaussian functions, with fixed centres and standard deviations from Anguiano et al. (2020) for all but the fourth Gaussian. The only free parameters were the normalisations for the thick disk population, halo population, and "fourth" population. The normalisation for the thin disk is given by the normalisation condition. The observations are shown in black while the best-fit model is shown in red. The contributions of the thin disk, thick disk, halo, and "fourth" populations are shown in blue, green, grey, and purple, respectively. The uncertainties for the observed histograms were estimated using the MC approach. The model Gaussians were appropriately re-binned. The resulting population fractions are stated in Table 4.2.2.

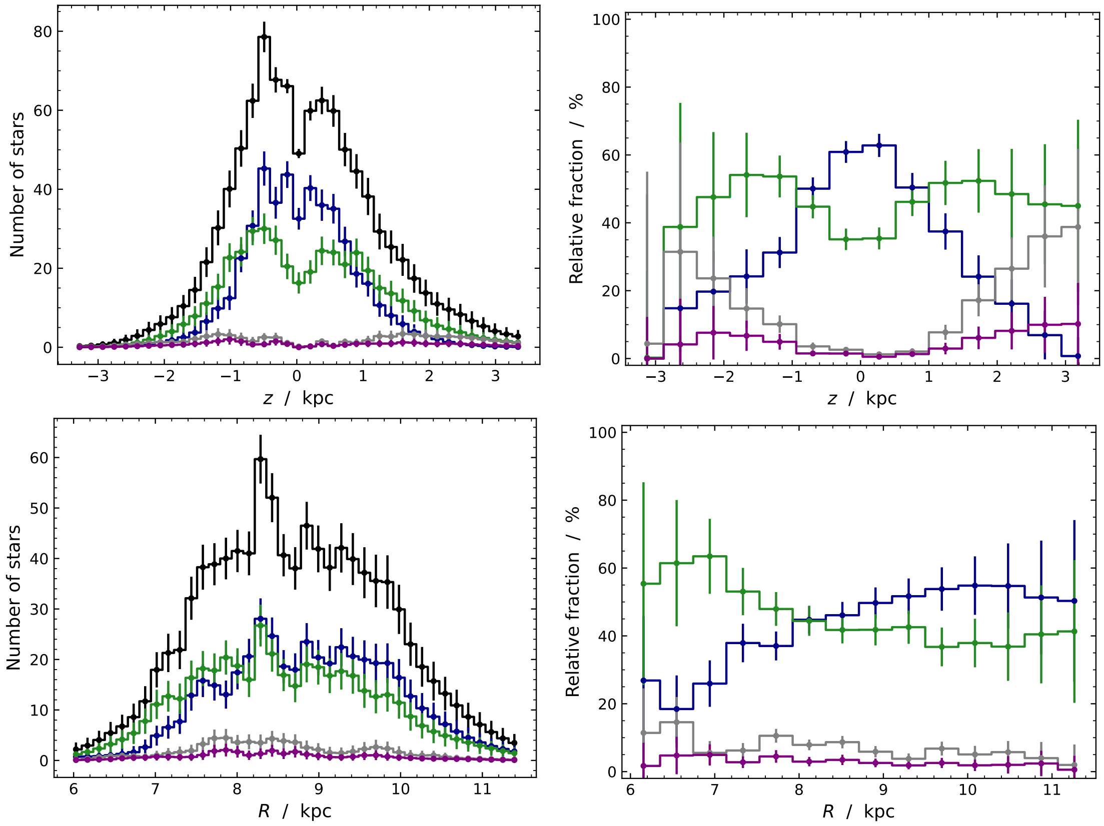

Figure 4.2.6. Absolute (left panels) and relative (right panels) histograms for the known hot subdwarf sample in height above the disk z (upper panels) and distance from the Galactic centre R (lower panels). The thin disk, thick disk, halo, and the "fourth" populations are shown in blue, green, grey, and purple, respectively. The combined bins are shown in black. The measurement uncertainties and fractional membership probabilities are considered using the MC method.

Orbits were calculated using the code developed by Irrgang (2014), based on model I of Irrgang et al. (2013). To allow accurate results for the eccentricity, the stellar trajectories were followed for 10 revolutions around the Galactic centre or at most for 15 Gyr. Uncertainties in the output parameters were estimated using an MC calculation with 50 000 samples.

As described in Sect. 4.2.5, the overall population fractions were then estimated by fitting Gaussian models to the U-, V-, and W-histograms. This method was applied to both the known hot subdwarf sample and the sample of Luo et al. (2021). Best fits for both samples are shown in Fig. 4.2.5. In both the sample of Luo et al. (2021) and the known hot subdwarf sample, there is a significant contribution of stars between $V = 70$ and $140\,\mathrm{km\,s^{-1}}$ that can not be modelled by the halo or thick disk populations. Therefore, a fourth Gaussian was introduced, centred at $V = 91\,\mathrm{km\,s^{-1}}$. While this Gaussian is necessary to reproduce the observed distribution of hot subdwarfs in V, it may not represent a single physical population of stars. Its standard deviation in V, $\sigma_V \approx 34\,\mathrm{km\,s^{-1}}$, was estimated using the sample of Luo et al. (2021). Anguiano et al. (2020) used a similar contribution centred at $V = 91\,\mathrm{km\,s^{-1}}$ to account for the skewed distribution of chemically selected thick disk stars in their much larger sample, although their standard deviation was larger at $\sigma_V \approx 115\,\mathrm{km\,s^{-1}}$ (cf. their fig. 4). Because nothing is known about the properties of this putative "fourth" population in U and W, it was centred at zero in these histograms, while the corresponding standard deviations were set to be intermediate between the thick disk and halo. The addition of the "fourth" population improved the fit for both the halo and thick disk populations, and reduced the contribution of the halo population. Due to this correlation between the halo and the "fourth" populations and the lack of information about the "fourth" population, there are rather large systematic uncertainties in the contributions of both populations. The best-fit models shown in Fig. 4.2.5 still over-estimate the number of retrograde halo stars, but otherwise provide a good fit to all three histograms.

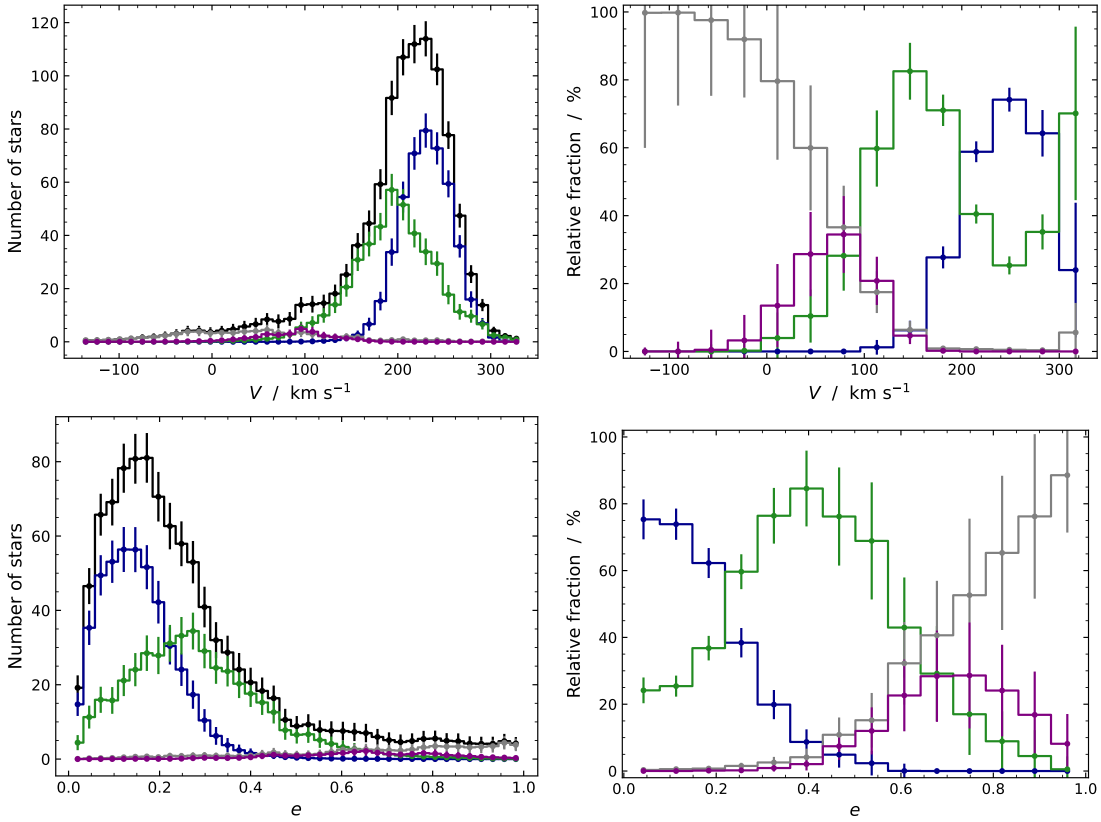

Figure 4.2.7. Like Fig. 4.2.6, but for the current circular velocity V and orbital eccentricity e.The colours are the same as in Figs. 4.2.5 and 4.2.6.

The resulting population fractions are compared with previous kinematic studies of hot subdwarfs in Table 4.2.2. Because the specific classification methods and sample selections differ between all studies, these results are not expected to be identical. Compared to the method of Luo et al. (2021), the $U/V/W$ histogram fitting method results in a lower fraction of thin disk stars in favour of the thick disk. All studies found their samples to be dominated by disk stars, including a large fraction of thick disk stars, much larger than the 10 % found for the WD population by Raddi et al. (2022), or the 17 % in the APOGEE sample of Anguiano et al. (2020). Although this may indeed indicate that hot subdwarfs from an old stellar population, the ratio of thin and thick disk stars also depends on the scale height of each sample. In particular the WD sample of Raddi et al. (2022) is much more local ($d \lesssim 300$ pc) than the known hot subdwarf sample, which extends to about 2 kpc from the Sun. The number of stars in the known hot subdwarf sample classified as halo is lower than in the sample of Luo et al. (2021), regardless of the classification method. This may be related to the stricter quality cuts for the known hot subdwarf sample, which exclude more binary stars and limit the maximum distance.

Sample selection effects become apparent in the spacial distribution of known hot subdwarfs. The left panels of Fig. 4.2.6 show the distribution of the known hot subdwarf sample in height above the disk z and planar distance from the Galactic centre r. The central dip in the absolute z-histogram and the increase in the fraction of thick disk stars towards the Galactic centre result from the fact that low Galactic latitudes are usually excluded in hot subdwarf surveys. This means that the line of sight quickly extends beyond the thin disk, which increases the contribution of the thick disk. This selection effect exists because hot subdwarfs are usually identified by their blue colors, which is more difficult at low Galactic latitudes where many stars are heavily reddened and where crowding presents an additional problem. A volume-complete sample of hot subdwarfs could remedy such selection effects. The sample of hot subdwarfs with good *Gaia* parallaxes does not extend beyond $|z| \approx 2$ kpc, which means that some halo substructures like the Sagittarius stream are excluded a priori: they are too distant (Naidu et al. 2020). Selection effects are less important for the relative z-histogram shown in the top right panel of Fig. 4.2.6. The relative

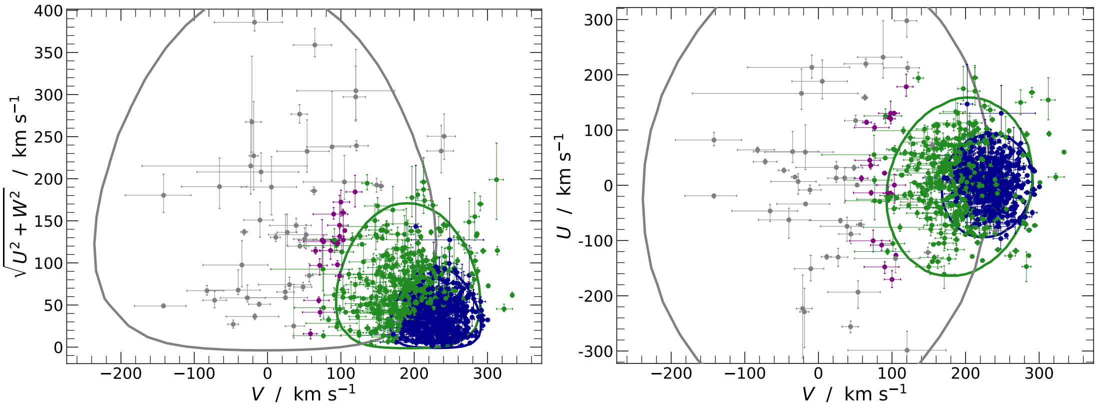

Figure 4.2.8. Distribution of the known hot subdwarf sample in the Toomre- and U-V diagrams. The 2-σ contours in the velocity diagrams are based on the results of Anguiano et al. (2020). The colors are the same as in Figs. 4.2.5 and 4.2.6.

fraction of thin disk stars exceeds 60 % at $|z| \lesssim 500$ pc, while the thick disk begins to dominate at $|z| \gtrsim 1$ kpc. The fraction of halo stars quickly approaches that of the thick disk at $|z| \gtrsim 3$ kpc.

As shown in Fig. 4.2.7 (top), the distribution of stars classified as thin and thick disk in the V-histogram is almost identical to the best-fit Gaussian models in Fig. 4.2.5 – the fraction of thick disk stars in the overlap between thin and thick disk is not suppressed, as would be the case using the contour-based method of Luo et al. (2021). A small fraction of stars is observed at $V > 300\,\mathrm{km\,s^{-1}}$, also seen in the logarithmic V-histograms in Fig. 4.2.5. While these stars are classified as thick disk, the probability density for the thick disk at $V > 300\,\mathrm{km\,s^{-1}}$ is low. They are not typical of any of the four considered populations and might be affected by bad data.

Although the eccentricity was not used for the classification, all four considered populations are well separated in the eccentricity histogram (Fig. 4.2.7, bottom). Almost all stars classified as thin disk have $e < 0.3$, while thick disk stars dominate between $e = 0.25$ and 0.6, but also contribute at lower eccentricities. Most stars in the “fourth” population have eccentricities between 0.5 and 0.8. Halo stars begin to dominate at $e > 0.8$, but are also present at low eccentricities.

The Toomre and U-V diagrams for the known hot subdwarf sample are shown in Fig. 4.2.8, where stars are coloured according to their most probable population membership. These diagrams also include 2σ contour lines from Anguiano et al. (2020), which seem to match the distributions of classified hot subdwarfs fairly well. In both diagrams, the “fourth” population seems to represent an over-density of stars in between the thick disk and the halo population. This is also the case in the L_z-e and E_{tot}-L_z diagrams shown in Fig. 4.2.9. The “fourth” fit component best matches the properties of the physical metal-weak thick disk population at $[\mathrm{Fe/H}] < -1$, for example as described by Naidu et al. (2020). The distinction between the metal-weak thick disk and the in-situ halo is however not strict because their kinematic properties overlap. Interestingly, Dorsch et al. (2021) have recently discovered that the heavy-metal sdOB EC 22536−5304 has a metal-poor sdF-type companion at $[\mathrm{Fe/H}] = -1.9$ and shares the kinematic properties of the metal-weak thick disk. This analysis was performed as part of this thesis and is presented in Sect. 3.3. Additional stars that fall in the “fourth” population are the bright heavy-metal iHe-sdOB Feige 46 (see also Latour et al. 2019a) and the extreme He-sdO Ton S 415.

Several halo stars are observed at high eccentricity and form an approximately “sausage”-shaped feature in the U-V diagram, centred around $V = 0\,\mathrm{km\,s^{-1}}$. These stars share the properties of the “Gaia-Sausage-Enceladus” (GSE) structure, which was similarly identified by Belokurov et al. (2018). The GSE consists of the remains of a dwarf galaxy that is thought to have merged with the Milky Way about 10 Gyr ago (Helmi et al. 2018). Its stars were found to have ages between 10 and 12 Gyr and a mean metallicity of $[\mathrm{Fe/H}] = -1.2$ (Feuillet et al. 2021). Because the kinematics of the Gaia-Enceladus population and those of the “in-situ” halo overlap, it is impossible to tell whether a high-eccentricity star is part of one or the other population. The brightest stars in the known hot subdwarf sample at $e > 0.75$ are the eHe-sdO

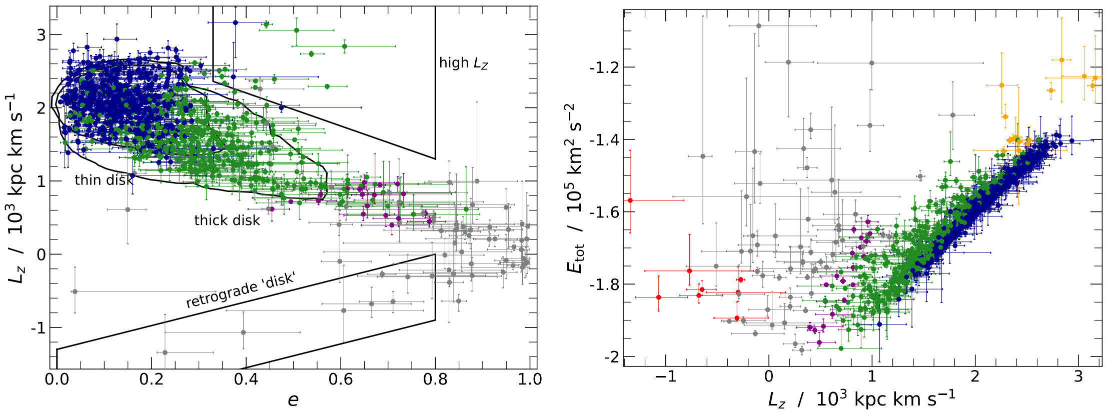

Figure 4.2.9. Like Fig. 4.2.8, but for the L_z-e and E_{tot}-L_z diagrams. The 2-σ contours in the L_z-e diagram are based on the sample of Buder et al. (2021), as shown in Fig. 4.2.2. In the E_{tot}-L_z diagram, the "high-L_z" population is marked in orange and the "retrograde disk" is coloured red, as defined by the boxes in the L_z-e diagram. The total energy is influenced by the choice of the Galactic potential, which can lead to offsets compared to literature analyses.

GALEX J191109.3-140654, the heavy-metal sdOB LS IV−14°116 (e. g. Randall et al. 2015), and the sdO GALEX J061937.8+343030. The sdO CBS 461 is the star with the highest orbital energy.

Some retrograde halo stars are observed at low eccentricity and form a "retrograde disk". Here, this "retrograde disk" is defined by a box in the L_z-e diagram (Fig. 4.2.9, left), covering eccentricities from $e = 0$ to 0.8 at negative L_z. Stars that fall in this box are coloured red in the E_{tot}-L_z diagram (Fig. 4.2.9, right). Most of these stars have a low orbital energy, so orbit deep in the Galactic potential. They may simply be associated with the high-α in-situ halo, with typical initial metallicities between [Fe/H] = −1 and 0 (Naidu et al. 2020) They also share some properties of the "Thamnos" structure discovered by Koppelman et al. (2019), which is also retrograde at low total orbital energies and relatively low eccentricities. According to Naidu et al. (2020), this substructure features a metallicity of [Fe/H] ≈ −1.9. Notable members of the "retrograde" disk are the eHe-sdO PG 1444+076 at $e = 0.39^{+0.12}_{-0.17}$ and the sdB Ton 1059 at $e = 0.23^{+0.10}_{-0.02}$.

In the L_z-e diagram (Fig. 4.2.9, left), the aforementioned high-V stars are located at high L_z and have eccentricities between about 0.2 and 0.6. To limit the overlap with the thin disk, a box for high-L_z stars in the L_z-e diagram was defined starting from $e = 0.33$. Stars within this box tend to have high total energies in the E_{tot}-L_z diagram, where they are marked in orange. These stars do not match the characteristics of any population and none of them are well studied; bright examples include the sdO PG 0314+180, UCAC4 682-031668, and UCAC4 653-001357.

4.2.7 Relation between kinematic and atmospheric parameters

The atmospheric parameters of many stars in the sample of Culpan et al. (2022) are known from spectroscopic analyses collected from the literature. This opens up the opportunity to study the relation between kinematic and atmospheric classes, analogous to the work of Martin et al. (2017) and Luo et al. (2021). A rough classification in iHe-sdB, sdB, sdO, iHe-sdOB, and eHe-sdO stars is shown in the left panels of Fig. 4.2.10 for both the known hot subdwarf and Luo et al. (2021) samples. This classification based on T_{eff} and helium abundance is the same as in Sect. 4.1.

In both samples, the kinematic constitution of the He-poor sdB and sdO populations is rather similar (Fig. 4.2.10, right panels). This is consistent with the widely accepted notion that many He-poor sdO stars are in a post-EHB evolutionary stage (Dorman et al. 1993). Because the kinematic properties of the iHe-sdOB population are clearly different from the He-poor sdBs, the often suggested evolutionary connection between these populations seems unlikely. Note that the many composite-SED iHe-sdOBs identified in Sect. 4.1 were not considered for the known hot subdwarf sample. In contrast, the kinematic properties of the remaining iHe-sdOBs and eHe-sdOs are identical within their uncertainties, which would allow the possibility of an evolutionary connection or their formation through coeval formation channels. The increased fraction of thick

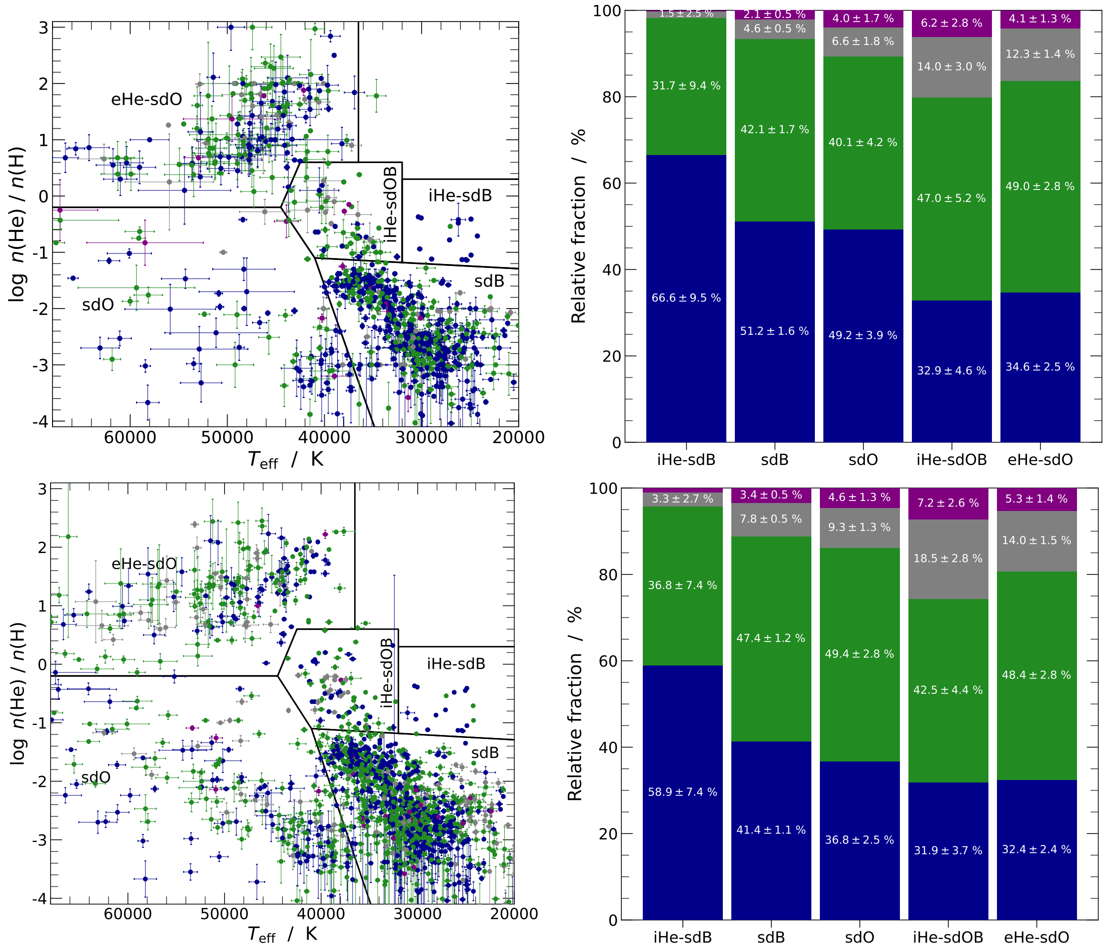

Figure 4.2.10. *Left:* Classification of the iHe-sdB, sdB, sdO, iHe-sdOB, and eHe-sdO populations, separated by black lines. Colours refer to the Galactic populations as in Fig. 4.2.6. *Right:* Fractions of Galactic thin disk, thick disk, halo, and "fourth" populations for these five spectroscopic classes in the known hot subdwarf sample (top) and the re-classified sample of Luo et al. (2021, bottom). Spectroscopic uncertainties and membership probabilities of individual stars were estimated using MC calculations, disregarding the fit uncertainties stated in Table 4.2.2.

disk and halo stars among the iHe-sdOBs and the eHe-sdOs suggests that these classes are on average older compared to the helium-poor sdB population. Old age is expected for a population of helium burning stars that was formed through the merging of two low-mass white dwarfs, given that such events are thought to be preceded by millions of years up to several Gyrs of gravitational wave emission, with delay times depending on the mass of the merging white dwarfs and their initial separation (Iben & Tutukov 1986b). As the only sub-population of hot subdwarfs discussed here, helium-rich sdB stars cooler than about 32000 K are predominantly thin disk stars, which indicates that these stars are on average younger than other hot subdwarf stars. These findings are consistent with the studies of Martin et al. (2017) and Luo et al. (2021).

Figure 4.2.11 conveys similar information: the fraction of spectroscopic classes among the kinematically defined populations. The largest spectroscopic class, the helium-poor sdBs, contributes to all kinematic populations. As expected, the fraction of helium-rich sdOB and sdO stars in the known hot subdwarf sample increases considerably in the halo, to a combined value of 49 %. This bears some resemblance to the results of Latour et al. (2018b), who found their sample of hot subdwarfs in the metal-poor and old globular cluster ω Cen to be dominated by intermediate He-sdOBs. However, the fraction of eHe-sdOs in the halo population is much larger than that of iHe-sdOBs, which is a clear difference to the ω Cen population. The re-classified sample of Luo et al. (2021) contains more He-poor sdB stars and shows less differences between the kinematic population. The latter may be related to larger uncertainties in their kinematic classification due to less strict quality cuts compared to the known hot subdwarf sample.

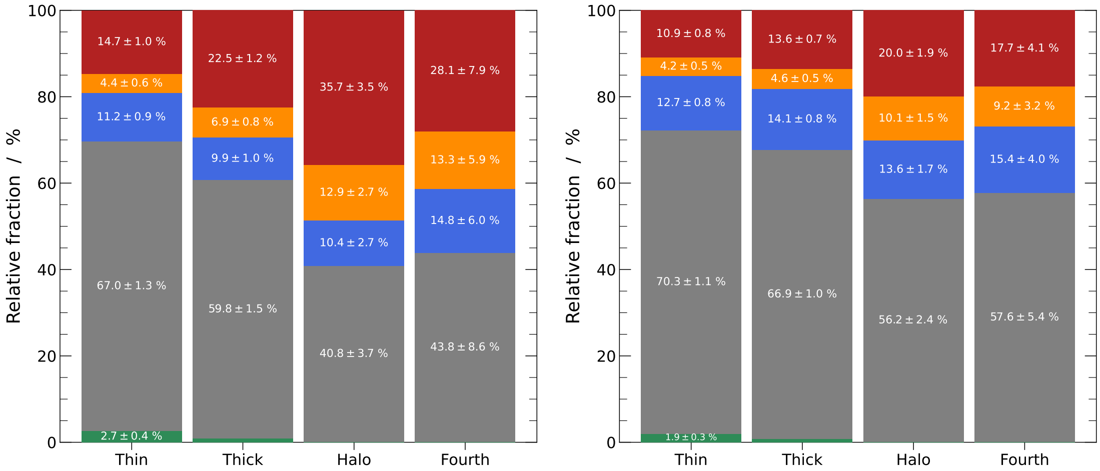

Figure 4.2.11. Like the right panels of Fig. 4.2.10, but for the fractions of iHe-sdB (green), sdB (grey), sdO (blue), iHe-sdOB (orange), and eHe-sdO (red) spectral classes among the four kinematic populations. The known hot subdwarf sample is shown on the left, while the re-classified sample of Luo et al. (2021) is shown on the right.

Figure 4.2.12 shows the distribution of classified stars in the known hot subdwarf sample in T_{eff} and helium abundance. The combined bin heights in the absolute diagrams on the left are determined by sample selection effects. This bias does not exist for the relative histograms shown on the right, which provide more significant insights in the relation between kinematic and spectroscopic population memberships. As already seen in Fig. 4.2.10, He-poor stars are more likely to be classified as thin disk than thick disk, with a ratio of about 60-to-40. This ratio reverses for He-rich stars. In addition, the number of halo and "fourth" stars with $\log n(\mathrm{He})/n(\mathrm{H}) < -1$ is far below 10 %. The relative contribution of the halo and "fourth" population increases sharply at $\log n(\mathrm{He})/n(\mathrm{H}) > -1$, which again indicates that kinematically hot and likely old stars have a larger contribution to the He-rich population. The situation is similar in the T_{eff} histogram, where the contribution of the thick disk and halo increases at $T_{\mathrm{eff}} \gtrsim 38000\,\mathrm{K}$.

4.2.8 Conclusions and Outlook

The analysis presented in this section provided estimates for the fraction of thin disk, thick disk, and halo stars in a large and high-quality sample of hot subdwarf stars based on the catalogue of Culpan et al. (2022). As listed in Table 4.2.2, the thin and thick disk each contribute about 44 % while halo stars seem to represent between 5 % and 10 % of the sample. A fourth population was required to match the distribution of hot subdwarfs in the current Galactic velocity space. This population is intermediate between the halo and thick disk populations and might be related to the metal-weak thick disk. Because the sample is not volume-complete, these numbers are affected by sample selection effects like missing stars in the Galactic plane and at distances $d > 2\,\mathrm{kpc}$.

The sample of hot subdwarfs contains stars from many different kinematic structures and stellar populations. The four populations discussed here are likely comprised of several subpopulations. One may therefore consider to replace the simple Gaussian model components used in the histogram fit with either more complex models or data-driven models as used by Anguiano et al. (2020), which would better represent the observed kinematics in large samples.

Membership probabilities to each of the four considered populations were assigned to all stars. This information can be combined with evidence from spectral, light curve, and SED analyses to constrain the evolutionary history of these stars. The relation between atmospheric parameters and kinematic population membership was briefly analysed in Sect. 4.2.7. The results are consistent with the findings of Martin et al. (2017) and Luo et al. (2021): in particular the helium-poor and helium-rich populations of hot subdwarfs show different kinematic properties. Helium-rich stars at $T_{\mathrm{eff}} > 32\,000\,\mathrm{K}$ seem to have a larger contribution by the thick disk and halo populations. The opposite is true for cooler helium-rich stars, which seem to be dominated by the

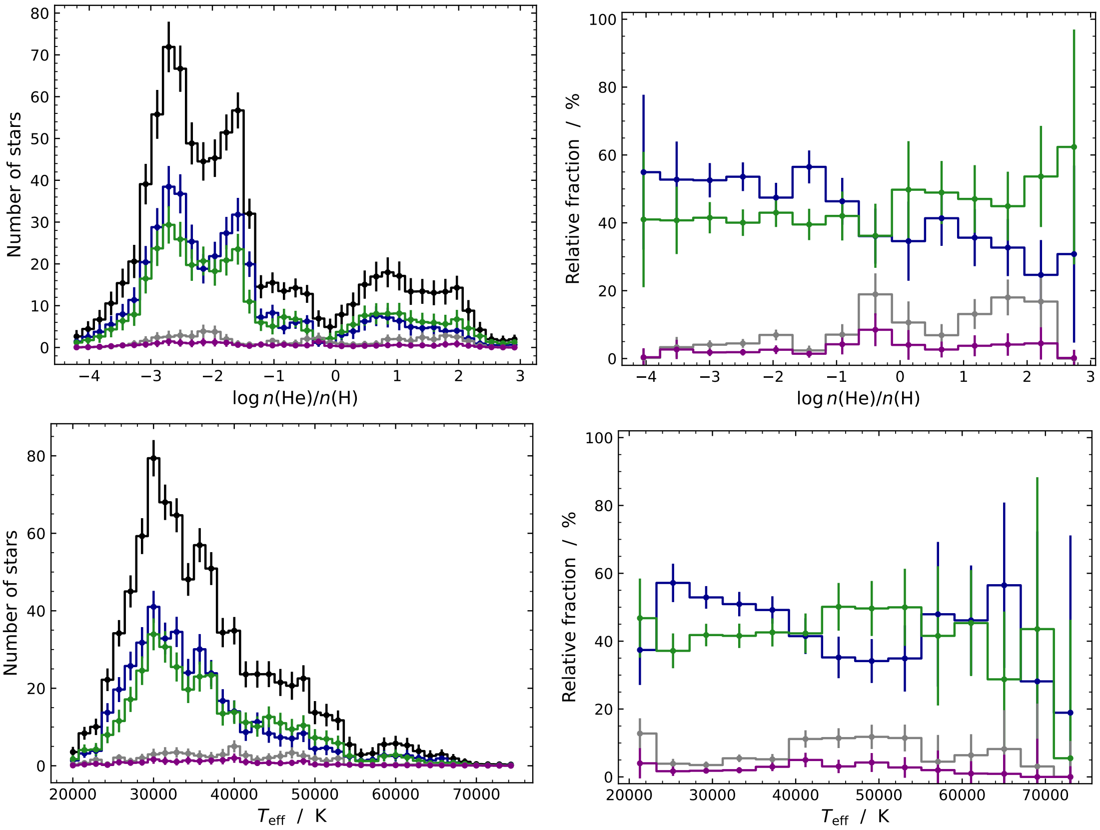

Figure 4.2.12. Like Fig. 4.2.6, but for the atmospheric parameters effective temperature T_{eff}, helium abundance $\log n(\mathrm{He})/n(\mathrm{H})$ of the known hot subdwarf sample.

thin disk, as already found by Luo et al. (2021). The differences in the contribution of kinematic populations to each spectroscopic class can be seen as an indicator of differing age or origin. Therefore, it seems likely that old stellar populations have larger fractions of iHe-sdOB and eHe-sdO stars. In addition, a general evolution of iHe-sdOB stars to become helium-poor sdB stars through atmospheric diffusion seems to be unlikely. Complementary and independent evidence of this was provided by Geier et al. (2022), who found the close binary fraction of iHe-sdOB and eHe-sdO stars to be much lower than that of helium-poor sdB stars.

While the analysis approach presented here can in many ways be considered an improvement over those of Pauli et al. (2006), Martin et al. (2017), or Luo et al. (2021), there is much room for future improvements, which should include the calculation and use of orbital actions J_R and J_z in addition to $J_\varphi = L_z$. Orbital actions represent important kinematic diagnostics for finding substructure in the Galactic halo (Lane et al. 2022). Furthermore, the Galactic models of Irrgang et al. (2013) used for the calculation of orbits should be updated using modern observational constraints such as the Galactic rotation curve of Eilers et al. (2019).

Neunteufel et al. (2021, 2022) have recently provided predictions for the kinematic properties of He-sdO/B stars ejected from single degenerate He-donor SNe. While all stars in the cleaned known hot subdwarf sample are bound to the Milky Way, the sample may still contain ejected stars and a larger kinematic sample of hot subdwarfs could be compared to these predictions. Most unbound stars like the known hypervelocity subdwarf US 708 are likely rejected from the current sample because they are too distant to meet our parallax quality criterion. Large surveys like 4MOST (de Jong et al. 2019), WEAVE (Dalton et al. 2014), and SDSS-V (Kollmeier et al. 2017) will take spectra of many more hot subdwarf stars and provide radial velocities for kinematic analyses. This will enable us to increase the size of the present kinematic studies manyfold. Such samples could further be extended beyond the about $d = 3\,\mathrm{kpc}$ achievable with *Gaia* EDR3 parallaxes by using spectroscopic distances if masses are assumed. In addition, *Gaia* DR4 will provide more accurate parallax distances. This will allow more detailed studies of hot subdwarfs in the halo, given that the halo begins to dominate at $|z| \gtrsim 3\,\mathrm{kpc}$ – just at the limit of *Gaia* EDR3.

Chapter 5

Summary and outlook

The hot subdwarf population encompasses many distinct varieties of hot evolved stars and so their origin and evolution must also be diverse. Many hot subdwarfs reside in binary systems. Close binaries (periods of hours to few days) host white dwarf or low mass stars, while wider binaries mostly have F/G/K-type main sequence companions. These systems must have formed through common envelope or Roche lobe overflow evolution. Single hot subwarfs are either formed by a merger involving at least one helium-core white dwarf or through internal mixing processes during the post-RGB evolution. It was the aim of this thesis to provide an observational overview of the properties of hot subdwarfs as an important step towards understanding their complex formation and evolution. Therefore, both the overall hot subdwarf population and several peculiar stars were studied in detail. These analyses and their results are summarised in the following.

5.1 Chemical footprints of stellar evolution

Hot subdwarf stars are chemically peculiar as a result of the interplay of nucleosynthesis, mixing and diffusion processes, as well as magnetic fields and mass loss. Their surface metal compositions range from very metal-poor to carbon-, nitrogen-, or oxygen-rich, and some stars even show extreme enhancement in heavy elements like zirconium and lead. Because stellar evolution can strongly affect the surface composition, such abundance patterns measured by detailed spectral analysis provide important information on the formation of hot subdwarf stars.

He-poor sdOB stars as a reference. Several of the detailed spectral analysis performed as part of this work dealt with peculiar helium-rich sdOB and sdO stars. However, it is important to also understand the more common He-poor sdOB stars as a reference. This is why we studied the surface abundances of CPD −56° 464 and the Schweizer-Middleditch (SM) star. Archival far-UV spectra are available for both stars, but had not been analysed before: the FUSE spectrum of CPD −56° 464 is among the best of any hot subdwarf while the SM Star was observed by both FUSE and HST/STIS-E140M, albeit at lower signal-to-noise. These spectra enabled the determination of 27 and 28 abundances for CPD −56° 464 and the SM Star, respectively. The surface compositions of both stars are similar. Both show a distinct CNO-cycle pattern and strong heavy metal lines, including As, Se, Kr, Y, Mo, and Sb, which were identified here for the first time in any He-poor sdOB. The heavy metal abundances are high compared to the Sun, ranging from 100- to 1000-fold enrichment, but they are low when compared to heavy metal stars like LS IV−14°116. Like several other He-poor sdOB stars at $T_{\rm eff} \gtrsim 32\,000$ K, the SM Star is completely devoid of silicon. This seems to be caused by the combined effect of diffusion and weak stellar winds, even if the details are not well understood. In contrast, the silicon abundance of CPD −56° 464, about one third solar, is among the highest observed in helium-poor sdOB stars.

Detailed studies of heavy metal stars. The next peculiar stars studied here are the zirconium-rich iHe-sdOB stars LS IV−14°116 and Feige 46. Many lines in their high-quality UVES spectra were identified with transitions of Ga III, Ge III-IV, Se III, Kr III, Sr II-III, Y II-III, Ga III, Zr III-IV, and Sn IV, many of which have not yet been observed in any star. The surface abundance of 19 metals in both stars were found to be nearly identical, except for slight differences in light metals (higher in Feige 46) and Zr, Sn, and Pb (lower in Feige 46). These patterns differ significantly from those of typical He-poor hot subdwarfs with similar effective temperatures, like CPD −56° 464 and the SM Star. The extreme overabundance of heavy metals (>4 dex above solar) is likely caused by strong atmospheric diffusion processes that affect both stars similarly. The C, N, O, and Ne abundances might be less affected by diffusion, in which case the fact that they are similar in both stars would provide evidence of a shared evolutionary origin.

The evolutionary models of Miller Bertolami et al. (2022) provide a promising scenario specifically for LS IV−14°116-like stars: the merging of a hybrid He/C/O white dwarf with a more massive helium-core white dwarf. This scenario is not only able to reproduce the correct atmospheric parameters and the confirmed single-star nature, but also their unique pulsations. Already Saio & Jeffery (2019) suggested C/O-enrichment in the envelope as the driver of pulsation in LS IV−14°116 and the proposed merger is naturally able produce exactly these over-abundances. In addition, the kinematic analysis performed here confirmed that both stars are part of the Galactic halo population. This is also consistent with the scenario of Miller Bertolami et al. (2022), given that the initial binary systems were likely old at the time of their merging.

An additional analysis was performed for the most lead-rich star known today: the helium-rich sdOB EC 22536−5304. This analysis shows that EC 22536−5304, in contrast to LS IV−14°116 and Feige 46, is part of a binary system. Its metal-poor subdwarf F companion is the most metal-poor known companion to a hot subdwarf star at $[\mathrm{Fe/H}] = -1.95 \pm 0.04$ and $[\alpha/\mathrm{Fe}] = +0.40 \pm 0.04$. This low metallicity and strong α-enhancement suggests an age of more than 10 Gyr for the system. The lead abundance obtained here corresponds to an extreme enrichment of $+6.3 \pm 0.3$ dex relative the Sun, which is hard to explain by pure diffusion. The enrichment is even larger with respect to the low initial metallicity of the system, namely that of the sdF.

Radial velocity variations, although poorly sampled at present, indicate that the binary system has an orbital period of about 457 days. The system was therefore formed through stable Roche lobe overflow. It represents the most extreme case of metal-poor post-RLOF hot subdwarf binaries and has the shortest orbital period among such systems, which may help constrain future RLOF models. A similar but helium-poor lead-rich sdOB in a binary system was identified simultaneously by Németh et al. (2021). The existence of these stars in post-RLOF binary systems shows that a stellar merger is not required to form lead-rich hot subdwarfs.

BD −7° 5977: a testbed for the RLOF scenario. BD −7° 5977 is one of the few known hot subdwarfs with a subgiant companion. Because of its brightness, the system was extensively observed with high-resolution far-UV, optical, and infrared spectrographs. This allows us to test the RLOF scenario by searching for chemical signatures of material transferred from the progenitor during the RLOF phase. The detection of a lowered $^{12}\mathrm{C}/^{13}\mathrm{C}$ isotopic ratio holds the key, which is best derived from high-resolution infrared spectroscopy in the K-band.

Due to its large radius of about $8\,R_\odot$, the companion dominates the optical and infrared ranges, which complicates the analysis of the system. It is the combination of all observed spectra with the system's SED that finally allowed us to derive the atmospheric properties of both stars. The $^{12}\mathrm{C}/^{13}\mathrm{C}$ ratio of the K-type companion is lowered to about 28 compared to the solar value of about 89. In addition, the companion is enriched in nitrogen, while its scaled carbon abundance is sub-solar. These features can all be explained by material processed by hydrogen fusion in the CNO bi-cycle. While this CNO-processed material might have been brought to the surface of the K-type by mass transfer from the sdOB's progenitor, it is likely that part of it originates from the K-type itself: convective mixing during the first dredge-up phase brings material from the hydrogen burning shell to the surface. To obtain more conclusive evidence for external pollution, subdwarf binaries with less evolved companions have to be targeted for K-band spectroscopy.

5.2 Discovery of magnetic He-sdO stars

Motivated by the presumed post-merger nature of most He-sdO stars and the sdB's similarity to the magnetic Ap/Bp stars, several surveys have searched for magnetic fields in hot subdwarf stars of all types. However, none of the about 40 stars observed using spectropolarimetry were found to host a magnetic field, with upper limits of about 1 kG. It was a low-resolution spectrum that serendipitously led to the discovery of the first magnetic hot subdwarf to be analysed: the He-sdO J0809-2627. Its analysis here was based on a follow-up X-shooter spectrum, which showed strongly Zeeman-split hydrogen, helium, and metal lines, reproduced by a strong magnetic field of $B \approx 350\,\mathrm{kG}$. While this X-shooter spectrum was reasonably well reproduced by our simple homogeneous field model, two UVES spectra taken nine months later clearly require a non-homogeneous geometry, which implies that the field geometry is variable, likely due to (slow) rotation. All spectra are consistent with atmospheric parameters of $T_{\mathrm{eff}} = 44900 \pm 1000\,\mathrm{K}$, $\log g = 5.93 \pm 0.15$, and a peculiar helium abundance of $\log n(\mathrm{He})/n(\mathrm{H}) = +0.28 \pm 0.10$. They also require a consistent radial velocity of $33 \pm 2\,\mathrm{km\,s^{-1}}$, which seems to exclude a binary nature. We have combined the spectroscopic atmospheric parameters with a photometric fit and the *Gaia* parallax to derive a stellar radius and luminosity that are typical for He-sdOs and place the star on the helium main sequence. Its mass of $0.93^{+0.44}_{-0.30}\,M_{\odot}$, although uncertain, appears to be remarkably high. All of these results combined provide overwhelming evidence that J0809-2627 is the remnant of a double degenerate merger. Nevertheless, the star is a slow rotator at $v_{\mathrm{rot}} \sin i \lesssim 25\,\mathrm{km\,s^{-1}}$.

Even before J0809-2627, three magnetic He-sdOs were discovered in the SDSS survey, but were never analysed. The first spectral analysis for these stars was performed here. Over a time span of several years, each star was observed multiple times using the WHT/ISIS spectrograph. All three stars closely resemble the prototype J0809-2627: their T_{eff} and $\log g$ place them on the zero-age helium main sequence and they share its unusual intermediate helium abundance. In addition, they have field strengths from 300 kG to 500 kG and seem to lack any radial velocity variability, which provides further evidence for their formation via a merger channel. The four magnetic He-sdOs also all show a roughly 60 Å wide and "V"-shaped absorption feature centred at 4631 Å, the origin of which remains unidentified. The occurrence of three magnetic He-sdOs in the SDSS sample suggests lower limits to the magnetic fraction of $0.15 \pm 0.10\,\%$ in the general hot subdwarf population and $1.8 \pm 1.2\,\%$ in the He-sdO population. The existence of now four magnetic He-sdOs provides evidence for merger-induced magnetic fields. The stars are likely to evolve to become white dwarfs with field strengths of 50 to 150 MG, assuming magnetic flux conservation.

5.3 Hot subdwarf population characteristics

The *Gaia* satellite has revolutionised many fields of astronomy, for example through its discovery of substructure in the Galactic Halo kinematics or the discoveries of multiple sequences in the white dwarf and Halo populations. Its measurements include photometry, proper motions, and parallaxes for more than a billion stars. Combined with large ground-based spectroscopic surveys and other photometric surveys, this huge dataset finally allows the study of statistically significant samples of the comparatively rare hot subdwarf stars. In the second part of this thesis, two analyses based on these datasets were performed. The analysis of spectral energy distributions (SEDs), from the UV to the infrared, combined with *Gaia* parallaxes provided fundamental stellar parameters and characterised the population F/G/K-type companions to hot subdwarfs. In addition, the computation of Galactic orbits based on radial velocities and *Gaia* astrometry provided age estimates for the various sub-populations of hot subdwarfs.

Photometric analysis. We have performed SED fits for the sample of spectroscopically identified hot subdwarfs (Geier 2020; Culpan et al. 2022). Hot subdwarfs with F/G/K-type companions are easily detectable due to their double-peaked SEDs. Here, 1518 known hot subdwarfs are classified as such composite-SED systems, which suggests that 27 % of all hot subdwarfs have cool MS companions. Since the known sample of hot subdwarfs is biased against these systems, this value may be regarded as a lower limit for the local hot subdwarf population. The population of cool companions is dominated by F-type and K-type stars on the main sequence. There seems to be an unexpected dearth of G-type companions that can not be explained by selection effects. This double-peaked T_{eff} distribution can be reproduced by two overlapping Gaussian components.

While it seems likely that most, if not all of these systems were formed by Roche lobe overflow, it is unclear why there should be two distinct populations. Current binary population synthesis models fail to reproduce the observed companion population. These models should be updated and matched to these new observational results in order to advance our understanding of Roche lobe overflow and the formation of hot subdwarf stars.

Precise *Gaia* parallax measurements are available for the majority of the spectroscopically identified hot subdwarf sample. Combined with the angular diameters from the SED, this allowed us to determine radii and luminosities, as well as masses using spectroscopic surface gravity measurements. The results were discussed by spectral class, that is for the He-poor sdB, He-poor sdO, iHe-sdB, iHe-sdOB, and eHe-sdO classes. As already suggested by Németh et al. (2012), there seem to be two main groups of He-poor sdB stars on the extreme horizontal branch: a cooler one centred at about 28 000 K (EHB1) and a hotter one at about 33 000 K (EHB2). As predicted by theory, our results show that these two groups evolve into He-poor sdOs, which also appear in two groups, namely a compact population of post-EHB2 stars that is located below the He-MS and a group of less compact post-EHB1 stars. More than 90 % of eHe-sdO stars show non-composite SEDs, which excludes F/G/K-type companions. They typically have masses between 0.5 $M_\odot$and 1 $M_\odot$, and are therefore on average more massive than other types of hot subdwarfs. This is strong evidence for their formation through merger channels, given that they also lack short-period radial velocity variability. The population of iHe-sdOBs is also split into two subgroups: a luminous one with a low fraction of composite-colour binaries and a more compact group that features a high fraction of such binaries. The more luminous iHe-sdOBs therefore seem to share the evolution of eHe-sdO stars and are formed by low-mass white dwarf mergers.

Kinematic analysis. Another way to characterise any star is its Galactic orbit, which is closely related to its age: stars in the Galactic halo and thick disk are likely to be older than most stars in the Galactic thin disk. *Gaia* DR3 provided position, parallax, and proper motion measurements for thousands of hot subdwarfs. The full six-dimensional phase space coordinates needed for the calculation of Galactic orbits further require knowledge of radial velocities, which were not provided by *Gaia* for these for hot stars. Our kinematic analysis was therefore performed for hot subdwarfs with literature radial velocities in the catalogue of Culpan et al. (2022). The Galactic radial (U), tangential (V), and vertical (W) velocity distributions were then used to estimate the fraction of thin disk (43 %), thick disk (44 %), and halo stars (10 %) in a combined χ^2 fit, where each population was represented by a Gaussian distribution. A fourth population, intermediate between the halo and thick disk, was required to contribute about 3 % to sample. While this population might be related to the metal-weak thick disk, the idea of distinct Galactic components is a simplification, given that there are many different kinematic structures in the Milky Way.

Using a Gaussian component-based method, kinematic population probabilities were assigned to all stars. These can directly be combined with atmospheric parameters from the literature, stellar parameters from the SED fits, and *Gaia* parallaxes. In particular the helium-poor and helium-rich hot subdwarfs show different kinematic properties: helium-rich stars at $T_\mathrm{eff} > 32\,000$ K have a large contribution by the thick disk ($\gtrsim$48 %) and halo populations ($\gtrsim$13 %), while He-poor sdB and sdO stars both have lower thick disk ($\approx$41 %) and halo ($\approx$5 %) factions. Cooler He-rich stars differ from both He-poor and hotter He-rich stars: they are dominated by the thin disk ($\approx$67 %).

Spectroscopic populations that share kinematic properties were likely formed by the same processes or are connected by evolutionary links. The latter is the case for most He-poor sdO stars, which seem to evolve from He-poor sdB stars. Given its large thin disk fraction, the iHe-sdB population must be the youngest of the hot subdwarf populations. In contrast, the iHe-sdOB and eHe-sdO populations seem to be comparable in age and are both older than the He-poor sdB and sdO populations. This excludes stars with composite SEDs, which were not considered in the kinematic analysis. Given the difference in kinematics, it is unlikely that most iHe-sdOB stars evolve to become He-poor sdB stars through atmospheric diffusion. This agrees with the results of a search for radial velocity variability by Geier et al. (2022), who found many He-poor sdBs in close binary systems, but only very few iHe-sdOB and eHe-sdO stars.

5.4 Outlook

Several of the methods used and analyses performed as part of this thesis represent excellent starting points for further studies of hot subdwarf stars. This final section discusses some of the most promising perspectives.

Chemical footprints and magnetic fields. Follow-up observations of the enigmatic heavy-metal subdwarfs LS IV−14°116 and EC 22536−5304 with HST's STIS-E140M spectrograph are in progress and will finally allow us to complete the study of their surface composition, including their iron abundances. They will very likely also identify additional heavy metals. Atomic data calculations specifically for these spectra are ongoing, as are theoretical predictions for the creation of heavy elements during the initial helium-flashes. Heavy metal stars are not the only peculiar hot subdwarf stars that would profit from far-UV spectroscopy – detailed abundance patterns of sdO stars can only be measured from their strong lines in the UV range. These surface compositions represent essential test cases for theoretical models of the formation and evolution of hot subdwarf stars, from close binary systems to stellar mergers. It is therefore necessary to apply for HST time to extend our studies to cover additional hot subdwarfs of all types.

As the next step in the study of magnetic He-sdO stars, the currently available SDSS and LAMOST databases should be checked for magnetic hot subdwarf stars by performing χ^2 fits with magnetic model spectra – such efforts are ongoing. Unlike the previous manual inspection, this method is able to detect weaker magnetic fields for which the Zeeman components are not quite resolved. Ongoing and future large surveys such as SDSS-V (Kollmeier et al. 2017), WEAVE (Dalton et al. 2014), DESI (DESI Collaboration et al. 2016), and 4MOST (de Jong et al. 2019) will very likely discover more magnetic merger products and allow statistically significant comparisons to theoretical predictions. The currently available models for low-mass WD mergers do not consider magnetic fields and should therefore be updated. Metal abundance predictions from these models could then be compared to measurements from HST spectra.

Binarity and stellar parameters. Because photometric data are widely available and the SED fit approach is quick, this method can be applied to samples of more than 100 000 stars. It should therefore be extended to all *Gaia* colour-selected candidate samples, such as the 60 000 hot subdwarfs of Culpan et al. (2022), the BHB sample of Culpan et al. (2021), and the extremely low-mass white dwarfs of Pelisoli & Vos (2019). These candidate samples should be further extended towards the main sequence and into the Galactic disk. Here, the SED method has the advantage that interstellar reddening can be estimated independently of reddening maps.

The mass distribution of hot subdwarfs has been predicted by population synthesis models, but for a long time, these predictions could not be tested due to a lack of observational masses of sufficient quality and quantity. The main challenge is to derive surface gravities of sufficient precision for a large sample. As a next step, the hot subdwarfs in the combined SDSS and LAMOST surveys should be re-analysed using a consistent spectral fit method. This analysis would provide more consistent measurements of atmospheric parameters and thus allow the identification of substructure in hot subdwarf populations. More consistent surface gravity measurements would significantly increase the precision of the resulting SED/parallax-based mass distributions.

Galactic kinematics. The strongest limitation for kinematic analyses of hot subdwarf is the scarcity of the multi-epoch radial velocity measurements, given the large fraction of close binary systems. In addition, the sample could be extended to more distant objects when spectroscopic distances become available. The upcoming large spectroscopic surveys will provide the necessary radial velocity and surface gravity measurements required for this. Larger samples could not only be used to search for hot subdwarfs in the various halo substructures discovered by *Gaia*, but also to search for runaway hot subdwarfs. The kinematic properties of He-sdO/B stars ejected from single degenerate He-donor SNe were recently simulated by Neunteufel et al. (2021, 2022), but could not yet be tested due to the limitations of *Gaia* EDR3 parallaxes. *Gaia* DR4 will provide more accurate parallax distances, allowing us to peer deeper into the Galactic halo, where such runaways are expected.

Chapter 6

Bibliography

Abbott T. M. C., et al., 2018, ApJS, 239, 18
Abbott T. M. C., et al., 2021, ApJS, 255, 20
Abia C., Palmerini S., Busso M., Cristallo S., 2012, A&A, 548, A55
Afşar M., Sneden C., For B. Q., 2012, AJ, 144, 20
Ahmad A., Jeffery C. S., 2005, A&A, 437, L51
Ahmad A., Behara N. T., Jeffery C. S., Sahin T., Woolf V. M., 2007, A&A, 465, 541
Alam S., et al., 2015a, ApJS, 219, 12
Alam S., et al., 2015b, ApJS, 219, 12
Allard F., Wesemael F., Fontaine G., Bergeron P., Lamontagne R., 1994, AJ, 107, 1565
Allen C., Santillan A., 1991, Rev. Mexicana Astron. Astrofis., 22, 255
Allende Prieto C., Lambert D. L., Hubeny I., Lanz T., 2003, ApJS, 147, 363
Aller L. H., Greenstein J. L., 1960, ApJS, 5, 139
Almeida-Fernandes F., et al., 2022, MNRAS, 511, 4590
Alonso-Medina A., Colón C., Zanón A., 2009, MNRAS, 395, 567
Alonso-Medina A., Colón C., Porcher P., 2011, Atomic Data and Nuclear Data Tables, 97, 36
Althaus L. G., Miller Bertolami M. M., Córsico A. H., 2013, A&A, 557, A19
Altmann M., Edelmann H., de Boer K. S., 2004, A&A, 414, 181
Andrae R., Schulze-Hartung T., Melchior P., 2010, arXiv e-prints, p. arXiv:1012.3754
Anguiano B., et al., 2020, AJ, 160, 43
Arcones A., Thielemann F.-K., 2023, A&A Rev., 31, 1
Asplund M., Grevesse N., Sauval A. J., Scott P., 2009, ARA&A, 47, 481
Aznar Cuadrado R., Jeffery C. S., 2001, A&A, 368, 994
Badami J. S., Rao K. R., 1933, Proceedings of the Royal Society of London Series A, 140, 387
Bagnulo S., Landstreet J. D., 2020, A&A, 643, A134
Bagnulo S., Landstreet J. D., 2021, MNRAS, 507, 5902
Bagnulo S., Landstreet J. D., Fossati L., Kochukhov O., 2012, A&A, 538, A129
Bagnulo S., Fossati L., Landstreet J. D., Izzo C., 2015, A&A, 583, A115
Bailer-Jones C. A. L., Rybizki J., Fouesneau M., Mantelet G., Andrae R., 2018, AJ, 156, 58
Balona L. A., et al., 2019, MNRAS, 485, 3457
Barlow B. N., Wade R. A., Liss S. E., Østensen R. H., Van Winckel H., 2012, ApJ, 758, 58
Barnard A. J., Cooper J., Smith E. W., 1974, J. Quant. Spectr. Rad. Transf., 14, 1025
Baschek B., Norris J., 1975, ApJ, 199, 694
Baschek B., Kudritzki R. P., Scholz M., Simon K. P., 1982a, A&A, 108, 387
Baschek B., Hoeflich P., Scholz M., 1982b, A&A, 112, 76
Battich T., Miller Bertolami M. M., Córsico A. H., Althaus L. G., 2018, A&A, 614, A136
Battich T., Miller Bertolami M. M., Serenelli A. M., Justham S., Weiss A., 2023, arXiv e-prints, p. arXiv:2311.04700
Bautista M. A., Romano P., Pradhan A. K., 1998, ApJS, 118, 259
Bayo A., Rodrigo C., Barrado Y Navascués D., Solano E., Gutiérrez R., Morales-Calderón M., Allard F., 2008, A&A, 492, 277
Beauchamp A., Wesemael F., Bergeron P., 1997, ApJS, 108, 559
Bédard A., Bergeron P., Brassard P., Fontaine G., 2020, ApJ, 901, 93
Beers T. C., Norris J. E., Placco V. M., Lee Y. S., Rossi S., Carollo D., Masseron T., 2014, ApJ, 794, 58
Behara N. T., Jeffery C. S., 2006, A&A, 451, 643
Behr B. B., 2003, ApJS, 149, 67
Belokurov V., Erkal D., Evans N. W., Koposov S. E., Deason A. J., 2018, MNRAS, 478, 611

Bergeron P., Wesemael F., Michaud G., Fontaine G., 1988, ApJ, 332, 964
Bessell M., Murphy S., 2012, PASP, 124, 140
Bethe H. A., 1939, Physical Review, 55, 434
Bianchi L., Shiao B., Thilker D., 2017, ApJS, 230, 24
Blanchette J. P., Chayer P., Wesemael F., Fontaine G., Fontaine M., Dupuis J., Kruk J. W., Green E. M., 2008, ApJ, 678, 1329
Bland-Hawthorn J., Gerhard O., 2016, ARA&A, 54, 529
Bloemen S., Hu H., Aerts C., Dupret M. A., Østensen R. H., Degroote P., Müller-Ringat E., Rauch T., 2014, A&A, 569, A123
Bohlin R. C., Gordon K. D., Tremblay P. E., 2014, PASP, 126, 711
Bonaca A., Conroy C., Wetzel A., Hopkins P. F., Kereš D., 2017, ApJ, 845, 101
Bonaca A., et al., 2020, ApJ, 897, L18
Bonaca A., et al., 2021, ApJ, 909, L26
Bonanno A., Schlattl H., Paternò L., 2002, A&A, 390, 1115
Bond N. A., et al., 2010, ApJ, 716, 1
Bovy J., Rix H.-W., Hogg D. W., 2012, ApJ, 751, 131
Breedt E., et al., 2017, MNRAS, 468, 2910
Brown W. R., Kilic M., Bédard A., Kosakowski A., Bergeron P., 2020, ApJ, 892, L35
Brown W. R., Kilic M., Kosakowski A., Gianninas A., 2022, ApJ, 933, 94
Buder S., et al., 2021, MNRAS, 506, 150
Buder S., et al., 2022, MNRAS, 510, 2407
Burbidge E. M., Burbidge G. R., Fowler W. A., Hoyle F., 1957, Reviews of Modern Physics, 29, 547
Burdge K. B., et al., 2020a, ApJ, 905, 32
Burdge K. B., et al., 2020b, ApJ, 905, L7
Burleigh M. R., Heber U., O'Donoghue D., Barstow M. A., 2000, A&A, 356, 585
Busso M., Gallino R., Wasserburg G. J., 1999, ARA&A, 37, 239
Busso G., Moehler S., Zoccali M., Heber U., Yi S. K., 2005, ApJ, 633, L29
Byrne C. M., Jeffery C. S., Tout C. A., Hu H., 2018, MNRAS, 475, 4728
Caiazzo I., et al., 2020, ApJ, 901, L14
Cannon A. J., Pickering E. C., 1918, Annals of Harvard College Observatory, 91, 1
Cantat-Gaudin T., Brandt T. D., 2021, A&A, 649, A124
Cantiello M., Fuller J., Bildsten L., 2016, ApJ, 824, 14
Capitanio L., Lallement R., Vergely J. L., Elyajouri M., Monreal-Ibero A., 2017, A&A, 606, A65
Carnall A. C., 2017, arXiv e-prints, p. arXiv:1705.05165
Carollo D., et al., 2019, ApJ, 887, 22
Cassisi S., Schlattl H., Salaris M., Weiss A., 2003, ApJ, 582, L43
Castellani M., Castellani V., 1993, ApJ, 407, 649
Catelan M., 2009, in New Quests in Stellar Astrophysics. II. Ultraviolet Properties of Evolved Stellar Populations. pp 175–189 (`arXiv:0708.2445`), doi:10.1007/978-0-387-87621-4_27
Catelan M., Valcarce A. A. R., Sweigart A. V., 2010, in de Grijs R., Lépine J. R. D., eds, Vol. 266, Star Clusters: Basic Galactic Building Blocks Throughout Time and Space. pp 281–292 (`arXiv:0910.1367`), doi:10.1017/S1743921309991153
Caughlan G. R., Fowler W. A., 1962, ApJ, 136, 453
Chambers K. C., et al., 2016, arXiv e-prints, p. arXiv:1612.05560
Charpinet S., Fontaine G., Brassard P., Dorman B., 1996, ApJ, 471, L103
Charpinet S., Fontaine G., Brassard P., Chayer P., Rogers F. J., Iglesias C. A., Dorman B., 1997, ApJ, 483, L123
Charpinet S., Giammichele N., Zong W., Van Grootel V., Brassard P., Fontaine G., 2018, Open Astronomy, 27, 112
Chayer P., Fontaine M., Fontaine G., Wesemael F., Dupuis J., 2006, Baltic Astronomy, 15, 131
Chen X., Han Z., Deca J., Podsiadlowski P., 2013, MNRAS, 434, 186
Chiappini C., Matteucci F., Gratton R., 1997, ApJ, 477, 765
Chiba M., Beers T. C., 2000, AJ, 119, 2843
Choi J., Dotter A., Conroy C., Cantiello M., Paxton B., Johnson B. D., 2016, ApJ, 823, 102
Chountonov G., Geier S., 2012, in Kilkenny D., Jeffery C. S., Koen C., eds, Astronomical Society of the Pacific Conference Series Vol. 452, Fifth Meeting on Hot Subdwarf Stars and Related Objects. p. 93 (`arXiv:1112.2921`)
Clausen D., Wade R. A., Kopparapu R. K., O'Shaughnessy R., 2012, ApJ, 746, 186
Colin J., et al., 1994, A&A, 287, 38
Condon E. U., Shortley G. H., 1935, The Theory of Atomic Spectra
Conroy C., Gunn J. E., White M., 2009, ApJ, 699, 486
Conroy C., Graves G. J., van Dokkum P. G., 2014, ApJ, 780, 33

Coplen T. B., et al., 2002, Pure and Applied Chemistry, 74, 1987

Copperwheat C. M., Morales-Rueda L., Marsh T. R., Maxted P. F. L., Heber U., 2011, MNRAS, 415, 1381

Cowan R. D., 1981, The theory of atomic structure and spectra

Cristallo S., Straniero O., Gallino R., Piersanti L., Domínguez I., Lederer M. T., 2009, ApJ, 696, 797

Culpan R., Pelisoli I., Geier S., 2021, A&A, 654, A107

Culpan R., Geier S., Reindl N., Pelisoli I., Gentile Fusillo N., Vorontseva A., 2022, A&A, 662, A40

Cunto W., Mendoza C., Ochsenbein F., Zeippen C. J., 1993, A&A, 275, L5

Cutri R. M., et al., 2003, VizieR Online Data Catalog, 2246

Cutri R. M., et al., 2021, VizieR Online Data Catalog, p. II/328

D'Cruz N. L., Dorman B., Rood R. T., O'Connell R. W., 1996, ApJ, 466, 359

DENIS Consortium 2005, VizieR Online Data Catalog: The DENIS database

DESI Collaboration et al., 2016, arXiv e-prints, p. arXiv:1611.00036

Dalton G., et al., 2014, in Ramsay S. K., McLean I. S., Takami H., eds, Society of Photo-Optical Instrumentation Engineers (SPIE) Conference Series Vol. 9147, Ground-based and Airborne Instrumentation for Astronomy V. p. 91470L (`arXiv:1412.0843`), doi:10.1117/12.2055132

Däppen W., Anderson L., Mihalas D., 1987, ApJ, 319, 195

Day R. W., Lambert D. L., Sneden C., 1973, ApJ, 185, 213

De Angeli F., et al., 2023, A&A, 674, A2

De K., et al., 2019, ApJ, 873, L18

Dearborn D. S. P., Eggleton P. P., Schramm D. N., 1976, ApJ, 203, 455

Dearborn D. S. P., Liebert J., Aaronson M., Dahn C. C., Harrington R., Mould J., Greenstein J. L., 1986, ApJ, 300, 314

Dhillon V. S., Littlefair S. P., Marsh T. R., Sarna M. J., Boakes E. H., 2002, A&A, 393, 611

Di Matteo P., Haywood M., Lehnert M. D., Katz D., Khoperskov S., Snaith O. N., Gómez A., Robichon N., 2019, A&A, 632, A4

Dorman B., Rood R. T., O'Connell R. W., 1993, ApJ, 419, 596

Dorsch M., Latour M., Heber U., 2019, A&A, 630, A130

Dorsch M., Latour M., Heber U., Irrgang A., Charpinet S., Jeffery C. S., 2020, A&A, 643, A22

Dorsch M., Jeffery C. S., Irrgang A., Woolf V., Heber U., 2021, A&A, 653, A120

Dorsch M., Reindl N., Pelisoli I., Heber U., Geier S., Istrate A. G., Justham S., 2022, A&A, 658, L9

Dreizler S., 1993, A&A, 273, 212

Dreizler S., Werner K., 1993, A&A, 278, 199

Dreyer J. L. E., 1888, MmRAS, 49, 1

Driebe T., Schoenberner D., Bloecker T., Herwig F., 1998, A&A, 339, 123

Drilling J. S., Heber U., 1987, in Philip A. G. D., Hayes D. S., Liebert J. W., eds, IAU Colloq. 95: Second Conference on Faint Blue Stars. pp 603–606

Drilling J. S., Jeffery C. S., Heber U., Moehler S., Napiwotzki R., 2013, A&A, 551, A31

Drlica-Wagner A., et al., 2021, ApJS, 256, 2

Dworetsky M. M., Lanning H. H., Etzel P. B., Patenaude D. J., 1977, MNRAS, 181, 13P

Edelmann H., 2003, PhD thesis, Friedrich Alexander University of Erlangen-Nuremberg, Germany

Edelmann H., Heber U., Altmann M., Karl C., Lisker T., 2005, A&A, 442, 1023

Edge A., Sutherland W., Kuijken K., Driver S., McMahon R., Eales S., Emerson J. P., 2013, The Messenger, 154, 32

Eilers A.-C., Hogg D. W., Rix H.-W., Ness M. K., 2019, ApJ, 871, 120

El-Badry K., Rix H.-W., Heintz T. M., 2021, MNRAS, 506, 2269

Elkin V. G., 1996, A&A, 312, L5

Elkin V. G., 1998, Contributions of the Astronomical Observatory Skalnate Pleso, 27, 452

Escorza A., et al., 2019, A&A, 626, A128

Eser S., Özdemir L., 2017, Acta Physica Polonica A, 132, 1284

Eser S., Özdemir L., 2018, Canadian Journal of Physics, 96, 664

Fekel F. X., Simon T., 1985, AJ, 90, 812

Ferguson D. H., Green R. F., Liebert J., 1984, ApJ, 287, 320

Fernández-Menchero L., Jeffery C. S., Ramsbottom C. A., Ballance C. P., 2020, MNRAS, 496, 2558

Feuillet D. K., Sahlholdt C. L., Feltzing S., Casagrande L., 2021, MNRAS, 508, 1489

Figer D. F., 2005, Nature, 434, 192

Fitzpatrick E. L., Massa D., Gordon K. D., Bohlin R., Clayton G. C., 2019, ApJ, 886, 108

Fontaine G., Chayer P., 1997, in Philip A. G. D., Liebert J., Saffer R., Hayes D. S., eds, The Third Conference on Faint Blue Stars. p. 169

Fontaine M., Chayer P., Wesemael F., Lamontagne R., Fontaine G., 2004, Ap&SS, 291, 371

Fontaine G., Brassard P., Charpinet S., Green E. M., Randall S. K., Van Grootel V., 2012, A&A, 539, A12

Fontaine G., Green E., Brassard P., Latour M., Chayer P., 2014, in van Grootel V., Green E., Fontaine G.,

Charpinet S., eds, Astronomical Society of the Pacific Conference Series Vol. 481, 6th Meeting on Hot Subdwarf Stars and Related Objects. p. 83
Fuhrmann K., 1998, A&A, 338, 161
Fuhrmann K., 2011, MNRAS, 414, 2893
Fuller J., Cantiello M., Stello D., Garcia R. A., Bildsten L., 2015, Science, 350, 423
Gaia Collaboration 2018, VizieR Online Data Catalog, 1345
Gaia Collaboration et al., 2016, A&A, 595, A1
Gaia Collaboration et al., 2018, A&A, 616, A11
Gaia Collaboration et al., 2021, A&A, 649, A1
Gallart C., Bernard E. J., Brook C. B., Ruiz-Lara T., Cassisi S., Hill V., Monelli M., 2019, Nature Astronomy, 3, 932
García-Berro E., et al., 2012, ApJ, 749, 25
Garstang R. H., Kemic S. B., 1974, Ap&SS, 31, 103
Geier S., 2013, A&A, 549, A110
Geier S., 2020, A&A, 635, A193
Geier S., Heber U., 2012, A&A, 543, A149
Geier S., Heber U., Edelmann H., Morales-Rueda L., Napiwotzki R., 2010a, Ap&SS, 329, 127
Geier S., Heber U., Kupfer T., Napiwotzki R., 2010b, A&A, 515, A37
Geier S., Heber U., Heuser C., Classen L., O'Toole S. J., Edelmann H., 2013a, A&A, 551, L4
Geier S., et al., 2013b, A&A, 554, A54
Geier S., Heber U., Edelmann H., Morales-Rueda L., Kilkenny D., O'Donoghue D., Marsh T. R., Copperwheat C., 2013c, A&A, 557, A122
Geier S., et al., 2014, A&A, 562, A95
Geier S., et al., 2015a, Science, 347, 1126
Geier S., et al., 2015b, A&A, 577, A26
Geier S., Raddi R., Gentile Fusillo N. P., Marsh T. R., 2019, A&A, 621, A38
Geier S., Dorsch M., Pelisoli I., Reindl N., Heber U., Irrgang A., 2022, A&A, 661, A113
Gigosos M. A., González M. Á., 2009, A&A, 503, 293
Gilmore G., Reid N., 1983, MNRAS, 202, 1025
Girard T. M., et al., 2011, AJ, 142, 15
Girven J., et al., 2012, MNRAS, 425, 1013
González-Riestra R., Cassatella A., Wamsteker W., 2001, A&A, 373, 730
Götberg Y., de Mink S. E., Groh J. H., Kupfer T., Crowther P. A., Zapartas E., Renzo M., 2018, A&A, 615, A78
Gourgouliatos K. N., Jeffery C. S., 2006, MNRAS, 371, 1381
Goy G., 1980, A&A, 88, 370
Gratton R. G., Carretta E., Bragaglia A., Lucatello S., D'Orazi V., 2010, A&A, 517, A81
Gray D. F., 2005, The Observation and Analysis of Stellar Photospheres
Gray R. O., McGahee C. E., Griffin R. E. M., Corbally C. J., 2011, AJ, 141, 160
Green R. F., 1976, PASP, 88, 665
Green R. F., Schmidt M., Liebert J., 1986, ApJS, 61, 305
Green E. M., et al., 2003, ApJ, 583, L31
Green E. M., et al., 2011, ApJ, 734, 59
Green E., Johnson C., Wallace S., O'Malley C., Amaya H., Biddle L., Fontaine G., 2014, in van Grootel V., Green E., Fontaine G., Charpinet S., eds, Astronomical Society of the Pacific Conference Series Vol. 481, 6th Meeting on Hot Subdwarf Stars and Related Objects. p. 161
Greenstein G. S., 1967, Nature, 213, 871
Greenstein J. L., 1973, A&A, 23, 1
Groth H. G., Kudritzki R. P., Heber U., 1985, A&A, 152, 107
Grundahl F., Catelan M., Landsman W. B., Stetson P. B., Andersen M. I., 1999, ApJ, 524, 242
Hall P. D., Jeffery C. S., 2016, MNRAS, 463, 2756
Hamilton A. J. S., Fesen R. A., Wu C. C., Crenshaw D. M., Sarazin C. L., 1997, ApJ, 481, 838
Hamilton A. J. S., Fesen R. A., Blair W. P., 2007, MNRAS, 381, 771
Han Z., 2008, A&A, 484, L31
Han Z., Podsiadlowski P., Maxted P. F. L., Marsh T. R., Ivanova N., 2002, MNRAS, 336, 449
Han Z., Podsiadlowski P., Maxted P. F. L., Marsh T. R., 2003, MNRAS, 341, 669
Han Z.-W., Ge H.-W., Chen X.-F., Chen H.-L., 2020, Research in Astronomy and Astrophysics, 20, 161
Härm R., Schwarzschild M., 1961, AJ, 66, 45
Harrison T. E., Marra R. E., 2017, ApJ, 843, 152
Hauck B., Mermilliod M., 1998, A&AS, 129, 431
Hayden M. R., et al., 2018, A&A, 609, A79
Heber U., 2009, ARA&A, 47, 211

Heber U., 2016, PASP, 128, 082001
Heber U., Hunger K., 1987, The Messenger, 47, 36
Heber U., Bade N., Jordan S., Voges W., 1993, A&A, 267, L31
Heber U., Reid I. N., Werner K., 2000, A&A, 363, 198
Heber U., Edelmann H., Lisker T., Napiwotzki R., 2003, A&A, 411, L477
Heber U., Geier S., Gaensicke B., 2013, in European Physical Journal Web of Conferences. p. 04002 (`arXiv:1211.5315`), doi:10.1051/epjconf/20134304002
Heber U., Irrgang A., Schaffenroth J., 2018, Open Astronomy, 27, 35
Heinze A. N., et al., 2018, AJ, 156, 241
Helmi A., 2020, ARA&A, 58, 205
Helmi A., Babusiaux C., Koppelman H. H., Massari D., Veljanoski J., Brown A. G. A., 2018, Nature, 563, 85
Henden A. A., Levine S., Terrell D., Welch D. L., 2015, in American Astronomical Society Meeting Abstracts #225. p. 336.16
Henden A. A., Templeton M., Terrell D., Smith T. C., Levine S., Welch D., 2016, VizieR Online Data Catalog, p. II/336
Herbig G. H., 1999, PASP, 111, 1144
Hidalgo S. L., et al., 2018, ApJ, 856, 125
Hinkle K. H., Lambert D. L., Snell R. L., 1976, ApJ, 210, 684
Hinkle K., Wallace L., Livingston W., 1995, PASP, 107, 1042
Hirsch H. A., 2009, PhD thesis, FAU, Germany
Hirsch H., Heber U., 2009, in Journal of Physics Conference Series. p. 012015, doi:10.1088/1742-6596/172/1/012015
Hirsch H. A., Heber U., O'Toole S. J., Bresolin F., 2005, A&A, 444, L61
Høg E., et al., 2000, A&A, 355, L27
Holdsworth D. L., Østensen R. H., Smalley B., Telting J. H., 2017, MNRAS, 466, 5020
Hollands M. A., Tremblay P. E., Gänsicke B. T., Gentile-Fusillo N. P., Toonen S., 2018, MNRAS, 480, 3942
Hönl H., 1925, Zeitschrift für Physik, 31, 340
Houck J. C., Denicola L. A., 2000, in Manset N., Veillet C., Crabtree D., eds, Astronomical Society of the Pacific Conference Series Vol. 216, Astronomical Data Analysis Software and Systems IX. p. 591
Howarth I. D., Heber U., 1990, PASP, 102, 912
Hoyle F., 1954, ApJS, 1, 121
Hu G., Shao Z., 2022, ApJ, 929, 33
Hu H., Tout C. A., Glebbeek E., Dupret M. A., 2011, MNRAS, 418, 195
Hubeny I., 1988, Computer Physics Communications, 52, 103
Hubeny I., Lanz T., 2017a, arXiv e-prints, p. arXiv:1706.01859
Hubeny I., Lanz T., 2017b, arXiv e-prints, p. arXiv:1706.01935
Hubeny I., Lanz T., 2017c, arXiv e-prints, p. arXiv:1706.01937
Hubeny I., Mihalas D., 2014, Theory of Stellar Atmospheres
Hubeny I., Hummer D. G., Lanz T., 1994, A&A, 282, 151
Humason M. L., Zwicky F., 1947, ApJ, 105, 85
Hummer D. G., Berrington K. A., Eissner W., Pradhan A. K., Saraph H. E., Tully J. A., 1993, A&A, 279, 298
Husfeld D., Butler K., Heber U., Drilling J. S., 1989, A&A, 222, 150
Husser T. O., Wende-von Berg S., Dreizler S., Homeier D., Reiners A., Barman T., Hauschildt P. H., 2013, A&A, 553, A6
IAEA 1995, Reference and Intercomparison Materials for Stable Isotopes of Light Elements. No. 825 in TECDOC Series, `https://www.iaea.org/publications/5471/reference-and-intercomparison-materials-for-stable-isotopes-of-light-elements`
Ibata R. A., Gilmore G., Irwin M. J., 1994, Nature, 370, 194
Iben Icko J., 1968, ApJ, 154, 581
Iben Icko J., 1990, ApJ, 353, 215
Iben I. J., Tutukov A. V., 1984a, ApJS, 54, 335
Iben I. J., Tutukov A. V., 1984b, ApJ, 284, 719
Iben Icko J., Tutukov A. V., 1986a, ApJ, 311, 742
Iben Icko J., Tutukov A. V., 1986b, ApJ, 311, 753
Irrgang A., 2014, PhD thesis, Friedrich Alexander University of Erlangen-Nuremberg, Germany
Irrgang A., Wilcox B., Tucker E., Schiefelbein L., 2013, A&A, 549, A137
Irrgang A., Przybilla N., Heber U., Böck M., Hanke M., Nieva M. F., Butler K., 2014, A&A, 565, A63
Irrgang A., Kreuzer S., Heber U., 2018, A&A, 620, A48
Irrgang A., Geier S., Kreuzer S., Pelisoli I., Heber U., 2020, A&A, 633, L5
Irrgang A., Dimpel M., Heber U., Raddi R., 2021, A&A, 646, L4
Istrate A. G., Marchant P., Tauris T. M., Langer N., Stancliffe R. J., Grassitelli L., 2016, A&A, 595, A35

Jacobs V. A., et al., 2011, in Schuh S., Drechsel H., Heber U., eds, American Institute of Physics Conference Series Vol. 1331, Planetary Systems Beyond the Main Sequence. pp 304–309 (`arXiv:1101.4158`), doi:10.1063/1.3556216

Jacobson-Galán W. V., et al., 2020, ApJ, 896, 165

Jeffery C. S., 2011, Information Bulletin on Variable Stars, 5964, 1

Jeffery C. S., Miszalski B., 2019, MNRAS, 489, 1481

Jeffery C. S., Saio H., 2006, MNRAS, 372, L48

Jeffery C. S., Zhang X., 2020, Journal of Astrophysics and Astronomy, 41, 48

Jeffery C. S., Simon T., Evans T. L., 1992, MNRAS, 258, 64

Jeffery C. S., Pereira C., Naslim N., Behara N., 2012, in Kilkenny D., Jeffery C. S., Koen C., eds, Astronomical Society of the Pacific Conference Series Vol. 452, Fifth Meeting on Hot Subdwarf Stars and Related Objects. p. 41

Jeffery C. S., et al., 2013, MNRAS, 429, 3207

Jeffery C. S., Ahmad A., Naslim N., Kerzendorf W., 2015, MNRAS, 446, 1889

Jeffery C. S., et al., 2017, MNRAS, 465, 3101

Jeffery C. S., Miszalski B., Snowdon E., 2021, MNRAS, 501, 623

Ji S., et al., 2013, ApJ, 773, 136

Johnson D. R. H., Soderblom D. R., 1987, AJ, 93, 864

Jorissen A., Boffin H. M. J., 1992, in Binaries as Tracers of Star Formation. pp 110–131

Jorissen A., Boffin H. M. J., Karinkuzhi D., Van Eck S., Escorza A., Shetye S., Van Winckel H., 2019, A&A, 626, A127

Justham S., Podsiadlowski P., Han Z., 2011, MNRAS, 410, 984

Kato M., Saio H., Hachisu I., 1989, ApJ, 340, 509

Kato M., Hachisu I., Kiyota S., Saio H., 2008, ApJ, 684, 1366

Kaur M., Nakra R., Arora B., Li C.-B., Sahoo B. K., 2020, Journal of Physics B Atomic Molecular Physics, 53, 065002

Kawka A., Vennes S., 2011, A&A, 532, A7

Kawka A., Vennes S., Schmidt G. D., Wickramasinghe D. T., Koch R., 2007, ApJ, 654, 499

Kawka A., Vennes S., O'Toole S., Németh P., Burton D., Kotze E., Buckley D. A. H., 2015, MNRAS, 450, 3514

Kepler S. O., et al., 2013, MNRAS, 429, 2934

Kepler S. O., et al., 2019, MNRAS, 486, 2169

Khalack V., Yameogo B., LeBlanc F., Fontaine G., Green E., Van Grootel V., Petit P., 2014, MNRAS, 445, 4086

Kilic M., Munn J. A., Harris H. C., von Hippel T., Liebert J. W., Williams K. A., Jeffery E., DeGennaro S., 2017, ApJ, 837, 162

Kilkenny D., Heber U., Drilling J. S., 1988, South African Astronomical Observatory Circular, 12, 1

Kilkenny D., O'Donoghue D., Stobie R. S., 1991, MNRAS, 248, 664

Kilkenny D., Koen C., O'Donoghue D., Stobie R. S., 1997, MNRAS, 285, 640

Kilkenny D., Worters H. L., O'Donoghue D., Koen C., Koen T., Hambly N., MacGillivray H., Stobie R. S., 2016, MNRAS, 459, 4343

Kirby E. N., Cohen J. G., Guhathakurta P., Cheng L., Bullock J. S., Gallazzi A., 2013, ApJ, 779, 102

Koen C., Orosz J. A., Wade R. A., 1998, MNRAS, 300, 695

Kollmeier J. A., et al., 2017, arXiv e-prints, p. arXiv:1711.03234

Koppelman H. H., Helmi A., Massari D., Price-Whelan A. M., Starkenburg T. K., 2019, A&A, 631, L9

Kramida A., 2019, Atoms, 7, 64

Kramida A., Yu. Ralchenko Reader J., and NIST ASD Team 2019, NIST Atomic Spectra Database (ver. 5.7.1), [Online]. Available: `https://physics.nist.gov/asd` [2019, October 28]. National Institute of Standards and Technology, Gaithersburg, MD.

Kreuzer S., 2021, PhD thesis, University of Erlangen–Nuremberg, Germany

Krogager J.-K., 2018, arXiv e-prints, p. arXiv:1803.01187

Kupfer T., et al., 2015, A&A, 576, A44

Kupfer T., et al., 2021, MNRAS, 505, 1254

Kupfer T., et al., 2022, ApJ, 925, L12

Kurucz R. L., 1993, SYNTHE spectrum synthesis programs and line data

Kurucz R. L., 1996, in Adelman S. J., Kupka F., Weiss W. W., eds, Astronomical Society of the Pacific Conference Series Vol. 108, M.A.S.S., Model Atmospheres and Spectrum Synthesis. p. 160

Kurucz R. L., 2002, A few things we do not know about stars and model atmospheres. pp 3–14, doi:10.1007/978-94-010-0393-3_1

Kurucz R. L., 2018, in Workshop on Astrophysical Opacities. p. 47

Kushniruk I., Schirmer T., Bensby T., 2017, A&A, 608, A73

Lagarde N., et al., 2021, A&A, 654, A13

Lallement R., et al., 2018, A&A, 616, A132

Landstreet J. D., Bagnulo S., 2019, A&A, 628, A1

Landstreet J. D., Bagnulo S., Fossati L., Jordan S., O'Toole S. J., 2012, A&A, 541, A100
Lane J. M. M., Bovy J., Mackereth J. T., 2022, MNRAS, 510, 5119
Lang R. J., 1928, Physical Review, 32, 737
Langer N., Kudritzki R. P., 2014, A&A, 564, A52
Lanz T., Hubeny I., 2003, ApJS, 146, 417
Lanz T., Hubeny I., Heap S. R., 1997, ApJ, 485, 843
Lanz T., Brown T. M., Sweigart A. V., Hubeny I., Landsman W. B., 2004, ApJ, 602, 342
Lara N., González M. Á., Gigosos M. A., 2012, A&A, 542, A75
Latour M., Randall S. K., Fontaine G., Bono G., Calamida A., Brassard P., 2014, ApJ, 795, 106
Latour M., Fontaine G., Green E. M., Brassard P., 2015, A&A, 579, A39
Latour M., et al., 2016, A&A, 585, A115
Latour M., Chayer P., Green E. M., Irrgang A., Fontaine G., 2018a, A&A, 609, A89
Latour M., Randall S. K., Calamida A., Geier S., Moehler S., 2018b, A&A, 618, A15
Latour M., Green E. M., Fontaine G., 2019a, A&A, 623, L12
Latour M., Dorsch M., Heber U., 2019b, A&A, 629, A148
Lawrence A., et al., 2007, MNRAS, 379, 1599
Lawrence A., et al., 2013, VizieR Online Data Catalog, 2319
LeBlanc F., Monin D., Hui-Bon-Hoa A., Hauschildt P. H., 2009, A&A, 495, 937
LeBlanc F., Hui-Bon-Hoa A., Khalack V. R., 2010, MNRAS, 409, 1606
Lei Z., Zhao J., Németh P., Zhao G., 2018, ApJ, 868, 70
Lei Z., Zhao J., Németh P., Zhao G., 2020, ApJ, 889, 117
Lei Z., He R., Németh P., Zou X., Xiao H., Yang Y., Zhao J., 2023, ApJ, 953, 122
Lemoine M., et al., 2002, ApJS, 140, 67
Levenberg K., 1944, Quart. Appl. Math., 2, 164
Li Z., Li Y., 2021, ApJ, 923, 166
Lindegren L., et al., 2021, A&A, 649, A4
Lisker T., Heber U., Napiwotzki R., Christlieb N., Han Z., Homeier D., Reimers D., 2005, A&A, 430, 223
Liu Z.-W., Röpke F. K., Zeng Y., Heger A., 2021, A&A, 654, A103
Livne E., 1990, ApJ, 354, L53
Löbling L., 2020, MNRAS, 497, 67
Loginov A. V., Tuchkin V. I., 2001, Optics and Spectroscopy, 91, 165
López-Sanjuan C., et al., 2023, arXiv e-prints, p. arXiv:2301.12395
Lorén-Aguilar P., Isern J., García-Berro E., 2009, A&A, 500, 1193
Luo Y., Németh P., Wang K., Wang X., Han Z., 2021, ApJS, 256, 28
Ma X.-Y., Zhu Y.-Y., Yan Q.-B., You J.-Y., Su G., 2020, MNRAS, 497, 2190
Magnier E. A., et al., 2020, ApJS, 251, 6
Maoz D., Mannucci F., 2012, PASA, 29, 447
Marquardt D. W., 1963, Journal of the Society for Industrial and Applied Mathematics, 11, 431
Martin B., Wickramasinghe D. T., 1981, MNRAS, 196, 23
Martin P., Jeffery C. S., Naslim N., Woolf V. M., 2017, MNRAS, 467, 68
Mathys G., Hubrig S., Mason E., Michaud G., Schöller M., Wesemael F., 2012, Astronomische Nachrichten, 333, 30
Maxted P. F. L., Heber U., Marsh T. R., North R. C., 2001, MNRAS, 326, 1391
McClure R. D., Fletcher J. M., Nemec J. M., 1980, ApJ, 238, L35
McMahon R. G., Banerji M., Gonzalez E., Koposov S. E., Bejar V. J., Lodieu N., Rebolo R., VHS Collaboration 2013, The Messenger, 154, 35
Mengel J. G., Norris J., Gross P. G., 1976, ApJ, 204, 488
Mermilliod J. C., 1994, VizieR Online Data Catalog, p. II/193
Michaud G., Bergeron P., Wesemael F., Fontaine G., 1985, ApJ, 299, 741
Michaud G., Richer J., Richard O., 2011, A&A, 529, A60
Michaud G., Alecian G., Richer J., 2015, Atomic Diffusion in Stars, doi:10.1007/978-3-319-19854-5.
Miller Bertolami M. M., 2016, A&A, 588, A25
Miller Bertolami M. M., 2022, ApJ, 941, 149
Miller Bertolami M. M., Althaus L. G., Unglaub K., Weiss A., 2008, A&A, 491, 253
Miller Bertolami M. M., Córsico A. H., Althaus L. G., 2011, ApJ, 741, L3
Miller Bertolami M. M., Battich T., Córsico A. H., Christensen-Dalsgaard J., Althaus L. G., 2020, Nature Astronomy, 4, 67
Miller Bertolami M. M., Battich T., Córsico A. H., Althaus L. G., Wachlin F. C., 2022, MNRAS, 511, L60
Milne E. A., 1921, MNRAS, 81, 361
Milne E. A., 1924, Philosophical Magazine, 47, 209
Moehler S., 2001, PASP, 113, 1162

Moehler S., 2010, Mem. Soc. Astron. Italiana, 81, 838

Moehler S., et al., 2014, A&A, 568, A9

Molina F., Vos J., Németh P., Østensen R., Vučković M., Tkachenko A., van Winckel H., 2022, A&A, 658, A122

Möller L., 2021, Master's thesis, Friedrich-Alexander University Erlangen-Nürnberg, `https://www.sternwarte.uni-erlangen.de/docs/theses/2021-07_Moeller.pdf`

Momany Y., et al., 2020, Nature Astronomy, 4, 1092

Moni Bidin C., Moehler S., Piotto G., Momany Y., Recio-Blanco A., 2009, A&A, 498, 737

Moni Bidin C., Villanova S., Piotto G., Momany Y., 2011, A&A, 528, A127

Morton D. C., 2000, ApJS, 130, 403

Naidu R. P., Conroy C., Bonaca A., Johnson B. D., Ting Y.-S., Caldwell N., Zaritsky D., Cargile P. A., 2020, ApJ, 901, 48

Napiwotzki R., 2008, in Werner A., Rauch T., eds, Astronomical Society of the Pacific Conference Series Vol. 391, Hydrogen-Deficient Stars. p. 257

Napiwotzki R., et al., 2003, The Messenger, 112, 25

Napiwotzki R., Karl C. A., Lisker T., Heber U., Christlieb N., Reimers D., Nelemans G., Homeier D., 2004, Ap&SS, 291, 321

Napiwotzki R., et al., 2020, A&A, 638, A131

Naslim N., Jeffery C. S., Ahmad A., Behara N. T., Şahìn T., 2010, MNRAS, 409, 582

Naslim N., Jeffery C. S., Behara N. T., Hibbert A., 2011, MNRAS, 412, 363

Naslim N., Geier S., Jeffery C. S., Behara N. T., Woolf V. M., Classen L., 2012, MNRAS, 423, 3031

Naslim N., Jeffery C. S., Hibbert A., Behara N. T., 2013, MNRAS, 434, 1920

Naslim N., Jeffery C. S., Woolf V. M., 2020, MNRAS, 491, 874

Németh P., Kawka A., Vennes S., 2012, MNRAS, 427, 2180

Németh P., Vos J., Molina F., Bastian A., 2021, A&A, 653, A3

Neunteufel P., 2020, A&A, 641, A52

Neunteufel P., Kruckow M., Geier S., Hamers A. S., 2021, A&A, 646, L8

Neunteufel P., Preece H., Kruckow M., Geier S., Hamers A. S., Justham S., Podsiadlowski P., 2022, A&A, 663, A91

Newville M., Stensitzki T., Allen D. B., Ingargiola A., 2014, LMFIT: Non-Linear Least-Square Minimization and Curve-Fitting for Python, doi:10.5281/zenodo.11813, `https://doi.org/10.5281/zenodo.11813`

Nissen P. E., Schuster W. J., 2010, A&A, 511, L10

Nomoto K., Kobayashi C., Tominaga N., 2013, ARA&A, 51, 457

O'Connell R. W., 1999, ARA&A, 37, 603

O'Donoghue D., Kilkenny D., Koen C., Hambly N., MacGillivray H., Stobie R. S., 2013, MNRAS, 431, 240

O'Reilly F., Dunne P., 1998, Journal of Physics B Atomic Molecular Physics, 31, 1059

O'Toole S. J., 2004, A&A, 423, L25

O'Toole S. J., Heber U., 2006, A&A, 452, 579

Ochsenbein F., Bauer P., Marcout J., 2000, A&AS, 143, 23

Oke J. B., Gunn J. E., 1983, ApJ, 266, 713

Oliveira C. M., Hébrard G., 2006, ApJ, 653, 345

Onken C. A., et al., 2019, PASA, 36, e033

Oppenheimer B. R., Hambly N. C., Digby A. P., Hodgkin S. T., Saumon D., 2001, Science, 292, 698

Oreiro R., Ulla A., Pérez Hernández F., Østensen R., Rodríguez López C., MacDonald J., 2004, A&A, 418, 243

Orlov V. G., Voitsekhovich V. V., Rivera J. L., Guerrero C. A., Ortiz F., 2010, Rev. Mexicana Astron. Astrofis., 46, 245

Østensen R. H., et al., 2011, MNRAS, 414, 2860

Østensen R. H., et al., 2012, ApJ, 753, L17

Østensen R. H., et al., 2020, MNRAS, 499, 3738

Ostrowski J., Baran A. S., Sanjayan S., Sahoo S. K., 2021, MNRAS, 503, 4646

Pacheco T. A., Diaz M. P., Levenhagen R. S., Coelho P. R. T., 2021, ApJS, 256, 41

Paczyński B., 1971, Acta Astron., 21, 1

Paczynski B., 1976. p. 75

Page M. J., et al., 2012, MNRAS, 426, 903

Parker Q. A., Xiang Z., Ritter A., 2022, Galaxies, 10, 32

Pauli E. M., Napiwotzki R., Altmann M., Heber U., Odenkirchen M., Kerber F., 2003, A&A, 400, 877

Pauli E. M., Napiwotzki R., Heber U., Altmann M., Odenkirchen M., 2006, A&A, 447, 173

Pelisoli I., Vos J., 2019, MNRAS, 488, 2892

Pelisoli I., Vos J., Geier S., Schaffenroth V., Baran A. S., 2020, A&A, 642, A180

Pelisoli I., et al., 2021, Nature Astronomy, 5, 1052

Pelisoli I., et al., 2022, MNRAS, 515, 2496

Pereira C., 2011, PhD thesis, Queens University Belfast, Ireland

Petit P., Van Grootel V., Bagnulo S., Charpinet S., Wade G. A., Green E. M., 2012, in Kilkenny D., Jeffery C. S., Koen C., eds, Astronomical Society of the Pacific Conference Series Vol. 452, Fifth Meeting on Hot Subdwarf Stars and Related Objects. p. 87 (`arXiv:1110.5227`)

Pietrukowicz P., et al., 2013, Acta Astron., 63, 115

Podsiadlowski P., Han Z., Lynas-Gray A. E., Brown D., 2008, in Heber U., Jeffery C. S., Napiwotzki R., eds, Astronomical Society of the Pacific Conference Series Vol. 392, Hot Subdwarf Stars and Related Objects. p. 15 (`arXiv:0808.0574`)

Powell M. J. D., 1964, The Computer Journal, 7, 155

Proffitt C. R., Sansonetti C. J., Reader J., 2001, ApJ, 557, 320

Przybilla N., Nieva M. F., Edelmann H., 2006, Baltic Astronomy, 15, 107

Quievy D., Charbonneau P., Michaud G., Richer J., 2009, A&A, 500, 1163

Raddi R., et al., 2022, A&A, 658, A22

Raineri M., Reyna Almandos J. G., Bredice F., Gallardo M., Reigueiros A. G., Pettersson S. G., 1998, J. Quant. Spectr. Rad. Transf., 60, 25

Ramírez I., Allende Prieto C., 2011, ApJ, 743, 135

Ramos P., Antoja T., Figueras F., 2018, A&A, 619, A72

Ramspeck M., Heber U., Edelmann H., 2001, A&A, 379, 235

Randall S. K., Bagnulo S., Ziegerer E., Geier S., Fontaine G., 2015, A&A, 576, A65

Ratzloff J. K., et al., 2020, ApJ, 902, 92

Rauch T., 1993, A&A, 276, 171

Rauch T., Werner K., Kruk J. W., 2010, Ap&SS, 329, 133

Rauch T., Werner K., Quinet P., Kruk J. W., 2014, A&A, 564, A41

Rauch T., Quinet P., Hoyer D., Werner K., Richter P., Kruk J. W., Demleitner M., 2016, A&A, 590, A128

Rauch T., Gamrath S., Quinet P., Löbling L., Hoyer D., Werner K., Kruk J. W., Demleitner M., 2017, A&A, 599, A142

Reddy B. E., Lambert D. L., 2008, MNRAS, 391, 95

Reed M. D., et al., 2018, Open Astronomy, 27, 157

Reindl N., et al., 2019, MNRAS, 482, L93

Renzini A., 2023, MNRAS, 521, 524

Richer H. B., Kerr R., Heyl J., Caiazzo I., Cummings J., Bergeron P., Dufour P., 2019, ApJ, 880, 75

Riello M., et al., 2021, A&A, 649, A3

Robin A. C., Reylé C., Derrière S., Picaud S., 2003, A&A, 409, 523

Robin A. C., Bienaymé O., Fernández-Trincado J. G., Reylé C., 2017, A&A, 605, A1

Saffer R. A., Bergeron P., Koester D., Liebert J., 1994, ApJ, 432, 351

Saffer R. A., Keenan F. P., Hambly N. C., Dufton P. L., Liebert J., 1997, ApJ, 491, 172

Safronova U. I., Johnson W. R., 2004, Phys. Rev. A, 69, 052511

Sahoo S. K., et al., 2020, MNRAS, 495, 2844

Saio H., Jeffery C. S., 2000, MNRAS, 313, 671

Saio H., Jeffery C. S., 2002, MNRAS, 333, 121

Saio H., Jeffery C. S., 2019, MNRAS, 482, 758

Sandquist E. L., et al., 2020, AJ, 159, 96

Sarna M. J., Dhillon V. S., Marsh T. R., Marks P. B., 1995, MNRAS, 272, L41

Saumon D., Marley M. S., 2008, ApJ, 689, 1327

Savanov I. S., Romaniuk I. I., Semenko E. A., Dmitrienko E. S., 2013, Astronomy Reports, 57, 751

Schaffenroth J., 2016, Master's thesis, Friedrich-Alexander University Erlangen-Nürnberg

Schaffenroth V., Classen L., Nagel K., Geier S., Koen C., Heber U., Edelmann H., 2014, A&A, 570, A70

Schaffenroth V., et al., 2021, MNRAS, 501, 3847

Schaffenroth V., Pelisoli I., Barlow B. N., Geier S., Kupfer T., 2022, A&A, 666, A182

Schindewolf M., Németh P., Heber U., Battich T., Miller Bertolami M. M., Irrgang A., Latour M., 2018, A&A, 620, A36

Schlafly E. F., Finkbeiner D. P., 2011, ApJ, 737, 103

Schlafly E. F., et al., 2018, ApJS, 234, 39

Schlafly E. F., Meisner A. M., Green G. M., 2019, ApJS, 240, 30

Schlegel D. J., Finkbeiner D. P., Davis M., 1998, ApJ, 500, 525

Schneider D. M., 2022, PhD thesis, Friedrich-Alexander-Universität Erlangen-Nürnberg (FAU)

Schneider D., Irrgang A., Heber U., Nieva M. F., Przybilla N., 2018, A&A, 618, A86

Schneider F. R. N., Ohlmann S. T., Podsiadlowski P., Röpke F. K., Balbus S. A., Pakmor R., Springel V., 2019, Nature, 574, 211

Schönberner D., 1978, A&A, 70, 451

Schöning T., Butler K., 1989, A&AS, 78, 51

Schönrich R., Binney J., Dehnen W., 2010, MNRAS, 403, 1829

Schork M., 2017, Die unterleuchtkräftigen O-Sterne HZ 44 und BD+75 325: Eine Radialgeschwindigkeitsstudie
Schuler S. C., King J. R., The L.-S., 2009, ApJ, 701, 837
Schwab J., 2018, MNRAS, 476, 5303
Schwab J., 2019, ApJ, 885, 27
Schwab J., Shen K. J., Quataert E., Dan M., Rosswog S., 2012, MNRAS, 427, 190
Schweizer F., Middleditch J., 1980, ApJ, 241, 1039
Seaton M. J., 1962, in Bates D. R., ed., Atomic and Molecular Processes. p. 375
Seaton M. J., Zeippen C. J., Tully J. A., Pradhan A. K., Mendoza C., Hibbert A., Berrington K. A., 1992, Rev. Mexicana Astron. Astrofis., 23, 19
Shamey L. J., 1969, PhD thesis, University of Colorado at Boulder
Sharma S., Hayden M. R., Bland-Hawthorn J., 2021, MNRAS, 507, 5882
Sharma S., et al., 2022, MNRAS, 510, 734
Shen K. J., Kasen D., Miles B. J., Townsley D. M., 2018, ApJ, 854, 52
Silvotti R., Ostensen R. H., Telting J. H., 2020, arXiv e-prints, p. arXiv:2002.04545
Skrutskie M. F., et al., 2006, AJ, 131, 1163
Solano E., et al., 2022, MNRAS, 514, 4239
Soubiran C., Bienaymé O., Siebert A., 2003, A&A, 398, 141
Spitoni E., Verma K., Silva Aguirre V., Calura F., 2020, A&A, 635, A58
Spitzer Science C., 2009, VizieR Online Data Catalog, p. II/293
Stark M. A., Wade R. A., 2003, AJ, 126, 1455
Stello D., Cantiello M., Fuller J., Huber D., García R. A., Bedding T. R., Bildsten L., Silva Aguirre V., 2016, Nature, 529, 364
Stroeer A., Heber U., Lisker T., Napiwotzki R., Dreizler S., Christlieb N., Reimers D., 2007, A&A, 462, 269
Sweigart A. V., 1997, ApJ, 474, L23
Tailo M., et al., 2015, Nature, 523, 318
Tailo M., et al., 2021, MNRAS, 503, 694
Tauheed A., Hala 2012, Phys. Scr, 85, 025304
Telting J. H., Geier S., Østensen R. H., Heber U., Glowienka L., Nielsen T., Oreiro R., Frandsen S., 2008, A&A, 492, 815
Tepper-García T., 2006, MNRAS, 369, 2025
Thejll P., Ulla A., MacDonald J., 1995, A&A, 303, 773
Tillich A., et al., 2011, A&A, 527, A137
Tinsley B. M., 1979, ApJ, 229, 1046
Tomley L., 1970, ApJ, 162, 239
Tremblay P.-E., Bergeron P., 2009, ApJ, 696, 1755
Tremblay P. E., Fontaine G., Freytag B., Steiner O., Ludwig H. G., Steffen M., Wedemeyer S., Brassard P., 2015, ApJ, 812, 19
Tremblay P., Beauchamp A., Bergeron P., 2020, ApJ, 901, 104
Ulla A., Thejll P., 1998, A&AS, 132, 1
Unglaub K., 2005, in Koester D., Moehler S., eds, Astronomical Society of the Pacific Conference Series Vol. 334, 14th European Workshop on White Dwarfs. p. 297
Unglaub K., 2008, A&A, 486, 923
Unglaub K., 2010, in Werner K., Rauch T., eds, American Institute of Physics Conference Series Vol. 1273, 17th European White Dwarf Workshop. pp 251–254, doi:10.1063/1.3527815
Unglaub K., Bues I., 2001, A&A, 374, 570
Unsöld A., 1955, Physik der Sternatmospharen, MIT besonderer Berucksichtigung der Sonne.
Uzundag M., et al., 2021, A&A, 651, A121
Vaccaro T. R., Wilson R. E., 2003, MNRAS, 342, 564
Valyavin G., Bagnulo S., Fabrika S., Reisenegger A., Wade G. A., Han I., Monin D., 2006, ApJ, 648, 559
Virtanen P., et al., 2020, Nature Methods, 17, 261
Viton M., Deleuil M., Tobin W., Prevot L., Bouchet P., 1991, A&A, 242, 175
Vos J., Østensen R. H., Németh P., Green E. M., Heber U., Van Winckel H., 2013, A&A, 559, A54
Vos J., Østensen R. H., Vučković M., Van Winckel H., 2017, A&A, 605, A109
Vos J., Németh P., Vučković M., Østensen R., Parsons S., 2018, MNRAS, 473, 693
Vos J., Vučković M., Chen X., Han Z., Boudreaux T., Barlow B. N., Østensen R., Németh P., 2019, MNRAS, 482, 4592
Vos J., Bobrick A., Vučković M., 2020, A&A, 641, A163
Vos J., et al., 2021, A&A, 655, A43
Wallerstein G., 1962, ApJS, 6, 407
Wallerstein G., Sturch C., Klemola A. R., 1963, PASP, 75, 61
Wallis K. F., 2014, arXiv e-prints, p. arXiv:1405.4995

Wamsteker W., Skillen I., Ponz J., de la Fuente A., Barylak M., Yurrita I., 2000, Astrophysics and Space Science, 273, 155
Webbink R. F., 1984, ApJ, 277, 355
Weiss A., Denissenkov P. A., Charbonnel C., 2000, A&A, 356, 181
Wenger M., et al., 2000, A&AS, 143, 9
Werner K., Dreizler S., Heber U., Rauch T., Wisotzki L., Hagen H. J., 1995, A&A, 293, L75
Werner K., Reindl N., Geier S., Pritzkuleit M., 2022a, MNRAS, 511, L66
Werner K., Reindl N., Dorsch M., Geier S., Munari U., Raddi R., 2022b, A&A, 658, A66
Whelan J., Iben Icko J., 1973, ApJ, 186, 1007
Wickramasinghe D. T., Martin B., 1986, MNRAS, 223, 323
Wild J. F., Jeffery C. S., 2018, MNRAS, 473, 4021
Winkler P. F., Hamilton A. J. S., Long K. S., Fesen R. A., 2011, ApJ, 742, 80
Wisotzki L., Wamstecker W., Reimers D. L., 1991, A&A, 247, L17
Wolf C., et al., 2018, PASA, 35, e010
Wollman E. R., 1973, ApJ, 184, 773
Wu C.-C., Crenshaw D. M., Fesen R. A., Hamilton A. J. S., Sarazin C. L., 1993, ApJ, 416, 247
Wu Y., Xiang M., Chen Y., Zhao G., Bi S., Li C., Li Y., Huang Y., 2021, MNRAS, 501, 4917
Xiang M., Rix H.-W., 2022, Nature, 603, 599
Yan T.-S., Shi J.-R., Tian H., Zhang W., Zhang B., 2022, Research in Astronomy and Astrophysics, 22, 025007
Yi S. K., 2008, in Heber U., Jeffery C. S., Napiwotzki R., eds, Astronomical Society of the Pacific Conference Series Vol. 392, Hot Subdwarf Stars and Related Objects. p. 3 (`arXiv:0808.0254`)
Yoon S. C., Podsiadlowski P., Rosswog S., 2007, MNRAS, 380, 933
Young A., Nelson B., Mielbrecht R., 1972, ApJ, 174, 27
Yu S., Jeffery C. S., 2010, A&A, 521, A85
Yu S., Li L., 2009, A&A, 503, 151
Yu J., Zhang X., Lü G., 2021, MNRAS, 504, 2670
Zhang X., Jeffery C. S., 2012, MNRAS, 419, 452
Zhang W., Palmeri P., Quinet P., 2014, European Physical Journal D, 68, 104
Zhang X., Hall P. D., Jeffery C. S., Bi S., 2017, ApJ, 835, 242
Zhang X., Hall P. D., Jeffery C. S., Bi S., 2018, MNRAS, 474, 427
Zhu C., Pakmor R., van Kerkwijk M. H., Chang P., 2015, ApJ, 806, L1
Ziegerer E., Heber U., Geier S., Irrgang A., Kupfer T., Fürst F., Schaffenroth J., 2017, A&A, 601, A58
de Boer K. S., Aguilar Sanchez Y., Altmann M., Geffert M., Odenkirchen M., Schmidt J. H. K., Colin J., 1997, A&A, 327, 577
de Jong R. S., et al., 2019, The Messenger, 175, 3
van Leeuwen F., 2007, A&A, 474, 653
van Regemorter H., 1962, ApJ, 136, 906
von Weizsäcker C. F., 1937, Physikalische Zeitschrift, 38, 176
von Weizsäcker C. F., 1938, Physikalische Zeitschrift, 39, 633
Østensen R. H., et al., 2010, MNRAS, 409, 1470

Appendix A

Supplementary analyses

A.1 Atmospheric convection due to He II / He III

While most hot subdwarf stars are helium-poor, there is a substantial group of sdO stars with atmospheres that are dominated by helium. The evolutionary status of these He-sdO stars has been a topic of debate since their discovery in the 1950s. Initially they were thought to be post-EHB or even post-AGB stars. More recently, formation models following a late He-flash or a merger of two white dwarfs were considered as preferred scenarios.

Atomic diffusion has been proposed to quickly transform He-rich atmospheres to He-poor ones (e. g. Miller Bertolami et al. 2008), which makes diffusion essential to understanding the evolution of hot subdwarf stars. However, diffusion due to gravitational settling and radiative levitation alone fails to explain the observed helium and metal abundances. In their diffusion calculations for BHB and sdB stars Michaud et al. (2011) require some mixing in the envelope to damp diffusion, which otherwise would lead to very low helium abundances and strong enrichment in iron. Weak stellar winds (Unglaub 2008; Hu et al. 2011) and surface convection zones (Groth et al. 1985; Unglaub 2010) have been suggested as processes to damp the effects of diffusion in the atmosphere.

Groth et al. (1985) suggested that the ionisation of He II to He III may lead to a convection region in the line forming region of sdOB stars, if their initial helium content is high enough. This atmospheric convection zone is thought to suppress the gravitational settling of helium. Later, Unglaub (2010) showed that the extend of such a thin surface convection zone may have a significant effect on the abundances carbon, nitrogen, and oxygen. In particular, he argued that a C-rich atmosphere as expected from the deep-mixing hot-flasher scenario of Miller Bertolami et al. (2008) may be turned into a N-rich one.

Since model atmospheres have changed significantly since the first non-LTE H/He models that were used by Groth et al. (1985) and no recent studies are available, it is interesting to see if their conclusions have since changed. Their methods can easily be applied to modern model atmospheres. In the following, the TLUSTY grid of Dorsch et al. (2019) is used to check if their results can be reproduced. This grid considers H, He, C, N, and Si in non-LTE.

A region in the atmosphere is considered unstable to convection if it fulfils the Schwarzschild criterion

$$\nabla_{\text{model}} \coloneqq \left(\frac{\partial \ln T}{\partial \ln P}\right)_{\text{model}} \quad < \quad \left(\frac{\partial \ln T}{\partial \ln P}\right)_{\text{ad}} \eqqcolon \nabla_{\text{ad}}, \tag{A.1.1}$$

where T is the local temperature and P is the total pressure, the sum of gas and radiation pressure. While the model temperature gradient can be derived directly from the TLUSTY models, the adiabatic temperature gradient may be computed following Groth et al. (1985) and Unsöld (1955) as

$$\nabla_{\text{ad}} = \frac{Z}{V} \cdot (1+\beta) \cdot \{1 + 4\beta + Wx \cdot [2x_0x_2(n_1+n_2) + x_0x_1n_1 + x_1x_2n_2]\}.$$

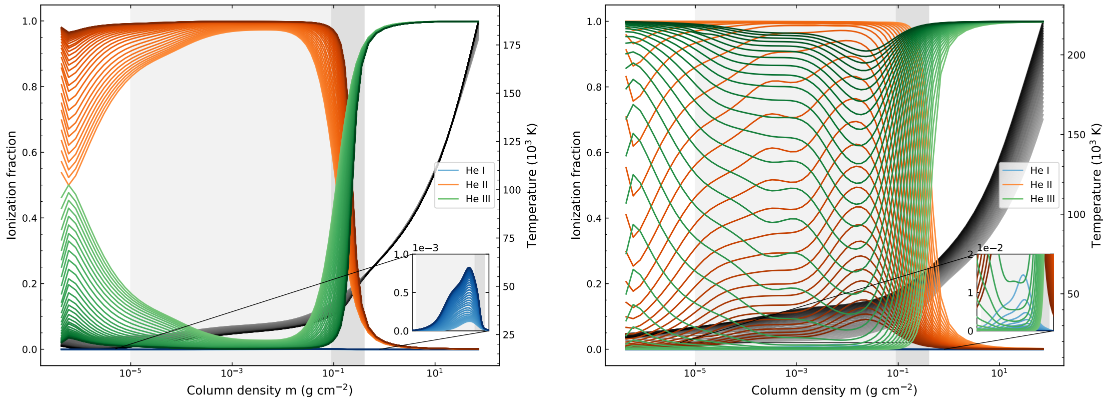

Figure A.1.1. Ionisation fractions of helium for models in the HeCNSi grid. The temperature stratification is shown in shades of grey. The line forming region is indicated approximately by the dark grey shaded background, while the extend of the strongest lines is shown with the light grey background. Left: from log y = –1 (light) to +3.4 (dark) with constant $T_{\rm eff}$ = 40kK and log g = 6. Right: from $T_{\rm eff}$ = 30kK (light) to 60kK (dark) with constant log n(He)/n(H) = 0 and log g = 6.

Here, the following abbreviations have been used:

$$x_1 = N_{\rm He^+}/N_{\rm He}, \qquad x_2 = N_{\rm He^{++}}/N_{\rm He}$$

$$x_0 = 1 - x_1 - x_2, \qquad y = N_{\rm He}/(N_{\rm H} + N_{\rm He})$$

$$x = (N_{\rm H} + N_{\rm He^+} + 2N_{\rm He^{++}})/(N_H + N_{\rm He}),$$

$$\beta = P_{\rm rad}/P_{\rm gas}, \qquad P_{\rm gas} = nk_BT, \qquad P_{\rm rad} = aT^4, \qquad a = 4\,\sigma_{\rm SB}/(3v_c)$$

$$n = n_{\rm e} + N_{\rm H} + N_{\rm He}, \qquad \xi_i = 5/2 + \chi_i/(k_BT), \qquad n_i = \xi_i + 4\beta, \qquad i = 1,2$$

$$Z = 1 + Wx\cdot(4\,x_2x_0 + x_1x_2 + x_1x_0),$$

$$V = [(4\beta + 5/2)^2 - 15/4]\cdot Z + Wx\cdot[Wx_0x_1x_2(\xi_1 - \xi_2)^2 + x_0x_2(n_1 + n_2)^2 + x_0x_1n_1^2 + x_1x_2n_2^2],$$

where n_e, $N_{\rm H}$, and $N_{\rm He}$ are the number densities of electrons, hydrogen, and helium while $N_{\rm He^+}$ and $N_{\rm He^{++}}$ are the number densities of (doubly) ionised helium. $P_{\rm rad}$ and $P_{\rm gas}$ are the radiative and gas pressures, while χ_i are the ionisation energies of helium. $k_{\rm B}$ is the Bolzmann constant, $\sigma_{\rm SB}$ the Stefan–Boltzmann constant, and v_c the speed of light. In the derivation of this expression, the Saha formula (see Eq. 2.1.14) has been used to calculate the derivatives of x_1 x_2, and x_0 – the non-LTE property of the models enters only through the temperature stratification. More details are given by Groth et al. (1985).

The convective instability is caused by the ionisation transition between He II and He III, which is shown in Fig. A.1.1. The left panel shows that the transition region between He II and He III shifts slightly outward in the atmosphere with increasing helium abundance. This is due to increased local temperatures with increasing helium abundance. A much stronger effect is seen when directly increasing the effective temperature (right panel): at the highest effective temperatures (60 kK), there is no transition since most helium ions are fully ionised in the atmosphere. At the lowest temperatures (30 kK), the transition from almost complete ionisation to predominantly singly ionised helium is located in the deeper regions of the atmosphere, below the line-forming region. Even in the coolest models, the population of neutral helium stays below 1.5 %. The He II/III transition reaches the line forming region only at 39 kK and the population of He III never drops below 80 % at temperatures higher than 54 kK.

As shown in Fig. A.1.2, the resulting adiabatic and model temperature gradients follow the behaviour of the transition region. Notably, the adiabatic gradient reaches a value of 0.4 at the bottom of the atmosphere – the same value as for a gas of fully ionised pure hydrogen. Partial

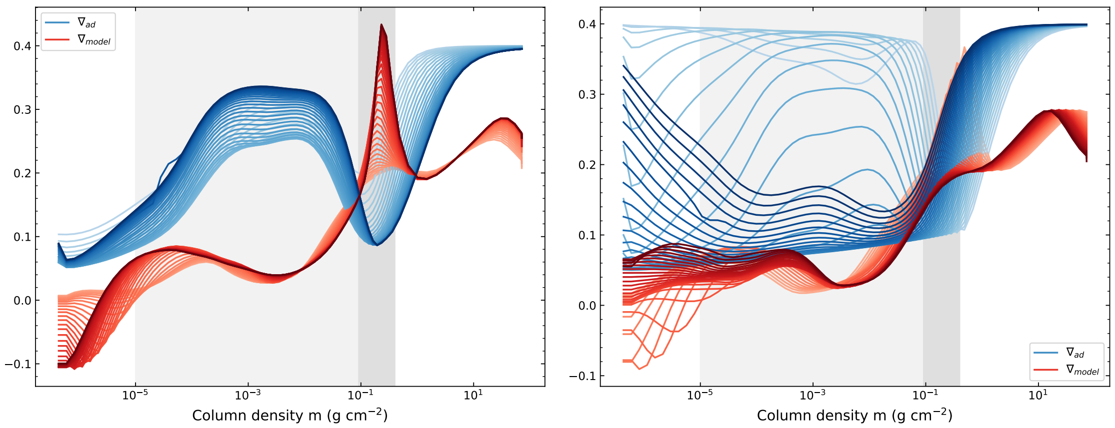

Figure A.1.2. Adiabatic and model gradients for the same models as in Fig. A.1.1. *Left*: from $\log n(\mathrm{He})/n(\mathrm{H}) = -1$ (light) to +3.4 (dark) with constant T_eff = 40 kK and $\log g = 6$. *Right*: from T_eff = 30 kK (light) to 60 kK (dark) with constant $\log n(\mathrm{He})/n(\mathrm{H}) = 0$ and $\log g = 6$.

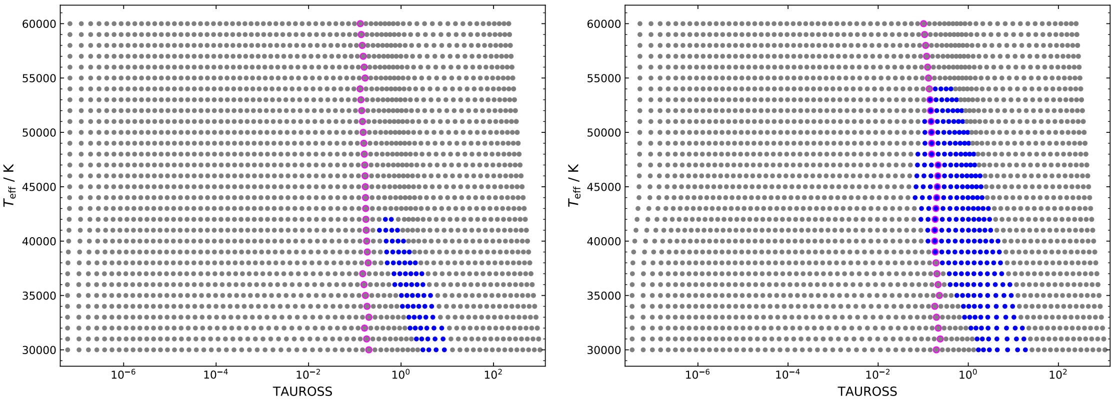

Figure A.1.3. Convective stability depending on temperature and optical depth in the atmosphere. Unstable depth points are marked in blue. The depth at which the H_β continuum forms is marked in pink. All models have $\log g = 6$. *Left*: $\log n(\mathrm{He})/n(\mathrm{H}) = -0.8$. *Right*: $\log n(\mathrm{He})/n(\mathrm{H}) = +0.0$.

ionisation of helium leads to a peak in the model temperature gradient and a dip in the adiabatic gradient. When increasing the abundance of helium, the peak and dip become more pronounced but only slightly change their position. This is due to the changes in the temperature structure as shown in the left panel of Fig. A.1.1. The drastic change in the ionisation stratification with temperature is reflected in the right panel of Fig. A.1.2, where not only the strength of the dip and peak change, but also their position.

As described by Eq. A.1.1, layers where the adiabatic gradient is larger than the model gradient are considered unstable to convection. While Fig. A.1.2 nicely shows the behaviour of the temperature gradients, it is hard to tell which model exhibits convection at which depth. This is better visualised in Fig. A.1.3, where unstable depth points are marked blue. The approximate depth at which the optical continuum forms is marked in pink. How this depth is determined is shown in Fig. A.1.4. It shows at which column densities in the atmosphere the monochromatic optical depth $\tau_\nu = 2/3$ is reached, i. e. where about half of the photons escape the photosphere. If convection occurs at this depth (the formation depth of the optical continuum), its effects will be detectable in the observed spectrum. Like Groth et al. (1985), we select the depth where the continuum at H_β forms to check for convectional instability. In this way, many of the cool ($T_\mathrm{eff} \lesssim$ 35 000 K) models, for which the He II/III convective region is located below the continuum forming region, are excluded. Convection due to the ionisation of He I would only become important at $T_\mathrm{eff} \lesssim 20\,000$ K. While the unstable region in a T_eff = 40 000 K subdwarf model does not reach the continuum forming region in a model with $\log n(\mathrm{He})/n(\mathrm{H}) = -0.8$ (left panel of Fig. A.1.3), the overlap becomes large in a model with $\log n(\mathrm{He})/n(\mathrm{H}) = +0.0$ (right panel of Fig. A.1.3).

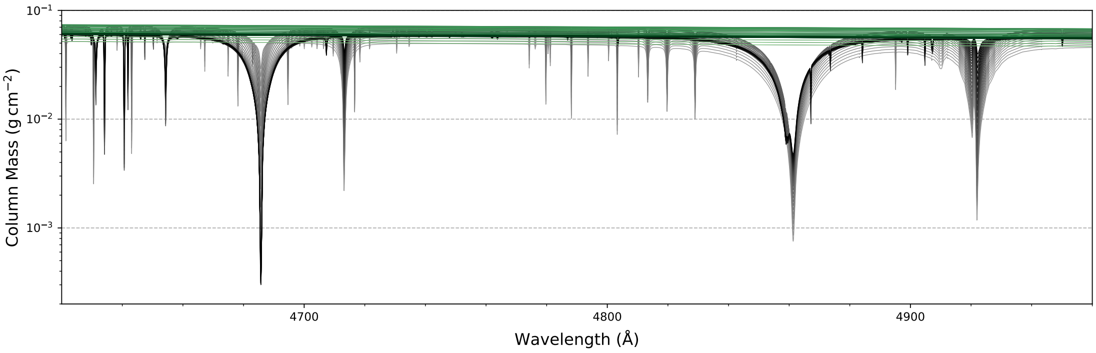

Figure A.1.4. Optical depth at $\tau_\nu = 2/3$ in models with $\log g = 6.0$, $\log n(\mathrm{He})/n(\mathrm{H}) = 0.0$, and temperatures from 30kK (light) to 60kK (dark). The green models show the location of the continuum without spectral lines, while the grey models also include spectral lines.

For a comparison with the observed subdwarf population in the $T_{\mathrm{eff}} - \log n(\mathrm{He})/n(\mathrm{H})$ diagram, all models in which the unstable region reaches the depth where the optical continuum is formed are marked blue in Fig. A.1.5. The predicted unstable region has a striking overlap with the observed population of helium-rich hot subdwarf stars, even at a relatively low surface gravity of $\log g = 4.8$. At higher $\log g$, the predicted unstable region shifts to somewhat higher effective temperatures as the optical continuum is formed further out in the atmosphere. A similar exercise can be done in the $T_{\mathrm{eff}} - \log g$ plane, as shown in the bottom four panels of Fig. A.1.5. Even though the predicted unstable region is broader in $\log g$ than the observed population, its slope with temperature matches the distribution of surface gravities well.

Despite the rough, simplified methods used here, the match of unstable regions to the observed helium-enriched subdwarf population is striking and encourages further investigation. Convection in the photosphere may dampen diffusion processes for He-sdO stars. Since the predicted convection zones are not very deep, their effect on the diffusion time-scale may not be very strong. However, it would be interesting to investigate these He II convection zones with hydrodynamic models, which have predicted deeper convection zones in the past. Even though the atmospheres of helium-rich subdwarf stars are at least partly convective, the radiative flux is much larger than the convective flux throughout the atmosphere. It is therefore not necessary to consider convection in the calculation of chemically homogeneous model atmospheres for these hot stars.

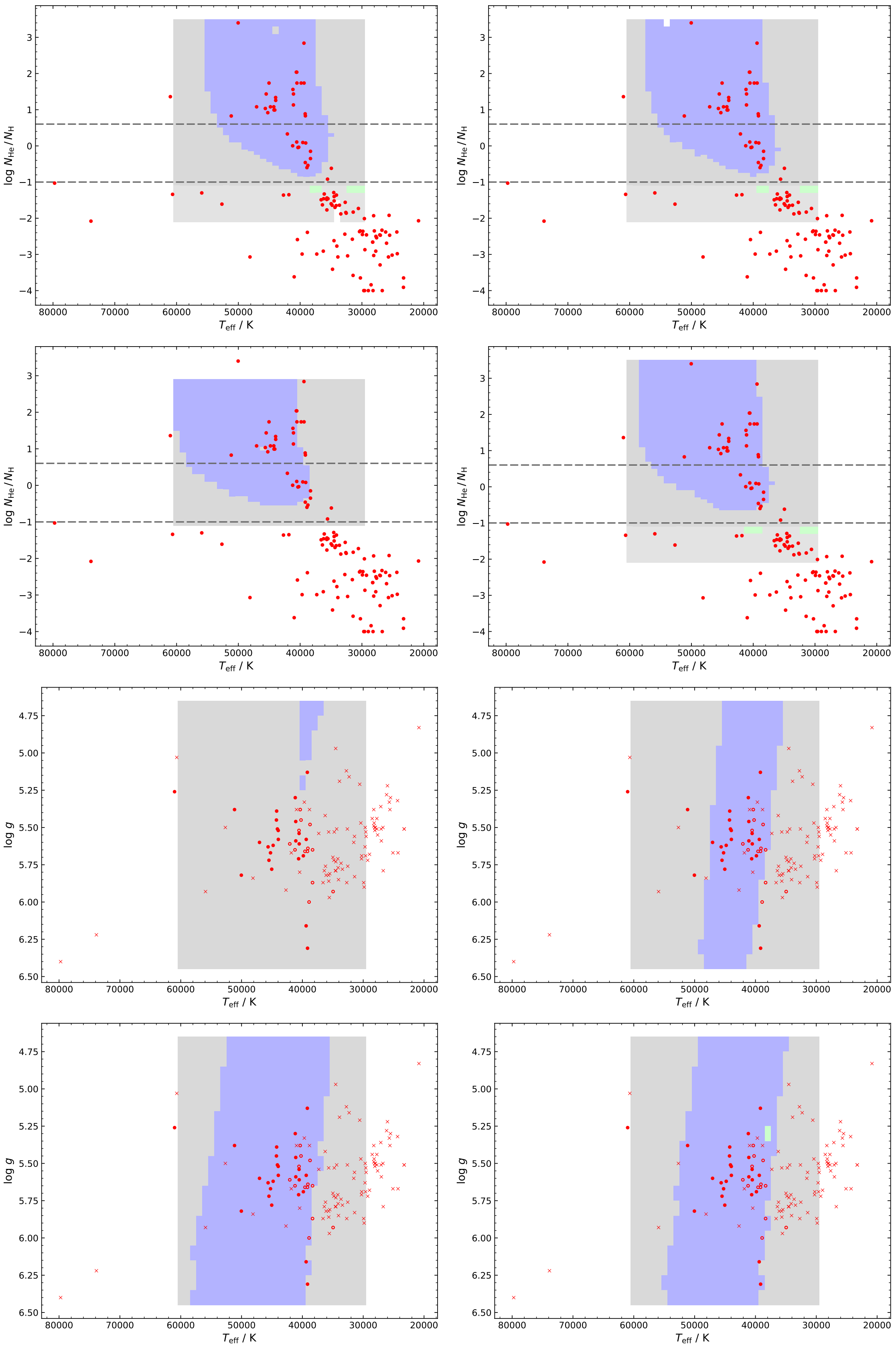

Figure A.1.5. *Top panels*: Convectionally unstable regions in the HeCNSi models compared with the observed hot subdwarf population of Lisker et al. (2005) and Stroeer et al. (2007). *Top panels*: In the $T_{\mathrm{eff}} - \log n(\mathrm{He})/n(\mathrm{H})$ diagram, where clockwise from the top left: $\log g = 4.8, 5.2, 5.6, 6.0$. *Bottom panels*: The $T_{\mathrm{eff}} - \log g$ space, where clockwise from the top left: $\log n(\mathrm{He})/n(\mathrm{H}) = -0.8, -0.4, +0.0, +0.4$. Stars with $\log n(\mathrm{He})/n(\mathrm{H}) > +0.6$ are marked with filled red circles, stars with $+0.6 > \log n(\mathrm{He})/n(\mathrm{H}) > -0.8$ with open circles, and the remaining stars with red crosses. Green patches indicate missing models.

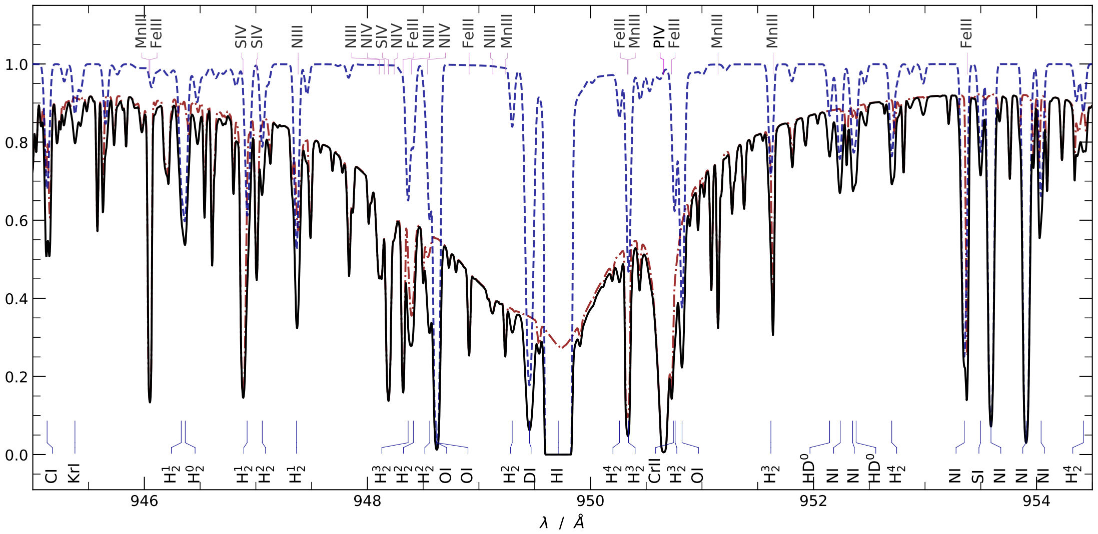

Figure A.2.1. Spectral range around the Lyman δ line in a model of the He-sdO BD+25° 4655. The predicted interstellar transmission is shown in blue, the normalised photospheric model in red, and the transmitted photospheric spectrum in black. Interstellar lines are labelled at the bottom while photospheric lines are labelled at the top.

A.2 Interstellar absorption

Ultra-violet spectra of hot stars show many strong lines. However, not all lines are photospheric; absorption by the interstellar medium (ISM) in the line of sight leads to additional lines that can easily be confused with photospheric lines. This is especially relevant at wavelengths below 1200 Å, where many transitions from the ground state of neutral and singly ionised ions are located (so-called resonance lines). Absorption by interstellar H_2, HD, and CO molecules contributes additional lines in this range. It is therefore important to model interstellar absorption when trying to derive metal abundances from far-UV spectra. This is illustrated in Fig. A.2.1, which shows numerous blends between interstellar and photospheric lines in a synthetic spectrum of the He-sdO BD+25° 4655.

Simple models of absorption by interstellar lines are easily computed when the column density in the line of sight is assumed as an input parameter for each ion individually. Usually, several components of the ISM are defined that are allowed to vary in radial velocity, temperature, turbulent velocity, and column densities. In this way, the contributions by several ISM clouds and the contributions by the different phases of the ISM can be considered. The following phases of the ISM are considered as separate components in the present analysis:

- Molecular regions containing the abundant molecules H_2, HD, and CO ($T \lesssim 100\,\mathrm{K}$).
- Cool atomic regions containing neutral hydrogen, deuterium, and metals ($T \approx 100\,\mathrm{K}$).
- Warm atomic regions containing singly ionised metals ($T \approx 8000\,\mathrm{K}$).
- Hot ionised regions, which can lead to absorption by strongly broadened C IV ($T \approx 10^5\,\mathrm{K}$) and O VI lines ($T \approx 10^6\,\mathrm{K}$). Such regions are present in the vicinity of very hot stars.

Since the focus of this work is photospheric rather than interstellar lines, the interstellar model used here is kept simple.

Due to the low density of the ISM, pressure broadening can be neglected. Instead, line profiles are assumed to be subject to Doppler broadening (thermal and turbulent) and natural broadening, only. In this case, their line profiles are described by Voigt-Hjerting functions

$$H(a, x) \equiv \frac{a}{\pi} \int_{-\infty}^{+\infty} \frac{e^{-y^2}}{(x-y)^2 + a^2}\, \mathrm{d}y\,.$$

According to Tepper-García (2006), this function can be analytically approximated to high precision in the relevant parameter range ($a \ll 1$) as

$$H(a, x) \approx H_0 - \frac{a}{\pi x^2} \cdot [H_0^2\,(4x^4 + 7x^2 + 4 + Q) - Q - 1]$$

where $H_0 \equiv e^{-2}$ and $Q \equiv 1.5x^2$. This treatment is used in VoigtFit and implemented in Python. It would be possible to compute the full Voigt-Hjerting function using the SciPy library (Virtanen et al. 2020). However, it is even faster to compute the approximation in a Fortran function, which is done here.

In the case of interstellar absorption, the damping parameter a is given by

$$a = \frac{\lambda_0 \cdot A_{\mathrm{ki}}}{4\pi \cdot b},$$

where λ_0 is the transition rest wavelength and A_{ki} is the transition probability. In a physical model, the Doppler broadening parameter b is computed from the component turbulent velocity υ_{tb} and the component temperature T as

$$b = \sqrt{\upsilon_{\mathrm{tb}}^2 + \frac{2k_{\mathrm{B}}}{m_{\mathrm{u}}} \cdot \frac{T}{A}},$$

where A is the standard atomic weight of the ion under consideration, m_{u} is the atomic mass constant, and k_{B} is the Boltzmann constant. The Doppler broadening parameter is usually dominated by the turbulent velocity and has values between about 5 and 20 $\mathrm{km\,s^{-1}}$ (except for hot ionised regions, where thermal broadening is dominant).

Finally, the wavelength-dependent transmission of a single line $I(\lambda)$ is computed as

$$I(\lambda) = e^{-\tau(\lambda)}$$

from the optical depth $\tau(\lambda)$, which is given by

$$\tau(\lambda) = \frac{\sqrt{\pi} e^2}{m_e c} \cdot N_{\mathrm{col}} \cdot f_{\mathrm{osc}} \cdot \lambda_0 \cdot H(a, x(\lambda)) \;/\; b,$$

where c is the speed of light, m_e is the electron rest mass, N_{col} is the column density of the considered ion, f_{osc} the transition oscillator strength, and $x(\lambda)$ is the distance from the line center

$$x(\lambda) = (\lambda - \lambda_0) \;/\; \lambda_D$$

in units of the Doppler wavelength $\lambda_D = b \cdot \lambda_0 \;/\; c$.

Apart from the user-defined ISM components, the only data required to produce the interstellar transmission spectrum are transition wavelengths λ_0, oscillator strengths f_{osc}, and transition probabilities A_{ki} for atomic lines and molecular lines. The interstellar line list used here is based on data collected for use with the IDL script OWENS (e. g. Lemoine et al. 2002; Oliveira & Hébrard 2006). OWENS is an interactive tool that allows modelling interstellar lines and was developed for the FUSE satellite. Since OWENS was found to be inconvenient for the present analysis, its core was converted into a simple Python script that produces transmission spectra using the equations stated above. It was found that the resulting implementation of the computation of optical depths was so similar to that used for the intergalactic line fitting tool VoigtFit (Krogager 2018) that it was possible to mostly adopt the existing implementation. Since VoigtFit is targeted at precise fitting of intergalactic lines towards quasars and does not consider a detailed model of a stellar photospheric spectrum, it could not directly be used here. For the purpose of this work it sufficient to adjust interstellar component parameters and column densities by eye (that is, without a χ^2 fit).

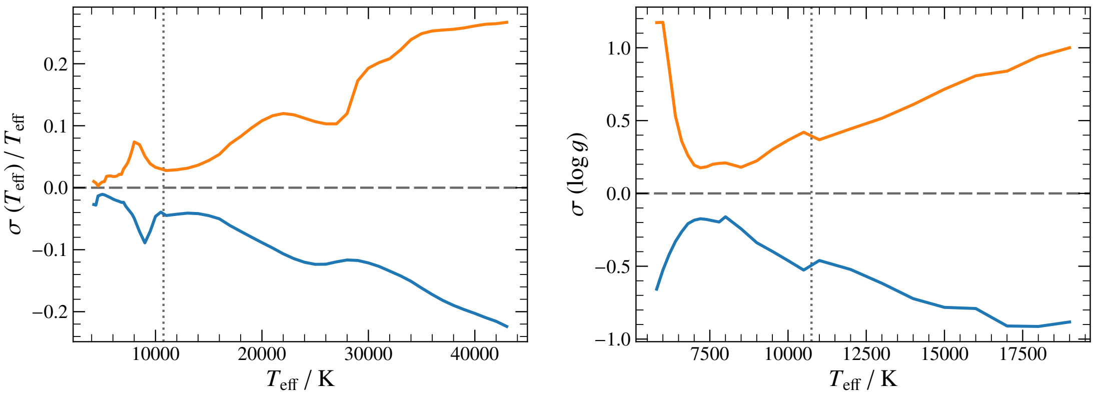

Figure A.3.1. Dependence of the lower (blue) and upper (orange) uncertainty of T_{eff} (left panel) and $\log g$ (right panel) on T_{eff} for fits to SEDs constructed from synthetic spectra. The dotted line separates Atlas12/Synthe models (left) from the ADS/sdB grid (right).

A.3 Temperatures and gravities from the SED

The accuracy and limitations of the SED fitting method are briefly evaluated in this section, in particular the T_{eff} and $\log g$ determination. To this end, synthetic magnitudes were computed from a model spectrum for a specific set of filters. This excludes uncertainties introduced by the model spectra, inaccurate photometric zero points, as well as erroneous filter functions. Here, the GALEX, SkyMapper, *Gaia*, 2MASS, and WISE (W1 and W2) filters are chosen because they are available for a large number of known hot subdwarfs and provide good photometric coverage – from the UV to the IR (compare Fig. 2.3.1).

Synthetic magnitudes formally have neither statistical nor zero point uncertainties. In a χ^2 fit, this would result in the trivial result that the fit parameters exactly equal the input parameters with zero uncertainty. To allow for a more realistic comparison to the uncertainty of real observations, a statistical uncertainty of 0.01 mag was assigned to all magnitudes. The SED fitting procedure further adds standard zero point uncertainties in quadrature, as is done for real observations. Interstellar extinction was applied to the model spectra before constructing the SED, in particular for a reddening parameter $R(55) = 3.02$ and a colour excess of $E(44-55) = 0.1$ mag, a typical value for hot subdwarfs at high Galactic latitudes. This is necessary to consider the uncertainty that arises from the strong correlation between T_{eff} and the colour excess caused by extinction.

Fits to these mock data were performed for a sequence of T_{eff} using the Atlas12/Synthe and ADS/sdB model grids. The helium abundance (solar) was kept fixed, while the colour excess, T_{eff}, $\log g$, and the metallicity [Fe/H] were free parameters. Because these four parameters are correlated, all of them need to be free for a good estimation of uncertainties. The input $\log g$ was set to 4.0 for the Synthe grid and 5.6 for the ADS/sdB grid, while the input metallicity was set to [Fe/H] = 0 for both grids. This corresponds to solar abundances for the Synthe grid and mean sdB abundances from Pereira (2011) for the ADS/sdB grid.

The input parameters were always reproduced by the χ^2 fit. As shown in the left panel of Fig. A.3.1, the relative uncertainty of T_{eff} increases drastically above about 29000 K. Temperatures beyond 43000 K are not shown because the upper uncertainties become very large. A notable feature is the local increase in T_{eff} uncertainty around 9500 K – this is likely related to the maximum strength of the Balmer jump which is reached at that temperature. The uncertainty of $\log g$, shown in the right panel of Fig. A.3.1, reaches its minimum at about 8000 K. For low T_{eff}, the uncertainty increases rapidly because the Balmer jump is not sensitive to $\log g$; for hotter stars, the flux maximum progressively shifts to shorter (UV) wavelengths while the Balmer jump steadily weakens. It should be noted that excellent real observations can perform better than this test if more magnitudes are available, or worse if less are available. In particular the GALEX observation is important at high T_{eff}, but is not always available.

Appendix B

Additional material

B.1 For Section 3.1

Table B.1.1. Remaining unidentified lines in the spectra of LS IV−14°116 and Feige 46. Estimated equivalent widths are given for LS IV−14°116. The detection limit is about 1.5 mÅ.

λ_{obs} / Å	EW / mÅ	Comment
3330.784	14.6	Kr III?
3439.421	13.3	Kr III, Rb III?
3457.789	11.3	Sr III?
3492.674	6.2	Kr III, Rb III?
3530.783	7.9	Zn III?
3570.183	4.5	Ne II?
3647.659	4.4	
3649.103	4.2	
3853.263	7.1	
3857.237	4.8	
3860.431	8.0	
3863.822	7.8	
3870.852	6.0	Ni III?
3873.239	3.0	
3901.527	5.3	
3912.595	4.5	Sr IV?
3915.091	5.3	
3931.572	5.2	
3931.572	5.2	
3935.767	9.5	
4013.975	4.1	
4037.023	6.5	
4050.439	4.8	
4058.837	4.4	
4059.791	2.6	
4088.011	4.7	
4148.989	13.0	
4181.054	7.5	Kr IV?
4184.853	5.1	
4210.418	1.8	
4211.177	1.8	
4479.618	14.0	
4636.534	35.0	not cov. for LS IV−14°116 broad
4814.473	14.0	
4820.085	9.2	
4879.165	5.3	
4972.468	8.1	
5102.885	16.5	weaker in Feige 46, Sn III?
5106.656	6.6	
5114.154	12.9	very broad
5135.913	13.9	broad
5167.776	6.2	
5207.452	4.1	
5208.282	3.5	
5210.208	2.8	stronger in Feige 46
5221.968	9.4	weaker in Feige 46
5232.749	5.9	
5234.305	5.7	not det. in Feige 46
5241.974	6.2	
5562.854	8.3	Zn III?
6756.452	16.3	not cov. for Feige 46

Figures B.1.1 and B.1.2 show the best-fit models (red) and observed UVES spectra (grey) of Feige 46 and LS IV−14°116, respectively. The strongest spectral lines are labelled and red labels identify line that lack oscillator strengths. Both spectra were normalised to match the model fluxes using a basic spline fit to represent the continuum.

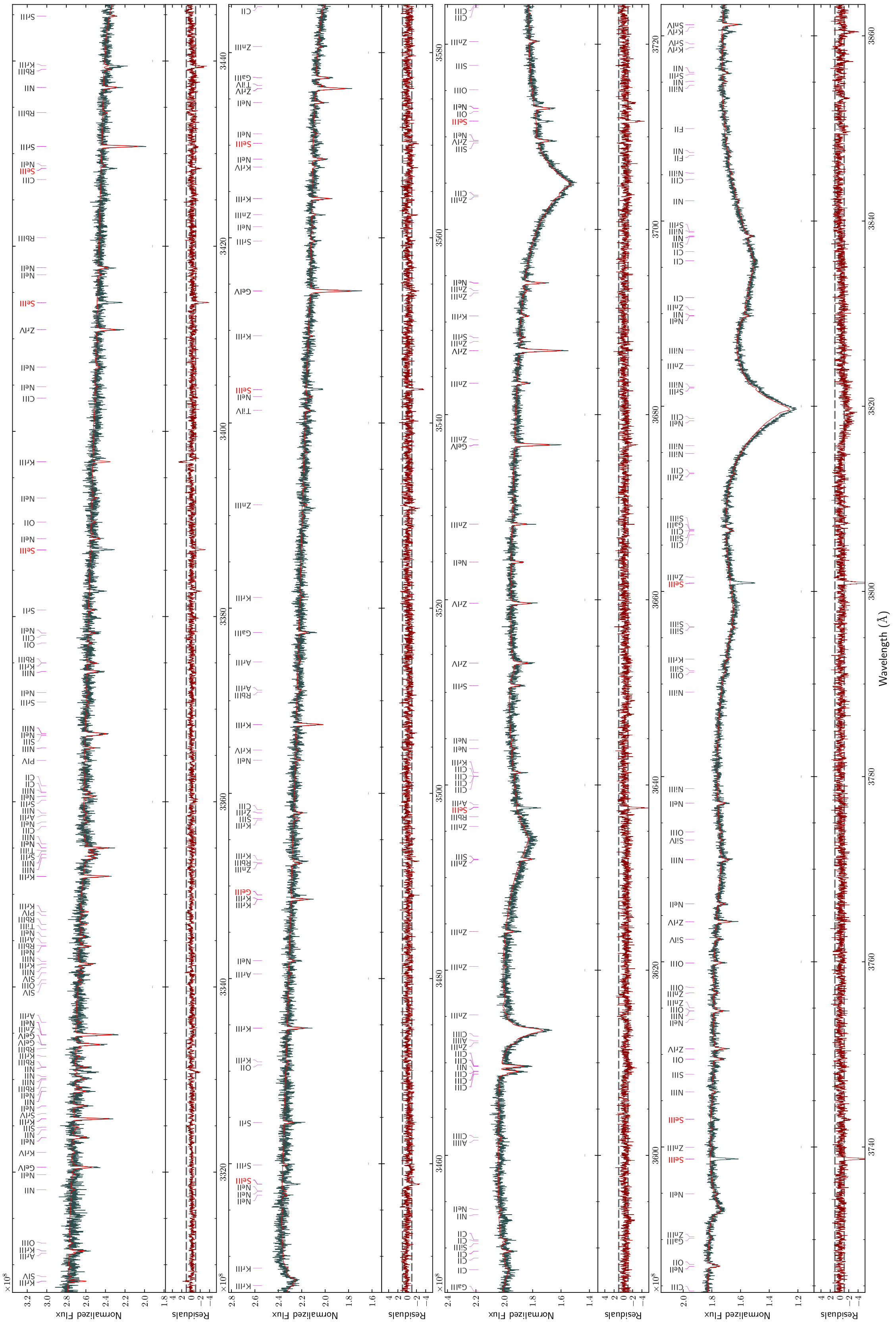

Figure B.1.1. UVES spectrum of Feige 46 (grey) and the final model (red). Adopted from Dorsch et al. (2020).

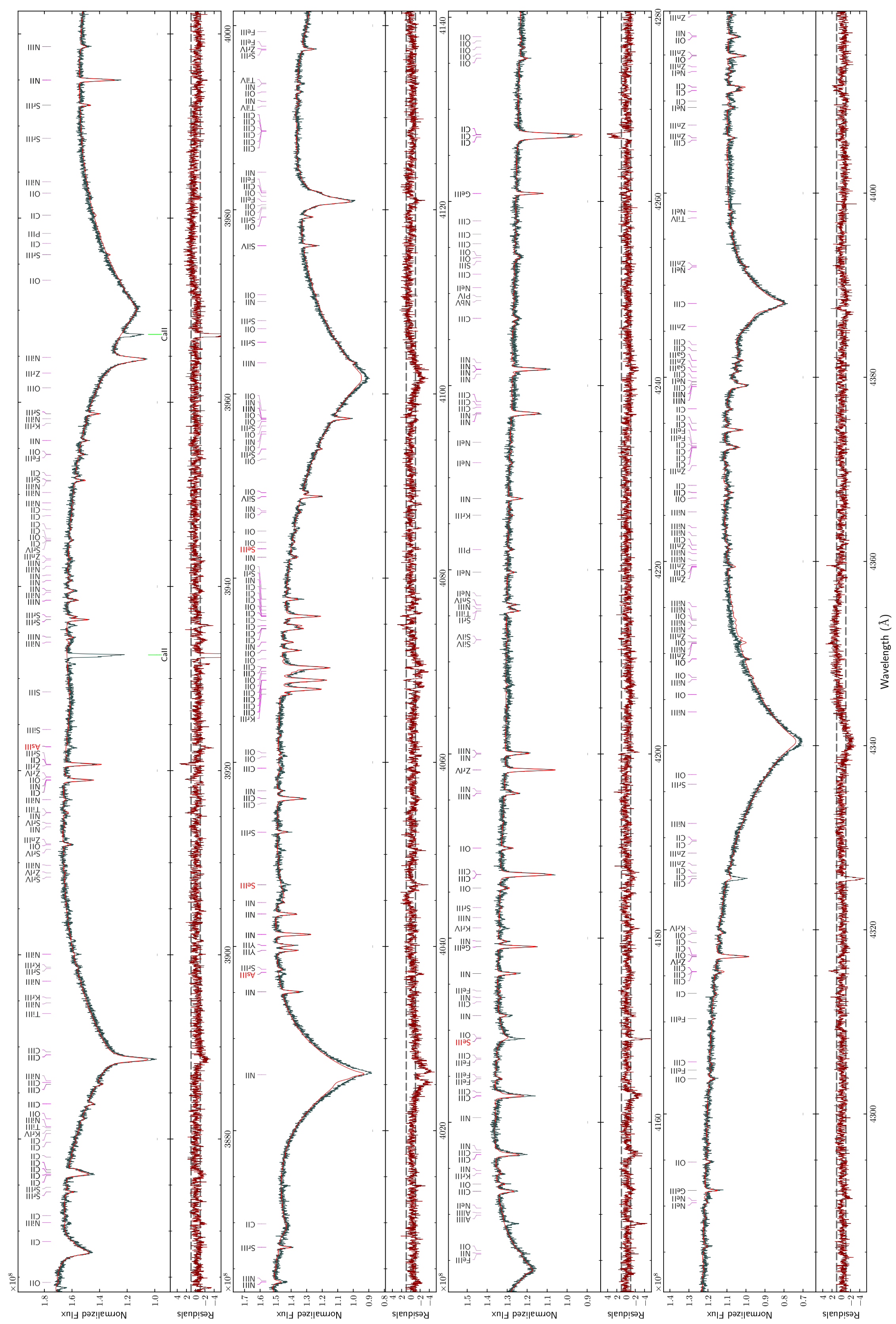

Figure B.1.1 (continued). UVES spectrum of Feige 46 (grey) and the final model (red). Adopted from Dorsch et al. (2020).

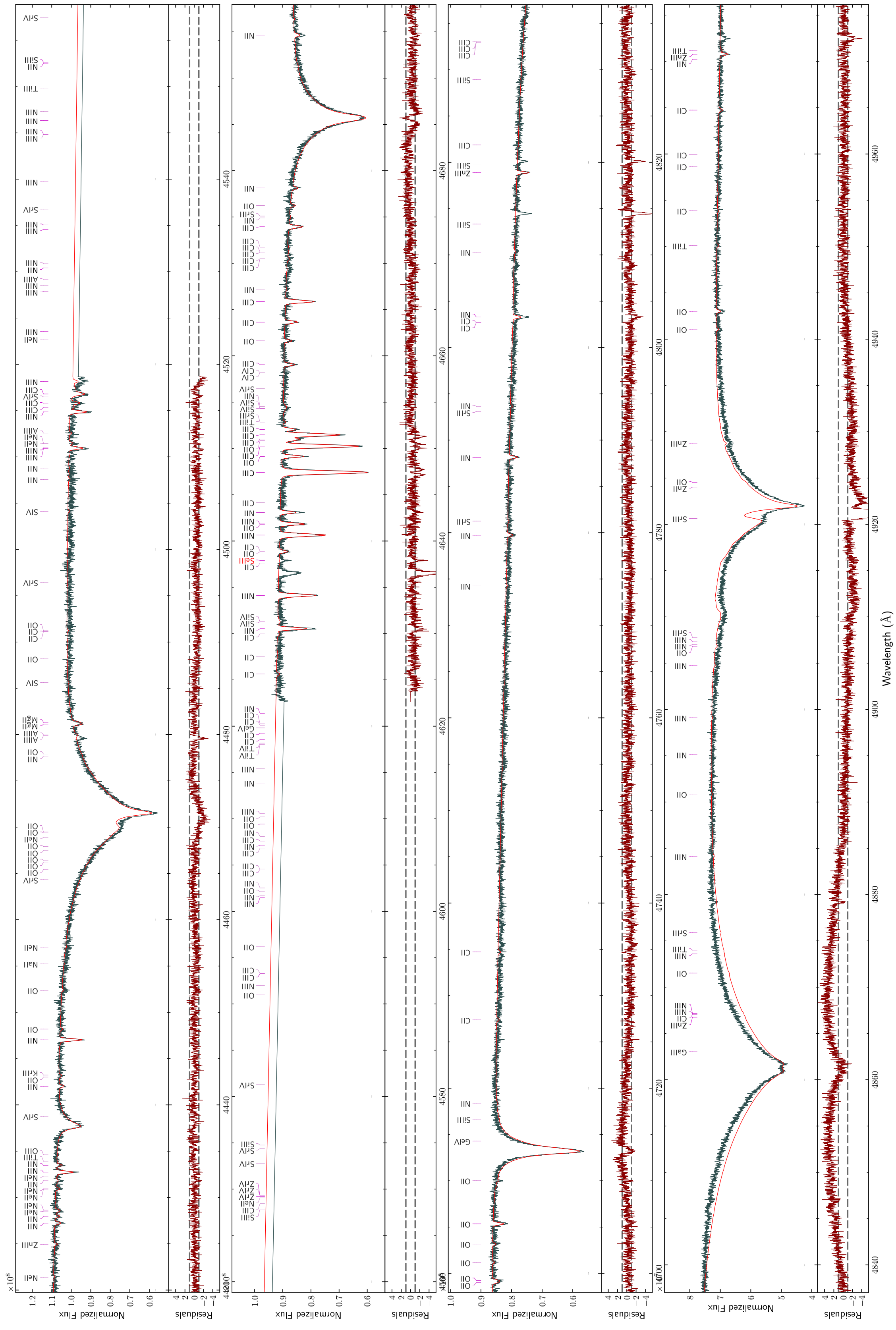

Figure B.1.1 (continued). UVES spectrum of Feige 46 (grey) and the final model (red). Adopted from Dorsch et al. (2020).

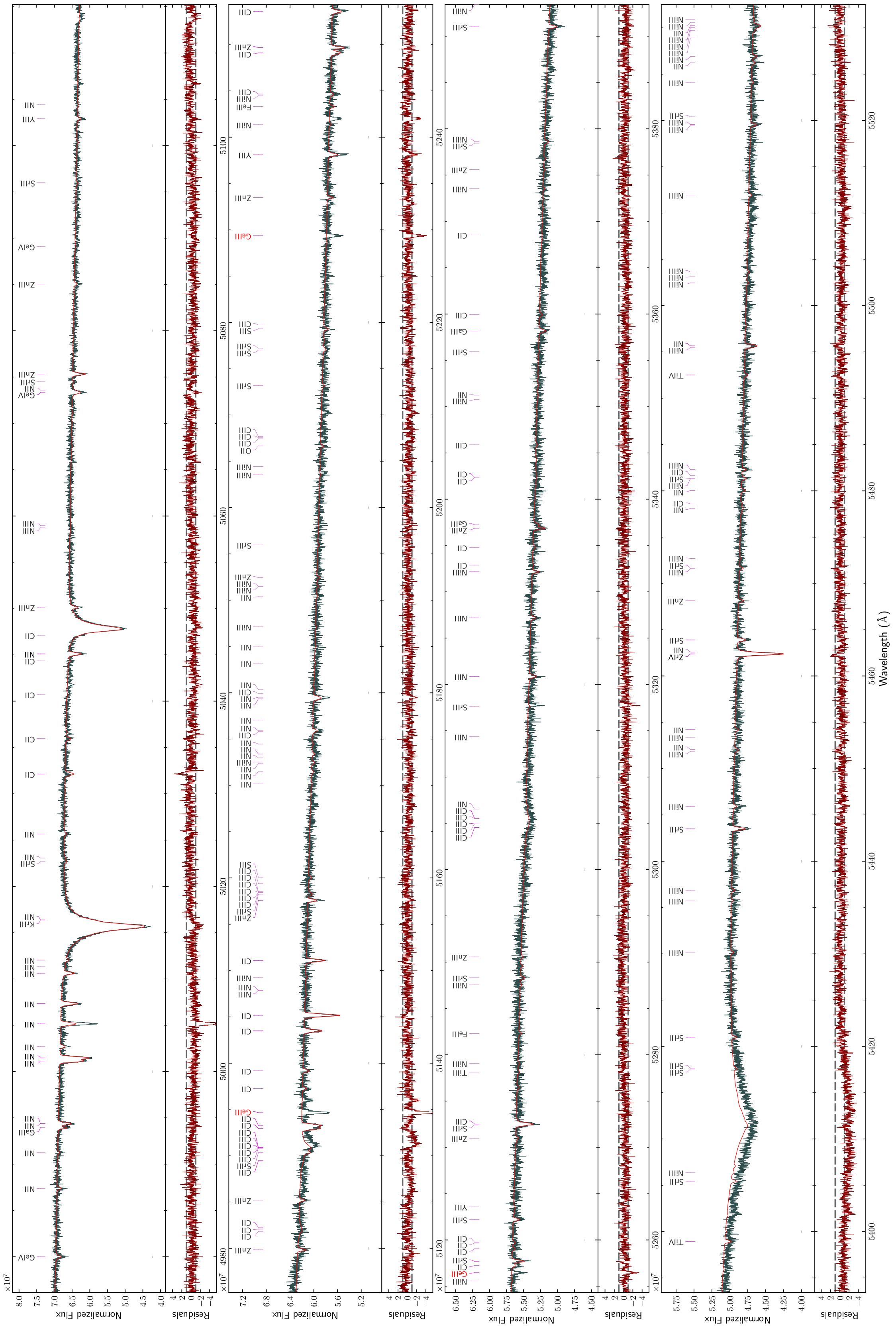

Figure B.1.1 (continued). UVES spectrum of Feige 46 (grey) and the final model (red). Adopted from Dorsch et al. (2020).

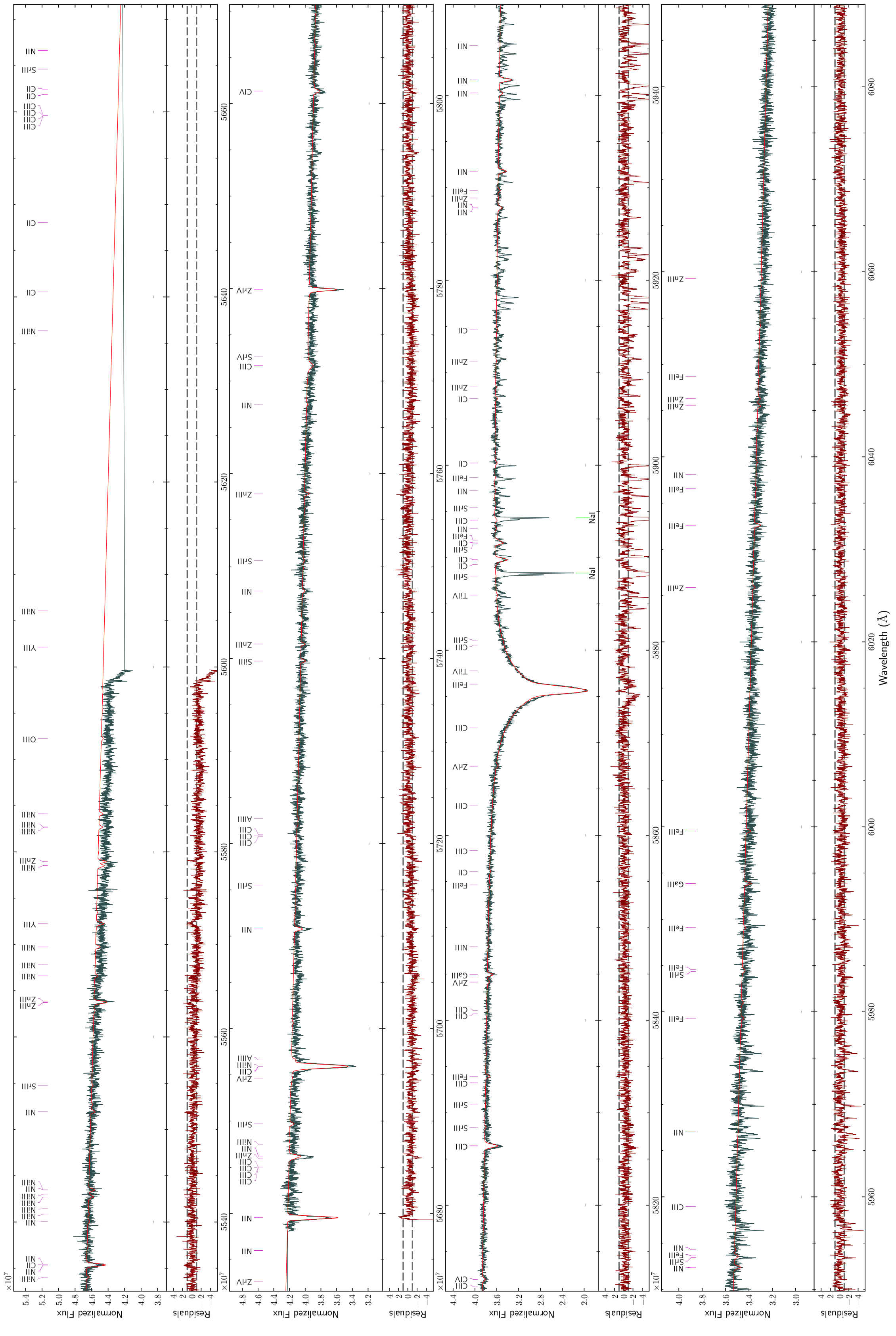

Figure B.1.1 (continued). UVES spectrum of Feige 46 (grey) and the final model (red). Adopted from Dorsch et al. (2020).

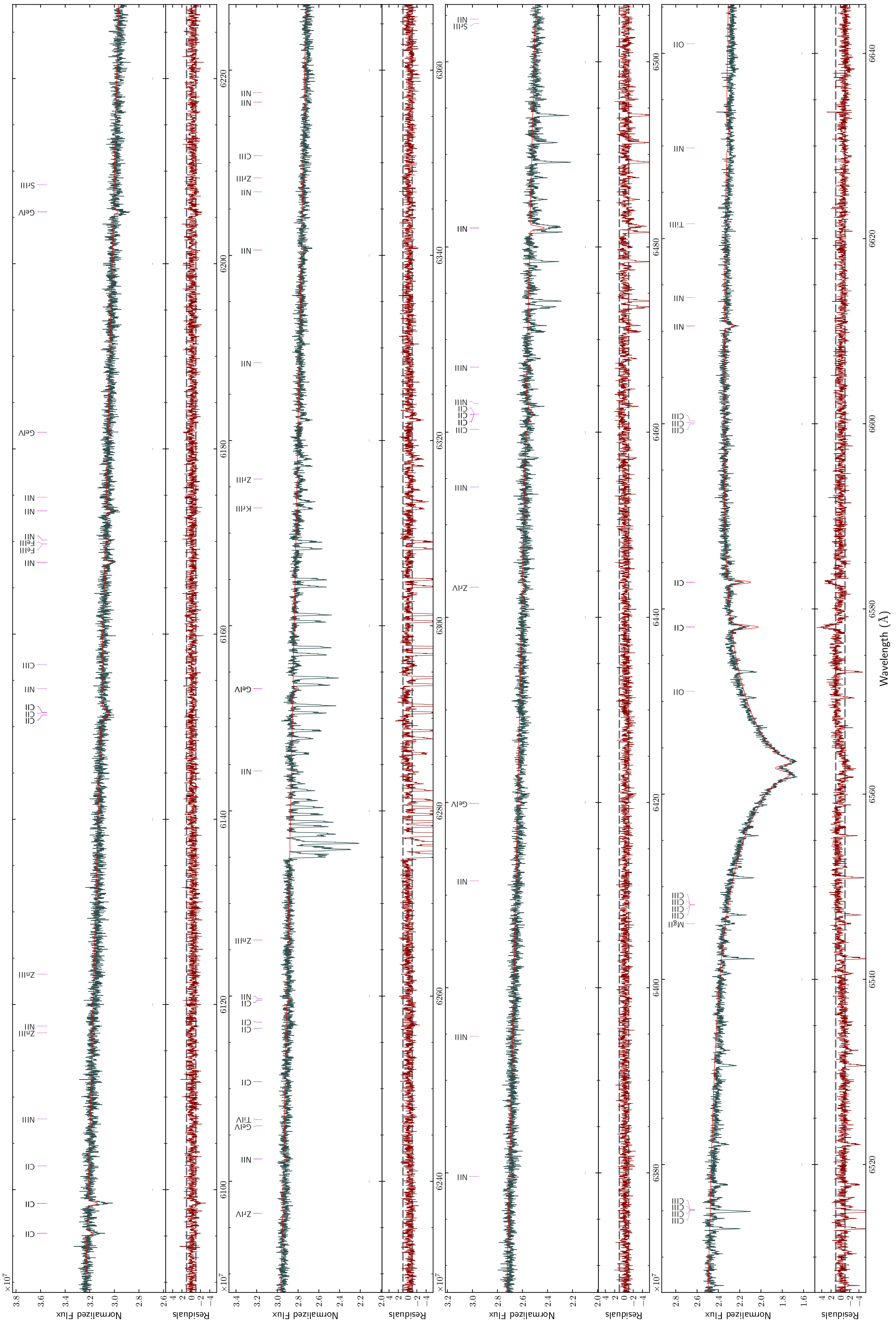

Figure B.1.1 (continued). UVES spectrum of Feige 46 (grey) and the final model (red). Adopted from Dorsch et al. (2020).

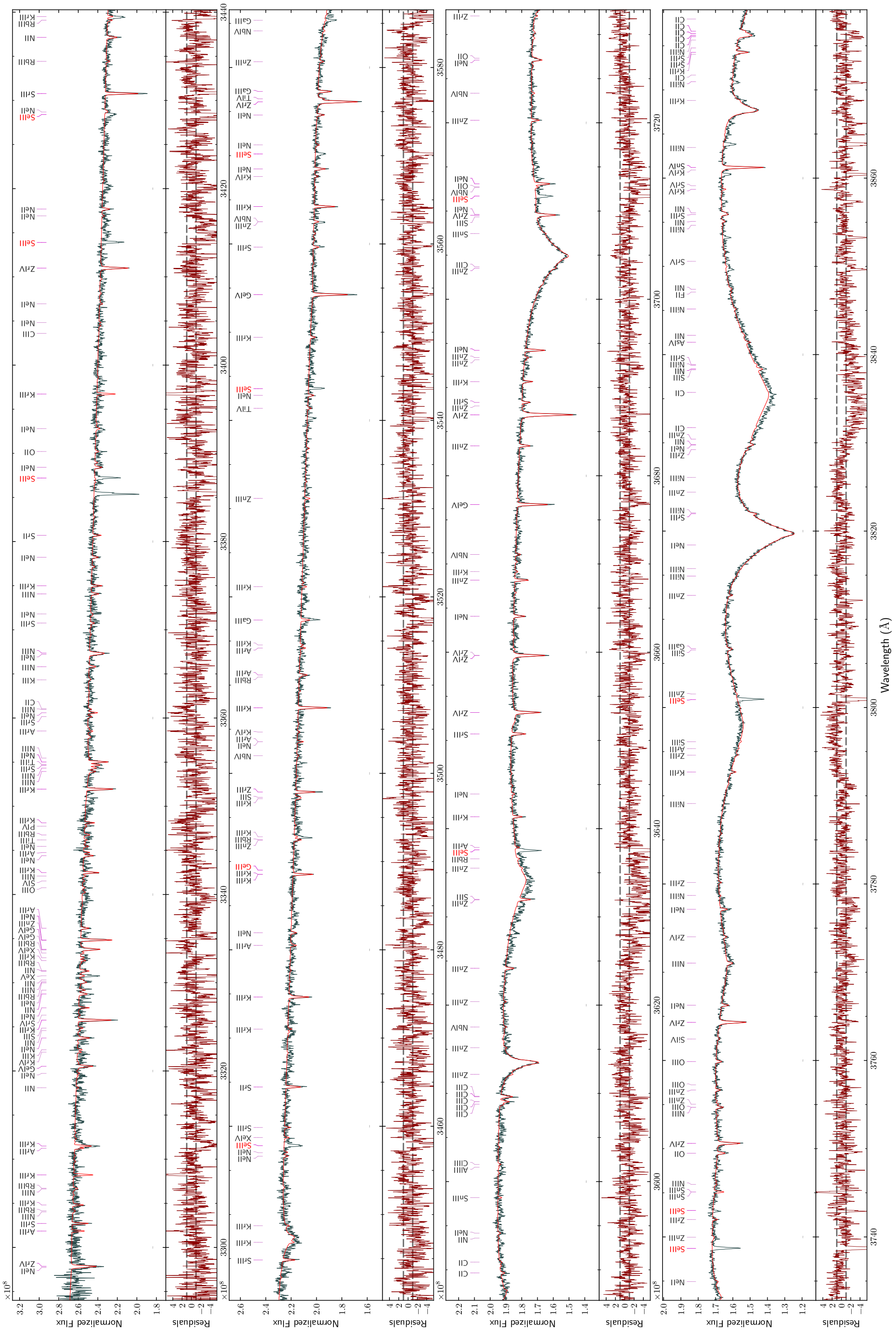

Figure B.1.2. UVES spectrum of LS IV−14°116 (grey) and the final model (red). Adopted from Dorsch et al. (2020).

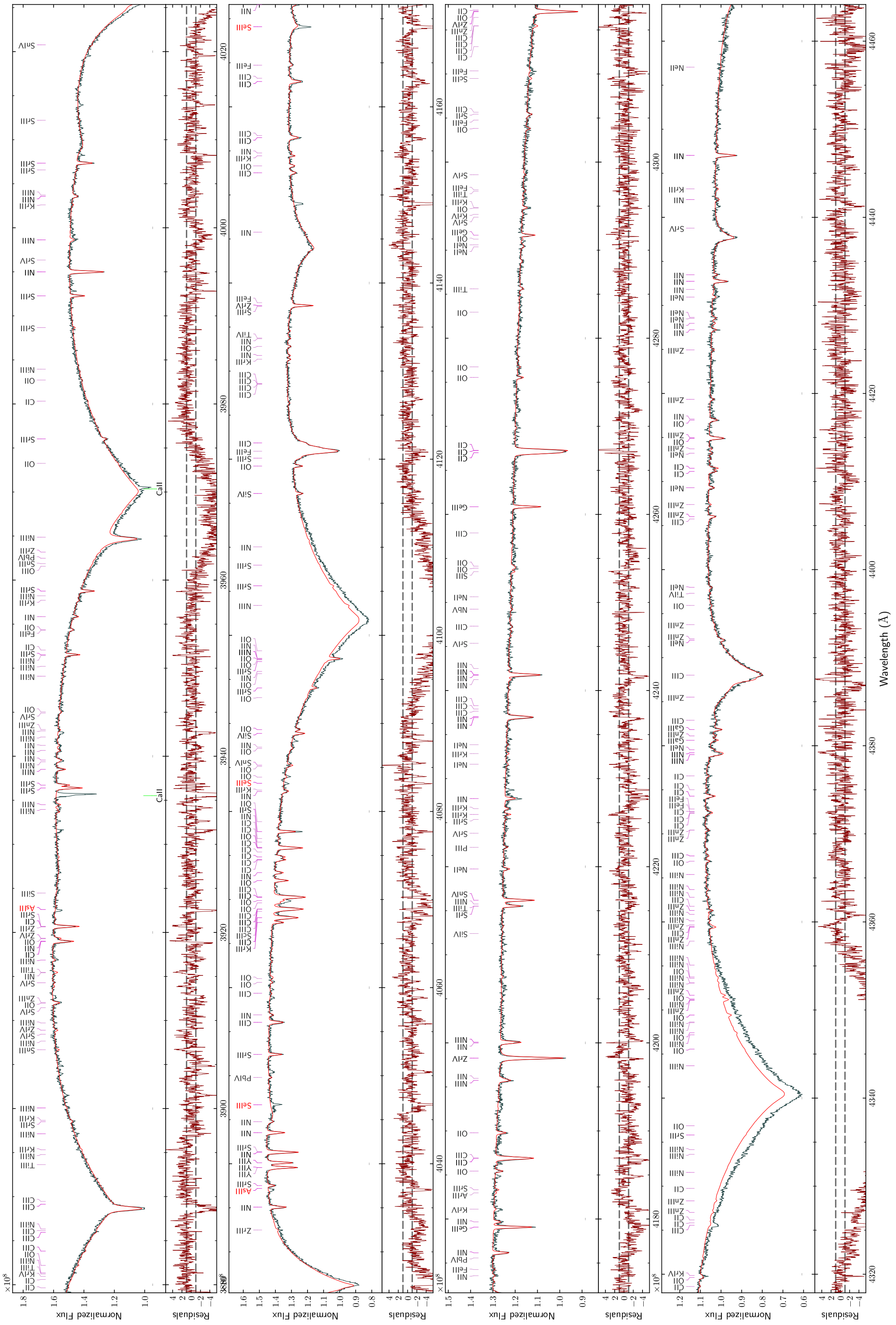

Figure B.1.2 (continued). UVES spectrum of LS IV−14°116 (grey) and the final model (red). Adopted from Dorsch et al. (2020).

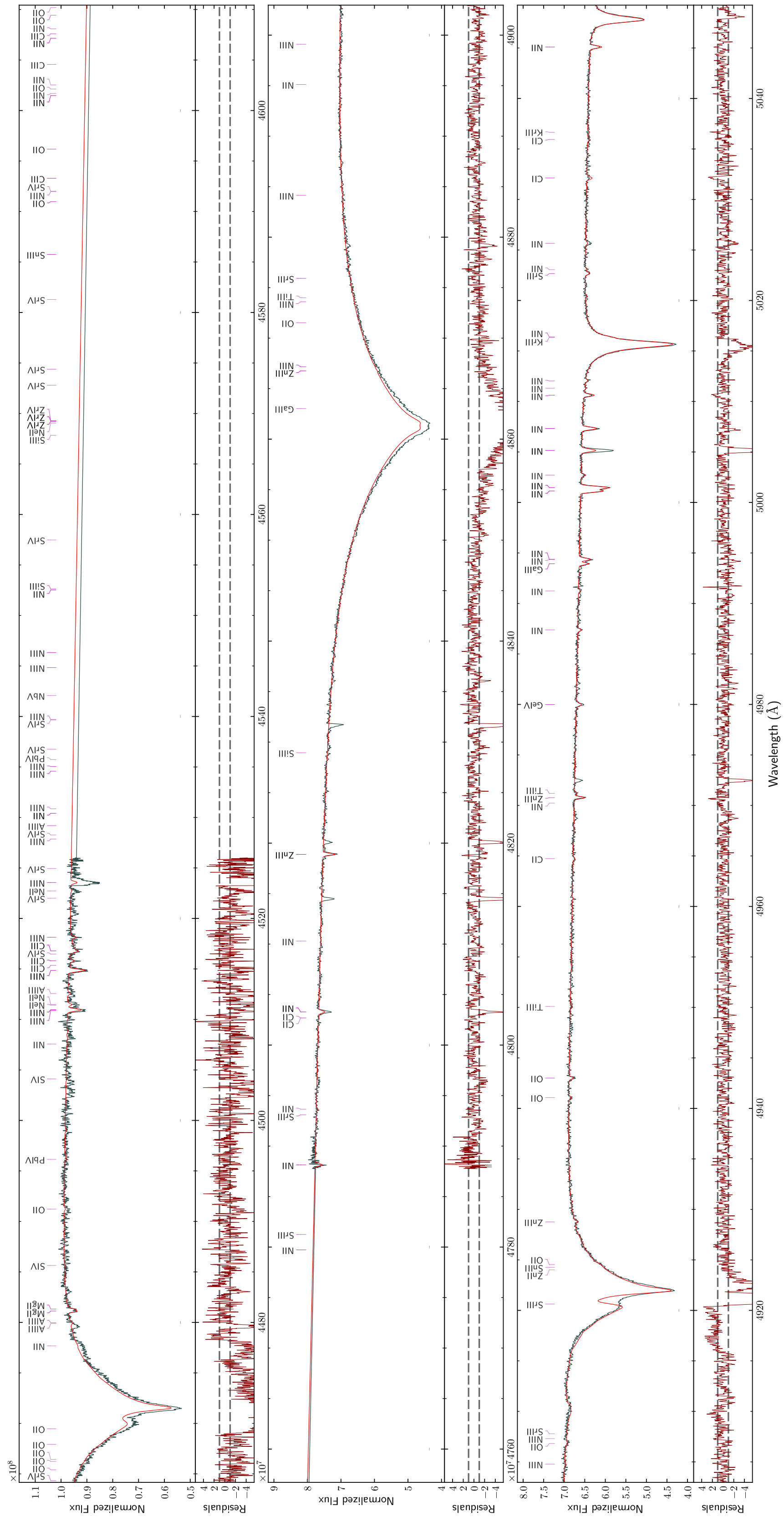

Figure B.1.2 (continued). UVES spectrum of LS IV−14°116 (grey) and the final model (red). Adopted from Dorsch et al. (2020).

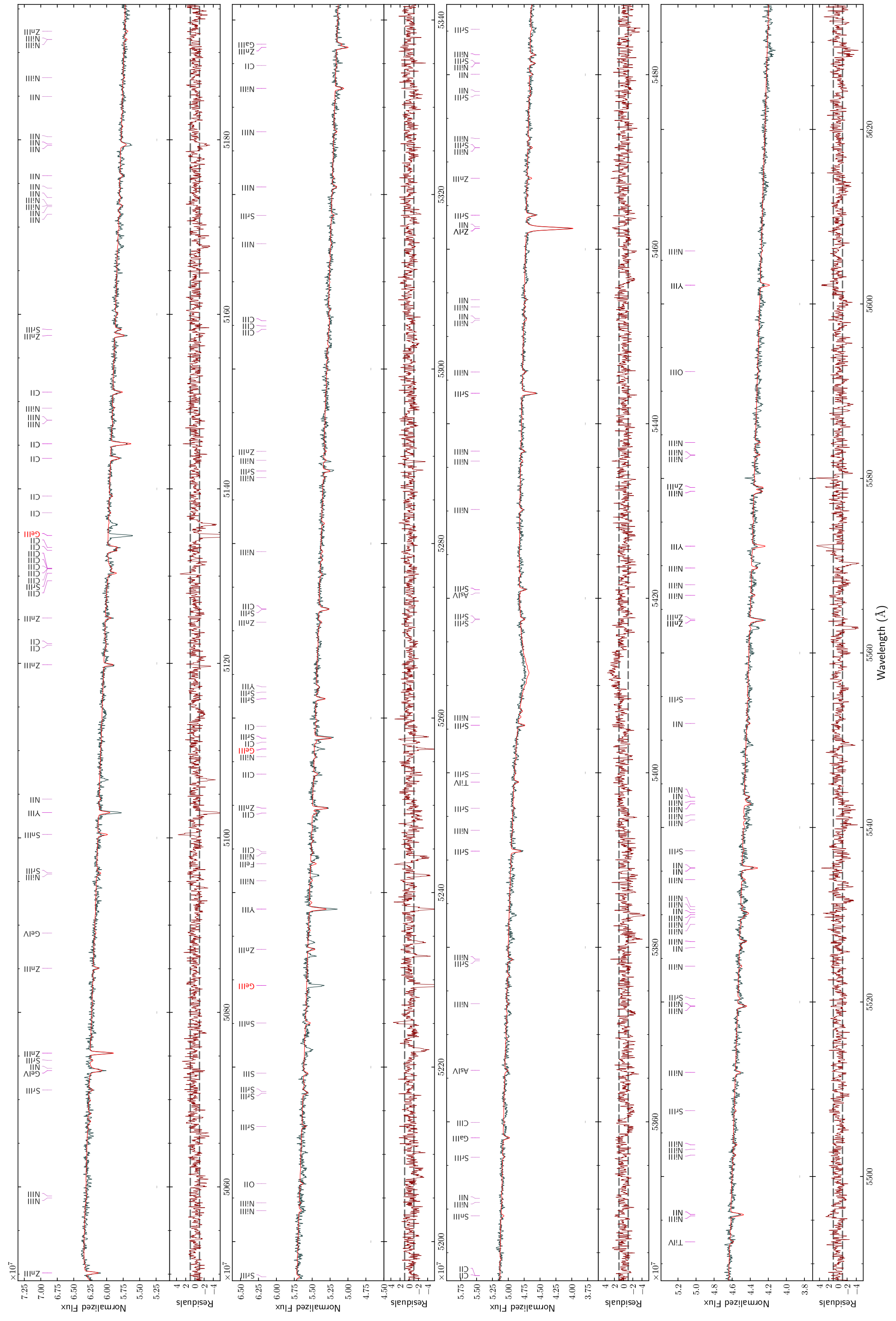

Figure B.1.2 (continued). UVES spectrum of LS IV−14°116 (grey) and the final model (red). Adopted from Dorsch et al. (2020).

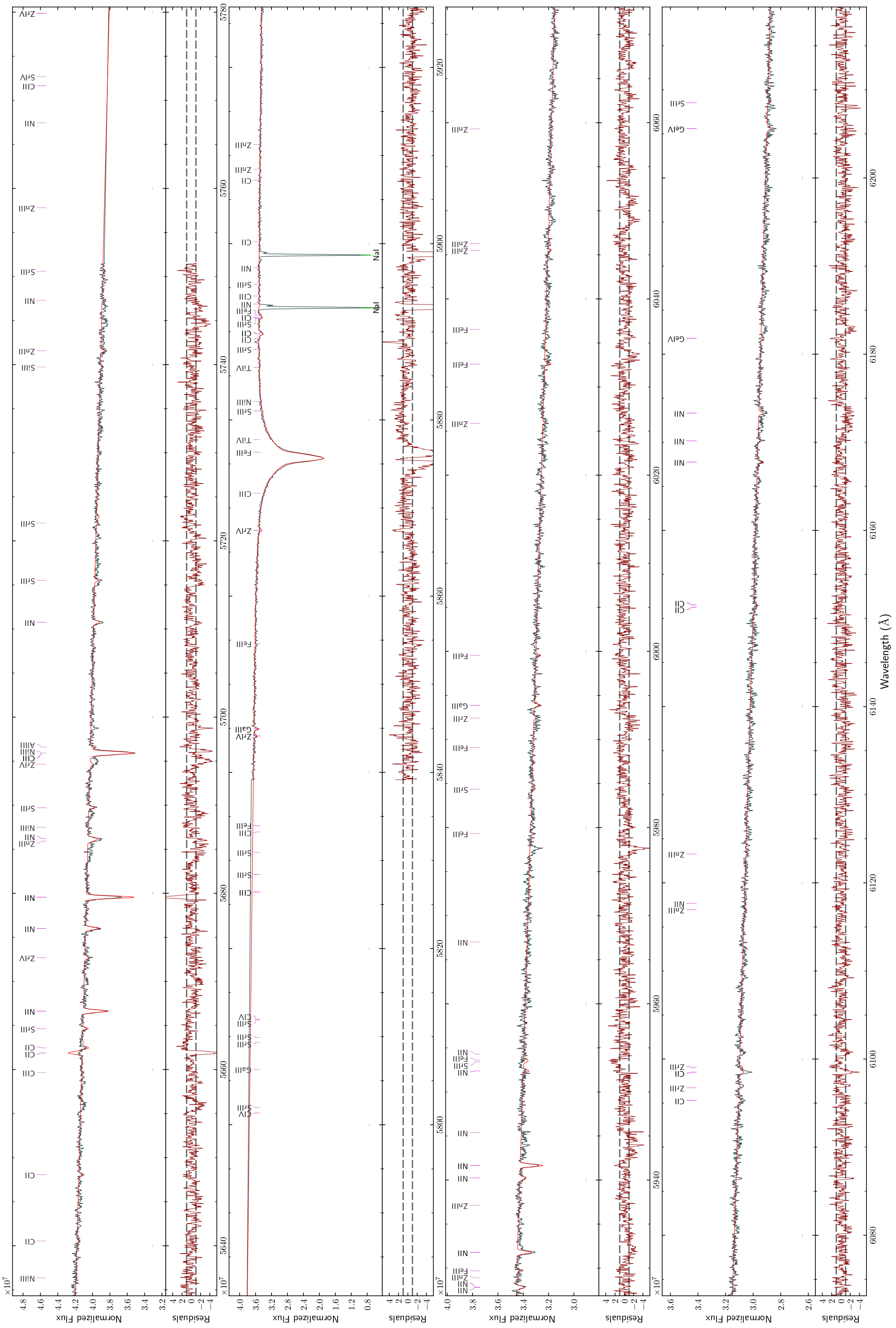

Figure B.1.2 (continued). UVES spectrum of LS IV−14°116 (grey) and the final model (red). Adopted from Dorsch et al. (2020).

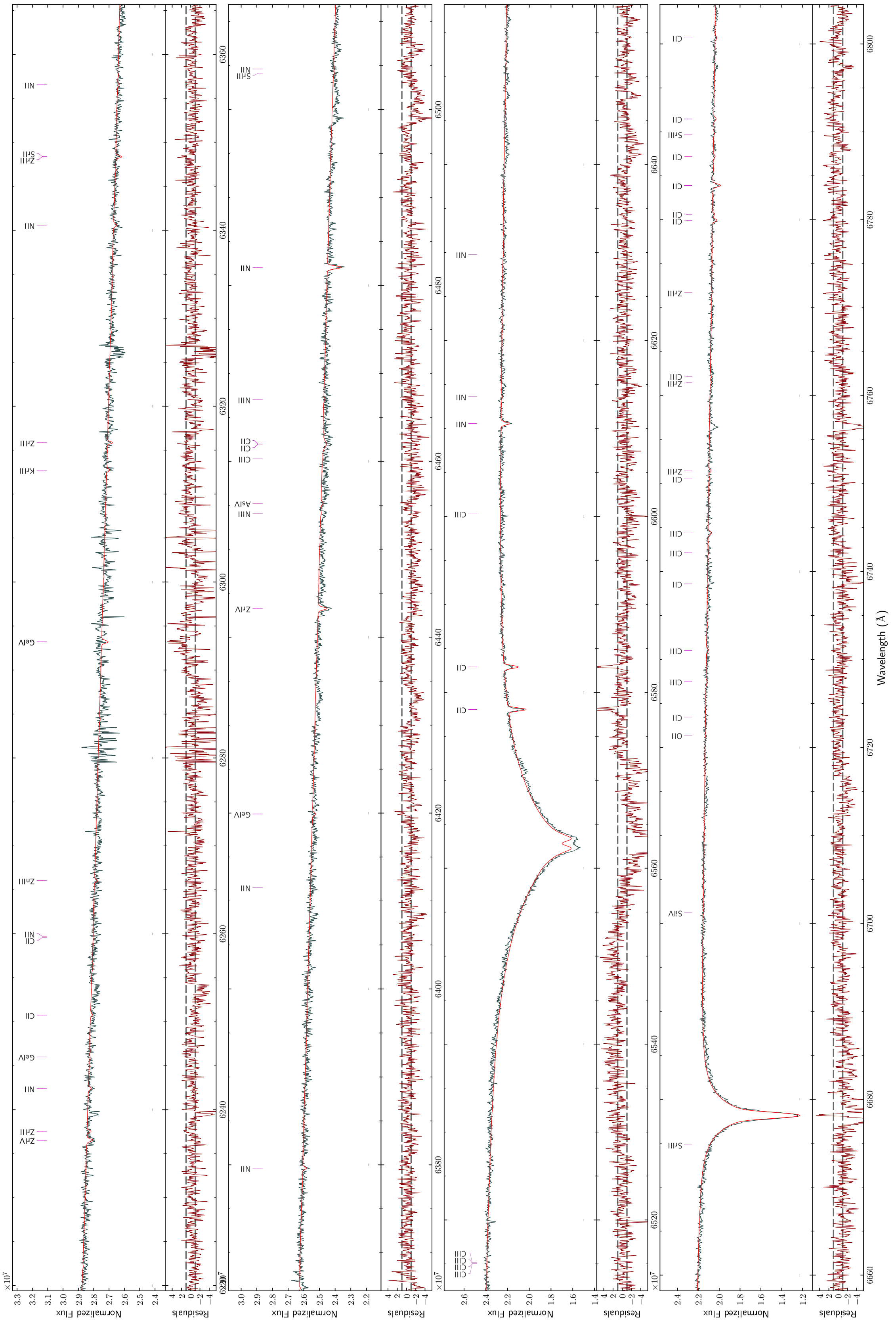

Figure B.1.2 (continued). UVES spectrum of LS IV−14°116 (grey) and the final model (red). Adopted from Dorsch et al. (2020).

B.2 For Section 3.2

This section presents the best fits to the full UV spectra of CPD −56° 464 and the SM Star as described in Sect. 3.2. In these plots, the best-fit model is shown in red while the observation is grey. Lines originating from heavy metals ($Z > 30$) are highlighted in blue. The contribution of absorption by the interstellar medium is shown by the light blue model. These lines were modelled as described in Sect. A.2; they are labelled at the bottom of each panel.

The FUSE spectrum of CPD −56° 464 is shown without binning in Fig. B.2.1. Because the FUSE spectrum of the SM Star features a high spectral resolving power but a low signal-to-noise ratio, it is shown with 4× binning in Fig. B.2.2. This spectrum also shows broad H I, N I, and O I emission lines. These are caused by the Earth's atmosphere and all affected regions were excluded from the analysis. Similar to the FUSE spectrum, 3× binning is applied to the STIS/E140M spectrum of the SM Star in Fig. B.2.3. As discussed in Sect. 3.2.2, two regions in the STIS spectrum are strongly affected by broad absorption features caused by ejecta associated with the foreground supernova remnant SN 1006.

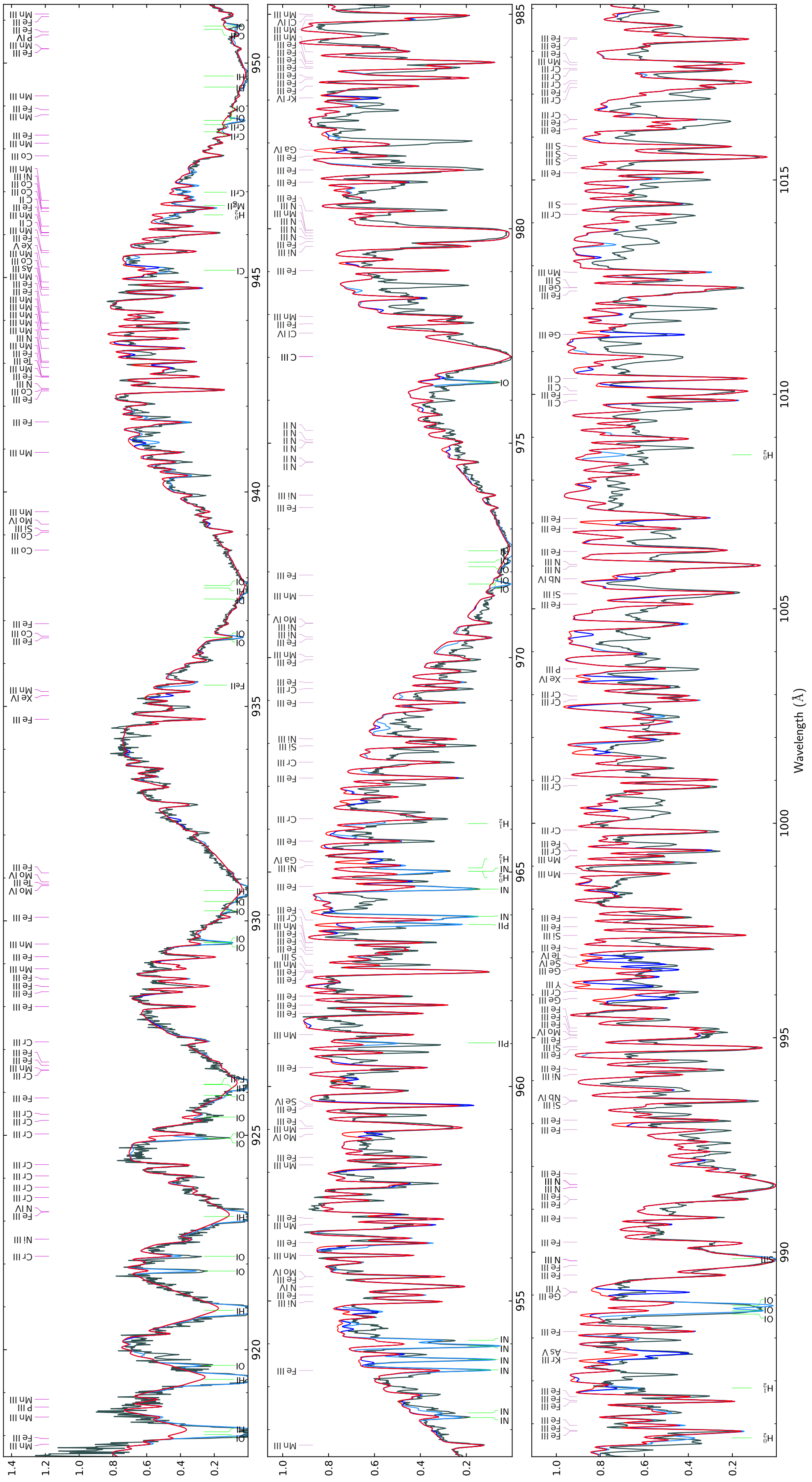

Figure B.2.1. FUSE spectrum of CPD −56° 464 (grey) and the best-fit model (red).

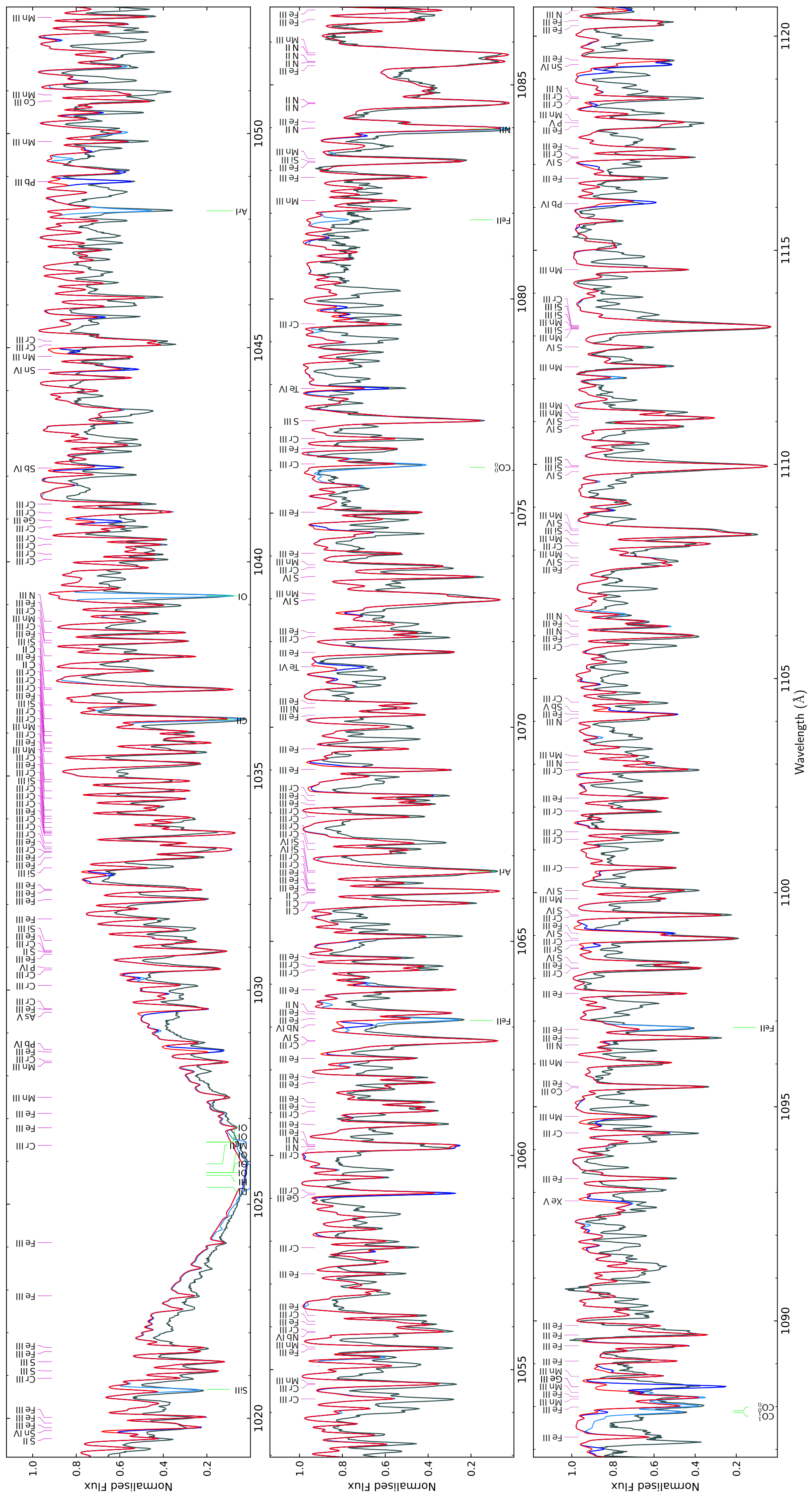

Figure B.2.1 (continued). FUSE spectrum of CPD −56° 464 (grey) and the best-fit model (red).

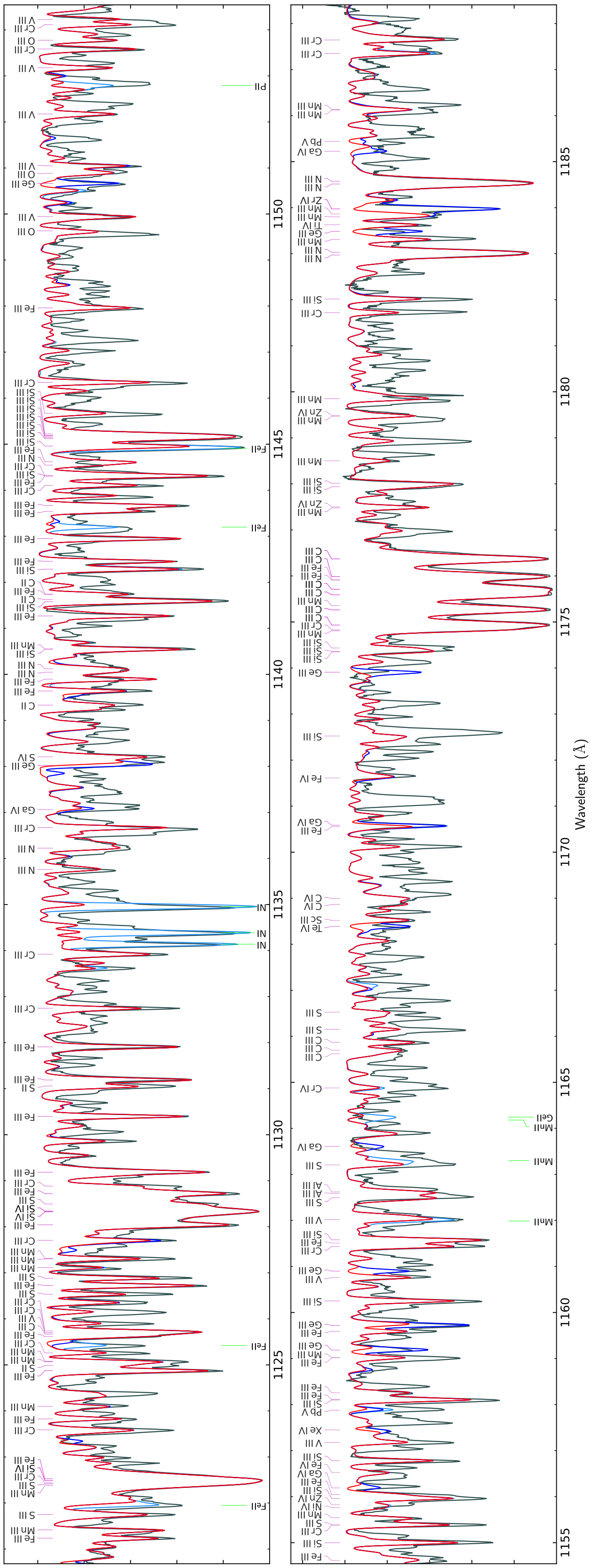

Figure B.2.1 (continued). FUSE spectrum of CPD −56° 464 (grey) and the best-fit model (red).

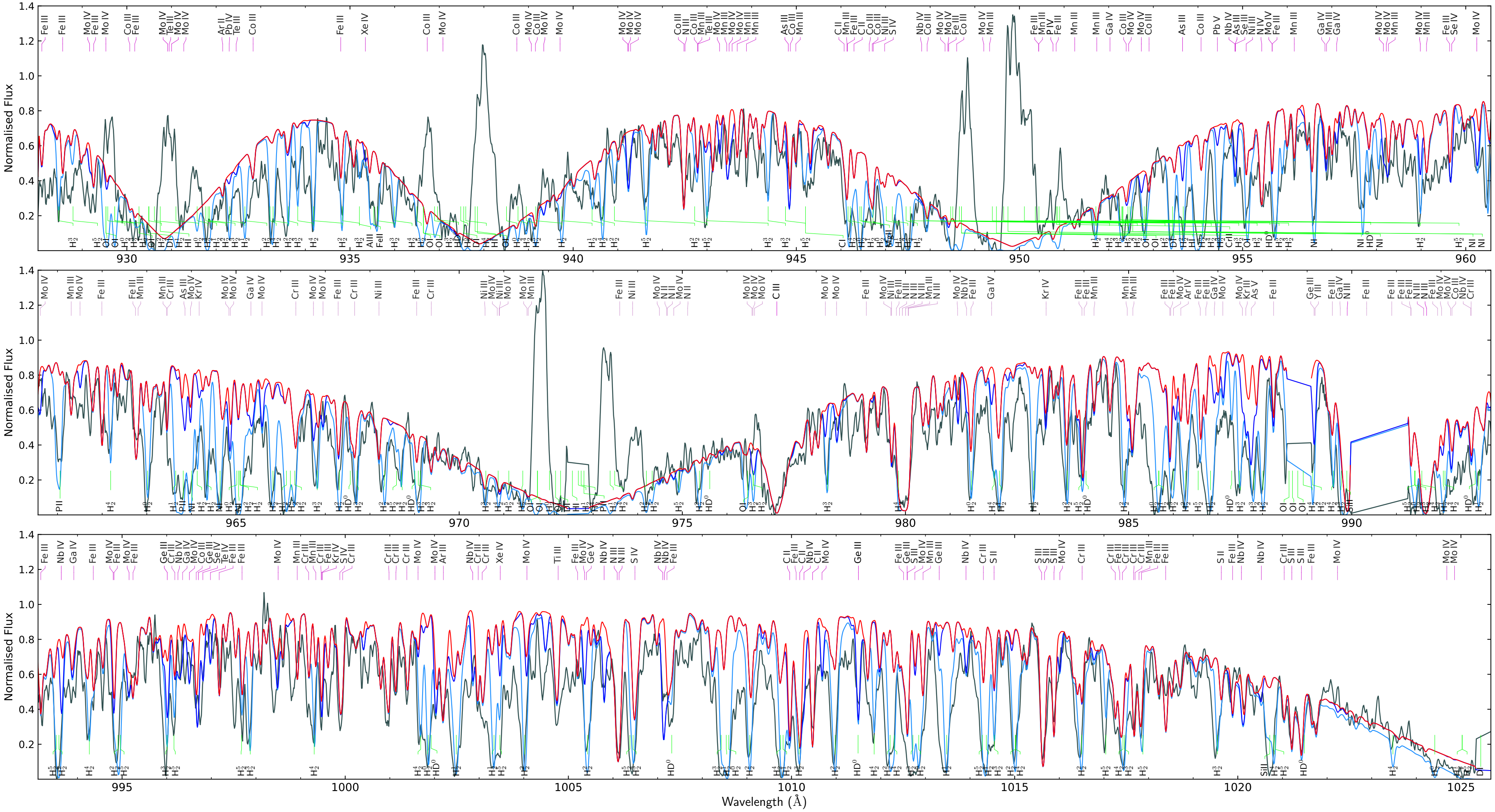

Figure B.2.2. FUSE spectrum of the SM Star (grey) and the best-fit model (red).

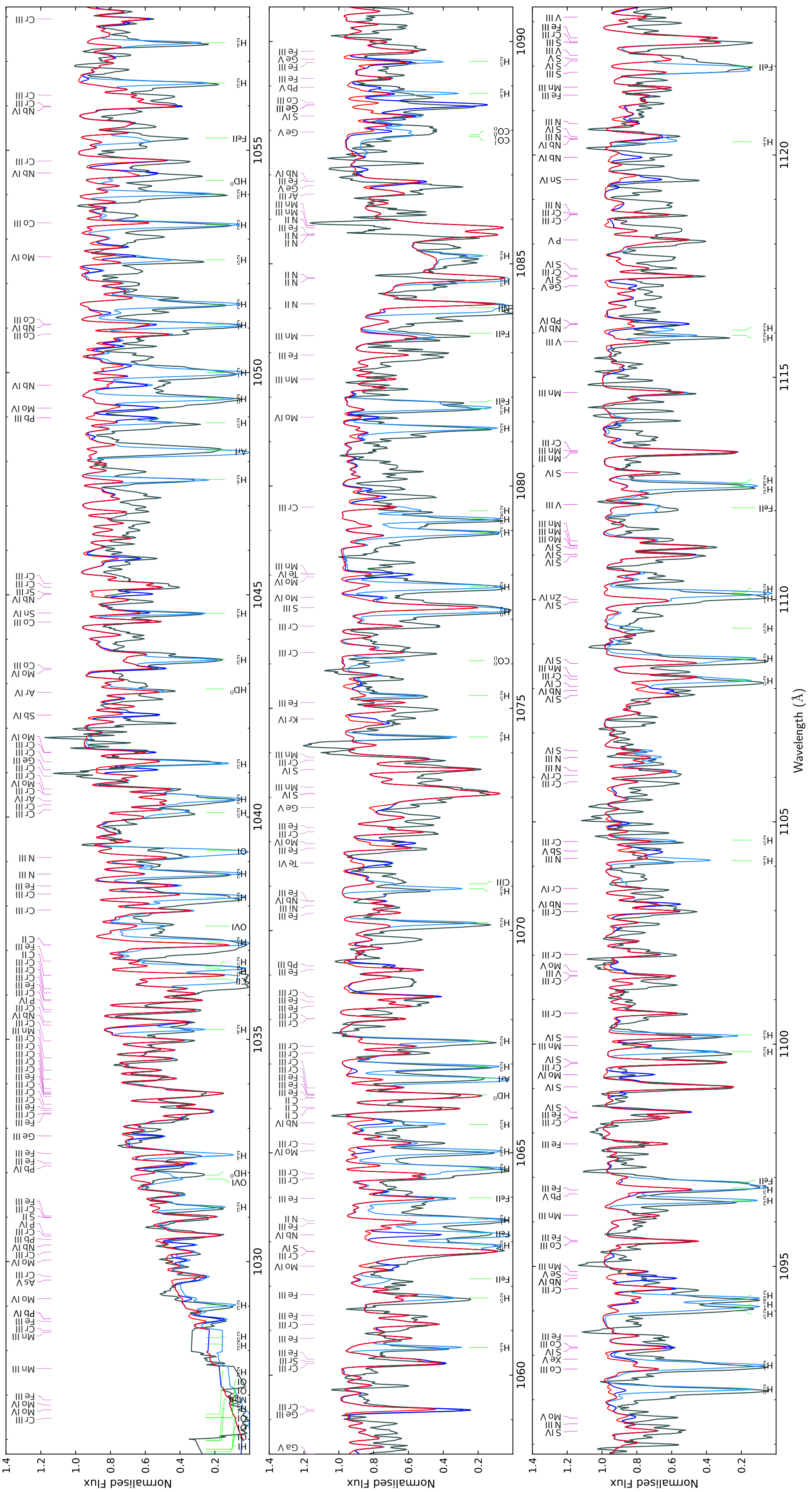

Figure B.2.2 (continued). FUSE spectrum of the SM Star (grey) and the best-fit model (red).

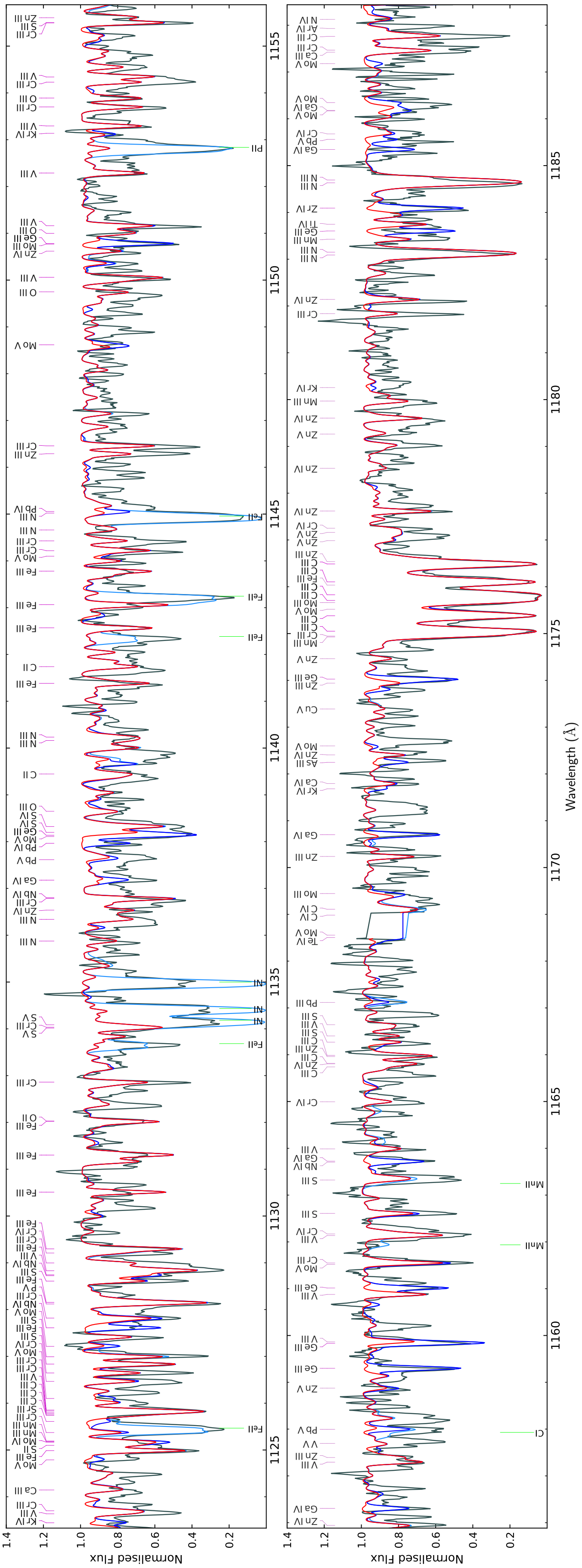

Figure B.2.2 (continued). FUSE spectrum of the SM Star (grey) and the best-fit model (red).

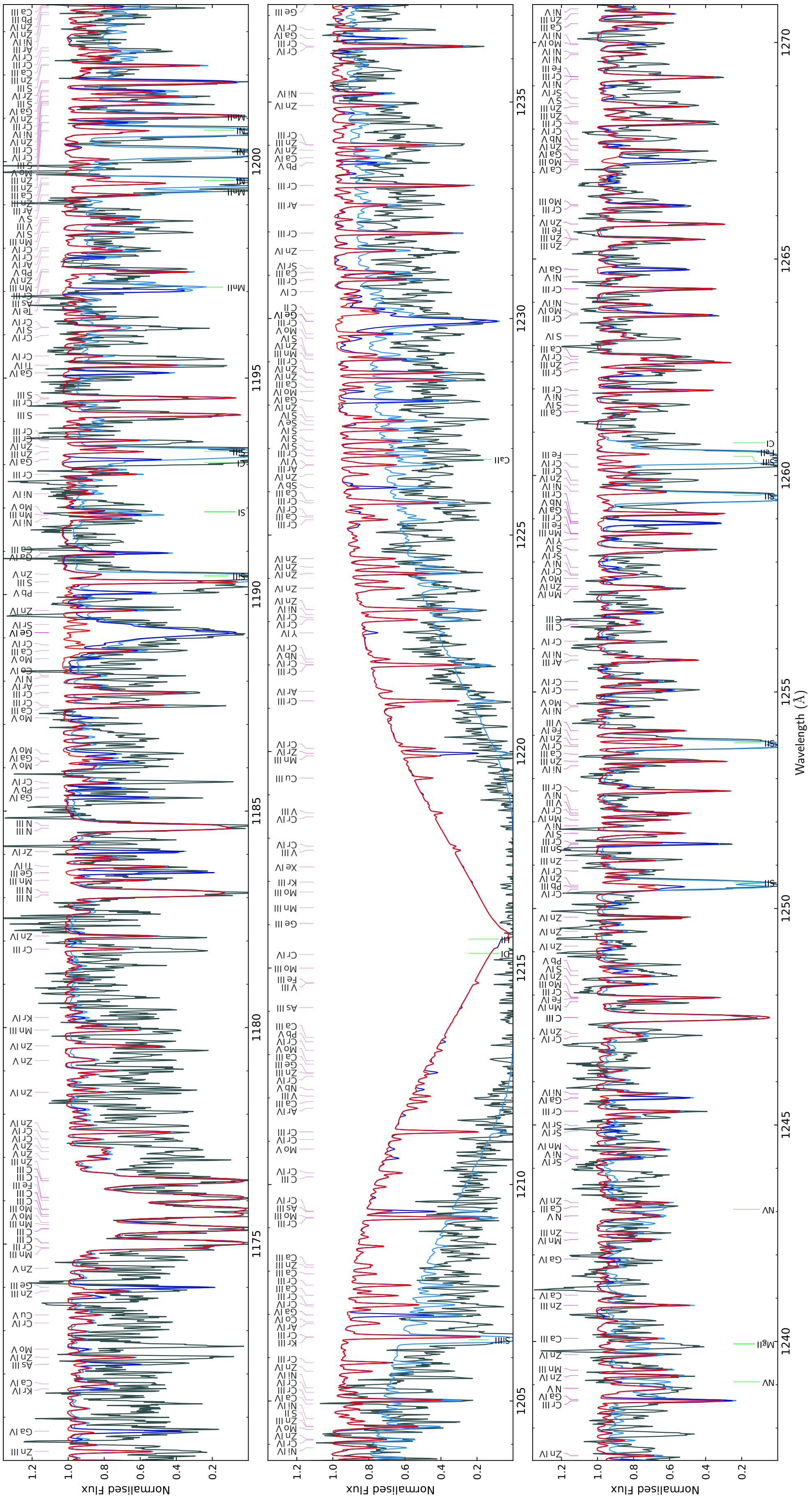

Figure B.2.3. STIS/E140M spectrum of the SM Star (grey) and the best-fit model (red).

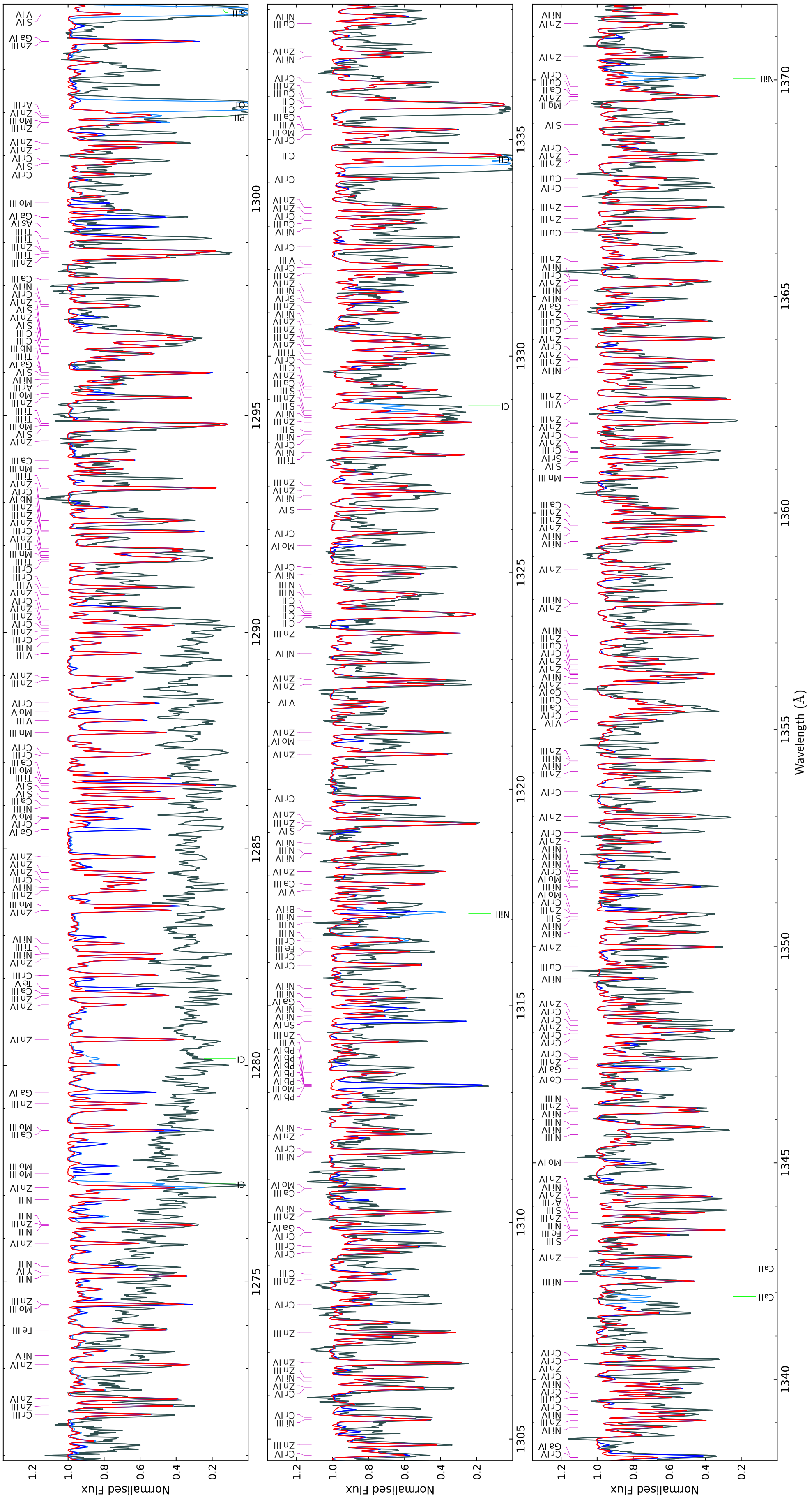

Figure B.2.3 (continued). STIS/E140M spectrum of the SM Star (grey) and the best-fit model (red).

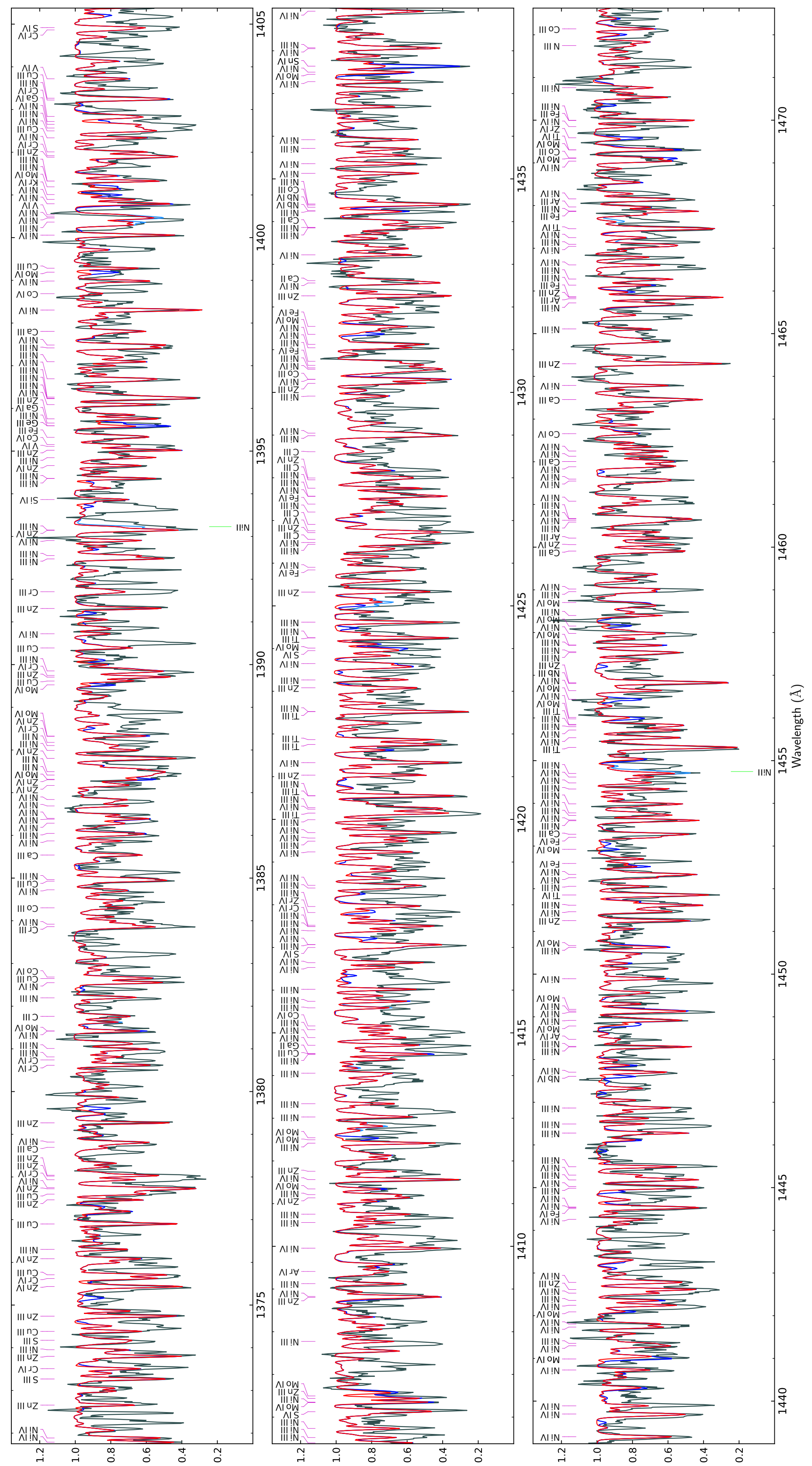

Figure B.2.3 (continued). STIS/E140M spectrum of the SM Star (grey) and the best-fit model (red).

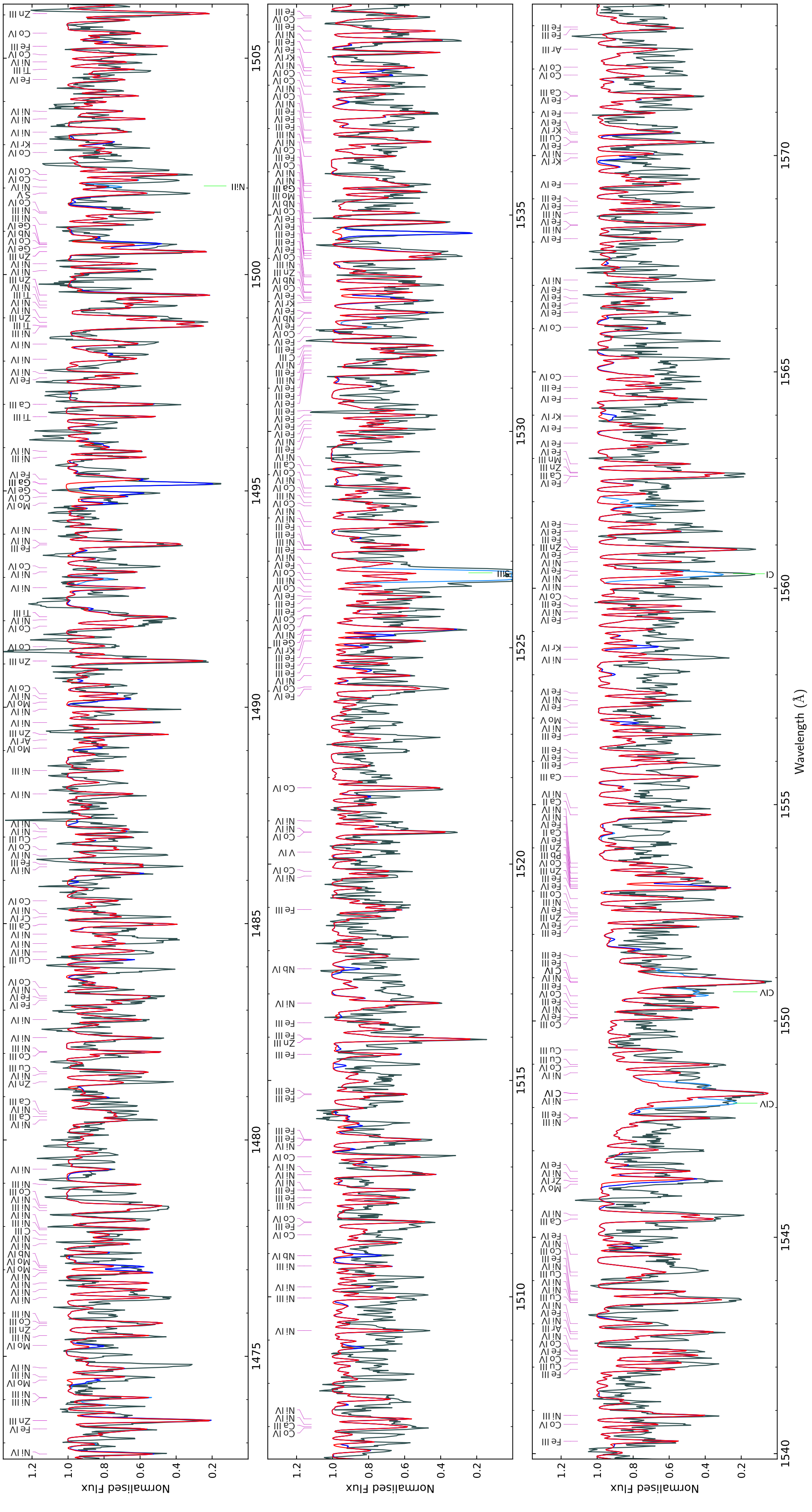

Figure B.2.3 (continued). STIS/E140M spectrum of the SM Star (grey) and the best-fit model (red).

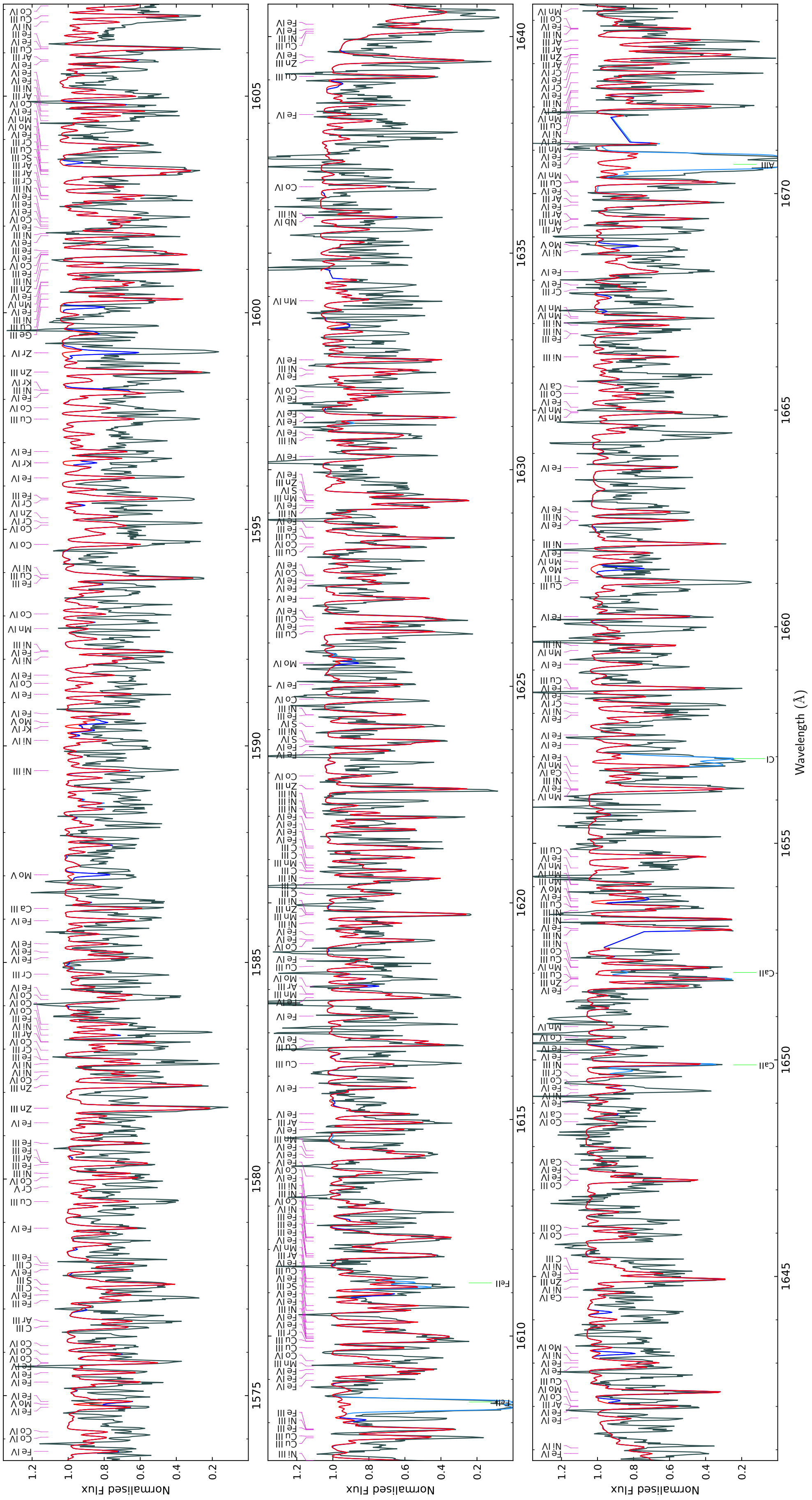

Figure B.2.3 (continued). STIS/E140M spectrum of the SM Star (grey) and the best-fit model (red).

B.3 For Section 3.3

Table B.3.1. Dimensions for the four grids of synthetic spectra used for the spectroscopic and SED analyses. For each parameter, the maximum and minimum values, as well as the step width are stated. As described in Sect. 3.3.4, the large and small Tlusty/Synspec grids were each computed using a fixed metal abundance pattern.

	Tlusty/Synspec		Atlas12/Synthe	
Parameter	large	small	large	small
$T_{\rm eff}$ (K)	27500	37300	4000	6150
	47500	38800	8000	6275
	1250	500	200	25
$\log g$	4.750	5.60	2.00	4.50
	6.125	6.00	5.20	4.80
	0.125	0.20	0.20	0.10
$\log n(\mathrm{He})/n(\mathrm{H})$	−1.00	−0.23	−1.07	−1.07
	+2.00	+0.07	−1.07	−1.07
	0.25	0.15	–	–
[Fe/H]	–	–	−2.00	−2.05
	–	–	+0.50	−1.85
	–	–	0.50	0.20
[α/Fe]	–	–	0.40	0.33
	–	–	0.40	0.44
	–	–	–	0.11
$v_{\rm tb}$ (km s^{-1})	5.0	0.0	0.0	1.5
	5.0	3.0	2.0	2.5
	–	3.0	1.0	1.0

Figures B.3.1 and B.3.2 respectively show the coadded HRS spectrum and a individual UVES spectrum of EC 22536−5304 (grey) along with the best-fit model (red) obtained in Sect. 3.3. The HRS spectrum was co-added from individual spectra using a common radial velocity for the He-sdOB component. Therefore, lines that originate from the sdF component are slightly broadened in this spectrum. Telluric lines were removed using the models of Moehler et al. (2014). In both figures, the contribution of the He-sdOB component is shown in blue (labelled at the top) while the sdF is shown in dark red (labelled at the bottom).

Table B.3.2. Unidentified lines in the HRS and UVES spectra of EC 22536−5304. Equivalent widths are stated for the composite spectrum. Rest wavelengths assume that lines originate from the sdOB.

λ / Å	EW / mÅ	Comment
4081.692	19	sharp
4182.414	11	sharp
4273.738	12	
4400.840	10	
4450.986	8	
4581.979	25	broad
4664.656	13	broad
4802.251	12	
5021.613	27	artifact?
5094.107	15	
5438.381	22	
7298.346	78	

Table B.3.3. Radial velocities with barycentric correction applied. The gravitational redshifts have not been corrected. The typical uncertainty is of the order $2\,\mathrm{km\,s^{-1}}$, depending on S/N. There may be a small systematic trend in the radial velocities derived from HRS spectra that were taken in 2019.

MJD	$\upsilon_{\mathrm{rad,B}}$ / km s^{-1}	$\upsilon_{\mathrm{rad,A}}$ / km s^{-1}	Spectrograph
55846.1	4.0	−14.6	UVES
55846.1	4.1	−15.7	UVES
55849.1	6.0	−12.2	UVES
55849.1	4.0	−13.0	UVES
55908.0	−1.2	−5.0	UVES
57891.0	−11.7	13.5	HRS
57891.0	−11.5	11.6	HRS
58437.0	−3.3	−3.2	HRS
58437.0	−4.2	−0.3	HRS
58612.0	2.4	−10.5	HRS
58612.0	2.6	−9.4	HRS
58616.0	1.9	−10.7	HRS
58616.0	2.1	−11.0	HRS
58617.0	2.0	−8.3	HRS
58617.0	2.3	−8.8	HRS
58619.0	4.1	−10.0	HRS
58619.0	2.9	−7.5	HRS
58620.0	2.5	−7.6	HRS
58620.0	4.9	−8.0	HRS
58621.0	3.9	−8.4	HRS
58621.0	3.8	−9.0	HRS
58624.0	3.4	−8.4	HRS
58624.0	3.0	−7.4	HRS
58625.0	3.4	−7.4	HRS
58625.0	4.1	−7.3	HRS
58626.0	3.3	−7.9	HRS
58626.0	4.1	−7.2	HRS

Table B.3.4. Orbital parameters for a sample of intermediate He sdOB stars studied by Martin et al. (2017) and recent additions (HZ 44, Feige 46, EC 22536−5304). The quantities $R_{\rm max}$, $R_{\rm min}$, and $Z_{\rm max}$ refer to the maximum and minimum distance from the Galactic centre, as well as the maximum distance from the Galactic disc. Known zirconium- or lead-rich stars are marked by †.

Star	$v_{\rm rad}$ km s^{-1}	±	$R_{\rm max}$ kpc	±	$R_{\rm min}$ kpc	±	$Z_{\rm max}$ kpc	±	V km s^{-1}	±	U km s^{-1}	±	W km s^{-1}	±	L_Z kpc^2 Myr^{-1}	±	e	±
PG 0909+276	20.0	2.0	9.23	0.18	8.59	0.05	0.42	0.03	249.1	2.1	−0.3	1.9	22.0	1.5	2.19	0.02	0.04	0.01
HD 127493†	−17.0	3.0	8.42	0.08	7.60	0.13	0.10	0.01	234.2	2.4	13.3	2.5	−3.2	1.8	1.98	0.02	0.05	0.01
UVO 0512−08	11.0	3.3	9.46	0.20	8.24	0.07	0.44	0.03	248.1	2.5	−21.0	2.9	−25.2	1.6	2.17	0.03	0.07	0.02
HE 1238−1745	−7.9	2.8	9.18	0.15	7.19	0.12	0.96	0.07	240.2	2.8	39.1	3.1	15.6	2.1	1.97	0.03	0.12	0.01
PG 1559+048†	−26.7	0.9	8.15	0.06	6.22	0.12	0.54	0.03	217.0	2.3	27.9	1.6	18.1	1.3	1.75	0.02	0.13	0.01
CPD −20 1123	−6.3	1.2	9.71	0.12	7.54	0.09	0.17	0.01	238.9	2.2	−41.4	1.5	8.4	0.7	2.10	0.02	0.13	0.01
SB 705	4.0	12.0	10.46	0.27	7.95	0.11	0.99	0.09	255.5	3.8	40.1	2.5	5.7	11.4	2.20	0.03	0.14	0.01
JL 87	−6.1	2.3	10.24	0.20	7.76	0.06	0.56	0.02	266.7	2.5	−27.6	1.9	5.7	1.5	2.17	0.02	0.14	0.01
UVO 0825+15†	56.4	0.5	9.63	0.10	7.18	0.10	0.16	0.01	232.0	2.1	46.8	1.3	6.4	0.8	2.04	0.02	0.15	0.01
PG 0229+064	7.6	4.0	9.16	0.08	6.67	0.14	0.67	0.05	210.8	2.6	31.1	3.0	19.1	3.1	1.90	0.02	0.16	0.02
HE 2357−3940	−18.4	14.2	9.59	0.21	6.95	0.12	0.96	0.12	236.1	2.6	54.5	5.1	9.6	13.4	1.97	0.03	0.16	0.02
TON 414	2.7	0.5	10.08	0.12	6.75	0.16	1.44	0.13	207.8	3.6	−54.1	3.0	35.5	1.8	1.96	0.03	0.20	0.02
HE 1310−2733	41.5	1.9	9.12	0.09	5.95	0.12	0.94	0.05	221.4	2.4	−67.9	2.7	19.2	1.4	1.77	0.03	0.21	0.01
FBS 1749+373†	−73.6	0.2	8.34	0.05	4.74	0.09	0.39	0.01	182.6	2.1	39.2	1.3	−2.5	0.8	1.51	0.02	0.28	0.01
HE 1136−2504	59.4	9.3	8.40	0.05	4.63	0.33	0.68	0.04	176.0	7.8	−30.4	1.6	5.6	5.5	1.48	0.07	0.29	0.04
TYC 3519-907-1	−62.7	0.2	9.30	0.08	5.12	0.09	0.30	0.01	195.5	2.1	73.5	2.2	2.7	0.9	1.66	0.02	0.29	0.01
PG 0240+046	63.4	2.0	10.57	0.11	5.36	0.13	0.57	0.03	196.9	3.1	93.4	2.8	0.6	2.1	1.78	0.03	0.33	0.02
HZ 44†	−12.7	0.4	9.30	0.07	4.48	0.11	0.41	0.02	177.3	2.7	76.8	2.3	10.2	0.8	1.52	0.02	0.35	0.02
EC 22133−6446	−21.0	10.0	9.30	0.20	3.58	0.26	0.44	0.05	159.1	7.9	101.3	8.7	−2.9	7.2	1.31	0.07	0.44	0.04
EC 22536−5304†	−3.3	5.0	8.21	0.05	2.51	0.13	1.50	0.12	113.2	4.2	−26.4	2.8	58.3	4.3	0.93	0.04	0.53	0.02
Feige 46†	90.0	4.0	9.64	0.09	1.13	0.12	0.68	0.04	63.5	5.2	115.5	3.7	13.8	4.4	0.55	0.04	0.79	0.03
LS IV−14°116†	−154.0	1.0	8.15	0.05	0.66	0.14	0.24	0.02	−42.5	6.8	21.2	2.7	0.1	2.9	−0.35	0.06	0.85	0.03

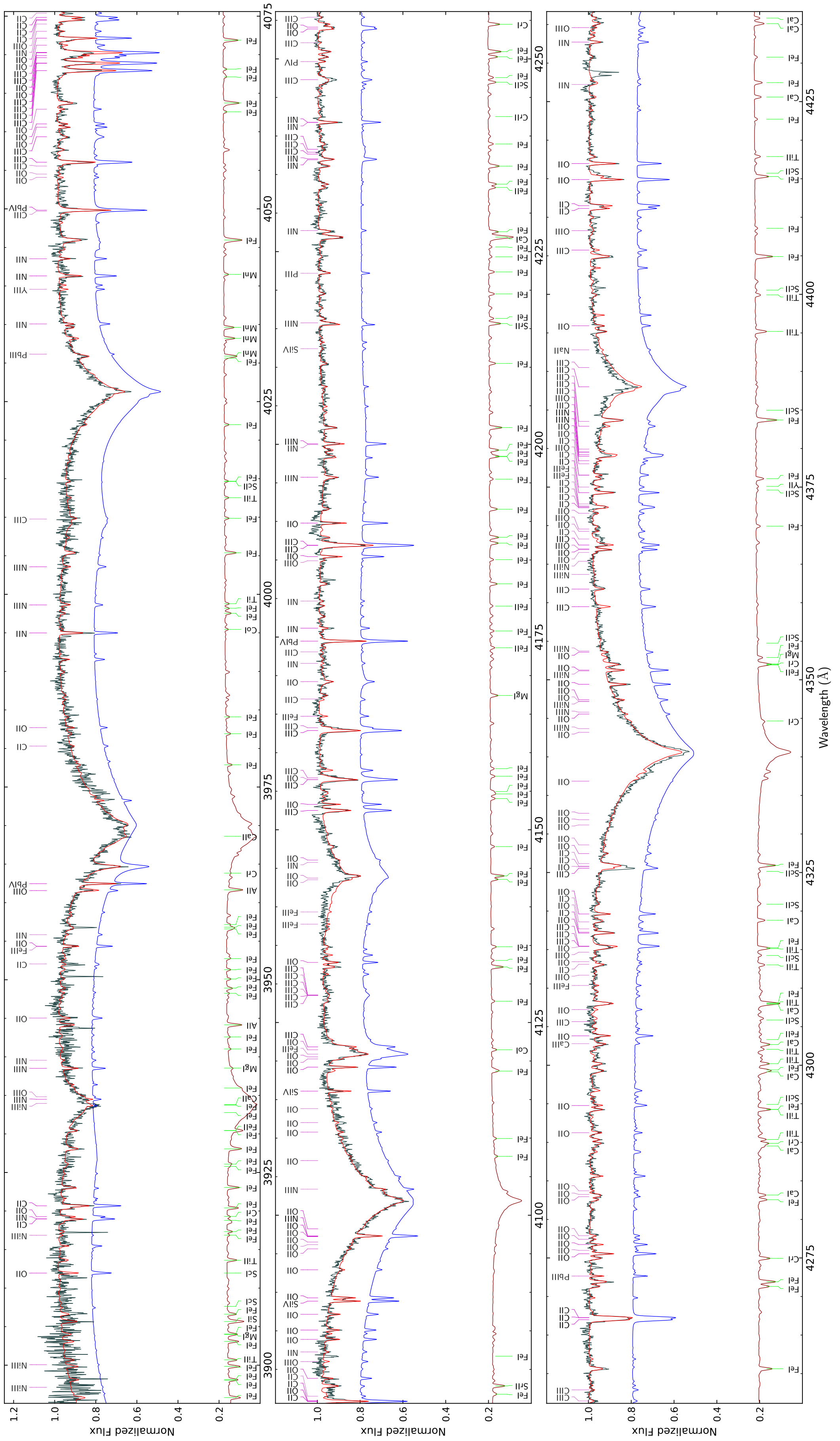

Figure B.3.1. The HRS spectrum of EC 22536−5304 (grey) and the combined (red) and individual models.

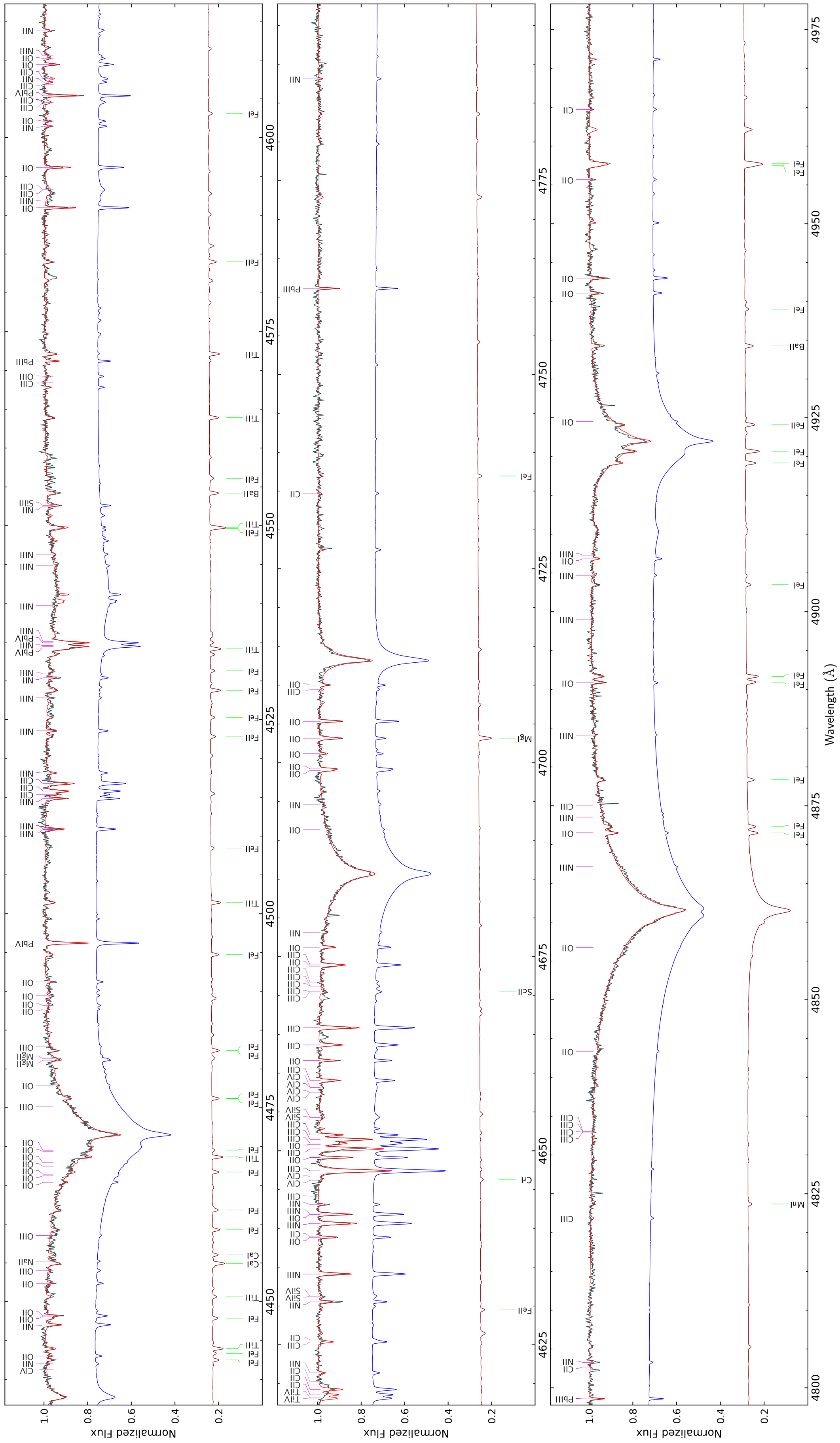

Figure B.3.1 (continued). The HRS spectrum of EC 22536−5304 (grey) and the combined (red) and individual models. Adopted from Dorsch et al. (2021).

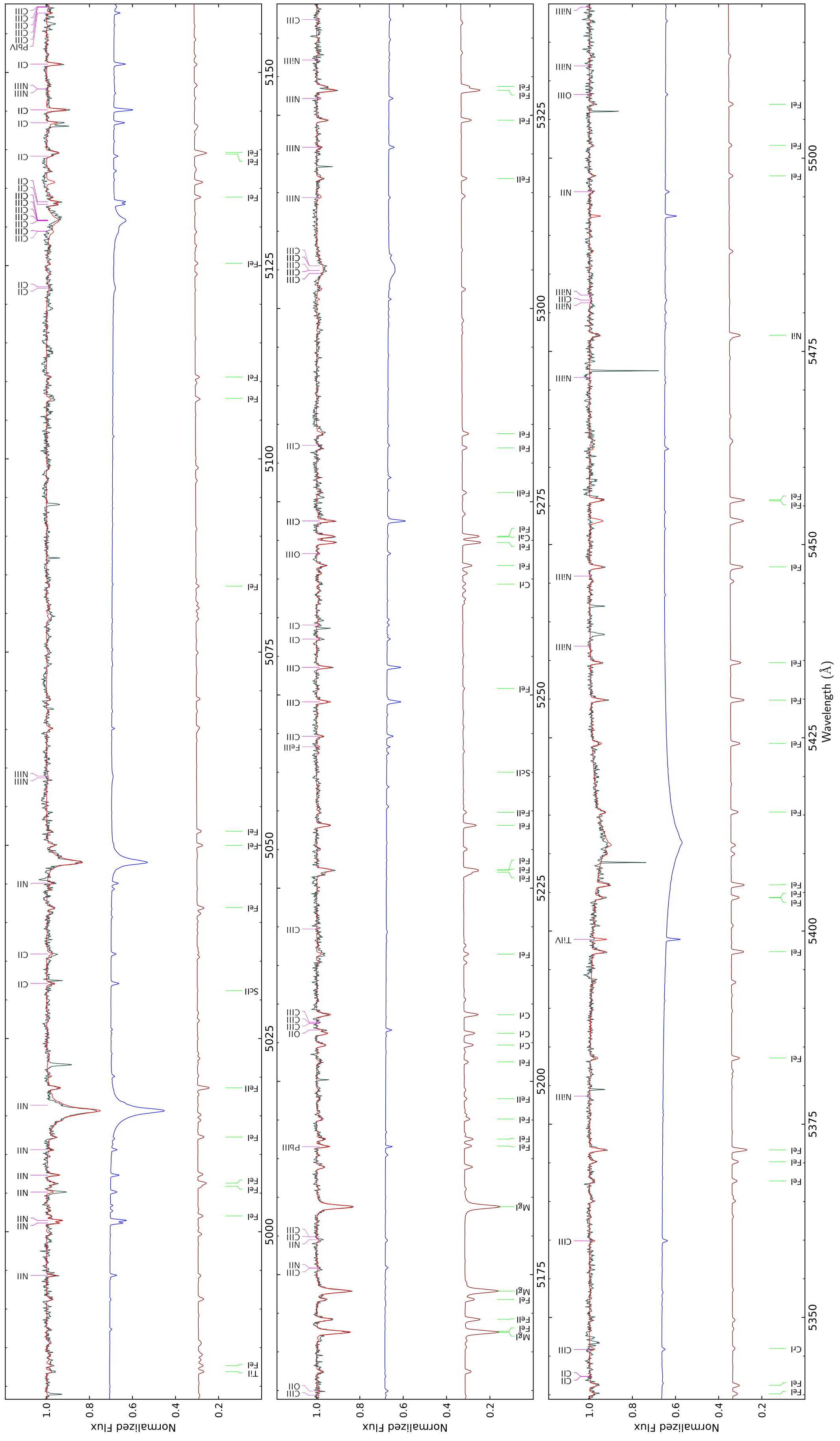

Figure B.3.1 (continued). The HRS spectrum of EC 22536−5304 (grey) and the combined (red) and individual models. Adopted from Dorsch et al. (2021).

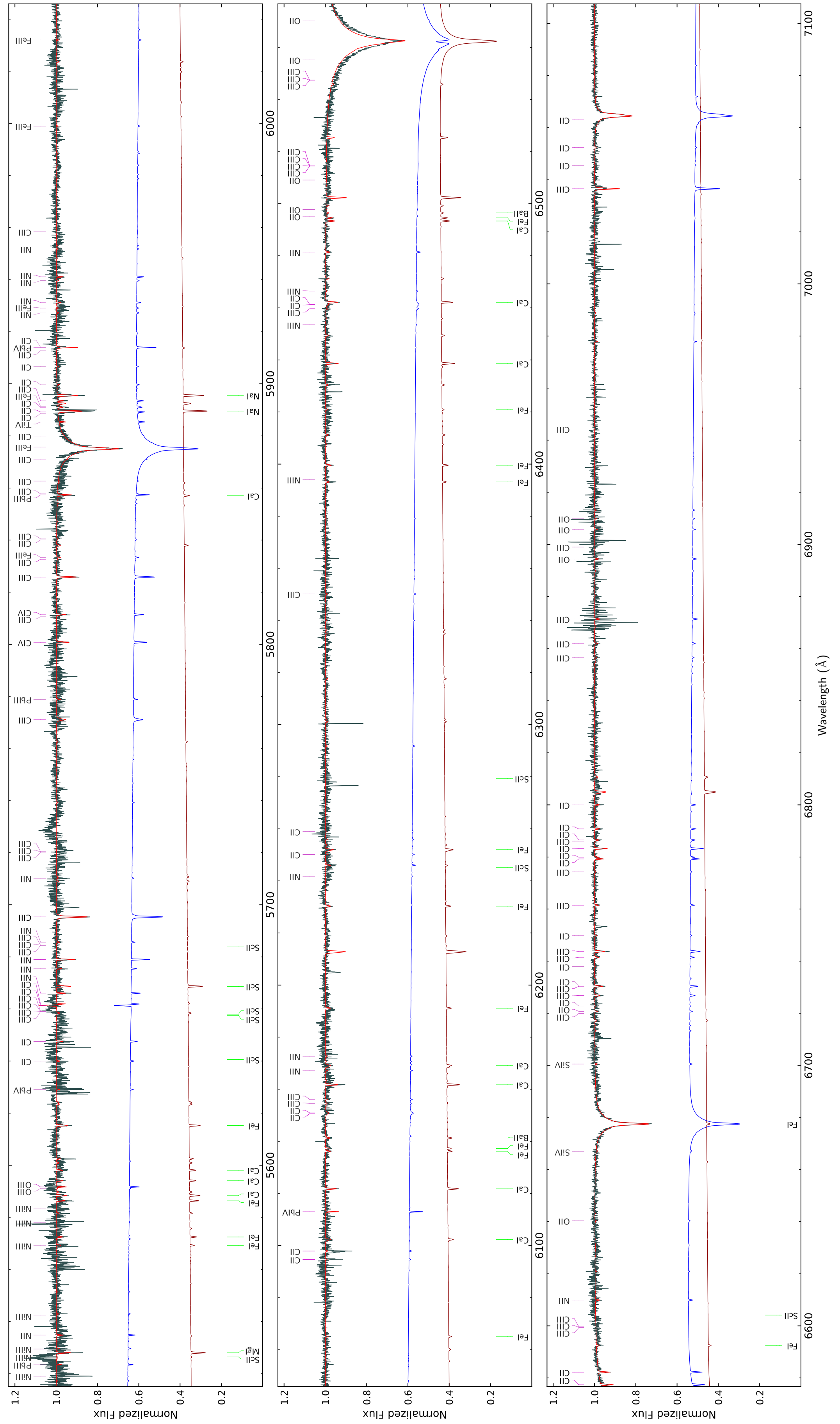

Figure B.3.1 (continued). The HRS spectrum of EC 22536−5304 (grey) and the combined (red) and individual models. Adopted from Dorsch et al. (2021).

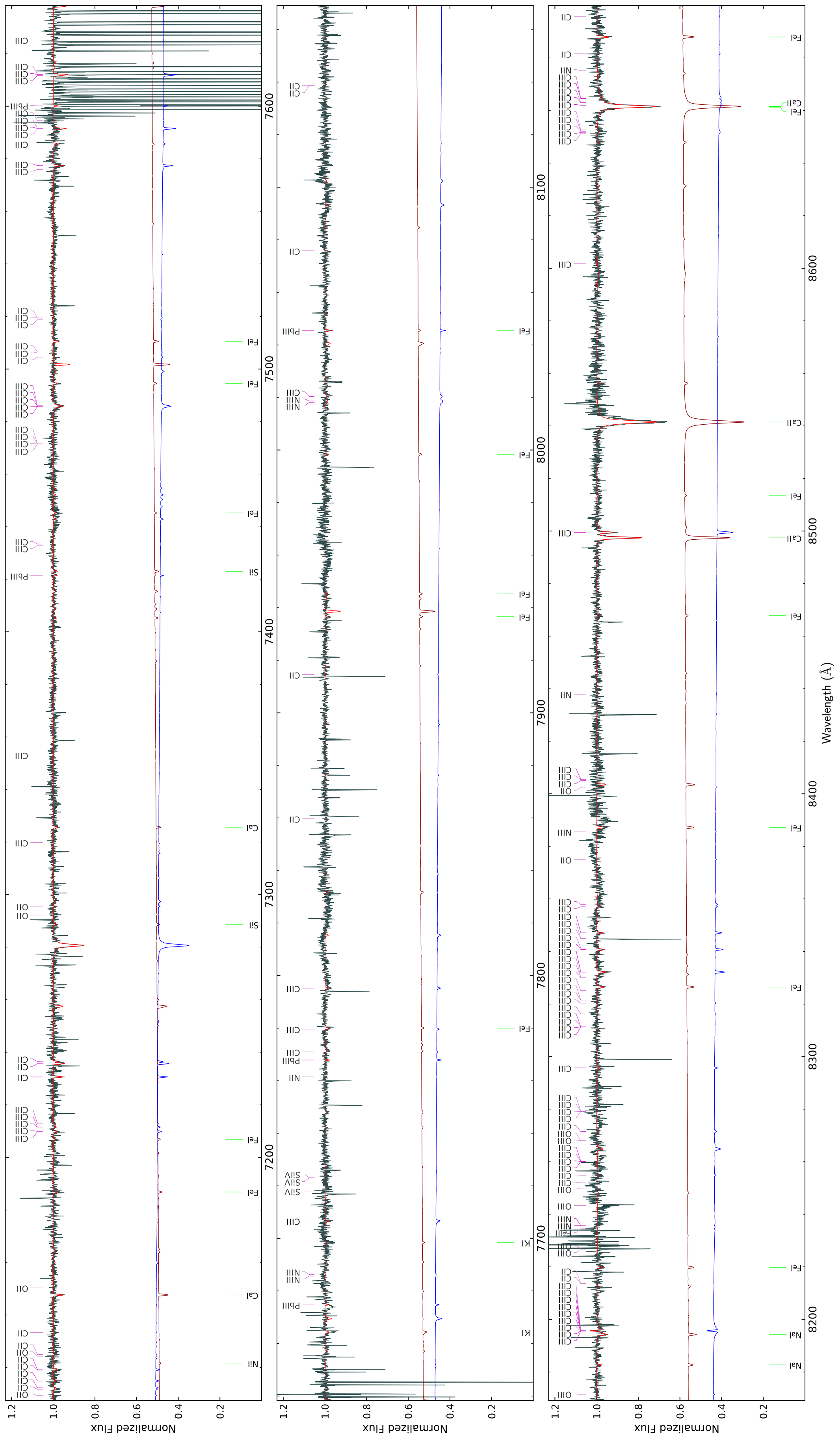

Figure B.3.1 (continued). The HRS spectrum of EC 22536−5304 (grey) and the combined (red) and individual models. Adopted from Dorsch et al. (2021).

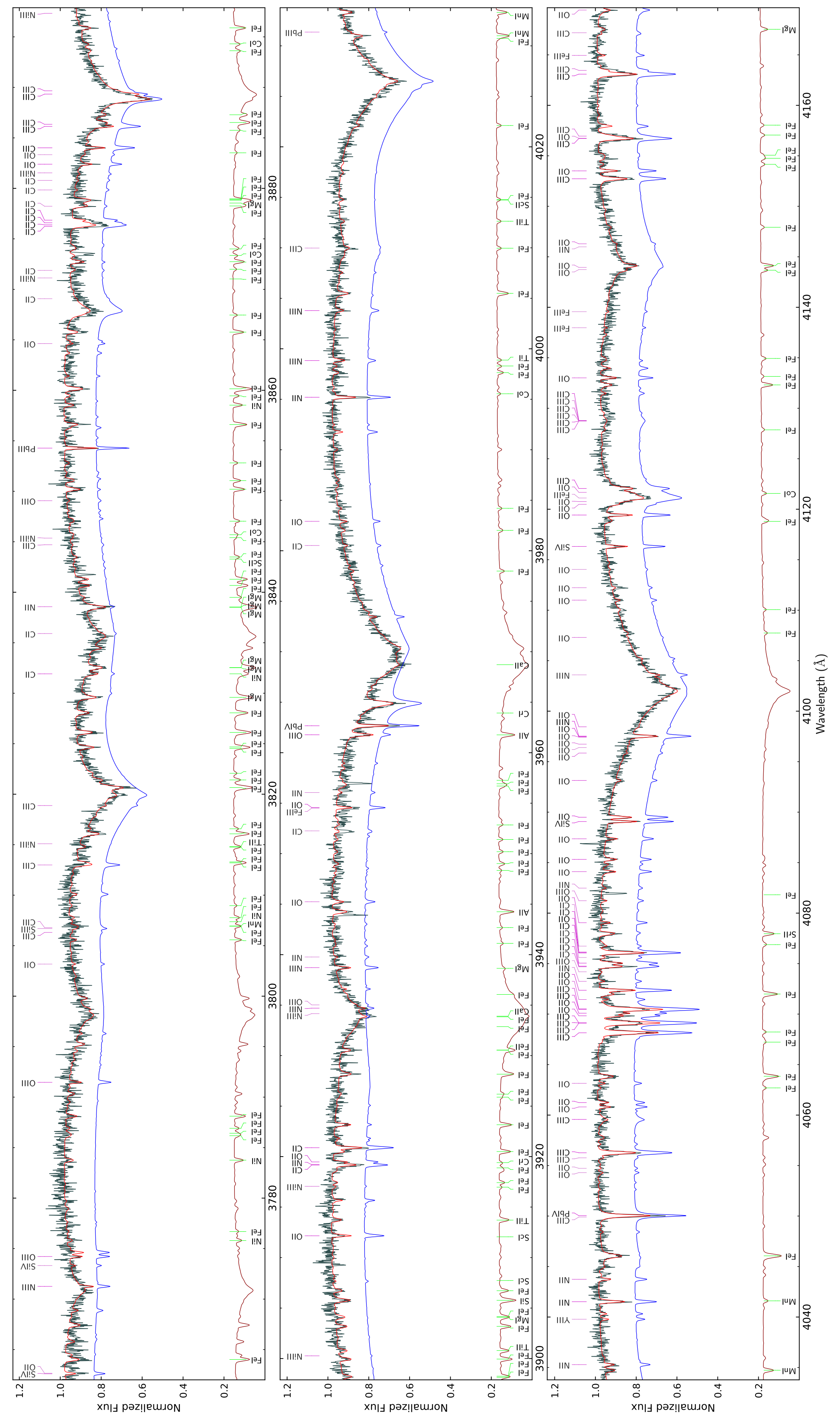

Figure B.3.2. The UVES spectrum of EC 22536−5304 (grey) and the combined (red) and individual models. Adopted from Dorsch et al. (2021).

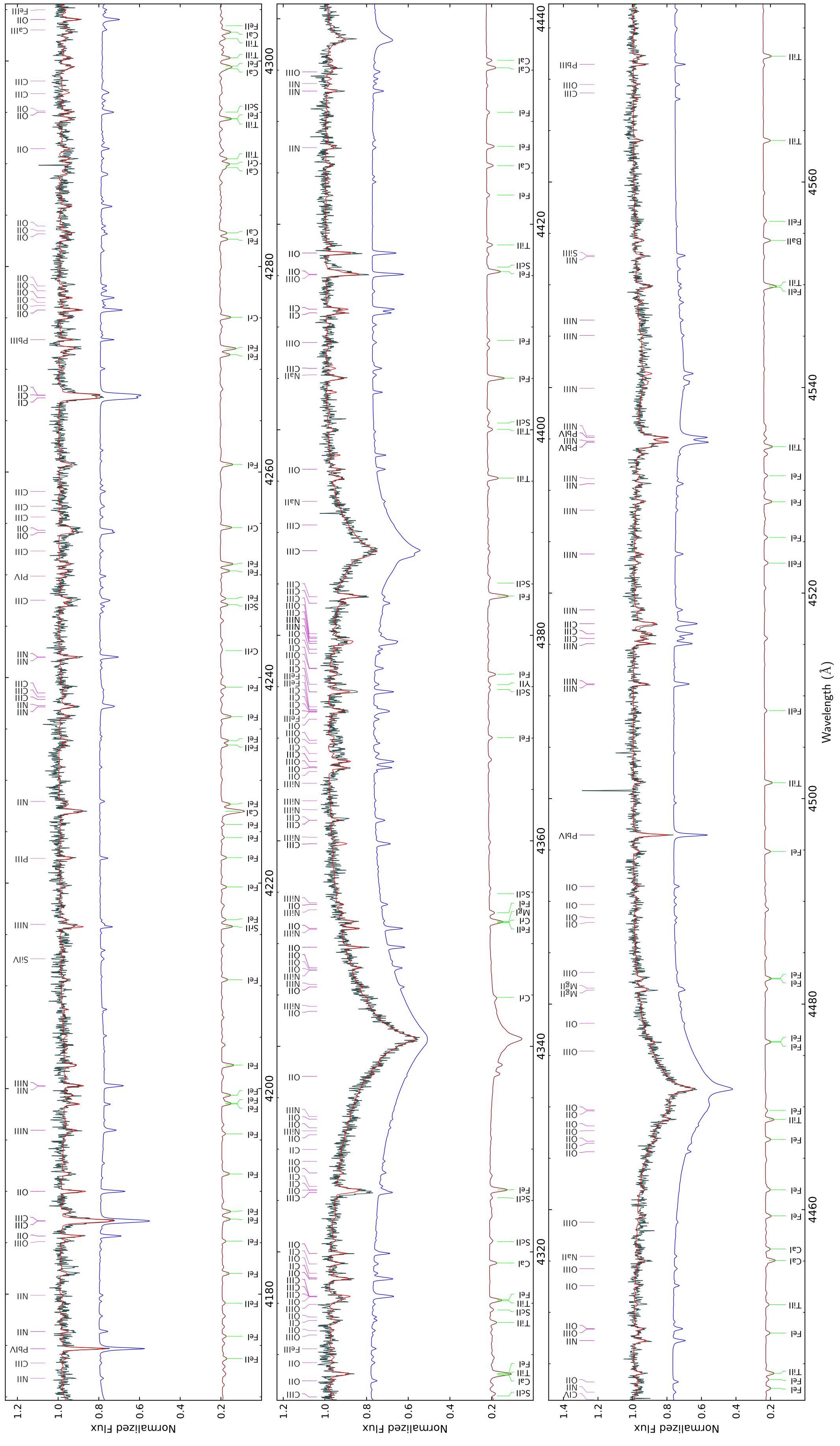

Figure B.3.2 (continued). The UVES spectrum of EC 22536−5304 (grey) and the combined (red) and individual models. Adopted from Dorsch et al. (2021).

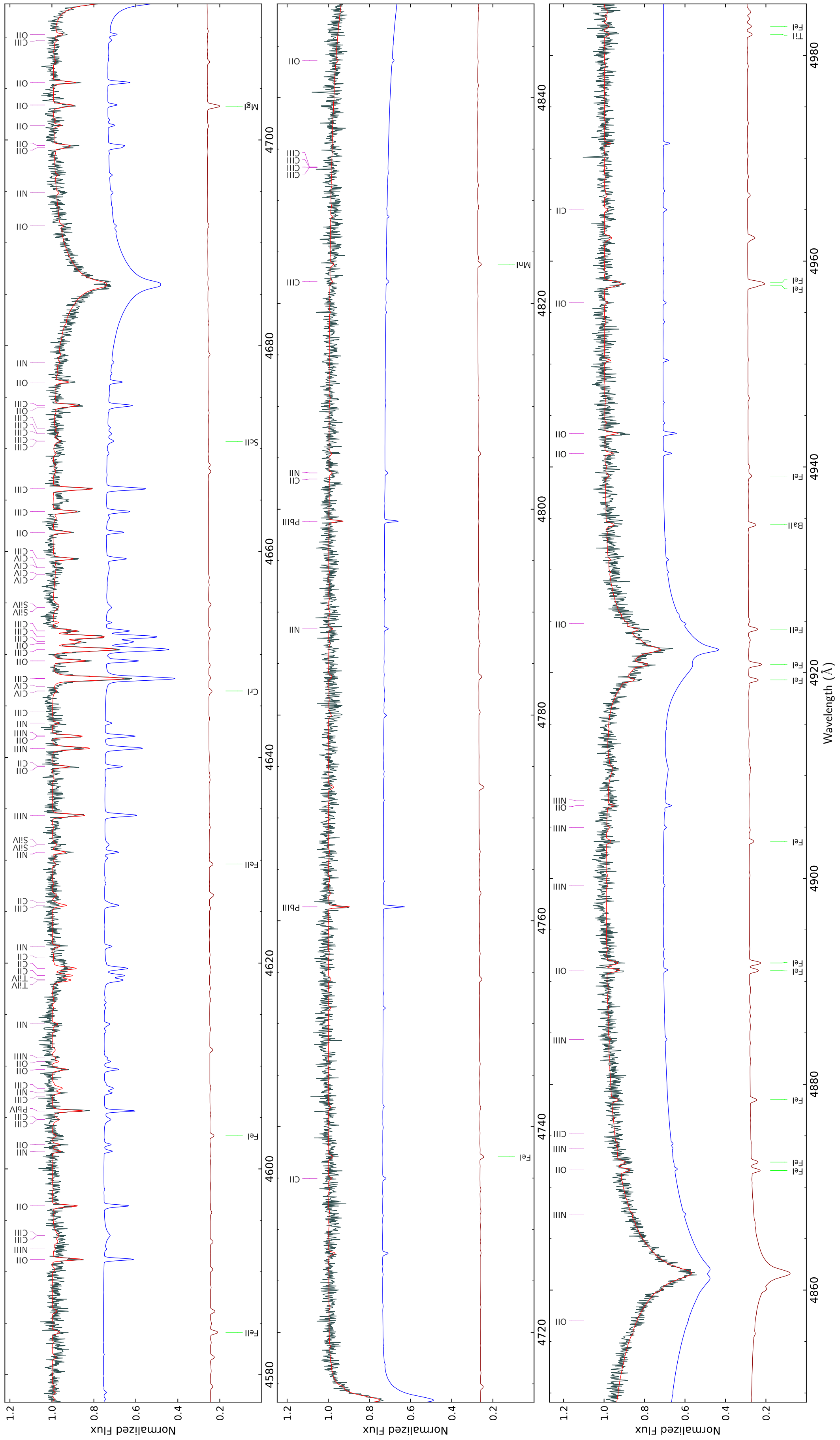

Figure B.3.2 (continued). The UVES spectrum of EC 22536−5304 (grey) and the combined (red) and individual models. Adopted from Dorsch et al. (2021).

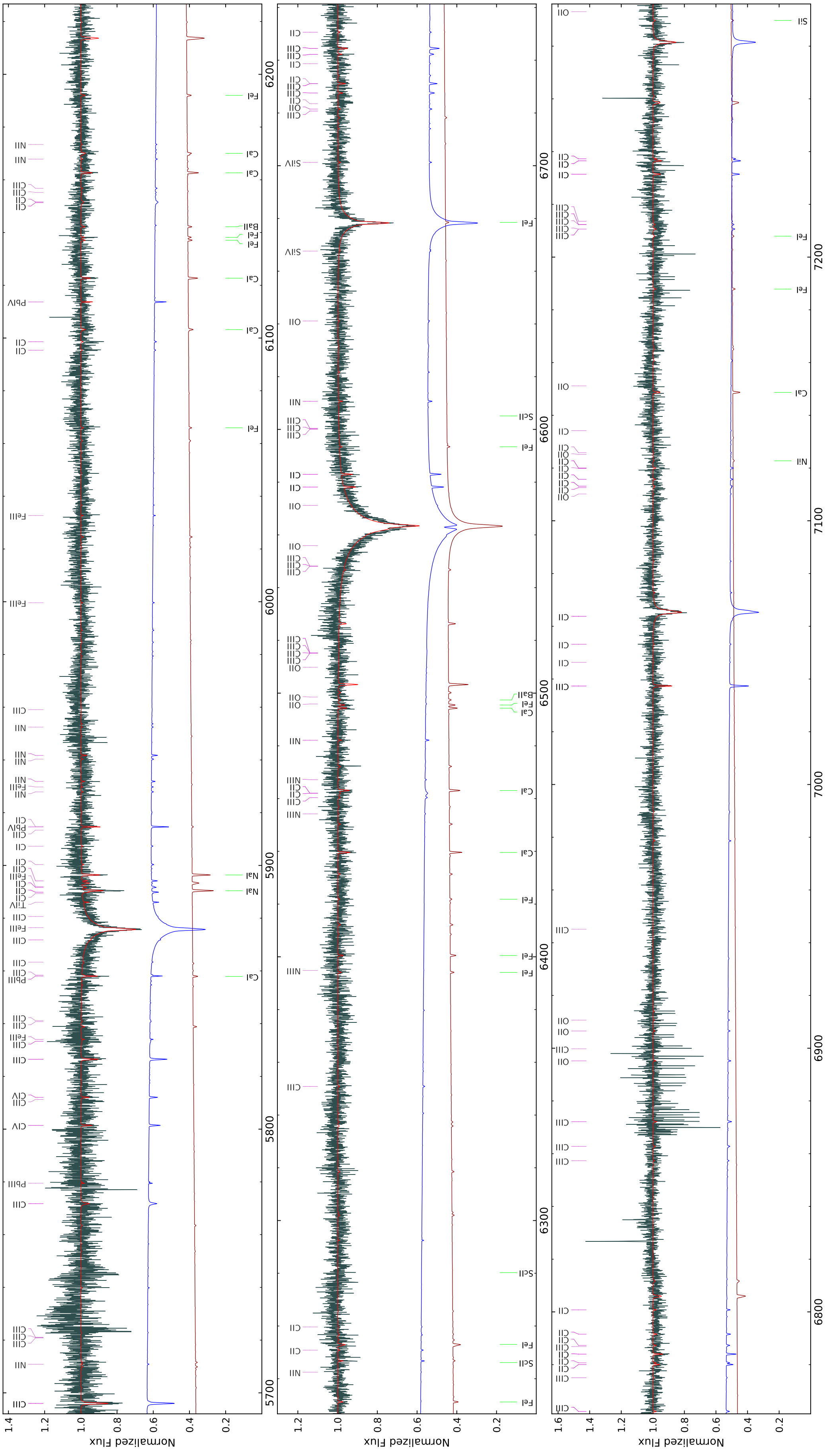

Figure B.3.2 (continued). UVES spectrum of EC 22536−5304 (grey) and the combined (red) and individual models. Adopted from Dorsch et al. (2021).

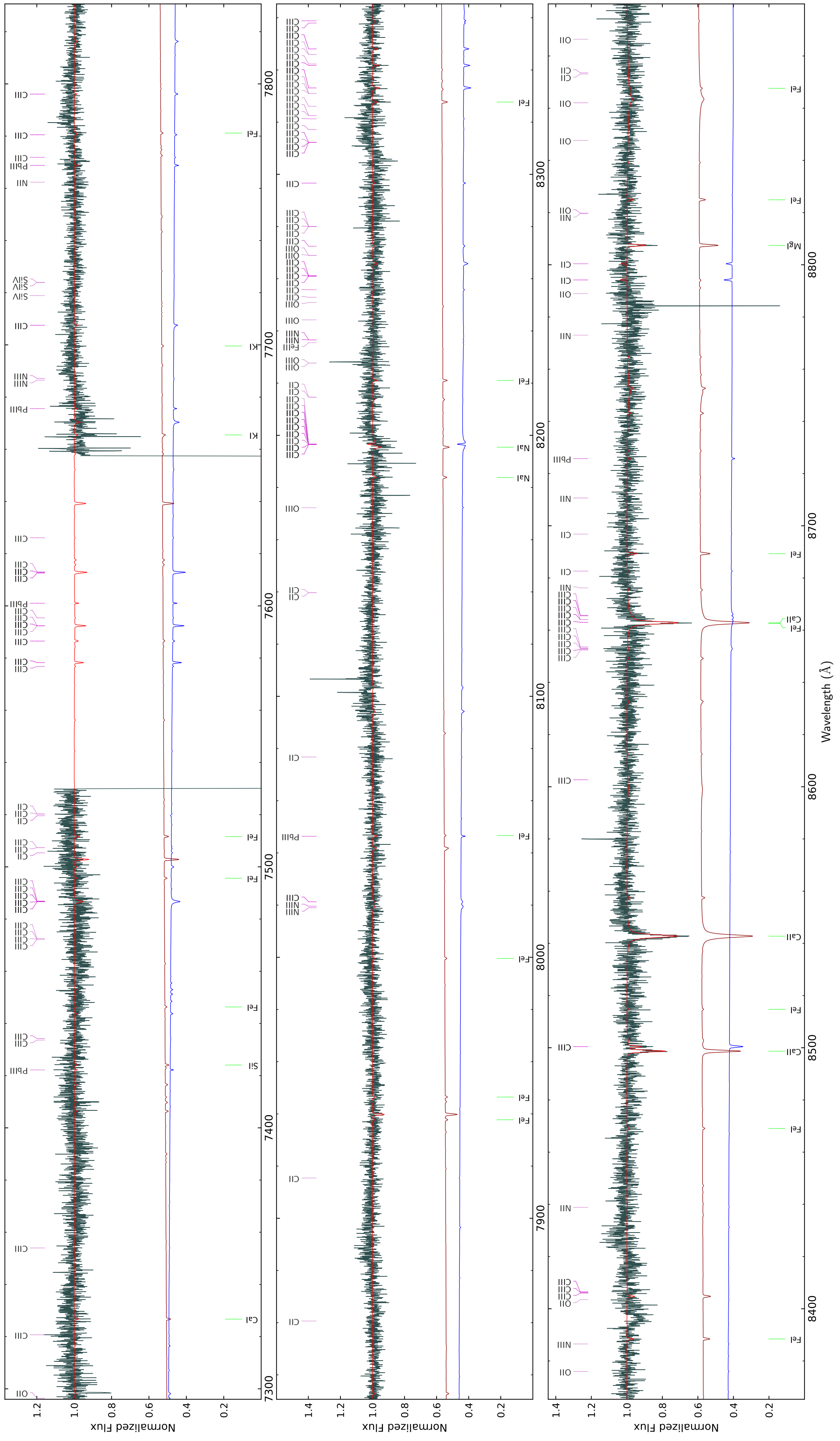

Figure B.3.2 (continued). UVES spectrum of EC 22536−5304 (grey) and the combined (red) and individual models. Adopted from Dorsch et al. (2021).

B.4 For Section 3.4

The first part of the FEROS spectrum of BD −7° 5977 is shown in Fig. B.4.1, where the K-type component is coloured dark red, the sdOB is coloured blue, and the combined spectrum is red. The full range and the HERMES and CARMENES spectra are not shown because they would cover dozens of pages. The CRIRES spectrum is shown in Fig. B.4.2; here only with the combined spectrum since the sdOB contributes very little in this infra-red range. All models shown here correspond to the best fit described in Sect. 3.4. Spectral regions that were excluded from the χ^2 fit are shaded grey.

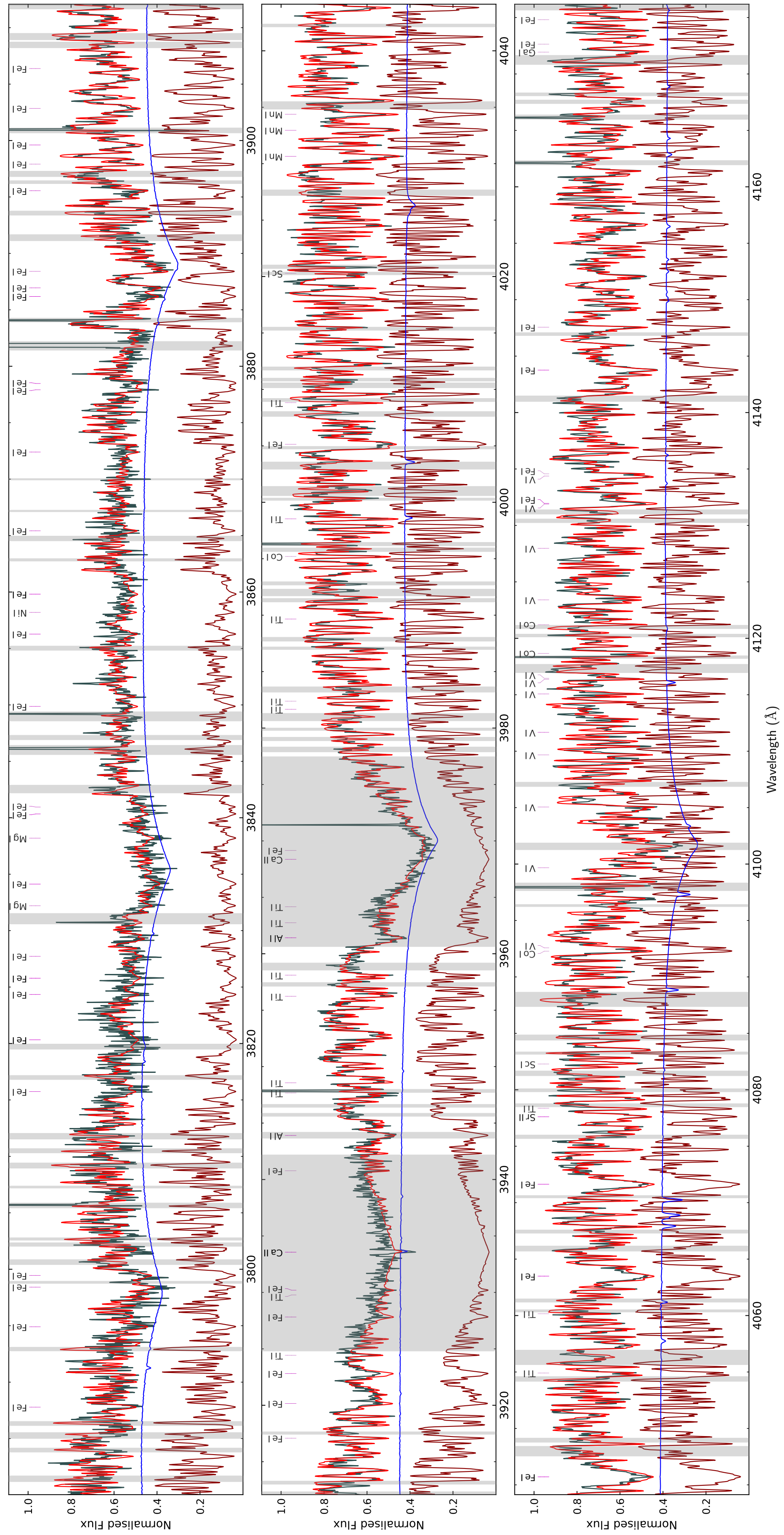

Figure B.4.1. The FEROS spectrum of BD −7° 5977 (grey) and the combined (red) and individual models.

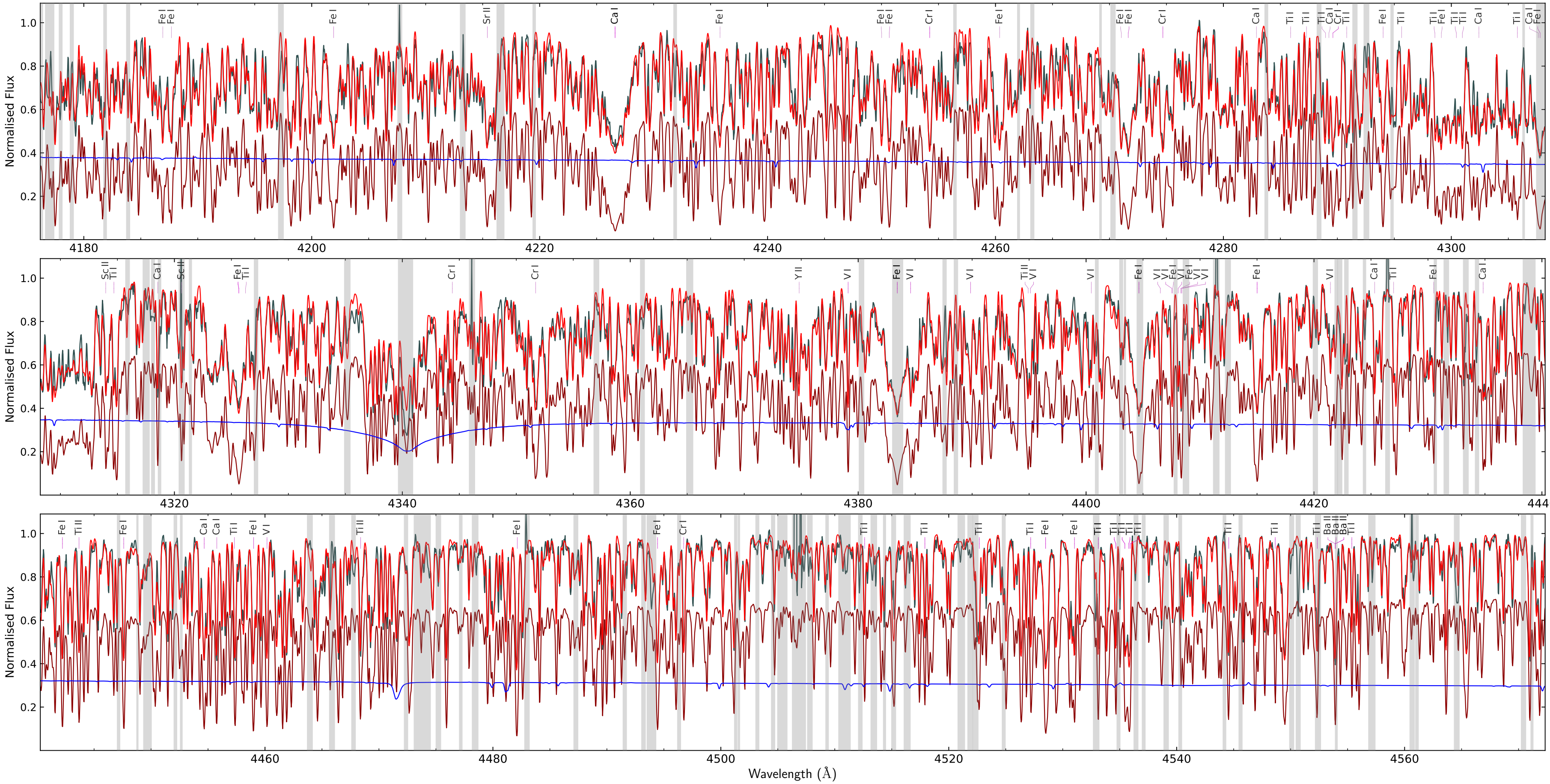

Figure B.4.1 (continued). The FEROS spectrum of BD −7° 5977 (grey) and the combined (red) and individual models.

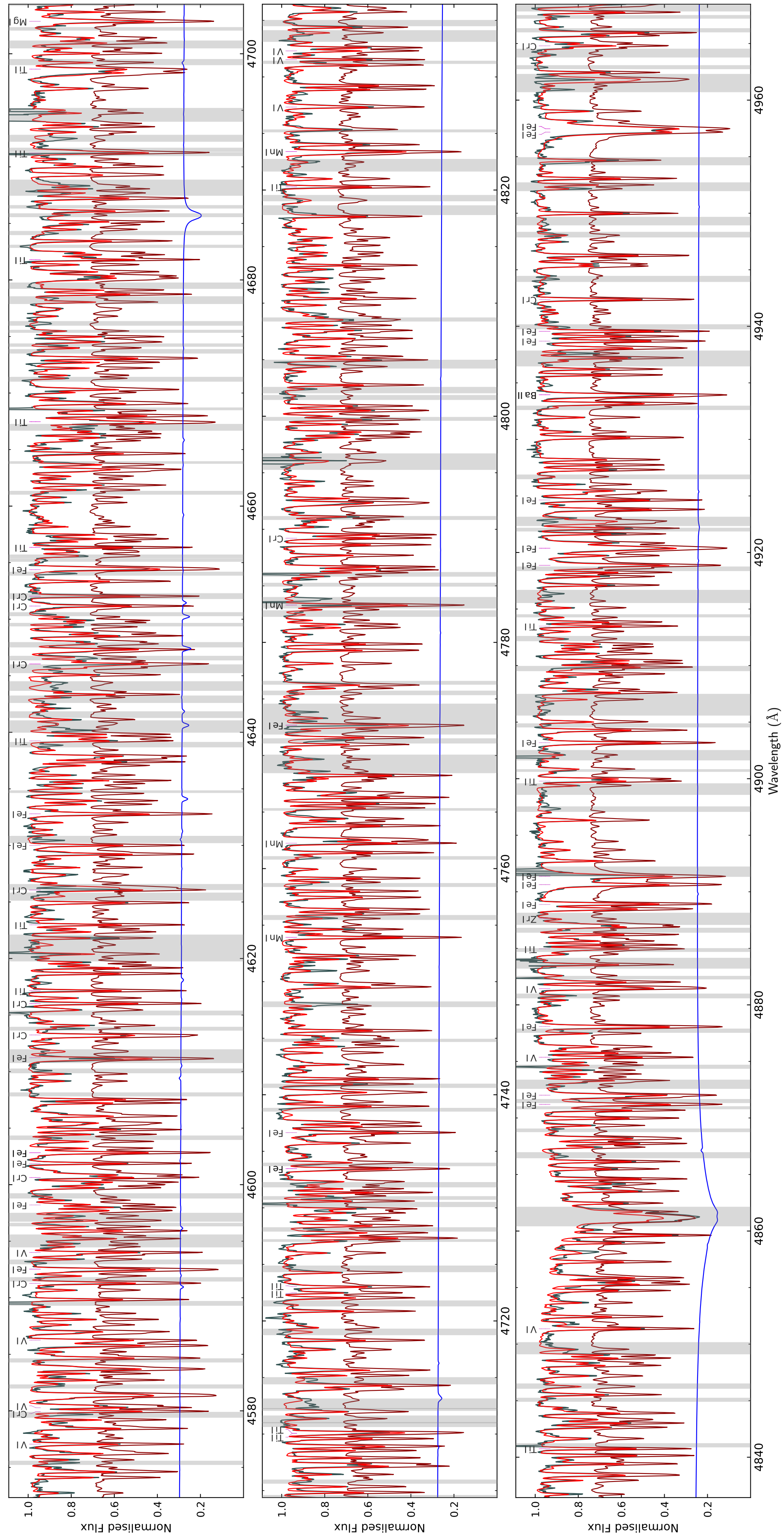

Figure B.4.1 (continued). The FEROS spectrum of BD −7° 5977 (grey) and the combined (red) and individual models.

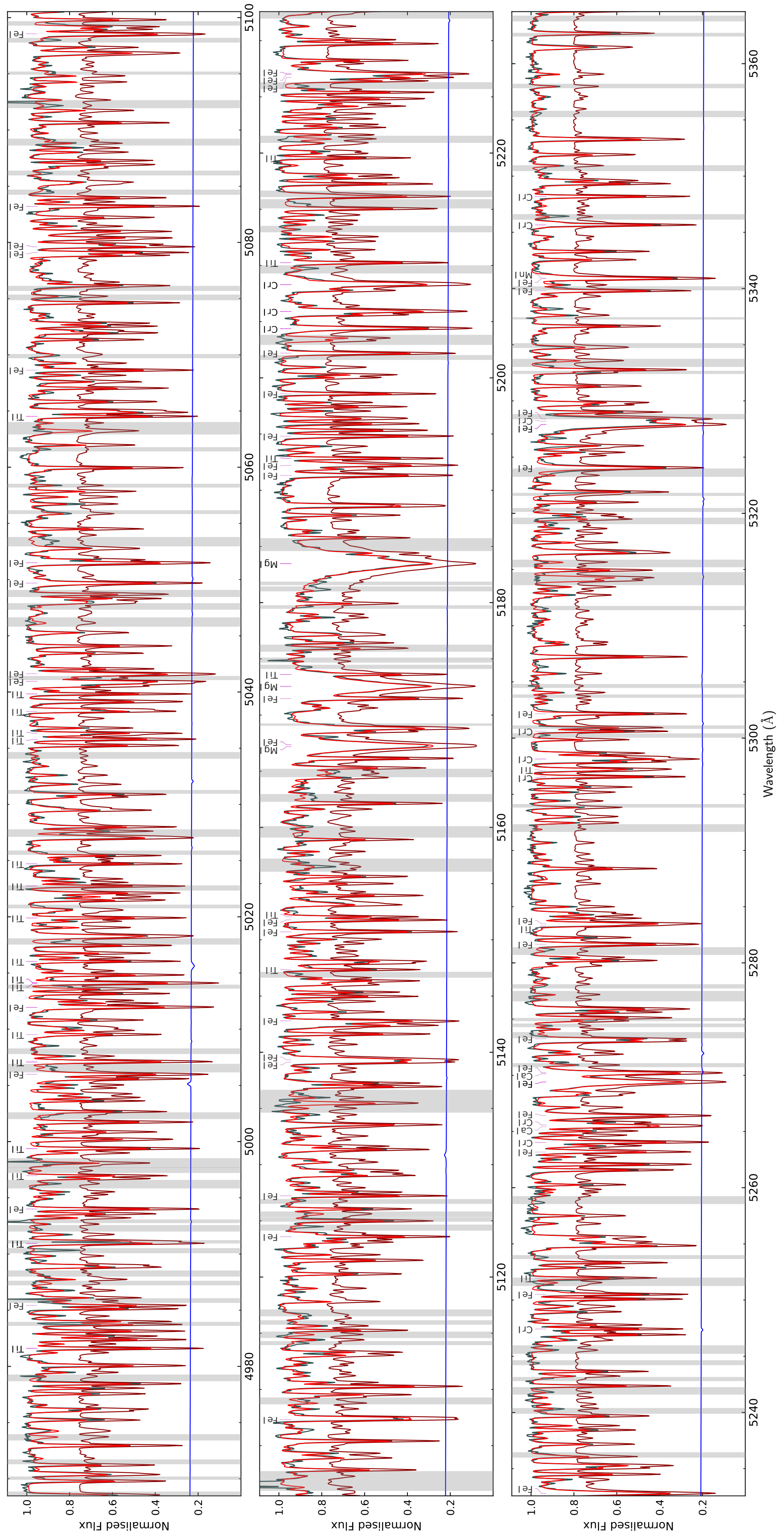

Figure B.4.1 (continued). The FEROS spectrum of BD −7° 5977 (grey) and the combined (red) and individual models.

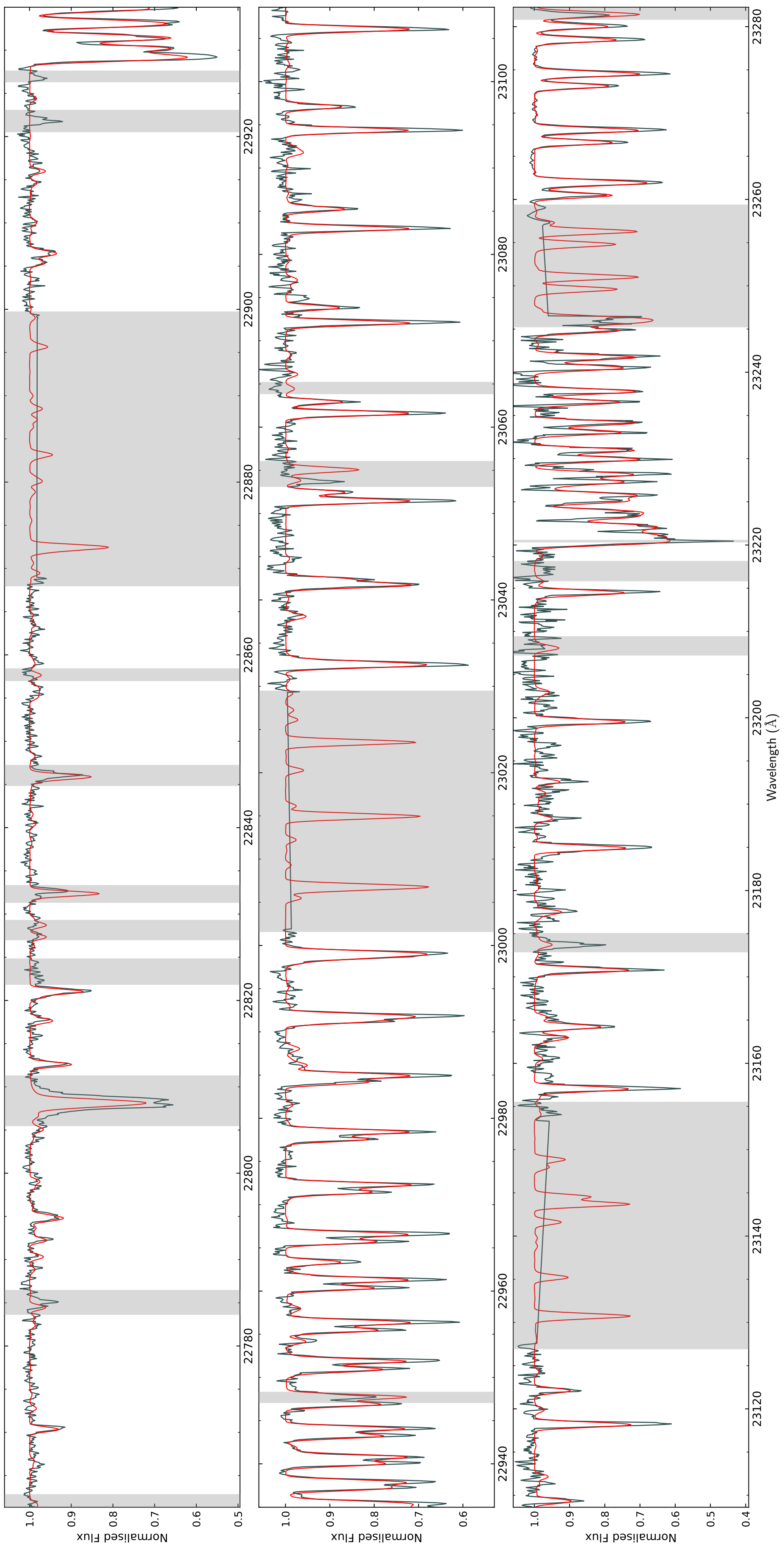

Figure B.4.2. The CRIRES spectrum of BD −7° 5977 (grey) and the combined (red) model.

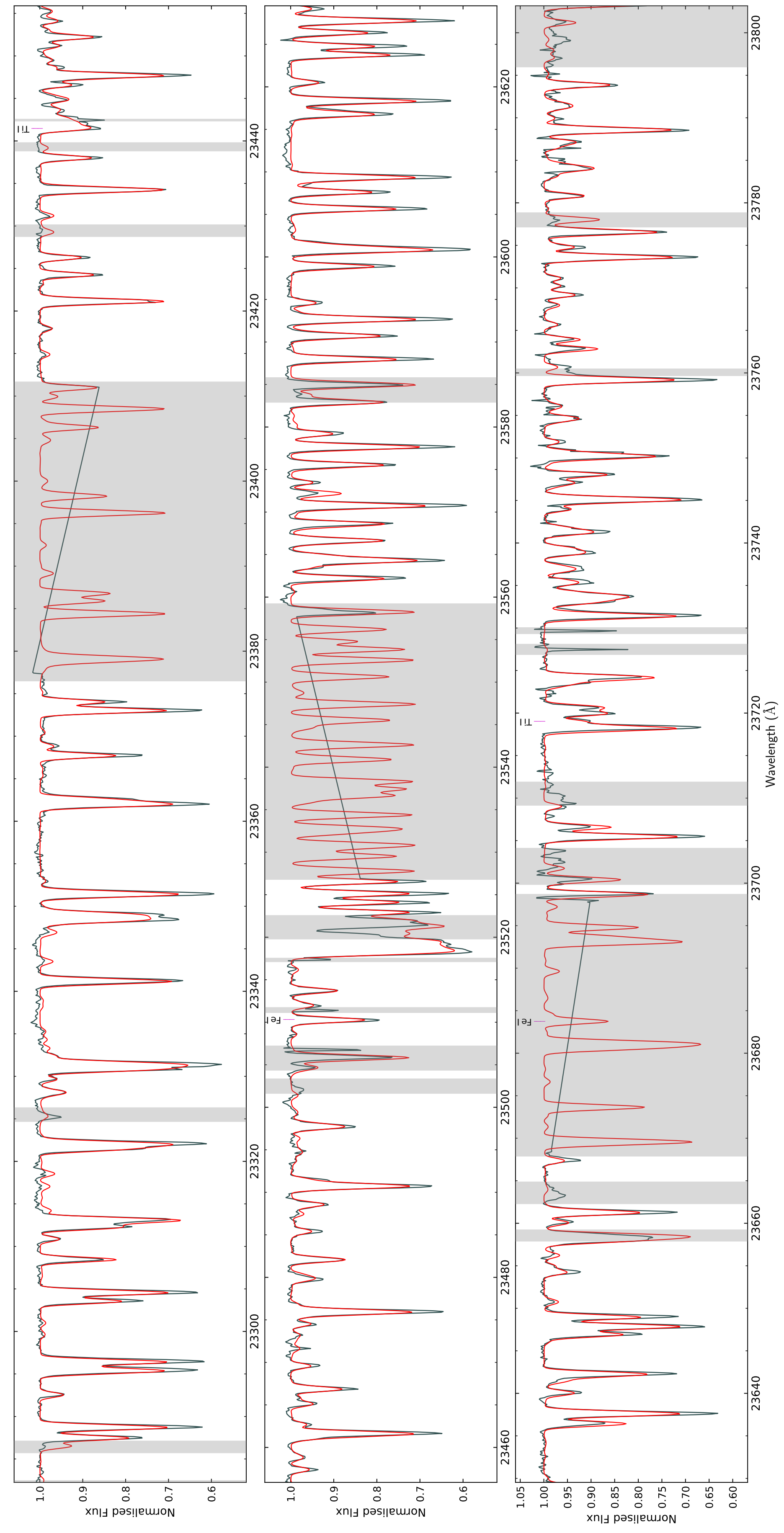

Figure B.4.2 (continued). The CRIRES spectrum of BD −7° 5977 (grey) and the combined (red) model.

B.5 For Sections 3.5 and 3.6

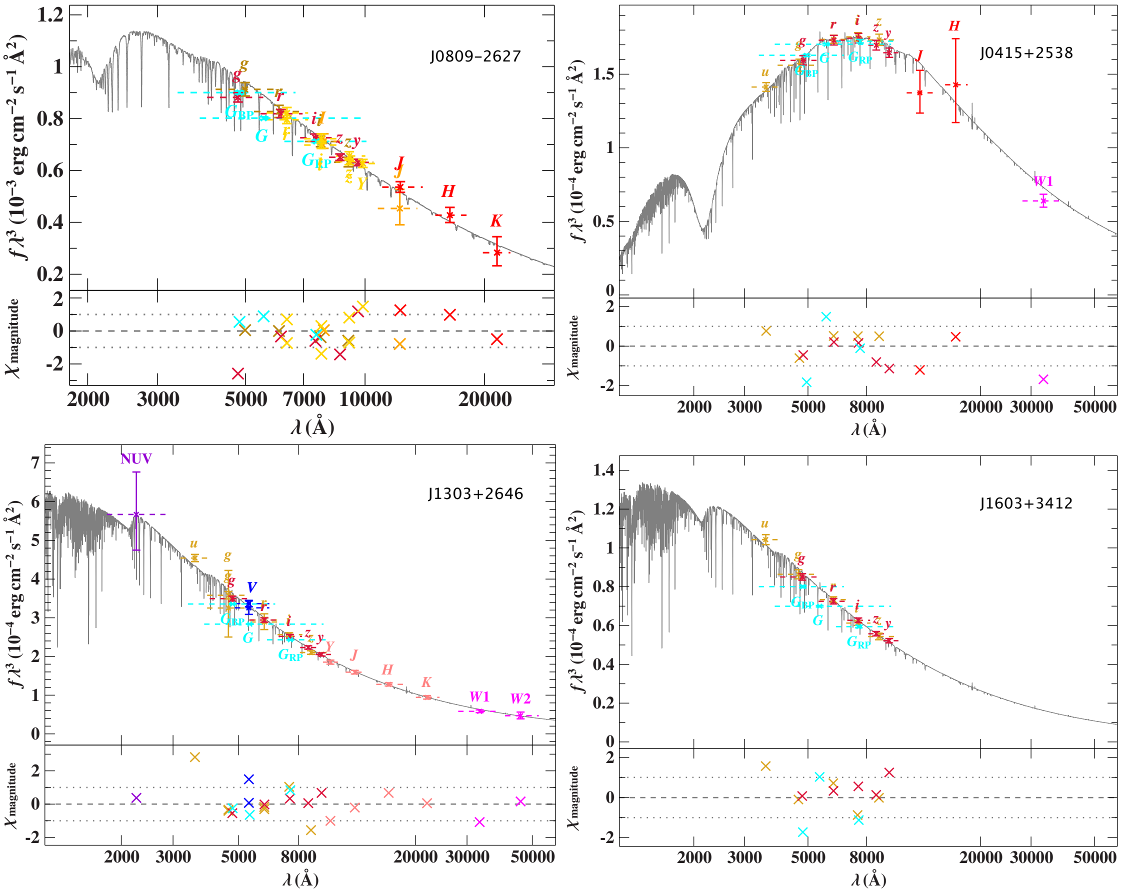

Figure B.5.1. SED fits for J0809-2627, J0415+2538, J1303+2646, and J1603+3412, where the grey line shows the final model. The following data were used: GALEX (purple, Bianchi et al. 2017), SkyMapper (dark gold, Onken et al. 2019), SDSS (ochre, Alam et al. 2015b; Henden et al. 2016), Johnson (blue, Kilkenny et al. 1988; Henden et al. 2016), Pan-STARRS (dark red, Magnier et al. 2020), *Gaia* EDR3 (cyan, Riello et al. 2021), DECam (gold, Schlafly et al. 2018; Drlica-Wagner et al. 2021), DENIS (orange, DENIS Consortium 2005), 2MASS (red, Skrutskie et al. 2006), UKIDSS (pink, Lawrence et al. 2013), and WISE (magenta, Schlafly et al. 2019). Adopted from Dorsch et al. (2022) and Pelisoli et al. (2022).

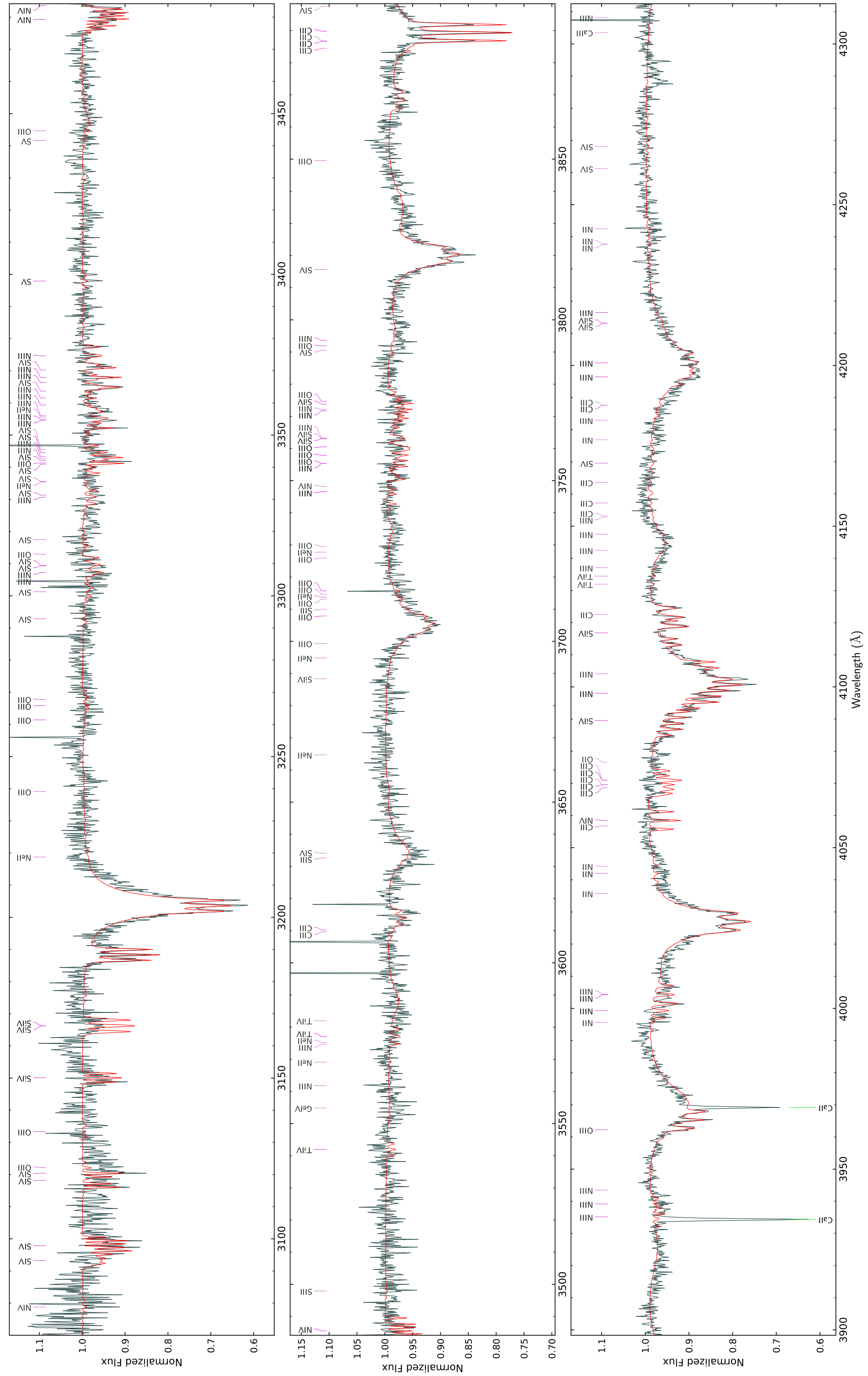

Figure B.5.2. X-shooter spectrum of J0809-2627 (grey) and the best-fit model (red). Adopted from Dorsch et al. (2022).

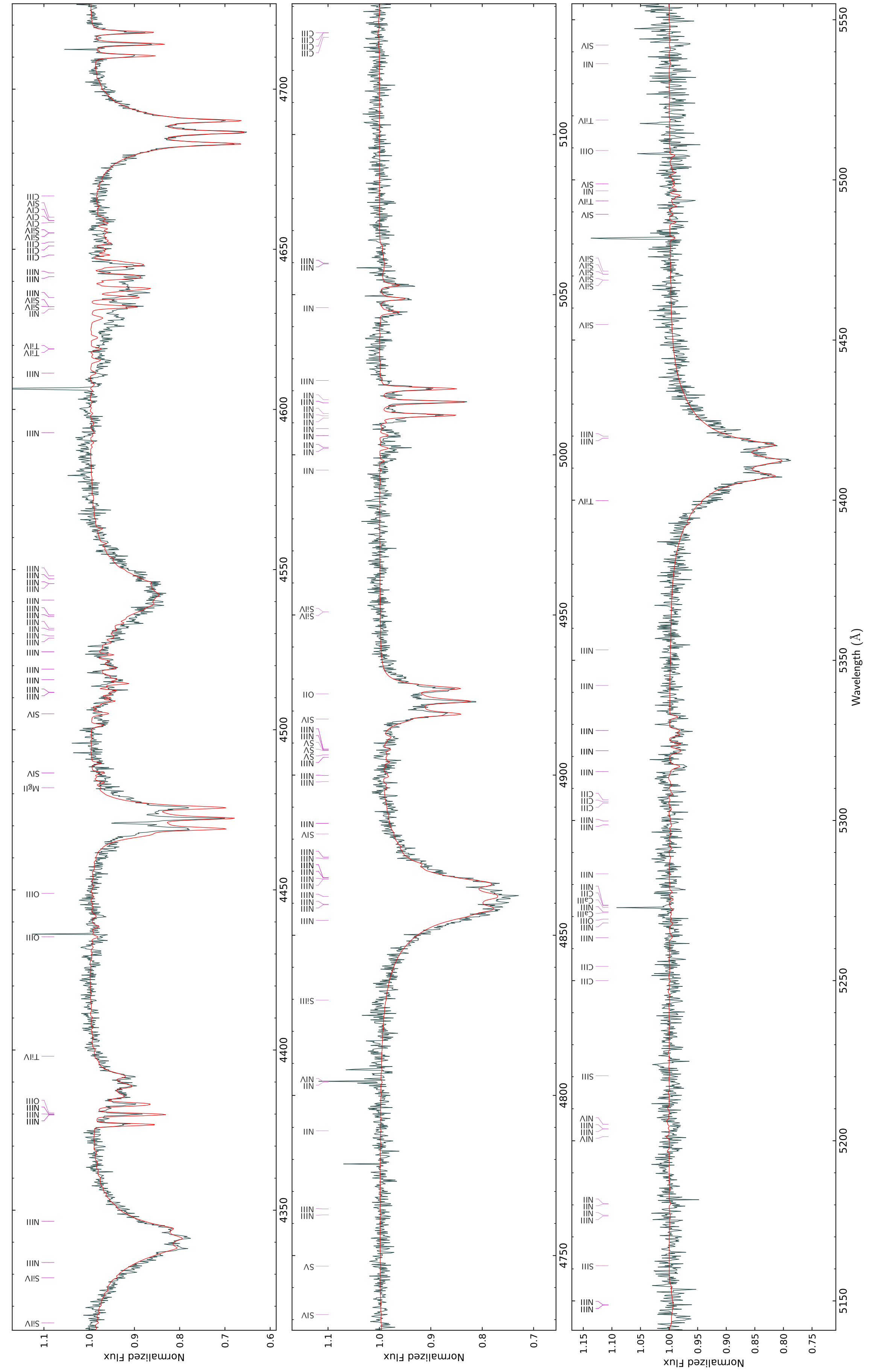

Figure B.5.2 (continued). X-shooter spectrum of J0809-2627 (grey) and the best-fit model (red). Adopted from Dorsch et al. (2022).

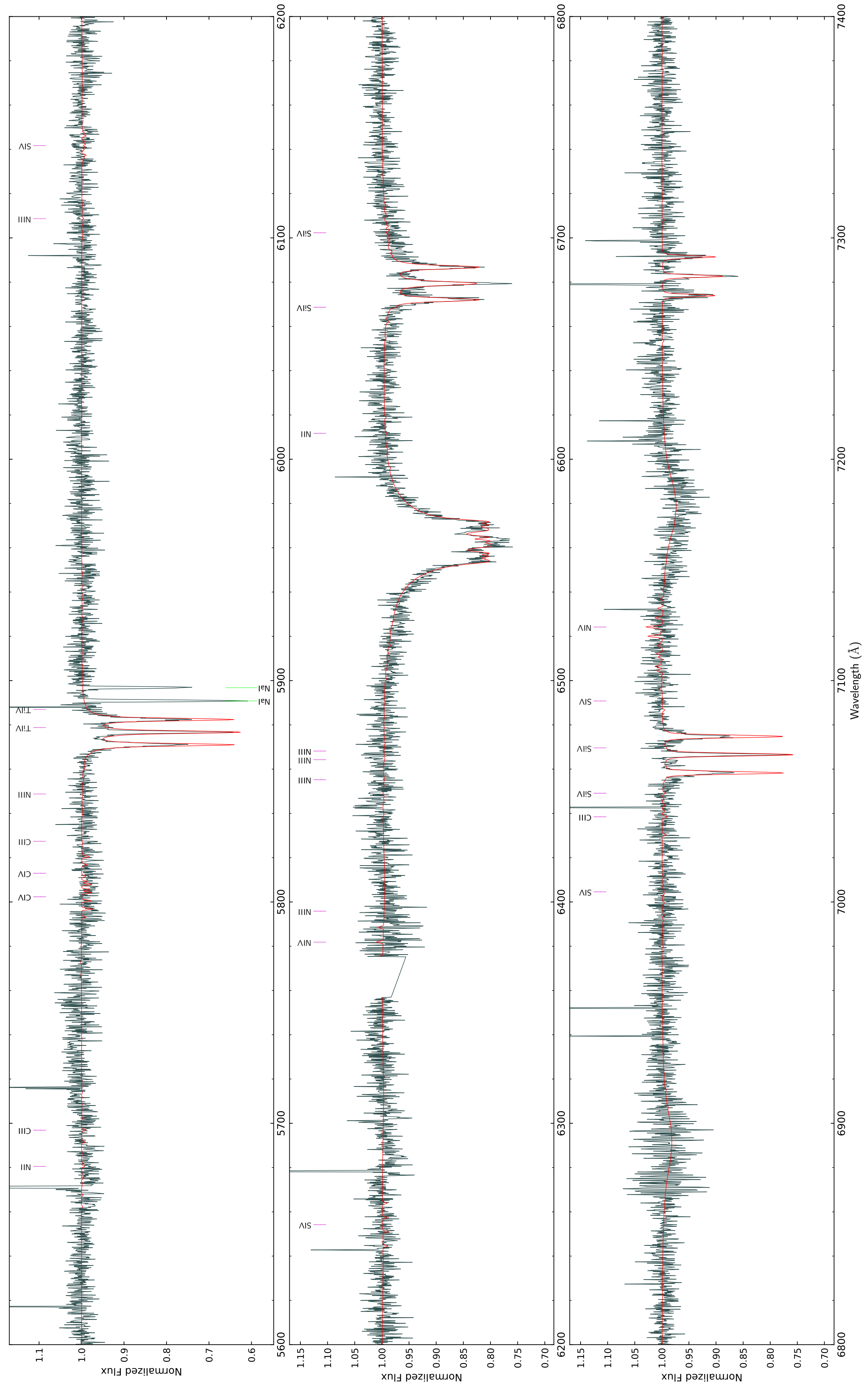

Figure B.5.2 (continued). X-shooter spectrum of J0809-2627 (grey) and the best-fit model (red). Adopted from Dorsch et al. (2022).

Table B.5.1. The magnetic fields of the individual components and their relative surface ratio for each of the three stars in our best-fit model to the individual WHT/ISIS spectra. The uncertainties for the surface ratios are one sigma statistical, whereas the uncertainties on the magnetic field strengths are estimated systematic uncertainties.

	J0415+2538	J1303+2646	J1603+3412
B_1 (kG)	270 ± 15	370 ± 20	292 ± 15
B_2 (kG)	430 ± 30	581 ± 20	390 ± 15
B_3 (kG)	–	439 ± 20	–
A_2/A_1	$0.260^{+0.014}_{-0.014}$	$0.70^{+0.13}_{-0.05}$	$0.81^{+0.16}_{-0.08}$
A_3/A_1	–	$0.56^{+0.23}_{-0.08}$	–

Table B.5.2 lists, to the best of our knowledge, all hot subdwarfs with determined atmospheric parameters that have upper limits or disputed claims of a magnetic field from spectropolarimetry. In addition, they all have spectra of similar quality or better than the stars discussed here, which would reveal Zeeman splitting for fields ~50 kG or more. Among the hot subdwarfs, the sdB HD 76431 has been studied by spectropolarimitry most extensively (Elkin 1998; Petit et al. 2012; Landstreet et al. 2012; Chountonov & Geier 2012), but no detection of a significant magnetic field was reported. Chountonov & Geier (2012) estimated the detection limit at 100 to 200 G. For other stars in Table B.5.2, no field could be reported at upper detection limits of 1 kG or better. For the four sdBs studied by Kawka et al. (2007) the limits turned out to be somewhat higher at several kG. The distribution of the stars listed in Table B.5.2 in the Kiel diagram is shown in Fig. 3.6.3. All subtypes are represented (sdB, sdOB, sdO, He-sdB, as well as both intermediate and extreme He-sdOs), though the majority are sdBs. Also some more luminous subdwarfs (e. g. LS IV-12 1, LSE 263, and LSE 153, marked with the prefix “l”) are included, which probably evolved from the AGB. HD 188112 is an underluminous sdB of too low mass for core helium burning, and Balloon 09010 0001 is a large amplitude pulsating V361 Hya star (Telting et al. 2008). The main types of binaries are also all represented: white dwarf or low-mass companion with short orbital period, main sequence or giant companions in long orbital period systems). Only seven stars lack sufficient $v_{\rm rad}$ measurements to allow conclusive remarks about binary status. An unconfirmed detection of a variable magnetic field was reported for BD+75 325 (see Sect. 3.6.3).

Table B.5.2. Hot subdwarfs with well-determined atmospheric parameters and upper limits on magnetic fields, typically of the order of a few kG. The $v_{\rm rad}$ variability is inferred from multi-epoch observations indicated in the notes. The orbital period is given in days when determined, and the entry "no" indicates no $v_{\rm rad}$ variations detected on long time scales (>months).

Name	Spectral class	$v_{\rm rad}$ variability	$T_{\rm eff}$	$\log g$	$\log n({\rm He})/n({\rm H})$	References	
						Atmospheric parameters	B limit
BD+75 325	iHe-sdO	no$^{\rm s17}$	52000 ± 2000	5.50 ± 0.20	+0.00	Lanz et al. (1997)	Elkin (1996, 1998)
HD 128220	lHe-sdO+GIII	871.78$^{\rm HH}$	40600 ± 400	4.5 ± 0.1	0.30 ± 0.05	Rauch (1993)	Elkin (1998)
BD+25 4655	eHe-sdO	no$^{\rm E}$	39500 ± 1000	5.8 ± 0.1	1.55 ± 0.15	Dorsch, priv. comm.	Elkin (1998)
Feige 87	sdB+G	936$^{\rm V}$	27270 ± 500	5.47 ± 0.15	$-2.56^{+0.22}_{-0.50}$	Vos et al. (2013)	Elkin (1998)
HD 76431	sdB	no$^{\rm R,Kh,CG}$	31180 ± 220	4.67 ± 0.03	−1.58 ± 0.05	Khalack et al. (2014)	Chountonov & Geier (2012)
GD 687	sdB+WD	0.37765$^{\rm G}$	24350 ± 360	5.32 ± 0.05	−2.38	Lisker et al. (2005)	Kawka et al. (2007)
GD 1669	sdB	no$^{\rm GH}$	34126 ± 360	5.77 ± 0.05	−1.36	Lisker et al. (2005)	Kawka et al. (2007)
GD 108	sdB+?	3.18095$^{\rm C}$	27760 ± 670	5.60 ± 0.11	< -3.0	Kawka et al. (2007)	Kawka et al. (2007)
WD 1153-484	sdB		30080 ± 660	5.15 ± 0.10	< -3.0	Kawka et al. (2007)	Kawka et al. (2007)
SB 290	sdB+K	uncertain$^{\rm G}$	26300 ± 100	5.31 ± 0.01	−2.52 ± 0.08	Geier (2013)	Landstreet et al. (2012)
HD 4539	sdB	no$^{\rm S,K,E}$	23200 ± 100	5.20 ± 0.01	−2.27 ± 0.24	Schneider et al. (2018)	Landstreet et al. (2012)
PHL 932	sdB	no$^{\rm K,E}$	33644 ± 500	5.74 ± 0.05	−1.64 ± 0.05	Lisker et al. (2005)	Landstreet et al. (2012)
PG 0133+114	sdB+WD	1.23787$^{\rm E}$	30073 ± 201	5.70 ± 0.04	−2.14 ± 0.04	Luo et al. (2021)	Landstreet et al. (2012)
SB 707	sdB+WD	5.85$^{\rm E}$	35400 ± 500	5.90 ± 0.05	−2.90 ± 0.10	O'Toole & Heber (2006)	Landstreet et al. (2012)
PG 0342+026	sdB	no$^{\rm E,S}$	26000 ± 1100	5.59 ± 0.12	−2.69 ± 0.10	Geier (2013)	Landstreet et al. (2012)
HD 127493	iHe-sdO	no$^{\rm E}$	42070 ± 180	5.61 ± 0.04	0.33 ± 0.06	Dorsch et al. (2019)	Landstreet et al. (2012)
HD 149382	sdB	no$^{\rm J}$	34200 ± 1000	5.89 ± 0.15	−1.60 ± 0.10	Saffer et al. (1994)	Landstreet et al. (2012)
HD 171858	sdB+WD	1.63280$^{\rm E}$	27200 ± 800	5.30 ± 0.10	−2.84 ± 0.1	Geier et al. (2010a)	Landstreet et al. (2012)
HD 188112	sdB+WD	0.6065812$^{\rm E}$	21500 ± 500	5.66 ± 0.06	−5.00	Heber et al. (2003)	Landstreet et al. (2012)
HD 205805	sdB	no$^{\rm E}$	25000 ± 500	5.00 ± 0.10	−2.00 ± 0.2	Przybilla et al. (2006)	Landstreet et al. (2012)
JL 87	iHe-sdB	no$^{\rm E}$	25800 ± 1000	4.80 ± 0.30	0.33	Ahmad et al. (2007)	Landstreet et al. (2012)
[CW 83] 0512-08	sdB	no$^{\rm E,S}$	38400 ± 1100	5.77 ± 0.12	−0.73 ± 0.10	Geier (2013)	Landstreet et al. (2012)
CPD-64 481	sdB+BD?	0.27726315$^{\rm Sch}$	27500 ± 500	5.60 ± 0.05	−2.50 ± 0.10	O'Toole & Heber (2006)	Landstreet et al. (2012)
CD-31 4800	eHe-sdO	no$^{\rm E}$	42230 ± 300	5.60 ± 0.1	2.61 ± 0.20	Schindewolf et al. (2018)	Landstreet et al. (2012)
PG 0909+276	sdOB	no$^{\rm E}$	35500 ± 500	6.09 ± 0.05	−1.00 ± 0.10	Geier (2013)	Landstreet et al. (2012)

LS IV-12 1	lsdO	no[E]	60000 ± 5000	4.50 ± 0.50	−0.95 ± 0.20	Heber & Hunger (1987)	Landstreet et al. (2012)
LSE 263	lHe-sdO	no[K]	70000 ± 2500	4.90 ± 0.25	>+1.0	Husfeld et al. (1989)	Landstreet et al. (2012)
LSE 153	lHe-sdO		70000 ± 1500	4.75 ± 0.15	>+1.0	Husfeld et al. (1989)	Landstreet et al. (2012)
BD+28 4211	sdO	no[L,H]	81300 ± 1200	6.52 ± 0.05	−1.12 ± 0.05	Latour et al. (2015)	Landstreet et al. (2012)
EC 11481-2303	sdO		55000 ± 5000	5.8 ± 0.3	−2.0 ± 0.3	Rauch et al. (2010)	Landstreet et al. (2012)
SB 410	sdB+WD	0.8227[E]	27600 ± 500	5.43 ± 0.05	−2.71 ± 0.10	Geier et al. (2010a)	Mathys et al. (2012)
SB 459	sdB		24900 ± 500	5.35 ± 0.10	−2.58 ± 0.10	Sahoo et al. (2020)	Mathys et al. (2012)
LB 1516	sdB+WD	10.3598[G2]	25200 ± 1100	5.41 ± 0.12	−2.78 ± 0.10	Geier (2013)	Mathys et al. (2012)
JL 194	sdB	no[E]	25770 ± 380	5.21 ± 0.06	−2.69 ± 0.06	Uzundag et al. (2021)	Mathys et al. (2012)
GD 1110	sdB+dM/BD	0.3131[Sch]	26500 ± 1100	5.38 ± 0.12	−2.54 ± 0.10	Geier (2013)	Mathys et al. (2012)
SB 815	sdB	no[K]	27200 ± 550	5.39 ± 0.10	−2.94 ± 0.01	Schneider et al. (2018)	Mathys et al. (2012)
Feige 66	sdB		33220 ± 370	6.14 ± 0.08	−1.61 ± 0.11	Lei et al. (2018)	Petit et al. (2012)
LS IV-14 116	iHe-sdO	no[JS,Ra]	35500 ± 1000	5.85 ± 0.10	−0.60 ± 0.10	Dorsch et al. (2020)	Randall et al. (2015)
Balloon 09010 0001	sdB	0.0041[T]	29446 ± 500	5.33 ± 0.1	−2.54 ± 0.2	Oreiro et al. (2004)	Savanov et al. (2013)
Feige 34	sdO		62550 ± 600	5.99 ± 0.03	−1.79 ± 0.04	Latour et al. (2018b)	Valyavin et al. (2006)

Notes. E = Edelmann et al. (2005) (variables published, non-variables: priv. com.), S17 =Schork (2017), S = Silvotti et al. (2020), J = Jacobs et al. (2011), K = Kawka et al. (2015), Kh = Khalack et al. (2014), R = Ramspeck et al. (2001), Ra = Randall et al. (2015), L = Latour et al. (2015), H = Herbig (1999), JS = Jeffery et al. (2015), R = Randall et al. (2015), C = Copperwheat et al. (2011), G = Geier et al. (2010b), GH = Geier & Heber (2012), T = Telting et al. (2008), HH=Howarth & Heber (1990), CG=Chountonov & Geier (2012), G2=Geier et al. (2014), Sch=Schaffenroth et al. (2014) V=Vos et al. (2013).

Acknowledgments

When I started to work on this project in late 2019, I was happy to be able to continue the research started in my MSc project and was exited to explore of the hot subdwarf population in more detail, and to broaden my understanding of astrophyics in general. Despite the unexpected COVID pandemic and the associated isolation, I thoroughly enjoyed freely working on my many projects. This is in large parts thanks to the extensive support of Uli Heber and Stephan Geier over several years.

For roughly the first two years of this project, I was working mainly from Bamberg and the Remeis observatory. During this time, Andreas Irrgang and Uli were always happy to answer my many questions; most of what I know I learned from our discussions. I also had a great time (not only) working with my Bamberg colleagues David Schneider and Steven Hämmerich, as well as all other members of the Remeis observatory. Thanks also to our admins Ingo Kreykenbohm and Philipp Weber for enabling me to extensively use the Remeis computer cluster.

My positive experiences continued throughout the second part of this thesis, which I spent in Potsdam in the working group of Stephan Geier. My Potsdam colleagues Veronika Schaffenroth, Nicole Reindl, Max Pritzkuleit, Harry Dawson, and Aakash Bhat made my time there very enjoyable. Thanks to Andrea Brockhaus for surely steering me through the shallow waters of Potsdam bureaucracy. Thanks also to Stephan your many interesting ideas, and for allowing me to work on this thesis when I really had a lot of other things to do. I had a great time observing at the INT and going to the sdOB10 conference in Liège, the 4MOST conferences in Potsdam and Brighton, the EUROWD22 conference in Tübingen, as well as the atomic data conference in Heidelberg.

Beyond Potsdam and Bamberg, I would also like to thank Marilyn Latour for our continued discussions and collaborations, which now span more than six years. Simon Jeffery also had a large influence on my work through our extensive collaborations, for example in our two papers on heavy metal stars, and well beyond. Ingrid Pelisoli was also always up for collaboration, for example in our paper about magnetic He-sdOs. Klaus Werner and Nicole Reindl allowed me to gain some insight into hot white dwarfs, which I found very interesting. I also enjoyed working on cooler sdBs with Thomas Kupfer and his students, and on F-type stars with Daniel Sebastian, even if this work was not related to this thesis. Finally, a big thank you to my parents for your generous support throughout all of my studies, even though they took a good ten years!

Based on observations collected at the European Southern Observatory under ESO programmes 087.D-0950(A), 088.D-0364(A), 088.C-0707(B), 089.D-0875(A), 095.D-0733(A), 0104.D-0206(A), 105.206H.001, and 108.225R.001. Based on observations obtained with the Southern African Large Telescope (SALT) under programmes 2017-1-SCI-004, 2018-2-SCI-033, and 2019-1-MLT-003. Based on observations with the Isaac Newton Telescope (under programme ID ING.NL.19B.005) operated on the island of La Palma by the Isaac Newton Group of Telescopes in the Spanish Observatorio del Roque de los Muchachos of the Instituto de Astrofísica de Canarias. Based on observations made with the NASA/ESA Hubble Space Telescope, obtained from the data archive (prop. ID 7349) at the Space Telescope Science Institute. STScI is operated by the Association of Universities for Research in Astronomy, Inc. under NASA contract NAS 5-26555. Support for MAST for non-HST data is provided by the NASA Office of Space Science via grant NNX09AF08G and by other grants and contracts. Based on FUSE data under Proposal IDs P114, I819, P205, and U106. Based on INES data from the IUE satellite. This work has made use of data from the European Space Agency (ESA) mission *Gaia* (`https://www.cosmos.esa.int/gaia`), processed by the *Gaia* Data Processing and Analysis Consortium (DPAC, `https://www.cosmos.esa.int/web/gaia/dpac/consortium`). Funding for the DPAC has been provided by national institutions, in particular the institutions participating in the *Gaia* Multilateral Agreement. The TOSS service (`http://dc.g-vo.org/TOSS`) used for this work was constructed as part of the activities of the German Astrophysical Virtual Observatory. We acknowledge the use of the Atomic Line List (`http://www.pa.uky.edu/~peter/newpage/`). This research made use of the lmfit python package developed by Newville et al. (2014). This research has made use of NASA's Astrophysics Data System.